

Superplastic forming of advanced metallic materials

Related titles:

Nanostructured metals and alloys

(ISBN 978-1-84569-670-2)

Nanostructured metals and alloys have enhanced tensile strength, fatigue strength and ductility and are suitable for use in applications where strength or strength-to-weight ratios are important. Part I of this important book reviews processing techniques for bulk nanostructured metals and alloys. Parts II and III discuss microstructure and mechanical properties, whilst Part IV outlines applications of this new class of material.

Tailor welded blanks for advanced manufacturing

(ISBN 978-1-84569-704-4)

Tailor welded blanks are sheets made from different strengths and thicknesses of steel pre-welded together before pressing and shaping into the final component. They produce high-quality components with the right grade and thickness of steel where they are most needed, providing significant savings in weight and processing costs in such industries as automotive engineering. Part I of this book reviews processing issues such as product design, production methods, weld integrity and deformation. Part II discusses applications in such areas as automotive and aerospace engineering.

Fundamentals of aluminium metallurgy

(ISBN 978-1-84569-654-2)

This book provides a comprehensive overview of the production, properties and processing of aluminium and its applications in manufacturing industries. Part I discusses different methods of producing and casting aluminium. Part II reviews metallurgical properties whilst Part III covers processing and applications in such areas as aerospace engineering.

Details of these books and a complete list of Woodhead's titles can be obtained by:

- visiting our web site at www.woodheadpublishing.com
- contacting Customer Services (e-mail: sales@woodheadpublishing.com; fax: +44 (0) 1223 832819; tel.: +44 (0) 1223 499140 ext. 130; address: Woodhead Publishing Limited, 80 High Street, Sawston, Cambridge CB22 3HJ, UK

If you would like to receive information on forthcoming titles, please send your address details to: Francis Dodds (address, tel. and fax as above; e-mail: francis.dodds@woodheadpublishing.com). Please confirm which subject areas you are interested in.

Superplastic forming of advanced metallic materials

Methods and applications

Edited by
Gillo Giuliano



Oxford Cambridge Philadelphia New Delhi

Published by Woodhead Publishing Limited,
80 High Street, Sawston, Cambridge CB22 3HJ, UK
www.woodheadpublishing.com

Woodhead Publishing, 1518 Walnut Street, Suite 1100, Philadelphia, PA 19102-3406, USA

Woodhead Publishing India Private Limited, G-2, Vardaan House, 7/28 Ansari Road,
Daryaganj, New Delhi – 110002, India
www.woodheadpublishingindia.com

First published 2011, Woodhead Publishing Limited
© Woodhead Publishing Limited, 2011
The authors have asserted their moral rights.

This book contains information obtained from authentic and highly regarded sources. Reprinted material is quoted with permission, and sources are indicated. Reasonable efforts have been made to publish reliable data and information, but the authors and the publisher cannot assume responsibility for the validity of all materials. Neither the authors nor the publisher, nor anyone else associated with this publication, shall be liable for any loss, damage or liability directly or indirectly caused or alleged to be caused by this book.

Neither this book nor any part may be reproduced or transmitted in any form or by any means, electronic or mechanical, including photocopying, microfilming and recording, or by any information storage or retrieval system, without permission in writing from Woodhead Publishing Limited.

The consent of Woodhead Publishing Limited does not extend to copying for general distribution, for promotion, for creating new works, or for resale. Specific permission must be obtained in writing from Woodhead Publishing Limited for such copying.

Trademark notice: Product or corporate names may be trademarks or registered trademarks, and are used only for identification and explanation, without intent to infringe.

British Library Cataloguing in Publication Data
A catalogue record for this book is available from the British Library.

Library of Congress Control Number: 2011929804

ISBN 978-1-84569-753-2 (print)
ISBN 978-0-85709-277-9 (online)

The publisher's policy is to use permanent paper from mills that operate a sustainable forestry policy, and which has been manufactured from pulp which is processed using acid-free and elemental chlorine-free practices. Furthermore, the publisher ensures that the text paper and cover board used have met acceptable environmental accreditation standards.

Typeset by RefineCatch Ltd, Bungay, Suffolk
Printed by TJI Digital, Padstow, Cornwall, UK

Contents

<i>Contributor contact details</i>	<i>xi</i>
<i>Preface</i>	<i>xiii</i>
Part I Superplastic forming methods	1
1 Metals for superplastic forming	3
N. RIDLEY, University of Manchester, UK	
1.1 Introduction	3
1.2 Historical aspects of superplasticity	4
1.3 Types of superplastic materials	7
1.4 Grain refinement	9
1.5 Processing of commercially significant alloys to develop superplastic microstructures	11
1.6 High strain rate superplasticity	16
1.7 Grain refinement by severe plastic deformation	17
1.8 Mechanisms of superplasticity	20
1.9 Sources of further information and advice	30
1.10 Acknowledgements	31
1.11 References	31
2 Standards for superplastic forming of metals	34
F. ABU-FARHA, Penn State Erie, USA and R. CURTIS, King's College London, UK	
2.1 Introduction	34
2.2 Need for standards	35
2.3 Existing standards	36
2.4 Issues with existing standards	37
2.5 Towards improved standards	41
2.6 References	46

vi	Contents	
3	Processes and equipment for superplastic forming of metals	49
	G. BERNHART, P. LOURS, T. CUTARD, V. VELAY, Ecole des Mines Albi, France and F. NAZARET, Aurock, France	
3.1	Introduction	49
3.2	Superplastic forming processes	50
3.3	Forming equipment	54
3.4	Forming dies	59
3.5	Conclusion	70
3.6	References	70
4	High-temperature lubricants for superplastic forming of metals	72
	P. A. FRIEDMAN and S. G. LUCKEY, Ford Research and Advanced Engineering, Michigan, USA	
4.1	Introduction	72
4.2	Lubrication mechanisms	73
4.3	SPF lubricants	74
4.4	Influence of friction and lubricant on forming	76
4.5	Testing and evaluation of lubricants	78
4.6	Production issues	78
4.7	Conclusions	80
4.8	References	81
5	The use of laser surface modification in combined superplastic forming and diffusion bonding of metals	83
	G. Q. WU and G. X. LUO, Beihang University (BUAA), China	
5.1	Introduction	83
5.2	Effect of laser surface modification on alloy surface	84
5.3	Diffusion bonding of laser surface modified alloys	91
5.4	Simulation of the bonding process	99
5.5	Conclusion	109
5.6	References	109
5.7	Appendix: List of symbols	111
Part II	Modelling of superplastic forming	113
6	Mathematical modelling of superplastic metal sheet forming processes	115
	G. GIULIANO, University of Cassino, Italy	
6.1	Introduction	115
6.2	Membrane theory	116
6.3	Flow rule	118

6.4	Analysis of superplastic free forming processes	119
6.5	Material constants from bulging tests	127
6.6	References	134
7	Finite element modelling of thin metal sheet forming J. BONET and A. J. GIL, Swansea University, UK	136
7.1	Introduction	136
7.2	Continuum model	137
7.3	Finite element formulation and time integration schemes	140
7.4	The incremental flow formulation	141
7.5	Pressure cycle algorithms	144
7.6	Die representation and contact algorithms	145
7.7	Commercial codes	145
7.8	Applications	146
7.9	Future trends and recommendations for further research	151
7.10	References	151
8	Constitutive equations for modelling superplastic forming of metals J. LIN and T. ZHU, Imperial College London, UK and L. ZHAN, Central South University, P. R. China	154
8.1	Introduction	154
8.2	Constitutive equations for superplastic alloys	154
8.3	Determination of constitutive equations from experimental data	160
8.4	Case study: simulation of superplastic forming	174
8.5	Conclusions	181
8.6	References	181
9	Predicting instability in superplastic forming of metals S. B. LEEN, NUI Galway, Ireland	184
9.1	Introduction	184
9.2	Theoretical considerations	185
9.3	Forming analyses and experiments	202
9.4	Results and discussion	209
9.5	Conclusions and future trends	220
9.6	References	222
Part III Applications of superplastic forming		225
10	Superplastic forming and diffusion bonding of titanium alloys M. JACKSON, University of Sheffield, UK	227
10.1	Introduction	227

viii	Contents	
10.2	Titanium alloys	228
10.3	The superplastic forming/diffusion bonding process	235
10.4	Applications	241
10.5	Sources of further information and advice	245
10.6	Acknowledgements	245
10.7	References	245
11	Superplastic forming of aluminium alloys R. GRIMES, University of Warwick, UK	247
11.1	Introduction	247
11.2	History	248
11.3	Superplastic aluminium alloys	249
11.4	Cavitation in superplastic aluminium alloys	258
11.5	High strain rate superplasticity	262
11.6	Exploitation of superplastic aluminium alloys	264
11.7	References	269
12	Quick Plastic Forming of aluminium alloys P. E. KRAJEWSKI and J. G. SCHROTH, General Motors, USA	272
12.1	Introduction	272
12.2	QPF process overview	273
12.3	Hot forming systems: prior deficiencies and new concepts	275
12.4	Integrally heated tool system	277
12.5	Tool heating system	282
12.6	Temperature distribution in a deck-lid inner panel tool	285
12.7	Ancillary benefits of integrally heated tools	286
12.8	Production validation experience	288
12.9	Material development	288
12.10	Lubrication	300
12.11	Conclusions	302
12.12	References	302
13	Superplastic forming of magnesium alloys R. GRIMES, University of Warwick, UK	304
13.1	Introduction	304
13.2	History	305
13.3	Properties of magnesium	306
13.4	Superplasticity in magnesium alloys	309
13.5	Manufacture of superplastic magnesium alloy sheet	313
13.6	Superplastic forming of magnesium components	320
13.7	References	323

14	Superplastic micro-tubes fabricated by dieless drawing processes	327
	T. FURUSHIMA and K. MANABE, Tokyo Metropolitan University, Japan	
14.1	Introduction	327
14.2	Industrial application of micro-tubes	328
14.3	Fundamentals of dieless drawing processes	329
14.4	Superplastic dieless drawing processes	336
14.5	FE simulation of superplastic dieless drawing processes	342
14.6	Grain refinement process of metal tubes for superplastic dieless drawing process	349
14.7	Other applications	355
14.8	Conclusion	357
14.9	References	358
	<i>Index</i>	361

Contributor contact details

(* = main contact)

Editor and Chapter 6

G. Giuliano
University of Cassino
DiMSAT
via DiBiasio, 43
03043 Cassino (FR)
Italy
E-mail: giuliano@unicas.it

Chapter 1

N. Ridley
School of Materials
University of Manchester
Grosvenor Street
Manchester
M1 7HS
UK
E-mail: norman.ridley@manchester.ac.uk

Chapter 2

F. Abu-Farha*
Mechanical Engineering
Penn State Erie
5101 Jordan Road
246 REDC Building
Erie
PA 16563
USA
E-mail: fka10@psu.edu

R. Curtis
King's College Dental Institute
King's College London
Floor 17, Guy's Tower
London
SE1 9RT
UK
E-mail: richard.curtis@kcl.ac.uk

Chapter 3

G. Bernhart, P. Lours, T. Cutard
and V. Velay
Institut Clément Ader EA814
Ecole des Mines d'Albi
Campus Jarlard
81013 ALBI
Cedex 09
France
E-mail: gerard.bernhart@mines-albi.fr

F. Nazaret
Aurock
Pépinière Albisia
81000 Albi
France

Chapter 4

P. A. Friedman* and S. G. Luckey
Ford Research and Advanced Engineering
2101 Village Road
MD 3135
Dearborn
MI 48121
USA
E-mail: pfriedma@ford.com

Chapter 5

G. Q. Wu* and G. X. Luo
Beihang University (BUAA)
China
E-mail: guoqingwu@buaa.edu.cn

Chapter 7

J. Bonet* and A. J. Gil
School of Engineering
Swansea University
UK
E-mail: J.Bonet@swansea.ac.uk

Chapter 8

J. Lin* and T. Zhu
Department of Mechanical Engineering
Imperial College London
Exhibition Road
South Kensington
London SW7 2AZ
UK
E-mail: Jianguo.Lin@imperial.ac.uk

L. Zhan
Institute of Metallurgical Machinery
School of Mechanical &
Electrical Engineering
Central South University Changsha
Hunan, 410083
P. R. China

Chapter 9

S. B. Leen
Mechanical and Biomedical Engineering
College of Engineering and Informatics
National University of Ireland Galway
Nun's Island
Galway
Ireland
E-mail: sean.leen@nuigalway.ie

Chapter 10

M. Jackson
Department of Materials Science and
Engineering
University of Sheffield
Sir Robert Hadfield Building
Mappin Street
Sheffield
S1 3JD
UK
E-mail: martin.jackson@sheffield.ac.uk

Chapters 11 and 13

R. Grimes
Warwick Manufacturing Group
University of Warwick
Coventry
CV4 7AL
UK
E-mail: roger.grimes@warwick.ac.uk

Chapter 12

P. E. Krajewski* and J. G. Schroth
General Motors Company
Research and Development Center
30500 Mound Road
Warren MI48090
USA
E-mail: paul.e.krajewski@gm.com

Chapter 14

T. Furushima and K. Manabe*
Department of Mechanical Engineering
Graduate School of Science and
Engineering
Tokyo Metropolitan University
1-1 Minamiosawa Hachioji
Tokyo 192-0397
Japan
E-mail: furushima-tsuyoshi@tmu.ac.jp;
manabe@tmu.ac.jp

Some metals, characterized by a fine and stable grain size when deformed under specific conditions of temperature and strain-rate, show an exceptional ductility known as superplasticity.

In superplastic sheet forming, those conditions are associated with uniform strains and very low flow stresses, which simplify the die's design, obtained through gas pressure

The elevated ductility of superplastic metals is useful for manufacturing products of complex forms in one operation, thereby eliminating unnecessary joints and rivets. Other benefits of superplastic forming include the reduction of residual stresses, the absence of springback, and the ability to form near net-shape parts that reduces machining costs and material waste. Because superplastic metals are light materials, superplastic forming helps to reduce the weight and the cost of the parts that they may replace. Therefore, superplastic metals can be of interest to the aerospace and transport industries, and in the fields of architecture, medicine and communications.

Relevant scientific activity has been intensely documented, and various specific conferences were promoted in order to include all the aspects of this technique: behaviour of the materials, tribology, tool design, modelling, etc.

This book aims to provide a neat and modernized synthesis of the various aspects of superplastic sheet metal forming. It is subdivided into three parts: methods, modelling and applications. In Part I, we introduce the types of metals and the mechanisms of superplasticity; the treatments that are used for refining the grain size; the equipment and procedures used for the characterization test; the types of lubrication; and the processes and equipment used for superplastic forming and for joining similar and dissimilar high-temperature metal materials.

Part II discusses the benefits and the limits of the mathematical and numerical modelling of the superplastic forming processes. Accurate constitutive equations and models for predicting instability are given in order to show the behaviour of the materials during the superplastic forming process. Finally, in Part III, the main superplastic metals of industrial interest are discussed, and some applications of superplastic forming are illustrated.

The aim of this book is to make available to engineers, researchers and students a useful means of consultation for their various roles. I thank all of the authors for their precious contributions, and all the members of the publishing team for their professionalism and patience.

Gillo Giuliano
University of Cassino, Italy

N. RIDLEY, University of Manchester, UK

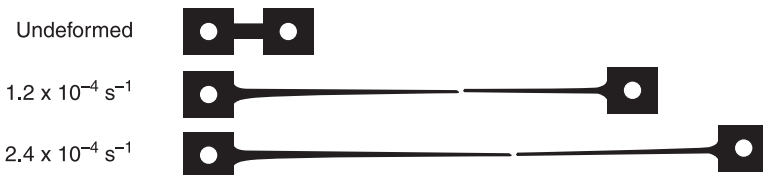
Abstract: This chapter deals with the requirements for superplastic behaviour and its characteristics, and outlines its potential as the basis of a commercially important shaping process. Historical aspects of the subject are dealt with. The different types of superplastic metallic materials are outlined, general methods for producing fine grain structures are considered, and specific methods for developing fine grain microstructures in commercially significant alloys are described. Observations of high strain rate superplasticity are reported and several procedures for producing ultrafine grain sizes using severe plastic deformation procedures are described. The final section deals with mechanisms of superplastic flow.

Key words: strain rate sensitivity of flow stress (m value), superplastic alloys, grain refinement, severe plastic deformation, mechanisms of superplastic flow.

1.1 Introduction

Superplastic (SP) materials are polycrystalline solids which have the ability to undergo exceptionally large tensile strains prior to failure, when they are deformed under a limited range of conditions (Fig. 1.1). In uniaxial tension, elongations in excess of $\sim 200\%$ are usually indicative of superplasticity, although Langdon¹ has proposed that this figure should be nearer 400% . However, it should be noted that elongation is influenced by specimen geometry and that the occurrence of cavitation during SP flow may lead to premature failure. Nevertheless, numerous metallic materials can show elongations of $500\text{--}1000\%$ or more, while Higashi² has reported an elongation of $\sim 8000\%$ for an aluminium bronze. Tensile strains typical of superplasticity are shown in Fig. 1.1.

This behaviour is related to the observation that the flow stress of a SP material is very sensitive to the rate of deformation. A characteristic equation which is



1.1 SP titanium alloy (IMI550) showing high elongations.

often used to describe SP deformation, at least over a limited range of strain rates, can be written:

$$\sigma = k\dot{\epsilon}^m \quad [1.1]$$

where σ is the flow stress, k is a constant, $\dot{\epsilon}$ is strain rate and m is the strain rate sensitivity of flow stress. A material is normally considered to be SP when it has an m value ≥ 0.3 although for many metallic materials m is in the range 0.4–0.8. During tensile deformation necks, which tend to form, lead to a local rise in strain rate, and to a sharp increase in the flow stress required to sustain plastic flow, i.e. strain rate hardening occurs within the necked region. Hence, high m confers a resistance to neck propagation and results in the high tensile strains characteristic of SP materials.

Superplasticity is a characteristic of materials which can be processed to develop a fine stable grain size, usually between 5–15 μm , when they are deformed at relatively slow strain rates normally in the range 10^{-4} s^{-1} – 10^{-2} s^{-1} , at temperatures $\geq 0.5 T_m$, where T_m is the melting point in degrees Kelvin. These deformation conditions are associated with low flow stresses, generally $< 10 \text{ MPa}$ and this, combined with the relatively high uniformity of plastic flow, has led to increasing commercial interest in superplastic forming (SPF).

SPF is a process whereby metallic materials in fine grained sheet form are gas pressure bulged into dies at elevated temperatures to give commercially useful products, often complex in shape, with high added value. These find a wide range of applications in aerospace, road and rail transport, architecture, and in the medical and communication fields. However, as the high value of m required to minimise differential thinning during forming is achieved at relatively slow strain rates, SPF is a slow process compared with conventional forming procedures.

Advantages of SPF are that it is a net shape forming process, it can lead to considerable savings in costs when a complex component which is normally built up of several parts can be formed as a single part, multiple parts can be produced in one operation, there is little spring back, and only one major tool is required. However, while a vast number of metallic materials have been shown to exhibit SP behaviour, most commercial SPF is concerned primarily with a relatively small number of Al and Ti alloys, although there is a developing interest in Mg alloys. There is also some commercial activity in the SPF of microduplex (α/γ) stainless steels, Ni-based alloys (e.g. IN738) and Zn–Al eutectoid.

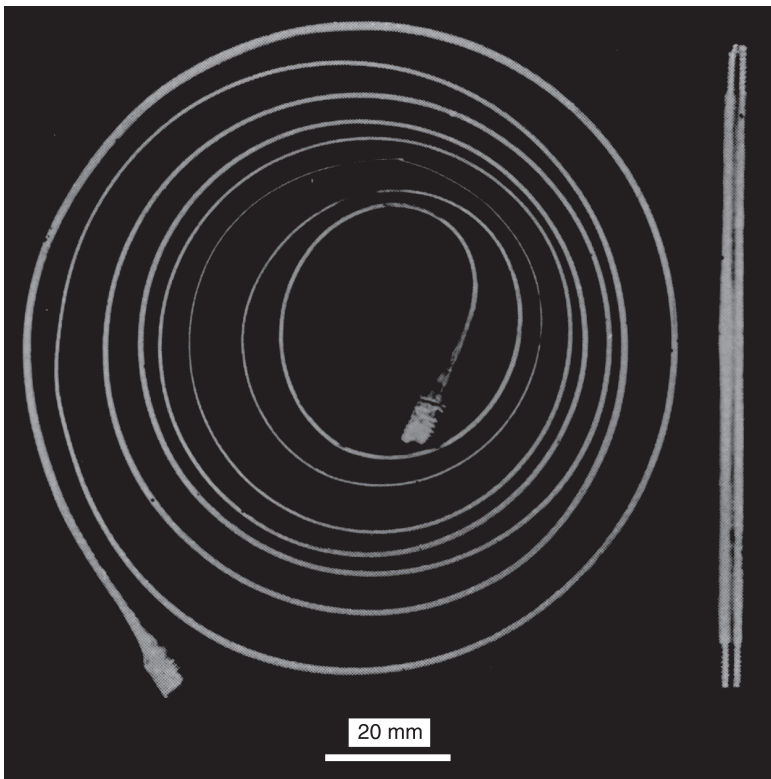
1.2 Historical aspects of superplasticity

The first recorded laboratory observation of what was almost certainly SP deformation was published in 1912 by Bengough³ who obtained an unusually high tensile elongation of 163% in 'complex' brass deformed at 700°C. There were further reports of SP behaviour in the early part of the twentieth century

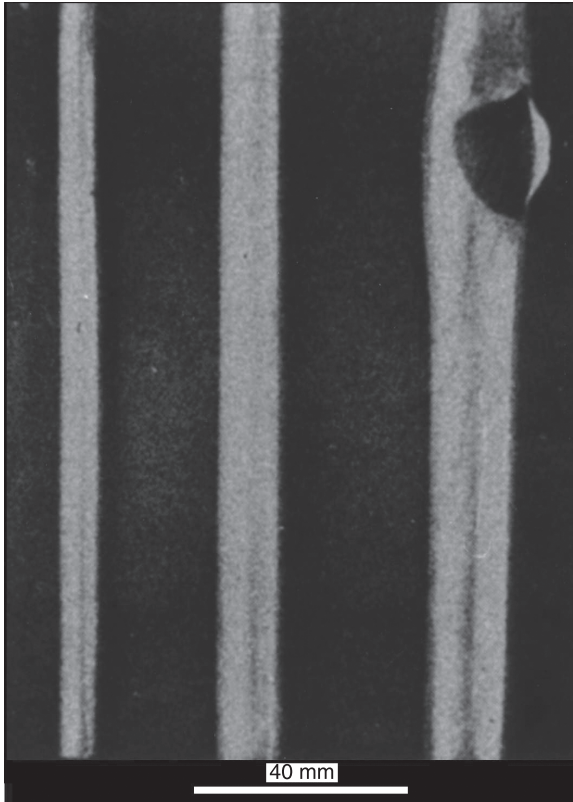
including the work of Jenkins⁴ in 1928 who achieved elongations of 350–400% in mechanically worked Cd–Zn and Pb–Sn eutectics.

However, the most spectacular of the earlier observations was seen in the work of Pearson in 1934.⁵ He recorded an elongation of 1950% during room temperature deformation of a screw threaded, extruded rod, tensile specimen of Bi–Sn eutectic. As the initial specimen was ~4 inches (100 mm) in length and was stretched to almost 2 metres, it had to be coiled up before the photograph shown in Fig.1.2 could be recorded. Further elongations of up to 1500% were obtained for extruded Pb–Sn eutectic alloy. Pearson also pressurised a tubular specimen of Pb–Sn eutectic and increased its internal volume by a factor of 9.1 prior to failure (Fig. 1.3). Although Pearson had unknowingly demonstrated the potential of SPF, he was not distracted from his main research interest which was the extrusion of metals. A short biography of Pearson and his 1934 observations has been given by Ridley.⁶

Following these earlier observations, there was no further interest in the phenomenon in the Western World for more than 25 years. However, work was carried out in Russia by Bochvar⁷ and co-workers during and after the Second World War with a number of publications on Zn–Al alloys, the first appearing in



1.2 Extruded Bi–Sn eutectic stretched to elongation of 1950%.⁵



1.3 Extruded Pb-Sn tube internally pressurised to failure.⁵

1945. The word Superplasticity is derived from the Russian for ultra-high plasticity. In 1962, Underwood⁸ reviewed the work carried out in Russia and it was this which aroused interest in the West. In 1964 Backofen⁹ and his colleagues at MIT demonstrated SPF by using air pressure to expand a tubular specimen of Zn-Al alloy into a die to produce a potentially useful shape.

Most of the ensuing work on SPF was carried out on Zn-22Al alloy, and the first patent was applied for by IBM in May 1965.¹⁰ In the late 1960s prototype parts were being produced in the USA for the computer industry, and in the UK for automotive panels. This early pioneering work on Zn-Al alloys also involved the development of SPF techniques, as outlined by Barnes.¹¹ The first commercial SPF company was set up in the UK in 1971, using an alloy based on Zn-22Al. However, while this and similar alloys had excellent formability their modest strength and relatively poor thermal stability restricted commercial exploitation.

In 1967 Lee and Backofen¹² demonstrated the SP deformation potential of titanium alloys, including Ti-6wt%Al-4wt%V (Ti-6/4) sheet material,

characterising tensile behaviour and recording elongations of >1000%. It was noted that the high plasticity exhibited might provide the basis of a viable method for shaping Ti alloys which overcomes processing problems associated with high strength, limited ductility and excessive spring back. Subsequent work at Rockwell International showed the feasibility of a fabrication process for Ti alloys which combined SPF and diffusion bonding (DB), with patents being taken out in 1975 by Hamilton and Asconi.¹³ Large numbers of demonstrator parts were produced and assessed as reported by Weisert and Stacher¹⁴ and Williams.¹⁵

Although most of the earlier studies of superplasticity involved 2-phase alloys, a move away from this situation occurred when several Al alloys containing <10% by volume of second phase, termed pseudo- or quasi-single phase, were processed to develop superplasticity. The first of these, developed in 1969 and later reported by Grimes *et al.*¹⁶ and Watts *et al.*,¹⁷ was not an existing alloy but was designed to be SP. The alloy, of wt% composition Al–6Cu–0.4Zr (AA2004) has the trade name Supral 100. Subsequent work by Hamilton *et al.*¹⁸ was carried out on existing high strength aerospace alloys of the 7000 series (Al–Zn–Cu–Cr) processed by the Rockwell Route, to develop a fine grain SP microstructure.

The high cost of fuel in the late 1970s encouraged the development of high strength Al–Li alloys for aerospace applications. The materials were designed to replace existing airframe alloys by matching their properties but also having an expected 10% reduction in density, and a 10% increase in stiffness. Many alloy compositions were investigated and several alloys were processed to develop superplasticity. Despite the considerable effort which went into the development of Al–Li alloys throughout the 1980s, the very low take-up of these materials by the aircraft companies resulted in research in this area coming to a halt in the early 1990s, at least in the Western World.

In 1982, because of the interest in superplasticity which had arisen, the first major international conference on ‘Superplasticity in Structural Materials’, edited by Paton and Hamilton¹⁹ was held in San Diego. This was followed by conferences in Grenoble in 1985 and Semi-ah-moo, Washington State, in 1988. This triennial sequence of meetings became known as the International Conference of Superplasticity in Advanced Materials, ICSAM, with further conferences being held in 1991 (Osaka), 1994 (Moscow), 1997 (Bangalore), 2000 (Orlando), 2003 (Oxford), 2006 (Beijing), and 2009 (Seattle), with a meeting in Albi, France, planned for 2012. Apart from ICSAM, many other meetings concerned with superplasticity have been held and numerous papers published, with the result that the literature on the subject is now considerable.

1.3 Types of superplastic materials

For a material to exhibit SP behaviour it must be capable of being processed to develop a fine grain equi-axed microstructure which will remain stable at the SP

deformation temperature. It is also considered important that the processing should lead to a predominance of high angle grain boundaries (lattice misorientation $>15^\circ$), consistent with the widely held view that grain boundary sliding is an important characteristic of SP flow.

There are two main types of SP metallic materials; pseudo single phase and microduplex. The former, which includes commercially significant aluminium alloys, are processed to develop a dispersion of fine precipitates (dispersoids) so that on recrystallisation the alloy will have a small grain size due to the pinning action of the dispersoids on the grain boundaries (i.e. Zener pinning). It has been predicted by Humphreys and Hatherly²⁰ that for a group of fine particles of volume fraction, F_v , and particle radius, r , Zener pinning will occur when the average grain size is equal to $\alpha r/F_v$, where α is a numerical factor ~ 1 . Further, fine precipitates will also inhibit grain growth which in Al alloys is a particularly important consideration since SP deformation is usually carried out at relatively high temperatures, $\geq 0.8 T_m$. The pinning effect of closely spaced, small particles may also inhibit subgrain growth and recrystallisation.

Although many aluminium alloys may exhibit superplasticity, those of commercial interest are listed in Table 1.1 and include SUPRAL 100 (AA2004), AA7475 and AA5083. These alloys can be divided into two groups: those which are recrystallised before SPF, and those which develop a SP microstructure during the early stages of hot forming. The former group includes the 7000 series alloys, e.g. AA7475 and AA5083, while the latter includes AA2004. Much effort was put into the development of Al–Li alloys for aerospace applications throughout the 1980s. While currently not of commercial interest, the two Al–Li alloys listed in Table 1.1 can be processed to develop SP behaviour by either of the above routes.

The microduplex alloys are also thermomechanically processed to develop a fine grain/phase size. Grain growth is limited by having a microstructure consisting of roughly equal proportions of two, or more, chemically and structurally different phases. These materials include α/β titanium alloys, α/γ stainless steels, γ/γ' nickel

Table 1.1 Compositions of SP aluminium alloys, optimum SPF temperatures, strain rates and typical elongations

Alloy	Composition, wt%	SPF temperature	Strain rate	Elongation %
2004	Al–6Cu–0.4Zr	460°C	$\sim 10^{-3} \text{ s}^{-1}$	800–1200
5083	Al–4.5Mg–0.7Mn–0.1Zr	500–520°C	10^{-3} s^{-1}	~ 300
5083 QPF*	Al–4.5Mg–0.7Mn–0.1Zr	450°C	$\sim 10^{-2} \text{ s}^{-1}$	~ 250
7475	Al–5.7Zn–2.3Mg–1.5Cu–0.2Cr	515°C	$2 \times 10^{-4} \text{ s}^{-1}$	800
8090	Al–2.4Li–1.2Cu–0.7Mg–0.1Zr	530°C	$5 \times 10^{-4} \text{ s}^{-1}$	1000
2090	Al–2.5Cu–2.3Li–0.12Zr	530°C	$\sim 10^{-3} \text{ s}^{-1}$	~ 500

*QPF – Quick Plastic Forming.

base alloys, α/β copper alloys, Zn–Al eutectoid and numerous eutectics such as Pb–Sn, and Al–33%Cu. Of these alloys, the α/β titanium alloys are of most commercial interest.

1.4 Grain refinement

General procedures for grain refinement will be considered before outlining the methods used for commercially important SP alloys. Grain refinement and grain size control has also been discussed by Wert.²¹ A further section will deal with high strain rate superplasticity, and also severe plastic deformation (SPD) procedures for producing ultrafine grain sizes.

1.4.1 Grain refinement by mechanical working

Duplex alloys

Grain refinement in duplex alloys can be carried out by hot working close to the SP deformation temperature of the material. This is likely to be near that which gives a microstructure consisting of equal volume fractions of the two phases. If the two phases have different characteristics, such that one is more brittle than the other, then working could fragment the harder constituent which would be infiltrated and dispersed by the softer phase. The two phases could then recrystallise or spheroidise during or after hot working. If the two phases have a similar mechanical character, hot working would elongate them and break them up by the development of shear bands. The structure can then be reformed with a much finer grain size by recrystallisation.

Grain growth during heat treatment and SP flow is restricted as the individual phases have different compositions. For grain growth to occur, solute must diffuse from the smaller grains of each phase through or around the other phase to the larger grains. A duplex material of high structural stability would be one in which the component metals show little or no mutual solid solubility. Examples of duplex materials which have been hot worked to develop fine grain structures include α/β titanium alloys, duplex stainless steels, α/β copper alloys, high carbon steels, and eutectic alloys such as Al–Cu, Pb–Sn and Bi–Sn.

Pseudo-single phase alloys

Pseudo-single phase alloys are primarily Al alloys which contain $\leq 10\%$ of second phase, most of which is in solution at the SPF temperature. The alloys are constituted such that fine grain sizes are produced by processes which involve static recrystallisation prior to SPF, or dynamic recrystallisation during the forming process, and stabilised by a relatively low volume fraction of small ($< 0.2 \mu\text{m}$) particles, i.e. Zener pinning.

In the former case, material is processed to develop a bimodal distribution of precipitates consisting of over-aged particles (1–2 μm) and fine particles (<0.1–2 μm) following heavy warm work. Rapid heating to a temperature close to that for SPF results in a large number of recrystallisation nuclei in the regions adjacent to the coarse precipitates (i.e. particle stimulated nucleation) and to fine equi-axed grains defined by high angle grain boundaries. At the high temperature, the larger precipitates dissolve and the smaller ones inhibit grain growth following recrystallisation and during subsequent SPF. Examples of Al alloys involving a bimodal distribution of precipitates include the 7000 series, i.e. AA7475 and AA7075, and AA5083.

In the processing leading to dynamic recrystallisation, hot/warm rolling is carried out in such a way that discontinuous recrystallisation does not occur. The conditions need to be such that the processes of static and dynamic recovery lead to relatively low levels of substructural internal energy in the sheet material. A microstructure consisting of bands – ribbons in three dimensions – of similarly orientated subgrains separated by aligned high angle grain boundaries is generated. These evolve during SP deformation into grains defined by high angle grain boundaries. Alloys processed in this way include AA2004 and AA8090.

1.4.2 Grain refinement by phase separation

Some duplex materials may be annealed at an elevated temperature where only one phase is stable. Rapid cooling from this temperature may result in a martensitic transformation or the retention of a supersaturated solid solution. Subsequent annealing in the two phase field will lead to the separation of individual equilibrium phases from the metastable microstructure. Processing of α/β Ti alloys by cooling from the β -phase field, followed by annealing and/or mechanical working in the two-phase field will lead to equiaxed α -phase in a β -matrix.

Another example of grain refinement by phase separation is the spinodal decomposition of Zn–22wt%Al alloy. Slow cooling leads to a lamellar decomposition product with poor SP properties, whereas on rapid cooling to room temperature a supersaturated solid solution is initially retained which decomposes spinodally to a very fine grain, highly SP, microstructure.

1.4.3 Grain refinement by phase transformation

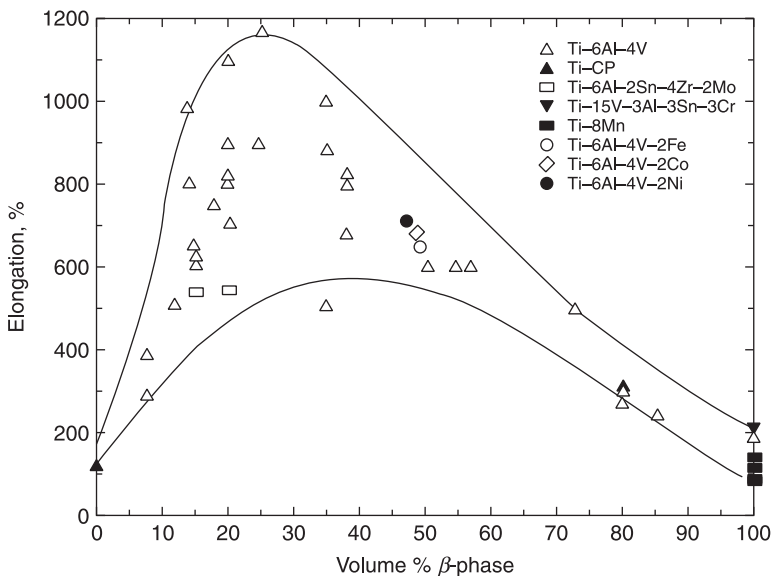
It has been observed that thermal cycling through a phase change can lead to grain refinement. This results from the nucleation of the reaction product at the grain boundaries of the parent phase, such that a single parent grain can be replaced by a number of smaller grains. Repeated cycling through the transformation temperature further refines the structure until a saturation grain size is reached. An example of this procedure is in the normalising of low/medium carbon steels which involves repeated cooling through the ($\alpha + \gamma$) range to below the eutectoid temperature.

Refinement can be further enhanced by controlled rolling of the steel above the transformation range such that a heavily deformed, yet uncrystallised, structure is produced. The deformation results in a large number of nucleation sites in the parent phase which transforms to a fine grain product on subsequent cooling. Controlled rolling coupled with phase transformation is exploited to develop small grain sizes in high strength low alloy steels and ultra-high carbon steels, and Cu–Al based alloys where the eutectoid reactions $\beta \rightarrow \gamma_2$ or $\beta \rightarrow \alpha + \kappa_3$ occurs on cooling.

1.5 Processing of commercially significant alloys to develop superplastic microstructures

1.5.1 Duplex α/β Ti alloys

The α and β phases have very different deformation characteristics. The close packed hexagonal (cph) α -phase has few slip systems and a self-diffusion coefficient which is two orders of magnitude less than that of the body centred cubic (bcc) β -phase. Although it might be expected that a large volume fraction of β -phase would enhance SP behaviour, it also leads to increased grain growth, such that a larger volume fraction of the α -phase would be required to maintain microstructural stability (Fig. 1.4). Hamilton²² has reported for a range



1.4 Elongation at respective SP deformation temperatures as a function of β -phase content for a range of α/β titanium alloys.²²

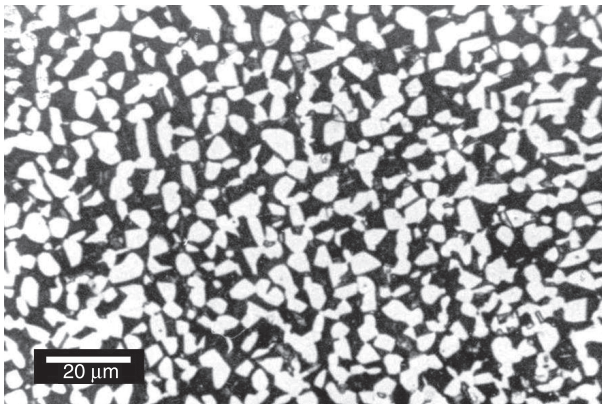
Table 1.2 Compositions of SP α/β titanium alloys, optimum SPF temperatures, strain rates and typical elongations

Alloy	Composition, wt%	SPF temperature	Strain rate	Elongation %
Ti-6/4	Ti-6Al-4V	880–920°C	$5 \times 10^{-4} \text{ s}^{-1}$	~1000%
SP700	Ti-4Al-3V-2Fe-2Mo	750–800°C	$3 \times 10^{-4} \text{ s}^{-1}$	≥300
Ti-6242	Ti-6Al-2Sn-4Zr-2Mo	850–940°C	$5 \times 10^{-4} \text{ s}^{-1}$	>500
IMI550	Ti-4Al-4Mo-2Sn-0.5Si	880–900°C	$5 \times 10^{-4} \text{ s}^{-1}$	>500
IMI834	Ti-5.8Al-4Sn-3.5Zr- 0.7Nb-0.5Mo-0.3Si-0.05C	950–990°C	$\sim 10^{-4} \text{ s}^{-1}$	~300

of α/β Ti alloys that at the respective SP deformation temperatures the optimum volume fraction of β -phase is ~40%. A list of α/β titanium alloys which have been processed to develop superplasticity is given in Table 1.2.

The alloy Ti-6/4 is usually produced in ingot form by vacuum arc melting of consumable electrodes. The as-cast structure is broken down by forging at 100–150°C above the β -transus. On cooling to room temperature the α -phase precipitates on β -phase grain boundaries and Widmanstätten α -phase forms within the grains to give a basket weave structure. Secondary processing, which has been discussed by Semiatin *et al.*,^{22,23} involves forging, extrusion, or plate or sheet rolling, below the β -transus to give an equi-axed α -phase (~5–10 μm) in a matrix of transformed β -phase (Fig. 1.5). Forming conditions for Ti-6/4 would usually be ~920°C, $5 \times 10^{-3} \text{ s}^{-1}$.

Table 1.3 includes other duplex alloys which have been processed to develop superplasticity.



1.5 Fine grain microstructure of a SP α/β titanium alloy.

Table 1.3 Compositions, optimum SPF temperatures, strain rates and typical elongations of miscellaneous alloys which have been processed to develop superplasticity

Alloy	Composition, wt%	SPF temperature	Strain rate	Elongation %
Al-Cu	Al-33Cu	480–500°C	$4 \times 10^{-3} \text{ s}^{-1}$ – 10^{-2} s^{-1}	400–1000
Zn-Al	Zn-22Al	200–250°C	$2 \times 10^{-5} \text{ s}^{-1}$ – $2 \times 10^{-3} \text{ s}^{-1}$	500–2900
Avesta	Fe-18Cr-5Ni- 3Mo-3RE60	1000°C	10^{-3} s^{-1}	>700
2205	Fe-22Cr-5.5Ni- 3Mo-2Mn	900–1000°C	10^{-4} s^{-1} – 10^{-3} s^{-1}	500–1000
IN-100	Ni-10Cr-15Co- 5Al-5Ti-3Mo	920–1050°C	$3 \times 10^{-4} \text{ s}^{-1}$ – $8 \times 10^{-4} \text{ s}^{-1}$	>800
IN738	Ni-16Cr-8Co- 3W-3Al-3Ti	~900°C	10^{-4} s^{-1} – 10^{-3} s^{-1}	~500
IN629	Cu-28Zn-15Ni- 13Mn	570° C	10^{-4} s^{-1} – $5 \times 10^{-4} \text{ s}^{-1}$	~450
Ni-Al Bronze	Cu-10Al-5Fe-5Ni	750–850	$5 \times 10^{-3} \text{ s}^{-1}$ – 10^{-1} s^{-1}	1000–8000 ²

1.5.2 Aluminium alloys (compositions given in weight %)

While a number of Al alloys have been processed to develop superplasticity, those which are of commercial interest are listed in Table 1.1 and include Supral 100 (AA2004), AA7475 and AA5083. The Al-Li alloys, AA8090 and AA2090, which have useful properties are also listed.

AA2004 (Al-6Cu-0.4Zr), Supral 100

The AA2004 alloy was not an existing material but was designed so it could be processed to develop superplasticity, while having useful ambient temperature properties typical of a medium strength Al alloy. The processing route has been described by Grimes *et al.*¹⁶ and by Watts *et al.*,¹⁷ while the events leading up to the development of this material and to its commercial use have been presented by Barnes *et al.*²⁵

The alloy is rapidly solidified from a high superheat (~780°C) to retain Zr in solution and to avoid the formation of coarse primary ZrAl₃ precipitates. It is then aged at 360°C when a homogeneous distribution of fine ZrAl₃ particles (~10 nm) is precipitated. After solution treatment at 500°C the alloy is hot rolled to break down the as-cast structure. The alloy is then heavily warm/cold worked to 80% reduction, during which operation recrystallisation is prevented by the pinning action of the ZrAl₃ particles.

The alloy can be formed at 460°C at a strain rate of ~ 10^{-3} s^{-1} and is capable of giving substantial tensile strains to failure of ~1000%. During forming, continuous dynamic recrystallisation of the heavily dislocated structure occurs and a fine

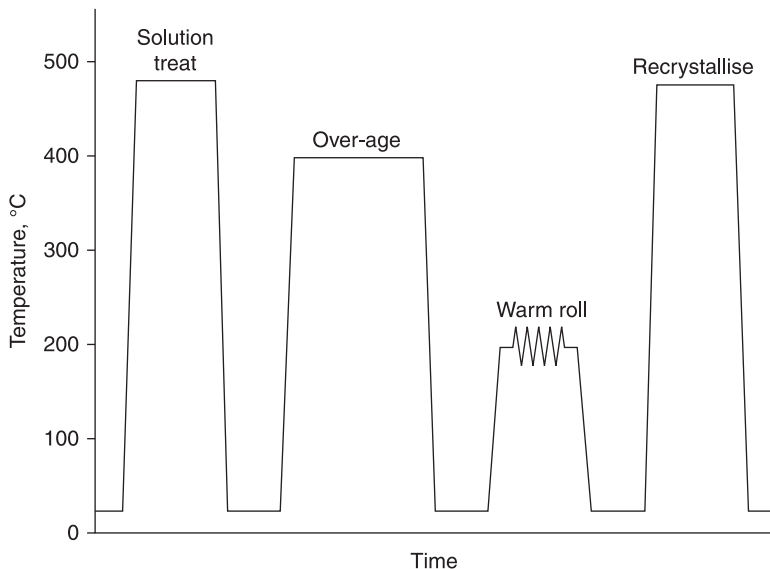
grain ($\sim 5\text{--}10\ \mu\text{m}$) SP microstructure evolves. The mechanism by which this occurs has been the subject of much investigation and has been discussed by Bate *et al.*²⁶

AA7475 (Al-5.5Zn-2.5Mg-1.5Cu-0.2Cr)

AA7475 material is an existing high strength alloy which can be thermomechanically processed to develop a fine grain size. There are several variants of the processing route but all involve the production of a microstructure with a grain size of $10\text{--}15\ \mu\text{m}$ by the static recrystallisation of a warm or cold worked alloy containing a bimodal distribution of precipitates. The Rockwell Route described by Hamilton *et al.*¹⁸ is the most well-known of these processing procedures and is illustrated in Fig. 1.6.

After hot working the cast alloy, it is solution treated at 480°C to dissolve all the precipitates except the Cr-rich dispersoids which are typically $0.1\text{--}0.2\ \mu\text{m}$ in diameter. It is quenched to retain solute in solution and then aged at 400°C for ~ 8 hours to produce an over-aged distribution of large precipitates of M-phase and T-phase. The alloy is then warm worked to give an $\sim 80\%$ reduction when these coarse particles lead to intense localised deformation and lattice rotation which provide sites for discontinuous recrystallization, i.e. particle stimulated nucleation.

Rapid heating to $\sim 480^\circ\text{C}$ results in a large number of recrystallisation nuclei in the locally deformed regions adjacent to coarse precipitates and to the development of a small grain size. At these temperatures, the large precipitates dissolve but the small Cr-rich precipitates inhibit grain growth following recrystallisation and,



1.6 Schematic of Rockwell Route for processing SP Al alloys.

during subsequent SPF, by exerting a drag effect on grain boundaries by Zener pinning. The processed material would then be capable of tensile strains to failure of 500–1000% under optimum deformation conditions (515°C and $2 \times 10^{-4} \text{ s}^{-1}$).

AA5083 (Al–4.5Mg–0.8Mn–0.1Cr)

AA5083 is a non-heat treatable alloy containing small varying amounts of the residual elements Fe and Si. It is a relatively inexpensive material, has medium strength, excellent cold formability and good corrosion resistance, and can be processed to give a moderate degree of superplasticity. It is now the dominant Al alloy used for the production of non-structural parts by SPF. The alloy also finds considerable use in the Quick Plastic Forming (QPF) process, described by Schroth,²⁷ which involves rapid forming ($\sim 10^{-2} \text{ s}^{-1}$) of automotive panels at $\sim 450^\circ\text{C}$.

After casting and hot rolling to plate, the alloy contains constitutive particles in the size range 1–5 μm which contain typically Al, Mn, Fe and Si, Al_6Mn precipitates of size 0.2–0.8 μm , and Cr-rich dispersoids. Following heavy cold work, 70/80% reduction, the larger particles act as nuclei for recrystallisation, while the smaller of the Al_6Mn precipitates and the Cr-rich dispersoids stabilise the grain size. The material can be recrystallised in the temperature range 350–550°C to give a grain size of 10–15 μm . SP tensile strains of 300–350% are observed at $\sim 525^\circ\text{C}$ for a strain rate of $\sim 10^{-3} \text{ s}^{-1}$. Matsuo²⁸ has demonstrated the benefit of reducing the Si and Fe levels to <0.04% (SKY high purity AA5083) on SP tensile ductility.

Al–Li alloys

A number of Al–Li alloys have been processed to develop excellent SP formability. Fine grain microstructures were produced by procedures which involved static recrystallisation prior to SPF, or by dynamic recrystallisation during the early stages of forming. Grimes²⁹ has reported that AA8090 (Al–2.5Li–1.2Cu–0.6Mg–0.1Zr) could be processed by either route. For material processed by the SUPRAL route, tensile elongations of >1000% were obtained for temperatures of 520/530°C and strain rates of $\sim 5 \times 10^{-4} \text{ s}^{-1}$.

1.5.3 Magnesium alloys

Magnesium alloys are the lightest structural metallic materials commercially available and there is an interest in the use of sheet products for applications as automotive body parts. The focus of research and development is to produce Mg alloy sheet with a random texture, avoiding anisotropy which reduces ambient temperature formability.

A processing route being widely investigated involves Twin Roll Casting (TRC) using a horizontal arrangement of rolls suitable for producing wide sheets.

The molten metal feed passes into the rolls and is rapidly cooled to give relatively thin sheet (2–10 mm) product which can then be hot rolled to the required thickness. The rapid cooling in TRC is believed to lead to a bimodal size distribution of intermetallic phases. Hence, on subsequent hot rolling to final thickness, the larger precipitates give rise to particle stimulated nucleation, while the fine precipitates stabilise the resulting fine grain size in which there is a randomisation of texture.

Several alloy compositions are being investigated including the long established AZ31 of wt% composition: Mg–3Al–1Zn–0.3Mn. Park *et al.*³⁰ have discussed the processing of Mg sheet. Material processed by the TRC route has shown SP behaviour with an elongation of 740% at 330°C at a strain rate of $5 \times 10^{-4} \text{ s}^{-1}$. Overview papers on the subject of Mg alloy processing appear in the TMS publication, *Journal of Metals (JOM)*, in August 2009.

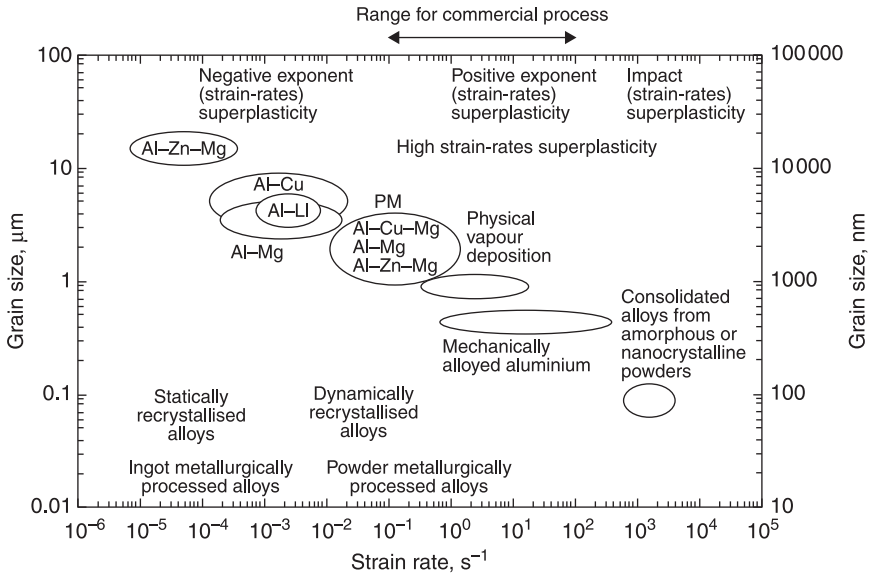
1.6 High strain rate superplasticity

In conventionally processed alloys, optimum superplasticity generally occurs at strain rates of 10^{-4} s^{-1} to $5 \times 10^{-3} \text{ s}^{-1}$, and there tends to be a decrease in tensile strains at slower and faster strain rates. However, in 1984 Nieh *et al.*³¹ conducted experiments on AA2124 reinforced with SiC whiskers and obtained high elongations at strain rates above $\sim 10^{-2} \text{ s}^{-1}$. This behaviour was subsequently termed High Strain Rate Superplasticity (HSRS) and is now defined by the Japanese Standards Association³² as superplasticity occurring at strain rates of 10^{-2} s^{-1} or greater.

Higashi³³ has reviewed studies on Positive Exponent Superplasticity, defined as superplasticity at very high strain rates $\geq 1 \text{ s}^{-1}$ which were observed in nanophase or near nanophase grain sizes produced in Al alloys by three advanced processing methods. These involved mechanical alloying, consolidation from amorphous or nanocrystalline powders, and physical vapour deposition. Studies carried out on these materials included tensile deformation using strain rates up to 6000 s^{-1} and also differential scanning calorimetry (DSC) measurements to determine their incipient melting points.

The optimum SP strain rates were found to be strongly dependent on the refinement of grain structure. It was also noted that maximum values of tensile elongation were observed at temperatures near or slightly above the incipient melting temperatures. It was proposed that small amounts of liquid phase at grain boundaries in alloys and interfaces in composites were responsible for enhancing the strain rate for superplasticity, and influencing the deformation mechanisms in these materials. The observations of Higashi, which show that the optimum strain rate increases as the grain size is decreased, are summarised in Fig. 1.7.

Although these are very interesting observations and show the important role of grain size in SP deformation, the procedures used to produce fine grain sizes would be difficult to scale up to produce bulk material. Other procedures which have been used more recently to produce very fine grain sizes have been based on



1.7 Optimum SP strain rates for Al alloys with a range of grain sizes (courtesy of K Higashi³³).

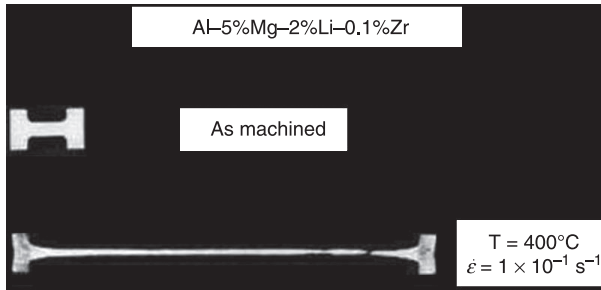
the use of severe plastic deformation. This topic has been reviewed by Valiev *et al.*³⁴ and is outlined in the next section.

1.7 Grain refinement by severe plastic deformation

1.7.1 Equi-Channel Angular Extrusion

During Equi-Channel Angular Extrusion (ECAE), the bulk solid is subject to very high plastic strains without any reduction in cross-sectional dimensions, and this differs very substantially from conventional working processes involving rolling, extrusion and drawing. In ECAE, a sample in the form of a bar or rod is machined to a size which fits into a channel in a die and is pushed through the die. Within the die the channel bends through an abrupt angle which is often close to 90° (Fig. 1.9(a)). As it passes through the region of intersection of the two parts of the die the specimen is subjected to shear. The imposed strain depends on the angle, ϕ , between the two parts of the channel, and is of the order of unity when $\phi = 90^\circ$.

As there is no gross change in the dimensions of the specimen, repetitive extrusion may be carried out on the same specimen to impose very high plastic strains. By control of the direction of rotation of the sample between successive passes, the temperature, and the number of passes, considerable redundant strains can be developed leading to very fine equi-axed recrystallised microstructures of submicron or nanometre dimensions. This technique has been mainly applied to



1.8 Al alloy 1420 processed by ECAE, strained at 400°C at 10^{-1} s^{-1} (courtesy of R Z Valiev³⁴).

Al alloys, and although the microstructures lack thermal stability at normal SPF temperatures, they can be deformed at appreciably lower temperatures and significantly higher strain rates, $\geq 10^{-2} \text{ s}^{-1}$, than the same alloy processed by conventional routes. This is illustrated in Fig. 1.8, which shows the results of work by Valiev and Islamgaliev³⁵ on AA1420 of wt% composition Al-5.5Mg-2.2Li-0.12Zr.

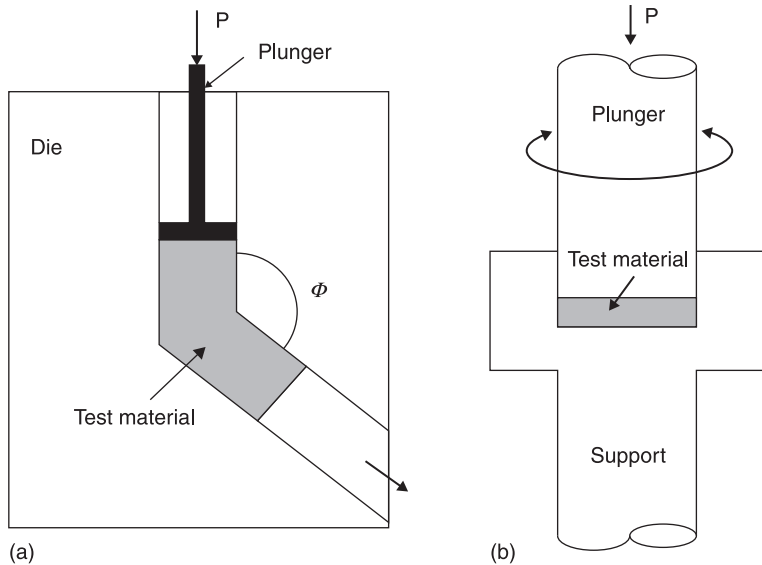
1.7.2 High-Pressure Torsion

High-Pressure Torsion (HPT) involves subjecting a sample in the form of a thin disc held between anvils to high pressure and simultaneous torsional straining (Fig. 1.9(b)). The discs are usually about 1 mm thick and 10–20 mm in diameter. It is generally found that an applied pressure of 5 GPa and five or more complete rotations of the sample in torsion are sufficient to produce an approximately homogeneous microstructure with a grain size of $\sim 200 \text{ nm}$ or less. It has been reported by Valiev *et al.*³⁶ that a miniature tensile test piece cut by electrical discharge from a strained disc of AA1420 and tested at 300°C at a strain rate of 10^{-1} s^{-1} gave an elongation of $\sim 400\%$.

1.7.3 Accumulative Roll Bonding

Both ECAE and HPT are valuable techniques for producing ultrafine grained SP materials which have been used in numerous interesting scientific investigations, the results of which have been the basis of many publications. However, it is unlikely that ECAE, and certainly not HPT, could be scaled up to produce significant quantities of material for commercial SPF at an acceptable cost. Tsuji *et al.*³⁷ have suggested that Accumulative Roll Bonding (ARB) may be a possible way of overcoming this problem.

For the production of large sheet material, the total strain during processing is limited because of the decreasing thickness of the sheet. In ARB the rolled sheet



1.9 Schematic illustration of principles of (a) ECAE and (b) HPT, where ϕ is the angle of intersection of the two channels and P is applied pressure (courtesy of R Z Valiev³⁴).

is cut into lengths, stacked and rolled again. ARB is both a rolling and a bonding process so that to achieve good bonding, surfaces must be cleaned by degreasing and wire brushing before stacking. For Al alloys rolling is carried out at $\sim 200^\circ\text{C}$ to achieve both bonding and strain accumulation. A study on AA5083 after 5 cycles, and an accumulated strain of 4, led to an initial grain size of $\sim 280\text{ nm}$. For a strain rate of $2 \times 10^{-3}\text{ s}^{-1}$ the material showed promising SP behaviour with elongations of $>400\%$ at 400°C , and $>200\%$ at 200°C .

1.7.4 Friction Stir Processing

Friction Stir Processing (FSP) is a relatively recent thermomechanical process which is very effective in producing fine grain equi-axed microstructures ($\sim 2\text{ }\mu\text{m}$). The procedure is an adaption of Friction Stir Welding (FSW) developed at The Welding Institute in 1991 as a solid state joining process for high strength aluminium alloys. In FSP a rotating tool, consisting of a cylindrical shoulder and a projecting concentrically located pin, is pushed into the surface of the material to be processed. Friction between the pin and the work piece combined with adiabatic heating due to metal deformation leads to a plasticised metal column (the 'stir zone').

When the shoulder of the rotating tool makes contact with the work piece, the tool is traversed in a predetermined manner to process a volume of material

defined by the processing path and the tool pin length. As the rotating tool traverses, softened material is displaced from the front of the pin to the back. Processing parameters include tool geometry, rotation rate and traverse speed. The distance between successive passes must be small enough to ensure some overlap of the stir zones so as to achieve a uniform microstructure throughout the processed region. The process can eliminate the large irregularly shaped constitutive particles often present in Al alloys, and which can initiate failure during SP deformation, and replace them with a uniform distribution of less deleterious fine particles.

Work on a range of Al alloys including AA7075, AA7475, AA2024, and AA5083 has shown that after processing they can be deformed at strain rates of $\sim 10^{-2} \text{ s}^{-1}$ at their normal SPF temperatures. FSP can be used to refine the microstructure in sheet, plate and cast material. Hayashi *et al.*³⁸ have reported that FSP of continuously cast AA5083 led to grain sizes in the range 1–3.5 μm , and on tensile testing at 450°C gave elongations of >1200% at 10^{-1} s^{-1} , while Smith *et al.*³⁹ demonstrated that FSP of low cost AA5083 sheet enabled superplasticity (uniform elongations >250%) to be developed.

1.8 Mechanisms of superplasticity

1.8.1 Constitutive equations

Equation [1.1], given in Section 1.1, may be re-written as:

$$\dot{\epsilon} = k_1 \sigma^n \quad [1.2]$$

where n , the stress exponent for deformation, is equal to $1/m$. The strain rate, $\dot{\epsilon}$, at which a SP material will deform, as defined by the simple relationship given in Eq. [1.2], can be restated in an expanded temperature dependent form by:

$$\dot{\epsilon} = \frac{AGbD}{kT} \left(\frac{b}{d}\right)^p \left(\frac{\sigma_{eff}}{G}\right)^n \quad [1.3]$$

This is the constitutive equation commonly used to describe elevated temperature deformation, in which G is shear modulus, b is the Burgers vector, k is Boltzmann's constant, T is absolute temperature, d is grain size and p is the exponent of inverse grain size, D is a diffusion coefficient ($= D_0 \exp(-Q_s/RT)$), where D_0 is a frequency factor, Q_s is the activation energy for the appropriate diffusion process and R is the gas constant. Deformation is driven by the deviatoric (shear) component of the effective stress field characterised by σ_{eff} , equal to $\sigma - \sigma_0$, where σ is the applied stress, and σ_0 is a threshold stress. A is a dimensionless constant. To establish a constitutive relationship for a material it is necessary to determine values for the material parameters m , p , Q_s and σ_0 . Procedures for determining these parameters have been outlined by Pilling and Ridley⁴⁰ and by Iwasaki *et al.*⁴¹

For constant stress and temperature it can be seen from the above equation that:

$$\dot{\epsilon} \propto \frac{1}{d^p} \quad [1.4]$$

Since the value of p lies between 2 and 3 for SP flow, the dramatic effect that a reduction in grain size could have on strain rate is clearly apparent, e.g. an order of magnitude reduction in grain size could lead to an increase of 10^2 – 10^3 in SP strain rate. Alternatively, for a given strain rate, a reduction in grain size could enable SPF to be carried out at a lower temperature, although this would usually be accompanied by an increase in flow stress. These observations are fully consistent with the results referred to in Sections 1.6 and 1.7 on grain refinement, whereby ultrafine grain sizes enable SP deformation to be carried out at significantly higher strain rates than those for conventionally processed material and/or at lower temperatures.

A high strain rate sensitivity of flow stress, m , is the most important mechanical characteristic of SP materials. It can be seen from Eq. [1.1] that if the relationship between flow stress and strain rate, $\dot{\epsilon}$ is plotted logarithmically then the slope of the plot is m , where:

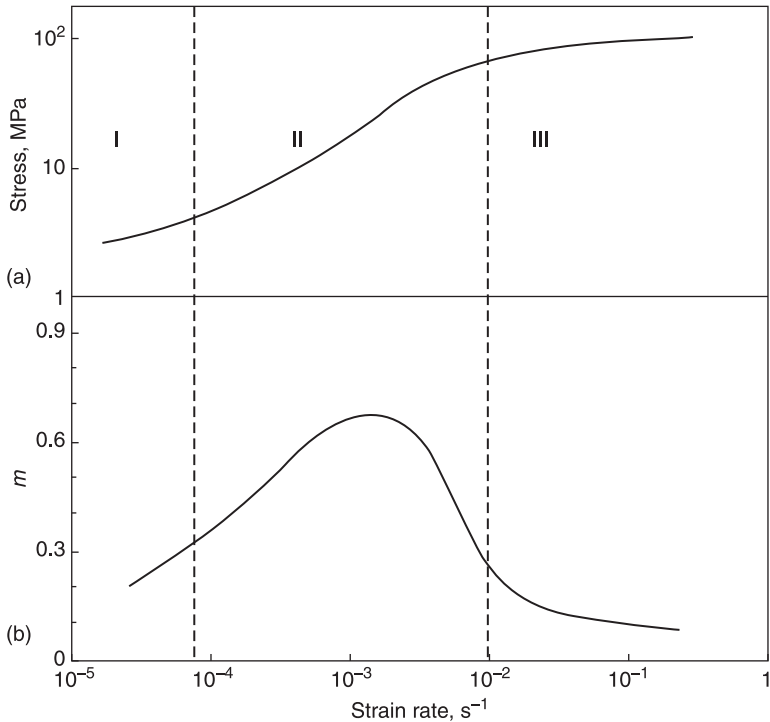
$$m = \frac{\partial(\log \sigma)}{\partial(\log \dot{\epsilon})} \quad [1.5]$$

For most SP materials the logarithmic plot has a sigmoidal shape, as illustrated in Fig. 1.10(a), and can be divided into three regions, labelled I, II, and III, although a Region 0 may be added as seen in Fig. 11.

The slope, m , of the sigmoidal curve when plotted against log strain rate, as seen in Fig. 1.10(b), shows that m passes through a maximum in Region II which is delineated by a value of $m > 0.3$. Regions I and III have m values in the range 0.1–0.3. Mechanical behaviour is affected by both temperature and grain size. Increasing temperature decreases the flow stress, particularly in Regions I and II. Maximum m is observed to increase with increasing temperature and decreasing grain size, and the strain rate for maximum m moves to higher values. For normally processed materials SP behaviour is usually observed for the strain rate range $5 \times 10^{-3} \text{ s}^{-1}$ to 10^{-4} s^{-1} .

Kashyap and Mukherjee⁴² have noted that during tensile deformation in Regions I and III the grains elongate in the direction of tension, and the change in shape of the specimen is consistent with the change in grain shape; grain elongation occurs such that the position of adjacent grains remains unaltered, and the number of grains across the cross-section is unchanged. These conditions correspond to deformation under non-SP conditions.

In contrast, during SP deformation (Region II) it was observed that the equiaxed shape and relatively small size of the grains remains unaltered after large elongations, although some strain enhanced grain growth usually occurs. They propose that grains change their neighbours by relative grain translation, i.e. grain



1.10 Schematic of: (a) logarithmic plot of stress versus strain rate p ; and (b) m versus log strain rate, for a typical SP alloy.

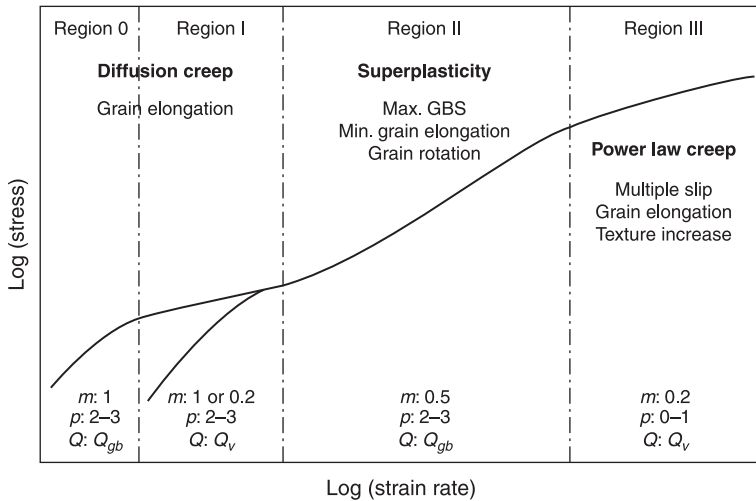
boundary sliding occurs, and the number of grains along the tensile direction increases with a corresponding decrease across the section, i.e. grains emerge from the interior. An overall reduction of texture occurs with increasing strain.

1.8.2 Other features of Region I and Region III

An expanded version of Fig 1.10(a) is seen in Fig. 1.11. Some of the characteristic values of the parameters p , n and Q , in the constitutive relationship and distinguishing microstructural and topological features, are shown on the figure.

Region I

At low strain rates the shape of the logarithmic stress–strain rate curve can vary. For many alloys m is low, ~ 0.2 , and this has been interpreted as evidence for the existence of a threshold stress for SP flow. However, it has been proposed that the existence of Region I is due to the segregation of impurity atoms to grain boundaries where they interact with moving boundary dislocations that contribute to grain boundary sliding.



1.11 Expanded version of the logarithmic plot of stress versus strain rate for SP alloy, where Q_{gb} is the activation energy for grain boundary diffusion, and GBS is grain boundary sliding.

Studies by Chaudhury and Mohammed⁴³ on Zn-22wt%Al showed that if impurities were reduced to very low levels (i.e. 6 ppm) then there was no evidence for the existence of Region I, although Region II and its transition to Region III were unaffected by purity levels.

However, as the strain rate is decreased for alloys which show a Region I, the slope has been observed to increase tending to unity. This has been cited as evidence for diffusion controlled flow with the activation energy being similar to that for volume diffusion. It has also been reported by Vale *et al.*⁴⁴ that m can initially decrease but further reductions result in a transition to a slope of 1, which has been termed Region 0 where true diffusion creep dominates with an activation energy of grain boundary diffusion. However, it should be noted that grain growth during slow strain rate deformation can affect the flow stress and complicate the interpretation of this region, as can the different testing techniques used to obtain stress-versus-strain rate data.

Region III

At high strain rates where $m \sim 0.2$ deformation involves recovery controlled dislocation creep (power law creep). Strain is accumulated by the glide of dislocations, but is dependent on the rate at which obstacles such as other dislocations, precipitates and solutes, can be bypassed. It is generally believed that dislocation climb is the rate controlling process. The activation energy for flow in this region is similar to that for lattice diffusion, and the strain rate is relatively insensitive to grain size. Other features of Region III are the observation

of slip lines, and the development of high dislocation densities in the grains. Crystallographic texture increases and significant grain elongation occurs.

1.8.3 Region II – the superplastic region

Although the microstructural requirements for superplasticity are well established, the exact mechanism of SP flow is less well understood. However, there is a widely held, although not unanimous, view, as indicated in Section 1.8.1, that strain is accumulated by the motion of grains, or groups of grains, relative to each other by sliding, and that grain boundary sliding, often referred to as Rachinger⁴⁵ sliding, is the dominant SP deformation process. The importance of grain boundary sliding is supported by a number of experimental studies of the displacement of marker lines on the surfaces of deformed SP specimens.

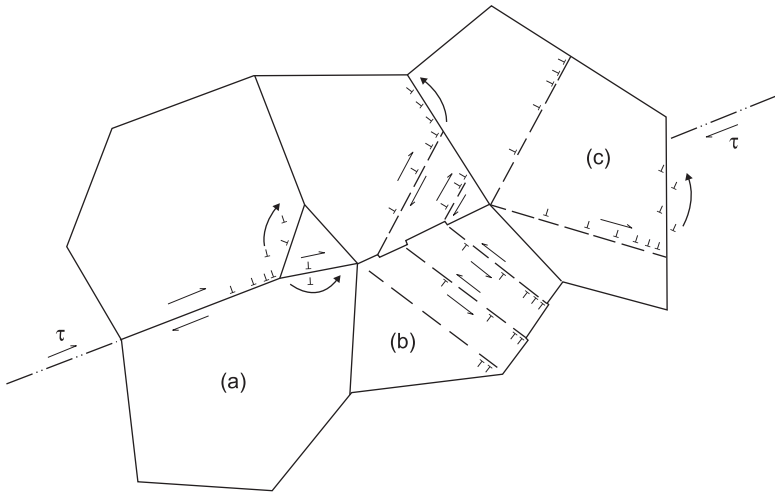
In work on a superplastically deformed microduplex Pb–Sn alloy of eutectic composition, extensive grain rotation was observed by Vevecka and Langdon.⁴⁶ However, there was not a build-up of rotation in any one grain, and the rotation angle increased or decreased up to about 30° as deformation proceeded. Observations also showed that intragranular dislocation movement only made a small contribution to the overall strain. Despite the possibility that movement of surface markers may not be representative of internal behaviour, similar observations of grain rotation were reported by Matsuki *et al.*⁴⁷ for a SP aluminium alloy with internal oxide markers.

If grain boundary sliding occurred in a completely rigid system, then voids would develop in the microstructure. However, as not all materials cavitate during SP flow, sliding must be accommodated. Accommodation is usually considered to involve dislocation and/or diffusion processes and the various models have been reviewed by Mukherjee,⁴⁸ Kashyap and Mukherjee,⁴² Langdon,⁴⁹ Gifkins,⁵⁰ Pilling and Ridley⁵¹ and by Nieh *et al.*⁵²

Dislocation models

When grain boundary sliding is obstructed by an unfavourably orientated grain, the resultant stress concentration may be relaxed by dislocation motion in the blocking grain. These dislocations pile up against the opposite grain boundary until the back stress prevents further activation of the source and stops sliding. Climb of the leading dislocation from the pile-up along the boundary into an annihilation site would allow another dislocation to be emitted from the source and a small increment of grain boundary sliding, i.e. strain, to be accumulated (Fig. 1.12). The stress and grain size exponents would both be predicted to have a value of 2, with an activation energy consistent with grain boundary diffusion (D_{gb}). The deformation rate would be given by:

$$\dot{\epsilon}_{II} = A_{II} \left(\frac{D_{gb} G b}{kT} \right) \left(\frac{b}{d} \right)^2 \left(\frac{\sigma}{G} \right)^2 \quad [1.6]$$



1.12 Composite diagram illustrating dislocation mechanisms involved in the relaxation of stress concentrations resulting from grain boundary sliding proposed by: (a) Gifkins,⁵⁰ (b) Mukherjee,⁴⁸ and (c) Ball and Hutchison,⁵³ where τ denotes shear stress.

In the original Ball and Hutchison⁵³ pile-up model it is proposed that groups of grains slide as a unit. In the Mukherjee model, grains slide individually rather than in groups, and grain boundary ledges can act as dislocation sources. The models lead to rate equations similar to Eq. [1.6], but the values taken by the parameter A_{II} are 12 and 2, respectively. In the Gifkins⁵⁰ model, sliding is considered to take place by the motion of grain boundary dislocations which pile up at triple points. The resulting stress concentration is relaxed by the dissociation of the leading dislocation into dislocations capable of moving in the other boundaries which make up the triple point, and/or into lattice dislocations which accommodate sliding.

These new dislocations then climb or glide in or near the two boundaries until they meet each other. They may annihilate or combine to form different boundary dislocations. The rate equation is identical to Eq. [1.5], except that A_{II} takes a value of ~ 64 . The grain boundary model is often referred to as the core and mantle model, as the accommodation of grain boundary sliding is assumed to occur only within a viscous mantle around a rigid core.

A composite diagram which illustrates from left to right the mechanisms of the (a) Gifkins, (b) Mukherjee, and (c) Ball and Hutchison models is seen in Fig. 1.12.

Arguments have been raised regarding the validity of dislocation models in that dislocation pile-ups are not observed, and may not be expected because of the relatively high temperatures at which deformation takes place. Also, grain elongation is implicit in any model involving dislocation glide/climb on any number of slip systems.

However, Falk *et al.*⁵⁴ have reported that after deformation of a SP copper alloy in Region II, transmission electron microscopy revealed an accumulation of matrix dislocations in coherent twin boundaries within the grains. Further, Valiev and Langdon⁵⁵ have measured intergranular strains in a SP Pb–62wt%Sn eutectic alloy over a wide range of elongations and observed the occurrence of non-uniform and oscillating intergranular strains within the lead and tin phases, but this strain made no net contribution to the total elongation.

Diffusion models

Ashby and Verrall⁵⁶ proposed a model which explains superplasticity as a transition between diffusion accommodated (D-A) flow operative at low strain rates and dislocation creep at high strain rates. For grains to maintain compatibility during deformation there is a gradual change in grain shape as matter is removed by diffusion. Grain boundary migration restores the original equi-axed shape but in a rotated orientation. However, because a transient but finite increase in grain boundary area results from the shape change, the model predicts a threshold stress for SP flow. The strain rate in the SP region is that due to diffusion but acting under an apparent stress, σ^* . This stress is equal to the applied stress, σ , less the stress required to create the additional grain boundary energy, σ_0 .

The total strain rate,

$$\dot{\epsilon}_{total} = \dot{\epsilon}_{diff-accom} + \dot{\epsilon}_{diff-creep} \quad [1.7]$$

$$\dot{\epsilon}_{diff-accom} = \left(\frac{100\Omega}{kTd^2} \right) \sigma^* D_v \left(1 + \frac{3.3\delta D_B}{dD_v} \right) \quad [1.8]$$

and

$$\dot{\epsilon}_{diff-creep} = A \left(\frac{D_v Gb}{kT} \right) \left(\frac{\sigma}{G} \right)^n \quad [1.9]$$

where Ω = atomic volume, d = grain size, D_v = volume diffusivity, k = Boltzmann's constant, δD_B = product of grain boundary width and diffusivity. In Eq. [1.8] $\sigma^* = \sigma - \sigma_0$ and $\sigma_0 = 0.72\gamma/d$, where γ = grain boundary free energy.

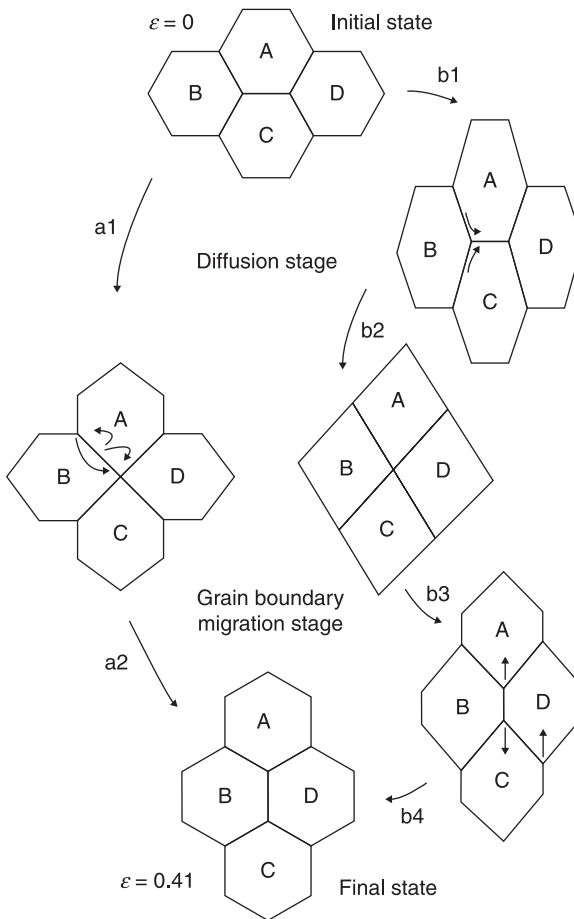
Within Regions I and II, diffusion accommodated flow was thought to account for >99% of the strain rate. Around the Region II/III transition, both mechanisms make important contributions to the flow process, and in Region III dislocation creep accounts for >99% of the strain rate.

As with the dislocation models, shortcomings were identified in the diffusion model and include:

- The diffusion paths proposed required that diffusion takes place in different directions on the opposite sides of the same grain boundary. The diffusion

paths were later modified by Spingarn and Nix⁵⁷ so that each grain within a cluster underwent the same change maintaining symmetry of deformation and a more realistic shape transient (Fig. 1.13).

- The strain rates predicted for Region II were about two orders of magnitude too fast.
- Experimentally measured σ_0 values were considerably lower and had the opposite dependence of temperature, and the opposite dependence of grain size compared with that predicted by the model, as observed by Smith *et al.*⁵⁸ in studies on a SP α/γ stainless steel. However, the model of Ashby and Verrall was the first to predict a sigmoidal logarithmic stress–strain rate relationship.



1.13 Grain switching model of Ashby and Verrall⁵⁶ (a1→a2) as modified by Spingarn and Nix (b1→b2→b3→b4).⁵⁷

1.8.4 Superplastic deformation in two-phase alloys

The phenomenological equations describing SP deformation given in the two previous sections have assumed a single phase microstructure, yet many such equations were often derived using measurements from two-phase materials. The materials parameters represented in these equations were either those of the softer phase or those given by a rule of mixtures. It is observed that SP flow seems to be accommodated almost exclusively in the softer phase (an isostress combination). Differences in the materials properties of each phase in the duplex microstructure would require the two phases to deform at quite different rates if an isostress rule was applied.

The material could be considered in terms of a non-Newtonian fluid, e.g. a soft β -phase with a stress exponent of >1 , containing hard undeformable particles, such as α -phase in α/β Ti alloys or α/β Cu alloys. Grain boundary sliding would occur by shear within a thin layer of β -phase in the vicinity of grain boundaries. The gliding dislocations in the β -phase would be more effectively obstructed by the α/β boundaries than the β/β boundaries. The dislocations might be expected to pile up in front of the α grains, climb along the interphase boundary (IPB) until glide within the β -phase could continue.

The probability of a gliding dislocation intersecting an α grain would increase as the volume fraction of the harder α -phase increased, while the glide distance would depend on the β -phase size. Suery and Baudalet⁵⁹ predicted a strain rate given by:

$$\dot{\epsilon}_H = A_H \left(\frac{1-f_\alpha}{f_\alpha} \right)^2 \left(\frac{D_{IPB}G}{kT} \right) \left(\frac{b}{d_\beta} \right)^2 \left(\frac{\sigma}{G} \right)^2 \quad [1.10]$$

where f_α is the volume fraction of α -phase and d_β is the grain size of the β -phase.

1.8.5 Cooperative grain boundary sliding

The models of SP flow outlined above consider sliding events which occur on a microscopic scale along boundaries of individual grains. However, Kaibyshev *et al.*^{60,61} have proposed that cooperative grain boundary sliding (GBS), in which grains in groups of mesoscopic dimensions slide along aligned grain boundary surfaces, is characteristic of superplasticity. When a sliding group meets an unfavourably orientated grain the resulting stress concentration can bring about dislocation generation in the blocking region. These lattice dislocations stimulate further sliding in the next suitably orientated grain boundary region. Hence, a band of shear occurs along aligned grain boundaries and crystallographic planes of several grains. The phenomenon gives rise to a pattern of shear markings on a polished surface.

Accommodation of the sliding can involve cooperative grain boundary migration and grain rotation. Relative displacements and rotations of groups of

grains also cause an increase in the number of grains lying along the direction of stress and a decrease in the transverse direction, which is characteristic of superplasticity. Kaibyshev *et al.*⁶⁰ have developed a model for SP deformation based on cooperative GBS which accurately reproduces the observed dependency of flow stress on strain rate. Cooperative GBS has been reported for both pseudo-single phase and microduplex alloys.

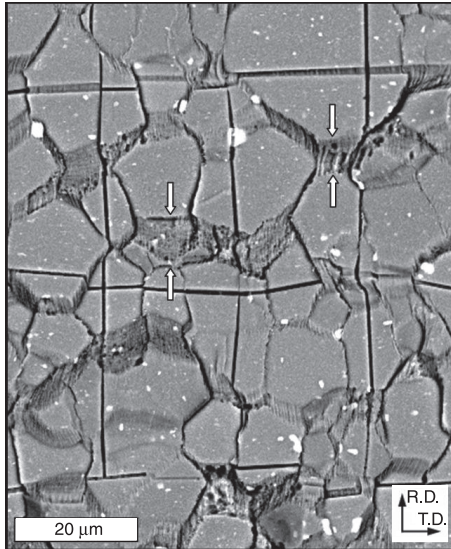
1.8.6 Mechanism of superplastic flow in aluminium alloys

The widely promoted view that grain boundary sliding is the dominant SP deformation mechanism is primarily based on surface measurements made on alloys such as microduplex Zn–22wt%Al and Pb–62wt%Sn. However, pseudo-single phase SP Al alloys represent a commercially significant group of materials for which substantial evidence of grain boundary sliding does not appear to be available. As outlined in an earlier section, these Al alloys fall into two groups: those with dynamically recovered structures, e.g. AA2004 Al–Cu–Zr and AA8090 Al–Li–Mg–Cu–Zr, and those with a recrystallised, near equi-axed microstructure which includes AA5083 Al–Mg–Mn and AA7475 Al–Zn–Mg–Cu–Cr.

Bate *et al.*²⁶ made studies of the effect of tensile strain at 450°C with a strain rate of 10^{-3} s^{-1} , on microstructure and texture of SP AA2004 (Supral). The m value remained essentially constant with strain at about 0.45. In this material texture was dominated by a component centred on $\{011\}\langle\sqrt{2}11\rangle$, which became weaker with deformation. The two variants of that texture allowed the identification of bands in the microstructure which acted as internal markers, and persisted to high strains. It was concluded that the texture and microstructure changes were not consistent with grain boundary sliding, and that a combination of rate sensitive slip and dynamic grain growth were better able to explain the behaviour of the material.

Bate *et al.*⁶² have also investigated the effect of deformation at 530°C, at a constant strain rate of $5 \times 10^{-4} \text{ s}^{-1}$, on the microstructure, texture and mechanical characteristics, of commercially processed Al–Li (8090) sheet. It was noted that m remained almost constant at ~ 0.5 during straining, despite a progressive change in microstructure. The initial sheet had a dominant cross rolled ‘brass’ texture centred on $\{011\}(11\sqrt{2})$, which became weaker with increasing strain, but it was also possible to identify similar orientations which remained aligned in the rolling direction for strains up to unity. The changes in microstructure and texture were not compatible with grain boundary sliding/Rachinger sliding.

Modelling studies, which assumed grain boundary sliding and incorporated measurements of dynamic grain growth and reductions in texture, showed that after a tensile strain of 0.5 the orientation alignment was completely removed. Hence, it was clear that grain boundary sliding as the primary deformation mechanism was not operative in AA8090, at least for SP strains up to 1.1 ($\sim 200\%$). However, it is likely that a limited amount of grain boundary sliding occurs as an



1.14 Examples of 'extension zones' (indicated by white arrows) for SP AA5083 with a coarse grid, strained at 530°C at $5 \times 10^{-4} \text{ s}^{-1}$ to $\epsilon \sim 0.3$; R.D. is rolling direction and T.D. is transverse direction (courtesy of K Sotoudeh).

accommodation mechanism to rate sensitive slip, which was considered to be the potential primary deformation mechanism for SP deformation in this alloy.

Sotoudeh and Bate⁶³ recently examined SP flow in AA5083 Al–Mg–Mn alloy using specimens with fine and coarse surface grids. Their observations showed that intragranular deformation in this alloy was very limited, consistent with the studies of Rust and Todd.⁶⁴ The grid lines showed grain boundary offsets, but interpreting these as being due to grain boundary sliding (Rachinger sliding) would only account for a small fraction of the overall strain. However, it was noted that there were 'grain extension zones' which made a significant contribution to the tensile direction offsets of the coarse grid lines (Fig. 1.14), and these can readily be considered as material accumulation zones resulting from diffusional creep. Diffusional creep can give rise to grain boundary offsets and an apparent grain boundary sliding phenomenon known as Lifshitz⁶⁵ sliding. These observations led to the conclusion that SP flow in this alloy is primarily a result of diffusional creep.

Overall, the above studies on Al alloys did not provide evidence of any significant involvement of grain boundary sliding, i.e. Rachinger sliding, in the SP deformation process for the conditions investigated.

1.9 Sources of further information and advice

The literature relating to superplasticity is substantial and papers describing original work frequently appear in materials science and related journals. A search

of the World Wide Web using the word ‘Superplasticity’ will yield many reference sources. The ICSAM Conferences referred to in Section 1.2 are published by Trans Tech Publications, Switzerland. Information on a range of aspects of superplasticity in metallic materials may also be found in: Pilling J and Ridley N, *Superplasticity in Crystalline Solids*, 1989, London, Institute of Materials; Kaikyshev O A, *Superplasticity of Alloys, Intermetallides and Ceramics*, 1992, Berlin, Springer-Verlag; Nieh T G, Wadsworth J and Sherby O D, *Superplasticity in Metals and Ceramics*, 1997, Cambridge, Cambridge University Press; Zhilyaev A P and Pshenichnyuk A I, *Superplasticity and Grain Boundaries in Ultrafine Grained Materials*, Cambridge, Cambridge International Science Publishing Co., 2010. A special issue of *Advanced Engineering Materials* in August 2010, Issue 8, is concerned with Bulk Nanostructured Materials and includes a review by Valiev RZ and Langdon TG, ‘The art and science of tailoring materials by nanostructuring for advanced properties by SPD techniques’, pp. 677–691.

1.10 Acknowledgements

The author is grateful to Dr K Sotoudeh and Dr Z C Wang for assistance with the preparation of illustrations.

1.11 References

1. Langdon T G, *J. Mater. Sci.*, 2009, 44, 5998–6010.
2. Higashi K, private communication, University of Osaka Prefecture, Japan, 1988.
3. Bengough D G, *J. Inst. Met.*, 1912, 7, 123–174.
4. Jenkins C H M, *J. Inst. Met.*, 1928, 40, 21–32.
5. Pearson C E, *J. Inst. Met.*, 1934, 54, 111–123.
6. Ridley N (ed.), *Superplasticity – 60 years after Pearson*, pp. 1–5, 1995, London, Institute of Materials.
7. Bochvar A A and Zviderskaya Z A, *Izves. Aka. Nauk. SSSR Otd Teku Nauk*, 1945, 9, 821–827.
8. Underwood E E, *J. Met.*, 1962, 14, 914–919.
9. Backofen W A, Turner I R and Avery D H, *Trans. ASM*, 1964, 57, 980–990.
10. US Patent Application No 445188, 2 April 1965.
11. Barnes A J, *Mater. Sci. Forum*, 2001, 357–359, 3–16.
12. Lee D and Backofen W A, *TM S-AIME*, 1967, 239, 1034–1040.
13. Hamilton C H and Asconi L A, U.S. Patents 3920175 (18 Nov. 1975), and 3927817 (23 Dec. 1975).
14. Weisert E D and Stacher G W, in Paton N E and Hamilton C H (eds), *Superplastic Forming of Structural Alloys*, pp. 273–289, 1982, Warrendale, TM S-AIME.
15. Williamson J R, in Paton N E and Hamilton C H (eds), *Superplastic Forming of Structural Alloys*, pp. 291–306, 1982, Warrendale, TM S-AIME.
16. Grimes R, Baker C, Stowell M J and Watts B M, *Aluminium*, 1975, 51, 720–723.
17. Watts B M, Stowell M J, Baikie B L and Owen D G E, *Metal Sci.* 1976, 10, 189–197.
18. Hamilton C H, Bampton C C and Paton N E, in Paton N E and Hamilton C H (eds), *Superplastic Forming of Structural Alloys*, pp. 173–189, 1982, Warrendale, TM S-AIME.

19. Paton N E and Hamilton C H (eds), *Superplastic Forming of Structural Alloys*, 1982 Warrendale, TM S-AIME.
20. Humphreys F J and Hatherley M, *Recrystallisation and Related Annealing Phenomena*, 2nd edn, 2004, Oxford, Elsevier.
21. Wert J A, in Paton N E and Hamilton C H (eds), *Superplastic Forming of Structural Alloys*, 69–83, 1982, Warrendale, TM S-AIME.
22. Hamilton C H, in Baudelet B and Suery M (eds), *Superplasticity*, 14.1–14.16, 1985, Paris, Centre National de la Recherche Scientifique.
23. Semiatiin S L, Seetharaman V and Weiss I, *Journal of Metals*, 1997, 6, 33–39.
24. Semiatiin S L, Fagin P N, Betten J F, Zane A P, Ghosh A K and Sargent G A, *Metall. Mater. Trans. A*, 2010, 41A, 499–512.
25. Barnes A J, Stowell M J, Grimes R, Laycock D B and Watts B M, *Key Engineering Materials*, 2010, 433, 11–30, Trans Tech Publications.
26. Bate P S, Humphreys F J, Ridley N and Zhang B, *Acta Mater.*, 2005, 53, 3059–3069.
27. Schroth J G, in *Advances in Superplasticity and Superplastic Forming*, Taleff E *et al.* (eds), pp. 9–20, 2004, Warrendale, TMS.
28. Matsuo M, in Ridley N (ed.) *Superplasticity – 60 years after Pearson*, pp. 277–283, 1995, London, Institute of Materials.
29. Grimes R, in *Superplasticity*, pp. 13.1–13.12, 1985, Paris, Centre National de la Recherche Scientifique.
30. Park S S, Park W-J, Kim C H, Yue B S and Kim N J, *Journal of Metals*, 2009, 61(8), 14–18.
31. Nieh T G, Henshall C A and Wadsworth J, *Scripta Metall.*, 1984, 18, 1405–1408.
32. Glossary of terms used in metallic superplastic materials, JIS H 7007, Japanese Standards Association, Tokyo, 1995.
33. Higashi K, in Ridley N (ed.), *Superplasticity – 60 years after Pearson*, pp. 93–102, 1995, London, Institute of Materials.
34. Valiev R Z, Islamgaliev R K and Alexandrov I V, *Prog. in Mater. Sci.* 2000, 45, 103–89, Elsevier Science.
35. Valiev R Z and Islamgaliev R K, *Mater. Sci. Forum*, 1999, 39, 304–306.
36. Valiev R Z, Islamgaliev R K, Stolyarov V V, Mishra R S and Mukherjee A K, *Mater. Sci. Forum*, 1998, 969, 269–272.
37. Tsuji T, Shiotsuki K, Utsunomiya H and Saito Y, *Mater. Sci. Forum*, 1999, 73–78, 304–306.
38. Hayashi J T, Menon S K, Su J-Q and McNelley T R, *Key Engin. Mater.*, 2010, 433, 135–140, Switzerland, Trans. Tech. Publications.
39. Smith C B, Mohan A, Mishra R S *et al.*, *ibid.*, pp. 141–152
40. Pilling J and Ridley N, *Superplasticity in Crystalline Solids*, pp. 48–64, 1989, London, Institute of Materials.
41. Iwasaki H, Hosokawa H, Mori T, Tagata T and Higashi K, *Mater. Sci. Eng.*, 1998, A252, 199–202.
42. Kashyap B P and Mukherjee A K, in Baudelet B and Suery M (eds), *Superplasticity*, 4.1–4 31, 1985, Centre National de la Recherche Scientifique, Paris.
43. Chaudhury P K and Mohamed F A, *Acta Metall.*, 1989, 36, 1099–1110.
44. Vale S H, Eastgate D J and Hazzledine P M, *Scripta Metall.*, 1979, 13, 1157–1162.
45. Rachinger W A, *J. Inst. Met.*, 1952, 81, 33–41.
46. Vevecka A and Langdon T G, *Mater. Sci. Eng.*, 1994, A187, 161–165.
47. Matsuki K, Morita H, Yamada M and Murakami Y, *Met. Sci.*, 1977, 11, 156–163.
48. Mukherjee A K, *Mater. Sci. Engin.*, 1971, 8, 83–89.

49. Langdon T G, *Metall. Trans*, 1982, 13A, 689–701.
50. Gifkins R C, in Paton N E and Hamilton C H (eds), *Superplastic Forming of Structural Alloys*, pp. 3–26, 1982, Warrendale, TM S-AIME.
51. Iwasaki H, Hosokawa H, Mori T, Tagata T and Higashi K, *Mater. Sci. Eng.*, 1998, A252, 65–101.
52. Nieh, T G, Wadsworth J and Sherby O D, *Superplasticity in Metals and Ceramics*, pp. 32–57, 1997, Cambridge, Cambridge University Press.
53. Ball A and Hutchison M M, *Metal Sci.*, 1969, 3, 1–7.
54. Falk L K L, Howell P R, Dunlop G L and Langdon T G, *Acta Metall.*, 1986, 34, 1203–1214.
55. Valiev R Z and Langdon T G, *Acta Metall. Mater.*, 1993, 41, 949–954.
56. Ashby M F and Verrall R A, *Acta Metall.*, 1973, 21, 149–163.
57. Spingarn J R and Nix W D, *Acta Metall.*, 1978, 26, 1389–1398.
58. Smith C I, Norgate B and Ridley N, *Scripta Metall.*, 1974, 8, 159–164.
59. Baudelet B and Suery M, *Res Mechanica*, 1981, 2, 163–170.
60. Kaibyshev O A, Pshenichniuka A I and Astanin V V, *Acta Mater.*, 1998, 46, 4911–4916.
61. Astanin V V, Kaibyshev O A and Faizova S N, *Acta Metal. Mater.*, 1994, 42, 2617–2622.
62. Bate P S, Ridley N and Zhang B, *Acta Mater.*, 2007, 55, 4995–5006.
63. Sotoudeh K and Bate P S, *Acta Mater.*, 2010, 58, 1909–1920.
64. Rust M A and Todd R I, *Mat-wiss u Werkstofftech*, 2008, 39, 289–292.
65. Lifshitz I M, *Sov. Phys. JETP*, 1963, 17, 909–920.

Standards for superplastic forming of metals

F. ABU-FARHA, Penn State Erie, USA and
R. CURTIS, King's College London, UK

Abstract: In this chapter, a review of the three main standards that describe the proper method for testing superplastic materials is presented, focusing on the critical issues that significantly impact testing results, and pointing out the points of agreement and disagreement among the three standards. In an attempt to resolve those issues, related investigations in the literature are reviewed and combined in an integrated testing methodology that covers the test specimen, clamping device and proper testing procedure. The methodology is hoped to provoke the development of a more universally accepted standard method for testing superplastic materials at elevated temperatures.

Key words: testing standards, superplastic metallic sheets, uniaxial tensile testing, specimen geometry, quick-mount grips, heating and holding time.

2.1 Introduction

The uniaxial tensile test is quite possibly the most common and the easiest testing procedure for characterising the mechanical behaviour of the various engineering materials. This is mirrored by the standardisation and versatility of the test's elements (specimen geometry, clamping device, test parameters) to fit the different material classes, in addition to the widespread use of uniaxial load frames by industrial, academic and research facilities where such standards are primarily adopted. Not surprisingly, the tensile test is the test of choice for studying, characterising and modelling the unique class of superplastic materials. For a start, the accepted definition for superplastic behaviour dictates the material achieving 200% elongation in simple tension (Pilling and Ridley 1989); therefore, the tensile test is essential for determining whether a material is superplastic or not, and then the range of conditions over which the material is expected to behave superplastically. Then, the flow stress/strain rate data derived from several tensile tests are plotted in the form of a sigmoidal (S-shaped) curve, uniquely associated with the class of superplastic materials. Also, there is the strain rate jump test, which is simply a uniaxial tensile test with multiple jumps in the applied strain rate (Comley 2008). The test is essential for the accurate determination of the strain rate sensitivity index of the material (known as m); the latter is a particularly important parameter for superplastic materials. While the sensitivity index of conventional metals does not exceed 0.3, even at elevated temperatures, superplastic materials are expected to have $0.3 < m < 0.7$ (Pilling and Ridley

1989). Finally, the efforts on constitutive modelling of superplastic deformation are predominantly based on the uniaxial loading case, hence requiring an abundance of tensile stress/strain data to calibrate and verify the proposed models. The latter are the mathematical relations necessary to describe and predict the deformation behaviours of superplastic materials. Yet, more importantly, they are the backbones of the finite element simulations that we completely rely on to produce the pressure–time profiles needed for regulating and controlling superplastic forming operations.

2.2 Need for standards

Superplastic materials have been studied for several decades now, yet they seem to have gained a greater attention recently due to the growing interest in lightweight alloys (titanium, aluminium and magnesium alloys) for energy-saving potentials; and the superplastic forming technique is known to go hand-in-glove with these particular alloys. While these materials are deformed pneumatically via the superplastic forming technique, resulting in predominant biaxial loading conditions, the fact is ‘we are still largely dependent on the uniaxial tensile test’ to study, characterise and model them, and then control their process deformation. Naturally, this dependence, combined with the growing interest, bring the need to regulate the multitude of testing activities in the field. Yet with superplastic materials in particular, the need is further accentuated from several perspectives.

Superplasticity in metallic materials is associated with warm/elevated temperatures, making standards like the ASTM E8/E8M (2009), ISO 6892-1 (2009), DIN EN 10002-1 (2009) and DIN 50125 (2004), not suitable for testing superplastic materials, from both specimen geometry and testing procedure points of view.

There are several standards, on the other hand, that describe the proper method for testing metallic materials at higher-than-ambient temperatures, such as the ASTM E21 (2009), ISO 783 (1999) and the DIN EN 10002-5 (1991). However, there are several reasons why they are not particularly suitable or applicable to superplastic materials. The prime one is the viscoplastic nature of superplastic materials, which is rather different to that of other non-superplastic materials, even at equivalent temperatures and stretching conditions. This viscoplasticity requires special attention with regard to the grip design, specimen geometry and heating path prior to testing. These items will be further elaborated in the next sections; yet it is worth mentioning at this point that none of the abovementioned standards describes a specimen geometry, nor a gripping device particularly tailored for higher-than-ambient temperature tensile testing.

Disparities in testing procedures and methodologies are clearly observed among the various efforts on superplastic tensile testing, despite the introduction of superplastic testing standards (covered next). Such disparities could be detrimental to the test results, since superplastic materials are very sensitive to the

conditions at which they are tested. Heating time, for example, is often not reported in superplastic studies; reported ones vary between 10 minutes (Abu-Farha *et al.* 2010), 20 minutes (Kim *et al.* 2001) and 30 minutes (Jäger *et al.* 2004), for the same alloy and testing temperature (Mg AZ31 at 400 °C). The resulting stress/strain curves have been shown to be different, thanks to the microstructural evolution in the material (Abu-Farha *et al.* 2007b).

Of all the testing facets, adopting a variety of test specimen geometries is one of the clearest and most detrimental forms of discrepancy. When reviewing the efforts on tensile testing of superplastic materials, one need not look for long before realising the disagreements among researchers on the issue. Selected examples of recent efforts in the field show that investigators adopt test specimens with different gauge lengths, varying from as long as 25.4 mm to as short as 4 mm (Verma *et al.* 1996, Lee and Huang 2004, Chino *et al.* 2004, Watanabe *et al.* 2005, Liu *et al.* 2009, Abu-Farha and Khraisheh 2007a, Chang *et al.* 2009, Hong *et al.* 2009, Ma and Langdon 1994). Moreover, the discrepancies are not limited to gauge length; they cover gauge width, gauge length-to-width ratio, fillet radius, and even the size of the grip region. All things considered, it is rather hard to find two efforts where the same specimen geometry is used. The aforementioned discrepancy is very crucial in testing superplastic materials, as specimen geometry has been shown to have great impact on the results of the tensile test (Johnson *et al.* 1994, Khaleel *et al.* 1996, Bate *et al.* 2008, Abu-Farha *et al.* 2010a, Nazzal *et al.* 2010). It was shown that specimens with smaller gauge length tend to produce higher values for maximum elongation before failure (Bate *et al.* 2008, Nazzal *et al.* 2010). The implications of this are detrimental in regard to our ability to cross-reference the results obtained by different investigators, provided the great variation in specimen geometry found in the literature.

These points highlight the need for standardising the method for tensile testing of superplastic materials; this is to unify current efforts and provide sufficient guidelines for prospective efforts in the field.

2.3 Existing standards

The highlighted need for standardisation was tackled recently, and the reader can find three major testing standards in the field. The first standard method for the tensile testing of superplastic materials was issued by the Japanese Standards Association in 2002, and was reaffirmed in 2007 (JIS H7501 2002). The American Society for Testing and Materials followed with a similar standard in 2005, which was reapproved in 2008 (ASTM E2448 2008). Finally, the International Organization for Standardization issued its standard in 2007 (ISO 20032 2007). Generally speaking, the ISO and JIS standards are quite similar in their contents, the items they cover, and the depth in which those items are covered. The ASTM one, on the other hand, is rather different and distinguishes itself from the others. It does cover the testing methodology more comprehensively, and it provides

more details on the various testing facets (Abu-Farha and Curtis 2009, Abu-Farha *et al.* 2010b).

2.4 Issues with existing standards

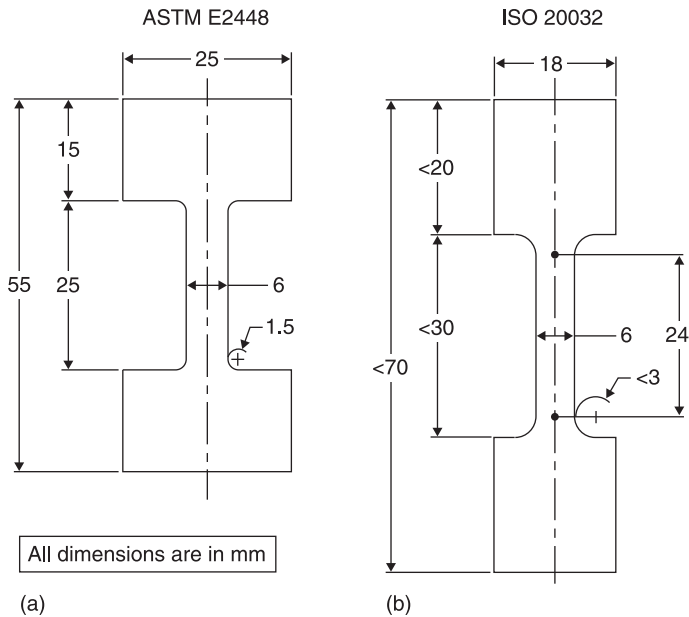
It is arguably true that the late arrival of the testing standards listed previously has led to the described state of discrepancies in the literature on superplastic tensile testing. However, even in the years that followed, such variations in the testing methodology (set-up and procedure) are still evident, and efforts referring to one or more of those standards are still limited. It is almost as though the standards are not being widely accepted in the field; and while allowing more time could change this perception, this may be attributed to:

- The standards do not agree on several important issues. The reader of the three standards gets conflicting messages on some of the detrimental items in superplastic tensile testing (such as the loading path: constant speed vs constant strain rate).
- The standards do not adequately or accurately address some of the main controversial issues in testing superplastic materials. The validity of this statement varies from one standard to the other. While the ASTM standard is more detailed and descriptive than the JIS or ISO standards, they all fail to provide guidelines on specific testing issues, such as the heating/holding time. Also, the standards do not fully explain or provide viable solutions to other issues, such as test specimen geometry and clamping device.

It might be safe to say here that this is almost entirely driven by the condition at which these materials are tested; elevated temperatures. By referring to other standards that simply deal with tensile testing at higher-than-ambient temperatures (DIN EN 10002-5 1991, ISO 783 1999, ASTM E21 2009), similarities in the drawbacks can be easily realised. One cannot find answers to several questions, particularly those related to the clamping (gripping) device, heating path, holding time and testing procedure. The above mentioned items will be discussed in detail here.

2.4.1 Test specimen geometry

First, the JIS H7501 and ISO 20032 standards propose two specimen geometries (one with flat sides and the other with curved sides), while the ASTM E2448 proposes only one. By focusing on the flat parallel-sided specimens proposed by each of the three standards, different proportions in terms of their geometrical parameters are noticed. Figure 2.1 shows a direct comparison between the specimen geometries as they appear in (a) the ASTM E2448 and (b) the ISO 20032. Disparities in the effective gauge length, fillet radius, and the ratio between the gauge and grip portions, are observed. Of most importance, the standards do



2.1 Tensile test specimen geometry according to: (a) ASTM E2448 and (b) ISO 20032.

not agree on the definition of the gauge length; while it is the distance between the shoulders according to the ASTM E2448, it is a selected distance within the parallel section according to the ISO 20032 (and similarly the JIS H7501). With the latter, stretching the test specimen will cause the entire length (from shoulder to shoulder) to deform, and that is what the testing machine will record for constructing the stress/strain curve. Without an extensometer, which is most often the case in superplastic tensile testing, it is not possible to track and record the deformation of a particular segment of the test piece (such as that proposed by the ISO 20032 and JIS H7501). As for the fillet radius, the larger fillet implies larger materials flow from the grip region into the gauge region; combined with the difference in how the gauge length is defined, one sees the significant impact on successive strain measurements.

Finally, and apart from these differences and their impact, none of the standards provide any guidelines on how those specimen geometrical parameters were selected. This may be unproblematic for conventional metals and ambient temperature testing, yet the viscoplastic behaviour of superplastic materials requires special attention. Several researchers have reported great impact on the test's outcome as a result of small changes in the geometry, hence indicating that some optimisation is needed (Johnson *et al.* 1994, Bate *et al.* 2008, Abu-Farha 2010a, Nazzal *et al.* 2010).

2.4.2 Clamping device (grip)

The clamping device issue is the most influential of all, since it affects the selection of the specimen geometry, and has a direct significant impact on the controversial issue of heating/holding time. The ISO 20032 standard hardly describes the clamping device. The JIS H7501 inadequately covers the issue, and indicates that the gripping device should impose pressure on the specimen surface to provide the gripping action. This is questionable, since doing so would adversely affect material flow from the grip region during testing. The ASTM E2448 standard, on the other hand, proposes a fairly simple clamping device, and provides a detailed description to the reader. In fact, it is the only one among all standards that deal with higher-than-ambient temperature tensile testing to provide the reader with a clamping device that suits this type of testing. Fundamentally, the proposed device imposes tensile loading on the shoulders of the specimen, and facilitates inserting the specimen into the grips in a short time, which is essential for testing at extreme temperatures. A detailed drawing of the clamping device can be found in different references (Comley 2008, ASTM E2448 2008).

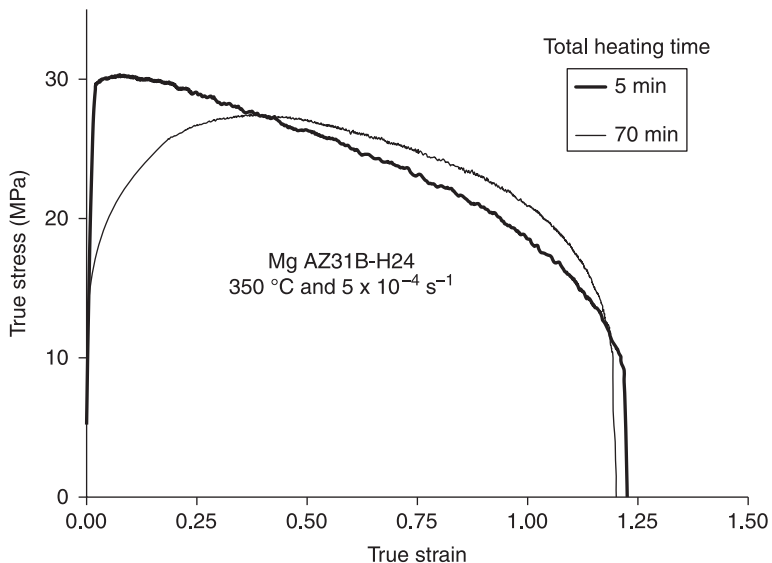
There are, though, some drawbacks and several aspects that could be further improved. The grips seem to target specimens prepared from sheets with a specific thickness, and shims are needed to accommodate other sheet thicknesses; this could complicate the specimen mounting process. Also, it is not clear how the grips would allow the specimen to expand freely during the heating phase, a matter which, if not guaranteed, could lead to imposing undesired compressive loads on the specimen. Finally, while the device is simple, every attempt should be made to optimise the means of mounting the specimen in the shortest possible time, as this produces the least impact on the heating/holding time issue.

2.4.3 Heating/holding time

The heating/holding time is a very controversial issue, yet it is the least adequately discussed of all superplastic tensile testing issues. The main divergence between the various standards starts with their different approaches for heating the specimen to the desired test temperature. The JIS H7501 and ISO 20032 standards indicate that the specimen is to be heated (alongside the testing set-up) from ambient to the targeted test temperature, and so that is what dictates the heating time. The ASTM E2448 standard provides clear instructions for heating the furnace (or heating chamber) to the desired test temperature before inserting the test specimen; and so heating time is simply the time needed for the furnace to re-establish the pre-set test temperature, after the interruption of opening it to insert and clamp the specimen. The first approach might be the easier one, particularly when testing at extremely high temperatures, where inserting the specimen into a hot furnace is troublesome. Yet this way of heating requires the load frame or testing machine to be able to accommodate the slow thermal expansion of all that lies inside the

furnace; a feature called ‘protect specimen’ that not all testing machines have. Additionally, this may cause undesirable changes to the microstructure of the material, which will be highly dependent on the test temperature. Consequently, this will make standardising the issue of heating time (and later holding time) particularly difficult. The other approach, on the other hand, is the more logical way to heat the specimen, if the hardship of gripping the specimen is overcome and made consistent, regardless of the test temperature.

After reaching the desired test temperature, there is the issue of holding time; the time that needs to be allotted before imposing tensile strain on the specimen. This time should be long enough to assure thermal equilibrium throughout the test specimen, yet not too long to cause significant alteration in the microstructure of the material, and hence distort the superplastic properties being evaluated. Unfortunately, opinion is divided on the subject here too. Both the JIS H7501 and ISO 20032 standards leave the issue without any firm guidelines: ‘Interested parties shall agree on the time of heating the test piece to the test temperature and the holding time at the test temperature before starting the test, provided that such agreement shall be made with full assurance of uniform temperature distribution over the test piece’ (JIS H7501 2002, ISO 20032 2007). According to the ASTM E2448, holding time is governed by reaching thermal equilibrium, which is detected by thermocouples readings, or when the cross-head beam ceases to move under the ‘protect specimen’ control. Referring to other standards on elevated temperature testing, the ASTM E21 dictates that this time should not be less than



2.2 Stress/strain curves obtained under identical conditions yet following different heating paths (Abu-Farha and Curtis 2009).

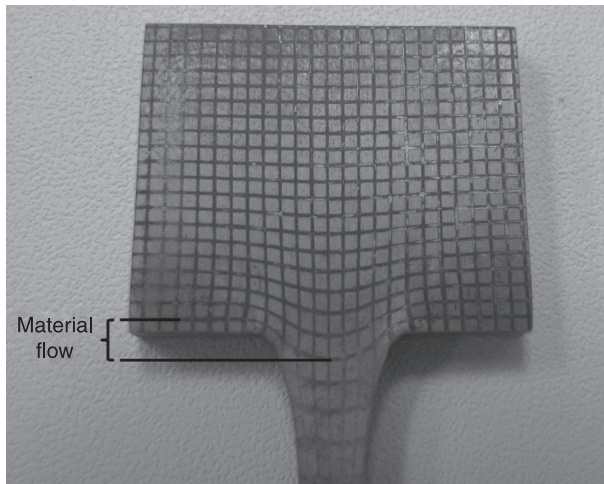
20 minutes, while both the ISO 783 and the DIN EN 10002-5 stipulates a 10-minute holding time regardless of the test temperature. As depicted, these disagreements leave a lot of room for the reader to choose such a detrimental factor. Figure 2.2 gives an example on the impact of the heating time on the resulting stress/strain curve of the material (Abu-Farha and Curtis 2009).

2.5 Towards improved standards

The previous discussion highlights the need to fill the gaps in the existing standards by seeking a methodology that tackles the most prominent testing issues. A significant amount of work has been carried out, and can be found in the literature, targeting the various facets of superplastic tensile testing. In this section, some of the results are gathered and used to draw the framework of a comprehensive testing methodology, to provide the grounds for an improved universally-accepted testing standard for the unique class of superplastic materials.

2.5.1 Test specimen geometry

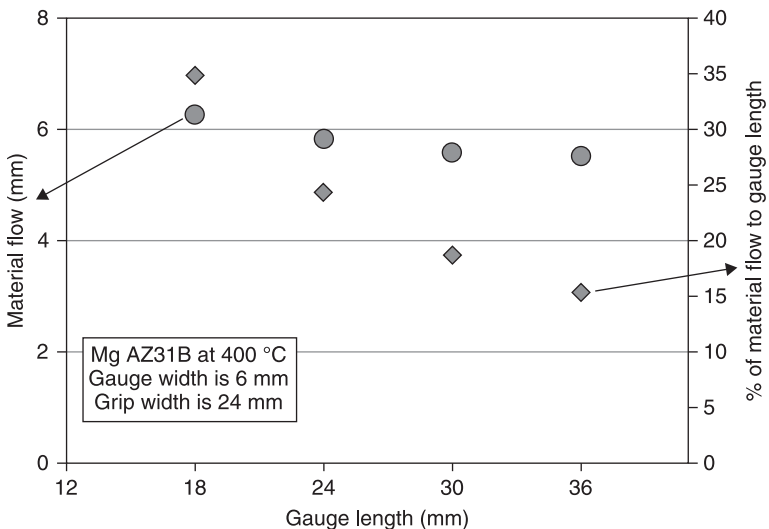
One of the major problems in the test specimen design is the unavoidable material flow from the grip region into the gauge region; illustrated in Fig. 2.3. This flow is inherent to the viscoplastic nature of superplastic materials, and must be minimised since it leads to inflated strain results (Bate *et al.* 2008, Nazzal *et al.* 2010, Abu-Farha *et al.* 2010a). Ma and Langdon (1994) suggest that as much as 60% of the extreme superplastic elongation of ~8000%, achieved in aluminium-bronze by Higashi and reported by Sherby and Wadsworth (1990), is associated



2.3 Material flow from the grip region into the gauge region in a superplastically deformed test specimen.

with material flow. Means of minimising this flow include the use of a smaller fillet radius at the specimen shoulder. In fact, a superplastic specimen should have as small a fillet radius as possible, since its presence affects the accuracy of the gauge length in the first place. Besides, a large fillet radius is not necessary, since stress concentration problems are not present with superplastic materials at elevated temperatures (unlike the case with conventional materials at near-ambient temperatures). Current machining and wire EDM cutting practices should be able to achieve fillet radii smaller than 2 mm. Using a smaller gauge width, and a smaller ratio between the gauge width and grip width, can also reduce material flow. With a nominal gauge width of 6 mm, as reported in most standards and testing efforts in the literature, a ratio of ~ 4 between the grip width and the gauge width is recommended (Nazzal *et al.* 2010). Also, alignment holes in the grip portion of the specimen should be avoided, as they were shown to promote material flow (Khaleel *et al.* 1996).

In addition to minimising material flow, proper selection of specimen geometry can minimise its effects on the apparent ductility of the material. The most detrimental geometrical parameter is the ratio between the gauge length and gauge width of the specimen, the effects of which were the focus of several investigators. Generally speaking, selecting a large gauge length-to-width ratio diminishes the error associated with material flow, as depicted by Fig. 2.4. However, it is not practical to have a very large gauge length; that is because superplastic tensile testing targets very large elongations, and so the physical limitations of the testing machine and the heating chamber should be taken into

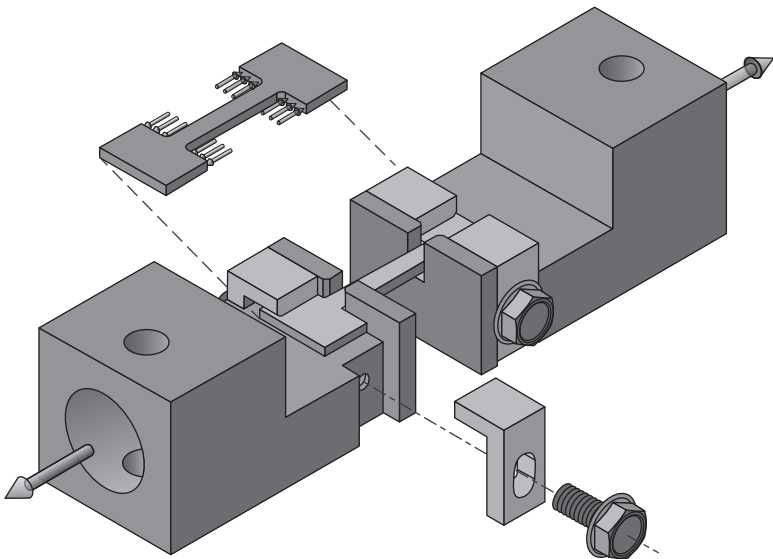


2.4 Material flow for various gauge length values (Abu-Farha *et al.* 2010a).

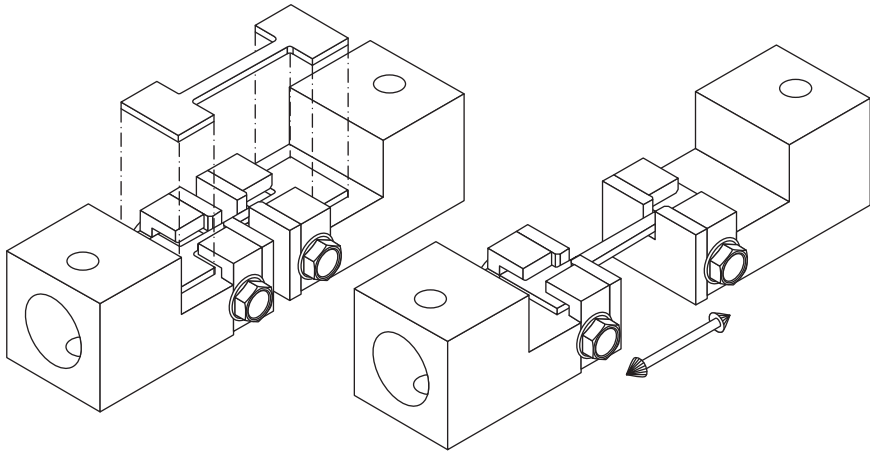
account. An optimum compromise is a gauge length-to-width ratio of ~ 4 , as concluded by most efforts in the field (ASTM E2448 2008, Johnson *et al.* 1994, Khaleel *et al.* 1996, Bate *et al.* 2008, Nazzal *et al.* 2009, Abu-Farha *et al.* 2010a).

2.5.2 Clamping device (grip)

By referring to the simple design proposed by the ASTM E2448 as a starting point, Fig. 2.5 shows a clamping device with modifications that aim to make it simpler and yet improve its suitability for testing superplastic materials at extreme temperatures (Abu-Farha and Curtis 2009, Abu-Farha *et al.* 2010a and 2010b). Similar grips were shown in the work of Bate *et al.* (2008). This grip design is centred about the ability to insert and mount the test specimen in the shortest possible time (labelled quick-mount grips in the figure). The grip is merely composed of a grip body and two L-shaped grip covers that are attached to the grip body's sides by two cap screws, and leaving a gap that corresponds to the thickness of the test specimen, hence allowing the specimen to simply slide into the grip. This gap can be easily altered to accommodate smaller and larger sheet thicknesses, since the grip covers are designed to glide along two slots on the sides of the grip body; this is clearly demonstrated by Fig. 2.5. As depicted in Fig. 2.6, gripping is simply achieved by sliding the specimen into the specified gap, which is aided by a slight chamfer on the inner edge of each of the grip covers. As a result, no pressure is applied to the grip region, hence material flow



2.5 Quick-mount grips specifically designed for testing materials at extreme temperatures.



2.6 A schematic demonstrating the ease of mounting a test specimen in the quick-mount grips.

is minimised. Furthermore, gripping the specimen does not require sliding/moving/fastening any of the clamping device's few components, which is a key feature for facilitating the testing procedure described later. Finally, tensile loading is exerted on (and transmitted through) the shoulders of the test specimen, and not the surface of the grip region. More details on the grips can be found in (Abu-Farha *et al.* 2009).

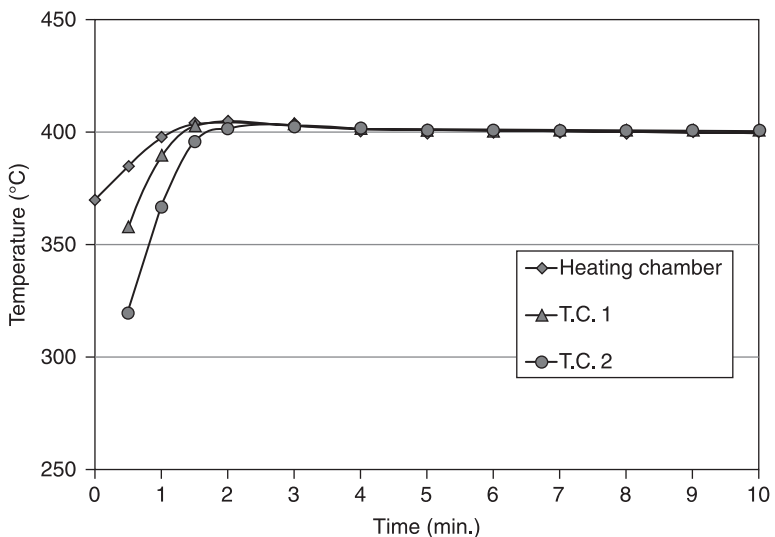
2.5.3 Testing procedure

The test set-up (furnace and the clamping device within) is first heated to the desired temperature, and then allowed sufficient time to equilibrate and permit the shafts, adaptors and grips to thermally expand and stabilise. This was shown to assist in controlling the later drop in temperatures during the gripping process, and bring the furnace back to the desired temperature in a short time. The crosshead beam is then moved so that the distance between the two grips is small enough for the specimen to be inserted without any interference. A test specimen is inserted into the space between the two grips as shown in Fig. 2.6, and left to slide by gravity into the top grip. After that, the cross-head beam is slowly moved so that the bottom shoulder of the specimen is in contact with the lower grip. The latter can be accurately sensed by monitoring the load cell reading, and making sure to stop as soon as the slightest force is detected. Finally, a certain holding time is allowed, and any needed adjustments (to compensate for any minute expansion in the specimen) are made, before the test is ready for initiation. It is important here to emphasise the specimen's freedom to thermally expand within the clamping device.

The described procedure can be done ideally without opening the furnace, and this is feasible from both the furnace and the clamping device perspectives.

Available furnaces or heating chambers often have an extra opening, excluding the top and bottom ones through which the grip shafts extend. For instance, INSTRON's 3119 environmental chamber has the extra opening on top, while MTS's 651 chamber has it on the side. Considering the grip, on the other hand, there is the very simple mounting aspect where there is no need to slide/move/fasten any parts. Recall that the operator's task is merely to deliver the specimen to the grips; once in place, the remaining steps are taken care of remotely by moving the cross-head beam. In addition, no matter how crude the specimen delivery process might be, mounting simplicity guarantees minimal chance of exerting non-axial loads on the specimen, and hence causing a distortion. Finally, note that the two grips are not supposed to be spaced by an exact distance for the specimen to glide in.

For the more traditional approach, where the furnace is opened and the specimen is inserted directly by the operator, the grips still allow for mounting/gripping in a very short time (around 5 seconds) (Abu-Farha *et al.* 2010a and 2010b). As will be expected, the furnace's temperature drops during those few seconds; nonetheless, the drop is quickly recovered, as demonstrated by the example presented in Fig. 2.7. In testing an Mg AZ31 specimen at 400 °C, actual temperature changes of both the furnace and the test specimen during the loading process were recorded. Two thermocouples were inserted at two different locations within the gauge length of a dummy test specimen. The thermocouples' temperatures were recorded against that of the furnace, as soon as the furnace is closed; a plot of



2.7 Example of temperature changes in both the furnace and the test specimen during the specimen mounting process in a tensile test at 400 °C (Mg AZ31B) (Abu-Farha *et al.* 2010b). T.C., thermocouple.

the results is presented in Fig. 2.7. As shown, the graphs confirm the test specimen reaching the furnace temperature in 2–3 minutes. Therefore, allowing a combined heating/holding time as short as five minutes would guarantee thermal equilibrium in the test specimen. It is to be mentioned here that specifying the exact amount of heating/holding time that different researchers shall be adopting is not intended; however, standardising this issue can be made easier with the quick-mount grips.

2.5.4 Heating/holding time

The ease of mounting the test specimen has a great impact on setting the guidelines for determining the heating and holding times. Not having to open the furnace means near-elimination of the ‘heating time’ issue, for two reasons. First: the temperature of the furnace will be maintained almost constant, since the only possible disturbance comes from introducing the test specimen. Second: the test specimen is anticipated to reach the test temperature soon after being inserted, due to its relatively small size; temperature measurements can be made to determine the precise length of time for the system being calibrated. Considering that situation, heating effects become less significant, and the short time that actually goes into heating the specimen can be simply associated with ‘holding time’. The latter can be easily determined for a specific system, and set to a small value (few minutes) that implies the minimal changes to the material’s microstructure. If, on the other hand, the second scenario (where the furnace had to be opened) is followed, then a combined heating/holding time needs to be determined through calibration and set. Note that it is more likely (with the proposed clamping device and testing approach) to be able to standardise this parameter and assign it smaller values, as was demonstrated in the example in Fig. 2.7.

2.6 References

- Abu-Farha, F. and M. Khraisheh, (2007a) ‘Analysis of Superplastic Deformation of AZ31 Magnesium Alloy’, *Journal of Advanced Engineering Materials*, vol. 9, no. 9, pp. 777–783.
- Abu-Farha, F. and M. Khraisheh, (2007b), ‘On the High Temperature Testing of Superplastic Materials’, *Journal of Materials Engineering & Performance*, vol. 16, no. 2, pp. 142–149.
- Abu-Farha, F. and R. Curtis, (2009) ‘Quick-Mount Grips: Towards an Improved Standard for Uniaxial Tensile Testing of Metallic Superplastic Sheets’, *Materialwissenschaft und Werkstofftechnik*, vol. 40, no. 11, pp. 836–841.
- Abu-Farha, F., M. Nazzal and R. Curtis, (2010a), ‘The Effects of Specimen Geometry on the Accuracy of Tensile Testing of Metallic Superplastic Materials’, *Key Engineering Materials*, vol. 433, pp. 325–331.
- Abu-Farha, F., J. Sabo and C. Herring, (2010b), ‘In Pursuit of an Integrated Methodology for Accurate Elevated Temperature and Superplastic Tensile Testing’, *Proceedings of the 5th International Manufacturing Science and Engineering Conference MSEC 2010*, Erie, PA, 12–15 October 2010.

- ASTM E8/E8M, (2009), 'Standard Test Methods for Tension Testing of Metallic Materials'.
- ASTM E21, (2009), 'Standard Test Methods for Elevated Temperature Tension Tests of Metallic Materials'.
- ASTM E2448, (2008), 'Standard Test Method for Determining the Superplastic Properties of Metallic Sheet Materials'.
- Bate, P., N. Ridley and K. Sotoudeh, (2008), 'Effect of Gauge Length in Superplastic Tensile Tests', *Materials Science and Technology*, vol. 24, no. 10, pp. 1265–1270.
- Chang, J., E. Taleff and P. Krajewsky, (2009), 'Effect of Microstructure on Cavitation During Hot Deformation of a Fine-Grained Aluminum–Magnesium Alloy as Revealed Through Three-Dimensional Characterization', *Metallurgical and Materials Transactions*, vol. 40A, no. 13, pp. 3128–3137.
- Chino, Y., H. Iwasaki and M. Mabuchi, (2004), 'Cavity Growth Rate in Superplastic 5083 Al and AZ31 Mg Alloys', *Journal of Materials Research*, vol. 19, no. 11, pp. 3382–3388.
- Comley, P., (2008), 'ASTM E2448 – A Unified Test for Determining SPF Properties,' *Journal of Materials Engineering and Performance*, vol. 17, no. 5, pp. 183–186.
- DIN EN 10002-1, (2009), 'Metallic Materials – Tensile Testing, Part 1: Method of Test at Ambient Temperature'.
- DIN EN 10002-5, (1991), 'Tensile Testing of Metallic Materials – Method of Test at Elevated Temperature'.
- DIN 50125, (2004), 'Test Pieces for Tensile Testing of Metallic Materials'.
- Hong, Y., C. RongShi and H. EnHou, (2009), 'Superplasticity of Mg-5.8Zn-1Y-Zr Alloy Sheet Fabricated by Combination of Extrusion and Hot-Rolling Processes', *Science in China Series E: Technological Sciences*, vol. 52, no. 1, pp. 166–171.
- ISO 6892-1, (2009), 'Metallic Materials – Tensile Testing, Part 1: Method of Test at Room Temperature'.
- ISO 783, (1999), 'Metallic Materials – Tensile Testing at Elevated Temperature'.
- ISO 20032, (2007), 'Method for Evaluation of Tensile Properties of Metallic Superplastic Materials'.
- Jäger, A., P. Luká, V. Gärtnerová, J. Bohlen and K. Kainer, (2004), 'Tensile Properties of Hot Rolled AZ31 Mg Alloy Sheets at Elevated Temperatures', *Journal of Alloys and Compounds*, vol. 378, pp. 184–187.
- JIS H 7501, (2002), 'Method for Evaluation of Tensile Properties of Metallic Superplastic Materials'.
- Johnson, K., M. Khaleel, C. Lavender, S. Pitman, J. Smith, M. Smith and C. Hamilton, (1994), 'The Effect of Specimen Geometry on the Accuracy of Constitutive Relations in a Superplastic 5083 Aluminum Alloy', *Materials Science Forum*, vols. 170–172, pp. 627–632.
- Khaleel, M., K. Johnson, C. Lavender, M. Smith and C. Hamilton, (1996), 'Specimen Geometry Effect on the Accuracy of Constitutive Relations in a Superplastic 5083 Aluminum Alloy', *Scripta Materialia*, vol. 34, no. 9, pp. 1417–1423.
- Kim, W., S. Chung, C. Chung and D. Kum, (2001), 'Superplasticity in Thin Magnesium Alloy Sheets and Deformation Mechanism Maps for Magnesium Alloys at Elevated Temperatures', *Acta Materialia*, vol. 49, no. 16, pp. 3337–3345.
- Lee, C., and J. Huang, (2004), 'Cavitation Characteristics in AZ31 Mg Alloys During LTSP or HSRSP', *Acta Materialia*, vol. 52, pp. 3111–3122.
- Liu, J., D. Chen, Z. Chen and H. Yan, (2009), 'Deformation Behavior of AZ31 Magnesium Alloy During Tension at Moderate Temperatures', *Journal of Materials Engineering and Performance*, vol. 18, no. 7, pp. 966–972.

- Ma, Y., and T. Langdon, (1994), 'Factors Influencing the Exceptional Ductility of a Superplastic Pb-62%Sn Alloy', *Metallurgical and Materials Transactions*, vol. 25A, no. 10, pp. 2309-2311.
- Nazzal, M., F. Abu-Farha and R. Curtis, (2010), 'Finite Element Simulations for Investigating the Effects of Specimen Geometry in Superplastic Tensile Tests', *Journal of Materials Engineering and Performance*, published online 6 August 2010. DOI: 10.1007/s11665-010-9727-9.
- Pilling, J., and N. Ridley, (1989), 'Superplasticity in Crystalline Solids,' The Institute of Metals, Maney Publishing, London.
- Sherby, O., and J. Wadsworth, (1990), 'Superplasticity in Metals, Ceramics and Intermetallics', M. J. Mayo *et al.* (eds), vol. 196, pp. 3-14, Materials Research Society, Pittsburgh, PA.
- Verma, R., P. Friedman, A. Ghosh, S. Kim and C. Kim, (1996), 'Characterization of Superplastic Deformation Behavior of a Fine Grain 5083 Al Alloy Sheet', *Metallurgical and Materials Transactions*, vol. 27A, pp. 1889-1898.
- Watanabe, H., A. Takara, H. Somekawa, T. Mukai and K. Higashi, (2005), 'Effect of Texture on Tensile Properties at Elevated Temperatures in an AZ31 Magnesium Alloy', *Scripta Materialia*, vol. 52, pp. 449-454.

Processes and equipment for superplastic forming of metals

G. BERNHART, P. LOURS, T. CUTARD, V. VELAY,
Ecole des Mines Albi, France and F. NAZARET, Aurock, France

Abstract: The industrial use of materials with superplastic behaviour has required the development of dedicated processes, including all the related tooling equipment. This chapter first describes the various superplastic sheet-forming processes. Then the industrial equipment is detailed along with the technological options that may be used for heating platens. Special focus is given to tools and dies, either metallic, ceramic or refractory concrete-based: their material grades and properties are discussed, as are the methods used for modelling them. Finally, emerging processes are identified.

Key words: superplastic forming, quick forming, single sheet, multiple sheet, diffusion bonding, forming equipment, press-furnaces, die materials, metallic tools, ceramic tools, die design, die simulation, emerging processes.

3.1 Introduction

Prior to discussing the details of the superplastic forming processes, it is of primary interest to review the most important features of the behaviour of superplastic materials. Indeed, most of the specific parameters related to forming are determined by this behaviour. At this time, only micrograin superplasticity is of importance in the fabrication of industrial parts, where fine grain size (lower or equal to 10 μm), fairly high temperature (typically greater than half the absolute melting temperature) and low, thoroughly-controlled strain rate (usually in the range 10^{-2} – 10^{-4} s^{-1}) are required to ensure high ductility. Both the strain-rate sensitivity of the material and the processing temperature have a major impact on the global achievable elongation. When properly conducted, i.e. when the above process parameters are controlled, superplastic forming (SPF) offers advantages over other fabrication methods in terms of attainable shapes and reduced parts count, as well as weight and cost savings.

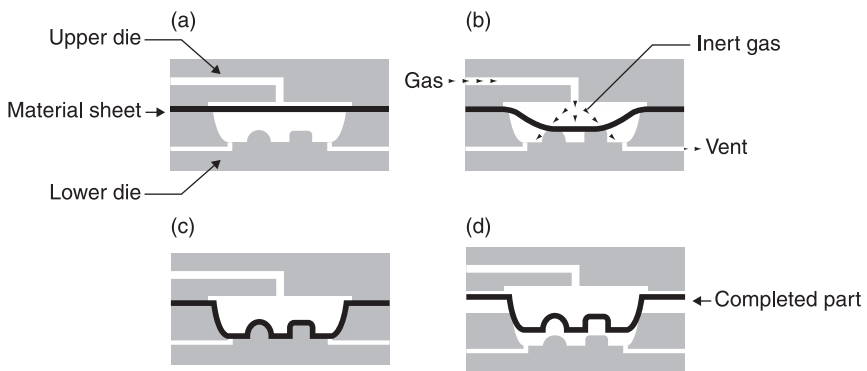
In industry today, SPF concentrates mainly on aluminium and titanium alloys. Even if general process features are the same, the requested forming temperatures (respectively 500°C and 900°C) have a major effect on equipment design, die alloy grades, lifetime and maintenance costs. Consequently, several parts of this chapter focus mainly on titanium SPF requirements.

3.2 Superplastic forming processes

The literature reports various methods and techniques for implementing SPF of dedicated materials.¹ Namely, blow forming, vacuum forming, thermo-forming, deep drawing or SPF combined with diffusion bonding (SPF-DB) for sheet materials, and forging or extrusion for bulk materials. Each of these methods is unique and specific in terms of its capability and its set of forming characteristics. For instance, SPF-DB is essentially conducted by combining diffusion bonding (DB) with blow forming and makes it possible to manufacture multiple-sheet structural parts and thus significantly enhance stiffness to weight ratio. Only those processes related to the blow forming of metal sheets, either single or multiple, are described in this chapter.

3.2.1 Single-sheet forming

Blow forming of single sheet is essentially based on the application of a gas pressure differential on the superplastic diaphragm, resulting in the deformation of the material into a given die configuration.² Pressure, typically in the range 10–30 bars, is applied through the injection, via a series of inlet tubes, of either air or a protective gas (typically argon), depending on the affinity to oxygen of the material to be formed. Figure 3.1, where a cross-section of the SPF die and sheet is shown, indicates the detail of the various successive sequences of the process. Die and sheet are maintained at the same temperature within a heating press. The gas pressure is imposed over the sheet causing the sheet to form into the lower part of the die. While it is being formed, the sheet simply vents to atmosphere the gas initially located within the lower die chamber. The lower die chamber may be



3.1 Single sheet blow forming of SPF materials showing the cross-section of die and sheet: (a) initial flat sheet inserted in between upper and lower dies; (b) progression of forming under gas pressure; (c) final shaped part in contact with lower die; and (d) removal of the part.

held either under vacuum or under some back pressure to control or even prevent cavitation in the formed material (e.g. aluminium alloys).

Generally speaking, the periphery of the sheet is maintained in a fixed position between upper and lower die and consequently does not draw in and slip as would typically be the case in a deep-drawing process. It is common to use machined grooves on the tooling to prevent the sheet from slipping and ensure tightness to prevent leakage of the forming gas. The sheet alloy can then stretch into the die chamber under the effect of the forming pressure. The process progresses further until the deformed sheet makes contact with the lower die cavity that dictates the shape of the part being manufactured. Of course, this results in considerable thinning of the sheet. For complex and deep-drawn parts, significant thickness gradients in the finished part may be encountered and can be avoided by prior appropriate localised chemical machining of the raw sheet. Reactivity between the sheet metal and the die material, which could result in sticking, thus making the finished part difficult to withdraw, is generally prevented by depositing a diffusion barrier, such as yttria or boron nitride, on the surface of the die.

Blow forming of a single sheet allows highly complex shapes to be manufactured, enhancing possibilities for creativity in the design and reducing lead times from concept to production. The process is carried out in one operation, thus reducing the number of joining or riveting operations required, and often allowing lower density alloys to be substituted for conventional materials.

3.2.2 Hollow cavity forming

Hollow cavity forming makes use of an initial tube, which is usually obtained after rolling and welding a flat sheet. The two ends of the tube are welded shut in order to create a closed cavity. Gas inlets are welded onto these in order to allow, first, an argon gas flow and then an internal pressure cycle to be applied. After deposition in the die forming cavity and a rise in the temperature, a complex final shape can be obtained. When compared to sheet forming no tightness is required between the dies. A formed part is shown in Fig. 3.2. Nevertheless, the sheet welding process requires special care as a local heterogeneous microstructure can cause non-uniform forming and/or local early rupture. In this respect, friction stir welding seems to be the more appropriate welding process as it allows optimisation of the local microstructure.³

3.2.3 Multi-sheet forming and diffusion bonding

In some cases, blow forming SPF can be beneficially combined with DB, which offers a dramatic extension to the process for fabricating high stiffness multi-sheet structures such as honeycomb components. Weight and cost savings are generally achieved by reducing the number of parts to be assembled and by promoting improved part consistency and interchangeability.



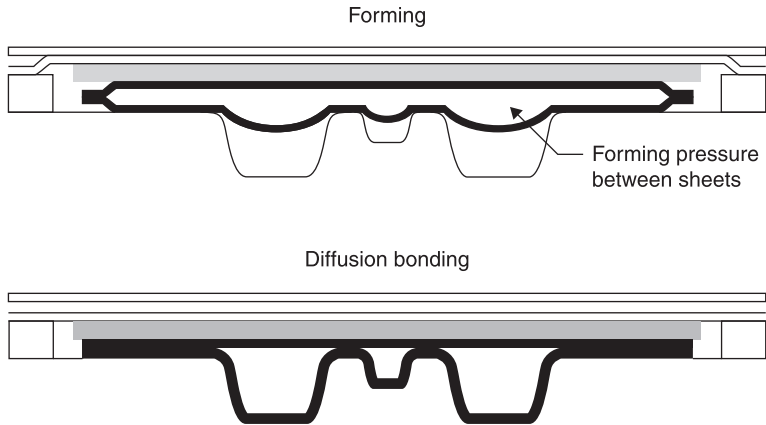
3.2 Hollow cavity SPF forming: steel tube after SPF (courtesy FormTech GMBH, www.formtech.de).

Basically, DB is a joining method carried out by promoting an intimate contact between two materials at high temperature. A low pressure, resulting in negligible strain, ensures that this contact is transformed into a bond. SPF and DB have evolved as a natural combination since the temperature requirements for both processes are essentially the same. In addition, it has been found that many superplastic alloys can be diffusion bonded under pressure in the same low range as that used for SPF.

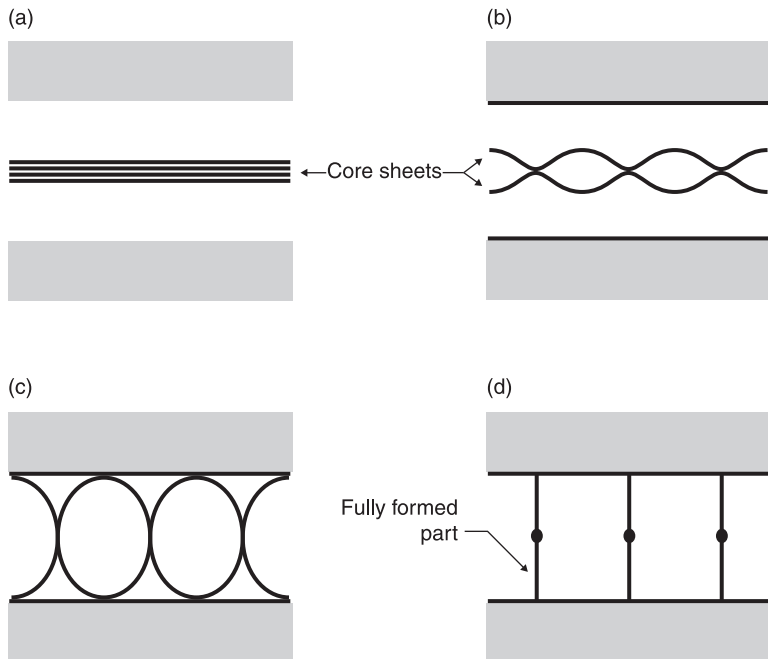
The SPF-DB process consists of different variations resulting in either two-sheet, three-sheet or four-sheet structural parts and is essentially based on the following sequence:

- DB of the sheets in given selected areas,
- subsequent expansion under the effect of the internal gas pressure.

For two-sheet parts (Fig. 3.3), one or both sheets are blown at unbonded locations. For three (or more) sheet structures, gas pressure forms the outer sheets (the skin) and the centre sheet(s) are stretched into a core configuration (Fig. 3.4). In order to develop diffusion bonds at predetermined localised zones, a parting agent or 'stop-off' acting as a diffusion barrier is deposited onto areas where no bonding is required. Which diffusion barrier is suitable may depend on the materials that are to be formed and also on the processing temperature, but the most widely used are yttria or boron nitride. These are also used to prevent



3.3 Two-sheet SPF blow forming and DB.



3.4 Four-sheet SPF blow forming and DB.

chemical-metallurgical reaction between the die and the sheet, as discussed above. Following DB, the area of the stop-off pattern is not bonded. Gas can be injected internally along the stop-off pattern, thereby causing the separation of the external sheets that progressively form and expand within a surrounding tool.

3.2.4 New rapid forming processes

In the last 15 years, the automotive industry has developed rapid forming processes with the aim of introducing SPF for mass production where required cycle times are less than a few minutes. Amongst them, two processes have been described in open literature for closure panel production:

- Quick Plastic Forming developed by General Electric.⁴
- High Cycle Blow Forming developed by Honda.⁵

These processes are based on the following key features: lubricant application and rapid preheating of blanks, hydraulic presses equipped either with heating platens supporting the dies or with self-heated insulated dies, and automated, fast sheet handling to ensure dimensional accuracy. In order to obtain forming steps of a duration of 1 to 2 minutes, special 5xxx aluminium alloy grades have been developed for low temperature ($\sim 450^\circ\text{C}$) and fast strain rate deformation (0.001 s^{-1} – 0.1 s^{-1}). Depending on the final shape, the forming operation may also include a hot-forming operation during die closure, so as to further reduce forming time.

3.3 Forming equipment

3.3.1 Standard press-forming equipment

Superplastic forming of industrial parts requires ‘press furnaces’. This equipment (Fig. 3.5) is composed of four-column hydraulic presses. On the lower and upper part, moving heating platens (see Section 3.3.2) are fitted on a metallic frame in order to heat the dies up to forming temperature, then to open the dies and give access to the sheet, and lastly to apply a closing pressure on the dies during the blow forming operation. The peripheral sides of the forming zone are heat-shielded with ceramic fibre blankets fixed on metallic frames. The size of the press is related to the size of the manufactured parts (or part set) and can vary from 60 tons (Research and Development platen size $80 \times 80\text{ mm}^2$) up to heavy industrial presses of several thousands of tons and platen sizes up to $5000 \times 3000\text{ mm}^2$. To achieve heating uniformity, the heating platens are generally divided into heating zones, each of which is individually temperature-controlled; the lateral heat shields may also be heated for thermal optimisation. The typical technical characteristics of a $2400 \times 1700\text{ mm}^2$ SPF press produced by ACB-PS company is given in Table 3.1.⁶

Two main blank removal techniques are used and these have an impact on press design:

- Manual or manual-assisted removal after opening of front door (Fig. 3.5), where an operator using blacksmith-type fire tongs removes the formed sheet directly from the hot zone of the furnace.



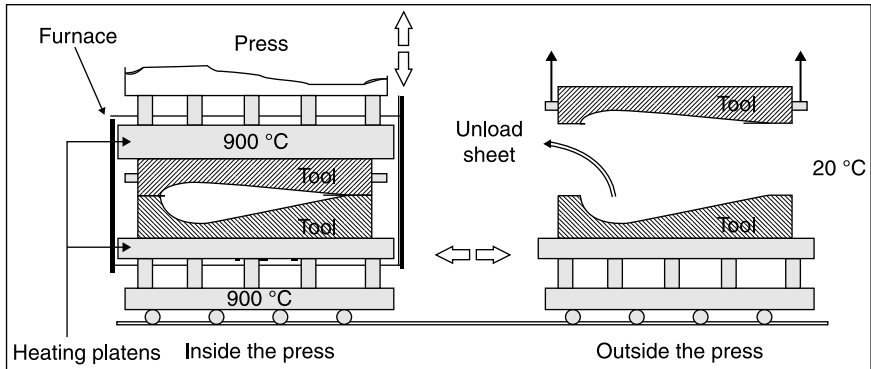
3.5 Standard SPF four-column press-furnace with manual blank removal after SPF (courtesy ACB-PS, www.acb-ps.com).

Table 3.1 Main characteristics of an SPF press

Platen dimensions	2400 × 1700 mm
Daylight of the press	2050 mm
Stroke of the press	1550 mm
Number of platen zones	18 per platen
Heating power per platen zone	12.5 kW
Heating zones in the heat-shields	1 in front plus 1 in rear
Heating power per heat-shield zone	12 kW
Installed heating power	474 kW

- Moving platen technology (Fig. 3.6) where the lower part of the press furnace (insulation, heating platen and die) is placed on a shuttle in order to allow sheet removal outside the heating zone.

A classic titanium alloy-forming production run is conducted as follows: heating of die till 900°C is achieved by conduction inside the press-furnace



3.6 Shuttle press with moving platen manufacturing principle.

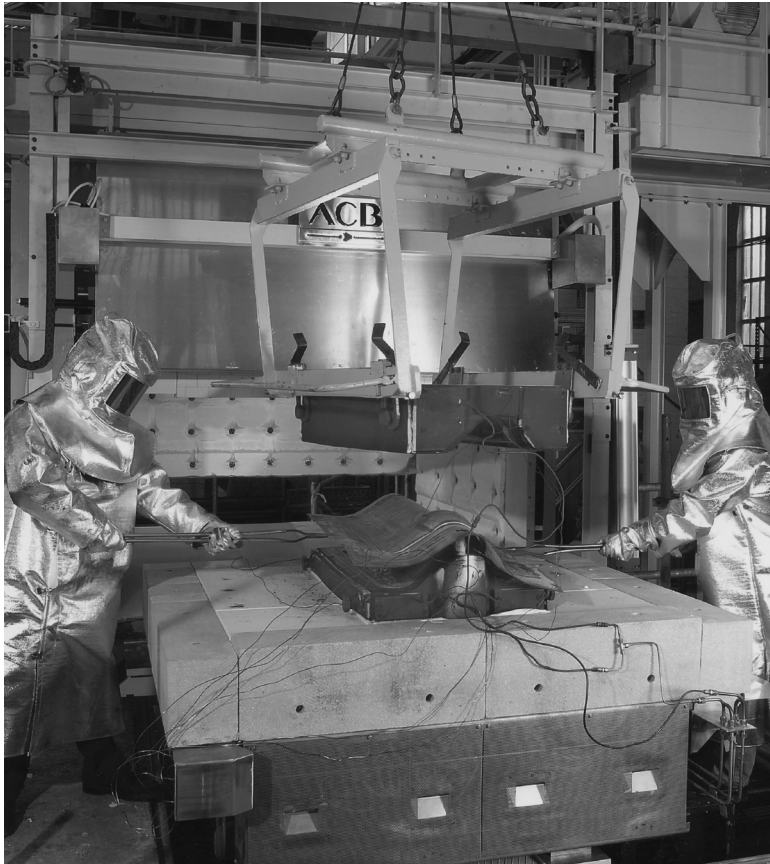
during a slow heating up. Duration of heating up can take 24 hours, depending on the heating rate: the higher the heating rate, the higher the transient stresses in the die during heating. After having reached quasi-isothermal conditions, the mould is taken out of the press using the mobile bottom-heating plate and the upper part of the mould, if present, is removed. Titanium sheet is placed in the die, which is pushed into the furnace, after closure of the die. As the die surface temperature drops during this operation, a waiting period that can reach up to one hour is required in order to return to an isothermal configuration.

Before sheet forming with a variable argon pressure, a clamping load is applied on the edge of the sheet in order to avoid gliding and to ensure that the mould remains airtight. After a forming period of approximately one hour, the gas pressure is withdrawn and the clamping load is removed, and the insulating door of the press-furnace is opened to withdraw the die and remove the formed titanium part (Fig. 3.7). This cycle is repeated as much as is necessary to superplastically form the number of components required during the given production run. At the end, the die is cooled down slowly in the furnace (a duration of about 24 hours).

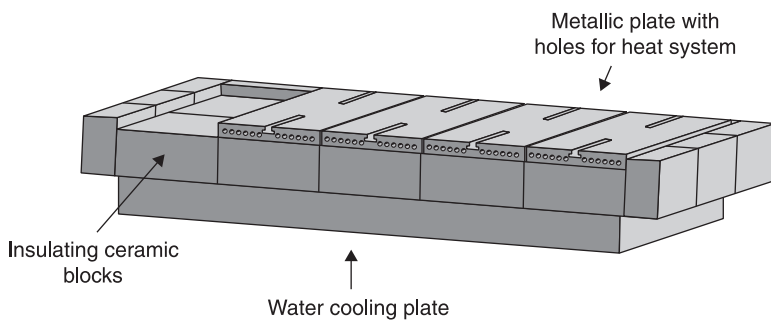
3.3.2 Heating platen technology

Heating platens are used in order to apply a uniform temperature as well as to provide the clamping loads on the SPF dies. Two main platen technologies are available in industry, either metallic or ceramic.

- *Metallic heating platens.* A monolithic heat resistant cast steel (HRCS) metallic platen is drilled with holes near the outer surface (Fig. 3.8) in order to allow the introduction of heating canes. Ceramic blocks are added to insulate the metallic frame of the press from heat transfer. Often a water-cooling plate is added between the ceramic insulation and the press structure. The main



3.7 Blank removal operation with a shuttle press (courtesy ACB-PS, www.acb-ps.com).



3.8 Metallic monolithic HRCS heating platen (courtesy EDM I).

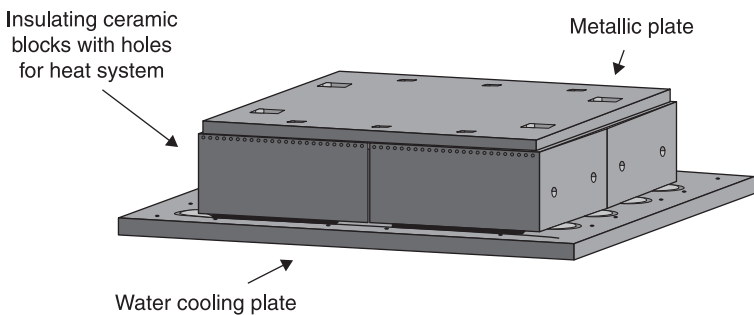
advantages of this system are that it makes it possible to perform rapid heating and to simplify the design of the upper SPF die fixing. Nevertheless, this solution has some drawbacks. First, the cost of this large, heavy platen is very high, as the requested grades contain more than 50% Ni and often also contain Molybdenum. Second, these platens are subjected to thermomechanical deformation that induces bad tool contact and accelerated degradation of the die. Finally, the gap between heating canes and hole can increase at high temperature due to thermal expansion and thus generate heat loss.

- *Ceramic heating platen technology.* This technology makes use of a ceramic heating block (Fig. 3.9) containing the heating system within it (heating canes as for metallic die technology). Sometimes a metallic plate can be fixed on the ceramic block but it is not mandatory. As in the previous solution, a water-cooling platen is used to insulate the press frame. The main advantage of this technology is that it divides the heating area into several heating zones, which means that maintenance costs are reduced when local damage occurs. Nevertheless, the cost of a standard heating platen made of vitreous silica remains high as this ceramic is brittle and can fracture rapidly. Another solution is to use reinforced refractory castables (see *Dies based on reinforced ceramic materials* in Section 3.4.3) with a quasi-brittle behaviour that avoids catastrophic failure. In such solutions heating threads may also be used instead of heating canes.

For all these set-ups, maintenance costs can vary for the same assembly design. The quality of the parts of the installation has a great influence on the lifetime of the structure.

3.3.3 Emerging innovative forming processes

Three emerging and innovative forming technologies have been reported in the literature which dramatically reduce heating costs and cut heating-platen maintenance costs whilst increasing productivity through reduced cycle time.



3.9 Ceramic heating platen technology (courtesy EDM).)

Two solutions aim to avoid costly die heating by applying the heat flux directly to the blank, either using one or more rapid moving Laser(s)⁷ or with infra-red heating lamps.⁸ The latter technique tries to promote rapid, local surface die heating using induction heating technology.⁹

All these processes are still under study at the laboratory scale.

3.4 Forming dies

3.4.1 Die environmental constraints

Tools employed in the SPF process are generally heated to the forming temperature and are subject to the internal gas pressure used to deform the sheets as well as to the clamping loads necessary to close the die and guarantee tightness. Generally speaking, the gas pressure is not high enough to constitute a critical design factor for a SPF die. More important are the clamping loads and the thermomechanical stresses involved in the implementation of the process, where successive sequences of heating and cooling are imposed on the dies. In addition, dies are subject to severe environmental conditions caused by the fairly high temperature and the oxidising atmosphere. Thermal stresses can provoke permanent die distortion, affecting the dimensional characteristics of the finished parts. Oxidation and possible spallation of the thermally-grown oxides can cause surface degradation, which tends to alter the surface finish of the manufactured parts and/or locally initiate cracking that can detrimentally propagate under the effect of the mechanical stress. A thorough selection of die materials showing high strength, satisfactory creep and thermomechanical fatigue resistance and oxidation resistance at the forming temperature can drastically reduce the risk of die degradation. It is preferable to use materials exhibiting a low thermal-expansion coefficient and which do not suffer from phase transformation within the typical process temperature range. Other important environmental factors are the metallurgical compatibility of the die material, the diffusion barrier that may be deposited on the die surface to minimise interaction and the sheet to be shaped, which can be highly reactive, as, for instance, in the case of Ti alloys.

3.4.2 Metallic dies

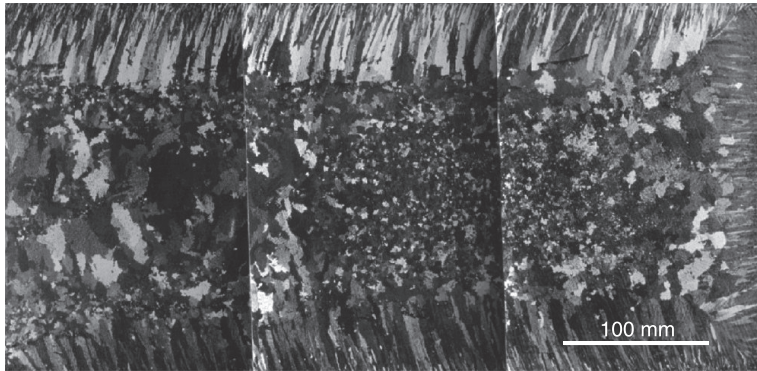
Numerous metallic grades have been developed over the years to address the requirement of the SPF environment for a temperature range of 700 °C–900 °C.¹⁰ They are elaborated by casting and are mainly in the family of Ni–Cr–Fe HRCS. These were mainly derived from CRES (Corrosion RESistant Steel) grades used in the petrochemical and metallurgical industries. Composition is often related to the location in the press-furnace, either heating platens and tanks (50% Ni), or inserts (40% Ni). Over the years, alloy composition has been carefully selected by die manufacturers (amongst them Aubert & Duval (France), Cronite (UK) and

RTI International Metals (USA)) so as to offer an optimal compromise between manufacturing, performance and cost. The most important factors in die design, apart from the cost of the alloying element, are castability, machinability and weldability before and after service.¹¹

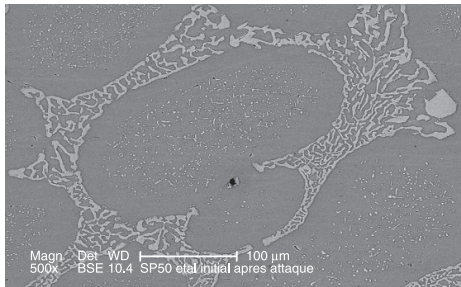
- *Composition and the effect of chemical elements.* As with many metallurgical issues, the optimisation of die alloy chemistry results from a complex compromise. A proper implementation of the process requires a composition appropriate to the specific requirements of SPF discussed above. Metal alloys used for dies are basically heat-resistant highly-alloyed cast steels with the following various elements. About 25wt% chromium and 0.5–2wt% silicon guarantees a fairly good resistance to oxidation. Nickel – in the range 20–50wt% and to a lesser extent manganese (circa 1wt%) – tends to stabilise the austenite phase and enhance creep resistance. Note that early dies were sometimes made with almost nickel-free ferritic alloys. However, those alloys, though very resistant to spallation subsequent to oxidation, showed poor creep properties and are no longer used. A ratio between the Ni and Cr content greater than 1 should drastically limit the sigma phase precipitation during long term exposure at high temperature (600 °C–900 °C) as well as the resulting alloy embrittlement. Though Si and Mn may promote the formation of a sigma phase, carbon inhibits this detrimental phase. However, depending on the die thickness and beyond 0.5wt%, carbon lowers the resistance to crack initiation and propagation caused by thermal shocks and thermal fatigue. Tungsten and/or niobium are generally added to form, as Cr does, primary eutectic carbides and secondary carbides that precipitate during high temperature ageing typically at 900 °C. These two carbides populations ensure mechanical strength and resistance to creep deformation and fracture. Typical die alloy compositions are given in Table 3.2.
- *Process, phases and ageing.* The dies are manufactured by sand casting. The macrostructure of the materials shows the typical thin outer equiaxe, and the intermediate columnar and the central equiaxe zones, with respective dimensions depending on the process parameters and the composition of the alloy (Fig. 3.10a). Primary dendrite arms are delineated by eutectic carbides that form an almost continuous network.¹² This network of connected $M_{23}C_6$ ($M = Cr, W, Fe$) and/or MC ($M = Nb$) particles is hard but brittle and guarantees to some extent the cohesion of the material. Dendrites are austenite phases in which secondary carbides, whose precipitation initiates during an ageing treatment at 900 °C, develop in the alloy in the manufacturing phase and complete their formation during high-temperature exposure once the die is in service. Figure 3.10 shows optical, scanning-electron and transmission-electron micrographs of a die alloy.
- *Oxidation and spallation.* Oxidation resistance of metallic alloys for SPF dies essentially results from the formation at high temperature of a slowly growing (parabolic rate constant at 900 °C, K_p in the range 1.3×10^{-12} to 1.9×10^{-12} g² cm⁴ s⁻¹) and fairly adherent oxide scale.¹³ This scale is a complex stratified layer composed of a thin amorphous silica SiO₂, located at the interface

Table 3.2 Chemical composition of typical heat-resistant cast steels for SPF dies (%)

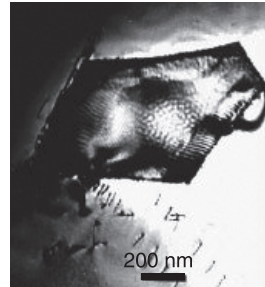
	Fe	C	Cr	Ni	Mn	Si	P	S	Mo	W	Nb	V
GX30NiCr35–25	Bal.	0.175	25.20	34.85	1.107	0.627	0.01	0.008	0.282	0.193	1.011	–
GX30NiCr39–24	Bal.	0.313	24.40	39.2	1.11	1.45	<0.001	0.0011	<0.020	<0.002	0.328	0.038
GX45NiCr49–27	Bal.	0.458	26.76	49	0.98	1.21	0.008	0.001	–	4.9	–	–



(a)



(b)



(c)

3.10 Macrostructure and microstructure of typical HRCS for a SPF die: (a) foundry structure; (b) dendrite arm, primary and secondary carbides; and (c) detail of a secondary Cr_{23}C_6 carbide.

with the metal alloy, an intermediate spinel MnCr_2O_4 and an outer Cr_2O_3 scale. Following cumulative SPF manufacturing that results in long-term exposure at high temperature in cycling conditions, this thicker outer scale can spall under the effect of the thermomechanical stress, especially for austenitic alloys showing a high difference in thermal expansion coefficient with the thermally grown oxide ($\alpha_{\text{substrate}} = 18 \times 10^{-6} \text{ }^\circ\text{C}^{-1}$ versus $\alpha_{\text{oxide}} = 8.5 \times 10^{-6} \text{ }^\circ\text{C}^{-1}$).

- **Mechanical strength and rupture (tensile, creep, fatigue, toughness).** Table 3.3 gives some thermomechanical properties of three metal alloys used to make dies, showing their moderate tensile mechanical characteristics, including a very poor ductility, even at high temperature. This fairly high brittleness,

Table 3.3 Mechanical and physical properties of typical heat-resistant cast steels for SPF dies

T (°C)	E (J/cm ²)	Yield stress (MPa)			Ultimate tensile strength (MPa)			Rupture strain (%)			Thermal conductivity (W/mK)			Creep behaviour: time (h) for 0.5% strain					
		20	500	750	900	20	500	750	900	20	500	700	900	850 °C/35 MPa	900 °C/35 MPa	950 °C/25 MPa			
	20	232	154	124	111	308	246	239	125	2.0	4.0	7.0	19	20	24	27	122	-	46
GX30NiCr35-25	15	220	175	-	77 (925 °C)	335	300	-	140	2.0	5.0	-	35 (925 °C)	18	23	26	209	27	152
GX30NiCr39-24	-	259	198	170	144	373	304	299	183	2.0	2.5	2.1	18	18	23	26	209	27	152
GX45NiCr49-27	6																		

resulting in impact strength energy lower than 15 J/cm² at room temperature and elongation to fracture lower than 10% up to 750 °C is directly related to the microstructure of the alloys. The soft austenite matrix cannot deform as it is embedded in a stiff, hard and brittle carbides network, prone to crack upon loading. On the other hand, these connected primary eutectic carbides – as well as the secondary carbides promoted by ageing – are effective in holding the whole microstructure as the alloy is strained in creep conditions. This results in rather good properties, as indicated by the time for 0.5% strain for various conditions of stress and temperature (Table 3.3).

- *Weld repair and life extension.* As a consequence of the high brittleness inherent to the microstructure of their constitutive alloys, metal dies are prone to crack upon cumulated thermal cycles generating thermomechanical fatigue. Cracks initiate and propagate along the hard, brittle primary carbides network. In order to extend the life of dies, multi-pass arc-welding repair (either with standard IN625 filler metal for cosmetic repair or with filler metals with composition close to that of the base metal for structural repair) can be carried out successfully.¹⁴ Unfortunately, thermal stresses resulting from welding usually generate the formation of new cracks because of the very low ductility of the base metal. The occurrence of weld-induced cracks can be avoided or at least limited using various means such as:
 - the pre-heating of the die (around 400 °C),
 - the surface decarburisation of the die, and/or
 - the buttering of the die using soft metal prone to accommodate weld stresses prior to weld repair. Buttering has proved to be very efficient in limiting the weld-induced cracking but drastically reduces the fatigue life of the material.

3.4.3 Ceramic based dies

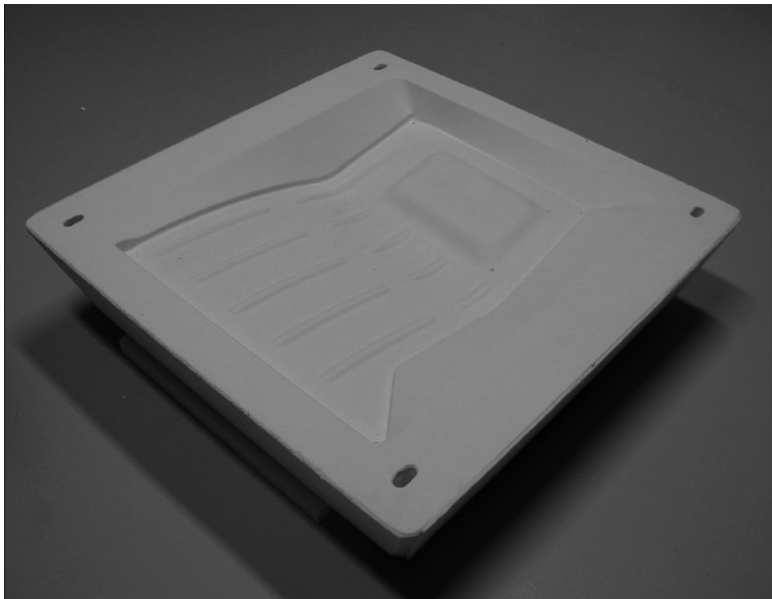
In some cases, SPF toolings made of HRCS suffer some limitations due to long lead times and high non-recurring costs. Various works have been done to develop SPF ceramic dies as a cheaper alternative versus HRCS for prototyping, both for small series and for low-rate production. On the one hand, dies based on non-reinforced ceramic materials have been considered, for example in the field of the SPF of medical or dental prosthesis. But in the field of industrial part production, their brittleness is the biggest limitation. On the other hand, reinforcement routes have been followed to develop tough dies based on reinforced ceramic materials for shaping TA6V aeronautical parts. Introducing reinforcement rods or short fibres in a ceramic material today allows for premature cracking of SPF ceramic dies to be avoided. The last remaining technical difficulty to overcome for ceramic dies is the question of surface degradations. Recent efforts have been made to develop hard or non-reactive coatings to protect the surface.

Dies based on non-reinforced ceramic materials

The first use of ceramic die technology for SPF manufacturing was reported in 1988.¹⁵ A slab of ceramic was manufactured with the desired shape cast into the top surface of the die and placed into a HCRC tank in order to support the forming stresses. Several trials have been conducted over the years by various industries for the use of such monolithic ceramics for industrial dies but these trials were not successful in the end.

For example, during a French research program dedicated to SPF tooling for shaping Ti alloy aeronautical parts, work was done to develop a fused silica-based refractory solution. The process is based on a slurry casting route followed by a 1200 °C firing. Such a process is well suited to obtain the required accuracy for SPF toolings in terms of geometry and of surface roughness. Figure 3.11 shows an example of a fused-silica SPF die. Due to their low thermal expansion coefficient, such materials exhibit a very high thermal shock resistance. Up to 950 °C, the materials are characterised by a brittle linear elastic behaviour and their rupture stress dispersion is characterised by a Weibull's modulus close to 15. But such toolings still suffer from their brittle behaviour and also from rather high costs.

A method of SPF forming using a ceramic moulding cavity set into a stronger cylindrical HCRC pressure vessel was developed for manufacturing titanium TA6V dental and medical implants.¹⁵ Phosphate-bonded investments have been



3.11 Prototype of a fused-silica-based SPF tooling for shaping a TA6V aeronautic part (courtesy, Prodem).

considered because they meet the different requirements for such applications. Particularly, they have sufficient strength and durability to resist hot creep deformation, have good resistance at high temperature under the forming pressure, exhibit a crack ‘initiation and/or propagation’, and are relatively weak in tension, thus allowing the fully-adapted sheet to be removed from the die surface even if there are re-entrant surfaces present in the die. This material makes use of the reaction that occurs when a blend of $\text{NH}_4\text{H}_2\text{PO}_4$ and MgO powders are mixed with water. Several works have shown that the main reaction product is Struvite ($\text{NH}_4\text{MgPO}_4\cdot 6\text{H}_2\text{O}$). Recent works using P solid-state MAS-NMR have provided additional information on the nature of the set microstructure.

Dies based on reinforced ceramic materials

For the Boeing Company, premature cracking was the biggest limitation for using ceramic tools. This problem was solved by adding high-strength (1300 MPa) reinforced rods made of fused silica oxides of silicon or alumina, which are cast directly into the ceramic aggregate.¹⁷ These rods are placed so as to diminish the twisting and deflection loads, primarily along the bending or expected flexural joints. The service life of such stand-alone ceramic dies has been increased substantially using this design technique. Figure 3.12 shows a picture of a reinforced die that has been used to produce titanium parts for commercial jetliners. For Boeing, if ceramic dies are to be used in a hot press, additional considerations must be taken into account for the press platen, bolster plate and insulation design. The main objective is to limit the consequence of a possible catastrophic failure of a ceramic die containing a pressurised part.

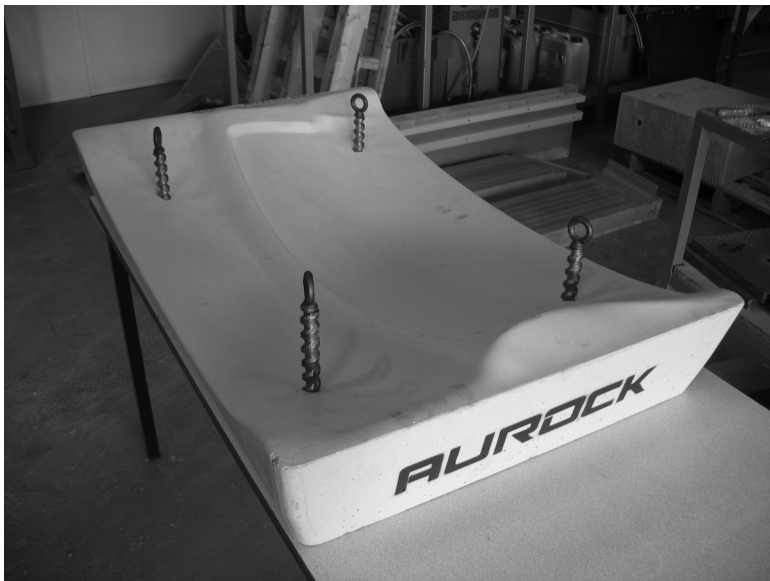


3.12 Ceramic die reinforced with fused silica rods for TA6V aeronautic parts forming (courtesy Dan Sanders, Boeing Company).

Another reinforcement route was followed by The Research Centre on Tools, Materials and Processes of Ecole des Mines d'Albi: it involved the reinforcement of a refractory castable with short metallic fibres (FRRC).¹⁸ The refractory castable is made of bauxite aggregates, fumed silica, alpha-alumina and an ultra-low content of a calcium-alumina cement. It is reinforced with 1.5vol% of short stainless-steel fibres. Precursors are first mixed in a planetary mixer and the material is then cast under vibration at room temperature. After drying, the FRRC is fired at high temperature to stabilise the material microstructure and the tooling geometry. Introducing metallic fibres drastically changes the mechanical behaviour of the refractory concrete. Brittle at the non-reinforced state, the refractory concrete's behaviour becomes non-linear and non-brittle when fibres are added. Such reinforcing effects are effective in the whole Ti alloy SPF temperature range (Fig. 3.13). Industrial FRRC dies are classically used for shaping aeronautic parts for prototypes and for small series. Up to now, they mainly consist of FRRC inserts placed in HRCS containers. Developments of stand-alone FRRC dies are now in progress. In order to address very high temperature of SPF forming (>950 °C), for example for refractory or TiAl alloys, ceramic fibre (i.e. Al_2O_3) reinforcements are under investigation.

Coatings on ceramic dies

Various works have been conducted, and are still in progress, to overcome the surface degradation of SPF ceramic tools. Boeing has completed the



3.13 Fibre reinforced refractory concrete (FRCC) SPF die for TA6V aeronautic parts forming (Aurock Company, www.aurock.com).

development of a cordierite-based ceramic glaze coating that can be plasma sprayed onto the ceramic die surface to create a hard protective shell. The Aurock Company is following other routes to develop oxide ceramic coatings for FRRC dies.

3.4.4 Die design and lifetime simulation

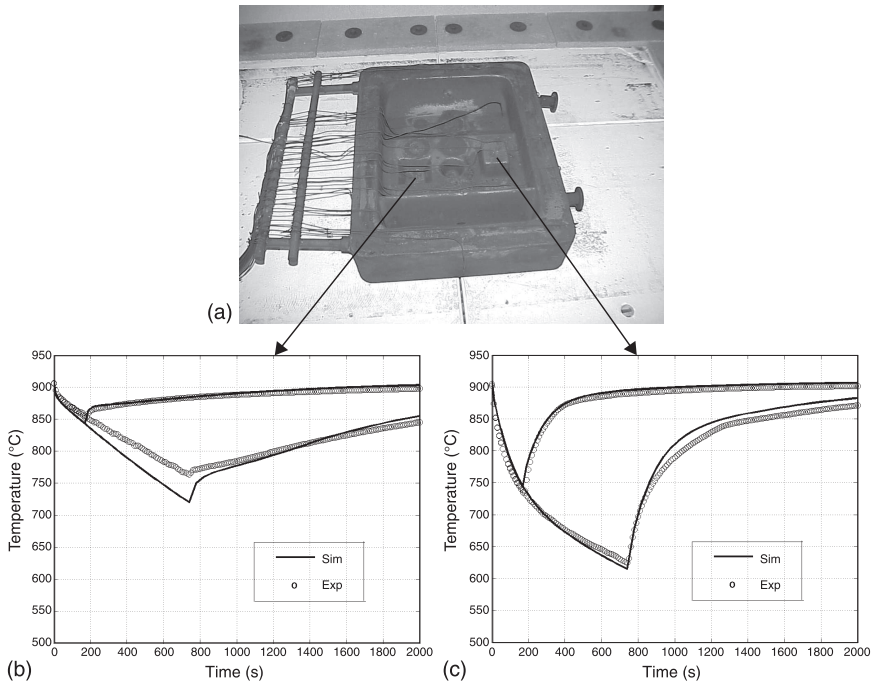
In order to optimise tool design and improve the lifetime, uncoupled thermo-mechanical modelling of SPF dies has been introduced. Different steps are required to successfully perform a thermo-mechanical simulation on a HRCS or reinforced ceramic die. First, the severe environmental conditions have to be taken into account as the die thermal cycle varies between a maximal temperature close to 900°C (inside the heating press) and a minimal temperature close to 400°C (outside the press and after sheet removal). These thermal cyclic conditions are repeated as many times as necessary to produce the required number of parts, and to induce mechanical stresses and cyclic plasticity creep or microcracking that may lead to the premature failure of the die. In order to assess the thermal gradient occurring in the die, a thermal Finite Element analysis is first calibrated using temperature measurements performed on industrial SPF dies. In a second step, a behaviour model has to be defined in order to provide accurate strain–stress responses when the material is subjected to industrial process conditions (i.e. cyclic loadings, viscous or damage effects). Last, the mechanical model needs to be implemented using a Finite Element software in order to simulate all the forming operations using the previous thermal analysis.

Transient thermal modelling of the HRCS SPF tool

Transient thermal modelling of SPF tools requires the knowledge of all the physical properties of the die material (density, thermal conductivity, heat capacity, emissivity) as well as the conductive, convective and radiative heat-exchange conditions inside and outside the furnace. The latter are identified by comparing calculated temperatures against the measured heating and cooling experiments done either on industrial dies or on laboratory model dies.^{19,20} Typical values are: emissivity of 0.82 for HRCS and 0.5 for ceramic dies; convective heat exchange coefficient $h = 5 \text{ W/m}^2/\text{K}$ and ambient temperature either 900°C in press-furnace or 25°C outside during blank removal. Figure 3.14 shows the good correlation between experimental and calculated thermal cycles measured at different surface locations of a HRCS model die containing holes and humps.

High-temperature HRCS die simulation

As the temperature cycling is complex, advanced cyclic behaviour and lifetime models are required to address such simulations. In order to take into account

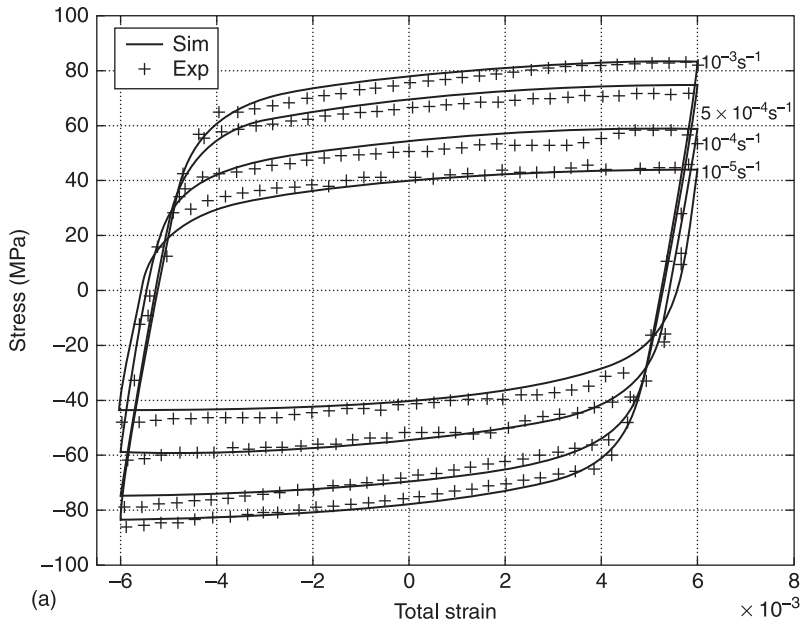


3.14 Comparison of experimental and calculated thermal cycles for two different locations at the surface of a test mould (a): (b) hole and (c) hump.

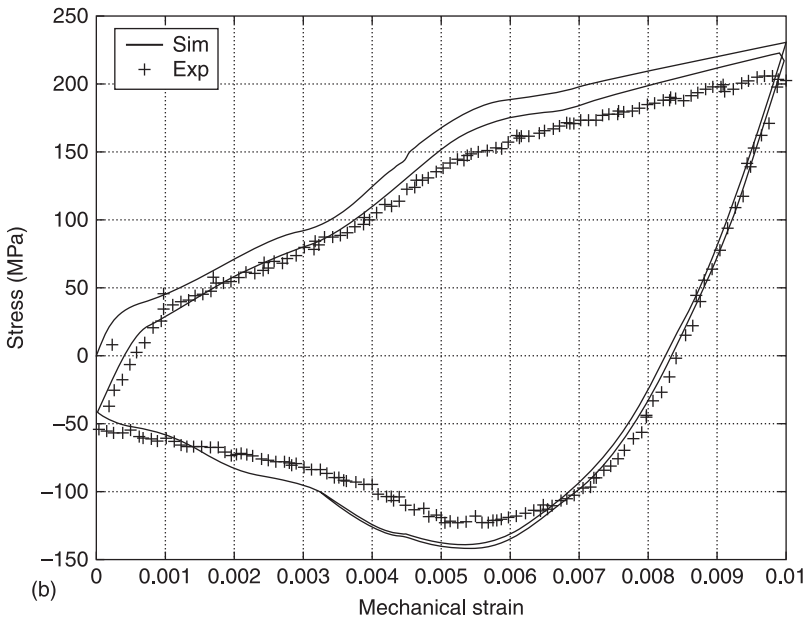
temperature and strain-rate dependent cyclic plasticity, two main approaches were adopted:

- An uncoupled plasticity-creep model, where cyclic plasticity is modelled using a non-linear kinematic hardening and creep deformation during dwell period using a power-law (Norton) creep,²¹ and a bilinear strain-range partitioning method for creep-fatigue life prediction.
- Coupled cyclic visco-plasticity, including non-linear kinematic hardening, isotropic hardening and power-law creep,²² and strain amplitude-based continuum damage models. This latter behaviour model has the advantage of taking account of strain-rate effects that are effective at high temperature.

Model parameters have to be identified in conducting high temperature isothermal cyclic fatigue tests, and their validation is performed by comparing model response with experimental complex anisothermal out-of-phase cyclic tests. Figure 3.15 shows such a comparison at 950 °C for several strain rates and in anisothermal conditions between 950 °C and 500 °C. After validation, behaviour



(a)



(b)

3.15 (a) Comparison between experimental and simulated loops at different strain rates for a temperature of 950°C. (b) Model prediction for an out of phase thermo-mechanical fatigue test.

and lifetime models were incorporated in commercial FE software for die calculation.

3.5 Conclusion

The SPF process allows complex parts to be shaped using low-deformable alloys. If technological costs for aluminium blank forming are reasonable, the high temperature required by Titanium-alloy forming (900°C) addresses many scientific and technological issues. Among them, resistive heating technology and die costs, lead-time and maintenance are limiting factors for SPF process dissemination.

Nevertheless recent improvements have been made by industry or are under investigation in research laboratories. This has, for example, permitted the introduction of this process in the automotive industry for aluminium-alloy mass production using QPF-like processes. On the other hand, the use of new low-cost die materials based on reinforced silica or castables reduces non-recurring costs and die-production lead times, and offers new opportunities for prototype manufacturing or part redesign. The future of SPF remains dependent on the capacity of scientists and engineers to introduce more sustainability in this process by trying to reduce environmental constraints (temperature, heatshield fibres, etc.) and cut operational costs (energy consumption), which are mainly related to huge heat loss in the standard press-furnace technology.

3.6 References

1. Padmattan K A and Davies G T (1980), *Superplasticity*, Germany, Springer Verlag.
2. Hamilton C H and Ghosh A K (1988), *ASM Handbook* 14, 853–873.
3. Sanders D, Edwards P, Grant G, Ramulu and Reynolds A, (2008), ‘Superplastically formed friction stir welded tailored aluminium and titanium blanks for aerospace applications’, [hal-00338221 – version 1], *EuroSPF 2008*, Carcassonne, France.
4. Krajewski P E and Schroth J G (2007), ‘Overview of Quick Plastic Forming Technology’, *Mat Sc Forum*, 551–552, 3–12.
5. Saito K, Watanabe J and Nakao K (2008), ‘Application of aluminium blow forming for automotive closure panel’, [hal-00349245 – version 1], *EuroSPF 2008*, Carcassonne, France.
6. Petiot A and Favre T (2007), ‘Tool thermal behaviour in SPF environment’, *Mat Sc Forum*, 551–552, 111–122.
7. Jocelyn A,(2010), ‘From Indirect to Direct Heating of Materials Using Lasers’, *Key Eng Materials*, 433.
8. Bernhart G, Cutard T, Le Maoult Y, Schmidt F and Arcens JP (2008), ‘Infra-red sheet heating assisted Superplastic Forming’, *EuroSPF 2008*, Carcassonne, France.
9. Matsen M, (2010), ‘Induction Heating Technology for Superplastic Forming and Diffusion Bonding of Titanium Sandwich Panels’, *Key Eng Materials*, 433.
10. Barnet P and Moraux J Y (2008), ‘25 years of experiment in the tools for superplastic forming of Ti alloys evolution of metallic materials and design in foundry’, [hal-00371031 – version 1], *EuroSPF 2008*, Carcassonne, France.

11. Bernhart G, Velay V and Lours P, (2010), 'Heat Resistant Ni-Cr-Fe Steels for Superplastic Forming Dies: From Material Microstructure to Die Design' *Key Eng Materials*, 433, 77–84.
12. Baleix S, Lours P and Bernhart G, (1999), 'High Temperature Mechanical behaviour of Ni-Cr-Fe heat resistant cast steel', *8th International Conference on Mechanical Behaviours of Materials*, Victoria (Canada) 2, 653–657.
13. Baleix S, Bernhart G and Lours P, (2002), 'Oxidation and oxide spallation of heat resistant cast steels for superplastic forming tools', *Mat. Science and Engineering A*, 372, (2), 155–166.
14. Branza T, Deschaux-Beaume F, Velay V and Lours P, (2009), 'A microstructural and low-cycle fatigue investigation of weld-repaired heat-resistant cast steels', *J of Mat Proc Technology*, 209 (1), 944–953.
15. Cadwell G, (1988) 'Advanced in Production Technology for SPF of Titanium', Society of Manufacturing Engineers, Effective applications of SPF and DB for the Engineering Specialist, Section 4.
16. Curtis R and Juszczak A, (2001), 'Dies for dental superplastic forming – preliminary experiments to quantify the effect of handling techniques on the strengths of investment materials', *EuroSPF 2001*, Villard-de-Lans, France.
17. Sanders G (2004), 'A Production System Using Ceramic Die Technology for Superplastic Forming', *Mat Science Forum*, 447–448, 153–158.
18. Bernhart G, Nazaret F and Cutard T., (2007), 'Fiber reinforced refractory castables: an alternative solution for SPF die manufacturing', *Mat Science Forum*, 551–552, 37–42.
19. Velay V, Cutard T and Guegan N (2008), 'Thermal Behaviour Modelling of Super Plastic Forming Tools', [hal-00348613 – version 1], *EuroSPF 2008*, Carcassonne, France.
20. Shang J, Leen S B and Hyde T H, (2006), 'Finite element based methodology for predicting the thermomechanical behaviour of superplastic forming tools', *Proc IMechE, Part L: J materials:Design and Applications*, 220 (L3), 113–123.
21. Deshpande A A, Leen S B and Hyde T H, (2009), 'High Temperature Experimental Characterisation of XN40F for Life Prediction of SPF Tools', [hal-00337989 – version 1], *EuroSPF 2008*, Carcassonne, France.
22. Velay V, Bernhart G, Martinier A and Moraux J Y, (2010), 'High Temperature Fatigue on SPF Die Ni-Cr-Fe Heat Resistant Nickel Chromium Cast Steels' *Key Eng Materials*, 433, 69–76.

High-temperature lubricants for superplastic forming of metals

P. A. FRIEDMAN and S. G. LUCKEY, Ford Research and
Advanced Engineering, Michigan, USA

Abstract: As in other sheet metal forming operations, sliding friction between the sheet material and the die surface during superplastic forming needs to be managed. In this chapter the use of lubrication during the superplastic forming process is discussed with specific focus on the controlling mechanisms of solid lubricants, the use of lubricants in commercial superplastic forming processes, the influence of friction and lubricant on final part quality and finally some thoughts on the preferred methods of testing and evaluating lubricants.

Key words: superplastic forming, solid lubricant, metal forming.

4.1 Introduction

As in other sheet metal forming operations, sliding friction between the sheet material and the die surface during superplastic forming (SPF) needs to be managed. In SPF, this is especially critical since the process is a net-thinning operation with no additional material flowing into the die cavity. Another requirement for a suitable SPF lubricant is the ability to mitigate adhesion of the forming material to the die surface. For some materials, such as aluminum, there is a strong tendency for the material to become *tacky* at elevated temperature. This can result in adhesion to the die surface and difficulty in both forming and part removal. As well as being prone to adhesion, many of the industrial materials used in SPF processes are in a soft condition at the elevated temperatures, and therefore prone to marring during the forming process. Hence, issues with the die surface, such as galling marks, can damage the surface of formed parts. The lubricant itself can also create unwanted marks and potentially premature fracture of the forming blank if it is allowed to build up on the die surface. Often the lubricant needs to be periodically cleaned off the die surface during production to minimize this build up. At lower volume, cleaning of the die can be performed on the tool once it is removed from the press and allowed to cool. However for higher volume applications, and hence longer production runs, cleaning of the die surface must be performed during forming runs without a significant loss of production time. The basic requirements of a lubricant for SPF include:

- Lubricity – ability of the material to slide along the die surface.
- Parting agent – mitigation of adhesion and ease of part release.

- Build-up – minimization of lubricant build-up.
- Die cleaning – relatively fast and easy *in-situ* cleaning.
- Part cleaning – ease of removal from the formed part surface.
- Economical – be of minimal cost to justify the business case to employ SPF.

While oil-based or waxy lubricants are typical in conventional stamping operations, these types of lubricants cannot withstand the high forming temperatures necessary for SPF. Consequently, solid lubricants such as graphite or boron nitride (BN) are often used. In addition to lubricants, surface coatings on the tools can be used to further reduce friction.¹ Together, the lubricant and die surface coating minimize the friction between the die surface and the sheet blank. The ability to characterize this friction state is vital to establishing the performance of the different frictional systems (lubricant plus coating) as well as to produce data to be used in CAE simulation of the process.

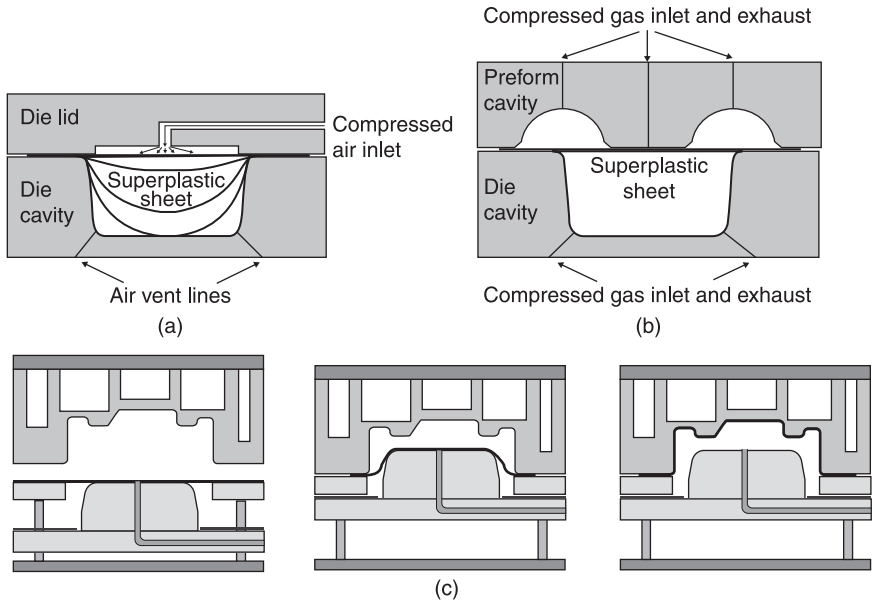
In the simplest embodiment of SPF, the blank is clamped between two flat binders and gas pressure is used to form the sheet into a one-sided die. A seal bead is often employed around the perimeter of the binder to ensure a good gas pressure seal. In this case, only one side of the sheet makes contact with the die surface so lubricant is only needed on the side of the sheet facing the forming cavity and the perimeter of the gas side.

A more advanced die system used in some production SPF processes combines elements of stamping (or mechanical forming) with SPF.²⁻⁵ This approach can reduce cycle time, thereby increasing possible production volumes. The simplest embodiment of this approach is either a plug-assist die or simply a die with a non-planar binder. A schematic of both a simple and complex SPF process is shown in Fig. 4.1. In either case, some degree of mechanical forming takes place by simply closing the die. The degree of mechanical pre-forming possible with this approach is limited by the panel shape and its propensity to wrinkle as the material is drawn into the die. In all of these processes, friction must be managed on both sides of the blank.

Other factors that must be considered in the selection of a suitable SPF lubricant are the application and removal of the lubricant from the sheet surface. As discussed below, the selection of an application process is both a function of the type of lubricant used and the production volume. Processes can range from one-off manual application prior to placing a sheet into the press, to coil coating of the lubricant at the aluminum mill. For removal of the lubricant, a cleaning system needs to be both capable of removing all traces of the lubricant, and properly sized to the production volume and part size.

4.2 Lubrication mechanisms

As noted above, lubricants that contain solid particles such as graphite or hexagonal BN are often used in SPF because of their ability to withstand the high temperature environment. Additionally, these lubricants can act like parting agents which helps prevent sticking of the part in the die at the end of forming. While



4.1 Schematic illustration of different types of SPF dies utilizing: (a) single-stage forming; (b) two-stage forming; and (c) double-action forming.

there is a tendency for solid lubricants such as these to build up on die surfaces, new processes have been developed that help strip the lubricant from them (see below). Solid lubricants work thanks to their lamellar crystal structure, where atoms are closely packed together on widely spaced planes. The atomic bonds are very strong within the plane, but relatively weak between planes. This allows for a shearing process where the planes slide past each other while under load.⁶ For a sheet metal forming process such as SPF, these solid lubricants need to be blended with some type of binder that helps the solid particles adhere to the sheet surface. It is critical to have sufficient bonding so that the solids adhere to the sheet surface during the forming process and do not build up on the die surface. However, after forming, these solid particles need to be cleaned from the sheet surface for downstream operations such as joining and painting. Hence, development of the binder system is a critical element in the formulation of these types of lubricants.

4.3 SPF lubricants

Typically, solid lubricants are applied to the blank via an evaporative solution having constituent ingredients that control and maintain viscosity, particulate dispersion, adhesion, and wetting. The most common primary active ingredients in SPF lubricants are either graphite or hexagonal BN. Other solid lubricants

successfully used in SPF include molybdenum disulphide and yttria. While these lubricants have demonstrated a higher friction relative to graphite and BN, they have been combined with various mixes of graphite and BN to tailor frictional conditions for specific applications in SPF.

Commercial SPF products are usually formed from specially-processed superplastic aluminum or titanium sheet alloys. In concept, the SPF press and die technology used to form these alloys are very similar, but the forming temperatures are quite different. While SPF of aluminum sheet is typically performed at temperatures ranging between 450 °C and 540 °C and does not require an inert atmosphere, titanium sheet requires an inert atmosphere at approximately 900 °C. For aluminum, both graphite and hexagonal BN are effective solid lubricants; however, graphite probably provides slightly better lubricity in the range of 500 °C. Conversely, BN has become the lubricant of choice for titanium SPF where it has demonstrated greater temperature resistance and higher lubricity.⁷

Lubricant selection must also be considered in the context of engineering requirements and the overall business case. For example, if blank pre-heat time must be minimized for technical or cost reasons, a coating of black graphite will more efficiently heat a blank than a blank coated with a white BN lubricant. In order to use the BN lubricant in these cases, a color additive may be needed to darken the appearance. The influence of the lubricant on downstream manufacturing must also be considered. For automotive aluminum applications, any residual graphite post-forming can have a deleterious effect on adhesives, sealants, and paint systems. Hence, before going to body assembly, superplastically-formed panels must pass through an elevated temperature, light-to-mild acidic (or caustic) wash to remove the solid lubricant. At the high temperatures required to superplastically form titanium aerospace panels, solid lubricants have the potential to react with the oxidizing sheet surface. If an undesired oxide layer develops, it must be removed post-forming. This may be done with a combination of grit blasting and an acidic bath treatment (pickling).⁷

These solid lubricants also function as parting agents. This not only prevents galling due to die and sheet adhesion but is critical to part extraction post-forming. After being fully formed within a die, a superplastically-formed panel continues to be deformable while at elevated temperature within the die. Great care, in both extraction from the die and cooling, must be taken until the panel has cooled and recovered enough yield strength for robust material handling. The parting agent serves to minimize the forces exerted on the panel for die release, thus reducing the potential for dimensional distortion.

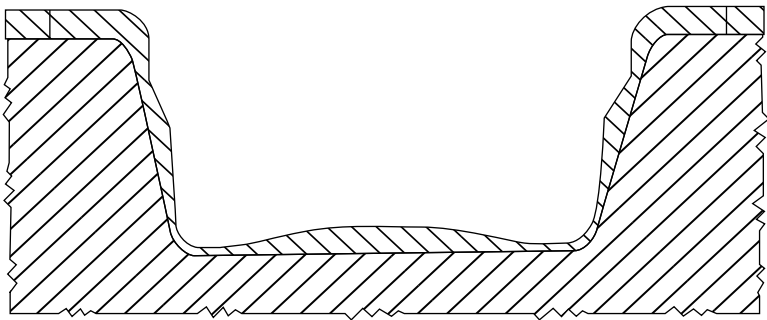
Until now, solid lubricants used in aerospace have also been generically applied for other industrial applications. As specialized SPF-based processes are developed for other industries, such as higher volume automotive manufacturing, optimizing the lubricant formulation to minimize graphite and BN content will continue to be an ongoing objective. These solids typically represent the most expensive ingredient for this class of lubricant. With increasing volume, the sensitivity of the

business case to consumable (lubricant) cost will also increase. In addition, high volume SPF processes will drive improvements in part release, clean-ability, and the overall manufacturing compatibility of SPF solid lubricants. These objectives will possibly be achieved by considering and optimizing the entire tribological system of die surface, solid lubricant, and sheet material.

4.4 Influence of friction and lubricant on forming

Friction has played a significant role in the development of SPF die technology and manufacturing practices. Relative to other sheet metal forming operations, such as stamping, the SPF sheet-solid lubricant-die interface is generally characterized as having a higher sliding friction. As it is a stretch-forming process, this can result in significant thickness variation, as depicted in the illustration of a simple plane strain section in Fig. 4.2.⁸

The thicker material at the top flange, bottom center of the cavity, and at the midpoint of the cavity walls, is caused by contact with the die early in the forming cycle where friction preserves metal thickness. Being the last region to form, the bottom corners can experience significant thinning thanks to a minimal feed of metal caused by earlier contact with the die bottom and walls. The necking just after each entry radius represents a common failure mode in SPF. Such necks develop when stretch-forming over radii which have a low radius to thickness ratio along plane strain and convex sections.⁹ The local neck begins after bending the sheet around the radius when the bulk gas forming of the blank begins. The free expansion of the blank into the cavity places significant tensile and normal stress on the material at the radius. This promotes localized thinning as the material slides over the radius. It becomes visually and physically apparent when the neck has slid from the radius onto the flat wall. The thinning in the corners and necking after radii may both impact the performance and quality of the panel with unacceptable levels of thinning, thickness variation, or may result in sheet splitting during forming.



4.2. Illustration of a typical thickness distribution for the SPF of a plane strain section.⁸

It is possible to have limited, local control of thickness variation by tailoring the friction condition. Differing amounts and types of solid lubricant, such as adjusting coating weight for graphite-based lubricants or percent content of BN for BN-based lubricants, can have a measurable influence on friction force.^{10,11,12} Referring to Fig. 4.1, a sheet with a low lubricant coating weight may split at the bottom corners due to excessive thinning; however, in some situations this may be prevented with an increase in lubricant thickness. As opposed to stretch-forming sheet into corners, the necking after the entry radius has an inverse relationship with friction.^{9,13} Low friction promotes stretch and sliding of the sheet on the radius where high friction works against stretch, and limits the sliding distance around the radius. This necking has been controlled in practice by locally applying parting agents such as magnesium hydroxide ($\text{Mg}(\text{OH})_2$) or yttria.^{14,15,16} Each has been demonstrated to have less lubricity than graphite and BN. Die and blank lubrication application methods for tailoring friction can be manual or automated operations using brushes, rollers, spray, and silk screening. A significant factor in selecting the appropriate lubricant application method is the manufacturing volume of the superplastically-formed panel.

While lubricant selection and adjusting coating weight can be useful in achieving successful panels, it is nevertheless limited in applicability and benefit. Another approach to mitigating undesired friction-induced thickness variation has been with single-die multistage SPF operations similar to those used in the polymer and glass thermoforming industries.¹⁷ Multistage SPF operations that take advantage of the high friction conditions of SPF have been effective at producing improved thickness uniformity.¹⁸ In multistage SPF, the sheet is preformed by mechanical action or gas pressure, or both, before using a final gas pressure cycle to finish the panel. The preform serves to locally pre-thin regions of the blank that experience the least thinning in the part cavity; hence, material is made available to increase thickness in more critical regions.^{19,20,21}

Superplastic forming die design has been greatly aided by the adoption of finite element analysis (FEA) by SPF manufacturers. A number of commercial FEA codes capable of forming simulation have friction models that include dependencies such as velocity and pressure. Unfortunately, such friction model coefficients and parameters are difficult to derive since no single experimental friction test can universally represent and fully characterize the SPF friction condition. Instead, a constant coefficient of friction (Coulomb friction) is typically used to model SPF, as is done in most production sheet metal forming analyses. While there has only been limited publication concerning SPF friction testing methods and results, a selection of friction coefficients are listed in Table 4.1. Although it is not an exhaustive listing, the data originate from current state-of-the-art test methods. Some have also been used to establish FEA correlation with forming trial results as well as in production die design. It is important to note that the coefficient of friction is an overly simple parameter describing a complex contact interface that is highly dependent on a number of factors that include

Table 4.1 Selection of reported constant coefficients of friction (COF)

Solid lubricant	Temp. (°C)	Sheet material	Die material	COF	Test method	Reported FEA correlation	Refs
BN-based	450–475	AA5083-H19	4140 steel	0.16–0.2	Sled test	Yes	10, 22
BN	Approx. 450	AA5083-H19	P20	0.3	Unknown	Yes	14
BN	900	Ti–6Al–4V	S310 SS	0.3–0.4	Sled test	Unknown	9
BN	500	AA5083-H19	A297-93 grade HN	0.21	Draw bead simulator	Unknown	23
Graphite	500	AA5083-H19	A297-93 grade HN	0.17	Draw bead simulator	Unknown	23

normal pressure, sheet velocity, and lubricant coating weight. For this reason, CAE analysts typically establish a constant coefficient of friction based on the available experimental friction data, inverse analysis that minimizes the difference between FEA and trial results by COF adjustment, and experience.

4.5 Testing and evaluation of lubricants

To develop an appropriate lubricant system, a method of characterizing the friction between the die surface and sheet is required. This is needed for two reasons. First, the ability to compare the effectiveness of lubricants is required in order to develop new lubricant solutions. Second, friction testing can be used to estimate the coefficient of friction which is required for accurate finite element simulation of the process. This is especially needed as SPF begins to be applied to higher volume applications. Several approaches have been used to characterize friction at elevated temperature including: strip drawing, draw-bead simulators, pin-on-disk and twist compression. Specific test methods for SPF have been developed based on these approaches.^{23,24,25} While these systems can be very useful in terms of one-to-one comparisons of lubricants, and for estimating the coefficient of friction, they are all lacking in that none of them include stretching of the material and hence do not simulate the creation of new surface area. Given that, they still have relevance as a quick method of screening lubricants for production usage and estimating the coefficient of friction for simulation purposes. To investigate lubricant more accurately during actual forming experiments, small-scale tooling coupled with FEA simulation and post-form thickness analysis can offer insight into the effectiveness of lubricants.⁹ For more information on various types of friction testing, see Azzam,²⁶ and Kitchen and Azzam.²⁷

4.6 Production issues

Development of SPF as a production manufacturing process has slowly matured over the past 40 years. Much of this work has been done in the aerospace industry

where there is a need for low volume processes to form extremely difficult to form materials. This paradigm favors the use of inexpensive tooling at the cost of longer cycle times and higher material costs. More recently, the usage of SPF for aluminum sheet has been increasing due to the expanded forming window associated with the process and the potential for part consolidation.²⁸ As production volume increases to those typical of the rail and automotive sectors, cycle time and material cost become the primary cost drivers and have greater influence on whether SPF can be used as a viable, cost-effective manufacturing option.

While substantial resources have been devoted to the science of superplasticity, the development of state-of-the-art SPF manufacturing processes, including the application and removal of lubricant, for higher volume remains an issue that continues to limit the application of this technology. The majority of the knowledge and expertise concerning production issues with SPF lubrication is distributed between a few select companies. While there are promising new technologies with respect to managing the complicated issue of tribology during SPF, in general these technologies are not presented in academic literature or trade magazines. In this section a short review is offered of the most critical aspects of managing lubrication during production SPF.

The application of lubricant to the sheet can be accomplished in several ways. For lower volume production, lubricant is often hand applied prior to insertion of the sheet into the press (or pre-heater). This is a labor intensive process which offers very little control over certain process parameters such as coating thickness. However, it is low cost and has been the de-facto method for many years of SPF production. For higher volume production, SPF purveyors have chosen to move to coating lines for the application of the lubricant. This can be done off-line where blanks are lubricated separately and then re-stacked or potentially coil-fed where coils are unwound, coated and re-coiled on one line. Another possible method is to lubricate the blanks at the head of an automated SPF line. An example of an integrated SPF line where lubrication can be applied at head of line can be found in Friedman (2007).²⁹

Binder systems used in SPF lubricants can sometimes smoke when heated. While this burn-off may not reduce the usefulness of the lubricant in terms of the ability to form the part, it may result in the need to evacuate air in the vicinity of the line. This is a significant issue that needs to be factored in both the development of a SPF lubricant and the layout of a manufacturing plant.

Lubricant build-up on forming dies is a critical issue in the consideration of lubricant selection. Build-up can have deleterious effects on panel quality and forming, and in some cases can result in premature tearing of the blank. Additionally, in some extreme cases, the lubricant build-up can alter the dimensions of the final part. Adhesion of the SPF lubricant to the sheet is critical to preventing build-up. Limiting the coating thickness can also help, in that less lubricant is introduced to the die on each forming cycle.

In low volume production, where the production runs tend to be smaller, dies can be removed from presses and cleaned at room temperature. This is a relatively simple and inexpensive method of mitigating the lubricant build-up issue. However, for higher volume production, cleaning of the die surface can be an expensive process that should be minimized. For large formings runs where dies must be cleaned between parts, several manufacturers have developed equipment and methods for the cleaning of SPF dies while in the press and at operating temperature. One of these methods uses propelled pellets of dry ice to mechanically remove lubricant from the die surface. Special nozzles have been designed to produce a knife-like stream of CO₂ pellets that can quickly clean the surface of the die. The obvious benefit of this approach is that the dry ice sublimates after contact with the die surface and therefore does not leave a residue inside the die. Additionally, the stream of CO₂ can be used to sweep the die surface of any other contaminants. Some high volume SPF users have automated this type of cleaning approach by placing the dry ice cleaning guns on robot.³⁰ This has obvious benefits in terms of speed, safety and accuracy.

One simple approach to mitigating the lubricant build-up issue is simply to use less lubricant. One enabler to this goal is the use of a die coating that reduces the tendency of the forming material to stick to the die surface. Coatings such as tungsten carbide cermet or chromium carbide cermet¹ have shown promise to either eliminate the need for lubricant or at least reduce the required amount. Other coatings such as hard chrome or Nickel–Boron can also be used. One important factor in selecting a coating is to find the appropriate surface roughness that offers both good lubricity and part release while also resulting in a good part finish. Another method that has been recently introduced is to coat the material rather than the die to remove the need for lubricant.³¹

4.7 Conclusions

When compared to other sheet metal forming operations, both the commercial lubricant product options and general tribological understanding for SPF remain relatively limited. To some extent, this is due to the extreme environment in which these lubricants must perform. It is also associated with the technical challenge of establishing test methods that can sufficiently represent the forming condition. Additional consideration might also be given to the limited number of manufacturers and researchers that practice SPF. The commercially-available SPF solid lubricants are readily applicable from a perspective of performance, manufacturing compatibility, and cost for the low-volume manufacturing of aluminum and titanium sheet panels. The graphite and BN-based lubricants offer sufficient lubricity to form very complex components. They also function effectively as parting agents to mitigate galling and promote part extraction from dies without incurring dimensional distortion. However, as other specialized SPF-based processes are developed, new lubricant systems will need to be developed

specifically for these new applications. This will no doubt require greater understanding of the tribology of the die-material interface to support the development of new solid lubricant formulations, die design, die coatings, and finite element formability analysis.

4.8 References

1. A. T. Morales, 'Evaluation of Die Coatings for Superplastic Forming Processes,' in E. Taleff *et al.* (eds), *Advances in Superplasticity and Superplastic Forming*, Proceedings of TMS Conference, Warrendale, PA, 2004, p. 51.
2. S. G. Luckey and P. A. Friedman, 'Hot Draw Mechanical Preforming of an Automotive Door Inner Panel,' *Proceedings of 2008 International Manufacturing Science and Engineering Conference*, October 7–10, 2008, Evanston, IL.
3. Y. Luo, S. G. Luckey, W. B. Copple and P. A. Friedman, 'Comparison of Advanced SPF Die Technologies in the Forming of a Production Panel,' *Journal of Materials Engineering and Performance*, 17(2): 142, 2008.
4. Y. Luo, S. G. Luckey, P. A. Friedman and Y. Peng, 'Development of an Advanced Superplastic Forming Process Utilizing a Mechanical Pre-Forming Operation,' *International Journal of Machine Tools & Manufacture* 48: 1509–1518, 2008.
5. G. Luckey, Y. Luo and P. A. Friedman, 'Method and Apparatus for Gas Management in Hot Blow-Forming Dies,' United States Patent No. 7,472,572, 2009.
6. F. J. Clauss, *Solids and Self Lubricating Solids*, Academic Press, New York, 1972.
7. J. D. Beal, R. Boyer and D. Sanders, 'Forming of Titanium and Titanium Alloys,' in S. L. Semiatin (ed.), *ASM Handbook Metalworking: Sheet Forming*, Vol. 14B, 2006, pp. 656–669.
8. J. R. Fischer, 'Prethinning for Superplastic Forming,' United States Patent No. 5,823,032, 1998.
9. N. R. Harrison, S. G. Luckey, P. A. Friedman and Z. C. Xia, 'Influence of Friction and Die Geometry on Simulation of Superplastic Forming of Al–Mg Alloys,' in E. M. Taleff, P. A. Friedman, R. S. Mishra, and J. C. Schroth (eds), *Advances in Superplasticity and Superplastic Forming*, TMS, 2004, pp. 301–309.
10. R. B. Kelly, S. B. Leen, I. R. Pashby and A. R. Kennedy, 'The Measurement of Friction for Superplastic Forming of Ti-6Al-4V,' in *Material Science Forum*, Vols 447–448, 2004, pp. 111–116.
11. P. A. Friedman, W. B. Copple, R. Allor and S. G. Luckey, 'High Temperature Lubricant Test for Superplastic Forming,' *Transactions of NAMRI/SME*, 33: 25–31, 2005.
12. K. Osada and K. Shirakawa, 'Influence of Lubrication on Aluminum Superplastic Forming,' *Material Science Forum*, 304–306: 813–818, 1999.
13. A. K. Ghosh and C. H. Hamilton, 'Superplastic Forming of a Long Rectangular Box Section Analysis and Experiment,' *Proceedings of ASM Process Modeling Fundamentals and Applications to Metals*, ASM, 1978, pp. 303–331.
14. S. P. Agrawal and E. D. Weisert, 'Method of Superplastic Forming using Release Coating with Different Coefficients of Friction,' US Patent No. 4,269,053, 1981.
15. P. E. Krajewski and A. T. Morales, 'Tribological Issues During Quick Plastic Forming,' *Journal of Materials Engineering and Performance*, 13(6): 700–709, 2004.
16. P. E. Krajewski, 'Lubrication System for Hot Forming,' United States Patent No. 5,8195,72, 1998.

17. D. S. Fields, D. L. Mehl and B. F. Addis, 'Thermoforming of Metals,' United States Patent No. 5,823,032, 1998.
18. W. Johnson, T. Y. M. Al-Naib and J. L. Duncan, 'Superplastic Forming Techniques and Strain Distributions in a Zinc–Aluminum Alloy,' *Journal of the Institute of Metals*, 100: 45–50, 1972.
19. D. B. Laycock and A. J. Barnes, 'Forming Ductile Materials,' United States Patent No. 4,045,986, 1977.
20. K. Nakamura, 'Manufacturing Method of Formed Product Having Required Wall Thickness by Superplastic Blow Forming Method,' Patent Abstract of Japan, No. 197020, 1989.
21. J. R. Fischer, 'Prethinning for Superplastic Forming,' United States Patent No. 5,823,032, 1998.
22. S. G. Luckey, P. A. Friedman and K. J. Weinmann, 'Correlation of Finite Element Analysis to Superplastic Forming Experiments,' *Journal of Materials Processing Technology*, 194(1–3): 30–37, 2007.
23. P. A. Friedman, W. B. Copple, R. Allor and S. G. Luckey, 'Lubricant Development for Superplastic Forming of Sheet Metals,' *Transactions of the North American Manufacturing Research Institute (NAMRI/SME)*, Vol. XXXIII, 2005.
24. P. E. Krajewski and A. T. Morales, 'Tribological Issues During Quick Plastic Forming,' *Journal of Materials Engineering and Performance*, 13(6): 700, 2004.
25. R. W. Davies, M. A. Khaleel, S. G. Pitman and M. T. Smith, 'Experimental Determination of the Coefficient of Friction During Superplastic Forming of AA5083 Aluminum Alloy,' in D. C. Duhnand and D. G. Sanders (eds), *First and Second International Symposia on Superplasticity and Superplastic Forming Technology*, ASM International, 2001 & 2002, pp. 39–43.
26. H. T. Azzam, 'Friction and Wear Testing Machines to Evaluate Tomorrow's Lubricants,' *Proceedings of ASLE Annual Meeting, May 23, 1968*, Preprint No. 68AIB-4.
27. G. Kitchen and H. T. Azzam, 'Realistic Friction Testing,' *Machine Design*, Vol. 39, 1967.
28. M. S. Rashid *et al.*, United States Patent No. 6,253,588 B1, 2001.
29. P. A. Friedman, R. Allor, W. Copple, G. Luckey and C. Young, 'System and Process for Superplastic Forming,' United States Patent No. 7,284,402, 2007.
30. A. T. Morales, E. F. Ryntz and N. T. Brinas, 'Hot Die Cleaning for Superplastic and Quick Plastic Forming,' United States Patent No. 6,516,645, 2003.
31. H. Uchida, Y. Nagai, T. Watanabe, H. Kazama, O. Yokoyama and K. Saito, 'Aluminum Alloy Sheet for Superplastic Forming,' United States Patent No. 7,575,811, 2009.

The use of laser surface modification in combined superplastic forming and diffusion bonding of metals

G. Q. WU and G. X. LUO, Beihang University (BUAA), China

Abstract: Combining superplastic forming/diffusion bonding (SPF/DB) with laser surface modification (remelting and cladding), provides a new approach to joining similar and dissimilar high-temperature metal materials. Sound surface layers with identical or similar microstructures and properties are gained at the intended bonding surfaces; and the solid state bonding of dissimilar alloys can be transformed into that of similar laser surface modified alloy layers. The new bonding approach is applied to the similar bonding of TiAl/TiAl alloys and the dissimilar bonding of TiAl/Ni (GH3044, K418) alloys, and diffusion bonding characteristics and mechanisms of laser surface modified alloys are studied systematically.

Key words: TiAl-based alloy, high temperature alloy, laser surface modification, superplastic diffusion bonding, modeling.

5.1 Introduction

Alloys based on the γ -TiAl intermetallic compound have been of much interest as lightweight structural materials for elevated temperature aerospace applications.¹⁻³ Successful joining and cost-effective fabrication methods for materials will increase their utility in engineering applications. Encouraging results have been obtained in a few studies by using conventional welding methods such as argon arc welding,⁴⁻⁶ electron beam welding,⁶⁻⁹ laser welding,³ linear friction welding,⁹ infrared joining,¹⁰ diffusion bonding (DB)⁹⁻¹⁵ and so on. Nakao¹¹ investigated the possibility of SPD of Ti-38wt%Al alloy and succeeded in obtaining sound joints. However, the process, heat-treating at 1300 °C with some bonding pressure which induces material degradation caused by microstructure changes, may prevent practical application. Kaibyshev¹⁶ used superplastic forming and diffusion bonding (SPF/DB) technology to realize a sound joint of TiAl alloys. According to the report, the use of low temperature superplasticity in TiAl intermetallic compound with a mean grain size of 0.4 μm enabled the temperature for solid state jointing (SSJ) to be reduced to 850 °C. It can be concluded that obtaining a fine grain structure for the SPF/DB process is the key to forming a sound joint of TiAl alloy at low temperature with short time. Laser-surface-modifying (LSM) technique provides a way to achieve it, and this can refine the microstructure on the surface and simultaneously preserve all the properties of the alloy parts.

Aimed at achieving sound bonding components, the laser surface treatment technique was used to obtain fine-grain microstructures which may be of benefit in SPF/DB. The effects of the laser surface treatment and post-heat treatment on the surface microstructural characteristics of the intended bonding parts of a TiAl-based alloy, Ni-based alloy and Ti-based alloy are investigated systematically. To predict the extent of SPD of different materials, a new model based on Derby and Hill's model was proposed. The effects of several factors, including bonding temperatures, bonding pressures, bonding times and different microstructures, on the SPD were investigated primarily.

5.2 Effect of laser surface modification on alloy surface

In this study, the intended bonding alloys, including TiAl alloys, Ni-based alloys and Ti-based alloys are cut into different sized pieces to carry out different laser surface treatments (LST). Those for laser surface remelting (LSR) are $60 \times 6 \times 5$ mm, those for laser surface clad (LSC) alloy-powder are $60 \times 20 \times 5$ mm, those for the laser surface clad (LSC) alloy slice are $60 \times 6 \times 5$ mm, and the alloy slice to laser surface clad are $60 \times (3\sim 5) \times (0.5\sim 0.7)$ mm. All laser surface treatments are carried out on the HGL-84 type CO₂ laser machine system, and the parameter combination of laser power, scanning rate and defocus distance are optimized to achieve sound surface appearance and microstructure which will aid good bonding.

5.2.1 Laser surface remelted TiAl alloy

Microstructural characteristics of TiAl alloy

Titanium aluminide alloy, Ti-46.5at%Al-2at%Cr-1.5at%Nb-1at%V (Ti-46.5Al, γ -TiAl), selected as experimental material, are prepared by the XD process and hot-isostatic-pressed (HIP) at 1260 °C/175 MPa for 3 h, and post-heated at 1350 °C for 10 min and then cooled in the furnace, which is characterized by the fully lamellar microstructure (consisting of γ -TiAl and α_2 -Ti₃Al phase) with a grain size of over 100 μm and lamellar width of about 1 μm .

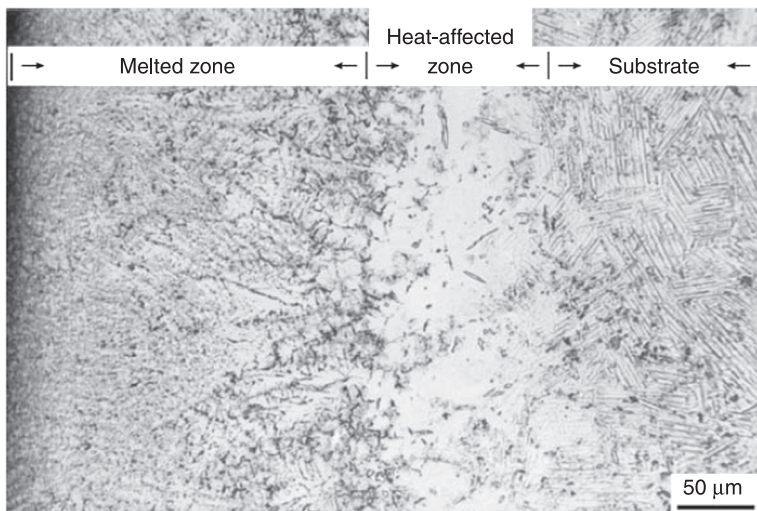
Microstructural characteristics of LSR-TiAl alloy

To investigate the effects of the laser process and post-heat-treatment on the microstructural characteristics of TiAl alloy, γ -TiAl alloy was laser-surface-remelted by 2 kW laser power, at a scanning rate of 10 mm/s, with defocus distance 32 mm and with a shielding gas of argon, and then post-heat-treated at different temperatures or different times.

After the laser surface remelts, the remelted zone and heat-affected zone are formed in γ -TiAl alloy. The remelted zone, with the depth of about 200 μm , is

characterized by a fine cellular dendrite structure (Fig. 5.1). The dendritic length is about 40–60 μm , and the cellular grain diameter is about 10–20 μm . The fine cellular dendrite structure in the melt zone of γ -TiAl alloy consists of α_2 -Ti₃Al and γ -TiAl, and the volume fraction of α_2 is larger than that of γ . The dendritic structure is not an ideal structure for SPF/DB.^{17,18} Nevertheless, according to the Ti–Al binary phase diagram, this dendritic structure in the laser-remelted zone of LSR γ -TiAl alloy is metastable. The surface layer under the laser beam is rapidly heated to a high temperature and remelted, at the same time, heat is dissipated locally within the target material through thermal diffusion, and the surface layer is rapidly quenched in a very short time; a large thermal gradient is developed from top to bottom in the melt pool. So, the α_2 phase obtained by laser surface melting is oversaturated and metastable and will be transformed under the post-heat treatment.

Below the remelted zone, there is a heat-affected layer with a microstructure different from the substrate. Its formation is attributed to the influence of the remelted zone. When the substrate is remelted by laser beam to form a melted pool which can be as the heating source, the substrate beneath the melted zone may be heated to the $\gamma + \alpha$ or α phase, and a microstructure is developed during quenching which is different from that of the substrate. During laser treatment, no change of microstructure was observed in the substrate, which is still composed of lamellar and equi-axed structure. Thereby, the material possesses the fine grain structure required in SPF/DB as well as keeping the original properties, especially properties at elevated temperatures.



5.1 Microstructure of the XD-TiAl alloy at the surface after laser surface treatment.

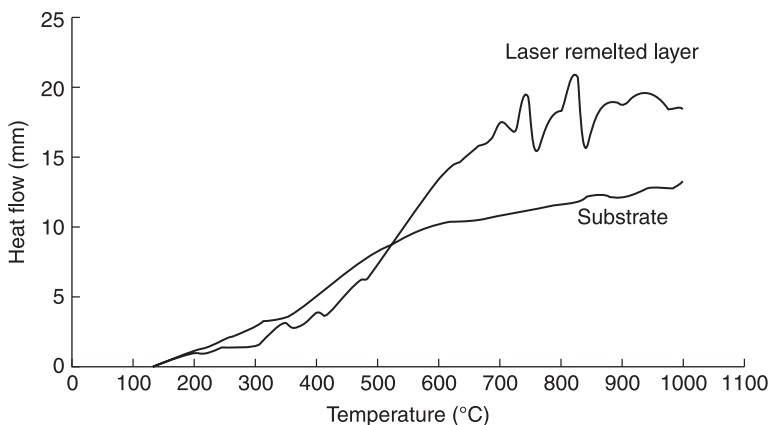
Microstructural transformation of LSR γ -TiAl alloy

The substrate shows high heat stability, while two exothermic peaks appear at 720–750 °C and 800–830 °C in the remelted layer of TiAl alloy respectively (Fig. 5.2). $\alpha_2 \rightarrow \gamma$ phase transformation takes place during the post-heat-treatment. It contains γ and α_2 phases in the quenched samples (some samples of laser remelted γ -TiAl alloy were held at 750 °C for 5 min and then quenched in water, and other samples were held at 860 °C for 5 min and then quenched in water), and the γ phase possesses a larger volume fraction than that of the LSR state.

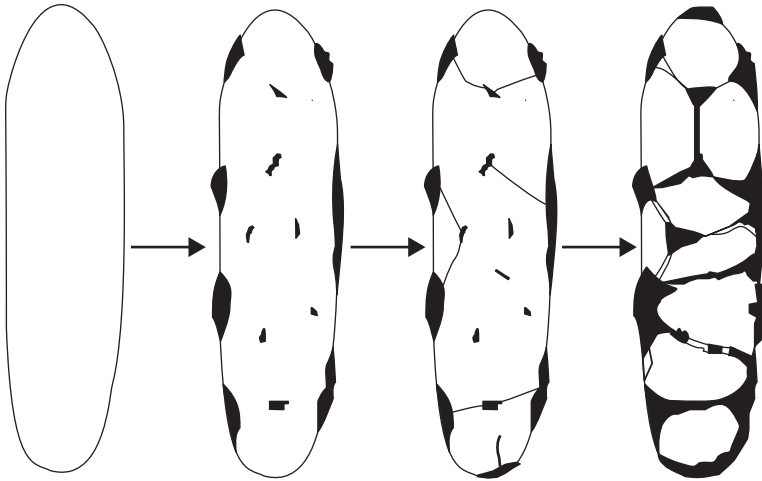
With an HM-100 ultra-high-temperature microscope, microstructural transformation of the laser surface-remelted TiAl was observed *in situ* during heating to temperatures of 800 °C, 850 °C, 900 °C and 950 °C, and the heating rate of 200 °C/min was adopted; results showed that the higher the heat treatment temperature, the shorter the time for structure change as expected. During heating at 800 °C, some structural variation can be observed after 150 min. At 900 °C, this time is shortened to 8 min, and most of the dendritic structure is transformed into fine equi-axed grains after 14 min. During post heating, no significant changes of microstructure were optically observed in the heat-affected zone and substrate, which indicate high stability of γ -TiAl substrate under the adopted temperature.

According to the results of *in situ* hot-stage observations with an ultra-high-temperature microscope, the structural changing process can be illustrated by Fig. 5.3. During the annealing treating, the microstructure transformation occurred first at the intergranular of the dendritic structure, then expanded into the transgranular, and finally changed to ultrafine equi-axed grain.

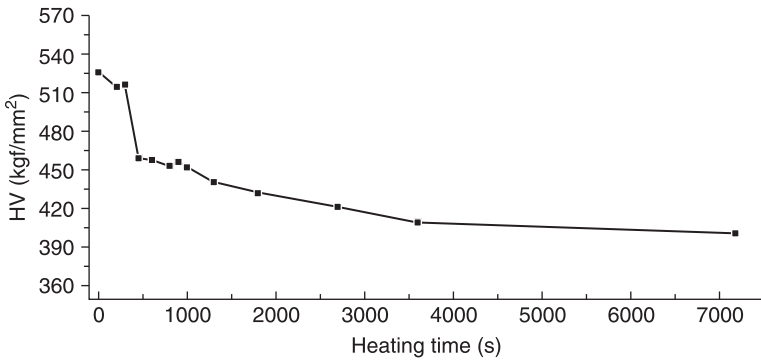
Following the structural transformation, micro-hardness of LSR γ -TiAl varies correspondingly. Figure 5.4 shows the relationship between post-heat treating time and the micro-hardness of LSR γ -TiAl alloy. It can be seen that the



5.2 Differential scanning calorimetry (DSC) results of the remelted zone and the substrate of TiAl alloy.



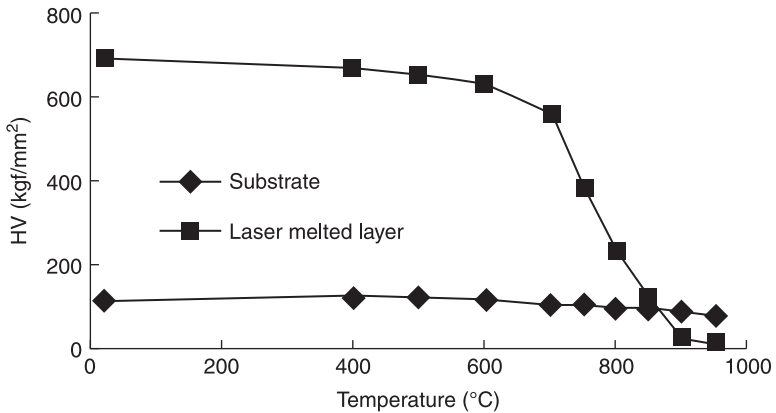
5.3 The illustration of dendritic structural transformation.



5.4 Micro-hardness (HV) curve of LSR γ -TiAl-based alloy varied with post-heating time.

micro-hardness decreases with the increase of post-heating time, and has a sharp decline between 300 s and 450 s. After being heat treated for 450 s, the micro-hardness slowly descends, then tends gently to stabilization. α_2 -Ti₃Al, the main phase of laser surface remelted TiAl based alloy, has higher moduli than the γ -TiAl phase, which is the main component of the LSR γ -TiAl alloy that is found post-heat treatment. The phase transformation and the relaxation of thermal residual stress both contribute to the decline of the micro-hardness.

Figure 5.5 shows the relationship between temperature and micro-hardness of the laser-melted layer and the substrate of TiAl alloy. It can be seen that the hardness of the substrate varies little and keeps relatively stable, while the hardness of the melted zone begins to descend sharply at about 750 °C. The



5.5 Relationship between temperature and micro-hardness of alloy (load, 2.45 N; load rate, 0.098 N/s; load holding duration time, 30 s).

variation is caused by the $\alpha_2 \rightarrow \gamma$ phase transformation. With a further increase of heating temperature, the hardness of the laser-melted layer is lower than that of the substrate above 850 °C, and the hardness of the melted zone is 1/3~1/6 of that of the substrate at 900~950 °C. Thereby, from the point of view of plastic deformation resistance, the resistance of the melted layer is lower than that of the substrate, and this change is apparently a benefit of solid state bonding. Additionally, apparently, the structure transformation of TiAl above 850 °C enhances the ability of SPF/DB.

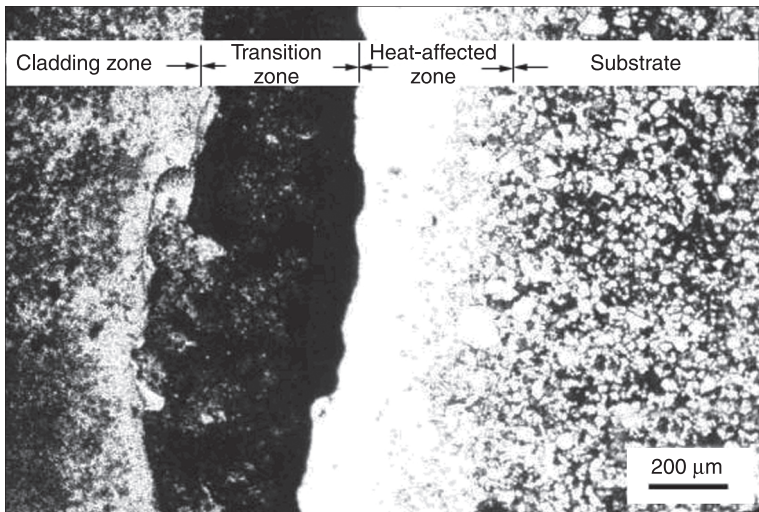
5.2.2 Ni–Cr–Ti–Al laser cladding layers

Gamma titanium aluminide alloys are attractive candidates for replacing the conventional Ni-based superalloy in engines to provide significant weight savings.^{1-4,19-22} Successful joining of TiAl alloys and Ni-based alloys is one of the critical factors for increasing their application as high-temperature structure materials in engineering. To successfully join TiAl alloy to Ni-based alloy with the LSM technique, suitable laser-modified layers should be determined to form the gradual change of composition and properties between two intended bonding alloys.

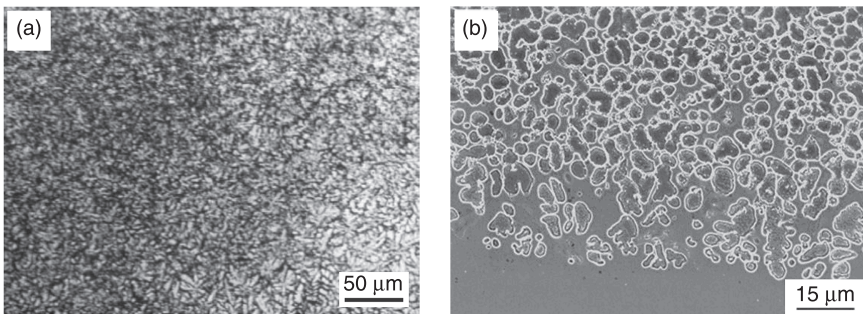
TiAl cladding layer on deforming Ni-based alloy

Ni-based deforming alloy, Ni–25wt%Cr–14.5wt%–1.5wt%Mo (marked as GH44), has a microstructure of a single austenite phase solution, and is extensively used in aerospace vehicles. A TiAl alloy sheet with a thickness of 0.5 mm was laser-clad on GH44 alloy with laser cladding parameters of 2 kW laser power, a scanning rate of 10 mm/s, and defocus distance of 32 mm.

Figure 5.6 illustrates the representative microstructure of the laser cladding TiAl alloy layer on the GH44 alloy. Three different zones, including a cladding zone, transition zone and heat-affected zone, are formed. The cladding zone characterized by dendritic structure (Fig. 5.7(a)), which is similar to that of LSR γ -TiAl alloy, consists of a α_2 -Ti₃Al phase and a γ -TiAl phase, and the volume fraction of the α_2 -Ti₃Al phase is larger than the γ -TiAl phase, which indicates that the metastable α_2 -Ti₃Al phase is obtained by the rapid cooling rate of laser surface modification. The phase transformation of $\alpha_2 \rightarrow \gamma$ takes place when the cladding layer is heat-treated at 900 °C for 1 h, and the dendritic microstructure is completely transformed into fine equi-axed grains, which provide a good structure



5.6 Microstructures of TiAl clad coating on GH3044 alloy.



5.7 Metallographs of: (a) the cladding zone after annealing heat treatment at 900 °C for 1 h and (b) the transition zone of TiAl laser clad coating on GH3044 alloy.

condition for SPF/DB. The transition zone, whose microstructure are shown in Fig. 5.7(b), contains $\text{Ni}_3(\text{Ti,Al})\text{C}$, $\alpha_2\text{-Ti}_3\text{Al}$ and Ti phases, and the $\text{Ni}_3(\text{Ti, Al})\text{C}$ phase possesses a larger volume fraction than the other two phases. Good elementary transition is formed between the cladding zone and the substrate. Through laser cladding treatment, a similar fine structure to laser-surface-remelted TiAl alloy was formed on the intended bonding surface of GH44 alloy, which is of great benefit to the SPF/DB.

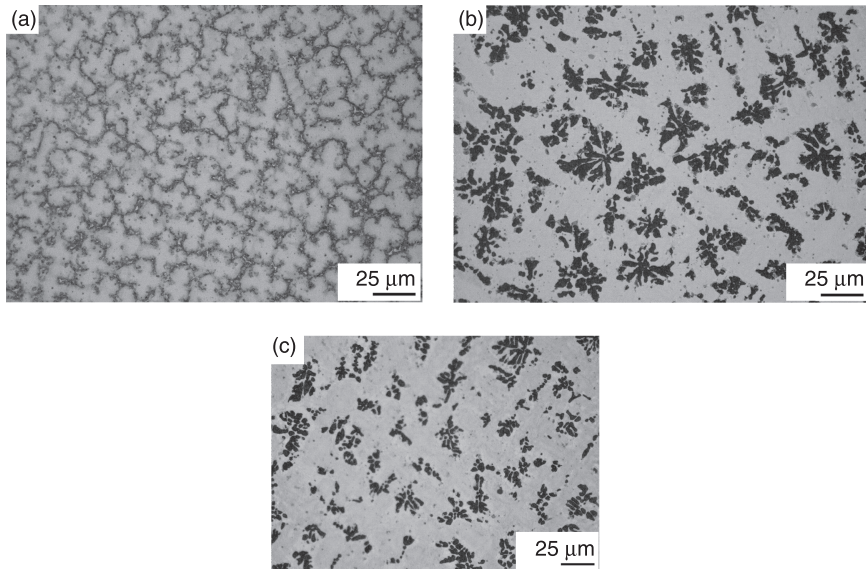
Ni–Cr–TiAl laser cladding layers on casting Ni-based alloy

The Ni-based alloy (type K418) contains mainly Cr (11.5~13.5wt%), Al (5.5~6.4wt%), Mo (3.8~4.8wt%), Nb (1.8~2.5wt%) and Ti (0.5~1.0wt%), and is generally used as the casting condition. K418 alloy was laser surface clad (LSC) with rich-Ni Ni–Cr–Ti–Al cladding. The laser cladding parameters were 1.7~2.0 kW, the scanning rate 100~200 mm/minute, and the beam diameter 4 mm. Ni–Cr–Ti–Al cladding materials, whose nominal chemical compositions are given in Table 5.1, were achieved by mixing pure Ni, Cr, Ti, Al powder ($\geq 99.9\%$, –200 grit) and $\gamma\text{-TiAl}$ alloy powder (Ti–46.5Al–2.5V–1Cr wt%, –60~140 grit) using a planetary ball mill equipped with agate ball grinding tanks and agate grinding balls.

The microstructure of K418 casting alloy is characterized by granular $\gamma\text{-Ni}_3(\text{Al, Ti})$ phases distributing dispersively in $\gamma(\text{Ni})$ matrix, MC and M_3B_2 distributing at grain boundary. Microstructural characteristics of Ni–Cr–Ti–Al clad coatings vary with the coating's composition. The $\text{Ni}_{61}\text{Cr}_{12}\text{Ti}_{14}\text{Al}_{13}$ cladding consists of dendritic $\text{Ni}_3(\text{Al, Ti})$ and a few interdendritic Ni_3Ti (Fig. 5.8(a)). The $\text{Ni}_{53}\text{Cr}_{11}\text{Ti}_{18}\text{Al}_{18}$ coating, with higher (Ti + Al) contents than the $\text{Ni}_{61}\text{Cr}_{12}\text{Ti}_{14}\text{Al}_{13}$ coating, contains dendritic $\text{Ni}_3(\text{Al, Ti})$, rosette interdendritic Ni_2TiAl (black phase) and a few interdendritic Ni_3Ti (Fig. 5.8(b)). The Ni_3Ti phase is replaced by a NiAl phase in the $\text{Ni}_{56}\text{Cr}_7\text{Ti}_{15}\text{Al}_{22}$ cladding by raising the ratio of Al/Ti on the base of the $\text{Ni}_{53}\text{Cr}_{11}\text{Ti}_{18}\text{Al}_{18}$ coating, and the microstructure of the $\text{Ni}_{56}\text{Cr}_7\text{Ti}_{15}\text{Al}_{22}$ coating is characterized by rosette or massive Ni_2TiAl and NiAl (black phase) distributing dispersively at interdendritic of the $\text{Ni}_3(\text{Al, Ti})$ phase (Fig. 5.8(c)).

Table 5.1 Chemical constitutions of Ni–Cr–Ti–Al cladding materials

Cladding materials (wt%)	Chemical constitution (wt%)				
	Ni	Cr	TiAl alloy	Ti	Al
$\text{Ni}_{61}\text{Cr}_{12}\text{Ti}_{14}\text{Al}_{13}$	68.97	12.17	18.86	–	–
$\text{Ni}_{53}\text{Cr}_{11}\text{Ti}_{18}\text{Al}_{18}$	62.43	11.02	26.55		
$\text{Ni}_{56}\text{Cr}_7\text{Ti}_{15}\text{Al}_{22}$	66.11	7.35	–	14.39	12.15



5.8 Representative structure of K418 alloy laser clad with rich-Ni Ni-Cr-Ti-Al coatings: (a) microstructure of the $\text{Ni}_{61}\text{Cr}_{12}\text{Ti}_{14}\text{Al}_{13}$ coating; (b) microstructure of the $\text{Ni}_{53}\text{Cr}_{11}\text{Ti}_{18}\text{Al}_{18}$ coating; and (c) microstructure of the $\text{Ni}_{56}\text{Cr}_7\text{Ti}_{15}\text{Al}_{22}$ coating.

5.3 Diffusion bonding of laser surface modified alloys

After laser surface modification and post-heating treatment, SPD was conducted on a Gleeble 1500 thermal imaging machine under the protection of an argon atmosphere, and the dimension of the alloy samples was $4.5 \times 2.5 \times 6 \text{ mm}^3$. To determine the bonding quality, the strength of three-point bending of the welding parts was tested in the comparison with that of the base alloy.

5.3.1 Bonding of TiAl alloys

Effects of LSR on strength of TiAl bonding couples

Table 5.2 summarizes the processes carried out on TiAl alloys and the results of shear tests at room temperature. Fully lamellar structural specimens (non-LSR γ -TiAl alloy) were investigated at bonding temperatures ranging from 900 °C to 1100 °C. The strengths of bonds made at higher temperature are expected to be higher, in fact, with the increase of bonding temperature below 1000 °C, the bonding quality enhances slowly. The ratios of shear strength of bonds to that of base metal (RSM) of specimens bonded at 900 °C and 1000 °C are 52% and 60%, respectively. When bonding temperature is up to 1100 °C, the bonding pressure of 60 MPa is not fit for bonding a TiAl workpiece directly, because the distortion

Table 5.2 Results of compression shear tests

Specimen	Process			Shear strength (MPa)	RSM (%)
	Pre-treatment	Bonding condition	Post-bond heat treatment		
1	Non-LSR	900 °C/60 MPa/60 min		243	0.52
2	Non-LSR	900 °C/60 MPa/120min		266	0.57
3	Non-LSR	1000 °C/60 MPa/60 min		282	0.6
4	Non-LSR	1100 °C/30 MPa/60 min		364	0.68
5	Non-LSR	900 °C/60 MPa/60 min	Post-H1200	318	0.68
6	LSR	900 °C/60 MPa/60 min		290	0.64
7	LSR	900 °C/60 MPa/90 min		335	0.72
8	LSR	900 °C/60 MPa/120min		384	0.82
9	LSR + Pre-H1000	900 °C/60 MPa/60 min		332	0.71
10	LSM	900 °C/60 MPa/60 min	Post-H1200	360	0.77
11	Base metal			464	

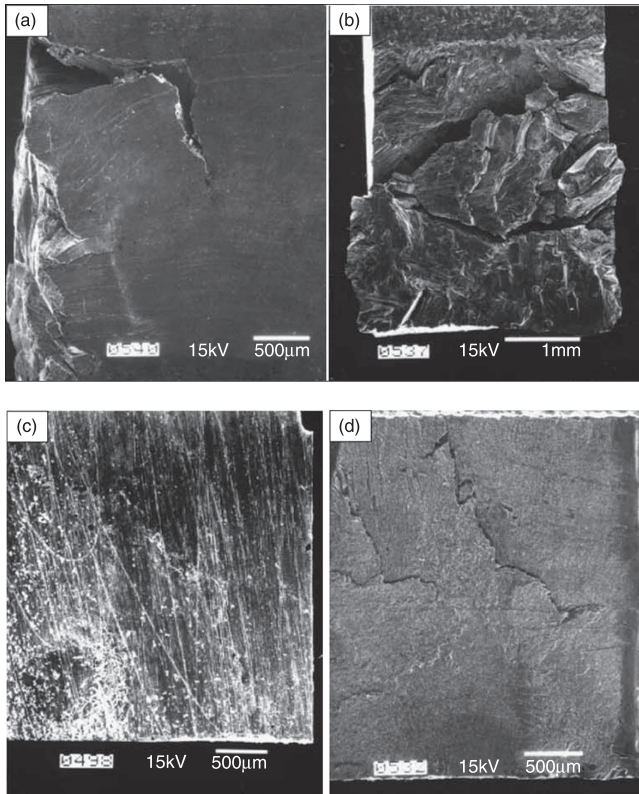
of the specimen is too heavy to use. A pressure of 30 MPa was used and the RSM of the specimen bonded at 1100 °C for 60 min is 68%. Prolonging the bonding time to 120 min, the RSM of the specimens bonded at 900 °C is only 57%. The above results show that a high bonding temperature plays a key role for fully lamellar structural specimens containing coarse grains. Additionally, the specimen bonded at 900 °C was post-bond heat treated at 1200 °C for 30 min, the RSM is 68%, which shows that post-bond heat treatment has a great effect on bonding strength.

To improve the bonding quality and decrease the bonding temperature of TiAl alloy, the bonding behaviors of specimens under different treatments were discussed at the same bonding conditions of 900 °C/60 MPa/60 min. For the bonding quality of the bonds without treatment, the RSM increases from 52% to 64%. The bonding quality can be further improved by the process of LSR + pre-bond heat treatment at 1000 °C for 60 min, with which the RSM of the specimen increases remarkably to 71%. As expected, with the process of LSR + post-bond heat treatment at 1200 °C for 30 min, the RSM of the specimen increases remarkably to 77%. Additionally, by bonding LSR TiAl alloy at 900 °C under a pressure of 60 MPa in 90 or 120 min, sound bonds could also be obtained. The RSMs of the specimens bonded at 900 °C in 90 and 120 min are 72% and 82%.

Fracture characteristics of LSR TiAl alloy

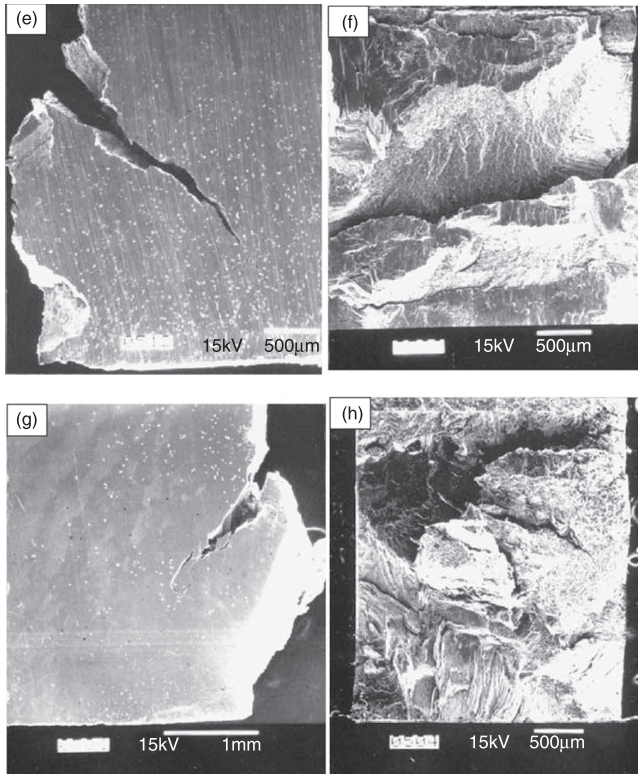
For analyzing the microstructural characteristics of DB process, the interface microstructure of a SPF/DB joint bonding at 900 °C/60 MPa for different times was observed through SEM. The observation reveals that, at the beginning of the bonding, the mating-surfaces were in point-contact due to the roughness in micro-scale. With deformation occurring, the mating-surfaces' contact area grew to a large fraction of the joint area, and the large voids disappeared due to the yield and creep deformation.²³ When the time increased (i.e. 0.5 h), the creep deformation by grain boundary diffusion occurred, and the micro-voids produced due to boundary immigration.²³ When the SPF/DB time was increased to 1 h, the micro-voids were eliminated, and a perfect joining interface formed. During this stage, the diffusion process plays a key role in void elimination by grain boundary rearrangement.²³

Figure 5.9 shows the representative fracture of the specimens shear-tested at room temperature. Conversely, Fig. 5.9(a) and (b) is the fracture of the specimen of



5.9 The sheared bonds of TiAl alloy couples treated with different processes: (a) microstructure of the sample side; (b) fractograph of the base metal; (c) micrograph of the sample side; (d) fractograph of fully lamellar structural specimen (bonding process: 1100 °C/30 MPa/60 min).

Continued



5.9 Continued. (e) Micrograph of the sample side; (f) fractograph of specimen of TiAl alloy treated by a process of laser surface melting + pre-heat treated at 1000 °C for 60 min (bonding process: 900 °C/60 MPa/60 min); (g) micrograph of the sample side; and (h) fractograph of specimen of TiAl treated by a process of laser surface melting + bonding process: 900 °C/60 MPa/60min + post-bond heat treatment at 1200 °C for 30 min.

base metal, it is apparent that the cleavage fracture occurs in the base metal and this base metal seems to be very brittle. The fractures of the fully lamellar structural specimens show that, though the fracture surfaces become rougher with the increase of bonding temperature, the specimens all fail from the bond line (Fig. 5.9(c)) with a lower bonding strength. The fracture failure mode of the sheared bonds is a sliding mode (II mode), as shown in Fig. 5.9(a). Figure 5.9(d) shows the fracture surface of specimen bonding at 1100 °C/30 MPa/60 min. It can be seen that, the specimen fails from the bond line, and the bonding interface is smooth, the fracture is observed, and brittle cracks take place and exist in a long range along the bond line, having a close relationship to the high crack sensitivity of the fully lamellar structure (FLS) specimens.

The shear test of the specimen treated by LSR shows that, though the bond quality is apparently improved, the bond strength is still low with an RSM of 64%,

and the specimen fails from the bond line as well as the fracture of the FLS specimen. With the processes of LSM + pre-H1000 or LSM + post-H1200, sound bonds are obtained with an RSM higher than 70%. Their fractures presenting an opening mode (I mode) also shows these results (Fig. 5.9(b)). From Fig. 5.9(e) and (g) it can be seen that the specimens bonded with the above mentioned two conditions both fail most away from the bond line, and the flaw spreads into the substrate. Their fractographs (Fig. 5.9(f) and (h)) show that the cleavage fracture occurs in the samples and there are no cracks between the LSR layer and the base metal.

As is the aim of this technique in the bonding of TiAl alloys, laser remelting is performed on the intended bonding surfaces. By laser surface modification, due to the very fine grain structure on the surface, sound bonds of TiAl alloys could be achieved at a lower bonding temperature of 900 °C than conventional SPD temperature, and the best shear strengths are greater than 80% of that of TiAl base metal.

5.3.2 Bonding of TiAl/Ni alloys

Bonding of TiAl and deforming Ni alloy

For the bonding of TiAl/Ni alloys, TiAl alloy and deforming high-temperature Ni alloy (GH44, Ni–25wt%Cr–14.5wt%W–1.5wt%Mo) undergo laser remelting and cladding of TiAl–alloy layer treatments respectively, and are post-heat treated at 900 °C for 1 h, and sound surface layers with identical microstructures and properties are gained at the intended bonding surfaces of TiAl alloy and GH44 alloy.

Diffusion bonding was carried out in a Gleeble 1500 thermal imitation machine with the vacuum degree of 1×10^{-4} Pa at different temperatures, with a pressure of 60 MPa for 1 h. The shear strength values are listed in Table 5.3. The results show that by increasing the bonding temperatures, shear strength values of the TiAl/GH44 bonded specimens increase rapidly due to higher diffusion at elevated temperature. When bonded at 800 °C, 850 °C and 900 °C, the shear strengths of TiAl/GH44 bonds using modified alloys exceed those of bonds by non-modified

Table 5.3 Shear strength of TiAl/GH3044 bonding couples

Specimens	Bonding conditions	Shear strength (MPa)
LSM-TiAl/GH44	800 °C/60 MPa/60 min	118
LSM-TiAl/GH44	900 °C/60 MPa/60 min	178
LSM-TiAl/GH44	950 °C/60 MPa/60 min	288
NLSM-TiAl/GH44	800 °C/60 MPa/60 min	95
NLSM-TiAl/GH44	850 °C/60 MPa/60 min	135
NLSM-TiAl/GH44	900 °C/60 MPa/60 min	181
TiAl alloy	950 °C/60 MPa/60 min	464

Note: NLSM (non-LSM) or TiAl/GH44.

alloys by 24%, 32% and 59%, respectively, indicating that bonding quality was significantly improved by utilizing laser surface modification.

A bond of laser modified alloys produced in the condition of 900 °C/ 60 MPa/ 1 h has a defect-free interface and fractured primarily in the cleavage mold, and exhibited a higher shear strength value of 288 MPa, which is up to 62% of that of a TiAl-base alloy. It can be concluded that, due to the very fine grain structure on the intended bonding surface of modified alloys, a perfect metallurgical bond can be obtained at lower temperature by grain boundary sliding and diffusion.

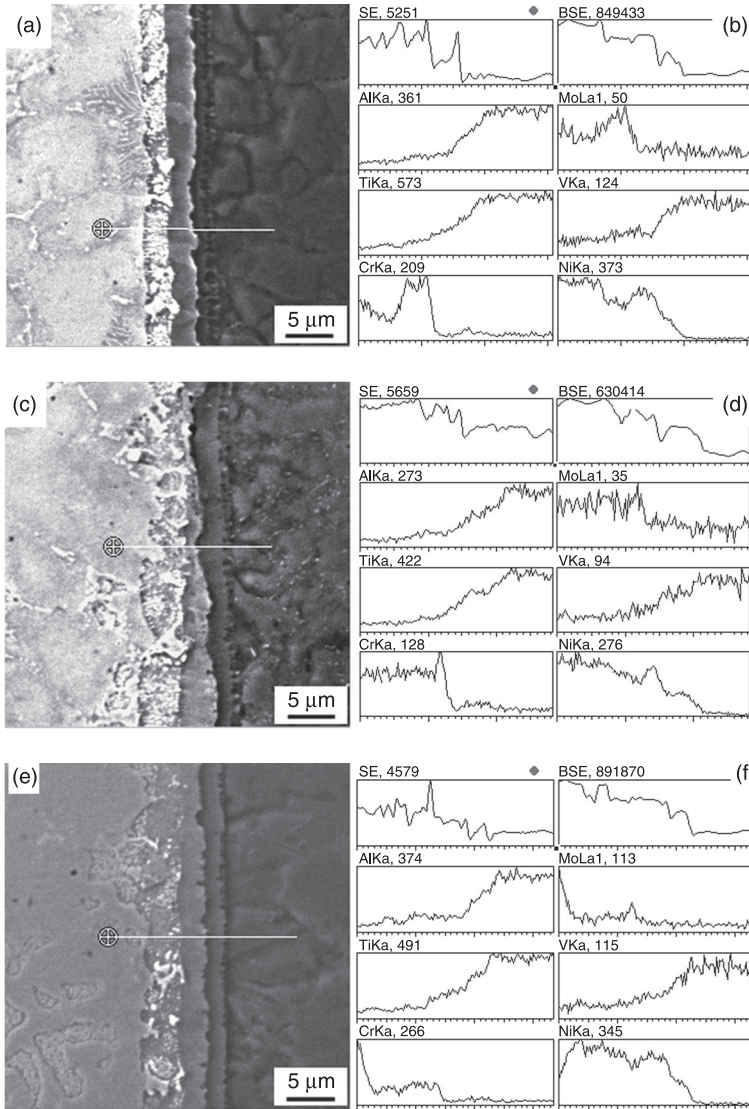
Bonding of TiAl and casting Ni alloy

For the bonding of TiAl/Ni casting alloys, TiAl alloy and casting high-temperature Ni alloy undergo remelting and cladding Ni–Cr–TiAl layer treatments respectively, and sound surface layers with identical or similar microstructures and properties are gained at the intended bonding surfaces.

At the SPD conditions of 950 °C/60 MPa/1 h, sound joints of LSM TiAl alloy to K418 alloy were achieved, and Fig. 5.10 shows their interfacial structure characteristics. It can be seen that, the compositions of Ni–Cr–Ti–Al coatings have significant effects on interfacial structures of laser surface modified (LSM) TiAl/K418 bonds. A composite interfacial structure consisting of at least three reaction layers is formed in each bond, and the width and shape of each interfacial reaction layer are varied with the composition of the Ni–Cr–Ti–Al cladding.

According to the results of EDS analysis, near the TiAl alloy side is the NiTiAl layer, the next is the Ni₂TiAl layer, and near the K418 alloy side is the reaction layer, obviously different in Cr content. In the TiAl/(Ni₆₁Cr₁₂Ti₁₄Al₁₃)K418 joint (Fig. 5.10(a)), massive Ni₃Ti is precipitated adjacent to the interface zone, the reaction layer near the K418 side contains significant amounts of Cr-rich (up to 47wt%, containing Ni approximately 28wt%) phase, the Ni₂TiAl layer is about 2.8 μm in width. The Ni₂TiAl phase in the the Ni₅₃Cr₁₁Ti₁₈Al₁₈ cladding has a relatively large size, and the reaction, Ni₂TiAl + TiAl → NiTiAl, occurs when the Ni₂TiAl phase contacts with TiAl alloy at bonding temperature, which increases the width of the NiTiAl layer at the corresponding location and results in the uneven width of the Ni₂TiAl layer and the NiTiAl layer in the interface zone of TiAl/(Ni₅₃Cr₁₁Ti₁₈Al₁₈)K418 joint (Fig. 5.10(c)). In the TiAl/(Ni₅₆Cr₇Ti₁₅Al₂₂)K418 joint, the content of the Cr-rich phase in the reaction layer near the K418 side obviously decreases, and the problem of Cr depletion in the adjacent location is improved, and the Ni₂TiAl and NiTiAl layers are uniform in width (Fig. 5.10(e)).

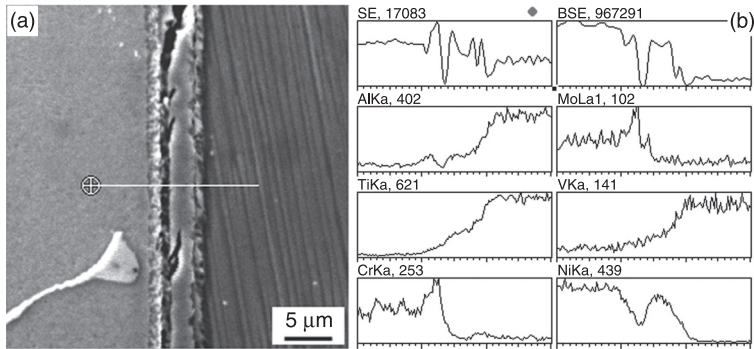
Some defects exist in the interfacial zone when TiAl alloy is directly diffusion bonded to K418 alloy at the same condition of 950 °C/60 MPa/1 h. There are obviously three reaction layers in the interfacial zone (Fig. 5.11(a)), and from the TiAl side to the K418 side are respectively NiTiAl, Ni₂TiAl and Ni₃(Al, Ti) layers with Cr content up to 19.5wt%, and Mo in the K418 substrate is segregated into the Ni₃(Al, Ti) layer as Cr, which is labeled with alloys in Fig. 5.11(b). Cracks are



5.10 SEM interface images and concentration profiles of major elements across the interface of LSM-TiAl/K418 joints: (a), (b) TiAl/(Ni₆₁Cr₁₂Ti₁₄Al₁₃)K418 joint; (c), (d) TiAl/(Ni₅₃Cr₁₁Ti₁₈Al₁₈)K418 joint; and (e), (f) TiAl/(Ni₅₆Cr₇Ti₁₅Al₂₂)K418 joint.

formed along the interface between the Ni₃(Al, Ti), Ni₂TiAl and NiTiAl layers, and simultaneously in the Ni₂TiAl layer.

The shear testing results show that the TiAl/(Ni₅₆Cr₇Ti₁₅Al₂₂)K418 joint has the shear strength of 359 MPa which is twice that of the TiAl/K418 direct bonding



5.11 Interfacial structure of TiAl/K418 direct bonding joint: (a) SEM image and (b) concentration profiles of major elements across the interface zone.

joint, the shear strengths of the TiAl/(Ni₅₃Cr₁₁Ti₁₈Al₁₈)K418 joint is similar to that of TiAl/K418, while the TiAl/(Ni₆₁Cr₁₂Ti₁₄Al₁₃)K418 joint has lower shear strength. These indicate that the shear strength of joints is strongly affected by the interfacial structure characteristics, and a Ni–Cr–Ti–Al laser clad coating with suitable composition and microstructure can obviously improve properties of the joints of TiAl alloy to Ni-base casting alloy.

For the bonding of TiAl/Ni alloys, TiAl alloy and casting high-temperature Ni alloy are treated by laser remelting and cladding with Ni–Cr–TiAl layer treatments respectively, and sound surface layers with identical or similar microstructures and properties were gained at the intended bonding surfaces. Under the same bonding condition, bonding of K418 alloys with Ni–Cr–Ti–Al laser clad coating to laser surface melted TiAl alloy is developed at lower temperature for less time, the shear strength of the TiAl/(Ni₅₆Cr₇Ti₁₅Al₂₂)K418 bond is greater than 100% of the TiAl/K418 directly bonding joints.

5.3.3 Bonding of TiAl/Ti alloys

When the LSM technique is applied to the SPD of TiAl alloy and Ti alloy, according to the lower SPD temperature of Ti alloy, the Ti alloy was laser-surface-remelted, and the TiAl alloy was either laser-surface-remelted or laser-surface-clad with Ti alloy. The effects of the microstructural characteristics of the intended bonding surface on the bonding strength of TiAl/Ti bonding couples were analyzed systematically.

Table 5.4 shows the shear strength of TiAl/Ti bonding couples with different intended bonding surface microstructures. It can be seen that the shear strengths of bonding couples between TiAl alloy with laser-surface-clad Ti layer and modified or non-modified Ti alloy is almost equal to that of non-modified TiAl/Ti bonding couples (under the same SPD condition of 800 °C/30 MPa/0.5 h, and

Table 5.4 Shear strengths of TiAl/Ti bonds with different intended surface microstructures

Bonding couple	Surface treating technology		Bonding parameter	Shear strength (MPa)	Ratio
	Ti alloy	TiAl alloy			
NLSM-Ti/TiAl	Non-modified	Non-modified	800 °C/30 MPa/0.5 h	304	0.65
LSM-Ti/(Ti)TiAl	Non-modified	LS-clad with Ti	800 °C/30 MPa/0.5 h	305	0.66
LSM-Ti _R /(Ti)TiAl-1#	LS-remelted	LS-clad with Ti	800 °C/30 MPa/0.5 h	297	0.64
LSM-Ti _R /(Ti)TiAl-2#	LS-remelted	LS-clad with Ti	850 °C/60 MPa /0.5 h	386	0.83
LSM-Ti _R /TiAl _R	LS-remelted	LS-remelted	800 °C/30 MPa/0.5 h	378	0.81
TiAl alloy	-	-	-	464	1

these increase up to 386 MPa when the SPD condition is adjusted to 850 °C/60 MPa/0.5 h). The above results indicate that the laser-surface-modification has no obvious improvement on the bonding strength of TiAl/Ti bonding couples, which is because the microstructural refining effectiveness resulting from laser surface modification is closely related to the properties of base alloys, and laser surface modification only slightly refines the microstructure of Ti alloy.

Compared with the similar shear strength of the bonding couples between laser-surface-remelted Ti alloy and TiAl alloy clad with Ti layer, under the same SPD condition of 800 °C/30 MPa/0.5 h, bonding couples between laser-surface-remelted Ti alloy and laser-surface-remelted TiAl alloy have the shear strength of 378 MPa – higher by 20% than that of non-modified TiAl/Ti bonding couples, which mainly benefit from the ultrafine microstructure of laser surface remelted TiAl alloy.

5.4 Simulation of the bonding process

The diffusion bonding process has an important influence on the design and manufacture of workpieces, since it is a great advantage to be able to bond similar or dissimilar materials. However, process conditions are often chosen by trial and error for there are so many control factors. Therefore, the simulation of the bonding process, to predict the extent of bonding when bonding different materials at given bonding temperatures, bonding pressures and bonding times, has been an important focus for researchers.^{24–29} Derby and Hill^{27–29} proposed a fully comprehensive quantitative model, in which seven mechanisms that operate in pressure sintering were considered in SPD. To predict the bonding process precisely, the actual information of roughness of the intended bonding

surfaces and the kinetic conditions of operating mechanisms in SPD should be considered.

Based on Derby and Hill's model, a new theoretical model containing the information of actual roughness of the intended bonding surfaces and the effect of the diffusion distance in a definite time was proposed. The model, effectively reflecting the characteristics of the real bonding process, realizes the visualization and simulation of the bonding process in which many voids disappear dynamically.

The surface source mechanisms play a key role in the voids closure in the initial stage of bonding, which leads to the change of voids from elliptical to circular cross section and, after that, the power law creep mechanisms and the interface source mechanisms act as two dominant ways leading to the voids shrinkage and disappearance. With the increase of the surface roughness of the intended bonding materials, the time for bonding prolongs as expected, and presents a trend of accelerated increase.

The metastable microstructure and the stable ultrafine microstructure could lead to the voids closure in much shorter bonding times than that of the original stable microstructure when bonding in the same bonding conditions. The couples with metastable microstructure, though with a grain size which is an order of magnitude larger than that of the samples with stable ultrafine microstructure, exhibit better bond characteristics than that of the stable ultrafine microstructure for its higher diffusion ability.

5.4.1 Modeling of voids shrinkage

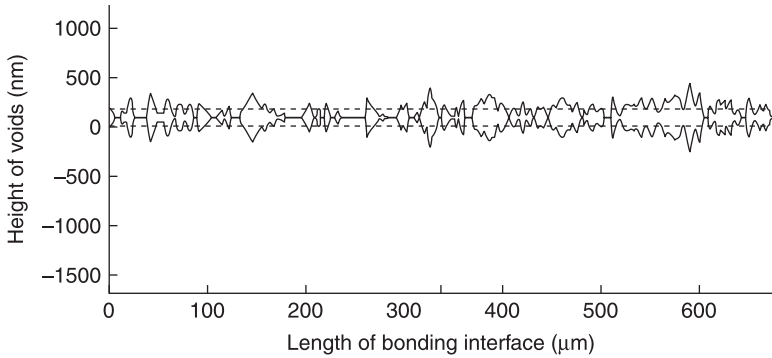
This new model considers the operating mechanisms during bonding as well as Derby and Hill's models,²⁷⁻²⁹ and the differences between the present method and Derby and Hill's methods are described below.

Application of the real rough surface in diffusion bonding

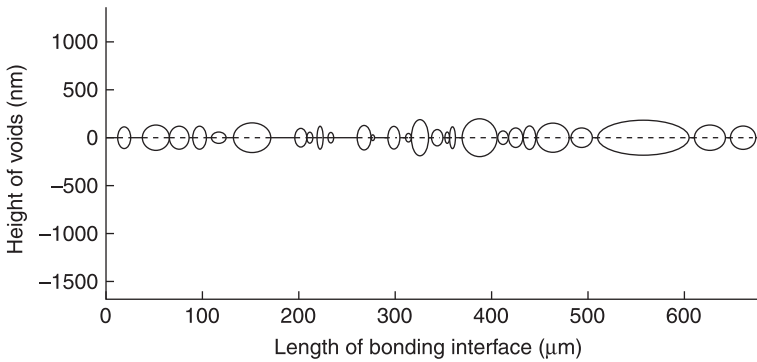
Because a real rough surface is used, it can be assumed that a linear relationship lies between the real contacting area and the load according to the principle of solid tribology,³⁰ and so the plastic flow occurs^{31,32} when

$$P_{eff} > \beta\sigma_y \quad [5.1]$$

where σ_y is the yield strength of the material at bonding temperature, and β is a coefficient. The plastic yielding deformation occurs instantaneously, and thus does not allow the time-dependent diffusion or creep to take place. At a given bonding temperature and pressure, after plastic contact, irregular bonding voids and discontinuous bonding lines are formed at the bonding interface (Fig. 5.12). To be suitable for simulation, the irregular voids are transformed into elliptical voids by keeping their volumes constant (Fig. 5.13).



5.12 Simulation result of the contacting surface with irregular voids and discontinuous bonding lines after plastic yielding deformation.

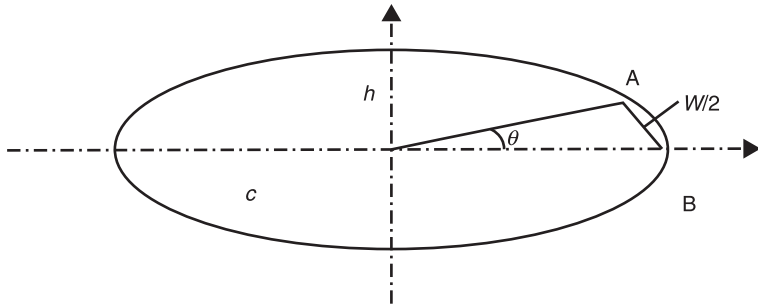


5.13 Simulation result of the contacting surface with elliptical voids.

Effect of the time limit of diffusion distance during diffusion bonding

The driving force of surface diffusion comes from the differences in surface free energy. Once there is a difference in surface curvature, mass is transferred along the surface to make the surface curvature consistent. Hill *et al.* assumed the driving force to be the difference between the maximum and minimum radii of curvature of the ellipse, which overestimates the effect of the surface source mechanisms. The simulation results show that most voids cease in a very short time and those left are too large compared to the original voids, which is inconsistent with the experimental results.^{24-26,33} In fact, the surface diffusion (mass transference) should have a distance limit in a definite time. Mullins gives an equation to calculate the length of spread of surface diffusion in a definite time of t .³⁴

$$W = 0.46 \cdot \left(\frac{D_s \cdot \delta \cdot \gamma_s \cdot \Omega}{k \cdot T} \cdot t \right)^{1/4} \quad [5.2]$$



5.14 Schematic diagram of the mass transference along the surface.

The term W becomes smaller and smaller with reduction of the time of t , and hence it can be assumed that the length of the curve from point B of minimum radii of curvature to point A of the longest length of surface diffusion in a definite time of t is approximately equal to $W/2$, and the radii of curvature of the point A can be calculated (Fig. 5.14).

$$d = \frac{(c^2 \cdot \sin^2 \theta + h^2 \cdot \cos^2 \theta)^{3/2}}{c \cdot h} \quad [5.3]$$

Therefore, the driving force should be the difference in the radii of curvature of point B and point A, and a new reduction factor $[(1/r_c) - (1/d)]$ is given. Hence the equation for the surface diffusion mechanism from a surface source to a neck now becomes

$$\dot{V}_1 = \frac{2 \cdot \Omega \cdot \delta_s \cdot D_s \cdot \gamma_s}{r_c \cdot k \cdot T} \cdot \left(\frac{1}{r_c} - \frac{1}{d} \right) \quad [5.4]$$

where

$$r_c = \frac{h^2}{c} \quad [5.5]$$

The equations of mechanism of volume diffusion from a surface source to a neck should also be changed correspondingly.

The simulation result of SPD in this model at the same conditions as in Hill's model shows more agreement with the experimental results from the phenomena of voids closure.

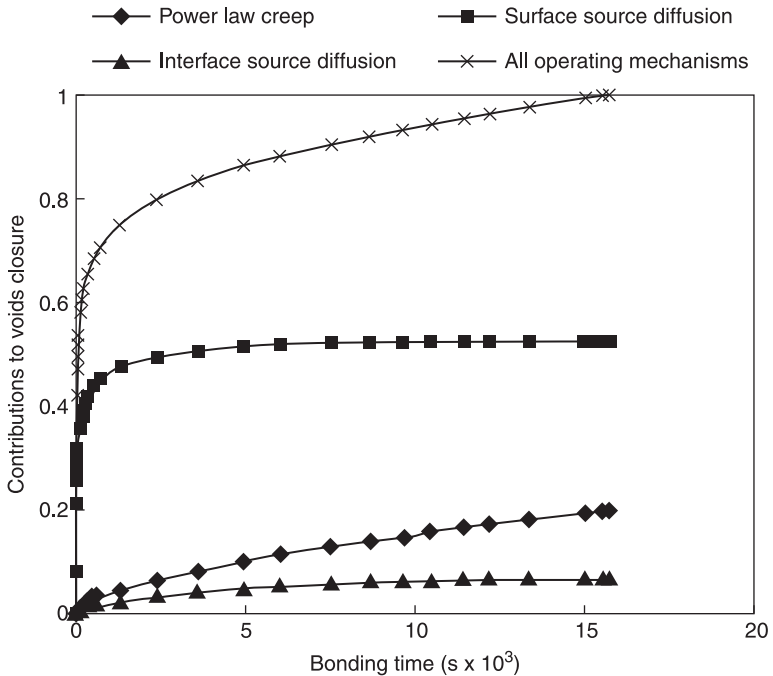
5.4.2 Effects of bonding conditions

The bonding conditions, including the bonding surface roughness, bonding time, bonding temperature and bonding pressure, act as four important control factors

in influencing the bonding characteristic in SPD, and the effects of these four parameters respectively on the bonding quality are discussed below.

The time needed for voids closure increases with the increasing degree of surface roughness. From the function of operating mechanisms, there is a gradual increase in the contribution to voids closure from creep deformation mechanisms with an increase in the degree of surface roughness. In this case, the contribution from the surface source mechanisms is gradually decreasing and the interface source mechanisms show relatively smaller contribution increases first, and decreases afterwards, to the voids closure. The analysis of the above simulation results reveal that a rough surface can severely decrease the rate of voids closure, and the heights of the voids formed after contacting will be lower as less-rough surfaces are used, which is a great contribution in realizing the SPD.

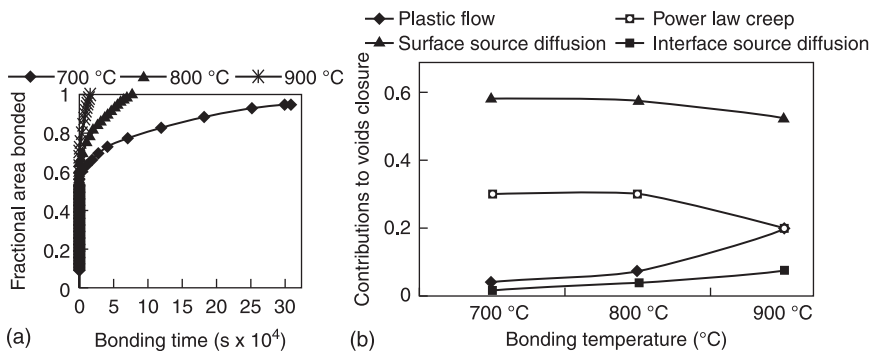
Figure 5.15 displays the contributions from the operating mechanisms to voids closure with the variations in bonding time. The result shows that the contribution from surface source mechanisms is dominant in the initial stage of bonding, which hence tends to change the voids from elliptical to circular cross-sections. After unity of the aspect ratios of the voids, the creep deformation mechanisms and interface source mechanisms act as two dominant manners to the voids elimination.



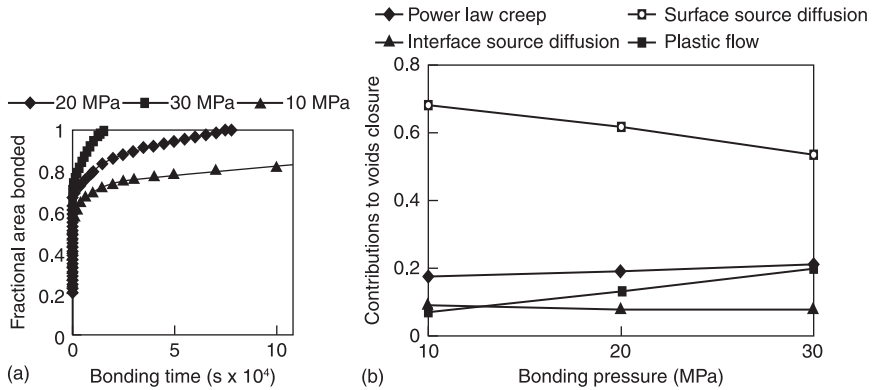
5.15 Variations in the contributions from each operating mechanism with the change of the bonding time.

When bonding in the given bonding pressure of 30 MPa and initially actual surface roughness ground with SiC-paper down to 1200 grit, a detailed investigation of the effects of bonding temperatures on bonding quality are shown in Fig. 5.16. The results illustrate that the bonding time for the voids elimination can be apparently shortened with the elevation of bonding temperature. At the bonding temperature of 700 °C, it takes 20 h to attain less than 80% of the rate of voids closure. However, compared to the previous bonding temperature, only 40 min is needed to achieve 80% of the rate of voids closure at the bonding temperature of 900 °C, and the voids are completely closed in 4 h, as indicated in Fig. 5.16(a). It also can be seen from Fig. 5.16(b) that, with the increase in bonding temperature, there is an increased contribution to the voids closure from the plastic deformation mechanisms, and the contribution from the creep deformation mechanisms and surface source mechanisms decreases relatively. By contrast with the above three mechanisms, the contribution to the voids closure from interface source mechanisms (which increases slightly with the elevation of the bonding temperature) is relatively low.

Besides the bonding temperature, the bonding pressure is considered as another key parameter in SPD. Figure 5.17 graphically shows the influence of different bonding pressures on the bonding quality when bonding in the case of a fixed, initial actual surface roughness and bonding temperature of 900 °C. The results show that the bonding time needed for the voids elimination is obviously shortened with the increase of bonding pressure. In the case of a bonding pressure of 20 MPa, more than 20 h is allowed to complete the voids closure, but the use of a higher bonding pressure of 30 MPa allows bonding time to decrease to little more than 4 h for voids elimination. With the enhancement of bonding pressure, there is an increasing contribution to the voids closure from both the plastic deformation



5.16 Prediction of the model illustrating: (a) effects of the bonding temperature on the voids closure and (b) contributions from all operating mechanisms to the voids closure with different bonding temperatures (bonding under a pressure of 30 MPa using a surface ground with SiC-paper down to 1200 grit).



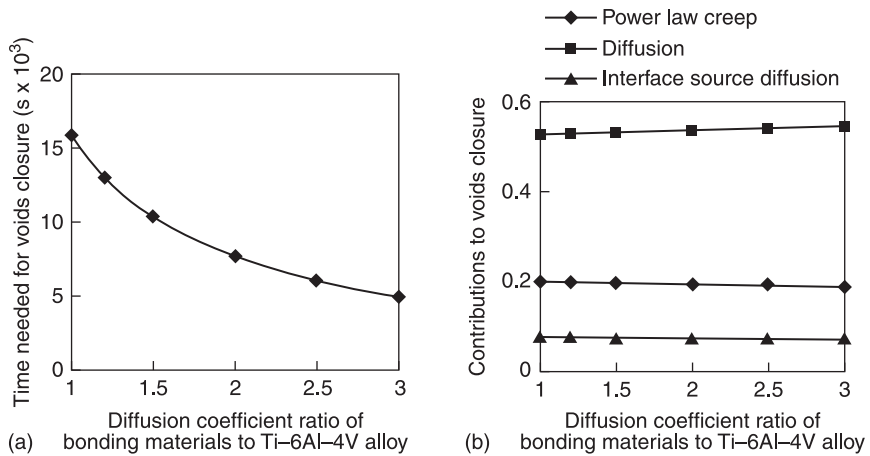
5.17 Prediction of the model indicating: (a) effects of the bonding pressure on the voids closure and (b) contributions from all operating mechanisms to the voids closure with different bonding pressures (bonding at 900 °C using a surface ground with SiC-paper down to 1200 grit).

mechanisms and the creep deformation mechanisms, but a slight decrease in the contribution from surface source mechanisms.

5.4.3 Effects of different microstructures on diffusion bonding

Previous research show that the elevated temperature hardness of the microstructure formed by laser surface melting is lower than that of the stable microstructure after exceeding a particular value of bonding temperature, which is consistent with the superplastic temperature of the microstructure formed by laser surface melting treatment. Therefore, with a suitable bonding temperature, the elevated temperature hardness of the metastable microstructure obtained by laser surface melting treatment, and the stable ultrafine microstructure formed by laser surface melting and pre-bond heat treatment, will be lower than that of the original stable microstructure. To further investigate the effects of each individual operating mechanism on the voids closure by using prepared surfaces with the above three typical microstructures respectively, the materials data of Ti-6Al-4V alloy is adopted as fundamental materials parameters for the original stable microstructure in the current model. According to the characteristic of the metastable microstructure and the stable ultrafine microstructure, the effects of the above three typical microstructures on the voids closure are discussed by adjusting each relative materials parameter.

Figure 5.18 shows the effect of the diffusion ability of the intended bonding materials on the voids closure. It can be seen from Fig. 5.18(a) that, in the case of a fixed initial surface roughness and bonding parameters, the rate of voids closure is accelerated as a result of the enhancement of diffusion ability within a particular range, and hence the bonding time for voids closure is apparently shortened.

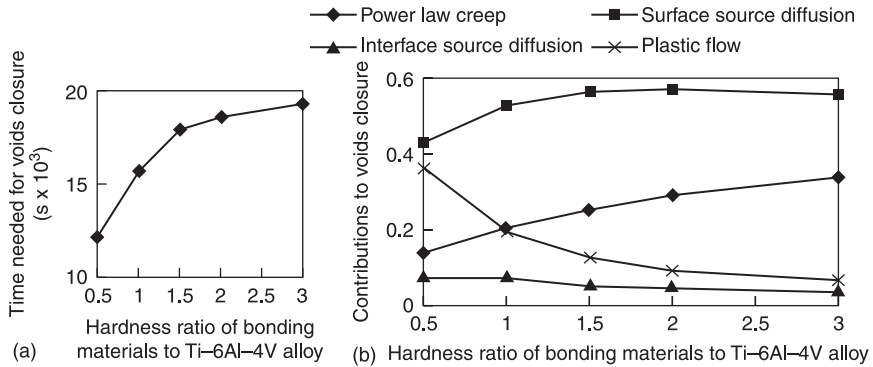


5.18 Prediction of the model displaying: (a) effects of the diffusion ability on the voids closure and (b) contributions from all operating mechanisms to the voids closure with different diffusion ability of the bonding materials (bonding at 900 °C under a pressure of 30 MPa using a surface ground with SiC-paper down to 1200 grit).

However, the diffusion ability, which is enhanced beyond a particular extent, shows a slight contribution to the voids closure. Figure 5.18(b) demonstrates the contribution from each operating mechanisms to the voids closure by using bonding materials with different diffusion abilities. It can be seen that each individual mechanism contributes slightly to the voids closure with the enhancement of its diffusion ability. The results mentioned above show that there is a significant contribution to the rate of voids closure from diffusion mechanisms, and the enhancement of diffusion ability, within a particular extent, will be helpful in accelerating the bonding process. In addition, although the creep deformation mechanisms show smaller contributions compared to that of diffusion mechanisms, their function in the SPD should not be ignored. As the interfacial diffusion channels and the creep properties of bonding materials will change with the variations of grain size, the contribution from grain boundary diffusion increases significantly.

In the initial stage of the bonding process, variations in quantity and size of voids will be induced as a result of the change of material hardness. In the bonding conditions of a given initial surface roughness and bonding process parameters, the process of voids closure is slowed with the enhancement of materials hardness, and the contribution from each operating mechanism is redistributed accordingly in the final stage of SPD (Fig. 5.19).

The characteristics of different microstructures, i.e. the original stable microstructure, the metastable microstructure formed by laser surface melting and the stable ultrafine microstructure formed by laser surface melting and post-bond heat treatment, have an important effect on the process of SPD. Table 5.5 gives the



5.19 Prediction of the model revealing: (a) effects of material hardness on the voids closure and (b) contributions from each operating mechanism to the voids closure with different hardness of the bonding materials (bonding at 900 °C under a pressure of 30 MPa using a surface ground with SiC-paper down to 1200 grit).

Table 5.5 Effects of different microstructures on times needed for the voids closure in bonding

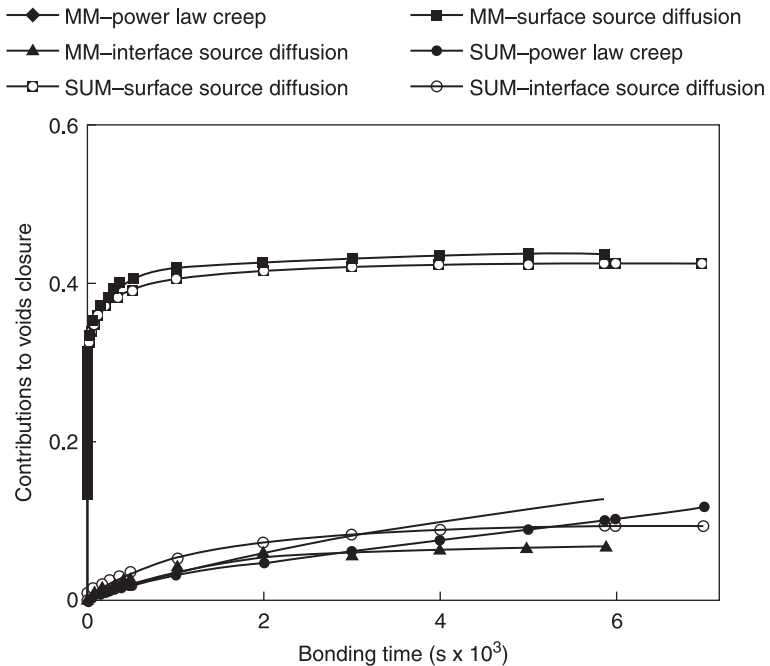
	Contributions from operating mechanisms on voids closure (%)				Voids closure times (s)
	Creep	Surface diffusion	Interface diffusion	Plastic yielding deformation	
Stable microstructure	20.3	52.9	7.2	19.6	15711
Metastable microstructure	13.1	43.8	7.0	32	5887
Stable ultrafine microstructure	11.6	42.9	9.5	32	6990

Note: diffusion bonding at 900 °C under a pressure of 30 MPa, surface ground with SiC-paper down to 1200 grit.

simulation result of bonding with different microstructures. The samples with the metastable microstructure (e.g. the microstructure formed by laser surface melted treatment) and the stable ultrafine microstructure represent a higher diffusion ability, smaller grain size and lower hardness at elevated temperature than the samples with the original stable microstructure. The former need less time (5887 s and 6990 s respectively) to complete the voids closure than the latter which needs a time of 15711 s. The simulation result agrees with the experimental results. From the contribution of operating mechanisms to the voids closure, it can be seen that the contribution from the plastic yielding deformation mechanisms increases greatly, and those from the surface source mechanisms and the creep deformation mechanisms decrease relatively. Comparing the effect of the

metastable microstructure on the voids closure with that of the stable ultrafine microstructure, the samples with the metastable microstructure need a shorter time for the voids closure than that of the samples with the stable ultrafine microstructure, as shown in Fig. 5.20. In addition, due to the higher diffusion coefficient of the metastable microstructure compared to that of the stable ultrafine microstructure, surface source mechanisms play a key role for the voids closure in the initial stage of SPD, which accelerate the voids closure and hence shorten the bonding time.

Additionally, from the contributions of operating mechanisms of diffusion, the interface source mechanisms operating in the samples with the stable ultrafine microstructure make a larger contribution than that of the samples with the metastable microstructure, for the former has a smaller grain-sized microstructure that increases the channels for interface diffusion. The contributions from the surface source mechanisms and the creep deformation mechanisms are correspondingly lower than those of the samples with the metastable microstructure. The samples with a metastable microstructure, though with a grain size which is an order of magnitude larger than that of the samples with stable ultrafine



5.20 Variations in the contribution from operating mechanisms to the voids closure with different bonding times by using the bonding samples with the metastable microstructure (MM) and the stable ultrafine microstructure (SUM) (bonding at 900 °C under a pressure of 30 MPa using a surface ground with SiC-paper down to 1200 grit).

microstructure, exhibit better bond characteristics than the stable ultrafine microstructure with its higher diffusion ability.

5.5 Conclusion

Combining SPF/DB with laser surface modification, new approaches to join similar or dissimilar metals are developed; a fine-grained microstructure at the intended bonding surface is produced by laser surface modification.

As for γ -TiAl alloy, a metastable dendritic structure on the intended bonding surface was obtained by laser surface remelting and cladding, and will be transformed into a uniform equi-axed stable microstructure during post-heat treatment, which can provide a suitable fine microstructure for SPF/DB. By laser surface remelting, sound bonds of γ -TiAl alloys were achieved at a lower bonding temperature of 900 °C and have higher shear strengths than conventional SPD temperatures.

Through the LSM treatment, the solid state bonding of TiAl/GH3044 alloy is turned to the solid state bonding of LSM TiAl layers, and sound bonds between LSM TiAl alloy and GH3044 alloy have been achieved at the lower temperature of 900 °C.

The Ni–Cr–Ti–Al coatings give a composition and property transition between TiAl alloy and casting Ni-base alloy, and have positive effects on their weldability. Solid state bonding of K418 alloys with Ni–Cr–Ti–Al laser clad coating to laser surface melted TiAl alloy is developed at a lower temperature in less time. Under the same bonding conditions, the shear strength of the TiAl/(Ni₅₆Cr₇Ti₁₅Al₂₂)K418 bond is more than 100% higher than that of TiAl/K418 directly bonding joints.

According to the simulation results, the metastable microstructure and the stable ultrafine microstructure could close the voids in much shorter bonding times than that of the original stable microstructure in the same bonding conditions benefitting from their greater diffusion ability. The metastable microstructure, though with a magnitude larger grain size, has higher diffusion ability and exhibits better bond characteristics than the stable ultrafine microstructure.

5.6 References

1. Y-W. Kim and D. M. Dimiduk, Progress in the understanding of gamma titanium aluminides. *JOM* 8 (1991) 40.
2. Y-W. Kim, Ordered intermetallic alloys, part II: Gamma titanium aluminides. *JOM* 7 (1994) 30.
3. S. Deevi, Intermetallics for the third Millennium. *Adv. Mater. Process.* 9 (1999) 44.
4. W. A. Baselack, Weldability of a titanium aluminide. *Welding J.* 68 (1989) 483.
5. M. J. Cieslak, Effect of thermal processing on the microstructure of Ti-26Al-11Nb_ Applications to fusion welding. *Met. Trans.* 21A (1990) 1273.

6. S. A. David, Weldability and microstructure of a titanium aluminide. *Welding J.* 69 (1990) 133.
7. M. C. Chaturvedi, N. L. Richards and Q. Xu, Electron beam welding of a Ti-45Al-2Nb-2Mn+0.8 vol.% TiB₂ XD alloy. *Mater. Sci. Eng.* A239/A240 (1997) 605.
8. M. R. A. Patterson, P. Martin, *et al.* Titanium aluminide – electron beam weld ability. *Welding J.* 69 (1990) 39.
9. P. L. Treadgill, Joining of intermetallic alloys – further studies. *Mater. Sci. Eng.*, A192/193 (1995) 640.
10. S. J. Lee, S. K. Wu and R. Y. Lin, Infrared joining of TiAl intermetallics using Ti-15Cu-15Ni Foil in the microstructure morphologies of joint interfaces. *Acta Mater.*, 46 (1998) 1297.
11. Y. Nakao, K. Shinozaki and M. Hamada, Diffusion bonding of intermetallic compound TiAl. *ISIJ Int.*, 31 (1991) 1260.
12. P. Yan and R.E. Wallach, Diffusion-bonding of TiAl. *Intermetallics*, 1 (1993) 83.
13. W. Glatz and H. Clemens, The high-temperature oxidation behaviour of Ti-47Al-2Cr-0.2Si and Ti-48Al-2Cr-2Nb compared with Ti-48Al-2Cr. *Intermetallics*, 5 (1997) 415.
14. G. Cam, K. H. Bohn, *et al.*, The fracture behavior of diffusion-bonded duplex gamma TiAl. *JOM*, 11 (1996) 66.
15. G. Cam, H. Clemens, *et al.*, Diffusion bonding of γ -TiAl sheets. *Intermetallics*, 7 (1999) 1025.
16. O. A. Kaibyshev, R. Ya. Lutfullin, R. V. Safillin and S. N. Fatullin, Problems and promises of developing integral technology of superplastic forming and diffusion bonding (SPF/DB). *Mat. Sci. Forum*, 170–172 (1994) 737–742.
17. R. M. Imayev, O. A. Kaybyshev and G. A. Salishchev, Mechanical behaviour of fine-grained intermetallic compound TiAl. *Phys. Met. Metallgr.*, 70(3) (1990) 179–186.
18. W. B. Lee, H. S. Yang and A. K. Mukherjee, Mechanical properties and microstructural characterization of a superplastic TiAl alloy. *Mater. Sci. Eng.*, A192–193 (1995) 733–740.
19. M. Lu, J. R. Bartett and T. J. Kelly, in *Proceedings of the 3rd International Symposium on Structural Intermetallics*, TMS, Jackson Hole, WY, 2001, pp. 225–232.
20. P. Bartolotta, J. Barrett, T. Kelly and R. Smashey, Use of cast Ti-48Al-2Cr-2Nb in jet engines. *JOM*, 49 (1997) 48.
21. B. Pettersson, P. Axelsson, M. Andersson and M. Holmquist, Cast XD gamma titanium aluminide turbine blade dampers, in Y. W. Kim, R. Wagner, M. Yamaguchi (eds), *Proceeding of the Symposium on γ -TiAl*, TMS, Las Vegas, 1995, pp. 33–40.
22. C. M. Austin and T. J. Kelly, Progress in implementation of cast gamma titanium aluminide, in M. V. Nathal (ed.), *Proceedings of the First International Symposium on Structural Intermetallics*, TMS, Champion, 1997, pp. 143–150.
23. P. J. Winkler, Diffusion bonding and superplastic forming two complementary manufacturing techniques, Superplasticity and Superplastic Forming, in C. Hamilton, N. E. Paton (eds), *Superplasticity Forming*, TMS, 1988, pp. 491.
24. C. H. Hamilton, *Titanium Science and Technology*, 1 (1973) 625 (New York, Plenum).
25. G. Garmong, N. E. Paton, A. S. Argon, *et al.*, Attainment of full interfacial contact during diffusion bonding. *Metallurgical Trans.*, A6 (1975) 1269–1279.
26. J. Pilling, The kinetics of isostatic diffusion bonding in superplastic materials. *Mater. Sci. Eng.*, 100 (1988) 137–144.

27. B. Derby and E. R. Wallach, Theoretical model for diffusion bonding. *Metal Science*, 16 (1982) 49–56.
28. B. Derby and E. R. Wallach, Diffusion bonding: development of theoretical model. *Metal Science*, 18 (1984) 427–431.
29. A. Hill and E. R. Wallach, Modeling solid-state diffusion bonding. *Acta Metall.*, 37 (1989) 2425–2437.
30. S. Z. Wen, *The Principle of Tribology*. Publishing Company of Tsinghua University, Beijing, China, 1991, pp. 364.
31. D. S. Wilkinson and M. F. Ashby, Mechanism mapping of sintering under an applied pressure. *Science of Sintering*, 10 (1978) 67–76.
32. E. Arzt, M. F. Ashby and R. A. Verrall, Interface controlled diffusion creep. *Acta Metall.*, 31 (1983) 1977–1989.
33. J. R. D. Williamson, *Welding Technology for the Aerospace Industry*, Proceedings of the Conference, Los Angeles: AWS. 1981, pp. 55.
34. W. W. Mullins, *Metal Surfaces*. ASM, 1963, p. 17.

5.7 Appendix: List of symbols

P_{eff}	Contacting pressure in the stage of plastic yielding deformation
β	Coefficient
σ_y	The yield strength of the material at bonding temperatures
W	The longest length of spread of surface diffusion in a definite time of t
D_s	Surface activation energy
δ	Diffusion layer thickness
γ_s	Surface energy
Ω	Atomic volume
t	Bonding time
k	Boltzmann's constant
T	Bonding temperature
r_c	Radius of curvature on major semi-axis
h	Height of unit cell, equivalent to minor semi-axis of ellipse
c	Major semi-axis of ellipse
θ	Equivalent circle angle
V_1	Rate of change of a volume with respect to time contributed by surface diffusion mechanism
δ_s	Surface layer thickness
d	Radius of curvature of the point of the longest length of surface diffusion in a definite time t .

Mathematical modelling of superplastic metal sheet forming processes

G. GIULIANO, University of Cassino, Italy

Abstract: The mathematical modelling of superplastic sheet forming processes is based on knowledge of the membrane theory and the flow rule to correlate the stresses to the strains in the plastic range. The modelling is limited usually to two special cases concerning bulge forming from a circular sheet and bulge forming from a rectangular sheet. In this chapter, mainly the free forming processes will be emphasized. Moreover, at the end of the chapter, some techniques will be suggested in order to determine the constants of the material from tests of inflation.

Key words: mathematical modelling, free forming process, circular and rectangular sheets, material constants, bulging tests.

6.1 Introduction

It is noted that all the superplastic metals showed optimal values of forming relative both to the temperature and to the strain rate; in fact, a superplastic behaviour emerges only in a narrow range of values of temperature and strain rate. If, during the deformation process, the temperature and the maximum strain rate values diverge from the optimal values, then exceptional superplastic elongations are compromised. Therefore, an accurate analysis and planning of the forming processes becomes indispensable. By developing approximate analytical models, for structure of simple geometry, it is possible to predict the thickness distribution of the part, to calculate the load cycle pressure-time and to examine the influence of the material constants on the process parameters and geometry of the formed part.

The mathematical modelling of superplastic forming processes is limited usually to two special cases concerning bulge forming from a circular sheet and bulge forming from a rectangular sheet. Both of them will be considered in this chapter. Moreover, at the end of the chapter, some techniques will be suggested in order to determine the constants of the material from tests of inflation.

The mathematical modelling is based on the following simple hypotheses:

1. The remarkable plastic deformations obtained during superplastic forming processes render the elastic deformations negligible.
2. As the strain rates employed during superplastic deformation are quite low (and in the range of 10^{-5} – 10^{-3} s⁻¹), in the equations of motion of the continuum

inertia forces can be neglected. Thus only the equilibrium equations can be considered.

3. In superplastic forming processes, the forming temperatures are in a narrow range of circa $0.5 T_m$, where T_m is the melting point in degrees Kelvin. Therefore, in the modelling it is necessary to consider an isothermal process.
4. The effects of increasing the grain size (strain hardening) or the growth and interlinkage of internally nucleated voids (soft hardening) are neglected.
5. The material is assumed to be isotropic and incompressible. Moreover, the relationship between the equivalent stress and the equivalent strain rate is defined by the classical power-law model valid in a narrow range of strain rates:

$$\bar{\sigma} = K \dot{\bar{\epsilon}}^m \quad [6.1]$$

where K is the strength coefficient and m is the strain rate sensitivity index.

6. The thickness of the sheet is very small so that the bending and shearing effects are negligible. Thus it is possible to use the membrane theory in order to describe the stress state in the deformed sheet (Carrino, 2007).

6.2 Membrane theory

The membrane theory can be used in order to describe the stress state in a thin sheet loaded by internal pressure, p . Figure 6.1 shows a surface of revolution characterized by lines, called meridians, and parallel circles. In the figure, s is the thickness of the sheet, R_θ and R_φ are the two radii of curvature of the shell.

Taking an element from the shell, consider the following assumptions:

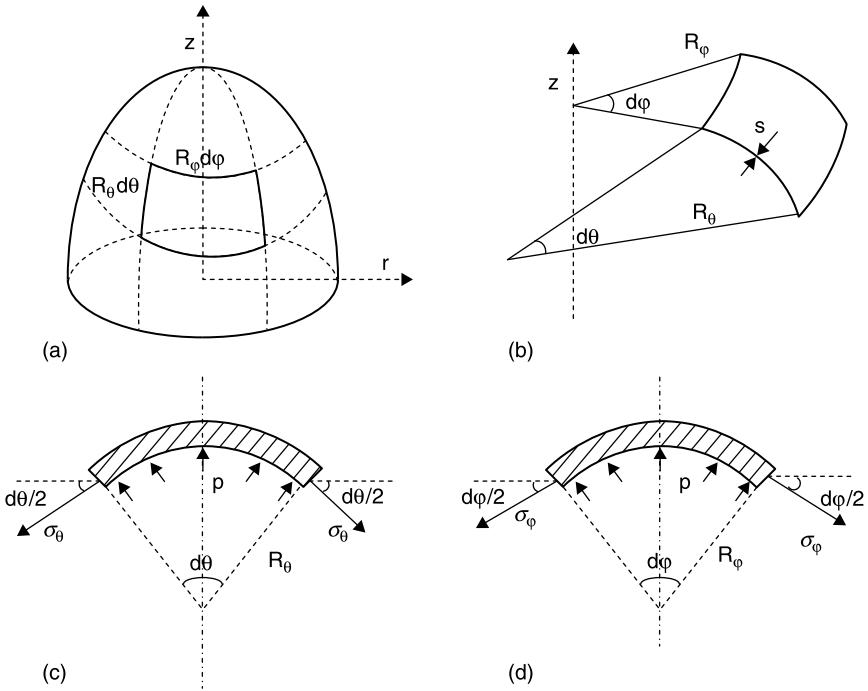
- the inertia forces can be neglected,
- because the thickness stress is much smaller than the tangential stress and the circumferential stress, it is neglected,
- the tangential and the circumferential stresses are uniformly distributed along the thickness.

A state of plane stress is assumed and the equilibrium equation of the shell element can be expressed as:

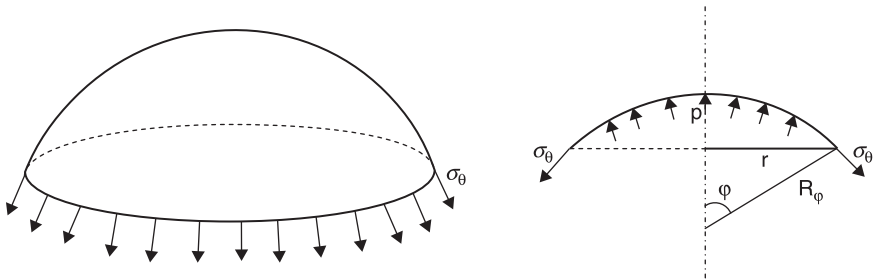
$$2\sigma_\varphi \operatorname{sen}\left(\frac{d\varphi}{2}\right) s R_\theta d\theta + 2\sigma_\theta \operatorname{sen}\left(\frac{d\theta}{2}\right) s R_\varphi d\varphi = p R_\varphi d\varphi R_\theta d\theta \quad [6.2]$$

Because, for a small angle, $\operatorname{sen}(d\alpha/2) = d\alpha/2$, the equilibrium equation can be written as:

$$\frac{\sigma_\varphi}{R_\varphi} + \frac{\sigma_\theta}{R_\theta} = \frac{p}{s} \quad [6.3]$$



6.1 Membrane theory of shells: (a) revolution surface characterized by meridians and parallel circles; (b) elements of the shell; and (c) and (d) stresses acting on the surfaces of the element.



6.2 Tangential stress acting on the shell.

With reference to Fig. 6.2, it is possible to estimate the tangential stress as:

$$\sigma_\theta \sin \phi \cdot 2\pi r s = p\pi r^2 \quad [6.4]$$

Taking into account that $r = R_\phi \sin \phi$, from Eq. [6.4] one can obtain the tangential stress as:

$$\sigma_\theta = \frac{pR_\phi}{2s} \quad [6.5]$$

Substituting Eq. [6.5] into Eq. [6.3], one can deduce that the circumferential stress equals:

$$\sigma_{\phi} = \frac{pR_{\phi}}{2s} \left(2 - \frac{R_{\phi}}{R_{\theta}} \right) \quad [6.6]$$

Equations [6.5] and [6.6] are the principal equations of membrane theory. Therefore, if the geometry of the shell and the forming pressure are known, it is possible to determine the stress state in the shell.

Invoking Von Mises criterion the equivalent stress for plain stress condition ($\sigma_t = 0$) can be written as:

$$\bar{\sigma} = \sqrt{\sigma_{\theta}^2 + \sigma_{\phi}^2 - \sigma_{\theta}\sigma_{\phi}} = \frac{pR_{\phi}}{2s} \sqrt{\left(\frac{R_{\phi}}{R_{\theta}}\right)^2 - 3\frac{R_{\phi}}{R_{\theta}} + 3} \quad [6.7]$$

6.3 Flow rule

In order to simplify the mathematical formulation, the elastic strain is negligible. Therefore, it becomes necessary to make reference to a theory that allows one to correlate the stresses to the strains in the plastic range (Carrino, 2007). Using the Levy-Mises flow rule one can obtain:

$$\begin{aligned} \dot{\epsilon}_{\theta} &= \frac{\dot{\bar{\epsilon}}}{\bar{\sigma}} \left[\sigma_{\theta} - \frac{1}{2}(\sigma_{\phi} + \sigma_t) \right] \\ \dot{\epsilon}_{\phi} &= \frac{\dot{\bar{\epsilon}}}{\bar{\sigma}} \left[\sigma_{\phi} - \frac{1}{2}(\sigma_{\theta} + \sigma_t) \right] \\ \dot{\epsilon}_t &= \frac{\dot{\bar{\epsilon}}}{\bar{\sigma}} \left[\sigma_t - \frac{1}{2}(\sigma_{\phi} + \sigma_{\theta}) \right] \end{aligned} \quad [6.8]$$

These equations are similar to those obtained from the elasticity theory except that:

- in place of $1/E$ the term $\dot{\bar{\epsilon}}/\bar{\sigma}$ is present (variable during deformation),
- in place of the Poisson coefficient a value equal to 0.5 is present.

In Eq. [6.8], $\dot{\epsilon}_{\theta}$, $\dot{\epsilon}_{\phi}$ and $\dot{\epsilon}_t$ are the tangential, circumferential and thickness strain rates respectively, while $\dot{\bar{\epsilon}}$ is the equivalent strain rate. From the Von Mises criterion and volume constancy ($\dot{\epsilon}_{\theta} + \dot{\epsilon}_{\phi} + \dot{\epsilon}_t = 0$), one can obtain the equivalent strain rate as:

$$\dot{\bar{\epsilon}} = \frac{2}{\sqrt{3}} \sqrt{\dot{\epsilon}_{\theta}^2 + \dot{\epsilon}_{\phi}^2 + \dot{\epsilon}_{\theta}\dot{\epsilon}_{\phi}} \quad [6.9]$$

6.4 Analysis of superplastic free forming processes

Approximated theoretical analyses of free forming and the forming into dies of simple shapes such as a conical die, V-shaped prismatic die, cylindrical cavity die and parallel walls die from circular or rectangular sheets appear in the literature (Fig. 6.3). The study of such processes gives the ability, in fair agreement with experimental data, to estimate the thickness distribution of the part manufactured, to determine the forming times, and to predict the load curve pressure-time that induces the optimal strain rate in the material.

Free forming makes the case simpler to analyse, because the sheet does not come into contact with the die walls: in the following sections this process is undertaken with greater emphasis. Forming into a die is more complex because, for an analytical model, intermediate conditions of contact between sheet and die comprised between the two limit conditions are necessary:

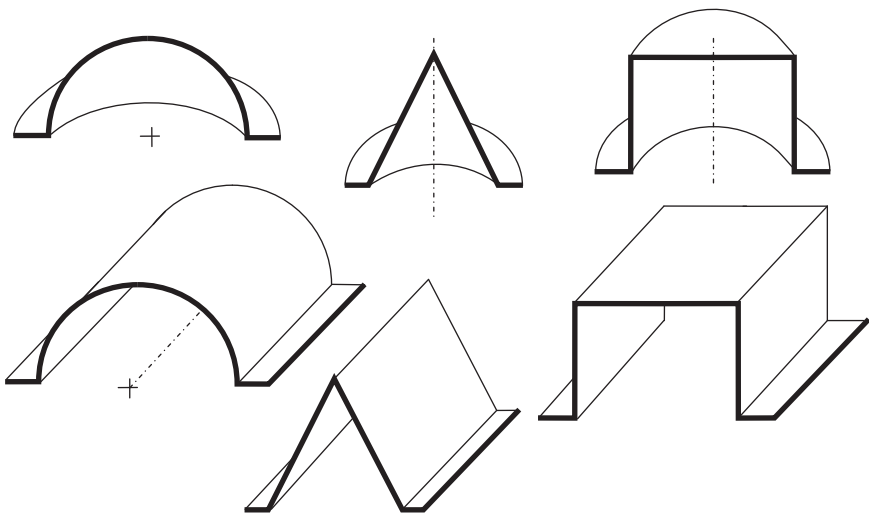
- free sliding,
- full adherence.

In these limit conditions, the sheet part once in contact with the die:

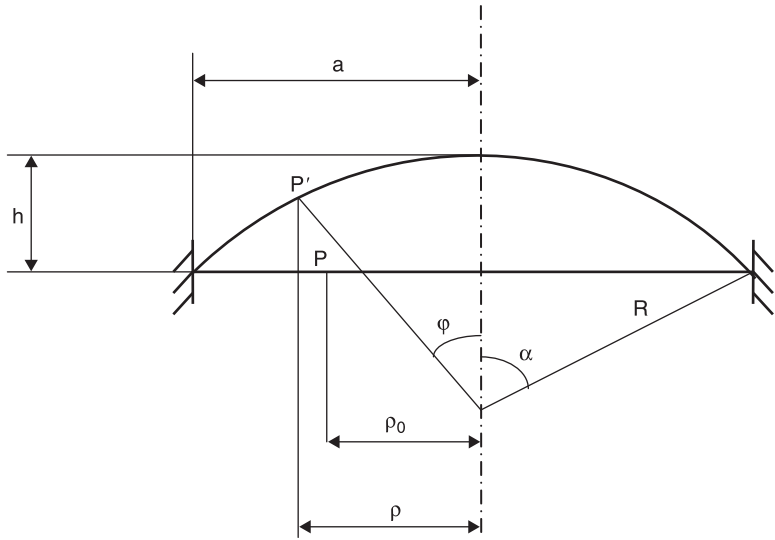
- continues to participate to the deformation,
- ceases to deform.

6.4.1 Free forming from a circular sheet

A circular sheet clamped around its periphery and loaded by a gas pressure is shown in Fig. 6.4. Jovane (1968), the first investigator of the approximate



6.3 Bulged parts starting with circular or rectangular sheets.



6.4 A circular sheet clamped around its periphery and loaded by gas pressure.

analysis of superplastic forming, assumed that the profile of the deformed sheet is part of a sphere. This hypothesis has been validated experimentally in first forming phases and for high values of the strain rate sensitivity index (Yang, 1992). Under such a hypothesis, based on the main equations of the membrane theory and Eq. [6.7], it is possible to define the stress state in every point of the sheet as:

$$\sigma_{\theta} = \sigma_{\varphi} = \frac{pR}{2s} \quad [6.10]$$

where R is the sphere radius.

Using the Levy-Mises equations and Eq. [6.9], it is possible to obtain the correspondent strain rates as:

$$\dot{\bar{\epsilon}} = -\dot{\epsilon}_t = 2\dot{\epsilon}_{\theta} = 2\dot{\epsilon}_{\varphi} \quad [6.11]$$

Jovane's model does not consider the non-uniform thickness that is determined at the moment of forming as successively evidenced from other authors (Cornfield, 1970; Holt, 1970; Ghosh, 1982; Chandra, 1993). In fact, close to the periphery of the sheet, the circumferential strain is negligible. In contrast with the equations of the membrane theory, the evidence from Eq. [6.8] shows that:

$$\sigma_{\theta} = 2\sigma_{\varphi} \quad [6.12]$$

The observed discrepancy is caused by the fact that, in proximity to the sheet periphery, the shear strains are considerable and could not be neglected. The plain

state determined in contact with the edge of the sheet leads to the following expressions for the stresses:

$$\begin{aligned} \sigma_{\theta} &= \frac{pR}{2s} \\ \sigma_{\phi} &= \frac{\sigma_{\theta}}{2} \\ \bar{\sigma} &= \sqrt{3}\sigma_{\phi} = \frac{\sqrt{3}}{2} \sigma_{\theta} \end{aligned} \tag{6.13}$$

and for strain rates:

$$\begin{aligned} \dot{\epsilon}_{\theta} &= 0 \\ \dot{\epsilon}_{\phi} &= -\dot{\epsilon}_t \\ \dot{\bar{\epsilon}} &= \frac{2}{\sqrt{3}} \dot{\epsilon}_{\phi} = -\frac{2}{\sqrt{3}} \dot{\epsilon}_t \end{aligned} \tag{6.14}$$

Therefore, indicating the pole and the edge of the sheet with the subscripts p and b respectively, from Eq. [6.5] one obtains:

$$\sigma_{\theta p} s_p = \sigma_{\theta b} s_b \tag{6.15}$$

therefore:

$$\bar{\sigma}_p s_p = \frac{2}{\sqrt{3}} \bar{\sigma}_b s_b \tag{6.16}$$

Substituting Eqs [6.1], [6.11] and [6.14] into [6.16] one obtains:

$$\frac{s_b}{s_p} = \left(\frac{2}{\sqrt{3}} \right)^{1+m} \left(\frac{\dot{\epsilon}_p}{\dot{\epsilon}_{t_b}} \right)^m \tag{6.17}$$

It is necessary to remember that the thickness strain rate is expressed as:

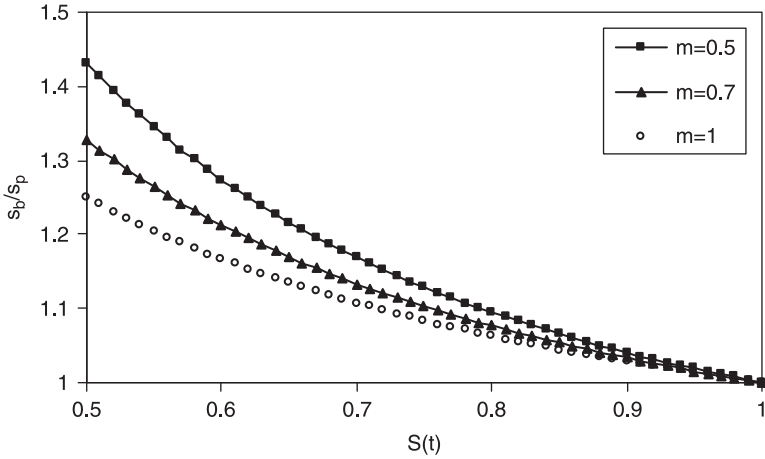
$$\dot{\epsilon}_t = \frac{\dot{S}}{S} \tag{6.18}$$

During the deformation process the thickness at the dome apex will endure such a thinning that:

$$s_p = S(t)s_0 \tag{6.19}$$

where s_0 is the initial thickness of the sheet and $S(t) \leq 1$.

Figure 6.5 shows that, during a free forming process, the thickness at the apex of the sheet is less than the thickness at the edge. Such non-uniformity is emphasized by diminishing of the strain rate sensitivity index value. Moreover, it is evidence a non-uniformity due to the different strain state that it is determined at the apex



6.5 Non-uniformity factor (s_v/s_p) during a free forming process for different m values.

and at the edge of the sheet during the inflation process will always be present that (also when $m = 1$ (ideal superplasticity)).

The thickness distribution in the generic configuration (instant t), has been suggested from Enikeev assuming that the meridian lines are uniformly stretched (Enikeev, 1994; 1995). With reference to Fig. 6.4:

$$\begin{aligned}
 \varepsilon_\varphi &= \ln\left(\frac{R\alpha}{a}\right) = \ln\left(\frac{\alpha}{\sin\alpha}\right) \\
 \varepsilon_\theta &= \ln\left(\frac{\rho}{\rho_0}\right) = \ln\left(\frac{\alpha \sin\varphi}{\varphi \sin\alpha}\right) \\
 \varepsilon_t &= \ln\left(\frac{s}{s_0}\right)
 \end{aligned}
 \tag{6.20}$$

where ρ_0 and ρ are the distance between a generic point of the sheet and the symmetry axis respectively at instants t_0 and t .

The thickness, s , in a generic point of the sheet (characterized from the angle φ) in the configuration for which half the angle subtended by a dome surface at its center of curvature is α , becomes:

$$\frac{s}{s_0} = \frac{\varphi \sin^2\alpha}{\sin\varphi \alpha^2}
 \tag{6.21}$$

Note that this expression is independent of the properties of the material. Considering thickness uniformity, simple geometric assumptions allow one to determine the value of R and the average thickness, \bar{s} , by means of the following relations:

$$R = \frac{a^2 + h^2}{2h} \tag{6.22}$$

and

$$\bar{s} = s_0 \frac{a^2}{a^2 + h^2} \tag{6.23}$$

where a is the initial radius of the sheet and h the dome height in a generic instant, t .

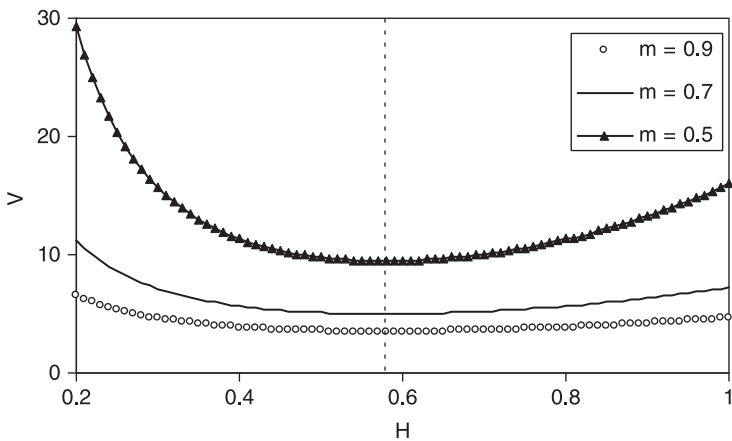
Introducing the relative dome height, $H = h/a$, and considering Eqs [6.10], [6.11], [6.18], [6.22] and [6.23] it is possible to determine the equivalent stress and strain rate using the following expressions:

$$\bar{\sigma} = \frac{pa}{4s_0} \frac{(1+H^2)^2}{H} \tag{6.24}$$

and

$$\dot{\bar{\epsilon}} = \frac{2H}{1+H^2} \dot{H} \tag{6.25}$$

Replacing Eq. [6.1] into Eq. [6.24] it is evident that, in a forming process at constant pressure, the strain rate varies continuously, also for various orders of magnitude at low values of m , and reaches the minimal value for $H^* \cong 0.58$ (Giuliano, 2009a). In a narrow range of values around H^* (the range is dependent on the value of m) it is possible to consider the strain rate as nearly constant. Showing $V = (4Ks_0/pa)^{1/m} \dot{\bar{\epsilon}}$ as the normalized strain rate, Fig. 6.6 shows that the m constant can influence the course of the strain rate during a forming process at constant pressure.



6.6 Normalized strain rate as a function of the relative dome height for a constant pressure application in free forming from a circular sheet and for different m values.

In the event in which the forming process happens at strain rate equal to the optimal strain rate, $\dot{\epsilon}_{opt}$ (that is the strain rate that, at the pre-chosen temperature, concurs to the material to reach the highest possible m values), through Eq. [6.24] and Eq. [6.25] it is possible to gain the load curve pressure-time (Giuliano, 2009a). Therefore:

$$p = \frac{4s_0 K \dot{\epsilon}_{opt}^m}{a} \frac{H}{(1 + H^2)^2} \tag{6.26}$$

where

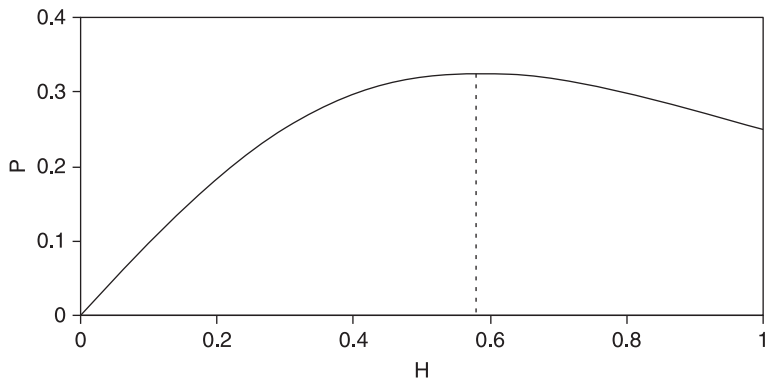
$$H = \sqrt{e^{\dot{\epsilon}_{opt} t} - 1} \tag{6.27}$$

Showing $P = (a/4s_0 K \dot{\epsilon}_{opt}^m)p$, the normalized pressure, Fig. 6.7 concurs to observe the variation during the deformation process. Such pressure reaches the maximum value for $H^* \cong 0.58$. Figure 6.8, obtained from Eq. [6.27], defining a normalized time $\tau = \dot{\epsilon}_{opt} t$, evidences the variation with the relative dome height H and the order of magnitude of the forming times necessary in order to obtain an hemisphere: if the optimal strain rate is equal at the 10^{-4} s^{-1} the forming time will be $0.69 \times 10^4 \text{ s}$.

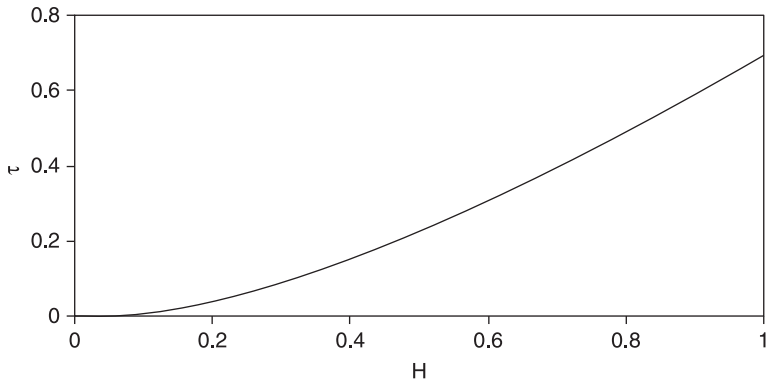
6.4.2 Free forming from a rectangular sheet

In the free forming process from a rectangular sheet (Ghosh, 1982; Ragab, 1983; Chandra, 1991; Vasin, 1999), with reference to Fig. 6.4, the basic hypotheses for an approximate analysis require that:

- the material is isotropic and incompressible,
- the elastic strains are neglected,



6.7 Normalized pressure as a function of the relative dome height for a constant strain rate application in free forming from a circular sheet.



6.8 Normalized time as a function of the relative dome height for a constant strain rate application in free forming from a circular sheet.

- the results of the membrane theory are considered,
- the sheet at any instant of the forming is equivalent to part of a cylindrical surface of infinite generatrix,
- during the forming plane strain state prevails.

As a result of this last assumption, Eq. [6.14] can be considered suitable in order to represent the strain state in every point of the sheet. Therefore:

$$\begin{aligned}\dot{\epsilon}_\theta &= 0 \\ \dot{\epsilon}_\phi &= -\dot{\epsilon}_t \\ \dot{\bar{\epsilon}} &= \frac{2}{\sqrt{3}} \dot{\epsilon}_\phi = -\frac{2}{\sqrt{3}} \dot{\epsilon}_t\end{aligned}\quad [6.28]$$

From the membrane theory, considering $R_\phi = R$ and $R_\theta = \infty$, it is possible to determine the circumferential stress, σ_ϕ , as:

$$\sigma_\phi = \frac{pR}{s} \quad [6.29]$$

From the Levy-Mises flow rule, considering $\dot{\epsilon}_\theta = 0$ one can obtain:

$$\sigma_\theta = \frac{\sigma_\phi}{2} \quad [6.30]$$

The stress state can be written as follows:

$$\begin{aligned}\sigma_\theta &= \frac{pR}{2s} \\ \sigma_\phi &= \frac{pR}{s} \\ \bar{\sigma} &= \sqrt{3}\sigma_\theta = \frac{\sqrt{3}}{2}\sigma_\phi = \frac{\sqrt{3}}{2} \frac{pR}{s}\end{aligned}\quad [6.31]$$

The radius of curvature of the sheet, R , and the thickness, s , can be evaluated, in any instant of deformation, as a function of the relative height, $H = h/a$.

Therefore:

$$H = \frac{1 - \cos \alpha}{\sin \alpha} = \operatorname{tg} \left(\frac{\alpha}{2} \right) \quad [6.32]$$

and

$$R = a \frac{1 + H^2}{2H} \quad [6.33]$$

while, from the incompressibility condition:

$$\frac{s}{s_0} = \frac{a}{R\alpha} = \frac{H}{1 + H^2} \frac{1}{\operatorname{arctg}H} \quad [6.34]$$

In conclusion:

$$\bar{\sigma} = \frac{\sqrt{3}}{4} \frac{ap}{s_0} \left(\frac{1 + H^2}{H} \right)^2 \operatorname{arctg}H \quad [6.35]$$

and

$$\dot{\epsilon} = \frac{2}{\sqrt{3}} \left[\frac{1}{(1 + H^2) \operatorname{arctg}H} - \frac{(1 - H^2)}{(1 + H^2)H} \right] \dot{H} \quad [6.36]$$

Replacing Eq. [6.1] into Eq. [6.35] it is possible to establish, in a forming process at constant pressure, the variation of the strain rate with the relative height according to the m constant. In fact, this gives:

$$\dot{\epsilon} = \left(\frac{\sqrt{3}}{4} \frac{ap}{Ks_0} \right)^{1/m} \left[\left(\frac{1 + H^2}{H} \right)^2 \operatorname{arctg}H \right]^{1/m} \quad [6.37]$$

Showing

$$V = \dot{\epsilon} \left(\frac{4}{\sqrt{3}} \frac{Ks_0}{ap} \right)^{1/m}$$

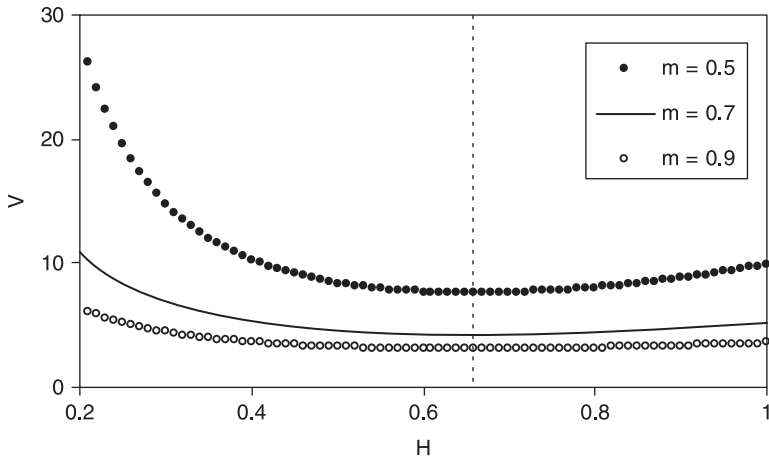
the normalized strain rate, Fig. 6.9 evidences the dependency from H and m . From Fig. 6.9, it is possible to note that the strain rate reaches a minimum for $H^* \cong 0.66$, and that it is constant for a narrow range of H values dependent on the m value.

In a process at constant strain rate, the load curve pressure-time and the H - t curve can be calculated by means of the following expressions:

$$P = \frac{4}{\sqrt{3}} \frac{s_0 K \dot{\epsilon}_{\text{opt}}^m}{a} \left(\frac{H}{1 + H^2} \right)^2 \frac{1}{\operatorname{arctg}H} \quad [6.38]$$

and

$$t = \frac{1}{\dot{\epsilon}_{\text{opt}}} \frac{2}{\sqrt{3}} \int_0^H \left[\frac{1}{(1 + x^2) \operatorname{arctg}x} - \frac{(1 - x^2)}{(1 + x^2)x} \right] dx \quad [6.39]$$



6.9 Normalized strain rate as a function of the relative dome height for a constant pressure application in the free forming from a rectangular sheet and for different m values.

6.5 Material constants from bulging tests

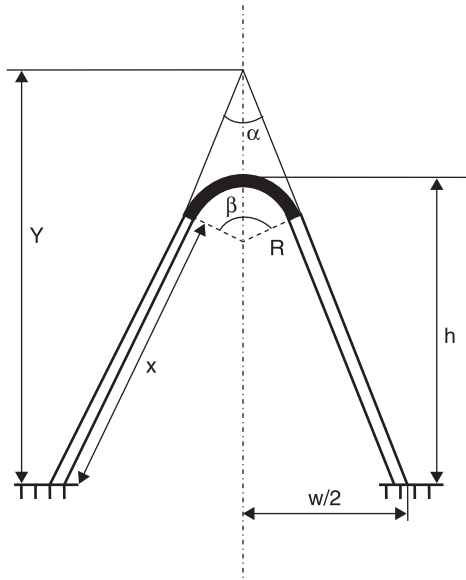
With reference to the classical power-law model, the value of the material constants using forming processes beginning with a circular or rectangular sheet represents an interesting solution regarding the traditional tensile test as:

- it is easier to prepare the test specimens regarding the standard specimen of the tensile test,
- the stress state that is determined during bulging tests is different from that of the uniaxial test, and is closer at the stress state determined during industrial forming processes.

The inflation tests present in literature are relative at free forming processes (Jovane, 1968; Enikeev, 1995; Cheng, 1996; Carrino, 2003; Giuliano, 2008), or at forming processes in a closed die (Ghosh, 1980; Lederich, 1982; Story, 1988; Goforth, 1988; Chandra, 1990; Carrino, 2001; Carrino, 2003). In general terms, various tests at constant pressure are necessary to record the evolution in the time of a parameter dependent of the sheet strain. It is possible thus to go back to the material constants m and K , by means of a simplified mathematical model, directly or through the determination of the equivalent stress–equivalent strain rate.

6.5.1 Bulging test into a conical die

The bulging test into a conical die was analyzed critically by Ghosh and Hamilton (Ghosh, 1980); even if successively it has been considered by other authors (Lederich, 1982; Goforth, 1988; Chandra, 1990; Carrino, 2003). Figure 6.10 shows a schematic layout of the forming process.



6.10 Schematic layout of the bulging test into a conical die.

Once the sheet comes into contact with the die, the profile of the uncontacted sheet region is assumed to be part of a sphere. Also the hypotheses used in the free forming of a circular sheet, and introduced in paragraph 6.4.1, are discussed here. In addition, it is assumed that a condition of full adherence in the contact region sheet-die exists. In the hypothesis of a balanced, biaxial stress state, it is well-known that the equivalent stress is equal to:

$$\mathbf{R}(\mathbf{x}_{n+1}^{k+1}, p_{n+1}^{k+1}) = \mathbf{T}(\mathbf{x}_{n+1}^{k+1}) - p_{n+1}^{k+1} \mathbf{G}(\mathbf{x}_{n+1}^{k+1}) = \mathbf{0} \tag{6.40}$$

where p is the forming pressure, R is the radius of curvature of bulge after contact with die walls and s is the instantaneous thickness.

The test was aimed at achieving constant flow stress by maintaining a constant forming pressure; therefore it is necessary to estimate the cone angle for which:

$$\frac{R}{s} = \text{const} \tag{6.41}$$

The surface strain rate, $\dot{\epsilon}_s$, is defined as:

$$\dot{\epsilon}_s = \frac{dS}{dt} \cdot \frac{1}{A} = \frac{\dot{S}}{A} \tag{6.42}$$

where S is the total surface of the deformed sheet at instant t , and A the surface not in contact with the die (the darkened portion in Fig. 6.10).

The total surface of the membrane is given from the sum of the spherical segment + the surface of the truncated cone formed from the portion of the sheet in contact with the die:

$$S = 2\pi R^2 \left[1 - \cos\left(\frac{\beta}{2}\right) \right] + \pi x \left[\frac{w}{2} + R \cdot \text{sen}\left(\frac{\beta}{2}\right) \right] \quad [6.43]$$

whose derivative is:

$$\dot{S} = 4\pi R\dot{R} \left[1 - \cos\left(\frac{\beta}{2}\right) \right] + \pi \dot{x} \frac{w}{2} + \pi \cdot \text{sen}\left(\frac{\beta}{2}\right) [x\dot{R} + \dot{x}R] \quad [6.44]$$

In Eqs [6.43] and [6.44], $\beta/2 = 90 - (\alpha/2)$, w is the diameter of initial sheet and x the apothem of the truncated cone.

Substituting Eq. [6.44] into Eq. [6.42], one can obtain:

$$\dot{\epsilon}_s = 2 \frac{\dot{R}}{R} + \frac{w}{4 \left[1 - \cos\left(\frac{\beta}{2}\right) \right]} \cdot \frac{\dot{x}}{R^2} + \frac{\text{sen}\left(\frac{\beta}{2}\right)}{2 \left[1 - \cos\left(\frac{\beta}{2}\right) \right]} \cdot \frac{\dot{x}R + x\dot{R}}{R^2} \quad [6.45]$$

where:

$$x = \frac{w}{2} \cdot \frac{1}{\text{sen}\left(\frac{\alpha}{2}\right)} - \frac{R}{\text{tg}\left(\frac{\alpha}{2}\right)} \quad [6.46]$$

and

$$\dot{x} = - \frac{\dot{R}}{\text{tg}\left(\frac{\alpha}{2}\right)} \quad [6.47]$$

Substituting Eqs [6.46] and [6.47] into Eq. [6.45], one can obtain:

$$\dot{\epsilon}_s = 2 \frac{\dot{R}}{R} - \frac{\cos\left(\frac{\alpha}{2}\right)}{\text{tg}\left(\frac{\alpha}{2}\right) \cdot \left[1 - \text{sen}\left(\frac{\alpha}{2}\right) \right]} \cdot \frac{\dot{R}}{R} \quad [6.48]$$

From volume constancy, can be written:

$$\frac{\dot{s}}{s} = -2 \frac{\dot{R}}{R} + \frac{\cos\left(\frac{\alpha}{2}\right)}{\text{tg}\left(\frac{\alpha}{2}\right) \cdot \left[1 - \text{sen}\left(\frac{\alpha}{2}\right) \right]} \cdot \frac{\dot{R}}{R} \quad [6.49]$$

that, integrated, it allows s/R to be estimated as:

$$\frac{s}{R} = \frac{s_1}{R} \left(\frac{R}{R_1} \right)^{-2 + \frac{\cos\left(\frac{\alpha}{2}\right)}{\operatorname{tg}\left(\frac{\alpha}{2}\right) \left(1 - \operatorname{sen}\left(\frac{\alpha}{2}\right)\right)}} \quad [6.50]$$

where, respectively, s_1 and R_1 are the thickness and the radius of curvature of the sheet in the first contact with the die.

So that the value s/R remains unchanged, it must impose a unitary value to the exponent of R/R_1 . Therefore:

$$\operatorname{tg}\left(\frac{\alpha}{2}\right) = \frac{\cos\left(\frac{\alpha}{2}\right)}{3 \cdot \left(1 - \operatorname{sen}\left(\frac{\alpha}{2}\right)\right)} \quad [6.51]$$

This relation is verified for a cone angle of 60° .

With the cone angle fixed to 60° , it is possible, with simple considerations, to estimate the equivalent strain rate and the equivalent stress as:

$$\dot{\bar{\epsilon}} = \frac{1}{A_1} \quad [6.52]$$

and

$$\bar{\sigma} = 0.385 \cdot \frac{W}{s_0} \cdot p \quad [6.53]$$

where A_1 is the angular coefficient of the following equation:

$$(t - t_1) = -A_1 \cdot \ln(Y - h) + A_2 \quad [6.54]$$

that is obtained recording, during the test, the $h-t$ trend. In Eq. [6.54], Y is the height of the cone, t_1 is the forming time to the end of the free-bulging stage (first contact sheet-die) and A_2 is a constant.

6.5.2 Bulging test into V-shaped die

In this bulging test (Ghosh, 1980; Lederich, 1982; Story, 1988; Carrino, 2001; Carrino, 2003), a pyramidal die rather than a conical die is used. During the bulging process, full adherence condition is assumed to prevail between the sheet which comes into contact with the die, while the non-contacted sheet deforms under plane strain state. So that a plane strain state is considered, the die must introduce a length at least five times greater to the width. Also, in this case, the bulged profile at any instant is circular.

With the width stress equal to:

$$\sigma_w = \frac{p \cdot R}{s} \quad [6.55]$$

R/s must be constant to maintain constant stress at constant pressure.

It is reasonable to define the width strain rate, $\dot{\epsilon}_w$, as:

$$\dot{\epsilon}_w = \frac{\dot{l}}{R \cdot \frac{\pi}{180} (180 - \alpha)} \quad [6.56]$$

In this expression, l represents the total width of the deformed sheet, and the denominator $R \cdot (\pi/180) \cdot (180 - \alpha)$ is the width of the sheet not in contact with the die walls (Fig. 6.10). From geometric considerations, one can obtain:

$$x = \frac{1}{\operatorname{tg}\left(\frac{\alpha}{2}\right)} \left[\frac{w}{2} \sqrt{1 + \operatorname{tg}^2\left(\frac{\alpha}{2}\right)} - R \right] \quad [6.57]$$

and

$$\dot{x} = -\frac{\dot{R}}{\operatorname{tg}\left(\frac{\alpha}{2}\right)} \quad [6.58]$$

where w is the initial width of the sheet.

The total width of the deformed sheet is:

$$l = 2 \cdot x + R \cdot \frac{\pi}{180} \cdot (180 - \alpha) \quad [6.59]$$

whose derivative is:

$$\dot{l} = 2 \cdot \dot{x} + \dot{R} \cdot \frac{\pi}{180} (180 - \alpha) \quad [6.60]$$

Substituting Eq. [6.58] into Eq. [6.60], one can obtain:

$$\dot{l} = -\frac{2 \cdot \dot{R}}{\operatorname{tg}\left(\frac{\alpha}{2}\right)} + \dot{R} \cdot \frac{\pi}{180} (180 - \alpha) \quad [6.61]$$

This equation, into Eq. [6.56], allows the width strain rate to be written as:

$$\dot{\epsilon}_w = \frac{\dot{R}}{R \cdot \frac{\pi}{180} \cdot (180 - \alpha)} \left[\frac{\pi}{180} \cdot (180 - \alpha) - \frac{2}{\operatorname{tg}\left(\frac{\alpha}{2}\right)} \right] \quad [6.62]$$

From the volume constancy, $\dot{\epsilon}_n = -\dot{s}/s$, and therefore after integration:

$$\frac{R}{s_0} \left(\frac{R}{R_0} \right)^{\frac{1}{180(180-\alpha)} \left[-\frac{2}{\operatorname{tg}\left(\frac{\alpha}{2}\right)} + \frac{\pi}{180}(180-\alpha) \right]} = \frac{s_0}{s} \cdot \frac{R}{s_0} \quad [6.63]$$

To maintain $R/s = \text{const}$, the geometry of the pyramidal die will have to be such that:

$$\frac{1}{\frac{\pi}{180} \cdot (180 - \alpha)} \cdot \left(-\frac{2}{\operatorname{tg}\left(\frac{\alpha}{2}\right)} + \frac{\pi}{180} \cdot (180 - \alpha) \right) + 1 = 0 \quad [6.64]$$

That is:

$$\frac{1}{\operatorname{tg}\left(\frac{\alpha}{2}\right)} = \frac{\pi}{180} (180 - \alpha) \quad [6.65]$$

The angle that verifies Eq. [6.65] is $\alpha \cong 46.4^\circ$. In this way, during the forming process, the value of the ratio between the radius of curvature of the sheet and its thickness remains constant.

Assuming $\alpha \cong 46.4^\circ$, the equivalent stress, $\bar{\sigma}$, and the equivalent strain rate, $\dot{\bar{\epsilon}}$, will be given from the following expressions:

$$\bar{\sigma} = 0.597 \cdot \frac{w}{s_0} p \quad [6.66]$$

and

$$\dot{\bar{\epsilon}} = \frac{2}{\sqrt{3}} \frac{1}{A_1} \quad [6.67]$$

where A_1 is obtained, as for the conical test, recording the h - t curve.

6.5.3 Free forming test

In the free forming processes at constant pressure from a circular or rectangular sheet independent of the approximate hypotheses, it is always possible to reach an expression in which (Jovane, 1968; Enikeev, 1995; Carrino, 2003; Giuliano, 2008):

$$J_m(H) \propto \left(\frac{pa}{Ks_0} \right)^{1/m} t \quad [6.68]$$

where $J_m(H)$ is an integral, estimated between the normalized heights H_0 and H , dependent of the adopted model and the m value. The variables p , s_0 and a

represent, respectively, the forming pressure, the initial thickness and the initial radius of the sheet (in the case of the circular sheet) or the width of the sheet (in the case of the rectangular sheet) while t is the forming time to pass from H_0 to H .

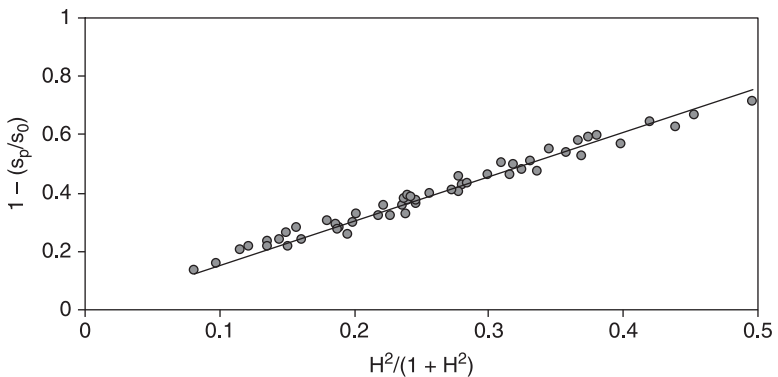
From Eq. [6.68] it is possible to determine, by means of two forming tests at the constant pressures p_1 and p_2 , the strain rate sensitivity index, m , as:

$$m = \frac{\ln\left(\frac{p_1}{p_2}\right)}{\ln\left(\frac{t_2}{t_1}\right)} \tag{6.69}$$

In this equation, t_1 and t_2 are respectively the forming times to reach the same normalized height, H .

Once m has been estimated, by means of Eq. [6.68], it is possible to go back at the K value. Such a value is strongly influenced by the adopted model; in particular, in the case of the circular sheet, from the approximate hypotheses used for the evaluation of the thickness at the sheet apex. The thickness at the sheet apex has been considered equal to the medium thickness of the sheet by Jovane (1968); different from the medium thickness and only dependent on geometric parameters by Enikeev and Kruglov (Enikeev, 1995); and dependent also of the material properties in a detailed geometric condition ($a = 30$ mm and entry radius of die = 2 mm) from Giuliano and Franchitti (Giuliano, 2008). In this last case, it has been verified experimentally (Giuliano, 2009b) for some superplastic Pb–Sn alloys (Fig. 6.11) that the thickness at the dome apex varies using the following expression:

$$1 - \frac{s_p}{s_0} = \delta \frac{H^2}{1 + H^2} \tag{6.70}$$



6.11 Experimental data for the PbSn60 alloy: a function of the normalized thickness at the dome apex versus a function of the normalized polar height, H .

Therefore, once determined the constant δ by means of preliminary tests, it is possible to estimate accurately the equivalent stress and the equivalent strain rate.

6.6 References

- Carrino, L. and Giuliano, G. (2001), 'Analysis of superplastic testing by using constant pressure in prismatic die', *Materials Science Forum*, 357–359: 219–224.
- Carrino, L., Giuliano, G. and Polini, W. (2003), 'A method to characterise superplastic materials in comparison with alternative methods', *Journal of Materials Processing Technology*, 138: 417–422.
- Carrino, L. and Giuliano, G. (2007), *La formatura superplastica*, Roma, Aracne editrice.
- Chandra, N., Kannan, D., Goforth, R.E. and Phillips, L. (1990), 'Mechanical characterization of superplastic materials using modified cone test', *Superplasticity in Aerospace*, II: 67–84.
- Chandra, N. and Chandy, K. (1991), 'Superplastic process modelling of plane strain components with complex shapes', *Journal of Material Shaping Technology*, 9: 27–36.
- Chandra, N. and Kannan, D. (1993), 'Superplastic sheet metal forming of generalized cup, Part II: non-uniform thinning', *Journal of Material Engineering and Performance*, 1: 813–822.
- Cheng, J.H. (1996), 'The determination of material parameters from superplastic inflation tests', *Journal of Materials Processing Technology*, 58: 233–246.
- Cornfield, G.C. and Johnson, R.H. (1970), 'The forming of superplastic sheet metal', *International Journal of Mechanical Science*, 12: 479–490.
- Enikeev, F.U. (1994), 'An analytical model for superplastic bulge forming of domes', *Materials Science Forum*, 170–172: 681–686.
- Enikeev, F.U. and Kruglov, A.A. (1995), 'An analysis of the superplastic forming of a thin circular diaphragm', *International Journal of Mechanical Science*, 37(5): 473–483.
- Holt, D.L. (1970), 'An analysis of the bulging of a superplastic sheet by lateral pressure', *International Journal of Mechanical Science*, 12: 491–497.
- Lederich, R.J., Sastry, S.M.L., Hayase, M. and Mackay, T.L. (1982), 'Superplastic formability testing', *Journal of Metals*, 16–20.
- Ghosh, A.K. and Hamilton, C.H. (1980), 'On constant membrane stress test for superplastic metals', *Metallurgical Transactions*, 11A: 1915–1918.
- Ghosh, A.K. and Hamilton, C.H. (1982), 'Influences of material parameters and microstructure on superplastic forming', *Metallurgical Transactions*, 13A: 733–743.
- Giuliano, G. and Franchitti, S. (2008), 'The determination of material parameters from superplastic free-bulging tests at constant pressure', *International Journal of Machine Tools and Manufacture*, 48(12–13): 1519–1522.
- Giuliano, G. (2009a), 'La formatura superplastica' in Suzzani R., *Manuale di Lavorazione della Lamiera*, Milano, Tecniche Nuove, 456–464.
- Giuliano, G. (2009b), 'Thickness and strain rate at the sheet dome apex in superplastic bulge forming tests', *Conference on Material Forming (ESAFORM 2009)*, Twente, Netherlands, April 27–29.
- Goforth R.E., Chandra N. and George D. (1988), 'Analysis of the cone test to evaluate superplastic forming characteristics of sheet metal', *Superplasticity in Aerospace*, I: 149–166.

- Jovane, F. (1968), 'An approximate analysis of the superplastic forming of a thin circular diaphragm: theory and experiments', *International Journal of Mechanical Science*, 10: 403–427.
- Ragab, A.R. (1983), 'Thermoforming of superplastic sheet in shaped dies', *Metals Technology*, 10: 340–348.
- Story, J.M. (1988), 'Incorporation of sliding friction into a closed-form model of plane strain superplastic forming', *Superplasticity and Superplastic Forming*, 297–302.
- Vasin, R.A., Enikeev, F.U. and Safiullin R.V. (1999), 'Mathematical modelling of superplastic forming of a long rectangular box section' *Materials Science Forum*, 304–306: 765–770.
- Yang, H.S. and Mukherjee A.K. (1992), 'An analysis of the superplastic forming of a circular sheet diaphragm', *International Journal of Mechanical Science*, 34: 283–293.

Finite element modelling of thin metal sheet forming

J. BONET and A. J. GIL, Swansea University, UK

Abstract: This chapter reviews the finite element simulation of superplastic forming processes. Both the traditional flow formulation and the incremental flow formulation are presented. The chapter reviews the finite element discretisation of the equilibrium equations describing the motion of a forming sheet including available strategies for the evaluation of a correct forming pressure, which is often one of the key outputs of the simulation. A number of examples are given in relation to applications in the aerospace industry as well as more recent applications in the biomedical field.

Key words: superplastic forming, finite elements, incremental flow formulation, pressure control, large strains, non-Newtonian viscous flow, contact conditions.

7.1 Introduction

Early reviews of the numerical simulation of superplastic forming (SPF) are given by Wood and Bonet¹⁹ and Bonet *et al.*³⁵ However, since these reviews, there have been further developments and literature on SPF in general and the finite element simulation of SPF in particular, hence the need for this current update.

Whilst analytical (or more precisely non-finite element) solutions for the simulation of SPF are available for simple geometries, the practical complexity of SPF components is such that the finite element method is the only viable route to simulation. This can be achieved using either explicit or implicit formulations and using membrane, shell or continuum elements as appropriate; see various papers in refs 19, 32 and 35. Nevertheless non-finite element solutions are often used in conjunction with simple bulge or cone tests in order to determine constitutive parameters,^{7,8} or pressure cycles.^{10,11,25}

Since superplasticity is a viscoplastic phenomenon, the flow formulation is the natural finite element approach in which the velocity of the forming material is the primary variable. This was first expounded by Thompson in 1969.¹ For non-steady state situations such as SPF, time integration is necessary to obtain the changing geometry. Although it had long been known that superplastic behaviour was a non-linear viscous flow process, it was not until 1984 that Argyris and St Doltsinis⁵ published what appears to be the first finite element paper specifically dealing with the simulation of SPF.

Since the publication of the first finite element simulation of SPF (FE-SPF),⁵ there has been a steady increase in the FE-SPF publication rate; however the adoption of FE-SPF by industry appears to remain at an early stage. This is due to a number of factors, namely: the extremely high level of skill in process design by personnel who have been associated with SPF since its inception in the aerospace industry in the 1960s; the required high level of skill needed to perform a finite element simulation involving complex mesh generation and the execution of a highly non-linear solution technique; and finally, the uncertainty regarding material properties including friction. However the aerospace industry does have the computational skills and does use FE-SPF whilst other industrial sectors are expressing a growing interest. In particular, superplasticity and SPF of dental and other biomedical prostheses has recently become an important new field of application. In this area, the ability of SPF to form complex parts is fully exploited. However, the patient-specific nature of the geometries involved implies that robust computational simulation processes need to be implemented in order to obtain predictable outcomes of component thickness. The application of numerical simulation to superplastically formed prostheses has been comprehensively described.^{27,33,37}

We continue with a brief discussion of superplasticity and the related issues concerning constitutive behaviour. Finite element formulation detail is provided by considering the developments undertaken by the authors, first, in respect of the 'classical' flow formulation and second, for the incremental flow formulation which is closely allied to finite deformation formulation. Existing commercial software capabilities will also be considered. A number of applications will be presented, followed by concluding thoughts on the future for finite element SPF simulation.

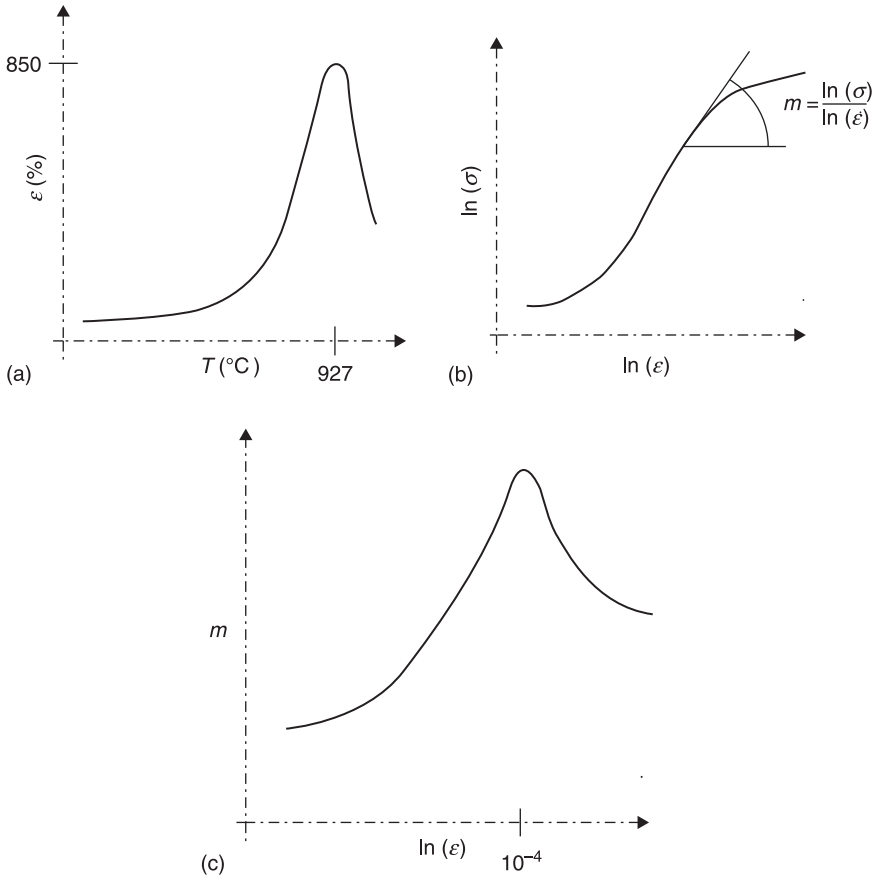
7.2 Continuum model

7.2.1 Uniaxial models

Superplastic forming behaviour of materials can conveniently be described as a non-Newtonian viscous flow. Such materials are generally characterised by a non-linear relationship between the Cauchy stress and the strain rate, and for superplastic materials this usually manifests as the sigmoidal curve shown in Fig. 7.1(b). The simplest constitutive equation^{3,6} is the Norton-Hoff power law relationship between Cauchy stress, σ the strain ϵ and the equivalent strain rate $\dot{\epsilon}$ as,

$$\sigma = K\epsilon^n \dot{\epsilon}^m, \quad m = \frac{\partial \ln \sigma}{\partial \ln \dot{\epsilon}} \quad [7.1]$$

where K is a constant and n and m are the strain hardening parameter and strain rate sensitivity index respectively. An alternative three parameter power law based model has been proposed.^{18,24}



7.1 Superplastic forming constitutive behaviour: (a) strain vs. temperature; (b) stress vs. strain rate in log–log scale; and (c) strain rate sensitivity index vs. strain rate in semi-log scale.

The power law can be augmented to include the effect of static and dynamic grain growth as,

$$\sigma = K(g, T) \dot{\epsilon}^{m(g, T)} \quad [7.2]$$

where g is the grain size and T the forming temperature.^{2,4,9,28,30} Since grain size changes during the forming process, a grain growth evolution equation is required. However, when using Eq. [7.2], many numerical simulations^{5,25} simply consider K and m as constant values and ignore their dependence with the grain growth. Whilst this may be satisfactory for simple geometries, the authors' experience is that the effect of grain growth evolution is an important factor that needs to be taken into account for an accurate simulation.^{33,35,37}

Many alternative hyperbolic sine-based constitutive equations for superplastic behaviour have been proposed,^{16,20,23,31} a typical uniaxial example employed by the authors²⁰ being as follows,

$$\sigma = \sigma_0 \left[\sinh^{-1} \left(\frac{\dot{\epsilon}}{\dot{\epsilon}_0} \right) \right]^m e^{\left(\frac{\sigma'}{RT} \right)}, \quad \sigma_0 = A_\sigma \left(\frac{g}{g_0} \right)^{P_\sigma}, \quad \dot{\epsilon}_0 = A_\epsilon \left(\frac{g}{g_0} \right)^{P_\epsilon} \quad [7.3]$$

where $\dot{\epsilon}$ is the strain rate and the dependency upon the grain size is revealed by g . Grain growth evolution is typically represented in terms of static and dynamic grain growth rates, over an increment in time Δt as,

$$g_{t+\Delta t} = g_t + [\dot{g}_{\text{stat}}(g, T) + \dot{g}_{\text{dyn}}(\dot{\epsilon}, g, T)] \Delta t \quad [7.4]$$

Complete parameter details for Eq. [7.3] and Eq. [7.4] are given in detail in refs 20 and 27.

7.2.2 General 3-dimensional constitutive equations

With the purpose of developing a 3-dimensional continuum approach to the phenomenon of superplasticity, the uniaxial constitutive equations derived in the above section are generalised within the framework of a viscoplastic energy potential Ψ . The von Mises equivalent stress $\bar{\sigma}$ can be formulated in terms of the equivalent strain rate $\dot{\bar{\epsilon}}$ by introducing a suitable viscoplastic energy density ψ as follows,¹²

$$\bar{\sigma} = \psi(\dot{\bar{\epsilon}}, g, T), \quad \bar{\sigma}^2 = \frac{3}{2} \sigma' : \sigma', \quad \dot{\bar{\epsilon}}^2 = \frac{2}{3} d' : d' \quad [7.5]$$

where σ' and d' are the deviatoric components of the Cauchy stress tensor and the rate of deformation tensor, respectively, derived as

$$\sigma' = \sigma - \sigma_m \mathbf{I}, \quad d' = d - \frac{1}{3} I_d \mathbf{I}, \quad I_d = \text{tr}d \quad [7.6]$$

being σ_m the mean stress or volumetric component of the Cauchy stress tensor and d the symmetric component of the spatial velocity gradient tensor $l = \nabla v$. Equation [7.5] can be re-expressed in terms of a viscoplastic energy potential Ψ as follows,

$$\bar{\sigma} = \frac{\partial \Psi(\dot{\bar{\epsilon}}, g, T)}{\partial \dot{\bar{\epsilon}}}, \quad \Psi(\dot{\bar{\epsilon}}, g, T) = \int_0^{\dot{\bar{\epsilon}}} \psi(\xi, g, T) d\xi = \int_0^{\dot{\bar{\epsilon}}} \bar{\sigma} d\xi \quad [7.7]$$

The deviatoric component of the Cauchy stress tensor σ' can be derived from the viscoplastic energy potential Ψ as,

$$\sigma' = \frac{\partial \Psi(\dot{\bar{\epsilon}}, g, T)}{\partial \dot{\bar{\epsilon}}^2} \frac{\partial \dot{\bar{\epsilon}}^2}{\partial d} = 2\mu d', \quad \mu = \frac{2}{3} \frac{\partial \Psi(\dot{\bar{\epsilon}}, g, T)}{\partial \dot{\bar{\epsilon}}^2} = \frac{\bar{\sigma}}{3\dot{\bar{\epsilon}}} \quad [7.8]$$

where μ is the non-linear viscosity parameter which clearly displays the non-Newtonian viscous constitutive nature of superplastic phenomena. The mean stress σ_m is usually obtained after defining a volumetric energy potential Ψ_m

introduced to enforce the incompressibility constraint (i.e. $I_d = \text{tr} \mathbf{d} = \nabla \cdot \mathbf{v} = 0$) by means of a κ -penalty approach as follows,

$$\sigma_m = \frac{\partial \Psi_m(I_d)}{\partial \mathbf{d}} = \sigma_m \mathbf{I}, \quad \Psi_m(I_d) = \frac{\kappa}{2} I_d^2 \quad [7.9]$$

Finally, combining Eq. [7.8] and Eq. [7.9], the Cauchy stress tensor results in

$$\sigma = 2\mu \mathbf{d}' + \kappa I_d \mathbf{I} \quad [7.10]$$

7.3 Finite element formulation and time integration schemes

In superplastic computational modelling, inertia effects are usually neglected, which enables the establishment of the equilibrium equations in a quasi-static framework. Following the classical mechanics principle of virtual work established over a domain V with boundary surface A , it must be verified that

$$\delta W(\mathbf{x}, \delta \mathbf{v}) = \delta W_{int}(\mathbf{x}, \delta \mathbf{v}) - \delta W_{ext}(\mathbf{x}, \delta \mathbf{v}) = 0 \quad [7.11]$$

where

$$\delta W_{int}(\mathbf{x}, \delta \mathbf{v}) = \int_V \sigma' : \delta \mathbf{d}' dV + \int_V \sigma_m \nabla \cdot \delta \mathbf{v} dV = \int_V (\sigma' + \sigma_m \mathbf{I}) : \nabla \delta \mathbf{v} dV \quad [7.12]$$

and

$$\delta W_{ext}(\mathbf{x}, \delta \mathbf{v}) = \int_A p \mathbf{n} \cdot \delta \mathbf{v} dA \quad [7.13]$$

In Eqs [7.11]–[7.13], \mathbf{x} symbolises the current spatial location of the forming component obtained after time integration of the velocity field \mathbf{v} , $\delta \mathbf{v}$ is a virtual velocity field compatible with the existing forming boundary conditions, $\delta \mathbf{d}'$ is the deviatoric component of the virtual rate of deformation tensor, p is the forming pressure acting on the boundary surface A , and \mathbf{n} is the outward unit normal to the surface.

Following an isoparametric finite element semi-discretisation procedure,³⁶ the different kinematic fields can be expanded in terms of standard finite element shape functions N^a associated to every node a of a Lagrangian mesh as

$$\mathbf{x} = \sum_a N^a \mathbf{x}^a, \quad \mathbf{v} = \sum_a N^a \mathbf{v}^a, \quad \delta \mathbf{v} = \sum_a N^a \delta \mathbf{v}^a \quad [7.14]$$

Substitution of above expressions [7.14] into the virtual work formulae [7.2] and [7.3], and taking into consideration the arbitrariness of the nodal virtual velocity $\delta \mathbf{v}^a$, results in a set of algebraic equations relating an assembled equivalent internal force vector \mathbf{T} and an assembled equivalent external force vector \mathbf{F} expressed in terms of the assembled velocity vector \mathbf{v} and the assembled spatial coordinates vector \mathbf{x} as

$$\mathbf{R}(\mathbf{x}, \mathbf{v}, p) = \mathbf{T}(\mathbf{x}, \mathbf{v}) - \mathbf{F}(\mathbf{x}, p) = \mathbf{0} \quad [7.15]$$

where

$$\mathbf{T}(\mathbf{x}, \mathbf{v}) = \mathbf{A}[\mathbf{T}_{(e)}^a], \quad \mathbf{T}_{(e)}^a = \int_{V_{(e)}} (\boldsymbol{\sigma}' + \boldsymbol{\sigma}_m \mathbf{I}) \nabla N^a dV \quad [7.16]$$

and

$$\mathbf{F}(\mathbf{x}, p) = \mathbf{A}[\mathbf{F}_{(e)}^a], \quad \mathbf{F}_{(e)}^a = p \int_{V_{(e)}} N^a \mathbf{n} dV \quad [7.17]$$

In the above set of equations, both nodal positions, which define the body geometry, and nodal velocities that define the deformation gradient and therefore the stresses, are unknowns at any time t . A time integration procedure is therefore required in order to advance the solution in time. This can be a simple forward Euler explicit scheme, namely,

$$\mathbf{x}_{n+1} = \mathbf{x}_n + \Delta t \mathbf{v}_n \quad [7.18]$$

which allows the equilibrium to be resolved only for the nodal velocities but has significant stability restrictions on the size of time step Δt that can be used. Alternatively, implicit schemes such as a trapezoidal rule,

$$\mathbf{x}_{n+1} = \mathbf{x}_n + \frac{1}{2} \Delta t (\mathbf{v}_n + \mathbf{v}_{n+1}) \quad [7.19]$$

lead to a set of equilibrium equations which are highly non-linear both in relation to the velocity and nodal positions. An alternative formulation, known as the *incremental flow formulation* that provides a more robust simulation process, is described below.

7.4 The incremental flow formulation

In the incremental formulation,^{13,21} the rate of deformation based material law which describes the phenomenon of superplasticity is approximated by a geometry based constitutive equation. The forming process is simulated as a sequence of solution steps in time, which enables the use of the displacement field as the primary variable, in contrast to the traditional flow formulation where the velocity field is regarded as the fundamental variable.

The configurations of an initial domain V_0 at two consecutive time steps t_n and t_{n+1} are symbolised as V_n and V_{n+1} , respectively. The incremental motion from \mathbf{x}_n to \mathbf{x}_{n+1} is represented by a general mapping Φ , with an associated deformation gradient tensor \mathbf{F} as,

$$\mathbf{x}_{n+1} = \Phi(\mathbf{x}_n), \quad \mathbf{F} = \frac{\partial \Phi}{\partial \mathbf{x}_n} = \nabla_n \Phi, \quad J = \det \mathbf{F} \quad [7.20]$$

In order to represent the flow equations in terms of geometrical quantities measured over a time step $\Delta t = t_{n+1} - t_n$, the incremental rate of deformation tensor $\tilde{\mathbf{d}}$ is defined as,

$$\tilde{\mathbf{d}} = \frac{1}{\Delta t}(\mathbf{C} - \mathbf{I}), \quad \mathbf{d} = \lim_{\Delta t \rightarrow 0} \tilde{\mathbf{d}} \quad [7.21]$$

where $\mathbf{C} = \mathbf{F}^T \mathbf{F}$ is the right Cauchy-Green deformation tensor. A simple incremental approximation to the equivalent von Mises strain rate $\dot{\tilde{\boldsymbol{\varepsilon}}}$, namely $\dot{\tilde{\boldsymbol{\varepsilon}}}$, is introduced as,

$$\dot{\tilde{\boldsymbol{\varepsilon}}}^2 = \frac{1}{3\Delta t^2}(\text{tr}\hat{\mathbf{C}} - 3), \quad \dot{\tilde{\boldsymbol{\varepsilon}}} = \lim_{\Delta t \rightarrow 0} \dot{\tilde{\boldsymbol{\varepsilon}}} \quad [7.22]$$

where the distortional component $\hat{\mathbf{C}}$ of the right Cauchy-Green tensor is defined as,

$$\hat{\mathbf{C}} = \text{III}_C^{-1/3} \mathbf{C}, \quad \text{III}_C = \det \mathbf{C} \quad [7.23]$$

For a simple Norton-Hoff viscoplastic potential, expressed in terms of the incremental equivalent strain rate $\dot{\tilde{\boldsymbol{\varepsilon}}}$ and two material parameters K and m as,

$$\Psi(\dot{\tilde{\boldsymbol{\varepsilon}}}) = \frac{K}{m+1} \dot{\tilde{\boldsymbol{\varepsilon}}}^{m+1} \quad [7.24]$$

the deviatoric component of the second Piola-Kirchhoff stress tensor \mathbf{S}' can be obtained after differentiation of the above expression with respect to $\tilde{\mathbf{d}}$,

$$\mathbf{S}' = \frac{\partial \Psi(\dot{\tilde{\boldsymbol{\varepsilon}}})}{\partial \tilde{\mathbf{d}}} = \frac{\mu \text{III}_C^{-1/3}}{\Delta t} \left(\mathbf{I} - \frac{1}{3} \text{I}_C \mathbf{C}^{-1} \right), \quad \mu = \frac{2}{3} \frac{d\Psi(\dot{\tilde{\boldsymbol{\varepsilon}}})}{d\dot{\tilde{\boldsymbol{\varepsilon}}}^2} \quad [7.25]$$

and the deviatoric component of the Cauchy stress tensor $\boldsymbol{\sigma}'$ can be obtained after a suitable push forward operation as,

$$\boldsymbol{\sigma}' = J^{-1} \mathbf{F} \mathbf{S}' \mathbf{F}^T = \frac{\mu}{J^{5/3} \Delta t} \left(\mathbf{b} - \frac{1}{3} \text{I}_b \mathbf{I} \right), \quad \text{I}_b = \text{tr} \mathbf{b}, \quad \mathbf{b} = \mathbf{F} \mathbf{F}^T \quad [7.26]$$

The mean stress or volumetric component of the Cauchy stress tensor $\boldsymbol{\sigma}_m$ is obtained from a volumetric energy potential Ψ_m , introduced to enforce the incompressibility constraint (i.e. $J = 1$) by means of a κ -penalty approach as follows,

$$\boldsymbol{\sigma}_m = J^{-1} \mathbf{F} \frac{\partial \Psi_m(J)}{\partial \tilde{\mathbf{d}}} \mathbf{F}^T = \boldsymbol{\sigma}_m \mathbf{I}, \quad \Psi_m(J) = \frac{\kappa}{2\Delta t^2} (J-1)^2, \quad J = \frac{V_{n+1}}{V_n} \quad [7.27]$$

Combination of Eq. [7.26] and Eq. [7.27] results in,

$$\boldsymbol{\sigma} = \frac{\mu}{J^{5/3} \Delta t} \left(\mathbf{b} - \frac{1}{3} \text{I}_b \mathbf{I} \right) + \frac{\kappa}{\Delta t^2} \left(\frac{V_{n+1} - V_n}{V_n} \right) \mathbf{I} \quad [7.28]$$

In anticipation of the need of a second order Newton-Raphson algorithm to solve the resulting set of non-linear algebraic equilibrium equations, the Lagrangian fourth order tangent moduli is obtained as,

$$\mathbf{C}' = 2 \frac{\partial \mathbf{S}'}{\partial \mathbf{C}} = 4\Delta t \frac{\partial^2 \Psi}{\partial \mathbf{C} \partial \mathbf{C}} \quad [7.29]$$

The Eulerian fourth order tangent moduli is formulated after a push forward operation as,

$$\mathbf{c}' = \frac{2\mu}{3J^{5/3}} \left(\frac{I_b}{3} \mathbf{I} \otimes \mathbf{I} - \mathbf{b} \otimes \mathbf{I} - \mathbf{I} \otimes \mathbf{b} + I_b \mathbf{i} \right) + \frac{(m-1)J}{3\mu\tilde{\epsilon}^2} \boldsymbol{\sigma}' \otimes \boldsymbol{\sigma}' \quad [7.30]$$

where \mathbf{i} represents an isotropic fourth order tensor with indicial components as,

$$i_{ijkl} = \frac{1}{2} (\delta_{ik}\delta_{jl} + \delta_{il}\delta_{jk}) \quad [7.31]$$

being δ_{ij} the well-known second order delta Kronecker tensor. Following a standard finite element implementation [7.14], the assembled residual equilibrium equations can be formulated as,

$$\mathbf{R}(\mathbf{x}, p) = \mathbf{T}(\mathbf{x}) - p\mathbf{G}(\mathbf{x}) = \mathbf{0} \quad [7.32]$$

where \mathbf{G} is an assembled external equivalent force vector corresponding to a normalised unit pressure. As can be observed, and in contrast to the classical flow formulation [7.15] where the nodal velocity \mathbf{v} plays the fundamental role, the incremental flow formulation [7.32] utilises the spatial nodal location vector \mathbf{x} as the primary variable. For a constant pressure field p , the non-linear algebraic equilibrium equations at a time step, t_{n+1} , namely $\mathbf{R}(\mathbf{x}_{n+1}, p) = \mathbf{0}$ are solved using a second order iterative Newton-Raphson procedure,

$$\mathbf{R}_{n+1}^{k+1} = \mathbf{R}(\mathbf{x}_{n+1}^{k+1}, p) \quad \mathbf{R}_{n+1}^k + \frac{\partial \mathbf{R}}{\partial \mathbf{u}} \Big|_{n+1}^k \Delta \mathbf{u} = \mathbf{0}, \quad \mathbf{u}_{n+1}^{k+1} = \mathbf{u}_{n+1}^k + \Delta \mathbf{u} \quad [7.33]$$

Hence, the update displacement vector $\Delta \mathbf{u}$ between two consecutive iterations k and $k+1$ yields,

$$\Delta \mathbf{u} = -[\mathbf{K}_{n+1}^k]^{-1} \mathbf{R}_{n+1}^k, \quad \mathbf{K}_{n+1}^k = \frac{\partial \mathbf{T}}{\partial \mathbf{x}} \Big|_{n+1}^k - p \frac{\partial \mathbf{G}}{\partial \mathbf{x}} \Big|_{n+1}^k \quad [7.34]$$

where an assembled symmetric stiffness matrix \mathbf{K} can be expanded into its main components in indicial form as,

$$[\mathbf{K}]_{ij}^{ab} = [\mathbf{K}^c]_{ij}^{ab} + [\mathbf{K}^\sigma]_{ij}^{ab} + [\mathbf{K}^v]_{ij}^{ab} + [\mathbf{K}^p]_{ij}^{ab} \quad [7.35]$$

where $[\mathbf{K}^c]_{ij}^{ab}$ is the constitutive deviatoric stiffness contribution as,

$$[\mathbf{K}^c]_{ij}^{ab} = \int_{V_{n+1}} \frac{\partial N^a}{\partial x_k} c_{ijkl} \frac{\partial N^b}{\partial x_l} dV \quad [7.36]$$

$[\mathbf{K}^\sigma]_{ij}^{ab}$ is the geometric or initial stress stiffness contribution as,

$$[\mathbf{K}^\sigma]_{ij}^{ab} = \int_{V_{n+1}} \delta_{ij} \sigma_{kl} \frac{\partial N^a}{\partial x_k} \frac{\partial N^b}{\partial x_l} dV \quad [7.37]$$

$[\mathbf{K}^v]_{ij}^{ab}$ is the constitutive volumetric stiffness contribution as,

$$[\mathbf{K}^V]_{ij}^{ab} = \frac{\kappa V_{n+1}^2}{\Delta t^2 V_n} (\bar{\nabla} N^a \otimes \bar{\nabla} N^b) + \int_{V_{n+1}} \sigma_m (\nabla N^a \otimes \nabla N^b - \nabla N^b \otimes \nabla N^a) dV \quad [7.38]$$

where $\bar{\nabla} N^a$ denotes the average gradient over the element corresponding to the shape function N^a and $[\mathbf{K}^p]_{ij}^{ab}$ is the follower load stiffness contribution defined as,

$$[\mathbf{K}^p]_{ij}^{ab} = p \int_{A_{n+1}} N^a \varepsilon_{ijk} \left(\frac{\partial N^b}{\partial \xi} \frac{\partial x_k}{\partial \eta} - \frac{\partial N^b}{\partial \eta} \frac{\partial x_k}{\partial \xi} \right) dA \quad [7.39]$$

where ε_{ijk} is the third order permutation tensor and ξ, η are the isoparametric coordinates of the parent finite element domain.

7.5 Pressure cycle algorithms

The ability to accurately control the forming of the SPF component, so that an optimum strain rate sensitivity index m is maintained throughout the deformation process, is fundamental for a successful outcome.¹⁴ Under these circumstances, the material is less prone to necking and a more uniformly distributed final thickness is likely to be attained. Pressure cycle calculations employ a variety of formulations, usually based on a maximum allowed desired target strain rate $\dot{\bar{\epsilon}}$ or target flow stress $\bar{\sigma}$ occurring anywhere in the forming material. Therefore, the forming pressure can be treated as an unknown variable whose value can be determined via an additional constraint equation (i.e. target strain rate, target flow stress). For a time varying pressure field, and following an incremental flow formulation, the system of non-linear algebraic equilibrium equations at time step t_{n+1} and at iteration $k + 1$ can be formulated as,

$$\mathbf{R}(\mathbf{x}_{n+1}^{k+1}, p_{n+1}^{k+1}) = \mathbf{T}(\mathbf{x}_{n+1}^{k+1}) - p_{n+1}^{k+1} \mathbf{G}(\mathbf{x}_{n+1}^{k+1}) = 0 \quad [7.40]$$

The spatial coordinates and forming pressure are iteratively updated as follows,

$$\mathbf{x}_{n+1}^{k+1} = \mathbf{x}_{n+1}^{k+1} + \Delta \mathbf{u}, \quad \Delta \mathbf{u} = \Delta \mathbf{u}_R - \Delta p \Delta \mathbf{u}_G, \quad p_{n+1}^{k+1} = p_{n+1}^k + \Delta p \quad [7.41]$$

where under a Newton-Raphson iterative scheme, the incremental displacement vector components $\Delta \mathbf{u}_R$ and $\Delta \mathbf{u}_G$ are formulated as,

$$\Delta \mathbf{u}_R = -[\mathbf{K}_{n+1}^k]^{-1} \mathbf{R}_{n+1}^k, \quad \Delta \mathbf{u}_G = -[\mathbf{K}_{n+1}^k]^{-1} \mathbf{G}_{n+1}^k \quad [7.42]$$

An additional constraint equation must be introduced to compute the incremental pressure. This constraint can be formulated, in a general manner, in terms of the spatial coordinates and the pressure as,

$$\mathcal{F}(\mathbf{x}_{n+1}^{k+1}, p_{n+1}^{k+1}) = 0 \quad [7.43]$$

A first order Taylor series expansion can then be applied to Eq. [7.43] to yield,

$$\mathcal{F}_{n+1}^{k+1} = \mathcal{F}(\mathbf{x}_{n+1}^{k+1}, p_{n+1}^{k+1}) \quad \mathcal{F}_{n+1}^k + \left. \frac{\partial \mathcal{F}}{\partial \mathbf{x}} \right|_{n+1}^k \Delta \mathbf{u} + \left. \frac{\partial \mathcal{F}}{\partial p} \right|_{n+1}^k \Delta p = 0 \quad [7.44]$$

Finally, combination of formulae [7.41] and [7.44] results in,

$$\Delta p = \frac{\mathcal{F}|_{n+1}^k + \frac{\partial \mathcal{F}}{\partial \mathbf{x}}|_{n+1}^k \Delta \mathbf{u}_R}{\frac{\partial \mathcal{F}}{\partial \mathbf{x}}|_{n+1}^k \Delta \mathbf{u}_F - \frac{\partial \mathcal{F}}{\partial p}|_{n+1}^k} \quad [7.45]$$

7.6 Die representation and contact algorithms

Accurate and valid geometric definition of the die is fundamental for a successful and accurate computational simulation. Smooth semi-analytical NURBS definition of the die surface can be employed, from which a faceted surface mesh is obtained. The initial geometric definition is likely to be in the form of a formatted file derived from some imaging technique. It is essential that the resulting surface definition is valid, in the sense that a unique connectivity must be defined, holes must not appear and unit normal vectors to the surface must be given in a consistent direction. In contrast to the mesh required for the discretisation of the forming material, the density of the die mesh must be considerably finer in order to capture complex features.

The mesh representing the forming sheet should be such that higher density meshes should be located in those areas anticipated to come into contact with die surfaces exhibiting complex detail, hence mesh refinement should be employed whereby mesh enrichment occurs when elements show excessive stretching or curvature based upon a computed error estimator.¹⁵

A numerical procedure must be implemented to enforce contact, by which it is ensured that the forming material remains on, and does not penetrate, the die.^{17,29} Inclusion of friction between the forming material and the die relates to those procedures which constrain the forming material to move tangent to the die surface according to classical friction laws. Including friction in the simulation of SPF is a challenge, since coefficients of friction are largely unknown and likely to change during the process. In practice, valuable information may be obtained from simulations assuming complete sticking or sliding contact between the forming sheet and the die. Sliding and frictional contact simulation is likely to be another source of convergence problems in implicit solution procedures where, for the latter, a non-symmetric tangent operator arises. As the die surface is comprised of facets, the equilibrium equations repeatedly solved within the Newton-Raphson algorithm alters as the node on the sheet moves from one facet to a neighbouring facet with a different unit normal.

7.7 Commercial codes

The finite element simulation of SPF can be categorised under a number of headings based on the formulation (velocity or displacement) and type of solution

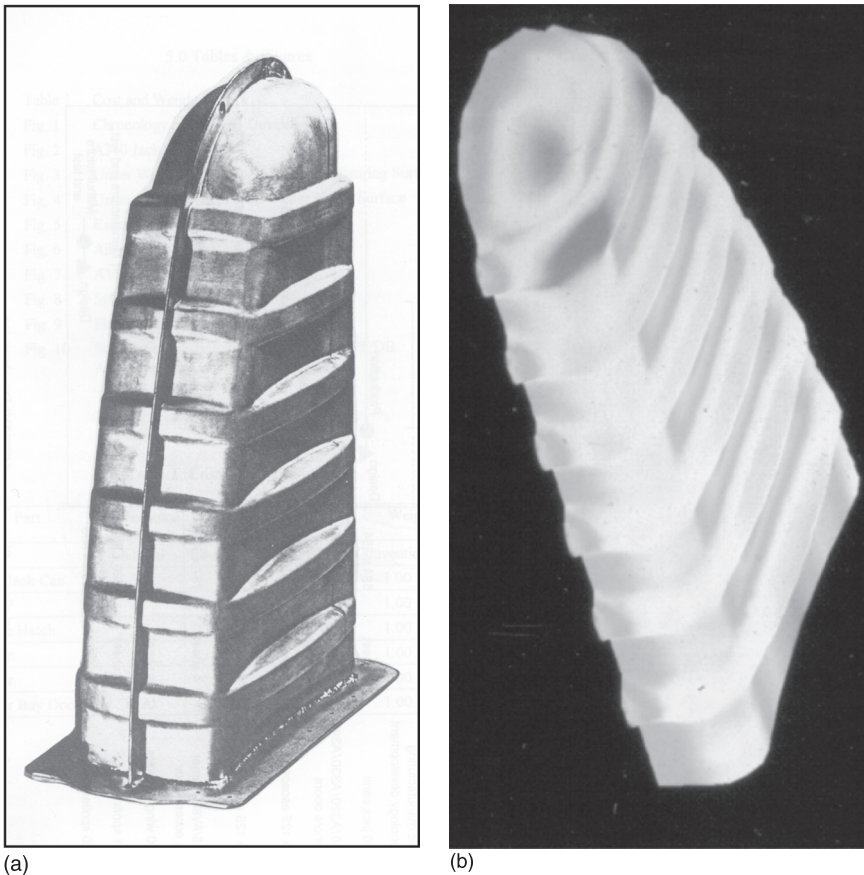
(explicit or implicit); discretisation (membrane, shell or solid); facility for mesh adaptation; complexity of constitutive equation (power or sinh law either with or without grain size dependency); inclusion of contact friction; inclusion of optimised pressure cycle calculation; complexity of component simulated (bulge, cone, aerospace, automotive, medical) and finally use of a commercial or privately developed program.

Implicit velocity based flow formulations dominate FE-SPF software, used by many individual developers; for example see Refs 22, 26, 30 and 35. Alternatively, implicit or explicit dynamic commercial codes such as MARC [<http://www.mscsoftware.com/Products/CAE-Tools/Marc-And-Mentat.aspx>] and the explicit PAMSTAMP code [<http://www.esi-group.com/products/metAl-forming>] are available. An implicit displacement based formulation is used by investigators employing the creep facilities of the commercial ABAQUS code [http://www.simulia.com/products/abaqus_fea.html]. A comparison between the ABAQUS and LS-DYNA (explicit dynamic) commercial codes for FE-SPF is provided.³⁴ Finally the authors have developed an implicit displacement based formulation known as the *incremental flow formulation* which has been presented above and is in use by the Aerospace industry through the code SNAPFORM.^{14,21,27}

7.8 Applications

Computational simulation of SPF processes started in the aerospace industry. An early example of a successful simulation is the jack can of the airbus A310, which houses the jack that deploys frontal slats. The overall size of the component is $500 \times 270 \times 70$ mm and the initial thickness of the sheet is 1.8 mm. The material is Ti-6Al-4V with an initial grain size of 8 μm . Just over 5000 triangular linear membrane finite elements are used to model the deforming sheet. The actual formed component is shown in Fig. 7.2, together with the final computed thickness distribution varying from 1.7 mm to 0.8 mm. Excellent agreement of thickness distribution was found between the computer model and the actual component. The actual forming time is 144 minutes which took 120 time steps in the calculation, requiring 290 Newton-Raphson iterations in total.

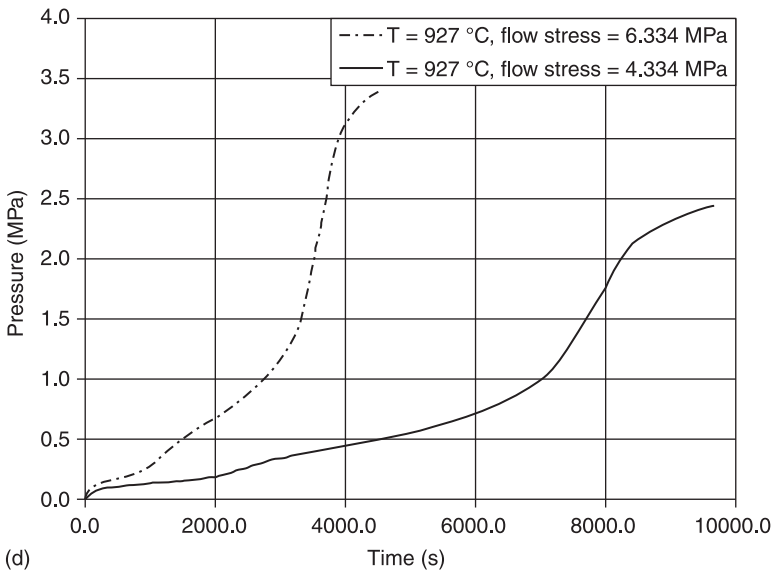
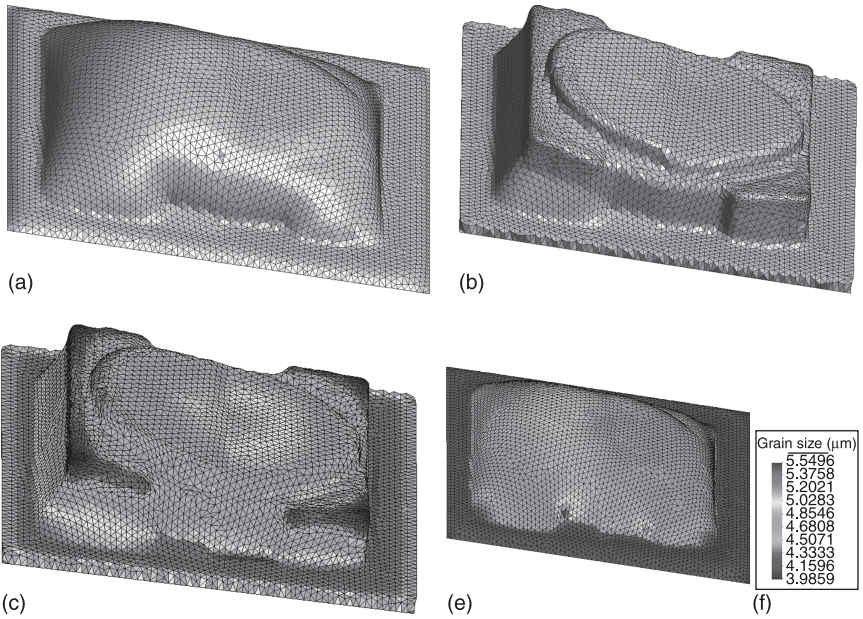
A second example relates to an automotive component that has been simulated using the incremental flow formulation described above. Initial meshes, comprising 8960 membrane elements for the sheet and 35770 elements for the die, were used with sticking assumed upon contact between the sheet and the die. The approximate size of the final formed component is $460 \times 410 \times 155$ mm; the initial thickness was 3 mm; the initial grain size 3.49 μm and the forming temperature was 927°C. Two configurations at different times together with the final thickness distribution are shown in Fig. 7.3(a), (b) and (c). The material is Ti-6Al-4V and the calculated pressure cycle, shown in Fig. 7.3(d) was determined



7.2 Jack can: (a) actual formed component and (b) final predicted thickness distribution.

using flow stress control with values of 4.334 MPa and 6.334 MPa. Finally Fig. 7.3(e) and (f) shows intermediate and final grain size distribution.

Recently, computational simulation technology has become an indispensable tool for researchers across the general discipline of Biomechanics. Crucial to the effectiveness of such a tool is its ability to simulate patient-specific problems. Superplastic forming has introduced interesting possibilities of creating prostheses at a lower cost and with more complex shapes than usual cold forming processes. Scanning of the patient's area of interest is employed to generate a geometrical model of the damaged area. Then, image-based mesh generation tools are used to obtain an accurate representation of the domain of interest. Thus, a valid computational die mesh can be obtained for the subsequent finite element simulation. It must be emphasised that attempts to generate complex prostheses

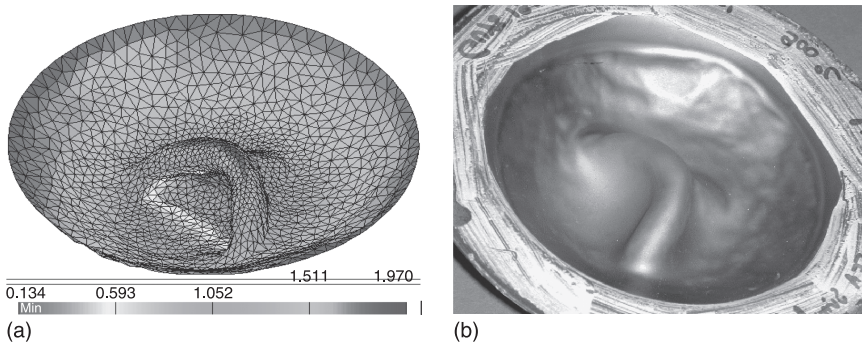


7.3 Automotive component: (a) intermediate configuration; (b) final shape; (c) final thickness distribution; (d) pressure histories at different flow rate stresses; and (e) and (f) intermediate grain size distribution.

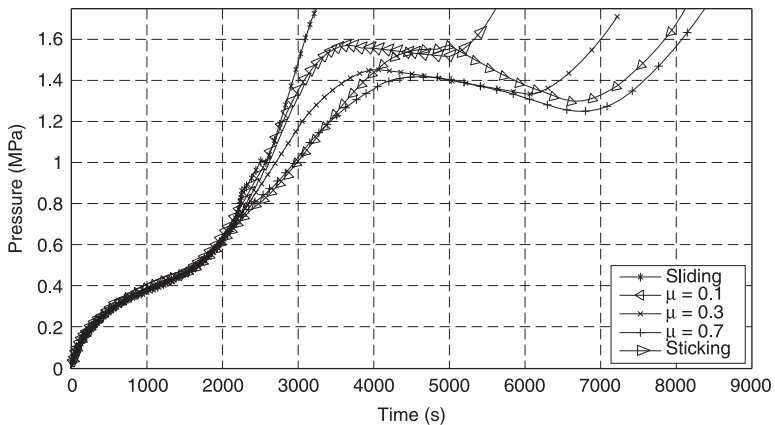
without prior numerical modelling to generate the pressure cycle can result in consistent ruptured prototypes.

The Ridge Augmentation membrane (RAM)²⁷ is a dental prosthetic device built for patients who have undergone ablative surgery or have suffered loss of hard tissue. The RAM prosthesis enables us to demonstrate the ability of the numerical simulation to predict suitable pressure cycles prior to the actual forming of the component. Figure 7.4(b) displays an image of the actual RAM prosthesis. The computational simulation was carried out under a forming temperature of 900°C, an initial grain size of 5 and an initial thickness of 2 mm. In addition, the pressure cycles were found using a target flow stress of 6.334 MPa, whose results are displayed in Fig. 7.5. Figure 7.4(a) displays the final thickness distribution obtained under sticking contact conditions.

Orbital cranioplasties³⁷ provide a considerable challenge for the maxillofacial and craniofacial surgeon in providing repair to the para-nasal sinuses and the



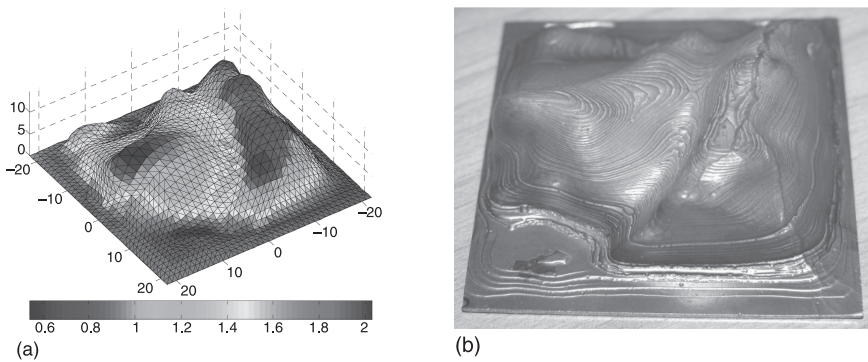
7.4 RAM computational analysis²⁷: (a) final thickness distribution (mm) and (b) final formed component.



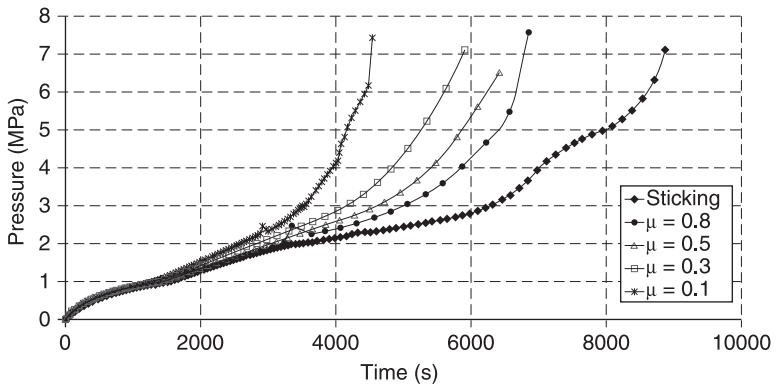
7.5 RAM pressure cycle for different contact conditions.²⁷

walls of the orbit. The most common cause for orbital floor repair is blunt trauma to the orbital rim. Data from a CT scan of both the normal orbital cavity and the orbital cavity with the defect are reconstructed as a 3-dimensional image. Where the floor of the orbit is missing on the affected side, the contours of the orbital floor and walls can be reconstructed by mirroring the data from the orbital cavity on the unaffected side. The area of interest is then selected and edited to produce an image of the newly contoured orbital floor, which is transferred to a rapid prototype to produce an anatomical model of the orbital floor contour. The titanium plate is then formed in the same way as previously described.

Figure 7.6(b) displays an image of the actual formed orbital floor prosthesis. The computational simulation was carried out under a forming temperature of 900°C, an initial grain size of 5 μm and an initial thickness of 2 mm. In addition, the pressure cycles were found using a target flow stress of 6.334 MPa, as can be observed in Fig. 7.7. Different predicted forming times were obtained ranging from 4600 s for friction coefficient $\mu=0.1$ to 9000 s for sticking conditions,



7.6 Orbital floor³⁷ computational analysis: (a) final thickness distribution (mm) and (b) final formed component.



7.7 Orbital floor pressure cycle for different contact conditions.³⁷

resulting in a maximum forming pressure of 7.5 MPa. Figure 7.6(a) displays the final thickness distribution obtained under sticking contact conditions.

7.9 Future trends and recommendations for further research

The application of SPF continues to expand into areas beyond aerospace and other manufacturing industries. Numerical modelling is particularly relevant in applications where the number of components is very limited, as is the case in biomedical applications where the geometries are invariably patient specific. The field of numerical simulation of SPF processes is now mature, with a number of commercial software packages available. Nevertheless, geometrically accurate predictions still require mesh refinement processes which are not yet fully developed for 3-dimensional applications. In addition, the development of rotation free shell elements would greatly enhance the membrane calculations that are currently common in SPF without significantly increasing the cost of the computation. Currently, given the quasi static nature of SPF processes, implicit algorithms are generally used in which equilibrium is sought at each step. Occasionally, at times of significant geometric changes, such as during sudden contact with concave parts of the die, reaching equilibrium may be difficult or expensive. In contrast, some authors have experimented with the use of explicit dynamic techniques with artificially enhanced inertia terms. This type of calculation avoids the need for reaching a converged equilibrium solution at each step and is therefore generally robust, although it can be inaccurate as the out-of-balance forces are turned into artificial inertia forces. Nevertheless, a robust and accurate combined algorithm could be developed that relies on the robustness of explicit calculations when sudden geometric changes take place, but takes advantage of the more accurate implicit calculations elsewhere.

7.10 References

1. Thompson E. G., Mack L. R. and Lin F. S. Finite element method for incompressible slow viscous flow with a free surface, in *Proceedings of 11th Midwest Mechanics Conference in Developments in Mechanics*, vol. 5, Iowa State University Press, 1969, pp. 93–111.
2. Ghosh A. K. and Hamilton C. H. Mechanical behaviour and hardening characteristics of a superplastic Ti–6Al–4V alloy, *Metallurgical Transactions A*, 1979, 10(6): 699–706.
3. Padmanabhan K. A. and Davies G. J., *Superplasticity: MRE Materials Research and Engineering*, vol. 2, Springer-Verlag, 1980, p. 312.
4. Ghosh A. K. and Hamilton C. H. Influences of material parameters and microstructure on superplastic forming, *Metallurgical Transactions A*, 1982, 13A: 733–743.
5. Argyris J. H. and St Doltsinis J. A primer on superplasticity in natural formulation, *Computer Methods in Applied Mechanics and Engineering*, 1984, 30: 83–132.

6. *Superplasticity*, AGARD-LS-154, Advisory Group for Aerospace Research and Development, NATO, August 1987, p. 204.
7. Goforth R., Chandra N. and George D. Analysis of the cone test to evaluate superplastic forming, in Heikkinen H. and McNelley T. (eds), *Superplasticity in Aerospace*, The Metallurgical Society, Warrendale, PA, 1988, pp. 149–166.
8. Pilling J. and Ridley N., *Superplasticity in Crystalline Solids*, Institute of Metals, Camelot Press Plc., 1989.
9. Hamilton C. H., Simulation of static and deformation-enhanced grain growth effects on superplastic ductility, *Metallurgical Transactions A*, 1989, 20A: 2783–2792.
10. Yang H.S. and Mukherjee, A. K. An analysis of the superplastic forming of a circular sheet diaphragm, *International Journal of Mechanical Sciences*, 1992, 34(4): 283–297.
11. Dutta A. and Mukherjee A. K. Superplastic forming: an analytical approach, *Materials Science and Engineering*, 1992, A 157: 9–13.
12. Chenot J. L. and Bellet M. The viscoplastic approach for the finite element modelling of metal forming processes, in: P. Hartley *et al.* (eds.), *Numerical Modelling of Material Deformation Processes: Research, Development and Applications*, Springer-Verlag, Berlin, 1992, pp. 179–224.
13. Bonet J. The incremental flow formulation for the numerical analysis of plane stress and thin sheet forming processes. *Computer Methods in Applied Mechanics and Engineering*, 1994, 114: 103–122.
14. Bonet J., Wood R. D. and Collins R. Pressure control algorithms for the numerical simulation of superplastic forming, *International Journal of Mechanical Sciences*, 1994, 36(4): 297–309.
15. Bonet J. Error estimators and enrichment procedures for the finite element analysis of thin sheet large deformation processes, *International Journal for Numerical Methods in Engineering*, 1994, 37: 1573–1591.
16. Mosher D. A. and Dawson P. R. An orthotropic flow rule for superplastic Ti–6Al–4V, *Mechanics Materials*, 1994, 19: 59–72.
17. Wriggers P. Finite element algorithms for contact problems, *Archives of Computational Methods in Engineering*, 1995, 2: 1–49.
18. Padmanabhan K. A. and Schlipf J. Model for grain boundary sliding and its relevance to optimal structural superplasticity, *Materials Science and Technology*, 1996, 12: 391–682.
19. Wood R. D. and Bonet J. A review of the numerical analysis of superplastic forming, *Journal of Material Processing Technology*, 1996, 60: 45–53.
20. Mosher D. A. and Dawson P. R. A state variable constitutive model for superplastic Ti–6Al–4V based on grain size, *Journal of Engineering Materials and Technology*, 1996, 118: 162–168.
21. Bonet J., Bhargava P. and Wood R. D. Finite element analysis of the superplastic forming of thick sheet using the incremental flow formulation, *International Journal for Numerical Methods in Engineering*, 1997, 40: 3205–3228.
22. K.S. Lee and H. Huh. Simulation of superplastic forming diffusion bonding with finite element analysis using the convective coordinate system, *J. Material Processing Technology*, 1999, 89–90: 92–98.
23. Lin J. and Dunne F. P. E. Modelling grain growth evolution and necking in superplastic blow forming, *International Journal of Mechanical Sciences*, 2000, 43: 595–609.
24. Padmanabhan K. A., Vasin R. A. and Enikeev F. U. *Superplastic Flow: Phenomenology and Mechanics*, Springer-Verlag, Berlin, 2001.

25. Garriga-Majo D. and Curtis R. V., Geometric analysis of thinning during superplastic forming, *Materials Science Forum*, 2001, 357–359: 213–218.
26. Bellet M., Fourment L., Corsini C., Paris L., Caussat J-J. and Spence P. J., Superplastic forming: from numerical modelling to automated process optimization, Euro-SPF 01, *1st. European Meeting on Super Plastic Forming*, Villard-de-Lans, May 2001, Presses Universitaires de Grenoble (PUG), 11–17, ISBN 2 7061 1106 2.
27. Bonet J., Wood R. D., Said R., Curtis R. V. and Garriga-Majo D. Numerical simulation of the superplastic forming of dental and medical prostheses, *Biomechanics and Modelling in Mechanobiology*, 2002, 1: 177–196.
28. Lin J. Selection of materials models for predicting necking in superplastic forming, *International Journal of Plasticity*, 2003, 19: 469–481.
29. Wriggers P. and Haraldsson A. A simple formulation for two-dimensional contact problems using a moving friction cone, *Communications in Numerical Methods in Engineering*, 2003, 19, 285–295.
30. Jin Q. and Liao X. Numerical simulation of superplastic forming and its microstructure evolution, *Materials Science Forum*, 2004, 447–448: 183–188.
31. Zhang B., Mynors D. J., Mugarra A. and Ostolaza K. Hyperbolic sine, *Materials Science Forum*, 2004, 447–448: 171–176.
32. Todd R. I. (Ed.) *Superplasticity in Advanced Materials ICSAM 2003*, Materials Science Forum, 2004, 447–448, ISBN 0–87849-937–7.
33. Wood R. D., Curtis R. V., Bonet J., Said R., Gil A. J., *et al.* Computer simulation of superplastic forming in restorative dentistry, *Materials Science Forum*, 2004, 447–448: 131–138.
34. Samekto H. and Roll K., Finite element simulation for superplastic forming processes of aluminium 5083, *Materials Science Forum*, 2004, 447–448: 117–122.
35. Bonet J., Gil A. J., Wood R. D., Said R. and Curtis, R. V. Simulating superplastic forming, *Computer Methods in Applied Mechanics and Engineering*, 2006, 195: 6580–6603.
36. Bonet J. and Wood R. D. *Non-linear Continuum Mechanics for Finite Element Analysis*, 2nd edn, Cambridge University Press, 2008.
37. Gil A. J., Curtis R. V., Bonet J. and Coward T. Finite element superplastic forming (FE-SPF) of patient-specific maxillofacial prostheses, *International Journal for Numerical Methods in Biomedical Engineering*, 2010, 26: 139–155.

Constitutive equations for modelling superplastic forming of metals

J. LIN and T. ZHU, Imperial College London, UK
and L. ZHAN, Central South University, P. R. China

Abstract: The chapter begins with the introduction of viscoplastic constitutive equations for superplastic alloys. The methods for solving and determining the constitutive equations are then presented. The optimization method and procedures for the determination of constitutive equations from experimental data are described. The chapter includes a case study of forming a rectangular box, which is used to demonstrate the whole superplastic forming simulation process. A summary is given at the end of the chapter.

Key words: superplastic constitutive equations, numerical integration, optimisation, objective function, superplastic forming simulation.

8.1 Introduction

To optimize complex superplastic forming (SPF) processes and to predict the microstructure distribution over formed parts, finite element forming process modelling needs to be carried out using physically based superplastic constitutive equations for the material. These equations should enable the experimentally measured stress–strain relationships and the microstructural evolution of the material during deformation to be accurately modelled. In addition, the hardening constituents such as strain rate hardening, dislocation hardening and the hardening due to grain growth also need to be identified.

Superplasticity contains specific features of the general viscoplasticity. It is a high rate creep problem. This chapter introduces the techniques for formulating general viscoplastic constitutive equations first, then for superplastic constitutive equations. Modelling of the hardening due to plastic deformation and grain growth are also discussed. Typical sets of superplastic constitutive equations are then presented and described. Numerical techniques for solving the equations and determining the equations from experimental data are also introduced. At the end of this chapter, a case study is given on how to use the unified superplastic constitutive equations for process modelling.

8.2 Constitutive equations for superplastic alloys

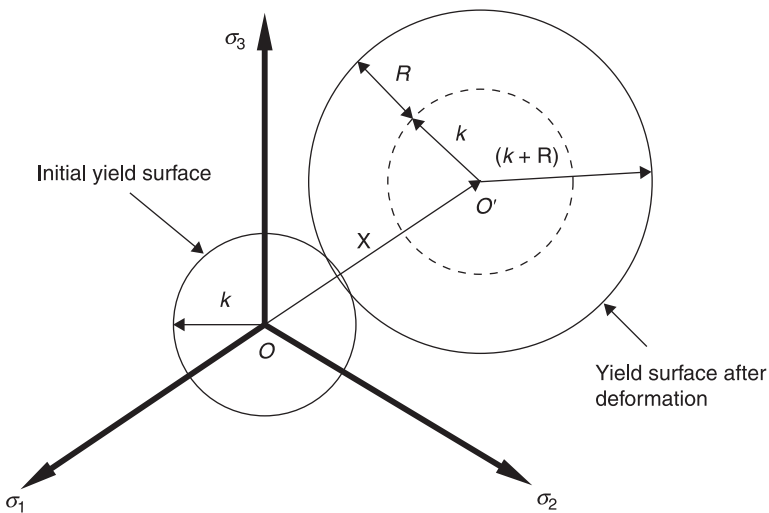
Application domain for viscoplasticity. As metals deform at a temperature above one-third of the absolute melting temperature, the flow stress of the material is

highly dependent on strain rate. This phenomenon is known as viscoplasticity. The theory of viscoplasticity describes the flow of matter by creep, which in contrast to plasticity, depends on time. For metals and alloys, it corresponds to mechanisms linked to the movement of dislocations in grains – climb, deviation, polygonization – with superposed effects of intercrystalline gliding, i.e., grain rotation and grain boundary sliding. These deformation mechanisms begin to arise as soon as the temperature is greater than approximately one-third of the absolute melting temperature. Viscoplastic behaviour of metals can be observed in warm and hot metal forming processes. Superplastic forming normally takes place at a temperature close to 0.5 of the absolute melting temperature of materials.

For viscoplasticity, the introduction of the corresponding flow rule needs the concept of the ‘elastic domain’ (Chaboche, 1977):

$$G = J_2 (\sigma_{ij} - X_{ij}) - R - k \leq 0 \quad i, j = 1, 2, 3 \tag{8.1}$$

where the components X_{ij} are related to the state of ‘kinematic hardening’, which *displaces* the centre of the yield surface (Armstrong and Frederick, 1966), as shown in Fig. 8.1. The scalar variable R is the amount of ‘isotropic hardening’, which *expands* the yield surface (Chaboche and Rousselier, 1983), and k the ‘initial threshold stress’, which describes the *initial yield surface* (Karim and Backofen, 1972). In plasticity the associated flow rule requires the orthogonality of plastic strain rate $\dot{\epsilon}_{ij}^p$ to the yield surface at the point σ_{ij} that belongs to the surface (Skrzypek, 2000). In viscoplasticity the point σ_{ij} lies outside the actual yield surface. In other words, $G > 0$ (Skrzypek, 2000). To accommodate the existence of the *viscoplastic*



8.1 Schematic diagram of cyclic hardening: plastic yield locus with isotropic and kinematic hardening.

potential as the extension of G beyond the yield surface, Rice (1970) suggested the *viscoplastic potential* $\psi = \psi(\sigma_{ij})$ as a power function of G :

$$\psi(\sigma_{ij}) = \frac{K'}{n+1} \left\langle \frac{J_2(\sigma_{ij} - X_{ij}) - R - k}{K'} \right\rangle^{n+1} \quad [8.2]$$

where n and K' are material parameters and $\langle \cdot \rangle_+$ denotes the positive part of $\langle \cdot \rangle$; $\langle \cdot \rangle_+$ equals to zero when $\langle \cdot \rangle < 0$. In particular, K' is dependent upon the temperature, microstructure and defect structure of the material. In view of the normality rule, the 'Mises-type viscoplastic flow rule for isotropic materials' is given as (Chaboche and Rousselier, 1983)

$$\dot{\epsilon}_{ij}^p = \frac{3}{2} \frac{(\sigma'_{ij} - X'_{ij})}{J_2(\sigma_{ij} - X_{ij})} \dot{\epsilon}_e^p \quad [8.3]$$

where

$$\dot{\epsilon}_e^p = \left\langle \frac{J_2(\sigma_{ij} - X_{ij}) - R - k}{K'} \right\rangle^n \quad [8.4]$$

is the effective viscoplastic strain rate, σ'_{ij} and X'_{ij} the deviatoric parts of the components σ_{ij} and X_{ij} , respectively. $\sigma'_{ij} - X'_{ij} = (\sigma_{ij} - X_{ij}) - (\sigma_{kk} - X_{kk})/3$ and $J_2(\sigma_{ij} - X_{ij}) = (\sigma_{ij} - X_{ij}) : (\sigma_{ij} - X_{ij})$ are deviatoric and effective parts of the stress, respectively.

8.2.1 Superplastic flow rule

Kinematic hardening is essential for modelling unloading and strain reversals, especially for predicting cyclic plasticity (Chaboche and Rousselier, 1983). In superplasticity, however, a material is normally deformed under tensile stresses to the point of fracture or until a desired shape is acquired. In these cases, strain reversals are normally not exhibited. Moreover, due to the occurrence of grain rotation that tends to eliminate the development of anisotropy, it is commonly recognized that the kinematic hardening is not necessary to be modelled in superplasticity (Cheong *et al.*, 2000). Therefore, X_{ij} and X'_{ij} in Eq. [8.4] can be disregarded:

$$\dot{\epsilon}_e^p = \left\langle \frac{J_2(\sigma_{ij}) - R - k}{K'} \right\rangle^n \quad [8.5]$$

Another important attribute of superplasticity is that the material behaviour is sensitive to grain growth (Arieli and Rosen, 1977; Ghosh and Hamilton, 1979), since grain rotation and boundary sliding is the dominant deformation mechanism. Small grains make the grain rotation easier, thus the flow stress is reduced. Thus

the effects of grain size d need to be incorporated into the formulation of the corresponding flow rule. This can be achieved by adjusting the value of K' in Eq. [8.5], which is related to the microstructure and defect structure of a material. By defining K' as a power function of d :

$$K' = Kd^{\frac{\mu}{n}} \quad [8.6]$$

Equation [8.5] becomes

$$\dot{\epsilon}_e^p = \left\langle \frac{J_2(\sigma_{ij}) - R - k}{K} \right\rangle_+^n d^{-\mu} \quad [8.7]$$

where μ is the *grain-size exponent*, K the material parameter. This is consistent with the experimental observations: that $\dot{\epsilon}_e^p \propto 1/d^\mu$ (Edington *et al.*, 1976; Ghosh and Hamilton, 1979).

Then, the *Mises-type superplastic flow rule for isotropic materials* is given as

$$\dot{\epsilon}_{ij}^p = \frac{3}{2} \frac{\sigma'_{ij}}{\sigma_e} \dot{\epsilon}_e^p \quad [8.8]$$

where

$$\dot{\epsilon}_e^p = \left\langle \frac{\sigma_e - R - k}{K} \right\rangle_+^n d^{-\mu} \quad [8.9]$$

and where σ_e is the Von-Mises stress.

8.2.2 Isotropic hardening

Isotropic hardening is related to the accumulated dislocation structure and expands the yield surface of a material under plastic deformation (Skrzypek, 2000). The evolution law for isotropic hardening takes the form (Chaboche and Rousselier, 1983)

$$\dot{R} = b(Q - R)\dot{\epsilon}_e^p \quad [8.10]$$

where b and Q are material parameters. Equation [8.10] describes a hardening behaviour that starts from zero but levels off as deformation progresses. The value of b is normally between 0.5 and 1 (Lin and Yang, 1999). It is related to the speed for R to saturate. On the other hand, the value of Q represents the level of saturation (Cheong *et al.*, 2000). The direct relationship between R and ϵ_e^p can be obtained after integration:

$$R = Q(1 - e^{-b\epsilon_e^p}) \quad [8.11]$$

Equation [8.11] was used in the work of Zhou and Dunne (1996), Lin and Yang (1999), and Cheong *et al.* (2000). This equation shows that the value of isotropic hardening is directly related to the amount of strain. The static recovery of

dislocations at high temperature is not considered. However, Eq. [8.10] or Eq. [8.11] is commonly used for the modelling of isotropic hardening in viscoplastic deformation of materials (Lin *et al.*, 1996).

In consideration of high temperature deformation mechanisms in superplasticity, static and dynamic recovery, an evolution equation for normalized dislocation density can be of the form (Lin *et al.*, 2005) with absence of the effect of recrystallization. (It is generally considered that no recrystallization takes place in superplastic deformation.) Then,

$$\dot{\bar{\rho}} = (d/d_0)^{\gamma_d} (1 - \bar{\rho}) \dot{\epsilon}_e^p - c_1 \bar{\rho}^{\gamma_2} \quad [8.12]$$

where d_0 , γ_d , c_1 and γ_2 are material constants. Normalized dislocation density $\bar{\rho} = 1 - \rho_i/\rho$, where ρ_i is the initial dislocation density and ρ the dislocation density in deformed materials. The normalized dislocation density varies from 0 (the initial state) to about 1 (the saturated state of a dislocation network). The first term in Eq. [8.12] represents the development of dislocation density due to plastic strain. Large average grain sizes result in dislocation density increasing quickly under plastic deformation since less grain boundary sliding takes place. The second term gives the effect of static recovery on the evolution of dislocation density. For example, for low strain rate deformation, the metal deforms at high temperature for a longer time, annealing takes place and the accumulated dislocations due to superplastic deformation can be reduced. The isotropic hardening can be expressed as a function of the normalized dislocation density directly:

$$\dot{R} = \frac{1}{2} B \bar{\rho}^{-1/2} \dot{\bar{\rho}} \quad [8.13]$$

where B is a constant. Integrating Eq. [8.13], $R = B \bar{\rho}^{1/2}$ can be obtained.

8.2.3 Grain growth

The interfacial energy associated with coarse-grained materials is lower than that with fine-grained structures, because of the smaller total boundary area (Zhou and Dunne, 1996). Therefore, grain growth can occur at temperatures above those required for diffusion processes to take place, as a natural mechanism to reduce the total boundary energy. It occurs by the migration of grain boundaries through short-ranged diffusion of atoms from one side of a boundary to the other (Zhou and Dunne, 1996).

By the consideration of the interfacial energy associated with grain boundaries, one of the earliest evolution laws for grain growth was developed by Shewmon (1969):

$$\dot{d} = \frac{M\vartheta}{d} \quad [8.14]$$

where M is the mobility of grain boundaries and ϑ the surface energy per unit area. M is dependent upon the strain rate; higher strain rates result in higher M -values. On the other hand, ϑ is dependent upon the temperature; higher

temperatures result in higher ϑ -values. Therefore, for a given set of M - and ϑ -values, the resulting prediction based on Eq. [8.14] can only be consistent with the grain growth at the given temperature and strain rate.

In order to incorporate the effects of strain rate, Kim and Dunne (1997) suggested a modified formulation:

$$\dot{d} = \frac{\alpha}{d^{\gamma_0}} + \beta \dot{\epsilon}_e^p \quad [8.15]$$

where α , γ_0 , and β are temperature-dependent material parameters; the term $M\vartheta$ in Eq. [8.14] is written as α . The grain-size dependence is accommodated by a power-law, and a linear plastic-strain-rate dependence is introduced. The presence of α/d^{γ_0} is needed for modelling *static grain growth* – as an experimental fact, grain growth occurs even without the accumulation of plastic strain at isothermal conditions (Ghosh and Hamilton, 1979). On the other hand, the plastic-strain-rate dependence is needed for modelling plastic-strain-induced grain growth, which is described by Eq. [8.15] *completely* independent of the grain size. Making use of Eq. [8.15], Kim and Dunne (1997) demonstrated that both static and dynamic grain growth can be modelled over a range of strain rates. Using a similar grain-growth equation, satisfactory results were also reported in the work of Lin and Yang (1999).

In order to allow for a higher degree of freedom, a more generalized formulation is introduced by Cheong *et al.* (2000):

$$\dot{d} = \alpha d^{-\gamma_0} + \beta \dot{\epsilon}_e^p d^{-\phi} \quad [8.16]$$

where ϕ is a new material parameter introduced here. If the plastic-strain-induced grain growth exhibited by a material is as that assumed by Kim and Dunne (1997), which is completely independent of the grain size, the value of ϕ should be equal to or close to zero. However, it is shown that the value of ϕ for AA7475 at 515 °C is close to unity. Equation [8.16] suggests that grain size may have different effects on static and dynamic grain growth.

8.2.4 Unified uniaxial superplastic constitutive equations

Summarizing the equations described above, a set of unified superplastic constitutive equations in the *uniaxial* form can be written as:

$$\dot{\epsilon}^p = \left\langle \frac{\sigma - R - k}{K} \right\rangle_+^n d^{-\mu} \quad [8.17]$$

$$\dot{R} = b(Q - R)\dot{\epsilon}^p \quad [8.18]$$

$$\dot{d} = \alpha d^{-\gamma_0} + \beta \dot{\epsilon}^p d^{-\phi} \quad [8.19]$$

$$\dot{\sigma} = E(\dot{\epsilon}^T - \dot{\epsilon}^p) \quad [8.20]$$

where $\dot{\epsilon}^p$ is the uniaxial plastic strain rate in the Power-law model, E the Young's

modulus. For Ti-6Al-4V at 927 °C, $E = 1000$ MPa and $k = 0.229$ MPa (Lin and Yang, 1999). Equation [8.17] is a typical power-law function.

The sinh-law based elastic-viscoplastic constitutive equations (Kim and Dunne, 1997) can be written as:

$$\dot{\epsilon}^p = A \sinh[B(\sigma - R - k)]d^{-n} \quad [8.21]$$

where $\dot{\epsilon}^p$ is the uniaxial plastic strain rate in the sinh-law model, A and B are material constants. Equations [8.18], [8.19] and [8.20] can also be coupled with Eq. [8.21] to form a set of sinh-law-based unified constitutive equations.

8.3 Determination of constitutive equations from experimental data

This is a curve fitting or optimization process. The constants within an equation set should be carefully chosen, so that the computed curves, such as stress–strain curves and grain size evolution curves can match the corresponding experimental data closely. The general uniaxial plastic strain rate $\dot{\epsilon}^p$ can be represented by a single power law (Eq. [8.17]) or a sinh-law (Eq. [8.21]). These simple constitutive equations can be determined easily from experimental data using analytical or numerical methods. However, the constitutive equations used to describe the viscoplastic/superplastic behaviour of materials become more complex as additional state variables are introduced to accurately describe the physical and mechanical phenomena of materials, such as grain growth, strain hardening and etc., before, during or after deformation (Lin and Dunne, 2001; Li *et al.*, 2002; Lin, 2003; Lin and Dean, 2005).

In order to determine the material parameters within constitutive equations from experimental data, three important aspects need to be considered. One is numerical integration methods for solving unified constitutive equations, which should be efficient and accurate. Another is objective functions, which should characterize particular features of the optimization problem. The third is the optimization algorithms used, which should be consistent with the convergence nature of the objective functions. These three aspects for determining superplastic constitutive equations are going to be introduced in this section in detail.

8.3.1 Methods of integrating constitutive equations

The constitutive equations applied to describe the superplastic behaviour of materials are a system of ordinary differential equations (ODEs), which, normally, cannot be solved analytically. A numerical integration method is required to solve the initial value problems. With the characteristics of more stability to solve the stiff problem (Cormeau, 1975), lower-order implicit integration methods are considered in this work. Although these require the Jacobian matrices to be calculated, the overall efficiency can be improved significantly, since the numbers of iterations required for integration are reduced and convergence is guaranteed.

Implicit methods

Vector y represents the integrated variables of the equations and vector \dot{y} within the equations indicates differentiation in terms of time, for example $[\dot{y}] = dy / dt$. The implicit Euler method is commonly used to integrate a set of stiff ODEs. The general form of the first-order of the implicit method is given by Willima *et al.* (2002) for the i^{th} equation and k increment:

$$[y_{k,i}^{(1)}] = [y_{k-1,i}] + \Delta t_k [\dot{y}_{k,i}] \tag{8.22}$$

The superscript (1) represents the first order integration. By linearizing the first-order implicit method as in Newton’s method (Willima *et al.*, 2002):

$$[\dot{y}_{k,i}] = [\dot{y}_{k-1,i}] + \left[\frac{\partial \dot{y}_j}{\partial y_i} \right] ([y_{k,i}] - [y_{k-1,i}]) \tag{8.23}$$

Then, the general form of the implicit integration [8.22] is rearranged into the form:

$$[y_{k,i}^{(1)}] = [y_{k-1,i}] + \Delta t_k \left[[I] - \Delta t_k \left[\frac{\partial \dot{y}_j}{\partial y_i} \right] \right]^{-1} [\dot{y}_{k-1,i}] \tag{8.24}$$

where $[y_{k,i}^{(1)}]$ represents the variables integrated from the i^{th} ordinary differential equations $\dot{y}_{k,i}$ using the first-order implicit Euler method. k is the current iteration of the integration, i and j vary from 1 to NE , where NE is the total number of differential equations within an equation set. Δt_k is the current step-size. $[\partial \dot{y}_j / \partial y_i]$ is a matrix with an order of $NE \times NE$ and is known as a *Jacobian Matrix* at the current k th iteration in the implicit numerical integration. Based on the implicit Euler scheme, stability can be obtained, but only first-order polynomials can be integrated exactly using a first-order method. Higher accuracy of the integration can be achieved by averaging explicit and implicit Euler methods according to the implicit trapezoid rule (Willima *et al.*, 2002), which is given by,

$$[y_{k,i}^{(2)}] = [y_{k-1,i}] + \frac{1}{2} \Delta t_k ([\dot{y}_{k-1,i}] + [\dot{y}_{k,i}]) \tag{8.25}$$

This method uses the average of the derivatives at $[\dot{y}_{k,i}]$ and $[\dot{y}_{k-1,i}]$ to compute $[y_{k,i}]$. The derivatives $[\dot{y}_{k,i}]$ are unknown, but can be obtained by linearization using Newton’s method in Eq. [8.23]. Then the second-order implicit integration, using trapezoid rule, can be represented by:

$$[y_{k,i}^{(2)}] = [y_{k-1,i}] + \Delta t_k \left[[I] - \frac{1}{2} \Delta t_k \left[\frac{\partial \dot{y}_j}{\partial y_i} \right] \right]^{-1} [\dot{y}_{k-1,i}] \tag{8.26}$$

This method has a second-order truncation error through Taylor series expansions, thus it is more accurate than Eq. [8.24]. Both implicit integration methods have good

features of convergence, but the disadvantage of the methods is that in each step, the Jacobian Matrix $[\partial\dot{y}_j/\partial y_i]$ must be firstly evaluated and then inverted to find $[y_{k,i}]$.

Error estimation and step-size control

The allowable truncation error, known as the tolerance, is normally used to control the integration accuracy. It can be measured by the difference between the first- and second-order solutions to the ODEs. The general form of the truncation error is commonly used (Dmitri *et al.*, 2002; Dmitri *et al.*, 2004) as,

$$O_i(\Delta t_k^2) = \left| [y_{k,i}^{(2)}] - [y_{k,i}^{(1)}] \right| \tag{8.27}$$

where $O_i(\Delta t_k^2)$ is the local truncation error for the i^{th} equations at the k^{th} iteration. It defines how far the numerical approximation is from the solution and can be used with a defined tolerance to dictate the maximum allowable error. In the present case, $[y_k^{(2)}]$ is the solution obtained using a second-order implicit scheme (Eq. [8.26]), as it improves the precision, while $[y_k^{(1)}]$ is the solution obtained using the first-order implicit Euler method (Eq. [8.24]).

To integrate a set of unified constitutive equations using a minimum number of iterations, adaptive step-size control is required. Step-size is normally determined according to the truncation error for individual equations. The truncation error of the first-order approximations to the ODEs through Eq. [8.22] and Eq. [8.25] can be defined as:

$$O_i(\Delta t_k^2) = \left| \frac{1}{2} \Delta t_k \left([\dot{y}_{k-1,i}^{(2)}] + [\dot{y}_{k,i}^{(2)}] \right) - \Delta t_k [\dot{y}_{k,i}^{(1)}] \right| \tag{8.28}$$

The truncation error $O_i(\Delta t_k^2)$ for the i^{th} equation is the first-order implicit Euler approximation to the ODEs through Taylor series expansions (Dmitri *et al.*, 2002). For the $(k + 1)^{\text{th}}$ (next) increment, the step-size is normally estimated according to the truncation error in the k^{th} (current) iteration. Replacing $O(\Delta t_k^2)$ by Tol_i in Eq. [8.28] results in:

$$\Delta t_{k+1,i} = \frac{[Tol]_i}{\left| \frac{1}{2} \left([\dot{y}_{k-1,i}^{(2)}] + [\dot{y}_{k,i}^{(2)}] \right) - [\dot{y}_{k,i}^{(1)}] \right|} \tag{8.29}$$

$$\Delta t_{k+1} = \text{Min} \{ \Delta t_{k+1,i} \} \quad i = 1, \dots, NE \tag{8.30}$$

where Tol_i is the tolerance specified for the i^{th} equation within an equation set. Δt_{k+1} is the estimated step-size for the next iteration of the integration. Having estimated the truncation error of the integration at the $(k + 1)^{\text{th}}$ iteration, a decision can be made as to whether to accept or reject the step-size.

In this error control method, the principal local truncation error remains less than a prescribed tolerance, so that the allowable error is under control. However,

it is difficult to specify tolerance for each equation in a complex equation set. It is unlikely to compare the error values due to different unit scales. Therefore, the inclusion of the tolerance as a restraint on the size of truncation error is ineffective, as each ODE would require a different value, and the minimum step-size is difficult to define uniquely due to the problem of different units. The unit values associated with the integrated variables need to be transformed to dimensionless numbers. However, this is beyond the scope of this chapter. More detailed numerical techniques about the step size control problems are given by Cao *et al.* (2008).

8.3.2 Objective functions for optimization

Many optimization methods, such as gradient-based (Zhou and Dunne, 1996; Kowalewski *et al.*, 1994) and Evolutionary Algorithm (EA)-based (Lin and Yang, 1999; Li *et al.*, 2002), have been developed for determining material constants within constitutive equations from experimental data. Various objective functions have been formulated to assess the errors between the experimental and computed data (Li *et al.*, 2002; Lin *et al.*, 2002). The objective functions should be able to 'guide' efficiently the optimization process to find the best fit to experimental data. The commonly used objective function is in *least square* form. An ideal objective function should obey the following criteria (Cao and Lin, 2008):

- Criterion 1: For a single curve.* All the experimental data points that the curve should be involved in the optimization and have an equal opportunity to be optimized, if the errors of its experimental data have been eliminated previously.
- Criterion 2: For multi-curves.* All experimental curves should have equal opportunity to be optimized. The performance of the fitting should not depend on the number of data points in each experimental curve.
- Criterion 3: For multi-sub-objectives.* An objective function should be able to deal with multi-sub-objective problems, in which the units of sub-objectives may be different and all the sub-objectives should have an equal opportunity to be optimized. Different units and the number of curves in each sub-objective should not affect the overall performance of the fitting.
- Criterion 4: Weighting factors.* The above criteria should be achieved automatically without choosing weighting factors manually, since they are difficult to choose in practice.

The problem

Objective functions (OF) are normally formulated based on minimizing the sum of the squares of differences between computed and experimental data at the same strain level. For example, the experimental stress–strain curve (symbols) and four curves derived using different sets of material constants for a set of superplastic constitutive equations are shown in Fig. 8.2(a). For a superplastic material model,

strains to failure are implicitly characterized by some of the material parameters, mentioned by Lin *et al.* (2002). The result of assessment of residuals between computed (solid lines) and experimental (symbols) stress–strain curves, for a viscoplastic damage constitutive model, is shown in Fig. 8.2(a). Four computed stress–strain curves are given in the figure, in which it can be seen that the computed curve 1 has a bad fitting with its low strain to failure. The curve 2 fits best to the experimental data. The curve 3 has quite close fitting within the experimental data, but beyond that, the curve has much higher strain to failure. The curve 4 is far away from the experimental data with its highest strain to failure.

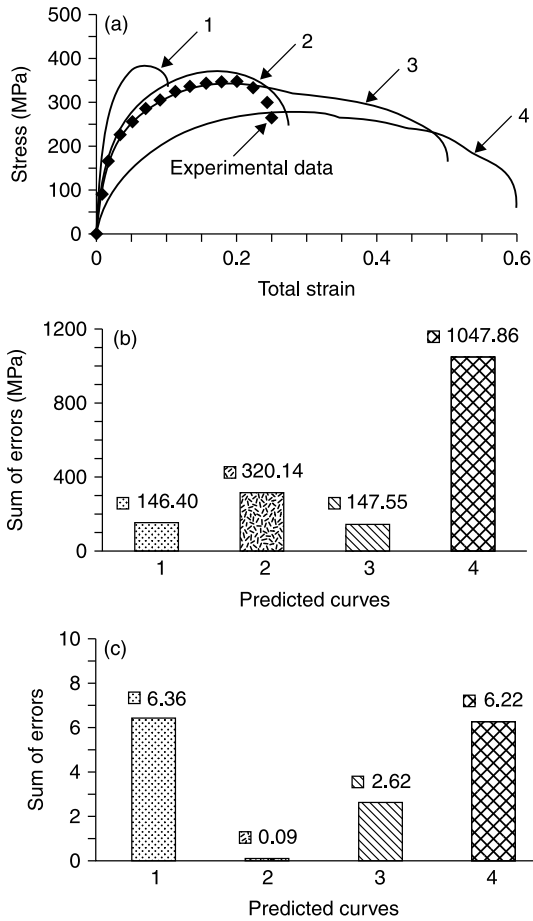
Figure 8.2(b) shows the corresponding sum of errors (stress differences at various strains) for computed curves in Fig. 8.2(a) when assessing the difference between computed and experimental stresses for the same strain level. From Fig. 8.2(b), it can be seen that the computed curve 4 has the largest error and curve 1 the smallest. It is obvious from Fig. 8.2(a) that curve 2 fits best to the experimental data according to ‘eyes’. The wrong assessment of errors indicates that if the predicted strain to failure is shorter than that of the experimental data points, such as computed curve 1 in Fig. 8.2(a), some of the experimental data cannot be involved in the error estimation. If the corresponding computed strain to failure is higher than that of experimental one, such as computed curves 3 and 4 in Fig. 8.2(a), the result of the fitting can be misleading as well. Figure 8.2(c) is plotted using Eq. [8.33] (the equation will be discussed later). It can be seen that curve 2 gives the lowest error and curves 1 and 4 are with higher errors. The fitting quality is consistent to the ‘eyes’ observation. Thus, the definition of an objective function for optimization should reflect both the ‘eyes’ observation and human judgement.

If the calculation is from both directions (strain and stress), another situation needs to be taken into account, in which the unit scales of strain and stress are significantly different. Thus, the most difficult task encountered in developing a universal objective function is to deal with these highlighted problems. To overcome the problems outlined above, a number of objective functions are formulated. Here the features of recently developed objective functions are introduced below.

Shortest distance method (OF_1)

This method was developed by Li *et al.* (2002) and used for the determination of a set of creep damage constitutive equations. In this method, errors are defined by the shortest distance between the experimental and the corresponding computed creep curves, which are $r^2 = \Delta\epsilon^2 + \Delta t^2$ as shown in Fig. 8.3. Here $\Delta\epsilon$ is the difference of experimental and computed data in creep strain (%) Δt and in creep time (in hours). In order to compensate for the different scales in strain and time, two weighting parameters α and β were introduced (Li *et al.*, 2002). The error for the i^{th} data point of the j^{th} curve is defined by

$$r_{ij}^2 = \alpha\Delta\epsilon_{ij}^2 + \beta\Delta t_{ij}^2 = \alpha(\epsilon_{ij}^c - \epsilon_{ij}^e)^2 + \beta(t_{ij}^c - t_{ij}^e)^2 \quad [8.31]$$

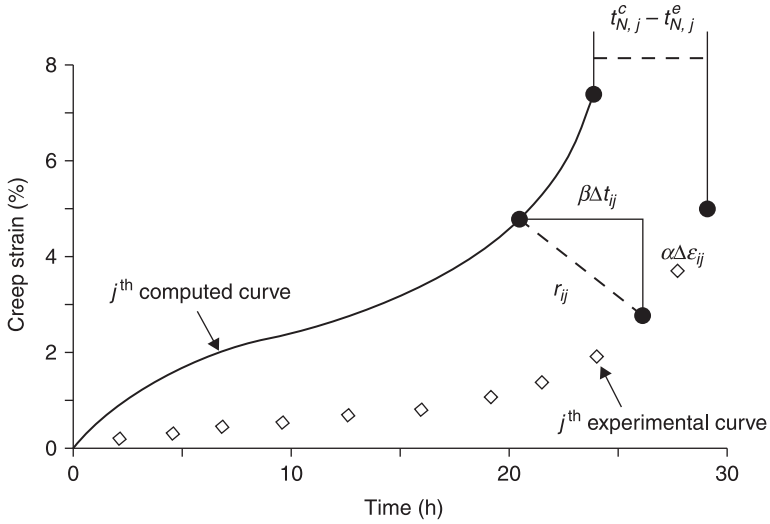


8.2 Comparison of experimental and computed stress–strain curves and errors analysis: (a) comparison of experimental (symbols) and computed (curves 1, 2, 3 and 4) stress–strain curves; (b) sum of the square of errors in stress; and (c) sum of the errors defined by Eq. [8.33].

By sum of r_{ij}^2 for all the data points of the curves, the objective function is expressed as:

$$f(x) = \sum_{j=1}^M \sum_{i=1}^{N_j} w_{ij} r_{ij}^2 + \sum_{j=1}^M W_j (t_{N_j,j}^c - t_{N_j,j}^e)^2 \quad [8.32]$$

where w_{ij} is the relative weight for the i^{th} data point of the j^{th} experimental creep curve. W_j is the relative weight for curve j . The superscripts, ‘c’ and ‘e’, represent the computed and experimental values respectively. The second term in Eq. [8.32] was introduced by Kowaleski *et al.* (1994) for determining creep-damage



8.3 Error definition for OF_I.

constitutive equations, in order to increase the sensitivity of the creep lifetime on the error estimation. In the calculation of the values r_{ij} , two scaling factors have been introduced to keep the unit scales compatible and at the same time to increase the sensitivity of the objective function. By choosing the weighting parameters properly, reasonable good fitting can be obtained. The results are presented by Li *et al.* (2002) for a set of creep damage constitutive equations. However, obtaining such a good result is due to experience of the particular problem. Weighting factors are difficult to choose for new problems. Thus, the objective function has a generic feature, but the weighting factors are problem-dependent and difficult to choose.

Universal multi-objective function (OF_II)

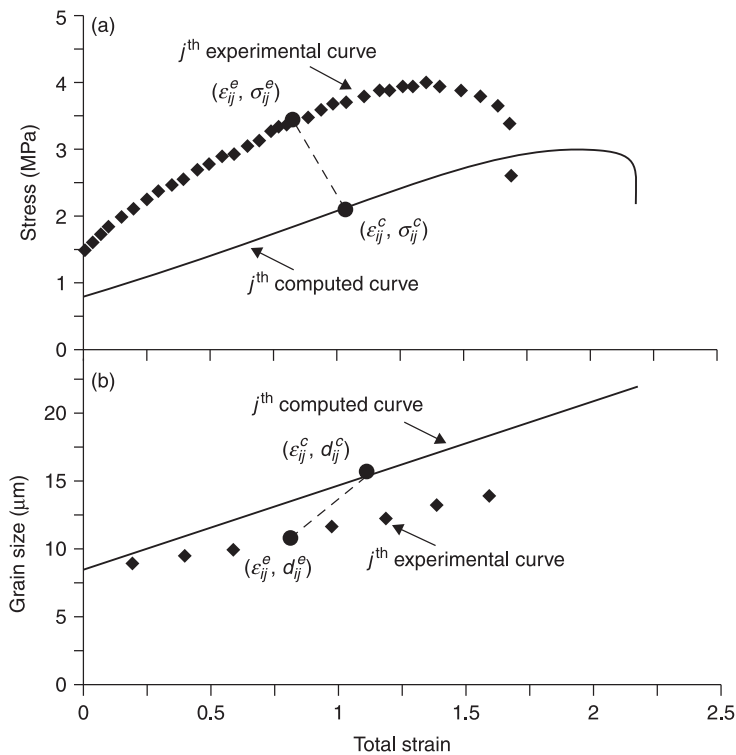
To overcome the difficulties associated with the differences between predicted and experimental strains to failure and the variation in unit scales, a dimensionless objective function was introduced by Lin *et al.* (2002) for the determination of a set of superplastic damage constitutive equations, in which multi-objectives are involved. Error definition for the multi-objective problem is shown in Fig. 8.4 and the objective function takes the form of:

$$f(x) = f_{\sigma} + f_d \tag{8.33}$$

$$f_{\sigma} = \sum_{j=1}^M \left\{ \left(\frac{1}{N_j} \right) \sum_{i=1}^{N_j} \left[\frac{\sigma_{ij}^e - \sigma^c \left(\epsilon_{N,j}^c \epsilon_{ij}^e / \epsilon_{N,j}^e \right)}{s_{\sigma,ij}} \right]^2 + \left[\frac{\epsilon_{N,j}^e - \epsilon_{N,j}^c}{s_j} \right]^2 \right\} \tag{8.34}$$

$$f_d = \sum_{j=1}^M \left\{ \left(\frac{1}{N_j} \right) \sum_{i=1}^{N_j} \left\{ \frac{d_{ij}^e - d^c \left(\epsilon_{N_{j,i}}^c \epsilon_{ij}^e / \epsilon_{N_{j,i}}^e \right)}{s_{d,ij}} \right\}^2 + \left[\frac{\epsilon_{N_{j,i}}^e - \epsilon_{N_{j,i}}^c}{s_j} \right]^2 \right\} \quad [8.35]$$

where f_σ is the residual for stress and f_d is the residual for grain size. $s_{\sigma ij} = 0.1 \sigma_{ij}^e$ and $s_{d,ij} = 0.1 d_{ij}^e$ for the i^{th} data point of the j^{th} curve and $s_j = 0.1 \epsilon_{N_{j,i}}^e$ for the j^{th} curve. N_j is the number of data points for j^{th} experimental curve and M the number of experimental curves involved in the optimization. In the first terms of Eq. [8.34] and Eq. [8.35], the experimental and corresponding computed data are normalized by their experimental data and the errors are transformed to dimensionless values. This approach enables multiple objectives to be dealt with, in which the residuals can be combined directly to form a multi-objective function without introducing weighting factors. The second terms in Eq. [8.34] and Eq. [8.35], which have similar function as in Eq. [8.32] (OF_I), are normalized by their biggest experimental strain values. This again results in a dimensionless error count. It ensures that the predicted strains to failure are close to the corresponding experimental one. The effect is all pervasive, because pushing $(\epsilon_{N_{j,i}}^c)$ towards $(\epsilon_{N_{j,i}}^e)$ ultimately means pushing all the predicted points towards their corresponding



8.4 Error definition for OF_II: errors in (a) stress (MPa) and (b) grain size (μm).

counterparts in the model. For normalizing the sum of errors against the number of data points, this ensures the two terms play the same important roles.

This objective function was successfully used for determining the material parameters arising in a set of superplastic-damage constitutive equations, which is expressed in Lin *et al.* (2002). For all individual experimental data points, it is important to obtain the corresponding computed data accurately. For a pair of experimental and corresponding computed curves, the same fraction is used to choose the corresponding data σ^c for the i^{th} experimental data point of the j^{th} curve. This ensures that all the experimental data are involved in the optimization. Moreover the predicted data will be *pushed* toward the corresponding experimental data.

General objective function (OF_III): true error definition (logarithmic error)

The assessment of residuals between the computed and the corresponding experimental i^{th} data point of the j^{th} curve can be measured by $\sigma_{ij}^c/\sigma_{ij}^e$. It has the advantage of being dimensionless, which naturally avoids the weighting parameters in OF_I and normalization in OF_II. The ratio of computed data against experimental data provides a measure of relative error. To consider the logarithmic scale expression, the feature of the square of the logarithmic scale in $\sigma_{ij}^c/\sigma_{ij}^e$ was studied. When σ_{ij}^c is far from σ_{ij}^e , the value of $(\ln(\sigma_{ij}^c/\sigma_{ij}^e))^2$ would be very large. It significantly increases sensitivity when value of $\sigma_{ij}^c/\sigma_{ij}^e$ becomes large similar to the true strain definition. A ‘true’ error definition for the i^{th} data point of the j^{th} experimental stress–strain curve can be expressed as $E = (\ln(\sigma_{ij}^c/\sigma_{ij}^e))^2$, in which the square is used to increase the sensitivity and ensures all errors are positives. This definition provides a true error assessment between computed and experimental data.

General objective function (OF_III): weighting factors

An automatic weighting factor for the i^{th} experimental data point of the j^{th} curve is introduced according to the features observed for the above error definitions, which may be expressed as:

$$\omega_{ij} = \phi \cdot \varepsilon_{ij}^e / \sum_{j=1}^M \sum_{i=1}^{N_j} \varepsilon_{ij}^e \quad \left(\omega_{11} + \omega_{12} + \dots + \omega_{N_j M} = \phi \right) \quad [8.36]$$

where $\phi = \sum_{j=1}^M N_j$ is a scaling factor, which is related to the total number of data points to increase the sensitivity of objective functions.

General objective function (OF_III): objective function

The same method for finding the corresponding computed and experimental data points defined in OF_II can be used. In consideration of the true error definition

and the weighting of the factors defined in Eq. [8.36], the residual in the fitting is defined using the ‘weighted distance’ in the true error coordinate system:

$$r_{ij}^2 = \omega 1_{ij} \left(\ln \frac{\varepsilon^c \left(\varepsilon_{N_{ij}}^c \varepsilon_{ij}^e / \varepsilon_{N_{ij}}^e \right)}{\varepsilon_{ij}^e} \right)^2 + \omega 2_{ij} \left(\ln \frac{\sigma^c \left(\varepsilon_{N_{ij}}^c \varepsilon_{ij}^e / \varepsilon_{N_{ij}}^e \right)}{\sigma_{ij}^e} \right)^2 \quad [8.37]$$

where $\omega 1_{ij}$ and $\omega 2_{ij}$ are relative weighting factors for ε_{ij}^e and σ_{ij}^e respectively. Based on Eq. [8.36], the factor of the i^{th} experimental data point of the j^{th} curve against the whole sum of data points is calculated automatically. This provides an equal opportunity for each data point to be optimized. The situation of losing features due to the logarithmic scale expression can be compensated and all points equally play the same roles. Together with the sum of the novel residual calculation r_{ij}^2 and automatic weighting factors, a general objective function is formulated as follows:

$$f(x) = \frac{1}{M} \cdot \frac{1}{N_j} \cdot \sum_{j=1}^M \sum_{i=1}^{N_j} r_{ij}^2 \quad [8.38]$$

The sum of the residuals is normalized against the number of experimental data points and curves. This ensures that assessment of residual is in an average dimensionless data point. Eq. [8.38] essentially provides a natural dimensionless average error and can be easily used for multi-objective problems. It gives an opportunity to deal with multi-sub-objectives, in which a different number of curves and units may be involved in the optimization. Together with the automatic weighting factors, it enforces compatibility with each data point, curve and objective, when dealing with the multi-objectives. All objectives play equally important roles. The objective, which has more experimental curves, does not give a representation biased towards the criterion that received more counts.

8.3.3 Optimization methods for determining the material constants

Background

One of the most difficult tasks encountered in materials modelling is to accurately determine material constants arising in equations from experimental data using current optimization techniques. Lin and Hayhurst (1993) developed an optimization technique and successfully determined the material constants for constitutive equations developed for leather where stress can be explicitly expressed as a function of strain. Kowalewski *et al.* (1994) developed a three-step method to determine the starting values of the constants in a set of creep damage equations for optimization. Zhou and Dunne (1996) proposed a four-step method to determine material constants for a particular set of the superplastic constitutive

equations. The above research was carried out using a *Gradient-based Optimization Method* and the difficulties associated with choosing proper starting values for the constants, were highlighted by the investigators. In addition, extra difficulties were met when the number of constants to be determined is large, e.g. more than 5 (Zhou and Dunne, 1996).

The introduction of a genetic algorithm (GA)-based optimization method to the problems by Lin and Yang (1999) has overcome the difficulty of choosing starting values and successfully solved the superplastic equations proposed by Zhou and Dunne (1996), which contain 13 constants. The method is based on classic GA and is inefficient in solving continuous problems (Fogel and Atmar, 1990). To improve the efficiency, Li *et al.* (2002) used an evolutionary programming (EP)-based optimization technique introduced by Yao *et al.* (1999). This algorithm has been applied with success to many constitutive equations and has been found useful particularly to determine unified creep damage constitutive equations and general viscoplastic constitutive equations (Li *et al.*, 2002). The details of the modern optimization methods are introduced elsewhere by Lin and Yang (1999) and Li *et al.* (2002) and are not presented here.

Determined set of constitutive equations for superplasticity

Equation Set 1: Uniaxial power-law model

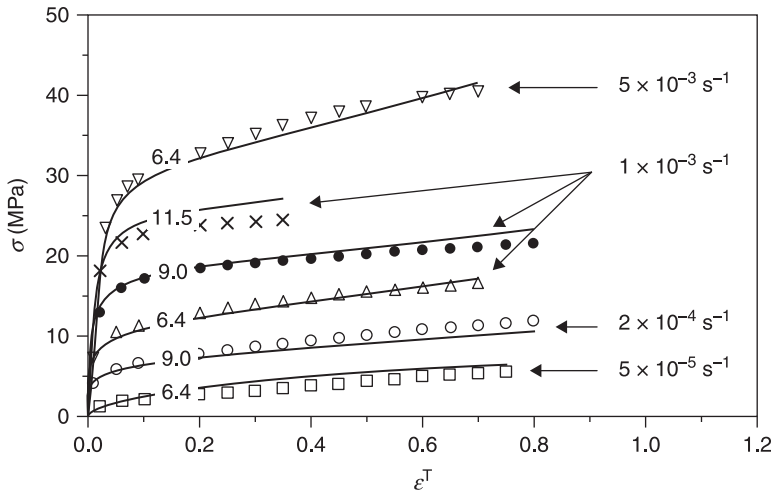
Equations [8.17]–[8.20] are a set of commonly used unified superplastic constitutive equations in the *uniaxial* form. The material constants within the equations can be determined from experimental data using the numerical techniques mentioned above and are listed in Table 8.1. The fitting results are shown in Fig. 8.5 for Ti–6Al–4V deforming at 927 °C for different strain rates with the initial grain sizes of 8.4, 9.0 and 11.5 µm.

Equation Set 2: Uniaxial sinh-law model

Equations [8.18]–[8.21] are a set of sinh-law based elastic-superplastic constitutive equations, which are used by Kim and Dunne (1997) for a range of materials deforming superplastically, with the difference that grain growth Eq. [8.19] is replaced by $\dot{d} = (\alpha_1 + \beta_1 |\dot{\epsilon}^p|) d^{-\gamma_0}$. The constants within the equations were determined from uniaxial experimental data for Ti–6Al–4V at 900 °C (Kim and Dunne, 1997), and are listed in Table 8.2.

Table 8.1 Material constants for Ti–6Al–4V at 927 °C

α	γ_0	β	ϕ	n	μ	K (MPa)	Q (MPa)	b	k (MPa)
73.408	5.751	2.188	0.141	1.400	2.282	60.328	3.933	2.854	0.229



8.5 Comparison of fitted (solid curves) and experimental (symbols) (Ghosh and Hamilton, 1979) stress–strain relationships for $\dot{\epsilon}^T = 5 \times 10^{-5}$, 2×10^{-4} , 1×10^{-3} , and $5 \times 10^{-3} \text{ s}^{-1}$; and $d^0 = 6.4, 9.0$, and $11.5 \mu\text{m}$.

Table 8.2 Material constants for Ti–6Al–4V at 900 °C

A	B	γ	Q	b	α_1	β_1	γ_0
0.2418×10^{-6}	0.1135	1.0170	3.9736	0.8801	0.2059×10^{-13}	0.6899×10^{-9}	3.0210

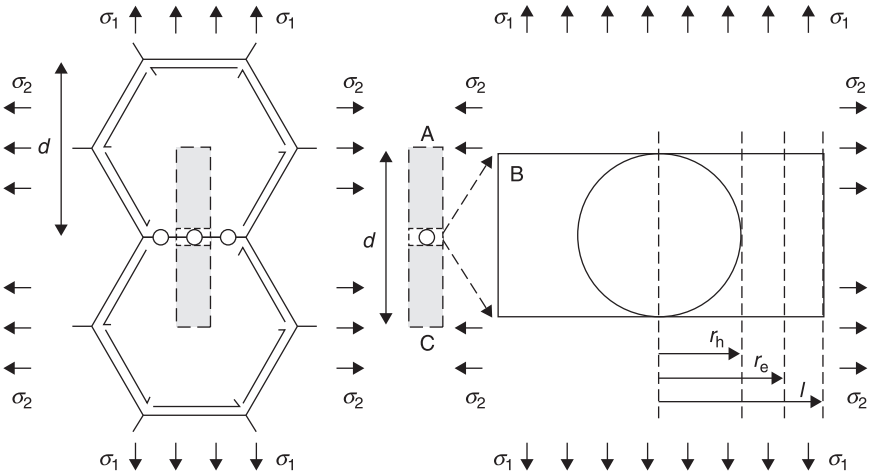
Equation Set 3: Uniaxial superplastic-damage constitutive equations

It is well known that grain-boundary sliding and grain rotation are important deformation mechanisms in superplastic alloys. The relative movement results in void nucleation and growth at grain boundaries. A schematic structure of void growth at grain boundaries of a cavitated superplastic material is shown in Fig. 8.6, where r_h is the radius of a spherical grain-boundary void, r_e the effective void radius, l the radius of the cylinder, which is also the cavity spacing, and d the average grain size.

Considering the damage mechanism – void nucleation and growth features in superplastic deformation, a set of constitutive equations can be written as (Cheong, 2002; Lin *et al.*, 2002):

$$\dot{\epsilon}^p = \dot{\epsilon}_{ss}^p \left[1 + \frac{2lf_h^{1/2}}{d} \left(\frac{\dot{\epsilon}_{cc}^p}{\dot{\epsilon}_{ss}^p} - 1 \right) \right] \tag{8.39}$$

$$\dot{\epsilon}_{ss}^p = \left\langle \frac{\sigma - R - k}{K} \right\rangle_+^n d^{-\mu} \tag{8.40}$$



8.6 Void growth at grain boundaries.

$$\dot{\epsilon}_{cc}^p = \left\langle \frac{\sigma^* - R - k}{K} \right\rangle_+^n d^{-\mu} \quad [8.41]$$

$$\dot{R} = b(Q - R)\dot{\epsilon}^p \quad [8.42]$$

$$\dot{d} = \alpha d^{-\gamma_0} + \beta \dot{\epsilon}^p d^{-\phi} \quad [8.43]$$

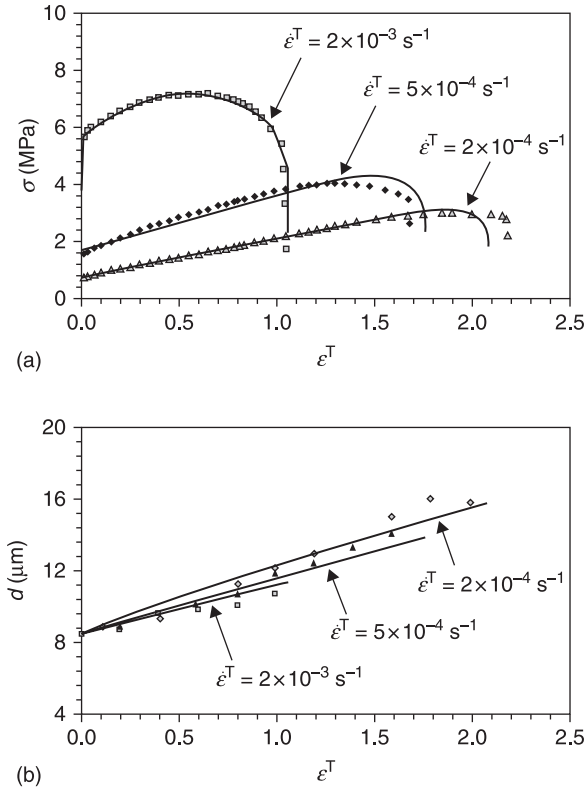
$$\dot{f}_h = \dot{\epsilon}_{cc}^p - (1 - f_h)\dot{\epsilon}_{ss}^p \quad [8.44]$$

$$\dot{f}_e = D(\dot{\epsilon}^p)^{d_1} + C \langle f_h - f_h^* \rangle_+ \quad [8.45]$$

$$\dot{l} = -\frac{1}{2} \dot{\epsilon}_{ss}^p \quad [8.46]$$

$$\dot{\sigma} = E(\dot{\epsilon}^T - \dot{\epsilon}^p) \quad [8.47]$$

where $\dot{\epsilon}^p$ is the uniaxial plastic strain rate for a superplastic material with the consideration of micro-damage. Equation [8.40] is the uniaxial plastic strain rate $\dot{\epsilon}_{ss}^p$ for undamaged part of the material, which can be the same as Eq. [8.17] or Eq. [8.21]. $\dot{\epsilon}_{cc}^p$ is the plastic strain rate of cavitated part of the material, $\sigma^* = \sigma/(1 - f_e)$ is the ‘effective’ stress of the cavitated material, f_e and f_h are damage variables defined as $f_e \equiv r_e^2/l^2$ and $f_h \equiv r_h^2/l^2$, respectively. For materials without pre-existing cavities, the initial values of f_e and f_h are chosen as 0. If the behaviour of a pre-cavitated material is to be modelled, appropriate initial values need to be given. The value of the cavity spacing l varies from an initial value l_0 to 0 and l_0 is



8.7 Comparison of computed (solid curves) and experimental (symbols) for Al–Zn–Mg at various strain rates. (a) Stress and strain and (b) grain size and strain.

regarded as a material parameter that is to be determined together with the others from uniaxial tensile test data.

The material parameters associated with the set of the superplastic damage constitutive equations ([8.39]–[8.47]) are: $k, K, n, \mu, b, Q, \alpha, \gamma_0, \beta, \phi, D, d_1, C, f_h^*, E$, and l_0 .

The constitutive equations are determined for Al–Zn–Mg at 515 °C from its experimental (symbols) stress–strain and grain-size data, as shown in Fig. 8.7. Given $E = 1000 \text{ MPa}$ and $d^0 = 8.47 \mu\text{m}$ (Pilling, 1985), the determination is carried out using the Evolutionary-Algorithm-based optimization technique developed by Lin *et al.* (2002). The determined material parameters are listed in Table 8.3 and the computed (solid curves) stress–strain and grain-size evolutions at strain rates $\dot{\epsilon}^T = 2 \times 10^{-4}, 5 \times 10^{-4}$, and $2 \times 10^{-3} \text{ s}^{-1}$ are shown in Fig. 8.7. It can be seen that a good correlation is obtained for both objectives.

Table 8.3 Material constants for Al–Zn–Mg at 515 °C.

k (MPa)	K (MPa)	n	μ	b	Q (MPa)	α	γ_0
2.9354×10^{-5}	28.7640	1.1299	2.0642	0.1186	5.5769	6.9000×10^{-2}	2.4000
β	ϕ	D	d_1	C	f_h^*	E (MPa)	l^0 (μm)
2.6000	5.5000×10^{-5}	3.7810×10^3	2.3973	32.3739	0.7557	1.000×10^3	4.3922

8.4 Case study: simulation of superplastic forming

8.4.1 Material model implementation for FE analysis

In a manner similar to that for creep deformation (Lin *et al.*, 1993), the uniaxial sinh-law model can be generalized by the consideration of a dissipation potential function. Firstly, the uniaxial plastic strain rate Eq. [8.21] without the hardening and grain growth variables is considered, which then reduces to

$$\dot{\epsilon}^p = \alpha \sinh(\beta\sigma) \tag{8.48}$$

Equation [8.48] can be generalized for multiaxial conditions by assuming an energy dissipation potential of the form

$$\psi = (\alpha / \beta) \cosh(\beta\sigma_e) \tag{8.49}$$

where $\sigma_e = (3S_{ij} \cdot S_{ij}/2)^{1/2}$ is effective stress and $S_{ij} = \sigma_{ij} - \delta_{ij}\sigma_{kk}/3$ are stress deviators. Assuming normality and the associated flow rule, the multiaxial relationship is given by,

$$\frac{d\epsilon_{ij}^p}{dt} = \dot{\lambda} \frac{\partial \psi}{\partial S_{ij}} = \frac{3\alpha}{2} \left(\frac{S_{ij}}{\sigma_e} \right) \sinh(\beta\sigma_e) \tag{8.50}$$

On re-introduction of the hardening and grain growth variables the effective plastic strain rate $\dot{\epsilon}_e^p$ for the sinh-law material model can be written as:

$$\dot{\epsilon}_e^p = \alpha \sinh[\beta(\sigma_e - R - k)]d^{-\gamma} \tag{8.51}$$

and then the set of multiaxial viscoplastic constitutive equations, implemented within a large strain formulation, may be written as:

$$D_{ij}^p = 3S_{ij}/(2\sigma_e)\dot{\epsilon}_e^p \tag{8.52}$$

$$\dot{R} = (C_1 - \gamma_1 R)\dot{\epsilon}_e^p \tag{8.53}$$

$$\dot{d} = (\alpha_1 + \beta_1 \dot{\epsilon}_e^p)d^{-\gamma_0} \tag{8.54}$$

$$\overset{\nabla}{\sigma}_{ij} = GD_{ij}^e + 2\lambda D_{kk}^e \tag{8.55}$$

in which D_{ij}^p is the rate of plastic deformation, D_{ij}^e the rate of elastic deformation, $\overset{\nabla}{\sigma}_{ij}$ the Jaumann rate of Cauchy stress, and G and λ are the Lamé elasticity constants.

The power-law based equation can be treated in the similar way.

The multiaxial constitutive equations can be implemented into large strain finite element solvers, such as ABAQUS, through one of user defined material subroutines, e.g. CREEP, UMAT, for FE SPF process simulation. The parameters, such as hardening, grain size, damage, etc., can be treated as state-variables in the process simulation.

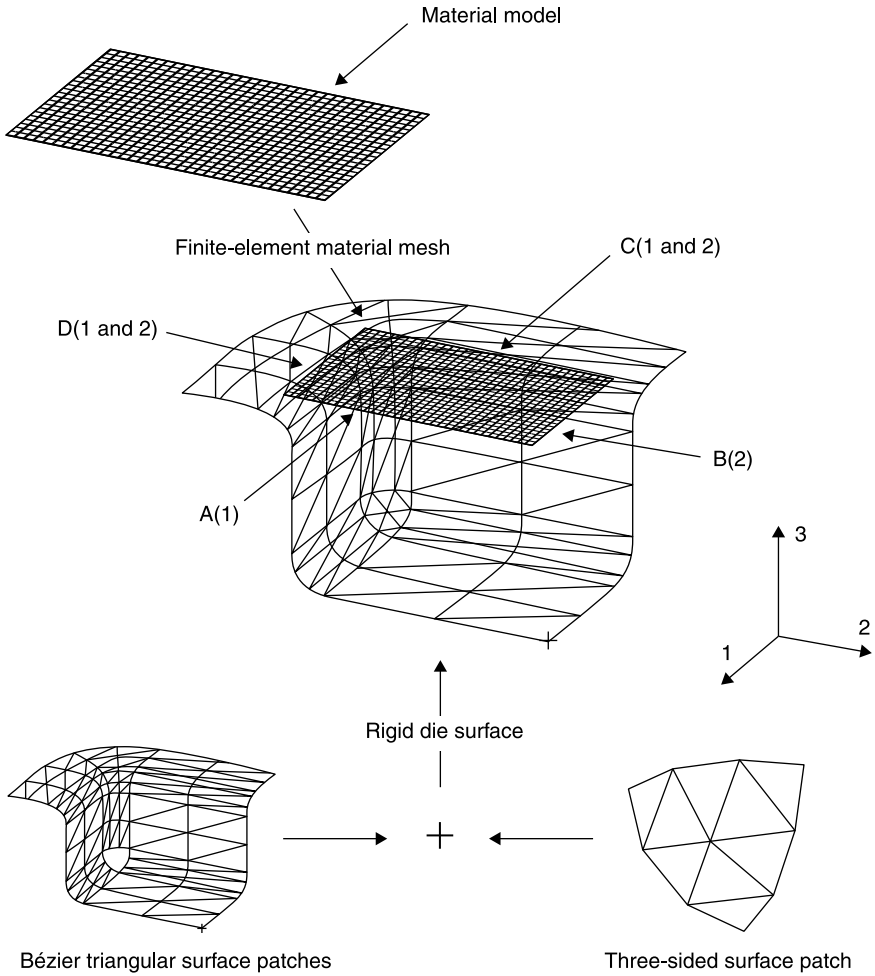
8.4.2 FE model

In a superplastic gas-blow forming process, a component is produced by applying gas pressure on a sheet material so that it deforms into a die cavity and acquires the die shape at an isothermal condition. This section introduces an integrated finite-element model for simulating such a forming process. The finite-element model is constructed using the industry-standard finite-element solver ABAQUS and is used in the following section for investigating the effects of initial grain size, their distributions, and target deforming rates on the superplastic gas-blow forming of a structural component.

A case study is presented for the gas-blow forming of a rectangular box. By virtue of symmetry, only a quarter of the sheet material needs to be modelled. Figure 8.8 shows the finite-element model. It can be seen that slightly more than a quarter of the die is constructed. This is to prevent the nodes at edges A and B from falling off the die surface as they are in contact, due to minuscule numerical discrepancies. The die surface is rigid and fixed in all directions. The boundary conditions for the sheet material are (as shown in Fig. 8.8): edges A and B are constrained in directions 1 and 2 respectively; while edges C and D are constrained in both directions 1 and 2 – considered as clamped to the die surface. The constraints are indicated in Fig. 8.8.

The finite-element analysis is divided into two stages:

- In the first stage, gas pressure is applied quickly and the sheet material deforms in a purely elastic manner. This stage takes only 0.7 s to complete and the applied gas pressure is only 960 Pa.
- Next, the gas pressure is varied accordingly such that the maximum strain rate over the deforming material is maintained at a target level $\dot{\epsilon}^{\text{target}}$. The material behaviour in this stage is characterized by the set of superplastic constitutive equations presented in the previous sections. The analysis terminates when the deforming material is completely in contact with the die surface. The normal distance from each of the nodes on the sheet to the die surface is monitored by the user-defined subroutine URDFIL. A contact is detected when the normal distance falls below a tolerance of $\text{DISTOL} = 1 \times 10^{-3}$ mm.



8.8 Integrated finite-element model for simulating the superplastic gas-blow forming of a rectangular box.

A set of superplastic constitutive equations (Equation Set 1) is implemented into ABAQUS through the user-defined subroutine CREEP. To allow for an efficient use of computational power, an adaptive implicit time incrementation scheme is employed. The parameter CETOL that is related to the accuracy of the numerical integration is set to 1×10^{-3} . This defines the maximum allowable difference in the plastic strain increments calculated from the plastic strain rates based on conditions at the beginning and the end of an increment.

ABAQUS allows the construction of complex-shaped three-dimensional rigid surfaces using Bézier triangular surface patches, provided that the elements over

the surfaces can be defined and their nodal normal directions are given. However, for free-form surfaces that involve compound geometries, the generation of the element and nodal information can be difficult. This is because most CAD systems perform surface characterization in terms of rectangular surface patches, rather than triangular ones. The regular assembly of rectangular surface patches necessarily leaves some *n-sided* holes, for instance the *3-sided* region on the die surface shown in Fig. 8.8. To accommodate such intractability, the technique demonstrated by Lin *et al.* (1998) that allows the characterization of *non-4-sided* regions is employed.

For the interaction between the surfaces of the die and sheet material, the Coulomb friction model is used and the friction coefficient is defined as $\mu^{fric} = 0.3$ and equivalent shear stress limit as $\bar{\tau}^{max} = 0.132$ MPa.

8.4.3 Modelling results

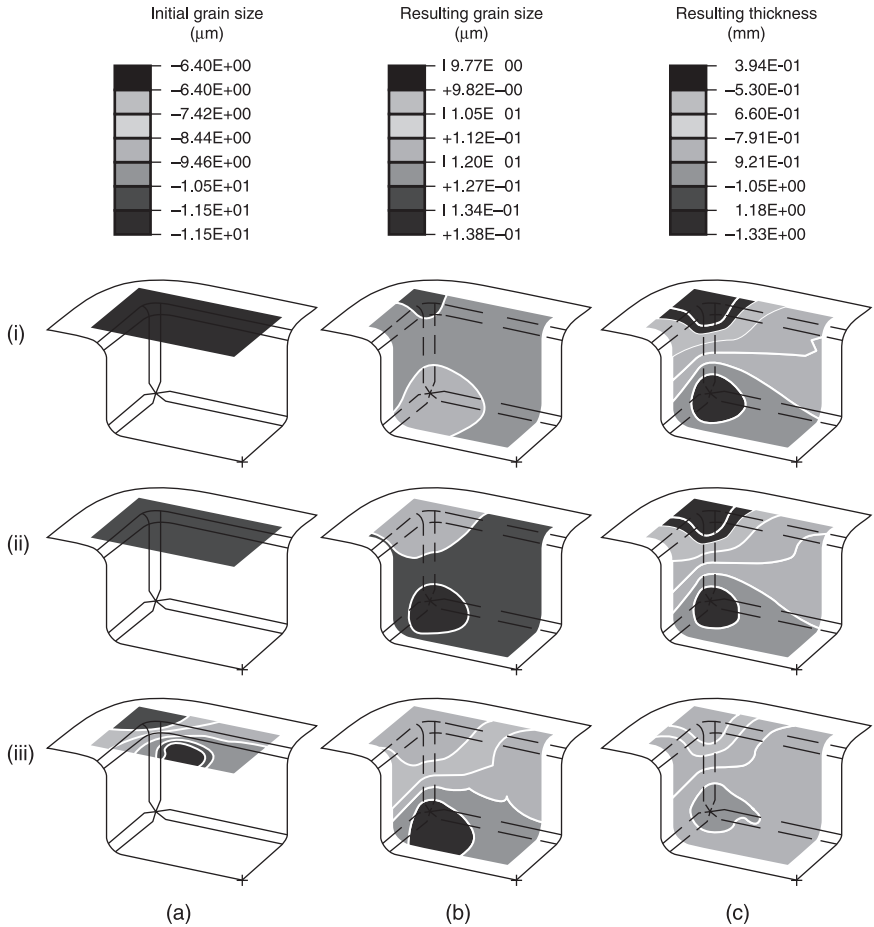
To investigate the effects of initial grain sizes, their distributions, and target deforming rates on the thinning of Ti–6Al–4V at 927 °C during the superplastic gas-blow forming of a structural component, finite-element simulations are carried out using the finite-element model described in detail in the previous section. The simulations are conducted with $\dot{\epsilon}^{target} = 5 \times 10^{-5}$ and $2 \times 10^{-4} \text{ s}^{-1}$, uniform initial sheet thickness $h^0 = 1.5$ mm, and initial grain-size fields as follows:

- $d^0 = 6.4 \text{ }\mu\text{m}$ (uniform) (Fig. 8.9, (a)(i)),
- $d^0 = 11.5 \text{ }\mu\text{m}$ (uniform) (Fig. 8.9, (a)(ii)),
- $6.4 \text{ }\mu\text{m} \leq d^0 \leq 11.5 \text{ }\mu\text{m}$ (non-uniform) (Fig. 8.9, (a)(iii)).

The non-uniform initial grain-size field $6.4 \text{ }\mu\text{m} \leq d^0 \leq 11.5 \text{ }\mu\text{m}$ is obtained by first dividing linearly the sheet material into six regions according to the resulting thickness obtained from the finite-element simulation with $\dot{\epsilon}^{target} = 2 \times 10^{-4} \text{ s}^{-1}$ and $d^0 = 6.4 \text{ }\mu\text{m}$ (Fig. 8.9(c)(i)), of which the resulting thickness field is $0.394 \text{ mm} \leq h^f \leq 1.330 \text{ mm}$. Then, the range of initial grain size $6.4 \text{ }\mu\text{m} \leq d^0 \leq 11.5 \text{ }\mu\text{m}$ is distributed linearly over the regions. In particular, the thinnest region corresponds to the coarsest grain size of $11.5 \text{ }\mu\text{m}$ and the thickest region to the finest grain size of $6.4 \text{ }\mu\text{m}$. The resulting non-uniform initial grain-size field is shown in Fig. 8.9(a)(iii). The resulting grain-size and sheet-thickness fields at $\dot{\epsilon}^{target} = 2 \times 10^{-4} \text{ s}^{-1}$ with the three initial grain-size distributions (Fig. 8.9(a)(i–iii)) are presented in Fig. 8.9(b)(i–iii) and 8.9(c)(i–iii), respectively.

Figure 8.10 shows the computed gas-pressure histories for $\dot{\epsilon}^{target} = 2 \times 10^{-4} \text{ s}^{-1}$ with the three grain-size distributions (Fig. 8.9(a)(i–iii)). It can be seen that the histories can be divided into three distinctive stages:

- For the first approximately 15% of the histories, the gas pressures increase with t/t^f , where t is time and t^f the time at which the associated forming process terminates.

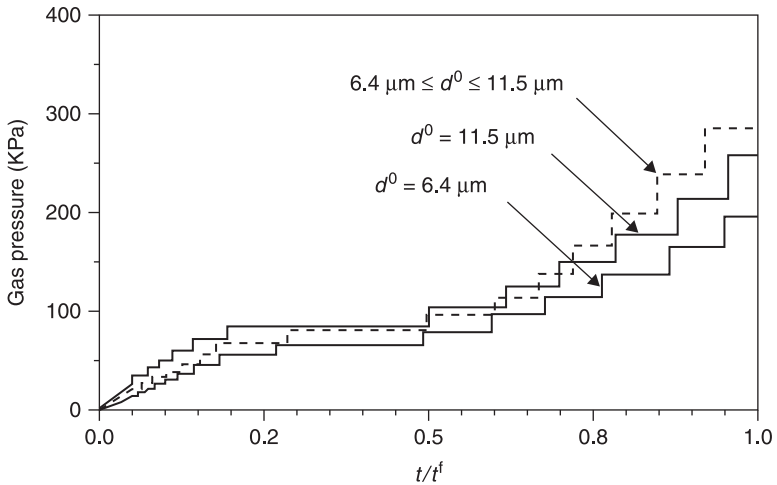


8.9 Field plots of: (a) initial microstructures; (b) resulting microstructures; and (c) resulting thickness for (i) $d^0 = 6.4 \mu\text{m}$; (ii) $d^0 = 11.5 \mu\text{m}$; and (iii) $6.4 \mu\text{m} \leq d^0 \leq 11.5 \mu\text{m}$

- Then, they remain at an almost constant level.
- Eventually, they increase with t/t^f again and this stage encompasses approximately 50% of the histories.

The increase of the gas pressures seen in the first stage is a result of the rapid increase in stresses mainly due to the hardening effects of grain growth and dislocation evolution. The sheet materials with $d^0 = 6.4, 11.5 \mu\text{m}$, and $6.4 \mu\text{m} \leq d^0 \leq 11.5 \mu\text{m}$ are deformed under free bulging in this stage.

Almost constant gas pressures are observed in the second stage (Fig. 8.9). These are a result of the balance between the material hardening due to grain growth and dislocation and the softening due to material thinning. The sheet



8.10 Gas-pressure histories for $d^0 = 6.4, 11.5,$ and $6.4 \mu\text{m} \leq d^0 \leq 11.5 \mu\text{m}$.

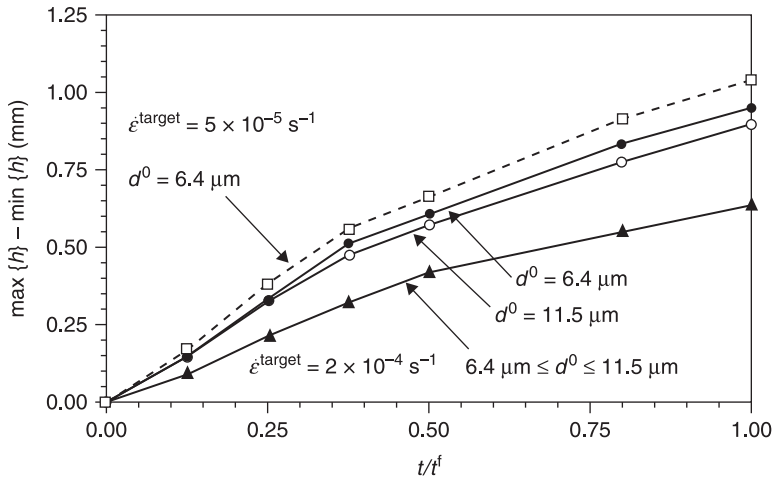
materials with $d^0 = 6.4, 11.5 \mu\text{m}$, and $6.4 \mu\text{m} \leq d^0 \leq 11.5 \mu\text{m}$ are also deformed under free bulging in this stage.

In the final stage, the gas pressures increase with t/t^f (Fig. 8.10). This indicates that part of the sheet material has come into contact with the bottom of the die surface. As a result, the deformation of the contacted material becomes locally restricted and the effective area on which the gas pressures are applied is decreasing. In this case higher gas pressures are required to maintain the maximum deformation rates at $\dot{\epsilon}^{\text{target}}$ while forming the rest of the sheets.

The computed gas pressure for $d^0 = 11.5 \mu\text{m}$ is generally higher than that for $d^0 = 6.4 \mu\text{m}$ (Fig. 8.10). This is because of the higher grain-growth hardening in the former sheet material (Fig. 8.9(b)(ii)) that possesses a coarser grain size than the latter (Fig. 8.9(b)(i)). Similarly, the computed gas pressure for $6.4 \mu\text{m} \leq d^0 \leq 11.5 \mu\text{m}$ lies between that for $d^0 = 11.5$ and $6.4 \mu\text{m}$ in the first and second stages (Fig. 8.10). However, the gas pressure for $6.4 \mu\text{m} \leq d^0 \leq 11.5 \mu\text{m}$ becomes the highest in the final stage. This is because the corner region of the formed part that comes into contact with the die eventually. The 3-sided region indicated in Fig. 8.8, possesses the greatest thickness (Fig. 8.9(c)(iii)), hence the lowest softening due to material thinning and coarsest grain size (Fig. 8.9(b)(iii)), the highest grain-growth hardening compared to that in $d^0 = 6.4$ and $11.5 \mu\text{m}$.

Figure 8.11 shows the histories of the difference between the maximum and minimum resulting sheet thickness $\max\{h\} - \min\{h\}$. Three computations are carried out at $\dot{\epsilon}^{\text{target}} = 2 \times 10^{-4} \text{ s}^{-1}$ with the three initial grain-size distributions shown in Fig. 8.9(c)(i–iii) while another at $\dot{\epsilon}^{\text{target}} = 5 \times 10^{-5} \text{ s}^{-1}$ with $d^0 = 6.4 \mu\text{m}$.

It can be seen from the figure that there is no significant difference between the profiles of $\max\{h\} - \min\{h\}$ for $d^0 = 6.4$ and $11.5 \mu\text{m}$ at $\dot{\epsilon}^{\text{target}} = 2 \times 10^{-4} \text{ s}^{-1}$. In particular, the values of $\max\{h\} - \min\{h\}$ for the two simulations at $t/t^f = 1.0 \dot{\epsilon}$



8.11 Histories of $\max\{h\} - \min\{h\}$; three computations are carried out at $\dot{\epsilon}^{\text{target}} = 2 \times 10^{-4} \text{ s}^{-1}$ (solid curves) with $d^0 = 6.4, 11.5$, and $6.4 \mu\text{m} \leq d^0 \leq 11.5 \mu\text{m}$, and one at $\dot{\epsilon}^{\text{target}} = 5 \times 10^{-5} \text{ s}^{-1}$ (dashed curve) with $d^0 = 6.4 \mu\text{m}$.

are 0.949 and 0.897 mm (Fig. 8.11) respectively, which give a difference of less than 4% of h^0 . The resulting sheet thickness distributions for the two simulations in Fig. 8.9(c)(i–ii) also show no significant difference. These indicate that coarsening *uniformly* the initial grain size from 6.4 to 11.5 μm is not capable of improving effectively the evenness of the resulting sheet thickness. This is because, when the maximum deformation rate is restricted, sheet materials with uniform values of d^0 are very likely to deform in a similar manner; the path of an infinitesimal material point on a sheet material from the initial position to the final is unlikely to be varied significantly.

Using the initial microstructural gradients shown in Fig. 8.9(a)(iii), it can be seen from Fig. 8.9(c)(iii) that the uniformity over the resulting sheet thickness is greatly improved compared to that in Fig. 8.9(c)(i–ii). The range of resulting sheet thickness in the former is narrower than that in the latter. Also, the history of $\max\{h\} - \min\{h\}$ for $6.4 \mu\text{m} \leq d^0 \leq 11.5 \mu\text{m}$ shown in Fig. 8.11 is generally lower than the others. In particular, the value of $\max\{h\} - \min\{h\}$ for $6.4 \mu\text{m} \leq d^0 \leq 11.5 \mu\text{m}$ at $t/t^f = 1.0$ is 0.636 mm, which is lower than that for $d^0 = 6.4 \mu\text{m}$ at the same $\dot{\epsilon}^{\text{target}}$ by 20% of h^0 . The resulting sheet thickness of the corner region for $6.4 \mu\text{m} \leq d^0 \leq 11.5 \mu\text{m}$ is also the highest among the three (Fig. 8.9(c)(i–iii)). However, its resulting microstructure (Fig. 8.9(b)(iii)) is rather non-uniform compared to the others (Fig. 8.9(b)(i–ii)). These show that the use of proper initial microstructural gradients is plausible for regulating the resulting thickness of a form part but with some unevenness over the resulting microstructure.

Figure 8.11 also shows the history of $\max\{h\} - \min\{h\}$ for the simulation with $\dot{\epsilon}^{\text{target}} = 5 \times 10^{-5} \text{ s}^{-1}$ and $d^0 = 6.4 \mu\text{m}$. It is generally higher than that for

$\dot{\epsilon}^{\text{target}} = 2 \times 10^{-4} \text{ s}^{-1}$ and $d^0 = 6.4 \text{ }\mu\text{m}$. This indicates that for the lower $\dot{\epsilon}^{\text{target}}$, the more severe the material thinning.

8.5 Conclusions

Process modelling techniques can be used to predict microstructure evolution and thickness distribution for superplastically formed parts, provided that the constitutive equations used for superplastic materials contain the features. This can be achieved by the introduction of state variables within the equations. Each state variable represents a particular physical parameter of the material deforming at the SPF temperature.

The unified superplastic constitutive equations cannot be solved analytically and need to be integrated numerically. The difficulties associated in integrating the equations accurately and efficiently are the step size control, since different equations within an equation set may contain different units. This makes the error assessment difficult. The unified superplastic constitutive equations need to be determined from experimental data using an optimization method. Apart from new search algorithms, the selection of suitable objective function for optimization is also very important.

8.6 References

- Arieli A and Rosen A (1977), 'Superplastic deformation of Ti-6Al-4V alloy', *Metallurgical Transactions A*, 8A(10), 1591-1596.
- Armstrong P J and Frederick C O (1966), *A Mathematical Representation of the Multiaxial Bauschiger Effect*, C.E.G.B. Report RD/B/N, 731.
- Cao J and Lin J (2008), 'A study on formulation of objective functions for determining material models', *Int J Mech Sci*, 50, 193-204.
- Cao J, Lin J and Dean T A (2008), 'An implicit unitless error and step-size control method in integrating unified viscoplastic/creep ODE-type constitutive equations', *Int J Numerical Methods in Engineering*, 73, 1094-1112.
- Corneau I (1975), 'Numerical stability in quasi-static elasto/visco-plasticity', *Int J Numerical Methods in Engineering*, 9, 109-127.
- Chaboche J L (1977), 'Viscoplastic constitutive equations for the description of cyclic and anisotropic behaviour of metals', *Bull Acad Polon Sci, Ser Sci Technol*, 25(1), 33-42.
- Chaboche J L and Rousselier G (1983), 'On the plastic and viscoplastic constitutive equations: Part 1 - Rules developed with internal variable concept', *J Pressure Vessel Technol*, 105(5), 153-158.
- Cheong B H (2002), *Modelling of Microstructural and Damage Evolution in Superplastic Forming*, PhD Thesis, Birmingham, University of Birmingham, 96-97.
- Cheong B H, Lin J and Ball A A (2000), 'Modelling of the hardening characteristics for superplastic materials', *J Strain Analysis*, 35(3), 149-157.
- Cheong B H, Lin J and Ball A A (2003), 'Modelling the effects of grain-size gradients on necking in superplastic forming', *J Mat Proc Technol*, 134(1), 10-18.
- Dmitri K, Philip B and Scott W S (2002), 'Adaptive backward Euler time stepping with truncation error control for numerical modelling of unsaturated fluid flow', *Int J Numerical Methods in Engineering*, 53, 1301-1322.

- Dmitri K, Philip B and Scott W S (2004), 'Truncation error and stability analysis of iterative and non-iterative Thomas-Gladwell methods for first-order non-linear differential equations', *Int J Numerical Methods in Engineering*, 60, 2031–2043.
- Edington J W, Melton K N and Cutler C P (1976), 'Superplasticity', *Progress in Mater Sci*, 21, 63–169.
- Fogel D B and Atmar J W (1990), 'Comparing genetic operators with Gaussian mutations in simulated evolutionary process using linear systems', *Bio Cybernet*, 63(2), 111–114.
- Ghosh A K and Hamilton C H (1979), 'Mechanical behaviour and hardening characteristics of a superplastic Ti–6Al–4V alloy', *Metall Trans A*, 10A(6), 699–706.
- Karim A U and Backofen W A (1972), 'Some observations of diffusional flow in a superplastic alloy', *Metall Trans*, 3(3), 702–712.
- Kim T W and Dunne F P E (1997), 'Determination of superplastic constitutive equations and strain rate sensitivity for aerospace alloys', *J Aero Engng*, 211, 367–380.
- Kowalewski Z L, Hayhurst D R and Dyson B F (1994), 'Mechanisms-based creep constitutive equations for an aluminium alloy', *J Strain Analysis*, 29, 309–316.
- Li B, Lin J and Yao X (2002), 'A novel evolutionary algorithm for determining unified creep damage constitutive equations', *Int J Mech Sci*, 44(5), 987–1002.
- Lin J (2003), 'Selection of material models for predicting necking in superplastic forming', *Int J Plasticity*, 19(4), 469–481.
- Lin J, Ball A A and Zheng J J (1998), 'Surface modelling and mesh generation for simulating superplastic deformation', *J Mat Proc Technol*, 80–81, 613–619.
- Lin J, Cheong B H and Yao X (2002), 'Universal multi-objective function for optimising superplastic-damage constitutive equations', *J Mat Proc Technol*, 125–126, 199–205.
- Lin J and Dean T A (2005), 'Modelling of microstructure evolution in hot forming using unified constitutive equations', *J Mat Proc Technol*, 167, 354–362.
- Lin J and Dunne F P E (2001), 'Modelling grain growth evolution and necking in superplastic blow-forming', *Int J Mech Sci*, 43(3), 595–609.
- Lin J, Dunne F P E and Hayhurst D R (1996), 'Physically-based temperature dependence of elastic viscoplastic constitutive equations for copper between 20 and 500 °C', *Phil Mag A*, 74(2), 655–676.
- Lin J, Hayhurst D R (1993), 'Constitutive equations for multi-axial straining of leather under uni-axial stress', *Eur J Mech A: Solids*, 12(4), 471–492.
- Lin J, Hayhurst D R and Dyson B F (1993), 'A new design of uniaxial testpiece with slit extensometer ridges for improved accuracy of strain measurement', *Int J Mech Sci*, 35(1), 63–78.
- Lin J, Liu Y, Farrugia D C J and Zhou M (2005), 'Development of dislocation based-unified material model for simulating microstructure evolution in multi-pass hot rolling', *Phil Mag A*, 85(18), 1967–1987.
- Lin J and Yang J (1999), 'GA based multiple objective optimization for determining viscoplastic constitutive equations for superplastic alloys', *Int J Plasticity*, 15, 1181–1196.
- Pilling J (1985), 'Effect of coalescence on cavity growth during superplastic deformation', *Mat Sci Technol*, 1, 461–465.
- Rice J R (1970), 'On the structure of stress-strain relations for time-dependent plastic deformation in metals', *Trans A.S.M.E., J Appl Mechanics*, 37, 728–737.
- Shewmon P G (1969), *Transformations in Metals*, New York, McGraw-Hill.
- Skrzypczek J J (2000), *Plasticity and Creep*, Hetnarski R B (ed.), London, CRC Press Inc.

Willima H P, Brian P F, Saula A and Willima T V (2002), *Numerical Recipes in C: The art of scientific computing*, London, Cambridge University Press.

Yao X, Liu Y and Lin G (1999), 'Evolutionary programming made faster'. *IEEE Trans Evolutionary Comput*, 3(2), 82–102.

Zhou M and Dunne F P (1996), 'Mechanism-based constitutive equations for the superplastic behaviour of a titanium alloy', *J Strain Analysis*, 31(3), 187–196.

Predicting instability in superplastic forming of metals

S. B. LEEN, NUI Galway, Ireland

Abstract: This chapter reviews the major approaches to the prediction of instability in superplastic forming. Theoretical and numerical approaches are treated. Key aspects include the effects of microstructure and the identification of an appropriate constitutive equation set. It is argued that the development of an easy-to-visualise superplastic forming limit diagram (SPFLD) concept is attractive as a vehicle to facilitate more widespread use of the superplastic forming (SPF) process, which is a key challenge to the technology. A case study on failure prediction for two titanium alloys is used for illustrative and comparative purposes with respect to a number of the key predictive techniques.

Key words: instability, necking, microstructure, inhomogeneity, superplastic forming limit diagram (SPFLD), damage mechanics.

9.1 Introduction

This chapter is concerned with the important topic of analysis of failure during superplastic forming (SPF). The benefits of SPF are well known (Pilling and Ridley, 1989), the key one being the ability to achieve large, uniform strains prior to failure (e.g. up to and greater than 1000% elongation), thus permitting the forming of complex parts. Typically, up to and beyond 500% elongation to failure can be obtained. Superplasticity may be classified into micrograin (microstructural) superplasticity and transformation (environmental) superplasticity. The present work is concerned with the former, which is associated with polycrystalline materials with a fine grain size, usually less than 10 μm , deformed within a specific (slow) range of strain-rates, e.g. 10^{-5} to 10^{-1} s^{-1} , and at temperatures greater than $0.5T_m$, where T_m is the melting point of the material. Another important benefit is the low flow stress normally associated with SP deformation. This phenomenon has been successfully exploited in both the aerospace and automotive industries for a considerable number of years, leading to significant benefits in relation to key components, e.g. titanium wide-chord fan-blades for gas turbine jet engines. More recently, SPF has found application in new areas such as biomedical, e.g. dental and cranioplastic prostheses, architectural, spacecraft and satellites. Clearly, in an era of increased awareness of the need for optimum use of material, energy and time, vis-à-vis sustainability of manufacturing processes, components and machinery, it is imperative that the limits of the SPF process be clearly understood and predictable. The phenomenon of SP is a highly complex,

non-linear material deformation process and analysis of the process is therefore also complex. This chapter is divided into four sections, as follows:

- Theoretical considerations.
- Forming analyses and experiments.
- Results and discussion.
- Conclusions and future trends.

The first section discusses the different mechanisms relevant to failure and instability during SP deformation and forming. This aspect is clearly important for the development of mechanisms-based models and phenomenological models. It is argued that an accurate representation of the mechanisms responsible for SP deformation is critical to SPF failure prediction. This section also describes the development of mathematical and numerical methods for SPF failure and instability across a range of materials and processes. The third section discusses the incorporation of failure prediction methods within commercial and academic process simulation software. Example applications of numerical modelling of SPF failure prediction will be given. This section also contains discussion of experimental test methods for the identification of SPF deformation and failure prediction constants.

One of the key challenges in relation to this point is the absence of a simple, easy-to-use and easy-to-visualise forming limit method, which nonetheless captures the salient complexities of the process, particularly with respect to microstructural evolution effects and strain-rate dependency. Hence, an important motivating theme of the present chapter is the development of a simplified forming limit diagram (FLD) approach for SPF, referred to here as a SPFLD.

It is argued that a critical issue in instability and failure prediction for SPF is that of an appropriate constitutive model. On the one hand, a sufficiently sophisticated model, incorporating key phenomena, such as flow stress dependence on strain-rate and strain and grain growth effects, e.g. Dunne and co-workers (Zhou and Dunne, 1996), is advisable, but on the other hand, it is preferable, where possible, to avoid overly complex material models. An important aspect here is validation against available test data, e.g. Ghosh and Hamilton (1979).

9.2 Theoretical considerations

9.2.1 Instability models

The onset of necking is commonly associated with plastic instability which, for negligible rate-dependence or for constant strain-rate conditions, in a tension test is given by the classical Considère condition for peak load. Thus, for such conditions, plastic deformation becomes unstable when the following condition is met:

$$\frac{1}{\sigma} \frac{d\sigma}{d\varepsilon} < 1 \quad [9.1(a)]$$

Hill (1952) and Swift (1952) independently proposed generalisations of the latter to predict respectively localised and diffuse necking in thin sheets under plane stress conditions. Swift established a condition for plastic instability under bi-axial tension, as follows:

$$\frac{1}{\sigma_1} \frac{d\sigma_1}{d\varepsilon_1} < 1 \quad \text{and} \quad \frac{1}{\sigma_3} \frac{d\sigma_3}{d\varepsilon_3} < 1 \quad [9.1(b)]$$

where σ_1 , σ_2 , ε_1 and ε_2 are the principal stresses and strains, leading to the following general expression for plastic instability:

$$\frac{d\sigma_{eq}}{\sigma_{eq} d\varepsilon_{eq}} \leq \frac{\sigma_1 \left(\frac{\partial f}{\partial \sigma_1} \right)^2 + \sigma_3 \left(\frac{\partial f}{\partial \sigma_3} \right)^2}{\frac{\partial f}{\partial \sigma_{eq}} \left(\sigma_1 \frac{\partial f}{\partial \sigma_1} + \sigma_3 \frac{\partial f}{\partial \sigma_3} \right)} \quad [9.2]$$

where $f(\sigma_1, \sigma_3)$ is the yield function, and σ_{eq} and ε_{eq} are the equivalent stress and strain, respectively. According to this equation, plastic strain is stable provided the increase in intrinsic yield strength of the material, due to strain hardening, is greater than the change in representative (equivalent) stress due to loading. Assuming $\sigma = K\varepsilon^n$ and employing the Levy-Mises equations for total strain (which are applicable for radial ε_1 - ε_3 strain-paths), as follows:

$$\left(\frac{\varepsilon_1}{\frac{\partial f}{\partial \sigma_1}} \right) = \left(\frac{\varepsilon_2}{\frac{\partial f}{\partial \sigma_2}} \right) = \left(\frac{\varepsilon_e}{\frac{\partial f}{\partial \sigma_e}} \right) \quad [9.3]$$

the limiting Swift principal strains for plastic stability under bi-axial plane stress are:

$$\varepsilon_1^f = \frac{\sigma_1 \left(\frac{\partial f}{\partial \sigma_1} \right)^2 + \sigma_3 \left(\frac{\partial f}{\partial \sigma_3} \right) \left(\frac{\partial f}{\partial \sigma_1} \right)}{\sigma_1 \left(\frac{\partial f}{\partial \sigma_1} \right)^2 + \sigma_3 \left(\frac{\partial f}{\partial \sigma_3} \right)^2} n = \frac{(2-a)^2 + a(2-a)(2a-1)}{(2-a)^2 + a(2a-1)^2} n \quad [9.4(a)]$$

$$\varepsilon_3^f = \frac{\sigma_3 \left(\frac{\partial f}{\partial \sigma_3} \right)^2 + \sigma_1 \left(\frac{\partial f}{\partial \sigma_1} \right) \left(\frac{\partial f}{\partial \sigma_3} \right)}{\sigma_1 \left(\frac{\partial f}{\partial \sigma_1} \right)^2 + \sigma_3 \left(\frac{\partial f}{\partial \sigma_3} \right)^2} n = \frac{a(2a-1)^2 + a(2-a)(2a-1)}{(2-a)^2 + a(2a-1)^2} n \quad [9.4(b)]$$

where $\sigma_3 = a\sigma_1$. The Hill equation for plastic instability, corresponding to localised necking along the line of zero extension, is as follows:

$$\frac{d\sigma_{eq}}{\sigma_{eq}d\epsilon_{eq}} \leq \frac{\frac{\partial f}{\partial \sigma_1} + \frac{\partial f}{\partial \sigma_3}}{\frac{\partial f}{\partial \sigma_{eq}}} \tag{9.5}$$

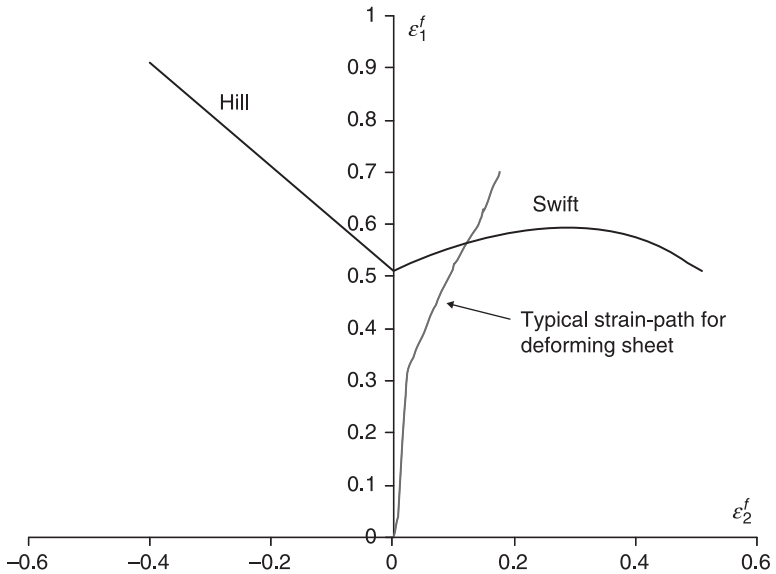
from which:

$$\epsilon_1^f = \frac{\frac{\partial f}{\partial \sigma_1}}{\frac{\partial f}{\partial \sigma_1} + \frac{\partial f}{\partial \sigma_3}} n \text{ and } \epsilon_3^f = \frac{\frac{\partial f}{\partial \sigma_3}}{\frac{\partial f}{\partial \sigma_1} + \frac{\partial f}{\partial \sigma_3}} n \tag{9.6}$$

so that:

$$\epsilon_1^f + \epsilon_3^f = n \tag{9.7}$$

The Hill and Swift conditions are commonly represented as the Hill-Swift FLD to define the onset of plastic instability, for the left-hand side and the right-hand side respectively of the principal strain space, as shown in Fig. 9.1.



9.1 Hill-Swift forming limit diagram.

Hart (1967) presented a theory of the tensile test for rate-dependent material behaviour, using on the growth of an inhomogeneity to define the onset of instability. Hence it was shown that the deformation is stable if:

$$\gamma + m \geq 1 \tag{9.8}$$

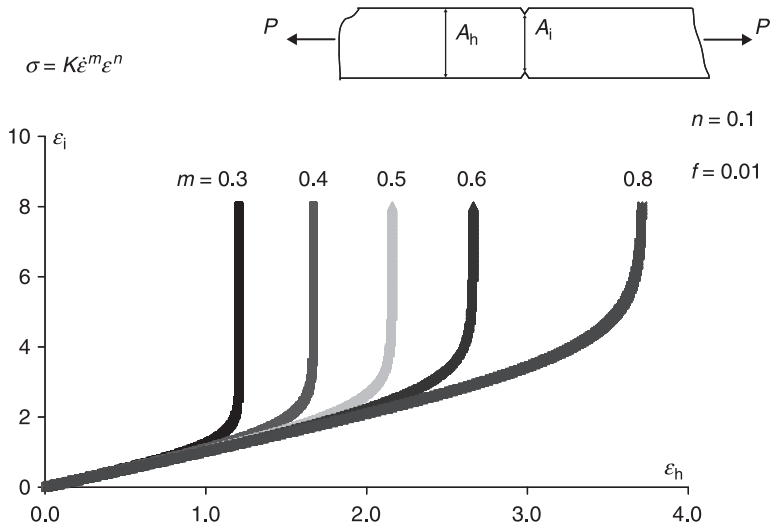
where

$$\gamma = \frac{1}{\sigma} \frac{d\sigma}{d\varepsilon} \quad \text{and} \quad m = \frac{\dot{\varepsilon}}{\sigma} \frac{d\sigma}{d\dot{\varepsilon}} \tag{9.8a}$$

are material parameters which vary through the deformation history in general. Hart went on to demonstrate that his model supported high ductilities for $m > 0.5$, approximately, corresponding to SP behaviour. Ghosh (1977) further qualified the analysis of Hart and explicitly demonstrated the role of high m -values in achieving high ductility by virtue of increasing the resistance of the material to the growth of inhomogeneities. Figure 9.2 shows the first order relationship between strain-rate sensitivity and ductility via strain localisation for a double power law of the form $\sigma = K\dot{\varepsilon}^m \varepsilon^n$. The curves in Fig. 9.2 were obtained by iteratively solving for inhomogeneous strain ε_i (strain inside the imperfection region) and homogeneous strain ε_h (strain outside the imperfection region or bulk strain) via the following force balance equation:

$$(1 - f)^{1/m} e^{-\frac{\varepsilon_i}{m}} \varepsilon_i^{\frac{n}{m}} d\varepsilon_i = e^{-\frac{\varepsilon_h}{m}} \varepsilon_h^{\frac{n}{m}} d\varepsilon_h \tag{9.9}$$

where A_i and A_h are the inhomogeneous and homogeneous cross-sectional areas,



9.2 Predicted effect of strain-rate sensitivity on growth of imperfections in tensile test specimen from Ghosh (1977).

as defined in Fig. 9.2, and f is a measure of the inhomogeneity defined by $A_i = (1 - f)A_h$. Clearly, high m -values, e.g. $m > 0.5$ to 0.6, lead to high bulk strain before localisation (necking). Ghosh pointed out and redressed an error in the Hart stability criterion. Hart ignored the second term in the following equation:

$$\delta\varepsilon = -\frac{\delta A}{A} + \frac{\delta A_o}{A_o} \tag{9.10}$$

which describes the initial imperfection (inhomogeneity) size. Ghosh has pointed out that this term is important in considering the growth or decay of any imperfection and showed that the resulting modified version of Eq. [9.8] was thus:

$$\gamma \geq \left[\frac{1 - m}{\left(1 - \frac{\delta \ln A_o}{\delta \ln A}\right)} \right] \tag{9.11}$$

so that no simple relationship exists between m and γ for instability; the initial imperfection size and the strain history must be accounted for. One possible approach for this is to treat the initial imperfection as a void and to use void growth models, e.g. see Zhou *et al.* (1988), to simulate the evolution of the imperfection and its subsequent effect and interaction with instability.

More recent work on the prediction of failure during SPF deformation has been presented by Chung and Cheng (2001), based on an instability criterion developed by Ding *et al.* (1997). Ding *et al.* considered a thin SP sheet under bi-axial stretching and, using a procedure analogous to that of Marciniak and Kuczynski (1967), analysed the conditions under which a local neck, assumed to form perpendicular to the major principal stress, σ_1 , becomes unstable. Furthermore assuming radial principal strain paths, a multi-axial generalisation of Hart's stability criterion was developed whereby stability is maintained as long as:

$$a\gamma + m \geq 1 \tag{9.12}$$

where

$$\gamma = \frac{1}{\sigma_{eq}} \frac{d\sigma_{eq}}{d\varepsilon_{eq}}, \quad m = \frac{\dot{\varepsilon}_{eq}}{\sigma_{eq}} \frac{d\sigma_{eq}}{d\dot{\varepsilon}_{eq}} \tag{9.12a}$$

and a is defined as

$$a = \sqrt{\frac{4}{3}(1 + \rho + \rho^2)} \quad \text{and} \quad b = \frac{1}{2 + \rho} \sqrt{3(1 + \rho + \rho^2)} \tag{9.13}$$

with

$$\rho = \frac{\varepsilon_3}{\varepsilon_1} = \frac{\dot{\varepsilon}_3}{\dot{\varepsilon}_1} \tag{9.14}$$

and

$$\boldsymbol{\varepsilon}_e = a\boldsymbol{\varepsilon}_1, \dot{\boldsymbol{\varepsilon}}_{eq} = a\dot{\boldsymbol{\varepsilon}}_1, \boldsymbol{\sigma}_{eq} = b\boldsymbol{\sigma}_1, \quad [9.15]$$

and

$$\boldsymbol{\varepsilon}_{eq} = \sqrt{\frac{2}{3}} \boldsymbol{\varepsilon}_{ij} \boldsymbol{\varepsilon}_{ij} \quad \dot{\boldsymbol{\varepsilon}}_{eq} = \sqrt{\frac{2}{3}} \boldsymbol{D}_{ij} \boldsymbol{D}_{ij} \quad \boldsymbol{\sigma}_{eq} = \sqrt{\frac{3}{2}} \boldsymbol{S}_{ij} \boldsymbol{S}_{ij} \quad [9.16]$$

with \boldsymbol{D}_{ij} as the plastic strain-rate tensor. Based on Eq. [9.12], Chung and Cheng proposed the concept of a flow localisation factor (FLF), ξ_{II} , to enable a quantitative description of the localisation process of unstable plastic flow, as follows:

$$\begin{aligned} \xi_{II} &= \frac{1 - a\gamma}{m} - 1 && \text{if } a\gamma + m < 1 \text{ (unstable)} \\ \xi_{II} &= 0 && \text{if } a\gamma + m \geq 1 \text{ (stable)} \end{aligned} \quad [9.17]$$

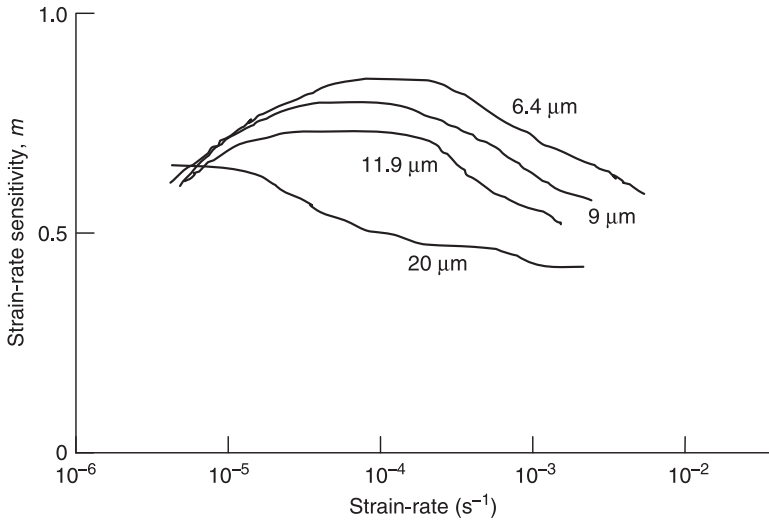
When the FLF is greater than -1 , a neck is predicted to start growing. The duration of neck growth is defined as the stage of flow localisation. Further work by Chung and Cheng (2002) presented evidence for the existence of a SP fracture criterion, defined by the integral of the FLF, C , reaching a critical value, C_{cr} , defined by calibration against forming failures. The integral C was defined as follows:

$$C = \int_0^{\boldsymbol{\varepsilon}_{eq}} J d\boldsymbol{\varepsilon}_{eq} \quad [9.18]$$

where $J = \xi_{II} + 1$ if $a\gamma + m < 1$ (unstable) and $J = 0$ if $a\gamma + m \geq 1$ (stable). It was argued that C_{cr} is a material property, only a function of material composition, grain size and temperature.

9.2.2 Microstructural analysis of SPF failure and instability

The failure mechanism in SP deformation is known to depend on the material. Many SP alloys, e.g. aluminium alloys, are known to cavitate and their SP ductility is limited by the cavitation process. However, one notable exception to this mode of failure is the alpha-beta titanium SPF alloys, e.g. Ti-6Al-4V; experimental studies suggest that these alloys can achieve very large elongations without significant cavitation (Pilling and Ridley, 1989) and that the SP ductility of these materials is controlled by inhomogeneous deformation, leading to localisation and necking. For micrograin superplasticity, grain size is arguably the predominant parameter; the other dominant parameter is strain-rate sensitivity, m . It has been shown: (i) that m depends directly on grain size (see Fig. 9.3), and (ii) that ductility has a first order relationship to m . Therefore, it is clear that grain size has a direct and critical influence on SPF ductility. A fine grain size leads to a low flow stress and a high m value. However, for real polycrystal materials, it is necessary to consider a distribution of grain size, since it is not possible to achieve a single

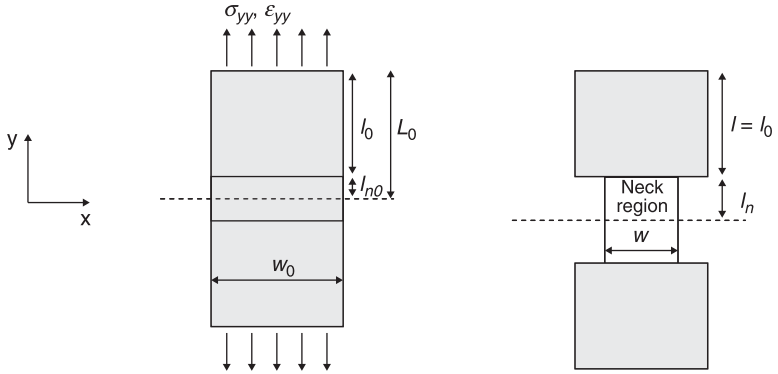


9.3 Schematic representation of measured effect of average grain size on strain-rate sensitivity, after Ghosh and Hamilton (1979).

uniform grain size throughout. Dunne and Kim (1999) and Dunne (1998) have presented an elucidating study on the effect of inhomogeneity of grain size on SPF failure and ductility. A key contributing factor in this important contribution to modelling of SP deformation was the incorporation of both static (temperature-driven) and dynamic (strain-rate controlled) grain growth kinetics. In terms of the importance of measured variations in grain size distributions in Ti-6Al-4V uni-axial test pieces to measured (uni-axial) SPF ductility, Dunne and Kim (1999) showed that: (i) for low strain rates, which give rise to diffusion-controlled grain growth, a reduction in the level of inhomogeneity is predicted, and hence increased failure strain, since distributions with small mean grain sizes have higher growth rates than those with large mean grain sizes; while (ii) for high strain rates, the initial levels of inhomogeneity tend to be maintained, leading to a reduction in failure strain.

A key phenomenon in instability is that of localisation, signalled by material softening and the associated stress drop. Dunne (1998) has presented a simple model which explains this phenomenon, in reference to Fig. 9.4. A ‘model’ neck is assumed to form and assuming plane strain and incompressibility, it was shown that:

$$\begin{aligned} \epsilon_{yy} &= \ln\left(\frac{l+l_n}{L_0}\right) \approx \ln\left(\frac{l_0+l_n}{L_0}\right) \\ \epsilon_{xx} &= -\frac{1}{2}\epsilon_{yy} = \ln\left(\frac{l_0+l_n}{L_0}\right)^{\frac{1}{2}} \end{aligned} \tag{9.19}$$



9.4 Schematic representation of neck formation under uni-axial SPF deformation, after Dunne (1998).

For a unit depth specimen, the cross-sectional area, A , is: $A = w$, and

$$\epsilon_{xx} = \ln \frac{w}{w_0} = \ln \left(\frac{l_0 + l_n}{L_0} \right)^{\frac{1}{2}}$$

so that

$$A = w = w_0 \left(\frac{l_0 + l_n}{L_0} \right)^{-\frac{1}{2}} \tag{9.20}$$

In the neck region, the cross-sectional area, A_n , is:

$$A_n = w_0 \left(\frac{l_n}{l_{n0}} \right)^{\frac{1}{2}} \tag{9.21}$$

Also,

$$\sigma_{yy} = \frac{F}{A} \tag{9.22}$$

$$\sigma_{yy}^n = \frac{F}{A_n} \tag{9.23}$$

and for perfect plasticity, with a yield stress k :

$$\sigma_{yy}^n = k = \frac{F}{A_n} \tag{9.24}$$

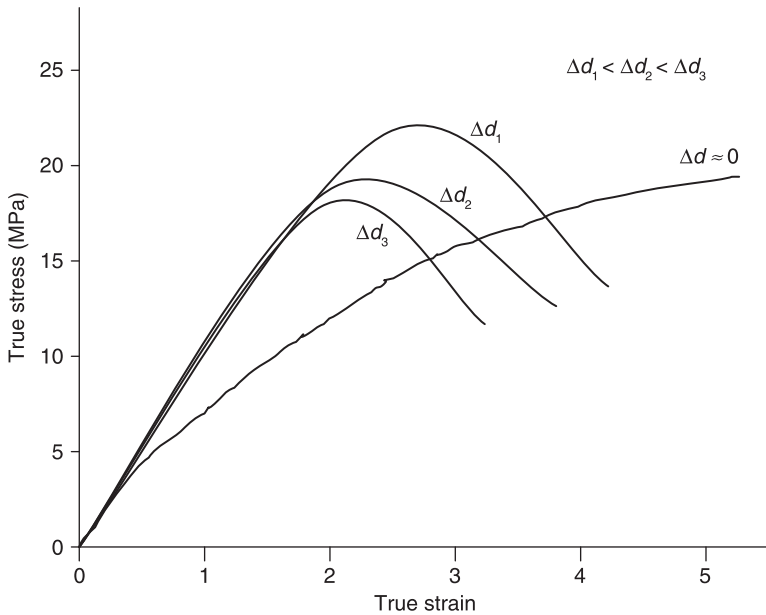
Hence,

$$\sigma_{yy} = k \frac{A}{A_n} \tag{9.25}$$

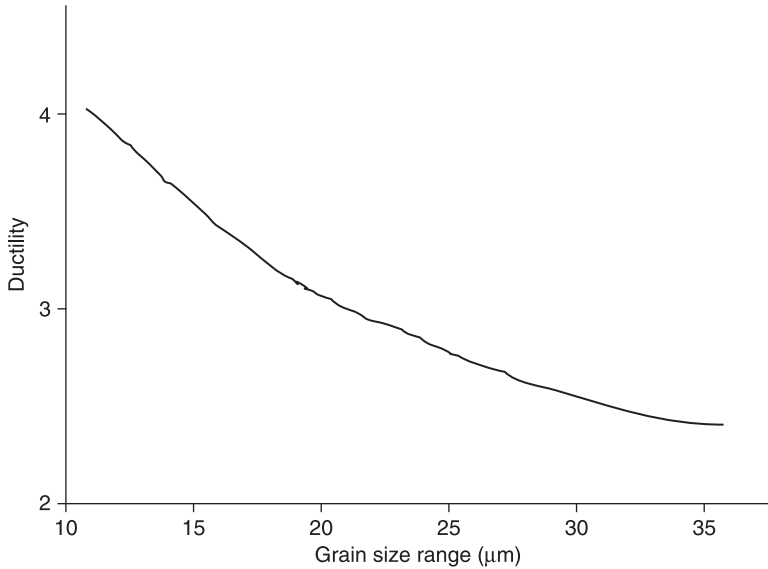
so that

$$\sigma_{yy} = k \left(\frac{l_{n0}}{L_0} \right)^{\frac{1}{2}} \left(1 + \frac{l_0}{l_n} \right)^{\frac{1}{2}} \tag{9.26}$$

Hence, when $l_n = l_{n0}$ and $L_0 = l_0 + l_{n0}$, $\sigma_{yy} = k$. As l_n increases, the neck develops, and the stress σ_{yy} decreases. Figure 9.5 shows a schematic representation of the predicted effect of grain size range, Δd , on the homogenised stress-strain response, and in particular, the effect of Δd on localisation and necking; in this case, the predicted localisation is entirely related to the inhomogeneous deformation induced by the microstructural (grain size) inhomogeneity, which is in turn related to the grain size range and the nature of the grain size distribution. It is clear that larger grain size ranges give smaller ductility and lower flow stress. Dunne showed that regions of higher grain size act as regions of reinforcement, with little deformation, and carry lower stresses than lower grain size regions. Also, it was concluded that these inhomogeneities lead to stress concentrations and hence



9.5 Schematic representation of the effect of initial grain size range (Δd) on localisation and necking under uni-axial SPF deformation, after Dunne (1998).



9.6 Schematic representation of the effect of initial grain size range (Δd) on ductility, after Dunne (1998).

strain localisation and ultimately necking and failure. Hence, a key significance of this work was the demonstration and FE simulation of the mechanism of failure for uni-axial SPF, viz. microstructure inhomogeneity-induced strain localisation. Dunne also presented an empirical, power-law relationship between ductility and grain size range, as follows:

$$\varepsilon_F = A(\Delta d)^\chi \quad [9.27]$$

where A and χ are constants, determined from tests. This is represented graphically in Fig. 9.6. The effect of increasing grain size range was shown to diminish rapidly for $\Delta d > 30 \mu\text{m}$, approximately.

9.2.3 Void growth models

As mentioned above, cavitation is an important phenomenon for failure and instability in SPF materials. It limits the ductility of the materials and reduces subsequent mechanical properties. Cavitation can be avoided forming by the superposition of a hydrostatic pressure. Zhou *et al.* (1988) have discussed the application of void growth models to SP deformation for cavity sensitive materials. It was pointed out that there are two main mechanisms for cavitation in SP materials, namely vacancy diffusion growth and plastic deformation controlled growth. The following equation for evolution of cavity volume with plastic strain was presented for plastically-controlled cavity growth, the more relevant to SP conditions:

$$C_v = C_{v0} e^{\beta(\varepsilon - \varepsilon_0)} \quad [9.28]$$

where C_{v0} is the cavity volume fraction at strain ε_0 and β is the cavity growth rate parameter. For the Rice and Tracey model, it was argued that

$$\beta = \beta_0 F(\sigma) \quad [9.29]$$

with β_0 related to material behaviour and experimental conditions and

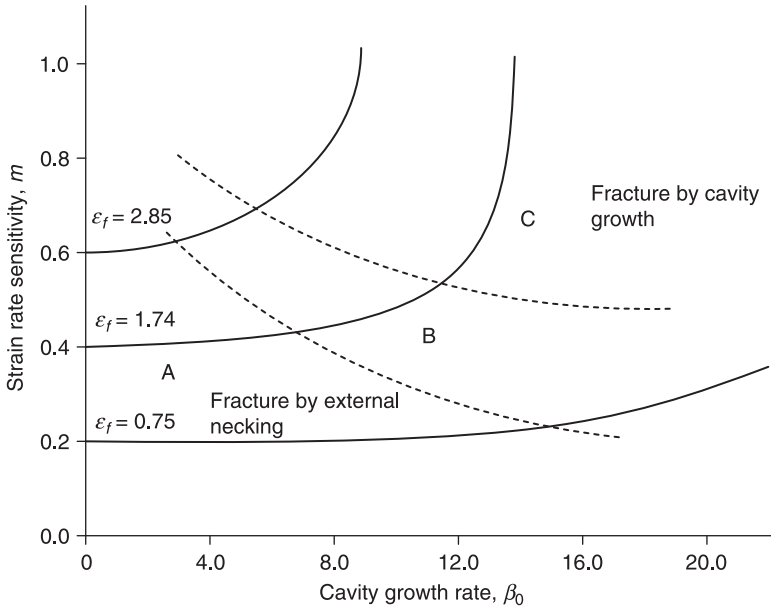
$$F(\sigma) = 0.558 \sinh\left(\frac{3\sigma_m}{2\sigma_{eq}}\right) + 0.008\nu \cosh\left(\frac{3\sigma_m}{2\sigma_{eq}}\right) \quad [9.30]$$

where σ_m is the mean hydrostatic stress and ν is the coefficient of strain-rate, given by $\nu = -3\dot{\varepsilon}_2/(\dot{\varepsilon}_1 - \dot{\varepsilon}_3)$, where $\dot{\varepsilon}_1 > \dot{\varepsilon}_2 > \dot{\varepsilon}_3$ are the principal strain rates. Equation [9.30] indicates that if the superimposed pressure P_h is large enough to make σ_m zero, then cavity growth will be suppressed. This condition occurs for P_h/σ_e greater than 1/3 and 2/3 for uni-axial and equi-bi-axial deformation, respectively. A modified version of Eq. [9.9] was employed to predict necking development under uni-axial tension incorporating cavity growth rate effects, as follows:

$$(1-f)^{1/m} e^{\frac{-\varepsilon_i}{m}} \left[1 - C_{v0} e^{\beta\varepsilon_i}\right]^{\frac{1}{m}} d\varepsilon_i = e^{\frac{-\varepsilon_h}{m}} \left[1 - C_{v0} e^{\beta\varepsilon_h}\right]^{\frac{1}{m}} d\varepsilon_h \quad [9.31]$$

Zhou *et al.* thus established the concept of a *superplastic fracture mechanism diagram*, which is shown schematically in Fig. 9.7. Based on the rationale that the two key parameters are strain-rate sensitivity, m , and cavity growth parameter, β_0 , the SP fracture mechanism diagram shows isostrain curves at fracture in the space of m and β_0 . The diagram is divided into three regions, labelled A, B and C. In region A, corresponding to small values of m and β_0 , the fracture curves are almost parallel to the β_0 axis, indicating negligible influence of cavity growth rate on fracture and predominant influence of m . In region C, where the fracture curves are almost parallel to the m axis, cavitation is the predominant influence leading to fracture without pronounced external necking. In region B, both external necking and cavity growth rate are of equal importance. Such diagrams, which can be plotted to different values of hydrostatic pressure, can be used to identify the process conditions required to change the fracture mode from cavitation fracture to macroscopic ‘necking’ fracture and consequently optimise the failure strain with respect to strain-rate sensitivity. Fracture mechanisms were presented for both uni-axial and bi-axial (bulging) SP deformation, but without specific application to any particular material(s).

It is possible to exploit the void growth model concept to develop a fracture locus in an FLD, as demonstrated by Leen *et al.* (2008). Following Yatomi *et al.* (2004), the Rice and Tracey void growth model can be represented as an equation



9.7 Schematic representation of the superplastic fracture mechanism diagram ($f = 0.005, C_{v0} = 0.001, P_h = 0$), after Zhou *et al.* (1988).

describing the effect of tri-axiality (ratio of hydrostatic stress, σ_m , to equivalent stress, σ_{eq}) on multi-axial failure strain, as follows:

$$\frac{\epsilon_f^*}{\epsilon_f} = \frac{0.521}{\sinh\left(\frac{3\sigma_m}{2\sigma_{eq}}\right)} \tag{9.32}$$

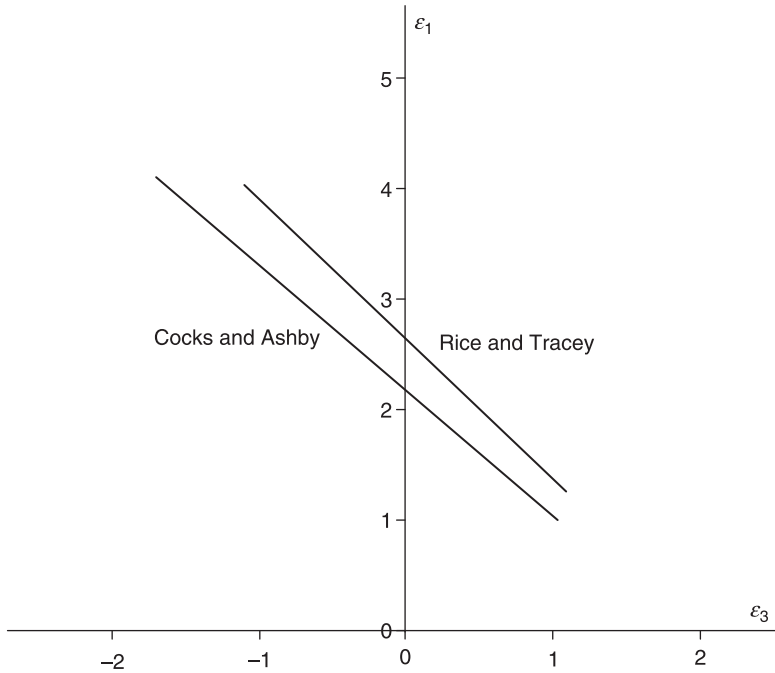
where ϵ_f^* , ϵ_f and ϵ_1^f are the multi-axial, uni-axial and major failure strains, respectively. Similarly, the Cocks and Ashby model can be represented as:

$$\frac{\epsilon_f^*}{\epsilon_f} = \sinh\left(\frac{1}{2}\left(\frac{2-m}{2+m}\right)\right) / \sinh\left(2\left(\frac{2-m}{2+m}\right)\frac{\sigma_m}{\sigma_{eq}}\right) \tag{9.33}$$

The major and minor failure strains are thus:

$$\epsilon_1^f = \frac{\epsilon_f^*}{\sqrt{\frac{4(1+\rho+\rho^2)}{3}}} \quad \epsilon_3^f = \rho\epsilon_1^f \tag{9.34}$$

Figure 9.8 illustrates Eq. [9.32] and Eq. [9.33] in the principal strain space as FLDs.

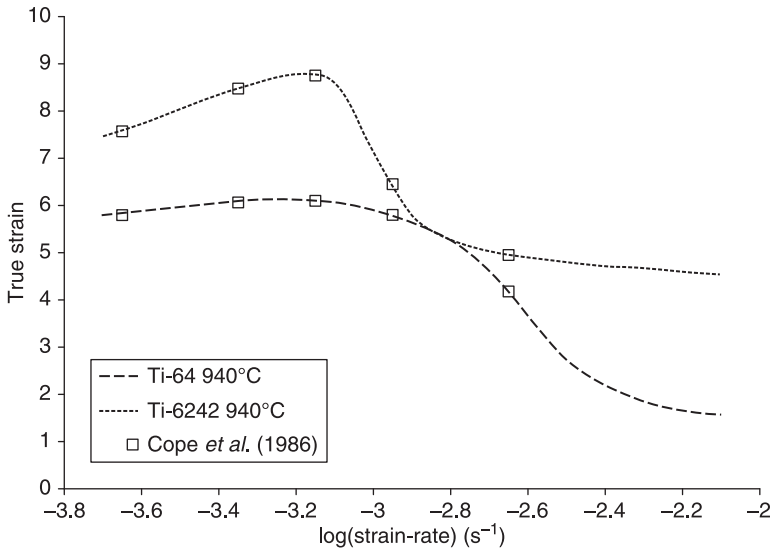


9.8 Schematic representation of FLDs based on Rice and Tracey and Cocks and Ashby void growth models, for assumed constant strain-rate.

9.2.4 Concept of the superplastic forming limit diagram

One of the key difficulties in applying the Hill-Swift, Rice-Tracey and Cock-Ashby FLDs to SPF is the strain-rate dependency, both of the deforming material and of the failure locus. One proposed solution to this is the concept of a SPF limit diagram (SPFLD), based on a strain-strain-rate approach for predicting the forming limits for SPF. The rationale is that a simple basis for predicting SP failure limits is the first order relationship between failure strain (ductility) and *m*-value (see Fig. 9.2, after Ghosh, 1977), which in turn has a direct relationship with strain-rate. Hence, a key relationship is that between strain to failure and strain-rate. A SPFLD is thus constructed as follows:

1. Establish the functional dependency of uni-axial strain to failure on strain-rate from uni-axial test data under constant strain-rate conditions, e.g. see Cope *et al.* (1986) for Ti-6Al-4V and Ti-6242 at a range of temperatures. If necessary, interpolate between different temperature and strain-rates.
2. Assume that this same functional dependency applies irrespective of the major strain, minor strain combination, i.e. across the 2D $\epsilon_1-\epsilon_3$ space for a given strain-rate, $\dot{\epsilon}$.
3. Then assume a specific 2D forming limit curve in $\epsilon_1-\epsilon_3$ space, for an assumed constant strain-rate. Any one of a number of different approaches could be



9.9 Curve fits for Ti-64 and Ti-6242 for sample failure strain versus strain-rate data published by Cope *et al.* (1986).

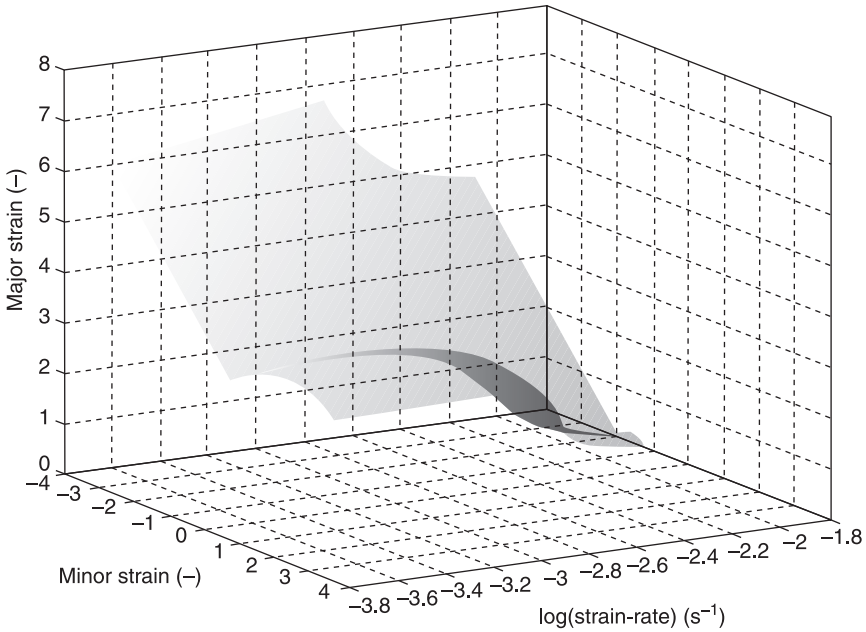
employed here, e.g. Lee and Zaveri (1982), Marciniak and Kuczynski (1967). In the present work, for illustrative purposes, the Hill-Swift combined instability limit curve is employed.

4. Thus construct a 3D SPFLD which represents a forming limit surface in ε_1 – ε_3 – $\dot{\varepsilon}_{eq}$ space covering the range of $\dot{\varepsilon}$ values occurring during forming processes.
5. To then use this SPFLD to predict failure for SPF, it is necessary to plot ε_1 – ε_3 – $\dot{\varepsilon}_{eq}$ loading (history) paths for sample (critical) points on the forming part (blank) in the 3D space, and then assess the intersection with the SPFLD. The most straightforward approach for this is to use a numerical technique, e.g. the FE method, particularly since the objective is a predictive capability. However, a key aspect of this model is the choice of constitutive equations.
6. Finally evaluate $\dot{\varepsilon}_{eq}$ using Eq. [9.16], plot the ε_1 – ε_3 – $\dot{\varepsilon}_{eq}$ paths in the 3D space and examine for intersection with the SPFLD.

Figure 9.9 shows typical elongation-strain-rate data from Cope *et al.* (1986) for Ti-64 and Ti-6242 at 940°C while Fig. 9.10 shows the 3D SPFLD which has been obtained for Ti-64 at 927°C using the above procedure and MATLAB™.

9.2.5 Damage mechanics models

A key shortcoming of the FLF approach and other approaches based on the Hart or even the Ghosh instability criteria is that it does not provide a means for simulating the development of the neck (imperfection or inhomogeneity);



9.10 Three-dimensional superplastic forming limit diagram for Ti-64 at 927°C.

the imperfection needs to be assumed *a priori*. Furthermore, a mechanisms-based material model, e.g. Zhou and Dunne (1996), which includes grain growth effects and has strain-rate independent material constants, identified from tests across a range of constant strain-rates, would be superior for identifying C_{gr} . However, the approach of Dunne (1998), discussed above in Section 9.2.2, directly circumvents this problem by inherent incorporation of microstructural inhomogeneity. The approach has only, thus far, been applied to uni-axial loading conditions.

Continuum damage mechanics (CDM) provides a framework for simulating the progressive development of material or geometric imperfections, without requiring an *a priori* assumption about the nature of this imperfection. At the same time, a CDM approach provides a basis for developing an improved SPFLD where the failure locus identification takes account of strain-rate effects more rigorously than Krohn *et al.* (2007) and implicitly permits generalisation from uni-axial to multi-axial (bi-axial) failure strains, in lieu of the Hill and Swift criteria (e.g. as in SPFLD), or the generalised Hart criterion (e.g. as in the FLF approach).

When rate effects are important, such as for SP deformation, then a viscoplastic constitutive equation of the following form is commonly employed:

$$\dot{\epsilon}^p = \left(\frac{\sigma}{K} \right)^{\frac{1}{m}} \tag{9.35}$$

where K and m are material constants identified as the stress axis intercept and slope, respectively, from a logarithmic plot of measured flow stress against strain rate, as obtained from constant strain-rate tests, for example. m is commonly referred to as the strain-rate sensitivity. Lin (2003) has derived K and m values of 7675.4 and 0.8614, respectively, for Ti-6Al-4V at 927°C from flow stress data at strain rates of $1 \times 10^{-3} \text{ s}^{-1}$ and $2 \times 10^{-4} \text{ s}^{-1}$.

One possible approach for the damage mechanics of SPF is to employ a method adopted from creep life prediction, e.g. the work of Hyde *et al.* (1996), which in turn is based on the work of Kachanov (1958). A scalar damage variable, ω , is defined as follows:

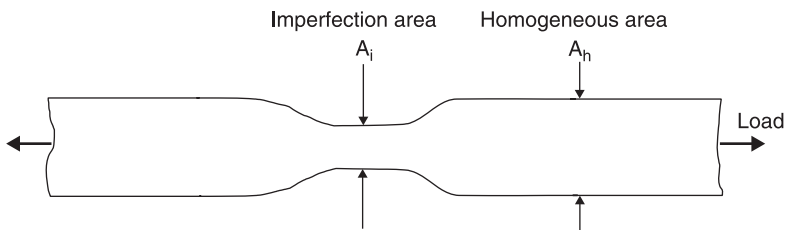
$$\omega = \frac{A_h - A_i}{A_h} = \frac{H_A - H_B}{H_A} \tag{9.36}$$

where A_i and A_h are defined in Fig. 9.11 as the inhomogeneous and homogeneous load-carrying areas, respectively, and similarly for H_A and H_B in Fig. 9.12. Thus, when the material is undamaged, or for material in undamaged regions, ω has a value of zero. With increasing damage, e.g. due to deformation localisation effects such as necking and/or cavitation, ω increases in value until failure is reached at some critical value ω_c . In damage mechanics, a key concept is that of effective stress, σ_{eff} , which is defined as follows:

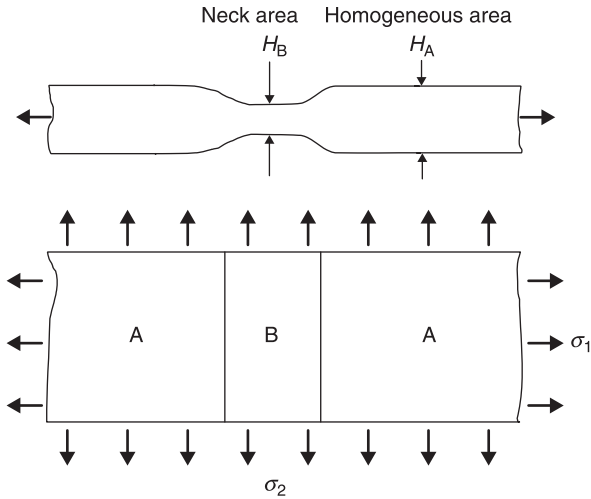
$$\sigma_{eff} = \frac{\sigma_o}{(1 - \omega)} \tag{9.37}$$

where σ_o is the nominal stress acting on the damaged load-carrying area, and σ_{eff} is the actual stress experienced by the damaged material due to the reduction in load-carrying area. The principle of strain equivalence (Lemaitre, 1996) states that the damage effect on constitutive equations can be included by replacing the stress term in the constitutive equation by the effective stress, σ_{eff} . Thus, the modified viscoplastic constitutive equation is as follows:

$$\dot{\epsilon}^p = \left(\frac{\sigma}{K(1 - \omega)} \right)^{\frac{1}{m}} \tag{9.38}$$



9.11 Assumed pre-existing geometric imperfection in tensile specimen, after Hart (1967) and Ghosh (1977).



9.12 Assumed neck (imperfection) in bi-axially stretched sheet under plane stress, after Marciniak and Kuczynski (1967), Ding *et al.* (1997) and Chung and Cheng (2002).

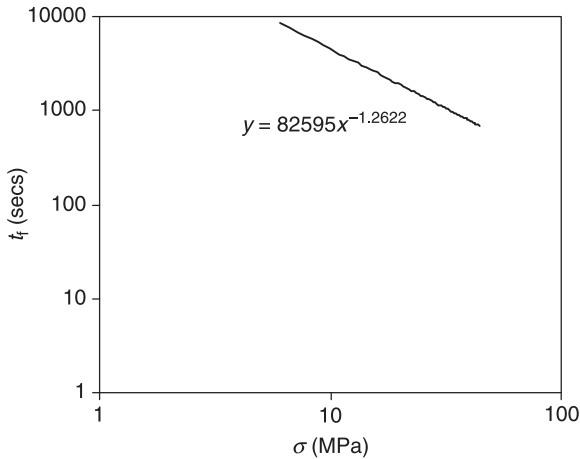
A key aspect is the identification of an appropriate damage evolution equation, which defines the development of inhomogeneities during SP deformation. The Kachanov damage mechanics evolution equation, commonly used for creep damage prediction, is one such approach. The following equation, as employed by Hyde *et al.* (1996), has been successfully applied to predict damage evolution for high temperature, constant stress creep of CrMoV and 9%Cr power plant steel alloys:

$$\dot{\omega} = M \left(\frac{\sigma}{1 - \omega} \right)^\chi \quad [9.39]$$

where M and χ are material rupture constants determined from uni-axial test data. The rupture constants for SPF can be determined as follows.

1. Identify the uni-axial strain to failure (ϵ_f) for the candidate material and temperature over a range of constant strain-rates. For example, this data has been interpolated from Cope *et al.* (1986), for Ti-6Al-4V at 927°C, as previously presented by Krohn *et al.* (2007).
2. Identify the (approximate) steady-state flow stress, σ , for each constant strain-rate test (via Eq. [9.35]).
3. Identify time to rupture, t_f , according to $t_f = \epsilon_f / \dot{\epsilon}$ for a given constant strain-rate.
4. Identify M and χ from σ - t_f rupture curve (e.g. Fig. 9.13), using the integrated version of Eq. [9.39], assuming ω_c is 1, as follows:

$$t_f = \frac{1}{M\sigma^\chi} \int_0^1 (1 - \omega)^\chi d\omega = \frac{\sigma^{-\chi}}{M(1 + \chi)} \quad [9.40]$$



9.13 Stress-life rupture data for Ti-6Al-4V at 927°C as inferred from Cope *et al.* (1986).

5. For Ti-6Al-4V at 927°C, for example, M and χ can thus be identified as 5.35×10^{-6} and 1.2622, respectively (units of MPa and seconds).

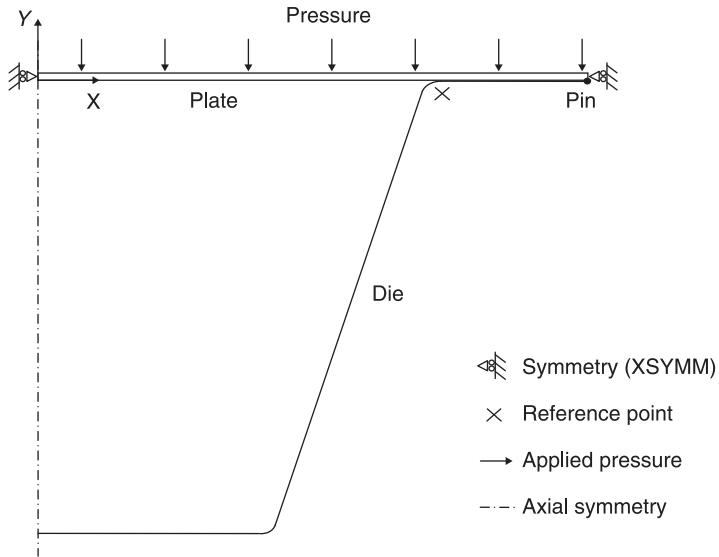
Lin *et al.* (2002) have presented a set of unified SP-damage constitutive equations for SP deformation of materials susceptible to cavitation, specifically Al-Zn-Mg and Al-7475 both at 515°C. The predicted uni-axial stress-strain curves showed excellent correlation with the measured ones for a range of strain-rates, including grain growth effects and hardening, as well as softening due to cavitation damage. The micro-damage modelled represents void nucleation and growth at grain boundaries, associated with the SP mechanisms of grain boundary sliding and grain rotation. The damage evolution equation adopted allows void growth to be a result of both diffusion and power-law creep. The approach requires 18 material constants, which were identified via a sophisticated data-fitting procedure, referred to as a universal multi-function objective function.

Giuliano (2006) presented the concept of a formability index, with application to the instability analysis of a PbSn alloy. The formability index is essentially similar to the SPFLD concept of Krohn *et al.* (2007).

9.3 Forming analyses and experiments

9.3.1 General

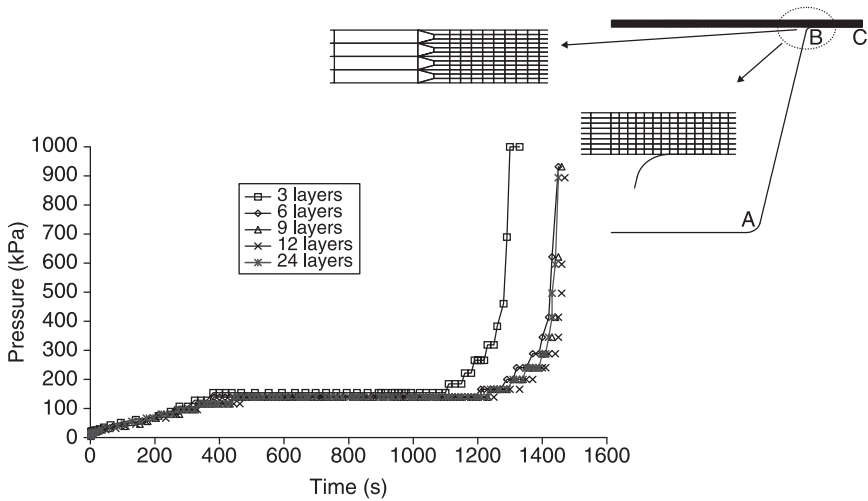
This section describes some tests carried out at the University of Nottingham with the specific purpose of generating failure during SPF in the titanium alloys,



9.15 Boundary and loading conditions of FEM.

One of the reasons for the importance of a FE-based failure prediction capability for SPF is the fact that FE modelling plays a key role in SPF, due to the need to control the strain-rate within an optimum range. Specifically, FE modelling is required for developing the SPF of new components and materials. Indeed, this issue highlights another reason why the use of a constitutive model with constants independent of strain-rate is required. In order to SP form a component under optimum strain-rate conditions, the instantaneous forming pressure needs to be varied so that some measure of current strain-rate for the forming sheet is maintained within an acceptable tolerance of the optimum (target) strain-rate. Different FE codes have different approaches for this. ABAQUS has a built-in capability to achieve this and this method is employed here. The technique determines the instantaneous pressure required to maintain the parameter r in the range $0.2 \leq r \leq 3.0$, where r is the ratio between the maximum instantaneous equivalent creep strain-rate, $\dot{\epsilon}_{max}^{cr}$, in the forming sheet and the target strain-rate, $\dot{\epsilon}_{target}$. A difficulty arises here with constitutive models where the constants are only valid for the target strain-rate: the same constants are implicitly assumed to be valid in the FE model for other strain-rates and the control algorithm ignores deviations of strain-rate on the lower side of the target, leading to errors.

An initial uniform coarse mesh simulation was performed; the mesh was then systematically refined at the die-entry radius and the bottom radius to achieve relative convergence, as shown in Fig. 9.16, with respect to the pressure–time curve.



9.16 Mesh refinement study with respect to the pressure–time curve.

9.3.2 Implementation of constitutive model

However, a key aspect of FE analysis for failure prediction is the choice of constitutive equations. Hence, based on the discussion above, the mechanisms-based sinh model is implemented here for the following reasons:

- the constants are independent of $\dot{\epsilon}$ and grain-size in a way which is consistent with the SP deformation mechanisms;
- it includes both static and dynamic grain growth effects, which are key to hardening behaviour and hence the σ – $\dot{\epsilon}$ – ϵ relationship in SPF;
- the required data is published for key titanium and aluminium alloys at the most commonly-used forming temperatures, e.g. Ti–6Al–4V at 927°C, and covering a range of $\dot{\epsilon}$ values.

The following set of large deformation mechanisms-based constitutive equations have been adopted here from the work of Zhou and Dunne (1996):

$$\dot{p} = \frac{\alpha}{d^\gamma} \sinh \beta (\sigma_{eq} - R - k) \tag{9.41}$$

$$D_{ij}^p = \frac{3S_{ij}}{2\sigma_{eq}} \dot{p} \tag{9.42}$$

$$\dot{R} = (C_1 - \gamma_1 R) \dot{p} \tag{9.43}$$

$$\dot{d} = \frac{\alpha_1}{d^\mu} + \frac{\beta_1 \dot{p}}{d^\mu} \tag{9.44}$$

$$\overset{\nabla}{\sigma} = 2GD_{ij}^e + \lambda D_{kk}^e \tag{9.45}$$

where $S_{ij} = \sigma_{ij} - \frac{1}{3}\delta_{ij}\sigma_{kk}$ and $\alpha, \beta, \gamma, \mu, \alpha_1, \beta_1, C_1, \gamma_1$ are material constants, d is grain size, G and λ are Lamé’s elastic constants, \dot{p} is the equivalent plastic strain rate, D_{ij}^p is the rate of plastic deformation tensor and $\overset{\nabla}{\sigma}$ is the Jaumann rate of Cauchy stress (Dunne and Petrinic, 2005). Equation [9.43] defines the evolution of R to a saturation value of C_1/γ_1 . A multistage analytical approach, developed by Lin and Yang (1999), has been applied to the data published by Ghosh and Hamilton (1979) to determine the constants for Ti–6Al–4V at 927°C for an initial grain size of 6.4 μm , which is consistent with the sheet material tested here. The values are given in Table 9.1.

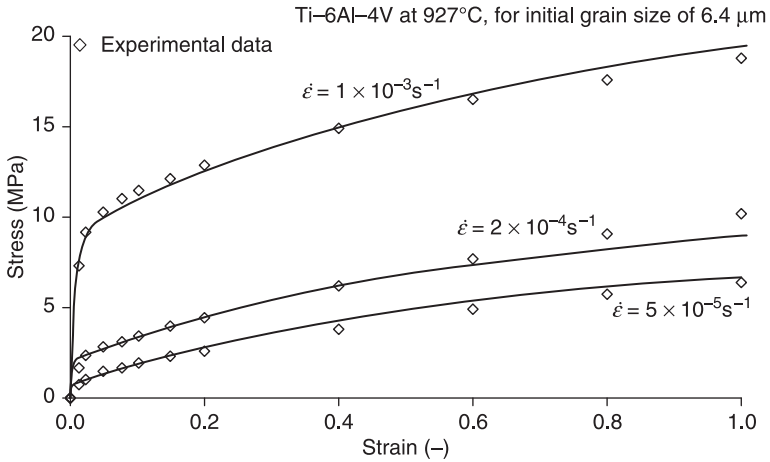
Table 9.1 Parameter values for unified-constitutive sinh model (Lin, 2003)

Constant	Value
α	2.115×10^{-5}
β	0.335×10^{-1}
γ	1.0
μ	4.995
α_1	0.13×10^{-16}
β_1	0.962×10^{-13}
C_1	12.442 MPa
γ_1	1.645
κ	0.5 MPa
E	1000 MPa

Figure 9.17 shows the validation (against the original test data of Ghosh and Hamilton, 1979) of the implementation of the above equation set within the CREEP user subroutine in ABAQUS for a FE model of a uni-axial test specimen under controlled strain-rate deformation conditions for three different constant strain-rates. Strain-rate control of the tensile specimen FE model was achieved by programming $v(t) = l_0 \dot{\epsilon}_0 e^{(\dot{\epsilon}_0 t)}$, where $\dot{\epsilon}_0$ is the target (constant) strain-rate, l_0 is the initial gauge length and t is the time in seconds, into the DISP user subroutine.

The multi-axial form of the coupled viscoplastic constitutive and damage evolution equations is as follows:

$$D_{ij}^p = \frac{3}{2} \left(\frac{\sigma_{eq}}{K(1-\omega)} \right)^{\frac{1}{m}} \frac{S_{ij}}{\sigma_{eq}} \tag{9.46}$$



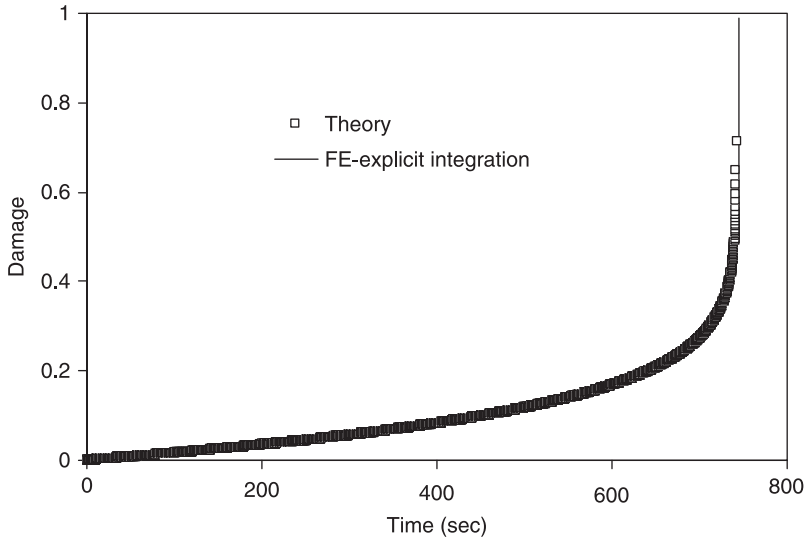
9.17 Validation of implementation of mechanisms-based sinh model for different strain-rates of $1 \times 10^{-3} \text{ s}^{-1}$, $2 \times 10^{-4} \text{ s}^{-1}$ and $5 \times 10^{-5} \text{ s}^{-1}$ against experimental data from Ghosh and Hamilton (1979) for a constant strain-rate tensile test specimen.

$$\dot{\omega} = B \left(\frac{\sigma_{eq}}{1 - \omega} \right)^x \tag{9.47}$$

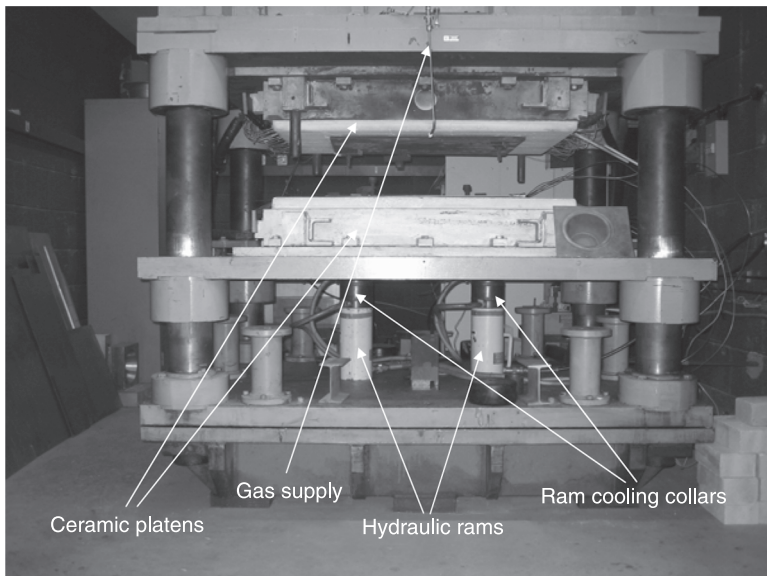
where σ_{eq} is the von Mises equivalent stress. Equations [9.46] and [9.47] have been implemented in a CREEP user subroutine in ABAQUS using explicit time integration, for large deformation, using the Jaumann rate of Cauchy stress defined by Eq. [9.45]. Figure 9.18 shows a validation of the FE-predicted damage evolutions versus time for a constant stress uni-axial condition against the theoretical solution.

9.3.3 Superplastic forming trials

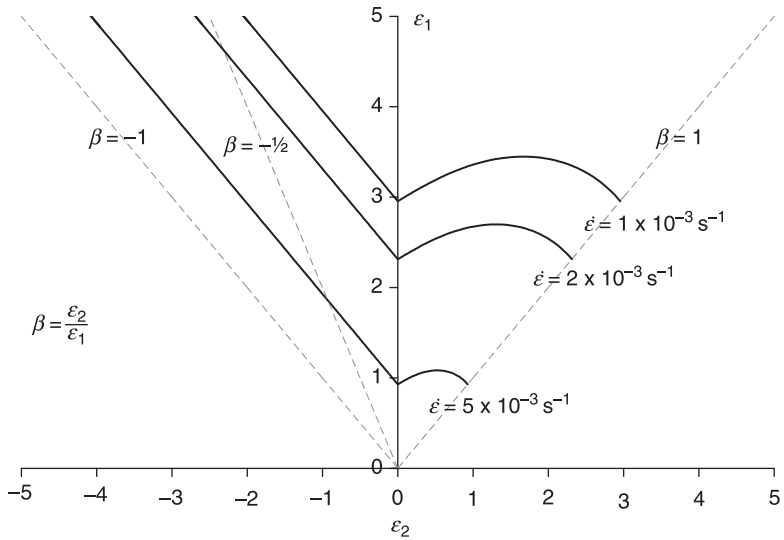
The SPF press, located at the University of Nottingham and shown in Fig. 9.19, was employed for the experimental phase of this investigation. The press consists of two ceramic platens, fitted with precision resistive heating wire, permitting forming temperatures of up to 990 °C, with an accuracy of approximately $\pm 5^\circ\text{C}$. Argon (Pureshield®) gas was used to apply the forming pressure to the upper surface of the plate and ensure an inert environment. Control of the gas pressure was achieved using a pair of mini-pumps, which are computer-controlled. The forming pressure-time curves required to form to specific target strain-rates are obtained from the FE analyses described above. Lubrication of the die-plate interface was provided using an aerosol-based Hexagonal Boron Nitride (HBN) applied to both the die and plate surfaces prior to forming. A large forming



9.18 Validation of FE-implementation of damage mechanics against the theoretical solution of damage for the constant stress uni-axial condition.



9.19 Image of the SPF press with annotation identifying key components.

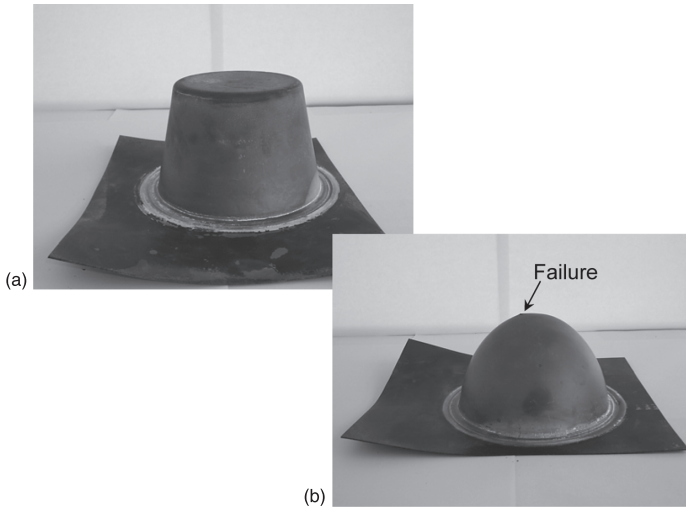


9.20 2D section views of SPFLD corresponding to strain-rates of $1 \times 10^{-3} \text{ s}^{-1}$, $2 \times 10^{-3} \text{ s}^{-1}$ and $5 \times 10^{-3} \text{ s}^{-1}$.

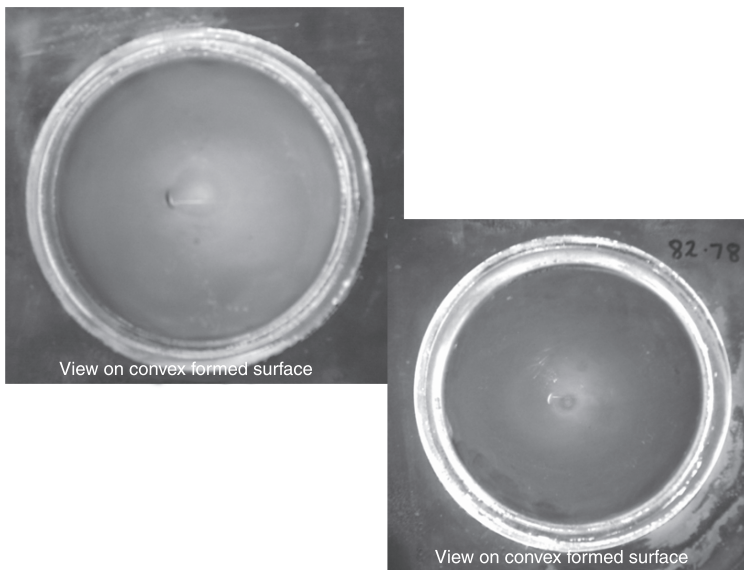
programme on 1 mm Ti-64 and 3 mm Ti-6242 sheet materials has been carried out; previous work included a large forming programme of work on Inconel 718 (SPF grade) to assess repeatability of failure depth and time etc. Repeatability with respect to both failure depth and time was shown to be within 5%. The relatively large thickness of the Ti-6242 sheet prohibited failure with the present die and practical strain-rates. Attention is focussed here on the Ti-64 sheet forming. Figure 9.20 shows 2D section views on the ϵ_1 - ϵ_2 plane of the SPFLD for three different $\dot{\epsilon}$ values of $1 \times 10^{-3} \text{ s}^{-1}$, $2 \times 10^{-3} \text{ s}^{-1}$ and $5 \times 10^{-3} \text{ s}^{-1}$, highlighting the difference in bi-axial failure strains associated with the different strain-rates. In particular, the failure strain is seen to reduce significantly with increasing strain-rate. Of course, there will be a distribution of strain-rate ($\dot{\epsilon}_{eq}$) over the forming sheet, but using the pressure control algorithm described above and the FE model, it is possible to establish pressure-time curves which correspond, within the constraints of the algorithm, to target strain-rates. Thus, the approach adopted here is to use the FE model to predict the pressure-time curve required to form at specific target strain-rates.

9.4 Results and discussion

The Ti-64 forming was undertaken at a target temperature of approximately 930 °C and a clamping load of 6.8 tonnes was applied to the SPF tool. Figure 9.21 shows two parts formed at target strain-rates of $1 \times 10^{-3} \text{ s}^{-1}$ and $5 \times 10^{-3} \text{ s}^{-1}$. The



9.21 SPF components formed at target strain rates of: (a) 1×10^{-3} and (b) $5 \times 10^{-3} \text{ s}^{-1}$.



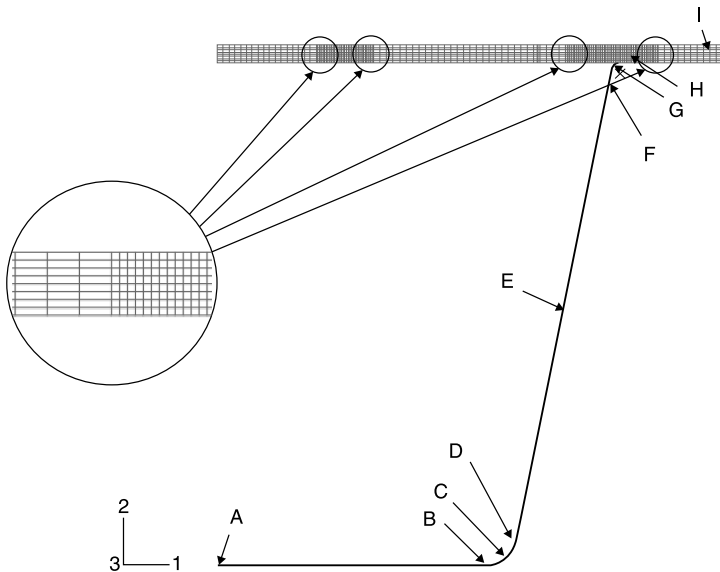
9.22 Different views of failed SPF part.

first formed successfully while the latter failed at a location near the centre of the dome, as shown. Figure 9.22 shows the failure for the faster strain-rate more clearly. The forming temperature for the Ti6242 sheets was 950°C and a range of strain-rates produced no fracture.

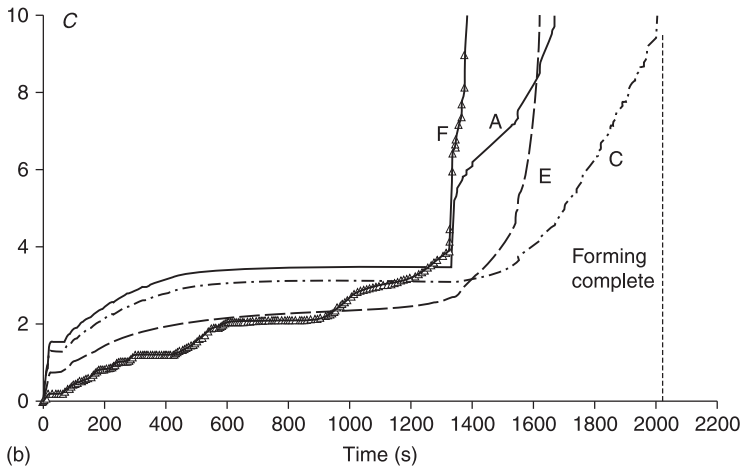
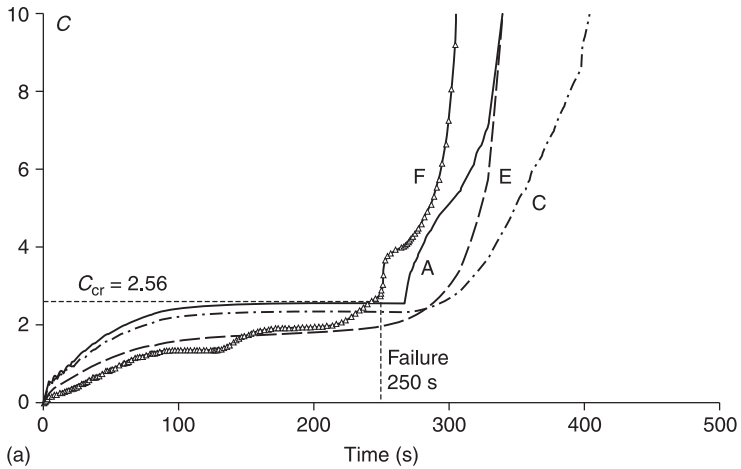
9.4.1 Application of FLF approach

The method used by Chung and Cheng (2002) to establish C_{cr} involved correlating a finite element predicted evolution of C as a function of forming time, with C_{cr} being the value corresponding to measured failure time. The value arrived at for C_{cr} for Ti-6Al-4V was 2.939 at 900 °C. This clearly relied on the use of a particular constitutive equation and in this case a double power law $\sigma = K\dot{\epsilon}^m\epsilon^n$ was used with one set of constants corresponding (presumably) to the target (optimum) strain rate for the forming process, although this information was not provided.

In the present work, the constitutive set defined by Equations [9.41]–[9.45] are employed. Figure 9.23 shows the labelling of points A to I on the forming sheet. Figure 9.24 shows the predicted results for the application of the FLF method to the Ti-64 forming trials described above. If the FLF method is calibrated, for the present case, using the failure C data from the $1 \times 10^{-3} \text{ s}^{-1}$ case, a C_{cr} value of 2.556 is thus identified. If this value is then applied to the $1 \times 10^{-3} \text{ s}^{-1}$ case, failure is predicted. This is inconsistent with the test data, whereby the $1 \times 10^{-3} \text{ s}^{-1}$ case formed successfully. The method also predicts failure for other strain-rates less than $1 \times 10^{-3} \text{ s}^{-1}$, which formed successfully. Although the C_{cr} value, determined here using the Dunne *et al.* equation set, is similar in value to that of Chung and Cheng (2002) for Ti-64 at 900 °C, C_{cr} is not a material constant, since it depends on the constitutive equation and using a double power law equation, for example, makes it depend also on strain-rate.



9.23 Axisymmetric FE model of a truncated cone die and sheet, showing labelled positions for prediction of strain-path history vis-à-vis SPFLD.



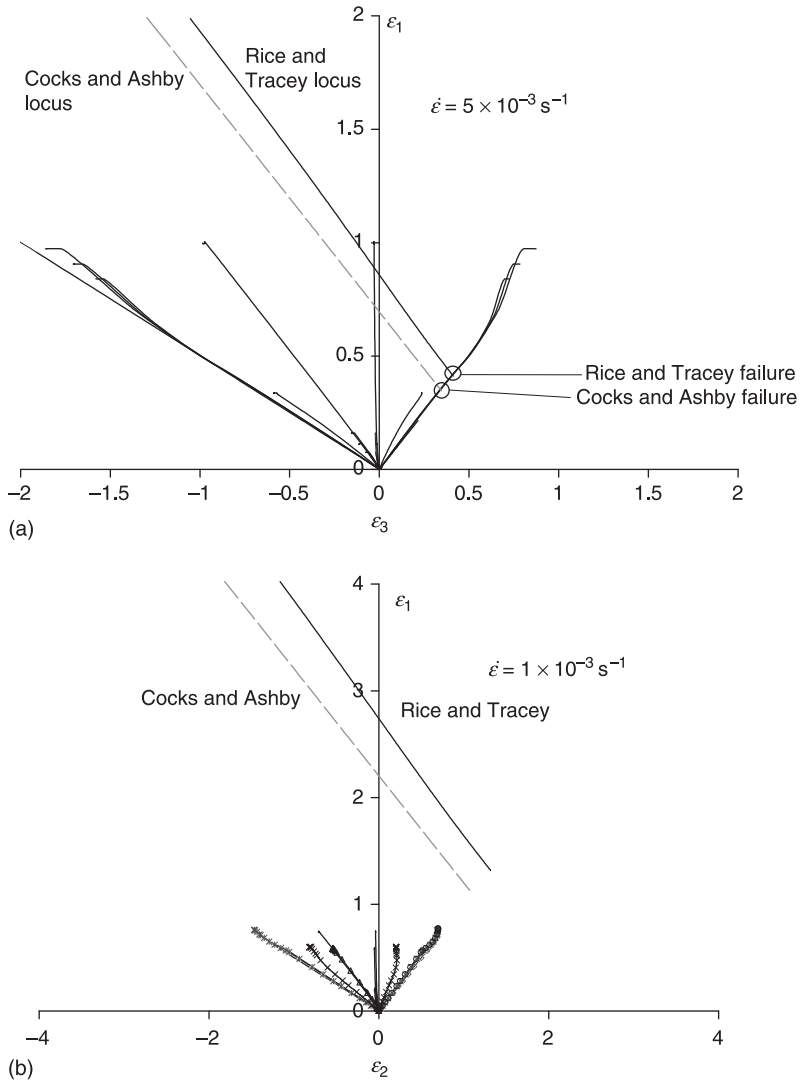
9.24 FE-predicted FLF predictions for: (a) $5 \times 10^{-3} \text{ s}^{-1}$ and (b) $1 \times 10^{-3} \text{ s}^{-1}$ forming tests.

In summary, the FLF approach is considered to have a number of shortcomings as follows:

1. It is based on the Hart criterion, which Ghosh has shown to be in error.
2. It purports to provide a SP fracture criterion which is argued to be a material property, but this is derived on the basis of a numerical model which relies upon a specific constitutive equation, which in turn is limited in terms of representation of deformation mechanisms and grain size effects, which are key to reliable SPF behaviour.
3. The method is complex and difficult to implement and interpret and, in light of the previous paragraph, it is not clear how grain size effects are dealt with.

9.4.2 Void growth models

Figure 9.25 shows the predicted strain-paths for points A to E on the forming sheet for target strain-rates of $5 \times 10^{-3} \text{ s}^{-1}$ and $1 \times 10^{-3} \text{ s}^{-1}$. Again, the constitutive set defined by Equations [9.41] – [9.45] are employed here. A number of observations can be made from these predicted results:



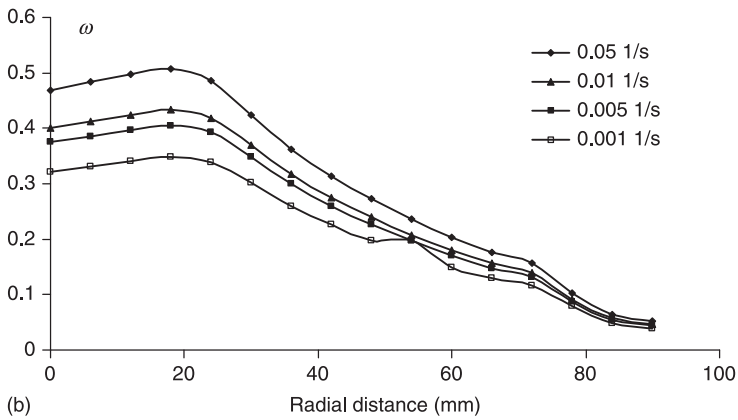
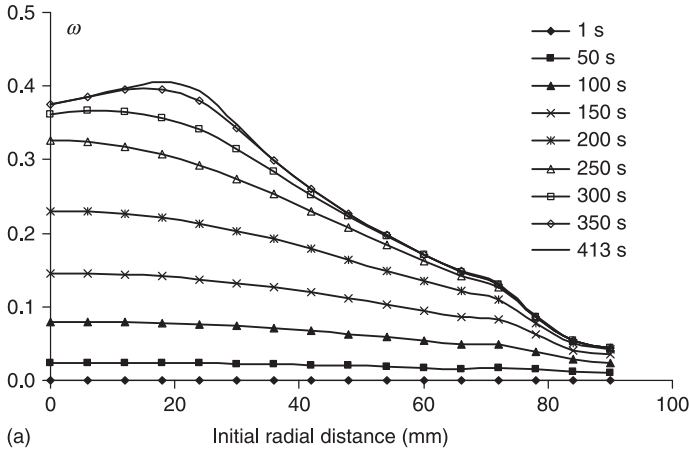
9.25 FE-predicted major-minor strain paths for a range of points in the forming blank vis-à-vis Rice and Tracey and Cocks and Ashby failure loci in strain space for: (a) $5 \times 10^{-3} \text{ s}^{-1}$ and (b) $1 \times 10^{-3} \text{ s}^{-1}$ forming tests.

1. The strain-paths generally exhibit approximately radial behaviour.
2. The $5 \times 10^{-3} \text{ s}^{-1}$ case is predicted to fail first at point A and then at point D.
3. The $1 \times 10^{-3} \text{ s}^{-1}$ case is predicted to give a significantly more homogeneous strain distribution over the forming sheet and is not predicted to give failure.
4. Both void growth models give predictions consistent with the failure of the $5 \times 10^{-3} \text{ s}^{-1}$ case and the successful forming of the $1 \times 10^{-3} \text{ s}^{-1}$ case.

However, these methods are ambiguous with respect to failure location. Despite not being suited to the failure mechanism in titanium alloys, which are not considered to cavitate, they do however provide a method for representing multi-axial failure strain.

9.4.3 Damage mechanics model

Four different target strain-rates of 0.001 s^{-1} , 0.005 s^{-1} , 0.01 s^{-1} , 0.05 s^{-1} were analysed using the coupled viscoplastic-damage equation, Eq. [9.46] and Eq. [9.47]. Figures 9.26 and 9.27 summarise the predicted damage results from the forming analyses for the different $\dot{\epsilon}_{\text{target}}$ values. Initially, damage is uniformly distributed but progressive forming damage begins to concentrate towards the centre (Fig. 9.26(a)). The final maximum damage is at $R = 20 \text{ mm}$, associated with concentrated thinning at that location, which is also evidently the last to come into contact with the die (corresponding to the bottom die radius). Figure 9.26(b) shows that damage increases monotonically with strain rate, and the spatial distribution trend is effectively independent of the strain-rate. Figure 9.27(a) shows that the damage rate is initially low, but increases with increasing deformation until die contact and decreases after contact; Fig. 9.27(b) shows the significant effect of $\dot{\epsilon}_{\text{target}}$ on damage rate. The forming trials presented above showed that failure occurred for 0.005 s^{-1} , but not for lower target rates. Although the damage constants have been obtained assuming a value for ω_c of 1.0, it is clear that this value is not predicted to occur in the forming sheet for rates which gave failure. A value of 0.33 for ω_c has also been suggested for use in failure prediction, based on grain boundary failure considerations (Lemaitre, 1996). If this value was employed here, failure would be predicted first at the centre of the sheet for the 0.005 s^{-1} case, which was the observed failure location in the tests, since this location is predicted to reach higher damage levels first (even if the $R = 20 \text{ mm}$ position has the final maximum predicted damage level). However, a key weakness of the present preliminary damage approach, which assumes monotonic damage rate to stress and stress to strain-rate relationships, is that it predicts successful forming with continually decreasing strain-rates, which is inconsistent with the well-known phenomenon of an optimum strain-rate (for maximum m value and SP ductility), above and below, which failure occurs at lower ductility.



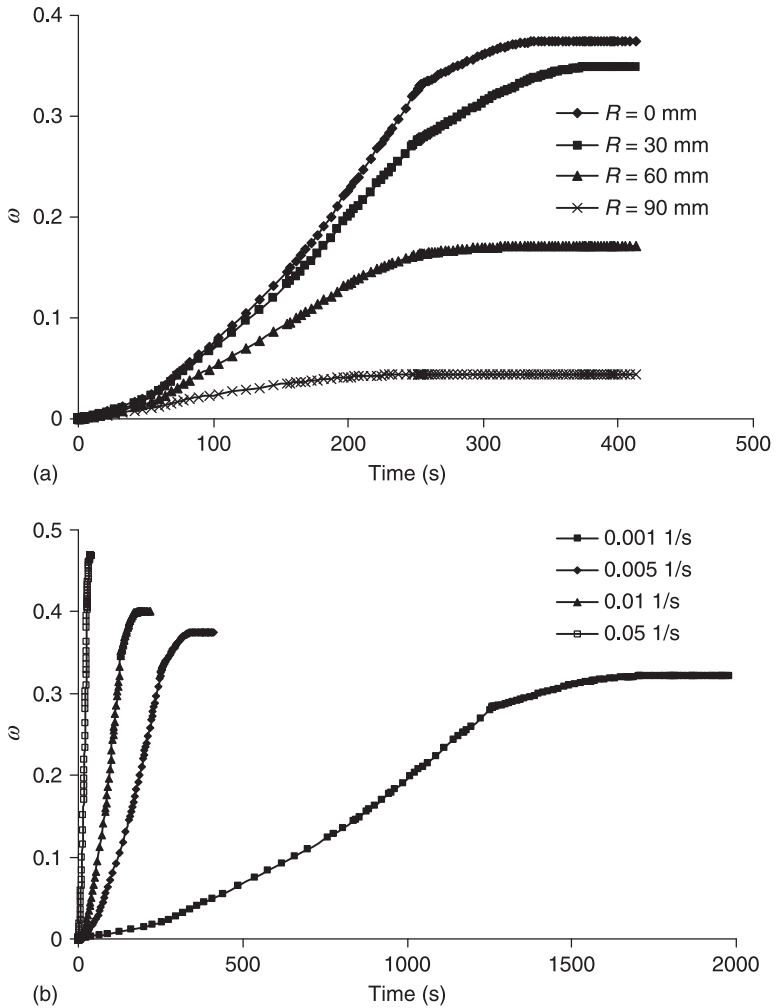
9.26 Predicted damage distributions: (a) versus (initial) radial position for $\dot{\epsilon}_{target}$ of 0.005 s^{-1} and (b) for different values of $\dot{\epsilon}_{target}$

9.4.4 SPFLD approach

Figures 9.28(a) and (b) show the FE-predicted $\epsilon_1-\epsilon_3-\dot{\epsilon}_{eq}$ paths for the sample positions (see Fig. 9.23) for the target strain-rates of $1 \times 10^{-3} \text{ s}^{-1}$ and $5 \times 10^{-3} \text{ s}^{-1}$, respectively. Figures 9.29(a) and (b) show the 2D section views of these same responses, i.e. $\epsilon_1-\epsilon_3$ plots, along with the corresponding 2D limit surfaces for the associated target strain-rates. Figures 9.30(a) and (b) show the $\epsilon_1-\epsilon_3-\dot{\epsilon}_{eq}$ paths on the SPFLD for both cases.

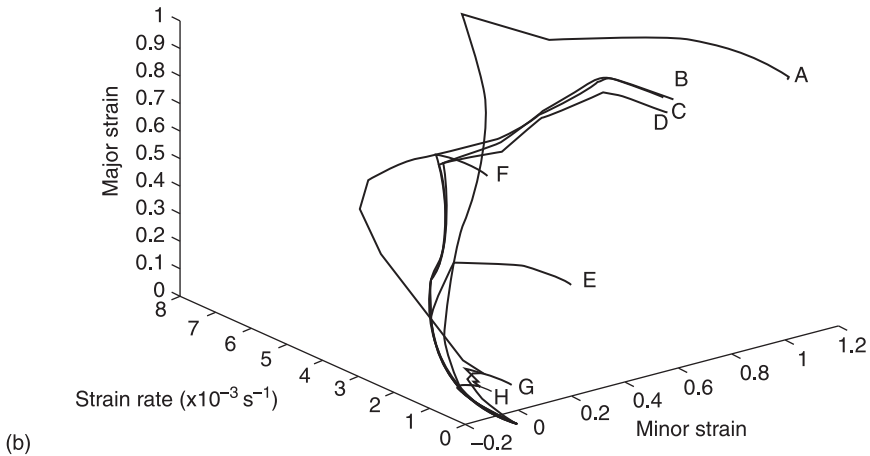
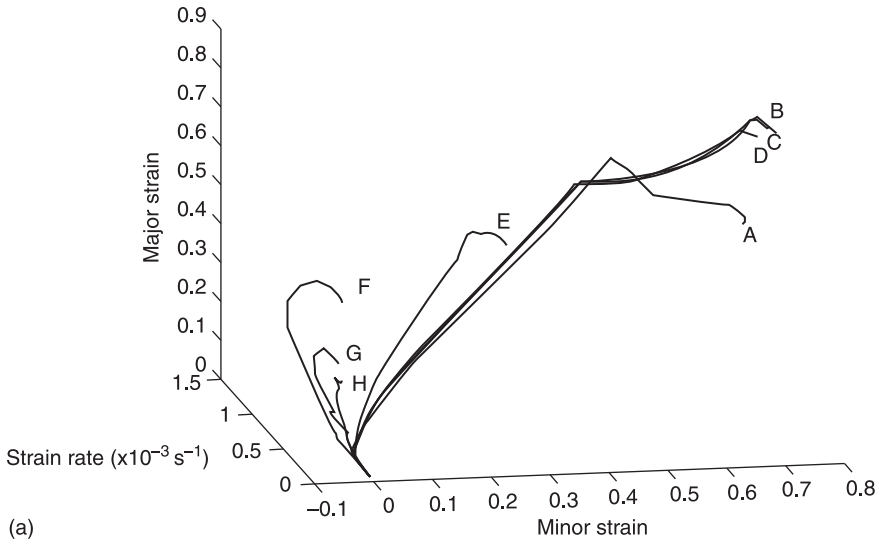
The following observations can be made in relation to these results:

1. The $\epsilon_1-\epsilon_3$ paths generally exhibit approximately radial behaviour.
2. The SPFLD approach predicts failure for the $5 \times 10^{-3} \text{ s}^{-1}$ case (Fig. 9.30(b)) and not for the $1 \times 10^{-3} \text{ s}^{-1}$ case (Fig. 9.30(a)), which is consistent with the forming trial results.



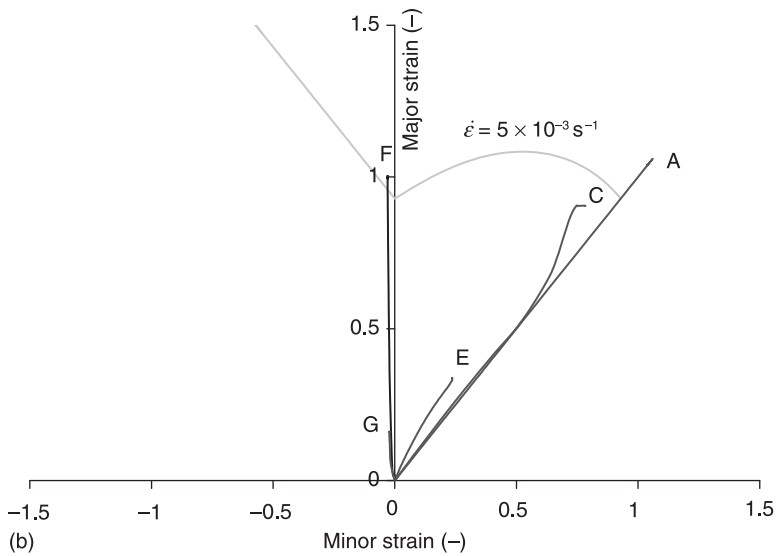
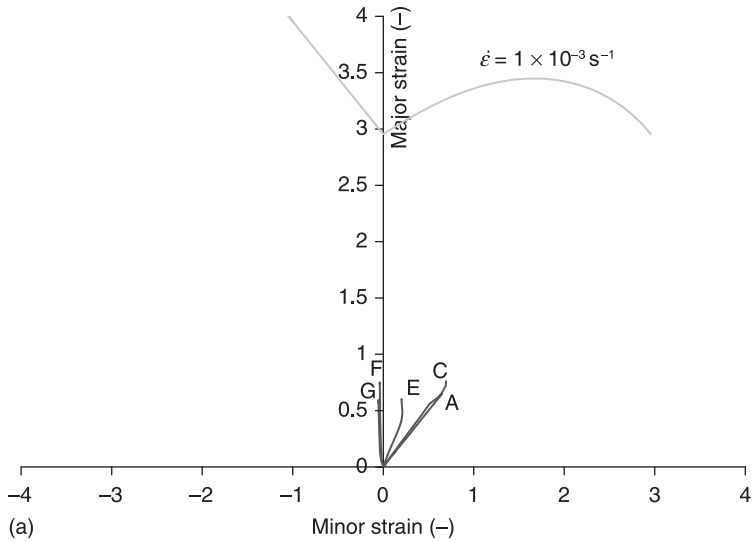
9.27 Predicted time-histories of damage: (a) at selected (initial) radial locations for $\dot{\epsilon}_{target}$ of 0.005 s^{-1} ; and (b) at $R = 0 \text{ mm}$ for different values of $\dot{\epsilon}_{target}$

3. Figure 9.29(a) shows that the $1 \times 10^{-3} \text{ s}^{-1}$ case is predicted to give a significantly more homogeneous strain distribution over the forming sheet.
4. The SPFLD-predicted location of failure for the $5 \times 10^{-3} \text{ s}^{-1}$ case is position A, which corresponds to the observed failure location in the forming trial.
5. The 2D section views, based on just $\dot{\epsilon}_{target}$ values, with just ϵ_1 – ϵ_3 paths, also provided useful information about failure, correctly predicting failure for the $5 \times 10^{-3} \text{ s}^{-1}$ case and none for the $1 \times 10^{-3} \text{ s}^{-1}$ case.



9.28 FE-predicted $\varepsilon_1-\varepsilon_3-\dot{\varepsilon}_{eq}$ paths for $\dot{\varepsilon}_{target}$ values of: (a) $1 \times 10^{-3} \text{ s}^{-1}$ and (b) $5 \times 10^{-3} \text{ s}^{-1}$, for positions A to H on the forming sheet.

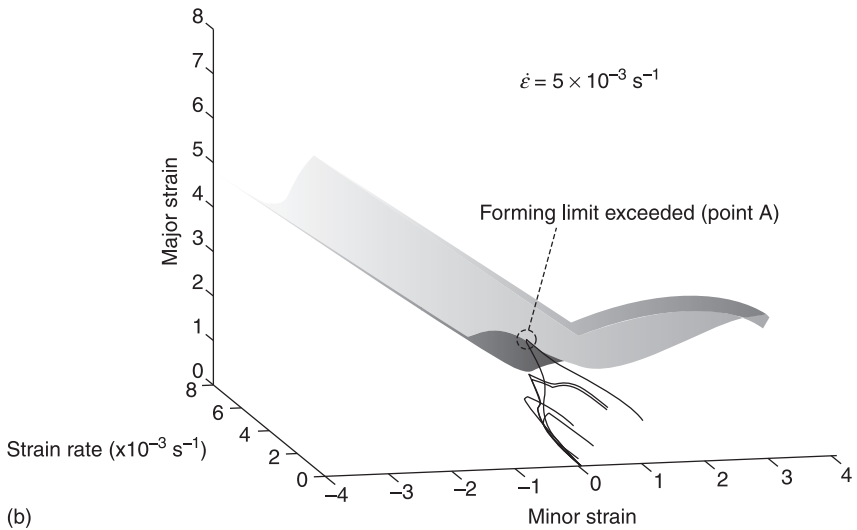
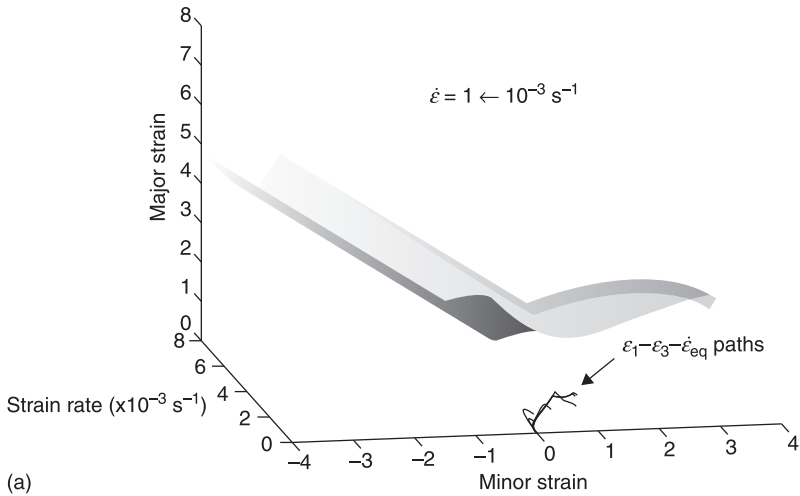
6. However, the 2D section views for the $5 \times 10^{-3} \text{ s}^{-1}$ case (similarly for the void growth approach of Fig. 9.25(a)) suggest failure at both positions A and F (die-entry radius), although first at A; this ambiguity does not occur for the SPFLD approach due to the incorporation of the $\dot{\varepsilon}_{eq}$ axis and associated data for the sample points on the blank.



9.29 2D section views of SPFLD showing FE-predicted ε_1 - ε_3 paths for $\dot{\varepsilon}_{target}$ values of: (a) $1 \times 10^{-3} \text{ s}^{-1}$ and (b) $5 \times 10^{-3} \text{ s}^{-1}$, for positions A to E on the forming sheet.

9.4.5 Discussion

Although results from only two forming trials are presented, previous forming experience with both titanium alloys, Ti-6Al-4V and Ti-6242, and Inconel 718, have indicated that scatter in such tests is not a significant issue. Nonetheless,



9.30 Comparison of FE-predicted $\epsilon_1-\epsilon_3-\dot{\epsilon}_{eq}$ paths with SPFLD for $\dot{\epsilon}_{target}$ values of: (a) $1 \times 10^{-3} \text{ s}^{-1}$ and (b) $5 \times 10^{-3} \text{ s}^{-1}$, for positions A to H on the forming sheet.

further testing would be helpful for different target strain-rates and for different materials to further assess the SPFLD approach. Initial work on the development of a SPFLD for Ti-6242, not presented here, has predicted no failure for the strain-rates tested on 3 mm thick sheets; thinner sheet material should facilitate forming failure.

A significant step forward would be the combining of the SPFLD concept with a failure criterion which directly includes strain-rate effects. The present

approach assumes that the Hill-Swift FLD can be used for constant strain-rates and that this can be mapped into the third dimension $\dot{\epsilon}_{eq}$ through the uni-axial SP ductility for different strain-rates. This is attractive because 2D section views of the SPFLD are familiar in the metal-forming field and only one new variable needs to be added, so that visualisation of the 3D SPFLD is straightforward. The integrated FLF approach, with C_{cr} , is promising but would need to be modified in the following respects:

- It would need to be based on a more comprehensive constitutive equation set, e.g. the mechanisms-based sinh equations of Dunne and co-workers.
- It would need to be modified to incorporate the shortcoming in Hart's criterion pointed out by Ghosh, with respect to modelling of initial imperfection size.

Furthermore, although the constitutive equations employed here are general with respect to strain-rate, they have nonetheless been developed and validated over a certain range of strain-rates. The extrapolation employed here is not significant so that it can be expected that the use of the model is still reasonable. Similarly, interpolation and some extrapolation has been employed with respect to the ductility versus strain-rate data of Fig. 9.9. Clearly, these issues could be addressed via further uni-axial testing of SPF materials.

9.5 Conclusions and future trends

The key conclusions from this chapter are as follows:

- Microstructural inhomogeneity (grain size distribution) is important for instability prediction in SP materials.
- There is a need for significant forming trials to support the development of a robust instability prediction tool for SPF.
- The concept of a SPFLD, as presented here, is one such easy-to-visualise tool; but this approach needs to be generalised so that the failure surface is obtained through a strain-rate failure mechanism, which also ideally encapsulates micro-structure effects.
- For non-cavitating SPF alloys, such as Ti-6Al-4V, this could be an approach based on the micro-structure heterogeneous approach of Dunne (1998), to identify the SPFLD failure surface for a range of bi-axial strain-strain rate paths. For cavitating alloys, such as Al-5083, a coupled viscoplasticity-damage mechanics material model, to incorporate softening effects due to void growth, is recommended. Again, this ought to be applied across a range of bi-axial strain-strain-rate paths to identify the SPFLD failure surface.
- Large-deformation, finite element methods play a critical role in SPF instability analysis, particularly for complex geometries and material behaviour.
- A key issue in SPF instability prediction is the identification, or development, of an appropriate constitutive equation set, which incorporates the key

phenomena, such as static and dynamic grain growth, strain-rate independence of material constants, strain-rate dependence, the key mechanisms, etc.

In terms of future trends related to instability in SPF, the following are some points worth considering:

- Exciting new developments in manufacturing, involving SPF, such as combined friction-stir welding (FSW) and SPF, e.g. see Sanders *et al.* (2008), will facilitate more widespread exploitation of the benefits of SPF, by allowing the manufacture of larger sheet components, no longer limited by the available dimensions of a SPF sheet. A key challenge related to this, however, will be the need for failure prediction methods which can account for the heterogeneous material zones created as part of the FSW process. Undoubtedly, computational modelling can play a central role in meeting this challenge. Another exciting, future and ongoing development is laser-induced SPF (Jocelyn *et al.*, 2010).
- Since microstructure (grain size, shape and evolution) is a primary parameter in SPF, it is clear that the development of multi-scale and multi-physics methods for instability is an important area for future development. For example, molecular dynamics simulation of the fundamental micro-structure mechanisms must be key for the future predictability of SPF, particularly for ultra-fine grain (UFG) grades of titanium alloys, with the potential for reduced forming temperatures or higher forming rates.
- New lightweight SPF materials, such as magnesium alloys, have the potential to improve fuel consumption in the transportation industry. The characterisation of such new materials for failure prediction, as well as SP deformation behaviour, is a requirement for successful exploitation.
- Superplastic forming has the potential to improve quality of life. For example, Richard Curtis (see Curtis *et al.*, 2010) has been a proponent of SPF manufacture of dental and maxillofacial implant structures. Such novel applications result in unique geometrical complexities which provide new challenges for failure prediction and more importantly for optimisation of pressure cycles.
- Renewable energy systems and sustainability: some key factors in the challenges facing the renewable energy industry are the development and/or identification of materials and structures which can:
 - resist corrosion on exposure to the environment, e.g. Ti for marine applications,
 - be manufactured at large length-scales to facilitate manufacture of wind turbine (WT) blades for increasing WT rotor diameters, for upscaling of power generation, e.g. combined use of FSW-SPF, as discussed by Sanders *et al.* (2010) for large-scale aerospace sheet components.
- Currently, polymer composites are the material of choice, but some doubts exist about the long-term durability of polymer composites in seawater, for

tidal turbines and wave energy generators, for example. Corrosion-resistant SPF alloys may well provide the answer here, providing the cost targets can be achieved. Aluminium SPF alloys, such as those described by Smith *et al.* (2010), are a more cost-effective alternative to titanium alloys for marine applications.

- There is a requirement for the development of standards and codes of practice for failure and instability prediction of SPF alloys.

9.6 References

- Chung, L.C. and Cheng, J.-H., 'Fracture criterion and forming pressure design for superplastic forming,' *Mat. Sci. Eng.*, A333, 2002, pp. 146–154.
- Chung, L.C. and Cheng, J.-H., 'The analysis of instability and strain concentration during superplastic deformation,' *Mat. Sci. Eng.*, A308, 2001, pp. 153–160.
- Cope, M.T., Evetts, D.R. and Ridley, N., 'Superplastic deformation characteristics of two microduplex titanium alloys,' *J. Mat. Sci.*, 21, 1986, pp. 4003–4008.
- Curtis, R., Omar, R., Bahra, J., Ditta, M., Chotai, A. and DiSilvio, L., 'Superplastic prosthetic forming – in vitro response,' *Key Engineering Materials*, 433, 2010, pp. 31–39.
- Ding, X.D., Zbib, H.M., Hamilton, C.H. and Bayoumi, A.E., 'On the stability of bi-axial stretching with application to the optimisation of superplastic blow-forming,' *Trans ASME, J. Eng. Mats. Tech.*, 119, 1997, pp. 26–31.
- Dunne, F.P.E., 'Inhomogeneity of microstructure in superplasticity and its effect on ductility,' *Int. J. Plasticity*, 14(4–5), 1998, pp. 413–433.
- Dunne, F.P.E. and Kim, T.-W., 'Inhomogeneous deformation and failure in superplasticity,' *Proc. R. Soc. Lond. A*, 455, 1999, pp 719–735.
- Dunne, F.P.E. and Petrinic, N., *Introduction to Computational Plasticity*, 2005, Oxford University Press, Oxford, UK.
- Ghosh, A.K., 'Tensile instability and necking in materials with strain hardening and strain-rate hardening,' *Acta Metallurgica*, 25, 1977, pp. 1413–1424.
- Ghosh A.K. and Hamilton C.H., 'Mechanical behaviour and hardening characteristics of a superplastic Ti–6Al–4V alloy,' *Metallurgical Transactions A*, 10A, 1979, pp. 699–706
- Giuliano, G., 'Failure analysis in superplastic materials,' *Int. J. Machine Tools & Manufacture*, 46, 2006, 1604–1609.
- Hart, E.W. 'Theory of the tensile test,' *Acta Metall*, 15, 1967, pp. 351–355.
- Hill R., 'On discontinuous plastic states, with special reference to localised necking in thin sheets', *J. Mechanics Physics Solids*, 1, 1952, pp. 19–30.
- Hyde, T.H., Xia, L. and Becker, A.A., *Int. J. Mech. Sci.* 38, 1996, pp. 385–403.
- Jocelyn, A., Keevil, A., Way, J., Flower, T., Fanourakis, A., *et al.* 'From indirect to direct heating of materials using lasers – a new beginning for superplastic forming,' *Key Engineering Materials*, 433, 2010, 63–68.
- Kachanov, L.M., *Proc. Acad. Sci. USSR Div. Engng. Sci.*, 8, 1958, pp. 26–31.
- Kelly, R.B., Leen, S.B., Pashby, I.R. and Kennedy, A.R., 'The measurement of friction for superplastic forming of Ti–6Al–4V,' *Materials Science Forum*, 447–448, 2004, pp. 111–116.
- Kröhn, M.A., Leen, S.B. and Hyde, T.H., 'A superplastic forming limit diagram concept for Ti–6Al–4V,' *Proc. Instn Mech. Engrs, Part L: J. Mats Design & Applications*, 221(L4), 2007, 251–264.

- Lee, D. and Zaveri, F. Jr., 'Neck growth and forming limits in sheet metals,' *Int. J. Mech. Sci.*, 24(3), 1982, pp. 157–173.
- Leen, S.B., Krohn, M.A. and Hyde, T.H., 'A comparison of failure prediction methods for superplastic deformation', *Int. J. Materials Forming*, DOI 10.1007/s12289-008-0205-y, 2008.
- Lemaitre, J., *A Course on Damage Mechanics*, 2nd edn, Springer, Berlin Heidelberg, Germany 1996.
- Lin J., 'Selection of material models for predicting necking in superplastic forming', *Int. J. Plasticity*, 19, 2003, pp. 469–481.
- Lin J., Cheong, B.H. and Yao, X., 'Universal multi-objective function for optimising superplastic-damage constitutive equations', *J. Materials Process. Technol.*, 125–126, 2002, pp. 199–205.
- Lin J. and Yang J., 'GA based multiple objective optimization for determining viscoplastic constitutive equations for superplastic alloys', *Int. J. Plasticity*, 15, 1999, pp. 1181–1196.
- Marciniak, Z and Kuczynski, K. 'Limit strains in the processes of stretch-forming sheet metal,' *Int. J. Mech. Sci.*, 9, 1967, pp. 609–620.
- Pilling, J. and Ridley, N. *Superplasticity in Crystalline Solids*, The Institute of Metals, London, UK, 1989.
- Sanders, D., Ramulu, M., Klock-McCook, E., Edwards, P., Reynolds, A. and Trapp, T., 'Characterisation of superplastically-formed friction stir welds in titanium 6Al–4V,' *J. Materials Engng Performance*, 17(2), 2008, 187–192.
- Smith, C.B., Mohan, A., Mishra, R.S, Mahoney, M., Miles, M., *et al.*, 'Friction stir processing of commercial grade marine alloys to enable superplastic forming,' *Key Engng Materials*, 433, 2010, 141–152.
- Swift H.W., 'Plastic instability under plane stress', *J. Mechanics Physics Solids*, 1, 1952, pp. 1–18.
- Yatomi, M., Bettinson, A.D., O'Dowd, N.P. and Nikbin, K.M., 'Modelling of damage development and failure in notched-bar multi-axial creep tests,' *Fatigue Fract. Eng. Mats. Structs*, 27, 2004, 283–295.
- Zhou, D.-J., Lian, J. and Suery, M., 'Numerical study of superplastic deformation with superimposed pressure for cavity sensitive materials,' *Materials Sci. Technol*, 4, 1988, pp. 348–353.
- Zhou, M. and Dunne F.P.E., 'Mechanisms-based constitutive equations for the superplastic behaviour of a titanium alloy', *J. Strain Analysis*, 31(3), 1996, pp. 187–196.

Superplastic forming and diffusion bonding of titanium alloys

M. JACKSON, University of Sheffield, UK

Abstract: The combination of titanium's excellent mechanical properties coupled with its natural ability to be superplastically formed and diffusion bonded has provided the aerospace industry with opportunities to manufacture stiff lightweight components with fewer joints/welds. This chapter firstly reviews the metallurgy, processing of sheet product and the phenomenon of superplasticity in titanium alloys. The second part reviews the superplastic forming (SPF) process itself, leading on to the exploitation of SPF coupled with diffusion bonding for many applications. A critical review of titanium product for low temperature SPF is also provided in this section. The chapter concludes with a brief review of aerospace applications.

Key words: aerospace, $\alpha + \beta$ titanium alloys, fine-grained Ti–6Al–4V, superplastic forming (SPF), diffusion bonding (DB), SPF/DB.

10.1 Introduction

Titanium (Ti) alloys exhibit excellent mechanical properties such as a high strength to weight ratio, unrivalled corrosion resistance and outstanding biocompatibility. Over the last four decades, engineers, designers and researchers have exploited titanium's natural ability to be superplastically formed and diffusion bonded at elevated temperatures and low strain rates to produce components and structures of optimum specific strength and stiffness, at minimum cost.

Historically, the aircraft and aero-engine manufacturers have driven the majority of developments for the superplastic forming (SPF) and diffusion bonding (DB) in Ti alloy systems, as opposed to the SPF of other light alloys such as Mg and Al where the automotive industry has had a more dominant role. And many readers, will have observed an array of hollow, wide-cord Ti fan blades sitting proudly at the front of a Rolls-Royce Trent series aero-engine (Fig. 10.1) while boarding a commercial aircraft; such components are an excellent example of SPF and DB technology. Over the last few years, with the advent of new aircraft build programmes, coupled with advances in SPF associated technology, and the development of Ti alloy grades that enable lower temperature (and thus, more economical) processing, the number of DB and SPF formed Ti components has significantly increased.

The first part of this chapter aims to provide a metallurgical introduction to Ti alloys and their superplastic behaviour and DB capability with respect to phase



10.1 Ti-6Al-4V hollow, wide-chord fan blades on a Rolls-Royce Trent series gas turbine engine (copyright Rolls-Royce plc).

chemistry and microstructure. In the second part of the chapter, the combination and exploitation of SPF/DB, leading onto the recent developments of Ti alloy grades that enable aerospace manufacturers to process at lower temperatures, and ultimately saving cost will be discussed. The chapter will conclude with a review of current and historical applications.

10.2 Titanium alloys

10.2.1 Titanium in today's aerospace industry: a brief note

Prior to any discussion on Ti alloys and their associated superplasticity capability, it is important to provide a degree of perspective with regard to the aerospace industry – the primary user of SPF of Ti alloys. The industry has been responsible for the majority of developments in SPF and DB of Ti alloys, for both airframe and

aero-engine components since the late 1960s. Today, with new fuel-efficient passenger aircraft consisting of a carbon fibre composite fuselage, empennage and wing, there is a materials selection requirement to employ an increased amount of Ti alloys for many components. For example, 120 million tonnes of Ti will be required per Boeing 787 aircraft, compared to 58 million tonnes on a Boeing 777 aircraft (Bolingbroke, 2010). This is due to Ti's superior galvanic corrosion resistance when in contact with the graphite, similar linear thermal expansion coefficients ($\sim 9.0 \times 10^{-6} \text{ K}^{-1}$) and Young's modulus/stiffness (110 GPa) to unidirectional CFRP (when loading parallel to fibres), compared to aluminium and steel. Aside from such properties, Ti alloys can be formed into complex structures using methods such as SPF/DB, further reducing the need for costly assembly and weight additive welds/rivets.

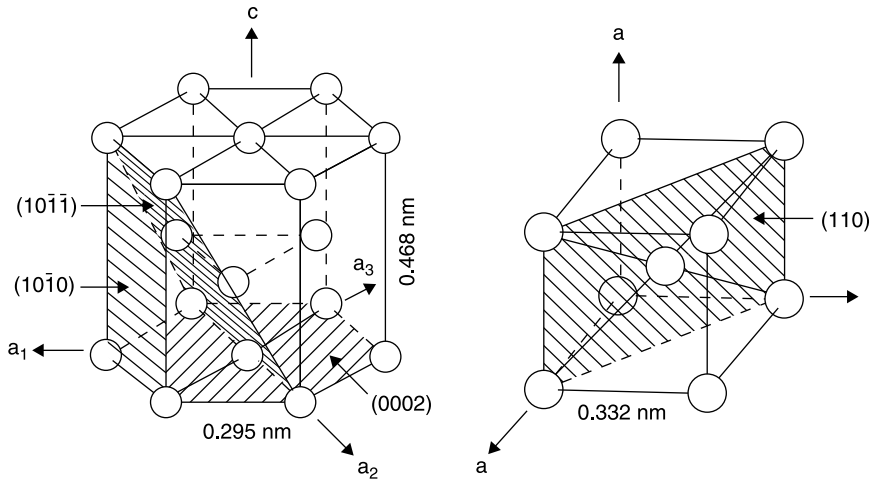
Annual global Ti sponge production has fluctuated around 100 000 tonnes over the last decade and with a worldwide demand of approximately 70 000 tonnes of mill product, Ti is dwarfed by commodity metal production: as a comparison, more stainless steel is produced in one day than the Ti industry produces in a whole year. More than half of the global Ti mill product feeds the highly cyclical aerospace industry, with other major markets including off-shore and chemical plant industries, which exploit titanium's excellent corrosion resistance. Over the last decade, both the aerospace and titanium industries have been badly affected by the aftermath of the 9/11 terrorist attacks, the SARS outbreak and, more recently, a global economic recession. However, since the recession of 2008–2009 and subsequent slump in the Ti industry, the current situation (as of mid-2010) is that orders for new aircraft are increasing once again. And although there are delays to 787, A380 and Joint Strike Fighter build programs, Ti producers are slowly benefiting from a requirement to double the amount of Ti on new aircraft platforms.

10.2.2 Metallurgy of titanium alloys

Titanium, being allotropic, can exist in two crystal forms known as alpha, α , which has a hexagonal close-packed (hcp) crystal structure and beta, β , which has a body-centred cubic (bcc) structure (Fig. 10.2). In unalloyed Ti, the α phase is stable at all temperatures up to 882.5°C, where it transforms to the β phase. This temperature is known as the β transus temperature. The β phase is stable from 882.5°C to its melting point of 1678°C.

The technologically important forms of Ti all contain deliberate alloying additions, which affect the phase equilibria and the microstructure by altering the relative thermodynamic stability of the two allotropic forms. Elements called α stabilisers (which include Al and the interstitial elements, O, N and C) preferentially concentrate in the α phase and raise the β transus. Beta-stabilisers can be subdivided into two types:

- the β isomorphous additions such as the bcc elements V, Mo and Nb, which continuously depress the β transus;



10.2 Unit cell of α phase and β phase (Lütjering and Williams, 2003).

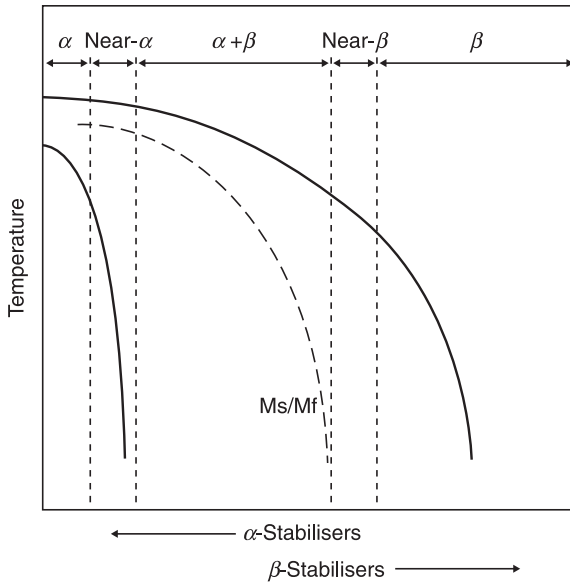
- the β stabilising eutectoid formers, such as Cu, Mn, Fe and Cr which also lower the β transus until a eutectoid reaction occurs.

Manipulation of the alloy chemistry coupled with thermomechanical treatment has produced Ti alloys with a wide range of mechanical properties. Ti alloys can be divided into five classes:

- α ,
- near- α ,
- $\alpha + \beta$,
- near- β ,
- β alloys,

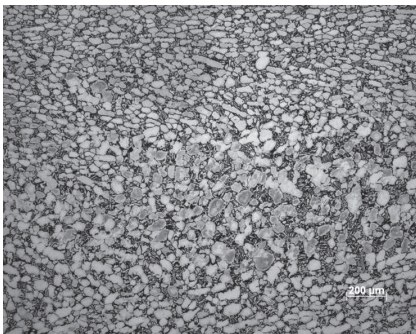
which reflect the contribution of the α and β phases to their microstructures and represented on a pseudo-phase diagram in Fig. 10.3. The $\alpha + \beta$ alloy Ti-6Al-4V accounts for ~90% of the Ti used in the aerospace market in forms ranging from sheet, plate, bar, die forgings, castings, and extrusions. This is due to Ti's good combination of producibility, strength, ductility, durability and damage tolerance properties. With regard to phase chemistry, Ti-6Al-4V contains sufficient β stabilisers (~4 wt% vanadium), as well as α stabilisers, to extend the $\alpha + \beta$ field to below RT, and therefore a two-phase morphology exists.

A mixture of α/β microstructures and volume fractions can be developed during thermomechanical processing (TMP). The lower the TMP temperature in the $\alpha + \beta$ field, the greater the stability of the β phase caused by increased solute enrichment of β stabilisers within the β phase. The morphology of the primary α (i.e. the α phase that remains untransformed as opposed to α formed by transformation from the β phase) can be equi-axial or lamellar. As the alloy is

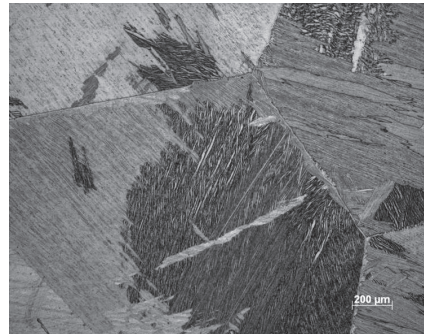


10.3 Schematic quasi-vertical section for ternary titanium alloys containing both α and β stabilisers (after Flower, 1990).

heated at temperatures in the $\alpha + \beta$ field, the volume fraction of the primary α diminishes as the β transus temperature is approached. The range of microstructural possibilities provided by $\alpha + \beta$ alloys (illustrated in Fig. 10.4) gives rise to a broad range of properties, which are particularly exploited in applications at temperatures approaching 300°C, due to the presence of the β phase, which degrades the creep resistance.



(a)



(b)

10.4 Ti-6Al-4V from the same billet: (a) as-forged in the $\alpha + \beta$ two-phase region and (b) forged and heat treated in the single β phase region for 2 hours. Manipulation of TMP conditions can drastically change the grain size and phase morphology.

10.2.3 Production of titanium sheet products

There is an abundant source of raw titanium oxide such as rutile and ilmenite in the Earth's crust; however, these oxides are thermodynamically more stable (i.e. high enthalpy of formation of its oxide) than other commodity metal oxides such as alumina and iron oxides. Therefore, it is more difficult to extract Ti from its oxide, which is a contributing factor to high extraction and processing costs of the supermetal. Preventing Ti from reacting with oxygen and other interstitial elements during downstream processing is even more energy intensive and costly.

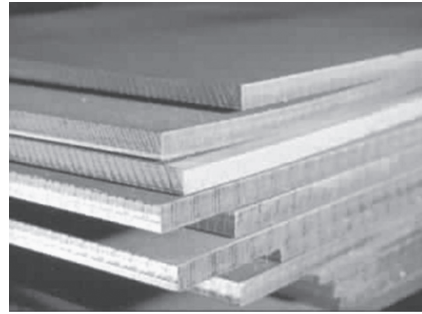
The current extraction method – the Kroll process, a metallothermic reduction process, has been the dominant commercial production route for Ti since the 1940s. It involves the carbochlorination of the oxide ores in a fluidised bed at 1300 K to produce an oxygen-free tetrachloride. Subsequent fractional distillation at 400 K removes most of the remaining ore impurities and the TiCl_4 is slowly fed into a large steel retort containing liquid magnesium between 1073 and 1173 K. Titanium sponge is formed in a highly exothermic reaction over long reduction times. The porous sponge product is crushed, alloyed and either consolidated into a welded electrode for vacuum arc remelting, as illustrated in Fig. 10.5, or fed directly into an electron beam cold hearth melting furnace, depending on the final product applications. The cast ingot from then undergoes extensive multi-step TMP stages such as hot forging around the β transus temperature in order to break down the microstructure and homogenise the chemistry before, in the case of sheet products, hot and warm rolling (Fig. 10.6) to achieve the final product shape, size and microstructure. Sheet and plate products account for 40% of all Ti product forms and a thorough description of the processing of $\alpha + \beta$ alloys is discussed in *Titanium* by Lütjering and Williams (2003). The titanium sheet is pack rolled to reduce surface oxidation. In pack rolling, a group of sheet blanks are sealed in a



10.5 Vacuum arc remelted titanium ingot (copyright Timet).



(a)



(b)

10.6 (a) Hot rolling of a titanium sheet and (b) a titanium sheet product (copyright Timet).

steel retort and hot rolled as a group. An inert parting agent prevents DB of the sheets during rolling. Subsequent cold rolling and cross rolling may be carried out to meet flatness, width and gauge tolerance requirements of customers. The resultant conventional sheet product will have a two-phase equi-axed α and β morphology with a grain size of $\sim 10 \mu\text{m}$.

10.2.4 Superplasticity in titanium alloys

As stated in previous chapters, superplastic behaviour can be attributed to localised tensile instability which results in an increase in flow stress, which then promotes straining in adjacent lower flow stress regions of the microstructure. Researchers since the late 1960s have investigated the optimum temperature and strain rate processing parameters that generate peak m -values and elongations for different Ti alloy chemistries. The effect of temperature on Ti-6Al-4V was first investigated by Lee and Backofen (1967), who illustrated that superplastic behaviour was confined to a subtransus temperature range of 815°C to 980°C . The upper limit of superplasticity being the β transus, which exceeded, will result in rapid grain growth in the single β phase. The lower limit being when the soft β phase is reduced promoting cavitation at α/α and α/β interfaces due to the limited slip systems of the dominant α phase. Therefore sheet produced with microstructural anomalies, such as large variations in grain size, elongated α or banding, will represent barriers to grain boundary sliding, which is generally accepted to be the dominant deformation mechanism for superplasticity in $\alpha + \beta$ Ti alloys such as Ti-6Al-4V.

Much of the seminal work determining the effects of microstructure and α/β phase volume fractions on superplasticity was carried out by Rockwell International (now part of Boeing) researchers N.E. Paton and C.H. Hamilton in the late 1970s and early 1980s (Paton and Hamilton, 1985). The combinatorial effect of temperature and strain rate on diffusion kinetics and deformation mechanisms in a two phase Ti alloy system is complex. As diffusion in the bcc β phase is two orders of magnitude

faster than the hcp α phase, it is important that a fine-grained α stabilises the microstructure during processing, preventing undesirable grain growth of the faster diffusing β phase. As with most superplastic materials, increasing grain size increases the flow stress and tends to reduce the maximum m-value as well as reducing the strain rate at which the maximum m-value is observed.

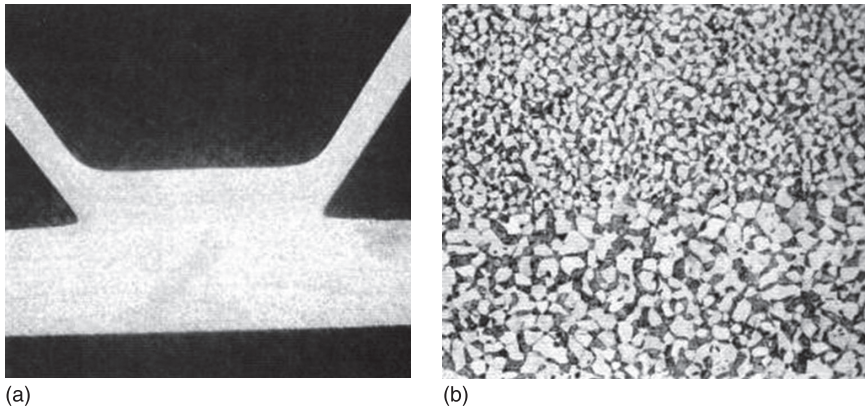
In summary, it is now widely accepted that the microstructural requirement for optimum superplastic behaviour in thin sheet Ti alloys is a fine equi-axed α/β morphology of grain size $\sim 10\ \mu\text{m}$ with approx. 30–50% volume of β at the processing temperature (i.e. $\sim 900^\circ\text{C}$ for a conventional Ti–6Al–4V sheet). In the literature, elongations easily in excess of 500% have been published particularly in the strain rates in the range of $10^{-4}\ \text{s}^{-1}$ to $10^{-2}\ \text{s}^{-1}$. However the majority of industrial parts do not require such excessive elongations; up to 300% ductility is sufficient. Lütjering and Williams (2003) make the point that the microstructural length scale must be consistent with the times required for diffusion over these distances to occur and quote that at temperatures of 875°C and a strain rate of $10^{-4}\ \text{s}^{-1}$ this length is about $20\ \mu\text{m}$, which is about the normal microstructural size scale in sheet products of this alloy after conventional mill processing.

Superplasticity is not only observed in Ti–6Al–4V, $\alpha + \beta$ alloys such as Timetal 550 (Ti–4Al–4Mo–2Sn) and Ti–62222 (Ti–6Al–2Sn–2Zr–2Mo–2Cr–Si) as well as near α alloy Ti–6242 (Ti–6Al–2Sn–4Zn–2Mo) have also been superplastically formed (Brewer, Bird and Wallace, 1998). It is also worth noting that substantial ductilities (i.e. up to 300%) have been observed in near β alloys such as Ti–10V–2Fe–3Al, Beta21S, β -CEZ and Ti–15V–3Cr–3Al–3Sn. Such alloys, when processed at relatively lower processing temperatures high in the $\alpha + \beta$ region or just above the β transus ($\sim 800^\circ\text{C}$), form fine single phase equi-axed structures through dynamic restoration processes, such as dynamic recovery or recrystallisation, and the formation of a fine subgrain network structure within the large β grains.

Finally, the deformation mechanisms and low flow stresses exhibited in fine equi-axed α/β Ti–6Al–4V have been exploited in other hot working processes such as extrusion, isothermal forging and hot isostatic pressing. Although starting microstructures are coarser and less uniform than those found in Ti–6Al–4V thin sheet, temperatures ($\sim 900^\circ\text{C}$) and strain rate regimes ($10^{-4}\ \text{s}^{-1}$ to $10^{-2}\ \text{s}^{-1}$) exploit enhanced plasticity through grain boundary sliding and diffusional creep mechanisms to produce near net shapes.

10.2.5 Diffusion bonding of titanium alloys

Diffusion bonding is the solid state joining of two surfaces under intimate contact and under high pressure and temperatures resulting in an undetectable original bond line, as grains from the two original parts form common boundaries along the original bond line, as illustrated in Fig. 10.7. In alloys such as Ti–6Al–4V, the prerequisite microstructural conditions and processing temperatures for DB are similar to SPF (described in section 10.2.3), as grain boundary sliding and



10.7 (a) A Ti-6Al-4V membrane panel diffusion bond and (b) microstructure at the bond line in a hollow, wide-chord fan blade (copyright Rolls-Royce plc).

diffusional creep are the dominant hot working mechanisms. Also DB exploits Ti's natural ability to diffuse its own surface oxide at temperatures above 600°C, enabling metal-metal contact and grain boundary diffusion to occur across the interface. To ensure good integrity bonds an inert or argon atmosphere is essential. As argon is insoluble in Ti, the engineers have to ensure that no gas remains entrapped at the interface.

A recent, comprehensive review on this topic, including detailed deformation mechanics of DB, has been presented by Sanders and Ramulu (2008) – who state a typical manufacturing cycle for the DB of thin sheet Ti-6Al-4V is 1.5 hours at a temperature of 900°C to 950°C with an applied force (usually argon gas) of 2 MPa. In the same review they state the conditions that govern the DB process to progress without bonding defects. For example, all surface oxides, oils and dirt must be removed to prevent contamination, and an inert atmosphere must also be applied to reduce the amount of oxygen-enriched surfaces which are brittle and prone to micro-cracking. The other important observation is that as the bonding time increases, the fast diffusing fine grains start to grow, due to time at temperature, resulting in a lack of diffusion when excessive grain growth has occurred.

Diffusion bonding in conjunction with SPF has provided the aerospace industry with a powerful forming technique that enables designers and engineers to form a single complex component from multiple sheet and is described in section 10.2.5.

10.3 The superplastic forming/diffusion bonding process

The combination of superplastic forming with diffusion bonding termed SPF/DB, where two or more sheets of Ti are fabricated into an integrally stiffened panel

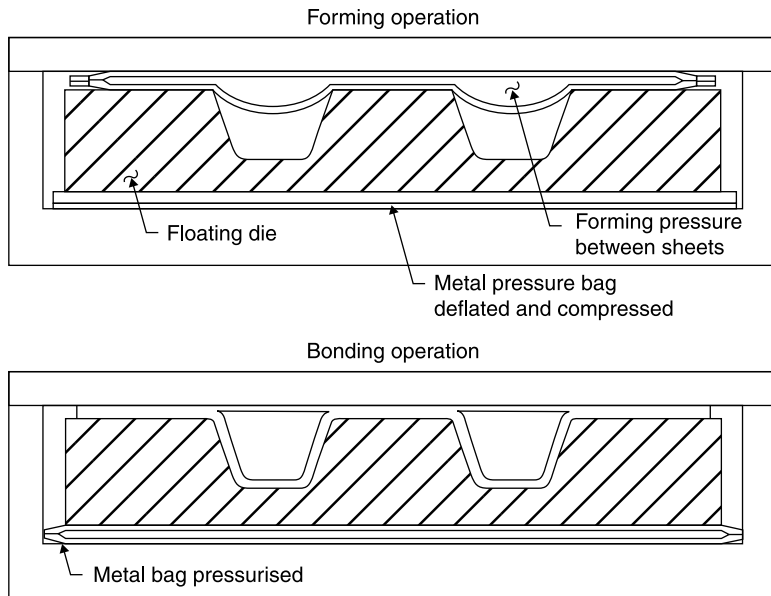
structure, has provided the aerospace industry with a unique forming and joining process over the last couple of decades. As described in section 10.2.4, DB occurs in alloys such as Ti–6Al–4V when two clean surfaces are pressed together at elevated temperatures to produce a sound metallurgical bond. As the process relies heavily on grain boundary diffusion across the interface, a fine equi-axed α/β grain structure during processing is preferred. Therefore, the microstructural requirements and processing temperature for DB are conveniently the same as that described for SPF in section 10.2.4.

The advantage of SPF/DB is the range of complex truss-core sandwich structures from a multi-sheet lay-up in one operation, significantly reducing the part count relative to conventional fabricated structures. Such stiffened sheet sandwich structures provide excellent weight savings thanks to the elimination of weldments, mechanical fasteners or rivets, as well as cost reductions while maintaining structural integrity. One of the initial applications of the SPF/DB process for a 2-sheet structure was for panels in the F-15E, and since then has gone from strength to strength and has been in commercial production for over 30 years. Boeing Company engineer, L.D. Hefti, on several occasions (2004, 2008) has stated the advantages of the SPF/DB process, which are:

- It replaces multi-piece assemblies with one monolithic component, which saves cost and weight and requires fewer tools.
- It is capable of producing complex geometry and sharp radii.
- The components contain very little, if any, residual stress with no spring back.
- Less assembly is required, which equates to lower cost and lighter weight along with better dimensional accuracy.
- The use of Ti improves the corrosion resistance of the component.

A seminal review by Stephens (1986) stated that SPF/DB enabled further weight savings if designers and engineers fully exploited the process capabilities to produce efficient and novel structural forms which could not or would not be considered appropriate for conventional manufacture.

Hefti (2004) described how the sheets were bonded by matched metal tooling. Figure 10.8 illustrates the forming and bonding operations using matched metal tooling for such components. In this example, argon gas expands the lower sheets, before a metal pressure bag is pressurised to enable the floating die to diffusion bond the lower sheet with the upper one. However, DB prior to expansion has commonly been used, where stop-off media is applied to inhibit bonding in certain areas. Hefti stated in a recent paper (2008) that the matched metal tooling method is more likely to produce non-bonds, resulting in scrap or a weld repair which adds further costs. He also makes the point in a 2004 paper at the International Conference on Superplastic Forming (ICSAM) that airplane engineers, designers and stress analysts, need to be assured that the process will yield quality hardware that meets structural requirements and that ‘engineers must be realistic’ – if there



10.8 Two-sheet SPF/DB process using matched metal tooling (Hefti, 2004).

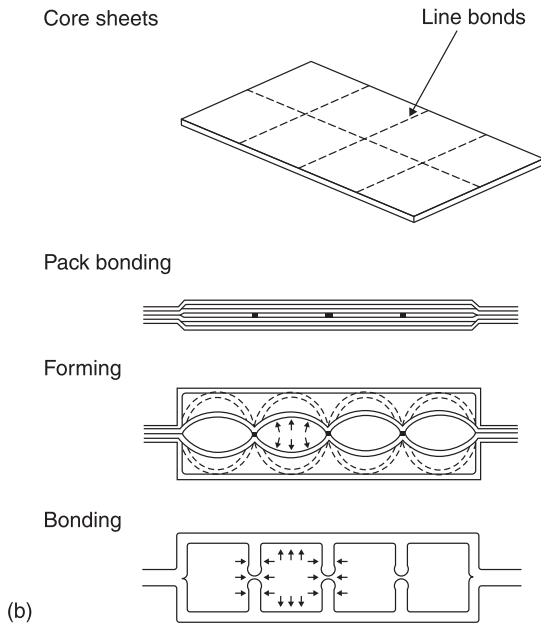
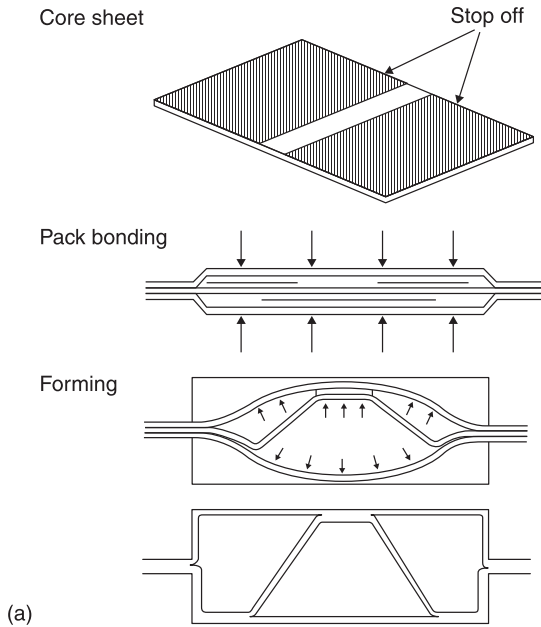
are areas that can tolerate non-bonds of a certain size and still be structurally acceptable, then the drawing should be zoned accordingly.

Hefti goes on to state that the stop-off process produces components with bond quality approaching 100%. The stop-off media can be applied by a silk screen method or a maskant/laser scribing method developed by Boeing.

Stop-off coatings such as BN and Y_2O_3 are used to prevent DB of the truss areas prior to the SPF stage.

Diffusion bonding of the sheet is carried out first under an inert atmosphere. Then argon gas is applied to superplastically deform the sheet structures as illustrated in the 3-sheet lay-up in Fig. 10.9(a). In a 3-sheet structure, for example, a variety of stiffening structures can be designed, such as a straight or sine wave structure. In a 4-sheet structure (Fig. 10.9(b)), cellular stiffened structures are achievable.

One of the practical advantages of SPF/DB are the low stresses on tooling, and thus subsequent low tool wear rates, compared to conventional forming routes. Although degradation due to high temperature cycling is significant and is a motivation for low temperature SPF/DB (section 10.4). In terms of product issues, there are excessive sheet thinning and unbonded regions. Designers and their finite element CAD models are sophisticated enough to predict thin regions in new complex structures without the need for costly trials and iterative component developments. Thinning occurs because of non-uniform stress levels in complex curvatures leading to variable forming rates and thicknesses. Engineers can



10.9 (a) Schematic of a 3-sheet SPF/DB lay-up (Stephens, 1986) and (b) schematic of a 4-sheet SPF/DB lay-up (Stephens, 1986).

combat such issues by using a starting product with a variable thickness, designing in selective reinforcement or innovative die design.

10.3.1 Low temperature superplastic forming/diffusion bonding

As stated in section 10.2.4, conventional Ti–6Al–4V sheet material with a grain size of $\sim 10\ \mu\text{m}$ can be formed at $\sim 900^\circ\text{C}$ into complex profiles. One of the drawbacks of SPF of Ti–6Al–4V at temperatures around 900°C is the reactivity of the sheet with residual oxygen in the high purity argon gas, and degradation of the costly tooling due to thermal cycling. At high temperatures, oxygen will diffuse into the surface of the component stabilising a β phase depleted region termed the ‘ α case’ up to tens of microns in thickness. As the α case layer is rich in oxygen, and thus harder and more brittle than the bulk material, it is prone to surface micro-cracking and consequently a reduction in fatigue strength. The removal of the α case is generally by sandblasting, chemical milling in HF/HNO₃ solutions which are costly and can lead to hydrogen embrittlement. Therefore, over recent times there has been attempts to carry out SPF/DB at lower temperatures that reduce the formation of deleterious surface phases as well as reducing energy and processing costs.

A decade or so ago, if you wanted a fine-grained α/β Ti material capable of SPF at temperatures lower than 900°C , manufacturers were limited to $\alpha + \beta$ alloy SP700 (Ti–4.5Al–3V–2Mo–2Fe) developed by NKK Corp., now JFE Steel Corp. in Japan. Since thermal expansion factor at the SPF temperature is very close to Ti–6Al–4V, the same dies were able to be used (Hefti 2009). Swale and Broughton (2003) from Aeromet International demonstrated that SP700 could be SPF’ed at $730\text{--}800^\circ\text{C}$ and have final mechanical properties equal to or better than the conventional Ti–6Al–4V.

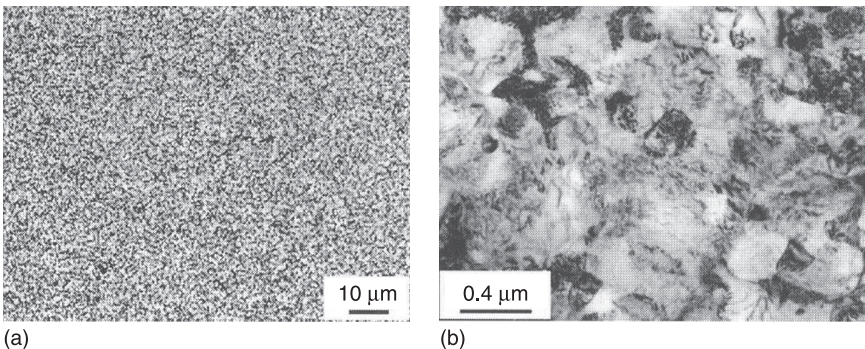
Aeromat International carried out analysis of manufacturing differences and benefits of SP700 and conventional Ti–6Al–4V. First, the lead time for part production was 6 weeks as opposed to 8 weeks for an equivalent Ti–6Al–4V part, due to the elimination of a number of processing steps associated with α case formation including: sand blasting, chemical milling, inspecting, and inspecting for hydrogen absorption during chemical milling. Other processing savings included a reduced set-up time, reduced electric consumption, extended element life, reduced ‘wear and tear’ of press structure and increased tool life. Swale and Broughton also made the point that there were reduced costs in disposing of spent (chemical etching) acids and contaminated sand in accordance with stringent UK environmental regulations. As a minimal amount of α case grew on the formed SP700 component at $730\text{--}800^\circ\text{C}$, thinner starting gauges can be used, they stated that a 20% reduction in starting stock thickness (0.96 mm compared to 1.22 mm) could be processed.

Hefti stated that parts continued to be fabricated using SP700 until the end of the Boeing 757 production in 2004, but as no extensive post-SPF mechanical

property evaluation had been conducted for the alloy, the material did not find extensive use in primary or secondary structures afterwards and a decision was made to stop manufacturing SP700 (Hefti 2008). In addition, research sponsored by NASA Langley showed that during roll seam welding trials in conjunction with SPF/DB for airframe sandwich structures, alloy SP700 had shown a tendency for extensive thinning (compared to other alloys) in the areas around the welds causing some concern about the utility of this alloy in such applications (Brewer, Bird and Wallace, 1998). However, as with Aeromet International, the Boeing engineers observed better die wear characteristics with no surface pitting and parts had a smooth finish, predominantly due to the low processing temperatures.

The SPF advantages demonstrated by SP700 provided a significant degree of research effort for low temperature SPF grade Ti–6Al–4V using the same gas pressures and forming cycles as those employed for conventional sheet material. At lower SPF temperatures the propensity for α case formation is severely reduced, the life of the tooling is increased and productivity increased due to reduced heat up times.

As stated in section 10.2.3, a greater volume fraction of grain boundaries, i.e. smaller grain size, equates to increased superplasticity at a given temperature and strain rate. Therefore, the key driver was to produce a sheet with submicron grain sizes. The Institute for Metals Superplasticity Problems (IMSP) in Ufa, Russia, developed a fine-grained (0.3–0.5 μm) sheet material which they termed sub-microcrystalline (SMC) Ti–6Al–4V, similar to that illustrated in Fig. 10.10. To produce a sheet with such fine grain sizes prior to pack rolling requires severe deformation thermomechanical processing such as a combination of near isothermal upset forging operations to continually refine the grain size and eliminate deformation dead zones (Salishchev *et al.* 2003). Multiple forged billets are finally forged into a pancake and machined into rolling blanks for the pack rolling procedure outlined in section 10.2.3. At around the same time, Verkhnyaya



10.10 Submicron-grained Ti–6Al–4V sheet, 2 mm thick: (a) microstructure in longitudinal cross section and (b) TEM image of sheet (Salishchev *et al.* 2003).

Salda Metallurgical Production Association (VSMPO-AVISMA) in Russia, currently the largest titanium producer (although projected to be eclipsed by the total output from China in 2011), also produced a fine-grained Ti-6Al-4V driven by collaborative research with Boeing. Levin *et al.* (2003) stated that the material had a grain size of 1–2 μm and ~65% α phase. This material has become the dominant material in many new SPF parts and VSMPO-AVISMA now regularly supply a fine grain Ti-6Al-4V material for an array of Boeing components. In 2010, the majority of SPF parts being produced by Boeing were from VSMPO-AVISMA fine grain Ti-6Al-4V, where forming temperatures are ~775°C (Hefti 2010), providing the industry with production advantages. With regard to α case formation, Comley (2003) stated that SPF of fine grain Ti-6Al-4V at 760°C produces a defined oxygen enriched layer of 13 μm compared to 30 μm for conventional Ti-6Al-4V at 900°C. A defined α case essentially due to an increase in the grain boundary volume fraction enables manufacturers to remove surfaces with more accuracy, again enabling thinner starting gauges and tighter tolerances.

However, in the author's opinion, if DB precludes the SPF operation, as in the case of the hollow wide-chord fan blade, metallurgical reasoning would suggest that significant grain growth will occur as a result of both thermal and straining effects, thus negating the benefits of the ultra-fine grained materials. Furthermore, over the last couple of years, work by Timet has shown that the severe TMP and associated high processing costs required prior to pack rolling to produce ultra-fine grain sheet may not be necessary (Kosaka and Gudipati 2010). $\alpha + \beta$ alloy Timetal®54M or Ti-54M (Ti-5Al-4V-0.6Mo-0.4Fe), which has an improved combination of strength, machinability and ballistic properties compared to Ti-6Al-4V, has also shown to be superplastic at temperatures as low as 750°C and at 'conventional grain sizes', i.e. 10 μm . Being slightly more β rich than Ti-6Al-4V, with Fe additions (which is a fast diffuser) and lower Al content, SPF flow stresses are reportedly 20–40% lower.

10.4 Applications

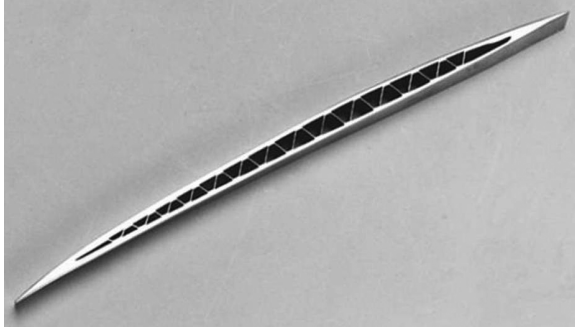
Ti-6Al-4V was first superplastically formed by CEGB Capenhurst in 1968 to representatives of the British Aircraft Corporation (a predecessor of what is now BAE Systems), who were so impressed that they set up a development facility in Filton (Grimes, 2001). In the USA, it was the Cold War that provided a lot of the driving force for SPF developments. Sanders and Ramulu (2004) provide a historical timeline of SPF developments from the B-1 Bomber to the F-15. The initial focus was to build monolithic, integrally stiffened hardware to replace built-up, fastened and welded assemblies for the B-1 Bomber airframe. This research was led by C.H. Hamilton at Rockwell International, who first combined SPF with DB for Ti sheet components. Follow-on work expanded to include McDonnell Douglas (now a subsidiary of Boeing) and SPF/DB monolithic panels for the F-15 Eagle which eliminated 726 detail parts and 10000 fasteners.

Applications on the F-15E were described by Hefti (2003) and included parts such as the keel, nozzle fairing, engine door and landing gear door.

Another major SPF/DB development initiated 30 years ago was the Rolls-Royce hollow, wide-chord fan blade (Fig. 10.11). The product was developed for the Trent series turbofans and provides almost 50% weight saving over solid wide-chord fan blades as well as improved efficiency. Two or more sheets of Ti-6Al-4V are diffusion bonded and then superplastically formed into a sleek hollow form with a stiffened girder structure (Fig. 10.12) and a unique camber and twist aerodynamic profile. The SPF/DB developments from applications such as the hollow wide-chord fan blade were exploited in the off-shore sector. High performance heat exchangers had complex truss-like internal structures which provided outstanding thermal gas cooling performance and enabled a more compact design compared to traditional plate/fin heat exchanger designs (Fowler, 1998). The use of titanium not only enabled the SPF/DB process to be used in the internal design, but provided the final product with excellent fatigue resistance, low weight and corrosion resistance.



10.11 Ti-6Al-4V hollow, wide-chord fan blades on a Rolls-Royce Trent series gas turbine engine (copyright Rolls-Royce plc).

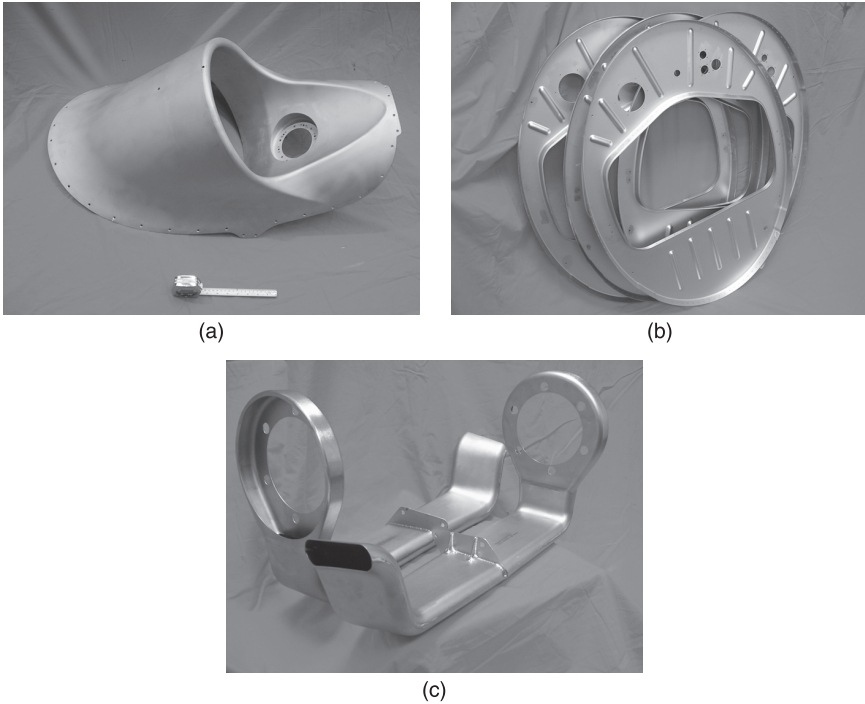


10.12 A 3-sheet stiffened girder structure in a hollow wide-chord Ti-6Al-4V fan blade (refer to Fig. 10.7 for corresponding bond line detail) (copyright Rolls-Royce plc).

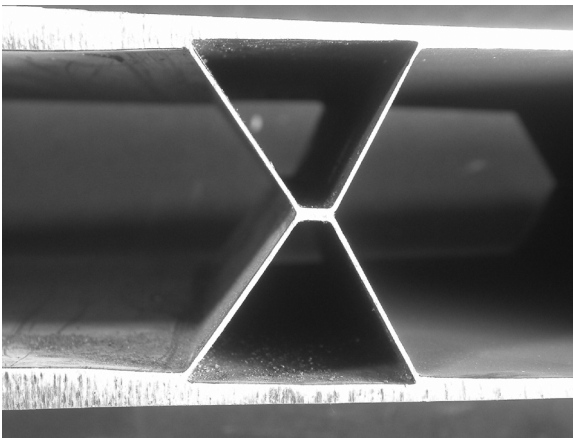


10.13 A 4-part SPF Ti pressing (copyright Aeromet International plc).

Aeromet International produce many complex aerospace components through SPF of Ti alloy sheet (Figure 10.13), such as tail cone sections and other complex assemblies. Figure 10.14 shows examples of the range of Ti products. Since their developments of the late 1960s, BAE Systems have traditionally been leaders in SPF/DB developments for both titanium and aluminium alloy components. The Eurofighter Typhoon is the latest example of a build program that is exploiting the technology in keel panels in the rear fuselage and structures in the foreplane (Fig. 10.15).



10.14 (a) A multi-part assembly of SPF formed Ti pressings for an access ducting, 450 mm diameter; (b) an SPF fire wall 800 mm maximum size; and (c) a welded assembly of two SPF tubular pressings, 500 mm long (copyright Aeromet International plc).



10.15 A segment of a 4-sheet Ti-6Al-4V 'X' core configuration of SPF/DB Typhoon foreplace (copyright BAE Systems).

10.5 Sources of further information and advice

Throughout the chapter, the author has highlighted further reading. In summary, for a critical review of the influence of microstructure and phase fractions on superplasticity in Ti Alloys, please refer to Paton and Hamilton (1985). An introductory review of SPF/DB was given by Stephens (1986) with excellent recent reviews from engineers at Boeing such as Sanders and Ramulu (2004), Comley (2004) and Hefti (2004). An overall understanding of titanium metallurgy, processing, properties and applications is provided by Lütjering and Williams (2003) in their book *Titanium*.

10.6 Acknowledgements

The author gratefully acknowledges Matthew Thomas (Timet UK), Bill Swale (Aeromat International Ltd), Mike Wallis (Rolls-Royce plc) and Peter Stewart (BAE Systems) for useful discussions and the supply of figures.

10.7 References

- Bolingbroke, R. (2010) Presentation to IOM3 Light Metals Committee, July.
- Brewer, W.D., Bird, R.K. and Wallace, T.A. (1998) 'Titanium alloys and processing for high speed aircraft', *Materials Science and Engineering: A*, 243(1): 299–304(6) (March).
- Comley, P.N. (2004) 'Lowering the heat: The development of reduced SPF temperature titanium alloys for aircraft production', *Materials Science Forum*, 447–448: 233–238.
- Flower, H.M. (1990) 'Microstructural development in relation to hot working of titanium alloys', *Materials Science and Technology*, 6: 1082–1092 (November).
- Fowler, J.O. (1998) *The application of titanium aero technology to compact heat exchanger manufacture*, in F.H. Froes, P.G. Allen and M. Niinomi (eds), *Non-Aerospace Applications of Titanium*, Warrendale, PA: The Minerals, Metals and Materials Society, pp. 237–243.
- Grimes, R. (2003) 'Superplastic forming: Evolution from metallurgical curiosity to major manufacturing tool?' *Materials Science and Technology*, 19: 3–10 (January).
- Hamilton, C.H., Ghosh, A.K. and Mahoney, M.M. (1982) 'Microstructure and phase ratio effects on the superplasticity of Ti–6Al–4V', in *Advanced Processing Methods for Titanium*, Warrensville Heights, OH: ASM International, pp. 129–144.
- Hefti, L.D. (2004) 'Advances in manufacturing superplastically formed and diffusion bonded components', *Materials Science Forum*, 477–448: 177–182.
- Hefti, L.D. (2008) 'Innovations in the superplastic forming and diffusion bonded process', *Journal of Materials Engineering and Performance*, 17(2): 178–182 (April).
- Kosaka, Y. and Gudipani, P. (2010) 'Superplastic forming properties of TIMETAL® 54M (Ti–5%Al–4%V–0.6%Mo–0.4%Fe) sheets', *Key Engineering Materials*, 433: 311–317.
- Lee, D. and Backofen, W.A. (1967) 'Superplasticity of some titanium and zirconium alloys', *Trans AIME*, 239: 1034.
- Levin, I.V., Kozlov, A.N., Tetyukhin, V.V., Zaitsev, A.V. and Berstov, A.V. (2003) 'Strain characteristics of Ti6–Al4–V alloy superfine grain sheets under SPF conditions',

- in G. Lütjering and J. Albrecht (eds), *Proceedings for the 10th World Conference on Titanium Ti-2003*, Weinheim: Wiley-VCH, pp. 577–588.
- Lütjering, G. and Williams, J.C. (2003) *Titanium*, Berlin/Heidelberg: Springer-Verlag, ISSN 1619–0181.
- Paton, N.E. and Hamilton, C.H. (1985) ‘Critical review: Superplasticity in titanium alloys’, in G. Lütjering, U. Zwicker and W. Bunk (eds), *Proceedings of the 5th International Conference on Titanium*, Frankfurt am Main: Deutsche Gesellschaft Für Metallkunde EV, pp. 649–672.
- Salishchev, G.A., Valiakhmetov, O.R., Galeyez, R.M. and Froes, F.H. (2003) ‘Production of submicron-grained Ti–6Al–4V sheets with enhanced superplastic properties’, in G. Lütjering and J. Albrecht, *Proceedings for the 10th World Conference on Titanium Ti-2003*, Weinheim: Wiley-VCH, pp. 569–576.
- Sanders, D.G. and Ramulu, M. (2004) ‘Examination of superplastic forming combined with diffusion bonding for titanium: Perspective from experience’, *Journal of Materials Engineering and Performance*, 13(6): 744–752 (December).
- Stephens, D. (1986) *Superplastic forming and diffusion bonding of titanium*, in *Designing with Titanium*, London: The Institute of Metals (ISBN 0 904357 89 9) pp. 108–124.
- Swale, W. and Broughton, R. (2004) ‘Applying superplastic forming principles to titanium sheet metal forming problems’, *Materials Science Forum*, 477–448: 239–246.

Superplastic forming of aluminium alloys

R. GRIMES, University of Warwick, UK

Abstract: The development of superplastically deformable aluminium alloys and their commercial exploitation over the past 40 years is outlined. At the outset it was not clear that it would be possible to develop such an alloy since all of the recognised alloys were of eutectic or eutectoid composition, but the addition of 0.5%Zr to an Al–6%Cu alloy proved to be the inventive step that made commercially useful superplastic aluminium a reality. Setting up the initial commercial forming operation with three small forming machines and the new alloy, AA2004 or Supral, is described; as well as the subsequent development of other alloys leading to exploitation around the world in new forming operations. From its early application, dominated by aerospace, the process has found major rail applications and, as the ability to make larger numbers of parts economically has increased, so automotive applications have rapidly grown.

Key words: Supral, superplasticity, innovation, zirconium.

11.1 Introduction

Superplastic behaviour in metallic alloys was probably first observed at the beginning of the twentieth century (Bengough, 1912) but remained a metallurgical curiosity until well into the second half of the century when interest was triggered by the publication of Underwood's review (Underwood, 1962). Even then, it was not until later that any thought appears to have been given to the possibility of commercially exploiting the superplastic phenomenon as a manufacturing technique (Backofen *et al.*, 1964). At this stage the general perception was that to exhibit superplasticity an alloy needed to be of, or near to, eutectic or eutectoid composition. The microstructure, it was believed, should consist of two, finely divided and stable phases. Superplastic behaviour was reported in Ti–6Al–4V in 1965 (Lyttle *et al.*, 1965) and exploitation of the remarkable superplastic properties of the Zn–22%Al eutectoid commenced in about 1968. As far as industrial exploitation was concerned, none of the apparently possible eutectics of aluminium, such as Al–33%Cu or Al–12%Si (a possible exception to this, somehow overlooked in the early investigations, was the Al–5.3%Ca eutectic and this is considered further below) possessed service properties appropriate to engineering components so that in the early stages of superplastic alloy development it was far from clear that a practically useful superplastic aluminium based alloy would even be possible.

11.2 History

The world's first practical superplastic aluminium alloy was jointly developed in the research organisations of the, then, Tube Investments Group [Tube Investments Research Laboratories (TIRL) and British Aluminium Research Division (BARD)]. TIRL had been conducting fundamental investigations into the deformation behaviour of the Al–33%Cu eutectic alloy so that this system seemed the logical starting point when the decision was taken to attempt the development of an industrially useful superplastic aluminium alloy. The copper content was immediately reduced to 6% as this represented the maximum addition regarded as acceptable in established aluminium alloys. However, the most significant step in the development proved to be the decision to add zirconium to the alloy. Initially added with the intention of refining the structure of the starting ingot, it duly transpired that the secret of its success lay in the provision of a dispersion of nano-scale particles of Al₃Zr that controlled the recrystallisation behaviour of the new alloy. The resultant Al–6%Cu–0.4%Zr alloy, commercially known as Supral, was internationally registered (in 1980 albeit superplasticity had been demonstrated in the alloy in 1969) as AA2004. A detailed description of the development of the alloy (now some 40 years old) was recently published (Barnes *et al.*, 2009). Probably the greatest significance of this development lay in the demonstration that it was possible to achieve excellent superplastic behaviour in an alloy that was, to all intents and purposes, a single phase alloy. Having established that a commercially useful superplastic aluminium alloy was possible, the TI Group decided to exploit it within their own companies by manufacturing the sheet within the British Aluminium Company and setting up a new company, (then called) TI Superform, to manufacture and sell engineering components from the sheet (Grimes, 2003). It was decided that Supral sheet would not be sold to third parties. This decision was very unpopular with some of the potential aerospace users who wanted to be able to fabricate their own components, and this probably accelerated development of other superplastic aluminium alloys by other organisations. Another factor encouraging the development of other superplastic alloys was the wish of aircraft companies to have a stronger alloy than AA2004 and, particularly, superplastic versions of established aircraft construction alloys such as AA7075/7475.

Development work, particularly by the Rockwell Company, led to a processing route to render AA7075 and AA7475 superplastic and, by the late 1970s, versions of AA7475 with good superplastic properties, in addition to their well-established service properties, were being manufactured by at least four aluminium companies.

At the end of the 1970s, and during most of the next decade, the development of Al–Li based alloys became, probably, the biggest aluminium alloy development ever undertaken and involved the world's major aluminium and aircraft companies together with national laboratories and academia. By 1982, superplasticity had been demonstrated in the alloy AA8090 and it soon became clear that variants

of most of the newly developed Al–Li based alloys could be rendered superplastic.

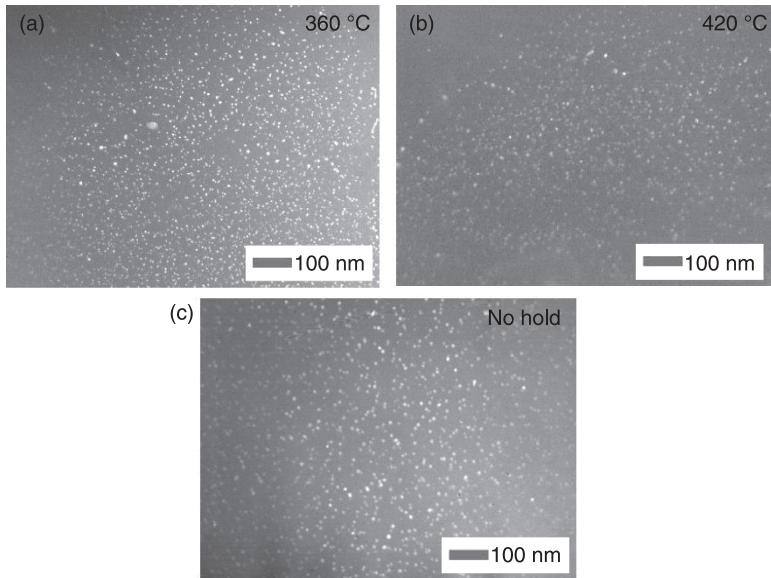
Chronologically, the next aluminium system to receive attention was that based upon Al–Mg alloys. Alusuisse introduced a series of alloys given the trade name Formal. In composition, these alloys were very close to AA5083 and, in the case of Formal 545, were within the AA5083 compositional specification. Japanese developments of Al–Mg based alloys followed on shortly and these are considered further in Section 11.3.5.

Further details of the superplastic aluminium alloys are given in the following sections.

11.3 Superplastic aluminium alloys

11.3.1 AA2004

AA2004 is the only surviving alloy developed primarily for its superplastic properties. The fact that it contains an abnormally high zirconium addition (~0.4% where the usual maximum zirconium addition is ~0.12%) confers it with exceptionally good superplastic properties, but also greatly increased the problems that had to be solved during development of its manufacturing route. In particular, Al–Zr alloys solidify with a peritectic reaction, the consequence of which is that the cooling rate during ingot casting has to be sufficiently high to suppress separation of coarse, primary Al_3Zr particles during solidification and leave virtually all of the zirconium in super saturated solid solution. For economic reasons, as conventional semi-continuous direct chill casting has to be employed for the production of the starting ingots, this need for rapid solidification severely restricts the maximum thickness of the ingot. Subsequent thermal mechanical processing is also critical if the optimum dispersion of fine scale Al_3Zr is to be precipitated from the super-saturated solid solution. Figure 11.1 demonstrates the considerable influence of different heating routes upon the Al_3Zr dispersion as the ingot is raised to the hot rolling temperature. In the intervening years, conventional wisdom has come to say that superplastic deformation takes place by grain boundary sliding (GBS) with some kind of accommodation mechanisms at the boundaries. In fact, before superplastic forming, AA2004 sheet has a heavily cold worked, completely unrecrystallised, structure that shows some limited recovery during heating to the deformation temperature, but it requires the combined effects of temperature and plastic strain to bring about recrystallisation. During the first stages of deformation, the wrought structure is gradually transformed into one of fine recrystallised grains and, if deformation continues, these grains gradually coarsen. When all of the processing conditions are correct, the superplastic performance of AA2004 probably exceeds that of any other commercially manufactured aluminium alloy; Table 11.1 shows the superplastic ductilities of AA2004 sheet produced from the



11.1 Influence of pre-heating conditions to hot rolling temperature on Al_3Zr dispersions. (a) Hold at 360 °C produces optimum dispersion, (b) hold at 420 °C is intermediate, and (c) direct heating to the rolling temperature of 480 °C is worst (courtesy of Dr G J Boyle).

Table 11.1 Ductilities of 1.5 mm sheet rolled in the first factory production trial of AA2004

Test temperature (°C)	Elongation (%)			
	Cast identity NVP		Cast identity NVQ	
	Longitudinal	Transverse	Longitudinal	Transverse
440	1084	1048	796	1192
450	1206*	1196	1170	1054
460	1150	1040	1210*	1210*
470	1016	970	1176*	1176*
480			806	1178

Note:

*without failing

first industrial rolling campaign after the alloy and its processing route had been developed.

Aluminium copper alloys are not noted for their corrosion resistance and so, initially, there was concern that the range of applications for which AA2004 would be suited would be restricted to those in non-corrosive environments. However, it was found that, if during hot rolling the material was clad on both

sides with a layer of 99.8% pure aluminium, the superplastic performance of the sheet was only marginally reduced but good corrosion resistance resulted. Commercially the clad version was known as Supral 150.

From the outset it was assumed that aerospace would represent a major outlet for superplastically formed (SPF) components since it was felt that, typically, such parts would be complex but required in only modest numbers. However, in the as-SPF condition the alloy is of only medium strength. The properties can be greatly improved by solution treatment and ageing, but a relatively high solution temperature is necessary and, since the alloy is fairly quench sensitive, rapid quenching from the solution treatment temperature is needed and problems from part distortion can arise. An indication of the superplastic properties of AA2004 is given in Table 11.2, and those of the service properties in Table 11.3, together with those of some other superplastic aluminium alloys.

11.3.2 AA7475

The philosophy behind the development of superplastic variants of 7XXX alloys was to take a composition that was already qualified as an aircraft structural alloy

Table 11.2 Superplastic properties of aluminium alloys under optimum deformation conditions

Alloy	Temperature (°C)	Strain rate (s ⁻¹)	Elongation (%)	m
AA2004	450	1×10^{-3}	1200	0.6
AA7475	516	2×10^{-4}	1000	0.85
Al-7%Ca	580	2×10^{-2}	850	0.78
Al-5%Ca-5%Zn	550	2×10^{-2}	600	0.5
AA8090	450	1×10^{-3}	1000	0.6
AA2195	490	1×10^{-3}	630	
AA5083	500	1×10^{-3}	325	0.5

Table 11.3 Ambient temperature mechanical properties of superplastic aluminium alloys

Alloy/condition	0.2% PS (MPa)	UTS (MPa)	Modulus (GPa)	Density (g/cm ³)
AA2004 as formed	120	240	74	2.83
AA2004 T6	315	410	74	2.83
AA7475 T76	462	524	70	2.8
Al-7%Ca as formed	165	190	72	2.69
Al-5%Ca-5%Zn as formed	158	180	72	2.71
AA8090 T6	350	450	78	2.55
AA2195 T6	585	620	79	2.7
AA5083 as formed	145	275	71	2.67

and to process it in such a way as to retain the established service properties at the same time as enabling superplastic deformation. Thus, it was essential to remain within the registered compositional limits, and additions, such as the large zirconium content of AA2004 could not be made. The developers also wanted to retain, to as great an extent as possible, the established manufacturing route of casting, homogenising and hot rolling. They then employed fairly conventional thermal mechanical treatments (TMT) of solution treating the hot blank, overaging to produce a dispersion of a very large number of particles of about 0.5 μm , heavily working and then employing particle stimulated nucleation (PSN) to create a fine recrystallised grain size of about 10–15 μm . While the initial development was performed by Rockwell International (Paton and Hamilton, 1978; Hamilton *et al.*, 1982) several variants on basically the same theme were developed by the interested aluminium companies (e.g. Ward *et al.*, 1984; or Mahon *et al.*, 1994).

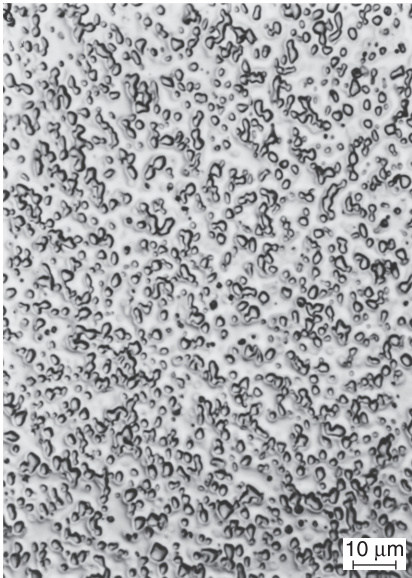
The superplastic performance of AA7475 sheet is very much influenced by the recrystallised grain size achieved in the sheet before deformation commences with GBS as the main mechanism. Slow grain growth accompanies increasing plastic strain. While SPF AA7475 is capable of large plastic strains, it is sensitive to both temperature and strain rate – achieving its best ductility at strain rates around $2 \times 10^{-4} \text{ s}^{-1}$ and temperatures fairly close to 516 °C. Superplastic properties are indicated in Table 11.2 and service properties in Table 11.3.

11.3.3 Aluminium–calcium based alloys

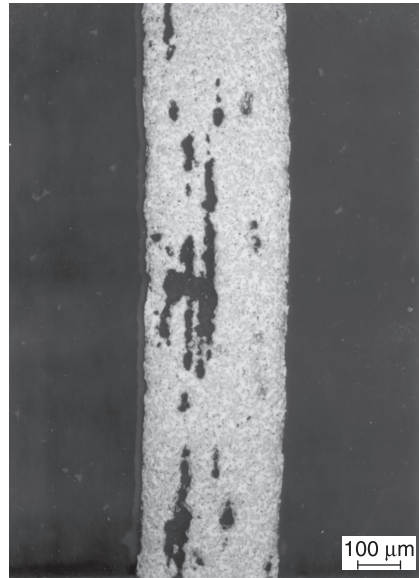
Although they failed to achieve commercial exploitation, two alloys based upon aluminium–calcium eutectics warrant inclusion in the overall story of superplastic aluminium alloys. Piatti *et al.* (1975) pointed out that on the aluminium rich side of the Al–Ca phase diagram there is a eutectic at 5.3%Ca. Unidirectional solidification resulted in a lamellar structure that, after hot rolling, broke down into a fine grained two phase structure of Al–Ca solid solution and the Al_4Ca intermetallic that exhibited good superplastic ductilities (Fig. 11.2). Although calcium is regarded as a fairly reactive element and therefore likely to lead to an aluminium alloy with poor corrosion resistance, the superplastic properties appeared comparable with those from AA2004. Within the British Aluminium Company, it was judged that the manufacture of a near to eutectic Al–Ca alloy would be simpler than the manufacture of AA2004, particularly in imposing fewer restrictions on casting the initial ingot, and so a number of full scale casting and rolling programmes was conducted. In fact, the corrosion behaviour proved to be no worse than that of AA2004 and the as-formed ambient temperature strength properties were similar to, or slightly better than, those of AA2004. However, ambient temperature ductility was poor, the temperature at which the best superplastic elongations were obtained was very high (~580 °C) and there were concerns that in industrial factory manufacture there would be the danger of Al–Ca scrap contamination of other alloys.



(a)



(b)



(c)

11.2 Microstructures of the Al-Ca eutectic alloy: (a) the lamellar, as-cast, eutectic; (b) after hot working; and (c) after 1050% tensile extension at 580 °C (note the remarkably low level of cavitation in this alloy system).

The second Al–Ca based alloy that came near to commercial production was investigated by Alcan International. They added zinc to the binary eutectic to produce a previously unknown ternary eutectic (Al–5%Ca–5%Zn) and this significantly improved ambient temperature ductility compared with the binary eutectic but had a negligible influence on the strength properties (Moore and Morris, 1980). Like the binary alloy, precipitation hardening would not be possible, so that any applications would have been confined to non-structural components. As with the binary alloy, fears of scrap contamination during the manufacture of other alloys loomed large in the decision not to continue with exploitation.

11.3.4 Aluminium–lithium based alloys

In the early 1980s, a series of new, lower-density alloys emerged based upon the Al–Li system and containing between ~1.75%Li and ~2.75%Li. They broadly divided into two families: those in which lithium was the major alloying addition and these were placed in the 8XXX alloy series; and those in which copper was the major alloying addition and these were placed in the 2XXX alloy series. While the new alloys were intended for general aerospace use in a wide range of tempers and product forms, it fairly quickly became apparent that superplastic deformation could readily be achieved with many of the new compositions. Table 11.4 indicates some of the Al–Li based compositions that were shown to be superplastic early in the development. Lithium precipitates from supersaturated solid solution as coherent spherical particles of δ' , Al₃Li. Several of the high strength 7XXX series alloys contain zirconium additions in order to provide a dispersion of Al₃Zr particles to control the grain structure. Virtually all of the new Al–Li alloys also

Table 11.4 Some early Al–Li based alloys exhibiting superplasticity

Ingot or powder	Composition (wt%)				Elongation (%)	Reference
	Li	Cu	Mg	Zr		
Ingot	2				320	A
Ingot	3.3			0.12	340	A
Ingot	3			0.5	1035	B
Ingot	2.7		2.8	0.15	680	A
Ingot	2.5	1.2	0.5	0.1	875	A
Ingot	3	4		0.5	925	B
Ingot	1.9	2.9	1	0.15	798	B
Powder	1.9	2.8	0.9	0.2	654	B
Powder	2.5	1.5	2	0.2	210	C
Powder	2	4		0.2	700	D

References: A – Grimes and Miller, 1983; B – Wadsworth *et al.*, 1983; C – Wadsworth and Pelton, 1984; D – Lederich and Sastry, 1983.

contained a zirconium addition at about 0.1%, but the role of the zirconium appears to have been more complex in that the Al_3Zr particles provided nuclei around which the isostructural δ' formed as a shell. The $\text{Al}_3\text{Zr}/\delta'$ particles inhibit recrystallisation, and hence made possible dynamically recrystallising superplastic variants in which the deformation mechanisms were closely analogous to those in AA2004, although the zirconium addition was far smaller. Other superplastic variants of Al–Li based alloys successfully employed Rockwell-type processing to generate a fine grain structure by static recrystallisation, although from a sheet manufacturing viewpoint the dynamically recrystallising product provides fewer problems.

Of the new alloys, AA8090 was probably the first actually to be used in component manufacture and for some time it appeared that this alloy would be the ideal superplastic aerospace aluminium alloy. It combined low density with a higher modulus, was capable of excellent superplastic behaviour at reasonably high strain rates ($\sim 10^{-3} \text{ s}^{-1}$), its forming temperature was above its solution treatment temperature and it exhibited low quench sensitivity thus avoiding the component distortion problems associated with separate solution treatment after forming. Additionally, the flow stress at the superplastic forming temperature was low thus allowing rapid pressurisation and de-pressurisation during part manufacture. The alloy was used in several applications on military aircraft (Fig. 11.3) but was found to have rather low impact resistance. The collapse of the former Soviet Union, together with the high price of Al–Li based alloys and certain unresolved technical issues, resulted in the termination of the so-called second generation Al–Li development programmes and AA2195 (Al–4%Cu–0.5%Mg–1%Li–0.4%Ag–0.12%Zr) is now the only superplastic sheet alloy available from that period. However, as ‘third generation’ Al–Li based alloys are now under development it seems likely that any developed for sheet application will also become available in superplastically deformable versions.

11.3.5 AA5083

When AA2004 and the Supral alloys were under development it was recognised that to cover the spectrum of likely applications a highly corrosion-resistant alloy would be desirable and that, although the clad version of AA2004 went some way towards this, it did not really offer a wholly acceptable solution. Thus, development continued of an alloy based on the established architectural alloy AA5251 but with a 0.4%Zr addition (Supral 5000) (Barnes *et al.*, 2009). However, before an entirely satisfactory commercial alloy resulted, Alusuisse announced their series of Formal alloys, also based upon the Al–Mg 5XXX system. In superplastic terms, the new alloys were little different from Supral 5000 but, unlike Supral 5000, they were produced by strip rolling from large, conventionally cast ingots resulting in a superior finish, better gauge control and a cheaper product. Other superplastic variants of Al–Mg alloys were announced over the next few years, including Neopral by



11.3 Inner structure of military aircraft door superplastically formed from the Al-Li based alloy AA8090.

Mitsubishi Aluminium (with a 0.5%Cu addition), SX01 by Sumitomo Light Metal Industries (with a 0.25%Cu addition) and ALNOVI 1 by Sky Aluminium. All of these alloys had the objectives of providing a material with reasonable superplastic capability, medium strength, high corrosion resistance, weldability and the ability to be anodised to a uniform finish. It should also be recyclable. Initially, it was the perception that such alloys would extend the range of applications open to SPF aluminium by being particularly suitable for architectural cladding where neither high strain capability nor high strength was required, but where corrosion resistance and a uniform attractive finished appearance were essential. While superplastic AA5083 has proved very successful in architectural applications (Fig. 11.4), the range of applications in which it is employed has rapidly expanded and the situation has now been reached where, in tonnage terms, superplastic AA5083 represents the most important superplastic aluminium alloy. Although AA2004 is still used for the most complex components and AA7475 for applications requiring high strength, AA5083 has taken over for the great majority of general engineering applications as well as automotive applications, architectural panels and some aerospace components. However, although the superplastic variants of AA5083 have carefully controlled minor additions (manganese and chromium) and impurity levels, the AA5083 plus copper variants have not achieved wide use.



11.4 Architectural application of superplastically formed AA5083 (courtesy Superform Aluminium).

Superplastic AA5083 is processed by heavy cold working and employing PSN to generate a fine, statically recrystallised grain structure on annealing. While, in principle, this is the same technique as that employed in the production of superplastic AA7475, the dispersed particles derive from the manganese and chromium additions and are both coarser and less numerous than those produced by precipitation from a solution treated blank in the case of AA7475. Thus, the grain sizes achieved in AA5083 tend, by superplastic standards, to be relatively coarse and the superplastic performance also modest. Quite small differences in the size and distribution of the PSN particles can result in sheet with significantly different superplastic capability (Kim *et al.*, 2004) while Verma (2004) demonstrated that by altering the hot and cold rolling schedules it should be possible to achieve a finer grained sheet without significantly increasing the cost of production. The success of AA5083 as a superplastic material, despite its

relatively coarse grain size, derives in part from the fact that it can deform by two primary deformation mechanisms. The finer grained material deforms by GBS at strain rates around 10^{-3} s^{-1} with an m value of about 0.5, while coarser grained material deforms by solute drag creep (SD) with an m value of about 0.3 (Taleff, 2010).

The superplastic properties of AA5083 are indicated in Table 11.2 and the service properties in Table 11.3.

11.4 Cavitation in superplastic aluminium alloys

Cavitation occurs during the superplastic deformation of all aluminium alloys and invariably increases with plastic strain. However, the extent of cavitation differs from alloy to alloy and, indeed, within any one alloy where there are differences in microstructure. While failure during superplastic deformation is not always the consequence of cavitation, it frequently is, and fracture is then dominated by the interlinking of cavities. In the extreme, the volume of cavities can reach about 10% when the material is close to failure. The phenomenon of cavitation was recognised at an early stage in the development of superplastic alloys (Stowell, 1982) and forming techniques and numerous investigations have been reported. Ridley and Zhang (1997) reviewed the earlier state of knowledge of the phenomenon, but Oh-ishi *et al.* (2004) point out that it is still not fully understood. In this respect, work at INP Grenoble (Blandin *et al.*, 2001) employing X-ray microtomography has enabled three-dimensional study of the growth and coalescence of cavities, contributing information that it was virtually impossible to obtain via the two-dimensional metallography necessarily employed in earlier investigations.

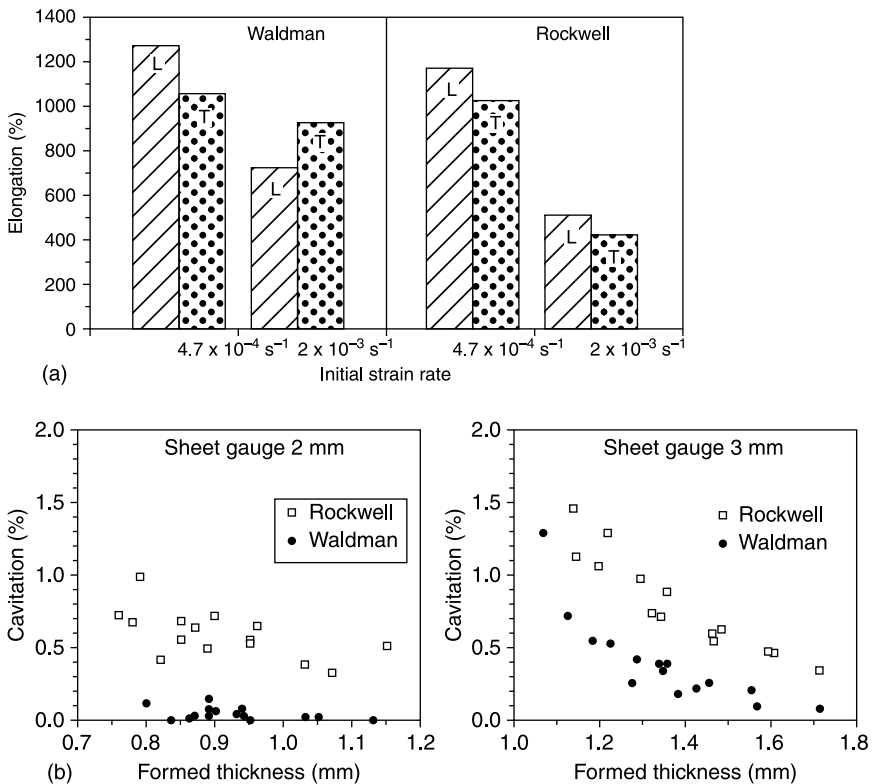
11.4.1 Cavity nucleation

All the industrially employed superplastic aluminium alloys contain a variety of finely distributed, second-phase particles, and sheet production of all of them involves large cold rolling reductions. Many of these particles are likely to be fractured during cold rolling and so exist as embryonic cavities in the sheet before superplastic deformation begins. New cavities are nucleated during superplastic deformation by GBS where the relative displacements of the grain boundaries require distribution of material by diffusion so that, if the strain rate is such that the accommodation processes cannot keep up, the build-up of stress concentrations may result in cavity nucleation. Cavities may also result from intra-granular slip intersections with particles on grain boundaries or from vacancy condensation on boundaries. The cavitation observed, therefore, after superplastic deformation is likely to be a combination of those that pre-existed in the as-rolled sheet and those that have nucleated and grown during deformation.

It is generally accepted that cavitation will be made worse if the grain size is increased. However, quite major improvements in cavitation may be achieved by

modifying the TMT employed. Thus, changing the processing route for superplastic AA7475 from one essentially based on the ‘Rockwell’ route to one employing a TMT process invented by Waldman and colleagues in 1974 (Mahon *et al.*, 1994), resulted in near to identical grain sizes of approximately 9 μm from both routes, but greatly reduced cavitation accompanying superplastic strain for the Waldman route material (Fig. 11.5). The resultant particle distributions were very different, the Waldman route resulting in far fewer but coarser particles than the Rockwell route.

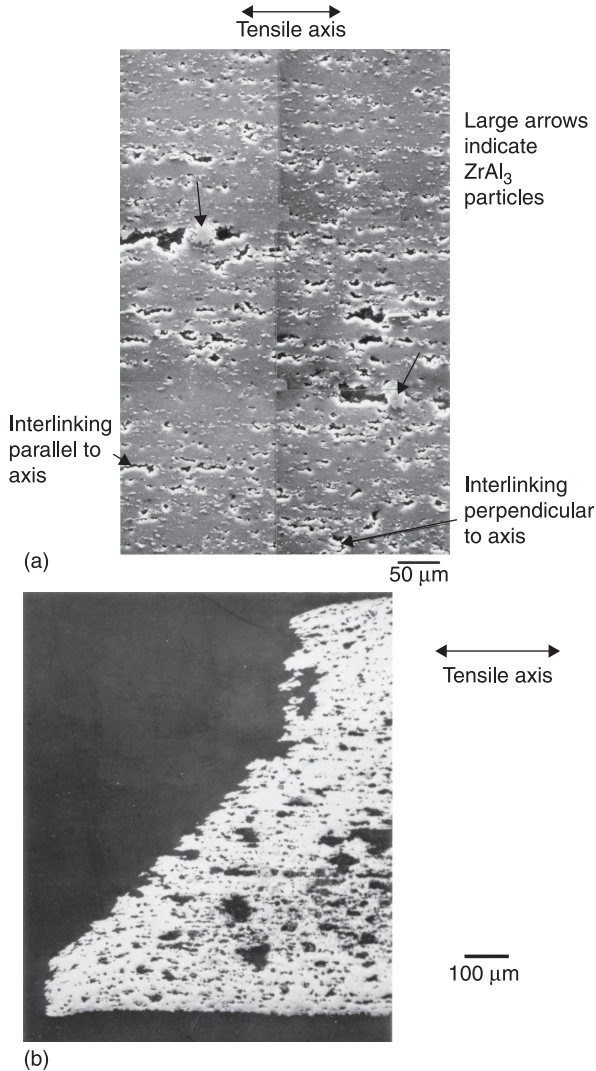
Bampton *et al.* (1999) demonstrated the benefit of a so-called secondary homogenisation treatment of AA7475 to reduce cavitation. A prolonged exposure of about 24 hours at the forming temperature of 516 °C reduced cavitation, particularly in material that had shown a high cavitation susceptibility. It was surmised that this was a consequence of out-gassing of hydrogen together with dissolution of any two-phase constituent particles that might otherwise melt during the forming operation.



11.5 Influence of the production route on the superplastic properties of AA7475: (a) superplastic ductilities in uniaxial tension (L = longitudinal, T = transverse) and (b) cavitation in material biaxially formed at a strain rate of approximately $2 \times 10^{-4} \text{ s}^{-1}$ (all tests at 515 °C) (after Mahon *et al.*, 1994).

11.4.2 Control of cavitation

Figure 11.6 illustrates cavitation nucleated at primary Al_3Zr particles in a tensile test specimen of AA2004 sheet deformed to a strain of 410%, together with the cavitation at the fracture of a sample from the same sheet that failed at an elongation of 800%. The tests were conducted with a constant crosshead velocity



11.6 Development of cavitation with tensile strain in AA2004: (a) after 410% strain, particularly showing cavities nucleated by coarse Al_3Zr particles and (b) section through fracture after 800% strain (courtesy of Dr M J Stowell).

and an initial strain rate of $1.7 \times 10^{-2} \text{ s}^{-1}$. Table 11.5 demonstrates the loss of mechanical properties that accompanies the formation of cavities in both as-formed and fully heat-treated material. The sheet had been biaxially formed into 'top hats' of different depths and tensile test pieces with the indicated equivalent strain cut from the base of the top hat. It is interesting to note that the thermal treatment involved in heat treating the material has reduced (in percentage terms) the strength reduction resulting from the cavitation.

At the maximum levels of equivalent strain found in the overwhelming majority of SPF aluminium components, the loss in properties resulting from cavitation is so small that it can be ignored. However, where the component is to be used in a highly stressed application, any cavitation damage becomes unacceptable and considerable development effort has been devoted to devising means, either of removing it or of preventing its occurrence in the first place. Perhaps the simplest approach employed to cope with cavitation was to take the formed component and subject it to a HIPping operation (Ahmed and Pearce, 1985). This treatment successfully closed the cavities, but a significant proportion reappeared on subsequent heat treatment, probably as a result of hydrogen dissolved in the alloy. The HIPping operation would, in any case, be both time consuming and expensive. A different approach was employed by Varloteaux and colleagues (1989), who adopted a strain/anneal procedure in which straining was interrupted to allow the cavities to anneal out by diffusion before further straining. They achieved good results with AA7475 by employing an alternating procedure of one minute straining followed by one minute of annealing. There have even been suggestions (Conrad *et al.*, 1991) that the application of an external electrical field during superplastic deformation of AA7475 resulted in a reduction in the nucleation rate at small strains.

However, it is clear that, apart from careful selection of material and processing conditions, the most effective way of processing superplastic aluminium alloys that are to operate in demanding environments is to conduct the forming operation under a superimposed hydrostatic pressure (so-called back pressure forming), such that cavities are not nucleated or, at least, do not grow. Bampton *et al.* (1983) conducted experiments within a chamber that allowed superimposed pressures of

Table 11.5 Influence of cavitation on service properties

Condition	Equivalent strain (%)	0.2% PS (MPa)	UTS (MPa)	Elongation (%)
As-formed	0	120	220	15
	100	100	165	4.5
	200	84	120	2.0
Heat-treated (T6)	0	285	450	14
	100	280	425	7
	200	280	400	4

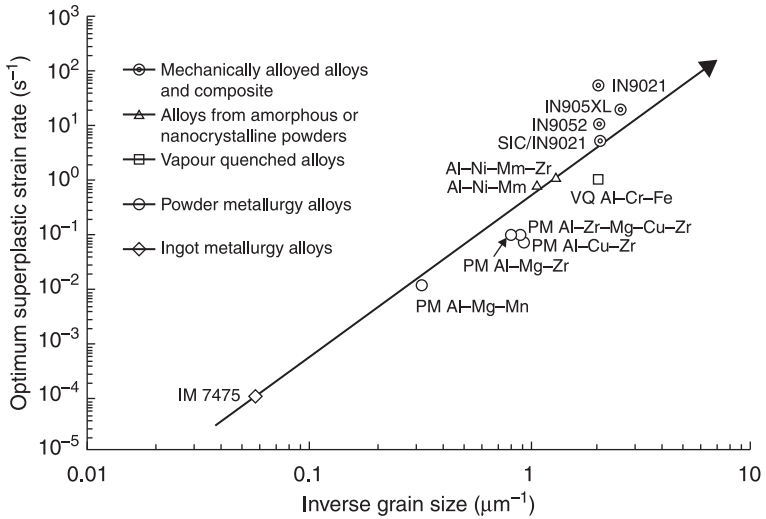
up to 7 MPa while conducting tensile tests on AA7475. They also conducted biaxial forming into a shallow rectangular die. It was concluded that when $p/\sigma_e \geq 0.6$, where p is hydrostatic pressure and σ_e flow stress, cavitation would be virtually completely suppressed. This applied under uniaxial tension, equi-biaxial or plane strain conditions. The application of the hydrostatic stress also significantly increased the strains to failure in their experiments, presumably because cavitation was suppressed.

Back pressure forming tends only to be used in the manufacture of high strength aerospace components from AA7475. It is generally not considered necessary with AA5083 in automotive and similar applications where the equivalent strains involved are usually quite low with only minor and well dispersed cavitation damage.

11.5 High strain rate superplasticity

The two biggest factors holding back wider exploitation of superplastic forming as a manufacturing technique have been the long forming times necessitated by low optimum strain rates together with the significant price premiums attached to superplastically deformable aluminium alloy sheet. Thus, when high strain rate superplasticity (HSRS) was first reported in about 1984 (Nieh *et al.*, 1984) it appeared that the first of these obstacles might be about to be removed. The initial observations of HSRS (strain rates from 10^{-2} s^{-1} to $> 10^0 \text{ s}^{-1}$ and frequently referred to as positive exponent superplasticity) were in metal matrix composites (MMC). However, further investigation demonstrated that material made via mechanical alloying, or consolidation from amorphous powders or nano crystalline powders or physical vapour deposition, could all be processed in such a way that they exhibited HSRS (Higashi, 1994). It quickly became apparent that the increase in optimum superplastic strain rate was closely related to refinement of the grain size (Fig. 11.7, Sherby *et al.*, 1994). However, arguments continued for some time over the mechanisms by which the high strain rate deformation was being achieved. There was agreement that the main mechanism was GBS, but disputes over the accommodation mechanisms required to relax the stress concentration resulting from the GBS. Since HSRS tended to be observed at very high temperatures, several of the investigators believed that there must be a liquid phase at the grain boundaries and that adiabatic heating from the rapid deformation would make this more likely. However, several later examples revealed HSRS in material at relatively low temperatures at which no melting could have occurred (Langdon, 1999).

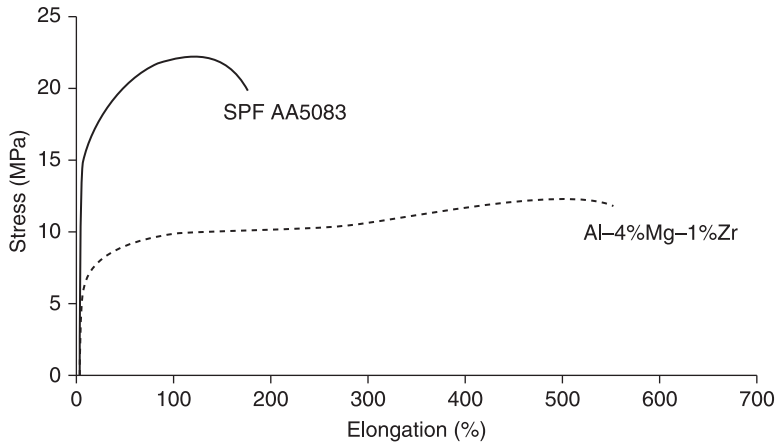
From an academic point of view the work on HSRS was very interesting, but the alloys in which it was demonstrated tended to be either of exotic composition or manufactured by expensive and impractical routes, or both. Thus, while they achieved one of the objectives for a commercial superplastic aluminium alloy, they failed dismally as far as either producing, or even



11.7 Plot from Sherby *et al.* (1994) illustrating the powerful relationship between refinement of grain size and increase in optimum strain rate. Where gas pressure is employed to form the sheet, it is doubtful whether there is any benefit from strain rates greater than 10^{-1} s^{-1} because the time taken to pressurise and de-pressurise the forming machine is large compared with the reduction in actual forming time (after Sherby *et al.*, 1994).

pointing to, a possible route to an economically viable alloy. Not surprisingly, virtually no work was done on the service properties of the early HSRS alloys.

The original superplastic aluminium alloy, AA2004, exhibits its optimum superplastic behaviour at a strain rate of about 10^{-3} s^{-1} , but at strain rates an order of magnitude higher can still achieve ductilities greater than 800% thus actually achieving the Japanese Standards Association requirement JIS H 7007 to be classified as a HSRS material. At least two programmes (Nieh and Wadsworth, 1993; Dashwood *et al.*, 2000) have taken the concept of the Supral alloys in employing a large zirconium addition, retaining it in supersaturated solid solution by rapid solidification and then generating a copious dispersion of very fine Al_3Zr particles to control the grain structure during HSRS deformation. Neither the AA2124 + 0.6%Zr of the Nieh and Wadsworth programme nor the Al-4%Mg-1%Zr of the Dashwood programme has been taken beyond the concept stage, albeit the latter programme was explicitly aimed at developing a HSRS alloy for automotive application and achieved promising results. Figure 11.8 compares the superplastic and ambient temperature strength properties of the Al-4%Mg-1.0%Zr alloy with those of the standard superplastic AA5083.



11.8 Superplastic performance of the experimental Al-4%Mg-1%Zr alloy compared with that of SPF AA5083. Ambient temperature properties of the experimental alloy were 0.2%PS 220 MPa and UTS 340 MPa, compared with 0.2%PS 145 MPa and UTS 320 MPa for the AA5083 (after Dashwood *et al.*, 2001).

11.6 Exploitation of superplastic aluminium alloys

11.6.1 The early days

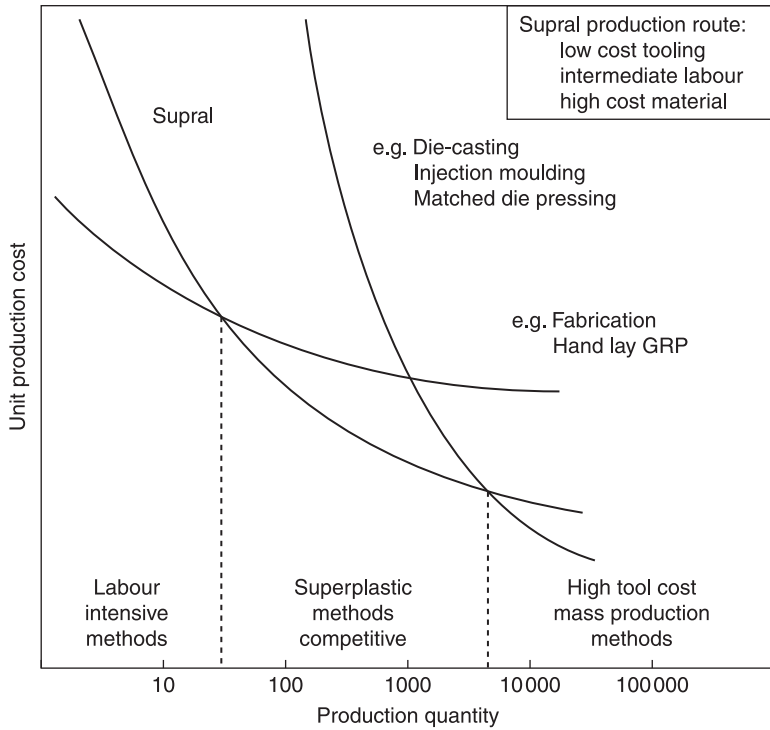
It is interesting to note that in 1964 Backofen and colleagues were the first to suggest that superplastic deformation might be exploited as a metal fabricating technique and, in frustration five years later in 1969, Backofen said (Steel, December 1969): 'When is industry going to get off its rump and put some of this to work? When will people discover that this is no longer a theory, but a hard, practical, established concept that can make someone a lot of money.' When the Tube Investments Group had invented and developed AA2004 a great deal of thought was devoted to how, in Backofen's words, it could be employed to make '... a lot of money'. The major issues that had to be resolved included the fact that in many situations the component that is under consideration for superplastic forming would probably be made from aluminium even if superplastic forming were not to be employed. Thus, as well as being in competition with other materials such as ABS, the superplastic former of aluminium sheet is in competition with aluminium castings or press formed aluminium or hand fabrication. After extensive research of the perceived likely markets it was concluded that there would be good prospects for a manufacturing operation based on the business identified by the market research (in very simplified form shown in Table 11.6). The major benefits from superplastic forming, when compared with conventionally formed metal components, were seen as greatly increased design freedom and, in particular, the ability to consolidate several smaller parts into a single larger part.

Table 11.6 Markets investigated before establishing Superform Metals

Aircraft	Numerous possibilities. Generally fewer than 100 per annum, occasionally up to 500 per annum. Substantial premium possible. Probably slow decision making.
Aircraft equipment	Seats, furnishings, ejector seat components. Good prospects of early sales.
Specialist cars	Major manufacturers able to write off tooling quickly so not seen as a good prospect, but six independent builders with annual vehicle numbers between 500 and 10000. Good prospects, particularly in replacing ABS.
Commercial vehicles – bodies	Fearred that impending impact resistance legislation would rule out aluminium in cab bodies.
Commercial vehicles – engines	Sumps of the majority steel pressings and SPF could not compete, but a smaller number require special sumps currently made from aluminium castings. Should be able to compete.
Buses and coaches	Most exterior panels in glass reinforced plastic (GRP) and too large for current SPF capability, but good trim and window fitting possibilities.
Caravans	Much interest shown because of superior fire performance compared with vacuum formed plastics, but probably not cost competitive. Components possible.
Boxes and cases	Appear very good prospects where equipment has to be stored and protected in boxes, but very difficult to define.
Buildings	Appear good prospects for decorative panels to 'break up' large flat surfaces, but will depend upon size.

Lower manufacturing costs arising from lower machine costs and much cheaper tooling would result in lower overall manufacturing costs for small to medium quantities (see Fig. 11.9). Compared with plastics the main benefit from superplastic forming was seen as superior product performance. Properties such as strength, stiffness, fire performance, electrical conductivity and electrical shielding favoured metal, but the relatively high cost of conventional metal forming techniques tended to favour plastics on a cost/performance basis. Superplastic forming would enable the exploitation of the superior properties of the metal while adding a styling capability that had previously been exclusive to plastics.

TI Superform (now Superform Aluminium) was formed in December 1973 with the objective of exploiting superplasticity by setting up a fabricating unit to manufacture SPF components. Initially the operation had three forming machines, two purpose built and very versatile, capable of male or female forming (one

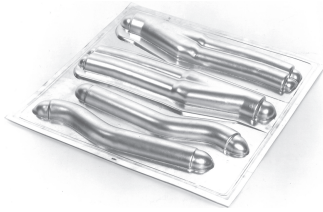


11.9 Superplasticity's techno economic niche – the region in which it was perceived superplastic forming would be economic at the time when TI Superform was established.

600mm × 600mm and one 900mm × 600mm), and one converted platen press (2100mm × 1200mm) capable of female forming larger parts. At that stage the only available superplastic aluminium alloy was AA2004 in either bare or clad form. The predictions for the business were largely borne out, although some surprisingly simple parts were made demonstrating that the superplastic route could, in the right circumstances, be economic even when very low forming strains were involved. Figure 11.10 illustrates some of the parts made in the early days of commercial exploitation of superplastic forming of aluminium alloys.

11.6.2 The present

Whereas exploitation of superplastic forming of aluminium alloys began with a single alloy and a single manufacturing unit in the United Kingdom, there are now forming operations in the United States, Japan, France, Germany, Lichtenstein, Switzerland and Ireland. Several aerospace companies have superplastic fabricating facilities to manufacture some of their requirements, while sub-contracting other parts to the specialist superplastic forming companies.



(a)



(b)

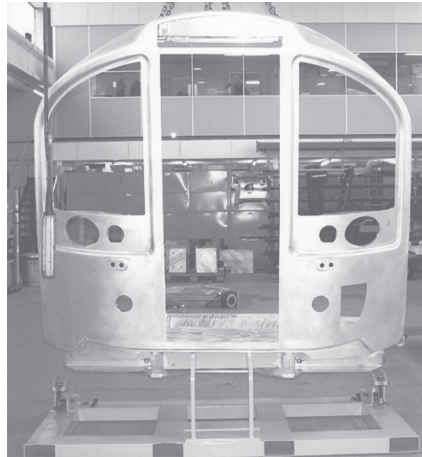
11.10 Parts made shortly after Superform Aluminium started operating: (a) very simple, small parts, but economic because it was possible to form four parts simultaneously (part of the exhaust system of a Lotus sports car). (b) Head box for Martin Baker ejector seat. Classic component for SPF – difficult, male formed, modest number requirements – enabled consolidation of parts from seven to two, together with weight reduction (courtesy of Superform Aluminium).

The automotive industry is increasingly employing superplastic forming of aluminium alloys and, at least where part numbers approach 100 000 per annum, setting up their own manufacturing facilities tailored to that type of operation as witnessed by GM in the United States and Honda in Japan. Of the sub-contracting operations, Superform Aluminium remains the biggest with manufacturing units in the United Kingdom and the United States. The predictions of market make-up, made back in the 1970s, proved reasonably accurate and have not changed dramatically in the intervening years. Caravans did not prove to be a market but rail, which did not figure in the original market research, became (and remains) significant, albeit it fluctuates as the rail building programmes fluctuate. Throughout the 1980s, aerospace represented around 60% of the United Kingdom business but this has now dropped back to, perhaps, 20% while automotive use has grown dramatically to close to half of the UK workload from being insignificant during the 1980s. In the United States, aerospace represents considerably more than half of the workload with automotive use taking up much of the balance.

While the maximum economic number of parts was judged to be about a total of 10 000 when superplastic manufacturing began, this has now increased to a current total of about 20 000 per annum. This increase has resulted from improvement in most of the operations involved in component manufacture. Overall handling has improved and the introduction of five axis CNC trimming after forming represents a major improvement on earlier, cruder methods. The forming tools are increasingly designed in such a way that significant parts of the forming operation are performed as the tools close, and gas pressure forming may be only a relatively small part of the operation. Component size capability has also greatly increased with machines now up to 3m × 2m × 600mm and employing



(a)



(b)

11.11 Current Superform Aluminium parts: (a) wings for Morgan sports car and (b) end of rail vehicle (formed in two halves and welded together) (courtesy of Superform Aluminium).

sheet up to 2.2 metres wide and 6 mm thick. Figure 11.11 shows some of the parts currently being manufactured at Superform Aluminium.

Virtually all the SPF aluminium components in current production are manufactured from one of the three alloys, AA5083, AA7475 and AA2004. In tonnage and part numbers, AA5083 dominates but cannot be used for the demanding high strength aerospace applications where AA7475 fulfils a significant and vital role. Equally, AA2004 has now come to occupy a niche role, particularly in aerospace components when the forming demands cannot be met by the other alloys.

11.6.3 The future

For the future the increasing demands to produce lighter vehicles are likely to lead to greater use of aluminium alloys generally, and this in turn is likely to increase the use of processes such as GM's quick plastic forming in volume vehicle manufacture but is also likely to make more opportunities for SPF panels in medium volume vehicles. While AA5083 has certainly now proved suitable for a very wide range of automotive parts, there are also those who would like to see a higher strength, corrosion resistant, weldable superplastic alloy, perhaps from the 6XXX series. The attempts to develop such an alloy have, so far, met with only limited success, but there seems little doubt that if a concerted effort were made such an alloy would be possible. The aircraft builders would like a superplastically deformable, non-precipitation hardening high strength alloy that would eliminate the problems of distortion that accompany separate solution

treatments or even precipitation hardening. An Al–5%Mg–1%Li alloy, partly modelled on the mechanically alloyed alloy IN5091 but made via spray casting, was under development between Oxford University and BAE Systems and showed appreciable promise (Hogg *et al.*, 2007), but funding was withdrawn and the development suspended. Since spray casting was the initial process, the alloy would not be cheap but if it simplified manufacturing compared with AA7475 the price might be justified, at least for military aircraft applications.

From its earliest days, superplastic forming has represented a low volume process and the fact that it takes a relatively expensive sheet, forms it relatively slowly into a complex shape, and employs relatively cheap tooling, locks it into what Barnes (1998) has described as a techno-economic niche. To break out of this niche requires an alloy that can be formed at strain rates of about 10^{-1} s^{-1} while being appreciably cheaper than the existing superplastic alloys and retaining the other good properties of AA5083. There is very little doubt that this could be done if the significant development costs that it would entail were available.

11.7 References

- Ahmed H and Pearce R, 1985, “Post-forming cavity closure in Supral 150 by hot isostatic pressing”, in R. Pearce and L. Kelly (eds), *Proceedings of International Conference on Superplasticity in Aerospace-Aluminium*, Cranfield, England, 146–159.
- Backofen W, Turner I and Avery D, 1964, “Superplasticity in an aluminium–zinc alloy”, *ASM Trans.*, 57: 980.
- Bampton C, Mahoney M, Hamilton C, Ghosh A and Raj R, 1983, “Control of superplastic cavitation by hydrostatic pressure”, *Metallurgical Transactions*, 14A: 1583–1591.
- Bampton C, Ghosh A and Mahoney M, 1985, “The causes, effects and control of cavitation in superplastic 7475 aluminium airframe structures”, in R Pearce and L Kelly (eds), *Proceedings of International Conference on Superplasticity in Aerospace-Aluminium*, Cranfield, England, 1–35.
- Barnes A, 1999, “Superplastic aluminium forming – expanding its techno-economic niche”, *Materials Science Forum*, 304–306: 785–796.
- Barnes A, Stowell M, Grimes R, Laycock D and Watts B, 2009, “Forty years since the invention of Supral alloys”, *Key Engineering Materials*, 433: 11–30.
- Bengough G, 1912, “A study of the properties of alloys at high temperatures”, *Journal of Institute of Metals*, 7: 123.
- Blandin J, Salvo L, Dendievel R and Rauch E, 2001, “Recent developments in superplastic forming activity at INP Grenoble”, *Proceedings Euro-SPF '01 Conference*, Presses Universitaires de Grenoble, France, 89–94.
- Conrad H, Cao W, Lu X and Sprecher A, 1991, “Effect of electric field on cavitation in superplastic aluminium alloy”, *Materials Science and Engineering*, A138: 247–258.
- Dashwood R, Grimes R, Harrison A and Flower H, 2001, “The development of a high strain rate superplastic Al–Mg–Zr alloy”, *Materials Science Forum*, 357–359: 339–344.
- Grimes R and Miller W, 1983, “Superplasticity in lithium containing aluminium alloys”, in T Sanders and E Starke (eds), *Aluminium–Lithium Alloys II*, Metallurgical Society of

- American Institute of Mining, Metallurgical and Petroleum Engineers, Warrendale, PA, 153–167.
- Grimes R, 2003, “Superplastic forming: evolution from metallurgical curiosity to major manufacturing tool?”, *Materials Science and Technology*, 19: 3–10.
- Hamilton H, Bampton C and Paton N, 1982, “Superplasticity in high strength aluminium alloys”, in Paton N and Hamilton H (eds), *Superplastic Forming of Structural Alloys*, Metallurgical Society of American Institute of Mining, Metallurgical and Petroleum Engineers, Warrendale, PA, 173–190.
- Higashi K, 1994, “Positive exponent superplasticity in advanced aluminum alloys with nano or near-nano scale grained structures”, *Materials Science and Engineering*, A166: 109–118.
- Hogg S, Palmer I, Thomas L and Grant P, 2007, “Processing, microstructure and property aspects of a spraycast Al–Mg–Li–Zr alloy”, *Acta Materialia*, 55: 1885–1894.
- Kim S, Balogh M and Waldo R, 2004, “Microstructural characterisation of superplastic forming (SPF) AA5083 sheet”, *Advances in Superplasticity and Superplastic Forming*, TMS, 139–147.
- Langdon T, 1999, “An examination of flow processes in high strain rate superplasticity”, *Materials Science Forum*, 304–306: 13–20.
- Lederich R and Sastry S, 1983, in T Sanders and E Starke (eds), *Aluminium–Lithium Alloys II*, Metallurgical Society of American Institute of Mining, Metallurgical and Petroleum Engineers, Warrendale, PA, 137–151.
- Lyttle J, Fischer G and Marder A, 1965, “Superplasticity in alpha-beta titanium alloys”, *Journal of Metals*, 17: 1055.
- Mahon G, Warrington D, Butler R and Grimes R, 1994, “An optimised manufacturing route for superplastic 7475 sheet”, *Materials Science Forum*, 170–172: 187–192.
- Moore D and Morris L, 1980, “A new superplastic aluminium sheet alloy”, *Materials Science and Engineering*, 43: 85–92.
- Nieh T, Henshall C and Wadsworth J, 1984, “Superplasticity at high strain rate in a SiC-2124 Al composite”, *Scripta Metallurgica*, 18: 1405–1410.
- Nieh T and Wadsworth J, 1993, “Effects of Zr on the high strain rate superplasticity of 2124 aluminium”, *Scripta Metallurgica et Materialia*, 28: 1119–1124.
- Oh-ishi K, Boyden J and McNelly T, 2004, “Deformation mechanisms and cavity formation in superplastic AA5083”, *Advances in Superplasticity and Superplastic Forming*, TMS, 119–126.
- Paton N and Hamilton H, 1978, “Method of imparting a fine grain structure to aluminium alloys having precipitating constituents”, US Patent, 4 092 181, May 30.
- Piatti G, Pellegrini G and Trippodo R, 1975, “Structures and properties of the Al–Al₄–Ca eutectic”, *Proceedings 6th International Conference on Light Metals*, Leoben/Vienna, Austria, 45–48.
- Ridley N and Wang Z, 1997, “The effect of microstructure and deformation conditions on cavitation in superplastic materials”, *Materials Science Forum*, 233–234: 63–80.
- Sherby O, Nieh T and Wadsworth J, 1994, “Overview on superplasticity research on fine grained materials”, *Materials Science Forum*, 170–172: 13–22.
- Stowell M, 1982, “Cavitation in superplasticity”, *Superplastic Forming of Structural Alloys, Conference Proceedings*, The Metallurgical Society of AIME, 321–336.
- Taleff E, 2010, “An overview of hot- and warm-forming of Al–Mg alloys”, *Key Engineering Materials*, 433: 259–265.

- Underwood E, 1962, "A review of superplasticity", *Journal of Metals*, 14: 914–919.
- Varloteaux A, Blandin J and Suery M, 1989, "Control of cavitation during superplastic forming of high strength aluminium alloys", *Materials Science and Technology*, 5: 1109–1117.
- Verma R, 2004, "Rolling process optimization for superplastic 5083 Al sheet", *Advances in Superplasticity and Superplastic Forming*, TMS, 159–170.
- Waldman J, Sulinsky H and Markus H, 1974, US Patent, 3 847 681.
- Ward B, Agrawal S and Ashton R, 1984, US Patent, 4 486 244.
- Wadsworth J, Palmer I, Crooks D and Lewis R, 1983, in T Sanders and E Starke (eds), *Aluminium–Lithium Alloys II*, Metallurgical Society of American Institute of Mining, Metallurgical and Petroleum Engineers, Warrendale, PA, 111–135.
- Wadsworth J and Pelton A, 1984, "Superplastic behavior of a powder-source aluminium–lithium based alloy", *Scripta Metallurgica*, 18: 387.

Quick Plastic Forming of aluminium alloys

P. E. KRAJEWSKI and J. G. SCHROTH,
General Motors, USA

Abstract: Quick Plastic Forming or QPF was developed as a high volume, hot blow forming process for making automobile closure panels from aluminum sheet. The chapter reviews the key drivers for developing the technology and identifies key differences between QPF and superplastic forming (SPF) technologies. The process is described in detail with a focus on heated die development, an important enabler for QPF. In addition, the material, lubricant, and modeling of the process are reviewed in detail.

Key words: Quick Plastic Forming (QPF), AA5083, heated tooling, biaxial bulge testing, lubrication.

12.1 Introduction

12.1.1 Definition

Quick Plastic Forming (QPF) refers to a commercial hot blow forming process developed by General Motors Company.^{1,2} The process has produced over 500 000 aluminum panels to date and enables complex shapes to be manufactured from aluminum sheet at traditional automotive volumes, i.e. tens of thousands of panels per annum.

12.1.2 Development drivers

QPF was developed in response to two key issues:

- an increased need to lower automotive structural mass to improve fuel economy;
- the lower formability of aluminum sheet materials compared to sheet steel.

When stamped under traditional ambient conditions, the formability of aluminum has limited its adoption for the complex panels that comprise doors, decklids and liftgates, because the required component shapes necessitated that potential parts should be broken up into multiple pieces to enable the desired shapes to be stamped. This, in combination with the higher cost of aluminum sheet, restricted the use of these materials. The attraction of a process which enabled aluminum to be manufactured into integrated panels more complex than those attainable with steel was the key driver for the QPF process development.

12.1.3 Differences from SPF

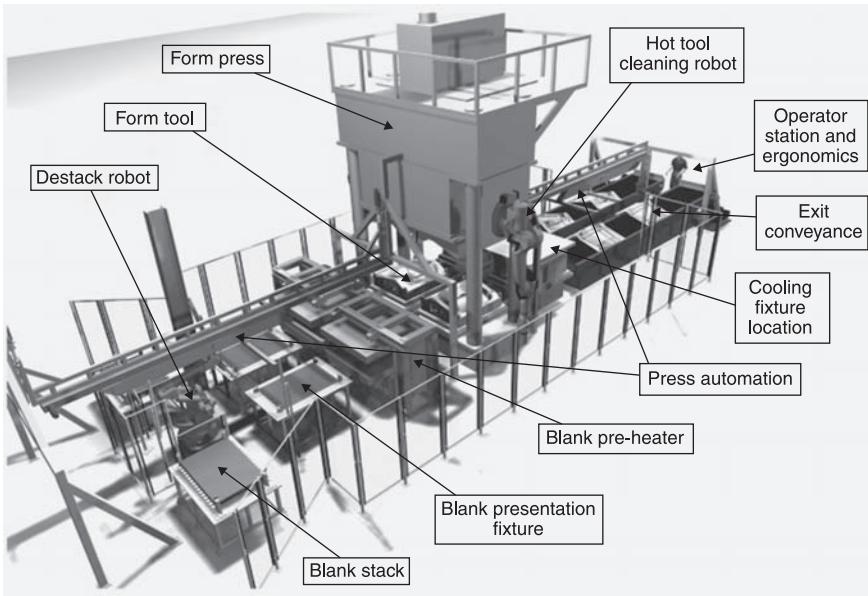
The QPF process is significantly different from traditional superplastic forming (SPF). In brief, the QPF process deforms the aluminum at strain rates greater than those associated with SPF, which are designed to maximize tensile ductility. The process also incorporates much more automation than traditional SPF processes in order to produce dimensionally correct components directly from a forming cell. The process is highly optimized around each specific components in an effort to minimize cycle time and maximize the productivity of the greater capital equipment installed for each product. Also, QPF generally produces parts of less complexity than could be obtained if longer cycle times (slower strain rates) were allowed. A number of these key process differences and associated drivers are summarized in Table 12.1.

Table 12.1 SPF and QPF process differences

Superplastic forming process	Quick Plastic Forming process
<p>Forming rates/temperatures chosen to exploit maximum material ductility</p> <p>Aerospace market</p> <ul style="list-style-type: none"> • Lower-volume (100s of panels/year) • High-price-point products • Hand re-work common for dimensional and surface quality <p>Manufacturing system</p> <ul style="list-style-type: none"> • Low level of automation, manual handling • Low capital, high piece cost <p>Typical SPF panels</p> <ul style="list-style-type: none"> • Extreme shapes • High forming strains – back pressure to limit cavitation • Maximum mechanical properties (including 2XXX, 7XXX alloys) <p>Niche process</p>	<p>Forming rates/temperatures chosen to maximize productivity consistent with final quality</p> <p>Automotive markets</p> <ul style="list-style-type: none"> • Higher-volume (tens of 1000s panels/year) • Low-price-point products (consumer goods) • Emphasize first-time dimensional and surface quality <p>Manufacturing system</p> <ul style="list-style-type: none"> • High level of automation, robotic handling • Higher investment, lower piece cost <p>Typical QPF panels</p> <ul style="list-style-type: none"> • Moderate shapes (but more complex than automotive metal stamping) • Moderate forming strains – back pressure not required • Moderate post-form properties (primarily 5XXX alloys) <p>High-volume process</p>

12.2 QPF process overview

A schematic representation of the automated forming cell used to carry out the QPF process is shown in Fig. 12.1. QPF manufacturing cells make use of a fully automated material handling system consisting of one floor-mounted robot, two



12.1 QPF forming cell for parallel processing of two panels simultaneously. Material flow is from left to right in this view.

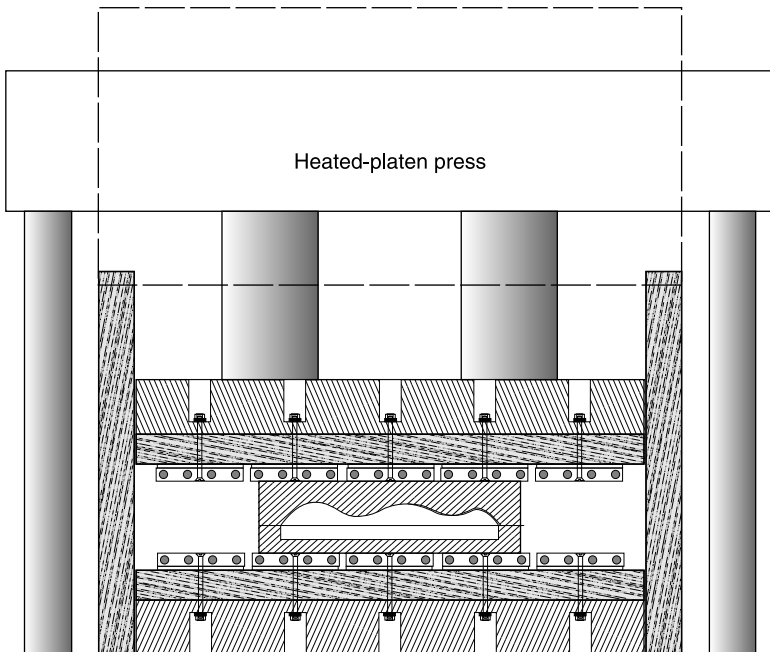
gantry robots, and a cooling conveyor which carries the formed panels out of the forming cell. Stacked, pre-lubricated blanks are placed at the entrance end of the cell in an area protected from intrusion by a light curtain. A floor-mounted robot is used to de-stack individual blanks and place them onto a locating presentation fixture. When the preheater opens, the first gantry robot picks the blank from its well-controlled position and places it within the preheater. The conduction preheater makes use of precision-heated platens and, when fully closed, maintains the blank within a very narrow gap that allows rapid heat transfer from the platens to the blank. The heated blank is raised on multiple pins after the preheater opens, at which point the gantry robot moves the heated blank to the now-open tool. The hydraulic press closes, produces a pressure tight seal at the tool/blank/tool interface, and imposes a pre-programmed pressure cycle to fully form the panel. Some tools incorporate additional mechanical actions or multiple pressurization steps as part of the forming cycle. After the pressurized air is exhausted, the tool is opened and the tool extraction system is cycled to strip the panel from the tool and hold it in a position from which the second gantry robot can grip it and move it to the waiting cooling fixture. The cooling fixtures are designed to support the panels as they cool to maintain proper dimensions. From the cooling fixture, the panel is placed on a slow-moving mesh cooling belt and travels through a distance of several panel widths before it reaches a 'tip-up' fixture at the end of the line. The panel is automatically rotated 90° in the tip fixture so that it is oriented in a

position from which it can be readily placed into a custom rack for transport and further processing. Overviews of QPF technology, which include forming cell descriptions, can be found elsewhere.^{1,2}

12.3 Hot forming systems: prior deficiencies and new concepts

Investigators have long recognized that the formability of aluminum is greater when it is processed at elevated temperatures.³ Prior work on hot blow forming of sheet aluminum near 500 °C has centered on processes that have typically been performed using presses which incorporate platen heaters⁴ to maintain tools at the desired forming temperature in an insulated environment (Fig. 12.2). Through the course of QPF development, several inadequacies of the heated-platen press system were identified:

- tool temperatures are difficult to control with precision;
- forming cycles with substantial 'tool-open' time lead to local tool temperature loss;
- substantial energy is lost to the environment through radiation and convection;
- handling equipment cannot be used in the hot oven-like environment;

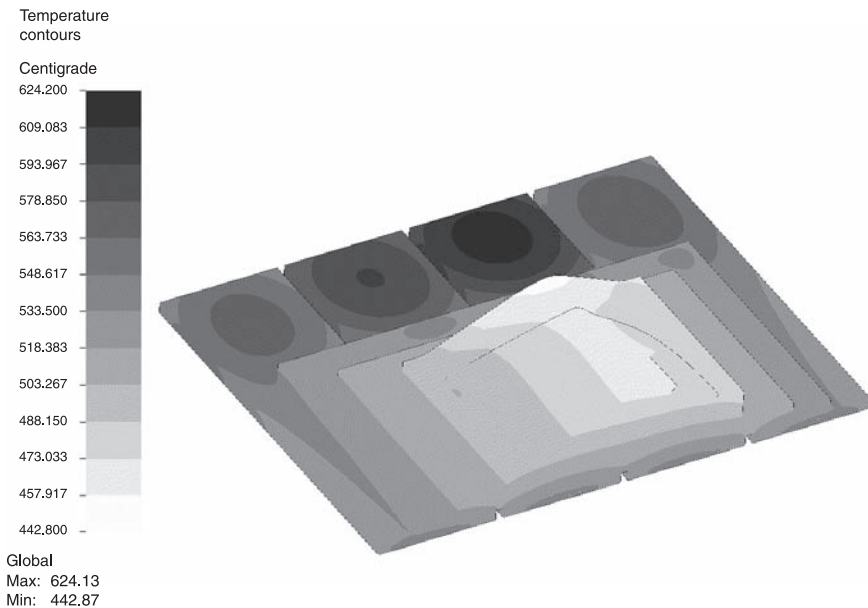


12.2 Traditional hot forming press with heated platens and insulated working volume.

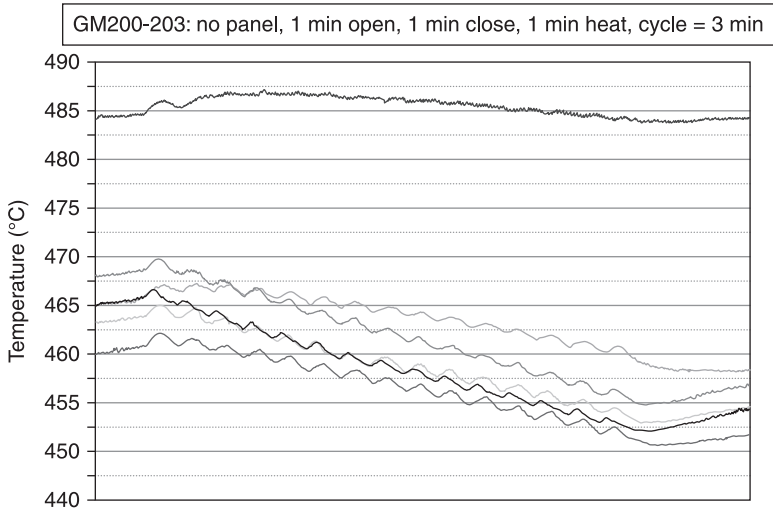
- rapid hot tool changeover is difficult and dangerous;
- automated tool-assist mechanisms cannot function in the heated-press environment.

It became apparent during the course of QPF development that the inability to adequately control tool temperature was a major barrier to exploiting hot blow forming technology for short cycle times. It is notable that although substantial effort has been directed at improved finite element (FE) modeling of hot aluminum sheet,⁵⁻⁶ the vast majority of recent work in that area continues to emphasize isothermal conditions during the forming process. That assumption is at odds with many of the actual production processes used to form hot sheet.⁷ Hence, a large part of QPF process development centered on predicting, validating, and ultimately improving thermal control in the hot forming tool to better achieve a stable, isothermal condition.

A key enabler for the improved thermal control was the development of a steady state thermal model based on the work of Caulk *et al.*^{8,9} Initial work with the thermal model examined the thermal distribution in press heated tools to understand the degree of the problems identified in the first three items above. Figure 12.3 shows the predicted temperature distribution of an unheated steel tool mounted to a heated-platen system within an insulated press. The temperature varies more than 60 °C over the working face of the tool even when it is held



12.3 Thermal modeling indicates that on the working surface of a simple tool, the temperature varies by nearly 60 °C when the base of the tool rests on heated platens.

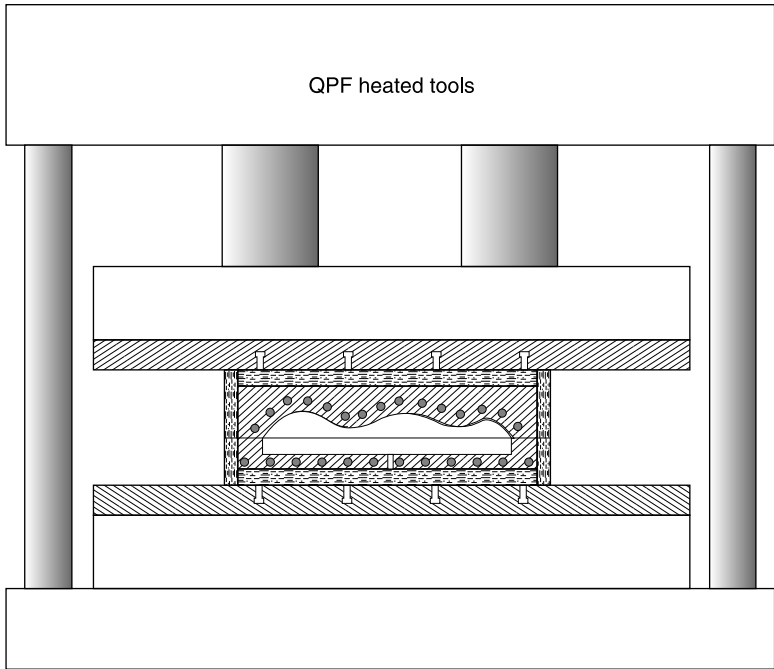


12.4 Physical experiments showed conclusively that temperatures within an unheated tool placed on heated press platens drop off as the insulated press is repeatedly opened and closed to simulate a steady-state manufacturing system.

at equilibrium with the press doors closed. When such a press is repeatedly opened, as would be required in a high volume production process, a surface temperature variation of $>100\text{ }^{\circ}\text{C}$ is predicted. These thermal gradients within such systems were confirmed experimentally. Figure 12.4 shows the temperature history of several locations monitored within an unheated tool mounted to a heated-platen press. Positions away from the platens within the tool undergo cooling as the press is repeatedly opened and closed. In this work, the doors of the press were opened and closed periodically to replicate a forming process with a 180-second cycle. Several cycle variations were explored, but in all cases, the tool cooled from the equilibrium temperature initially obtained within a closed press and thermal gradients over the working surface of the tool increased. The implication from many similar experiments is that in order to provide reasonable temperature control at the working surface of a large tool, heat sources must lie closer to the surface to be maintained at a target temperature. With this result in mind, the heated press system was abandoned in favor of a system for which the heating system is moved to within the tool itself and the resulting heated tool is insulated (Fig. 12.5). A detailed overview of the design of the integrally heated tool system and its integration into the QPF forming cell is provided below.

12.4 Integrally heated tool system

Although integrally heated tooling is common in other manufacturing systems, such as for injection molding of plastics, it had not typically been applied to the

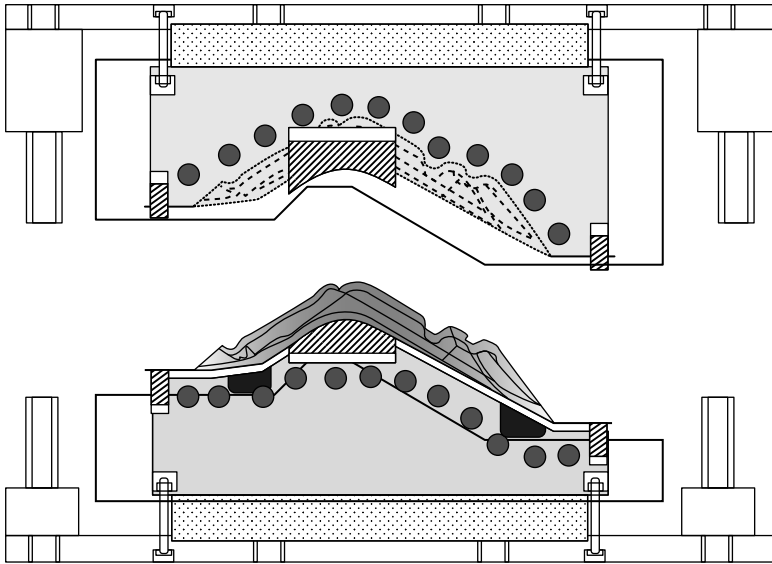


12.5 Hydraulic press with heated and insulated tool system.

higher temperatures required for hot forming of aluminum. Figure 12.6 shows a schematic picture of the heated and insulated tool system developed for QPF. Each half of the tool is composed of three segments:

- a heated working detail that makes up a portion of the pressurized forming cavity;
- load-bearing insulation that thermally isolates the working tool detail from the surrounding environment while transmitting the applied press loads;
- unheated mounting details that provide the interface of the heated/insulated tool to the press bed and ram.

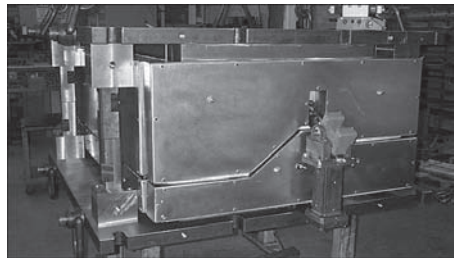
The tool halves must be designed to impart high loads, i.e. the press tonnage, while also isolating the heated tool portion. The insulated tool concept allows the heating elements to be placed within the tool in a manner that allows much better control of the temperature at the working surfaces of the tool, and also allows installation of the tool within a conventionally constructed hydraulic press. The tool exterior and working surfaces for the deck-lid inner panel shown schematically in Fig. 12.6 are shown together in Fig. 12.7. This typical QPF tool configuration will now be discussed in more detail.



12.6 Heated/insulated tool concept.



(a)



(b)

12.7 QPF tool: (a) working surface and (b) exterior views.

12.4.1 Tool exterior temperature target

The ability to use a heated/insulated tool system increases significantly if the outside of the tool package in the closed configuration can be maintained at a low temperature. Pneumatic systems can be operated to nearly 204 °C with high-temperature seals. Below about 93 °C, hydraulic systems such as those used for automated tool clamping can survive. For QPF tools, the target exterior temperature for the tool package was set at 55 °C to facilitate handling of tools in and out of a press in the heated state. The heated/insulated tool system will also transfer heat into the press into which it is placed. The insulation package must be capable of restricting this heat flow to a rate that the press can dissipate, or supplementary cooling must be introduced to the system.

12.4.2 Peripheral insulation development

The insulation around the outside vertical surfaces of the tool serves multiple purposes:

- it improves the temperature uniformity within the tool;
- it minimizes the energy required to maintain the tool at temperature during operation;
- it isolates the near-tool environment from the high temperatures required for QPF.

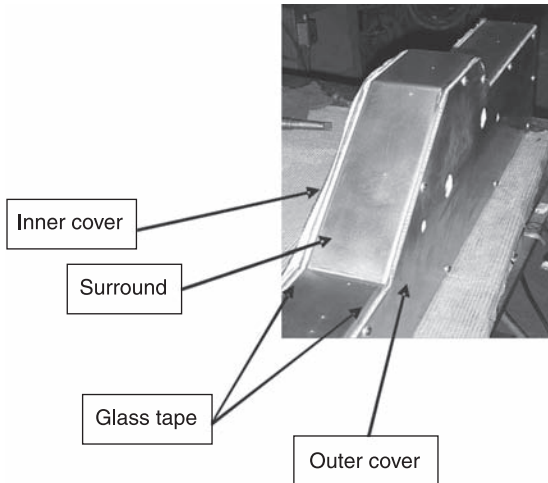
All three attributes are maximized when the insulating characteristics of the insulation package are maximized.

With normal convection cooling on the outside surface of the insulation package, calculations of convective heat flow from the surface and conductive heat flow through the insulation were used to determine the required insulation thickness of ~125 mm to provide acceptable heat loss from the surface. Minimization of the peripheral insulation thickness is important because it minimizes the tool plan-view dimensions and allows larger tool working areas to be used in the existing press footprint.

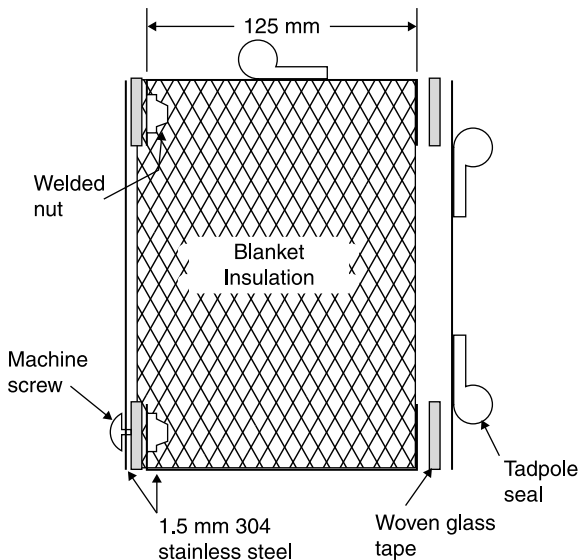
In the final QPF tool configuration, the peripheral insulation is maintained in the form of multi-segment 304 stainless steel enclosures containing a ceramic fiber blanket (Fig. 12.8). The ceramic insulation was chosen for its flexibility, low conductivity, and capability for filling irregularly shaped enclosures. The insulation containers were constructed from multiple segments (Fig. 12.9) separated by insulating glass tape to limit heat transfer between the metal components. The use of slotted holes and insulating glass tapes drastically reduces gross thermal distortions after the tool is heated, but the differential expansion of the hot and cold sides of the insulation packages must be taken into account in the design. Additional linear 'tadpole' seals were riveted to the insulating enclosures on the tool side covers. Each tadpole seal comprised a closed loop on the inner cover of the insulating detail and isolates the air space between the tool and the insulation to minimize convective air flow between the tool and insulation.

12.4.3 Top and bottom insulation

In the QPF tool, each heated half is bolted to a base-plate, which is in turn bolted to the bed or ram of the press. Between the tool and base-plate, an insulating system is used to thermally isolate the hot tool from the hydraulic press. During the design of the top and bottom insulation packages, a trade-off was made between minimizing heat flow and maintaining adequate strength. Low density, low strength insulation is more capable of restricting heat flow. However, higher strength, yet more conductive materials, are required to transfer the press loads without failure.



12.8 The peripheral insulation around the tool consisted of blanket insulation encapsulated in a package consisting of three 304 stainless steel elements: inner and outer covers, and a surround element. Stainless steel details are thermally isolated from each other with glass tape to minimize heat transfer across the enclosure. The outer covers were attached with machine screws that passed through slotted holes to allow relative motion between the various insulation enclosure elements.



12.9 Schematic of tool peripheral insulation system.

In the QPF process, for moderately sized tools consistent with automotive closure panels formed under ~500 psi maximum pressure, the upper and lower insulation packages had to be capable of withstanding distributed loads of >10 MN. The current QPF tooling system was developed around a combination of high-mechanical-property metallic alloy posts and surrounding low-density, low-thermal-conductivity fibrous insulation. Austenitic alloys with relatively low thermal conductivity were used since it was desired that thermal transport between the working and mounting tool details was minimized. Nickel based superalloys, such as those covered by ASTM B637, are particularly attractive for this application due to their hot strength and stability with respect to long term exposure at 500 °C.

The load-carrying capability of the insulation system determines the required area of high-load-carrying elements. From that starting point, simple linear thermal analysis was used to estimate an appropriate insulation height to fully define the required insulation package. By combining the low conductivity, low strength blanket insulation with the more conductive but higher strength alloy supports, a balance of insulating and load-transferring capabilities were obtained. Thermal modeling showed that ~100 mm of insulation achieved the dual requirements of both high load capacity and minimal heat loss, and led to a predicted heat transfer rate of ~3 kW into the press. This is moderate in comparison to the heating capacity of most tools (>100 kW). The predicted behavior was confirmed through actual experiments. Operationally, a very minor amount of external cooling can be implemented in the press to eliminate any problems of heat transfer between tool and press. Steps must be taken to interface the very strong load posts to the adjoining tool members so as to prevent local deformation under load.

12.5 Tool heating system

12.5.1 Power requirements

Tool heating systems are sized to allow heating of tools over reasonable time periods, e.g. <8 hours. In order to heat a 10000 kg tool to 450 °C in that time period, the maximum power requirement was predicted to be about 90 kilowatts. This power need dictates the size and density of the electric resistance heating elements.

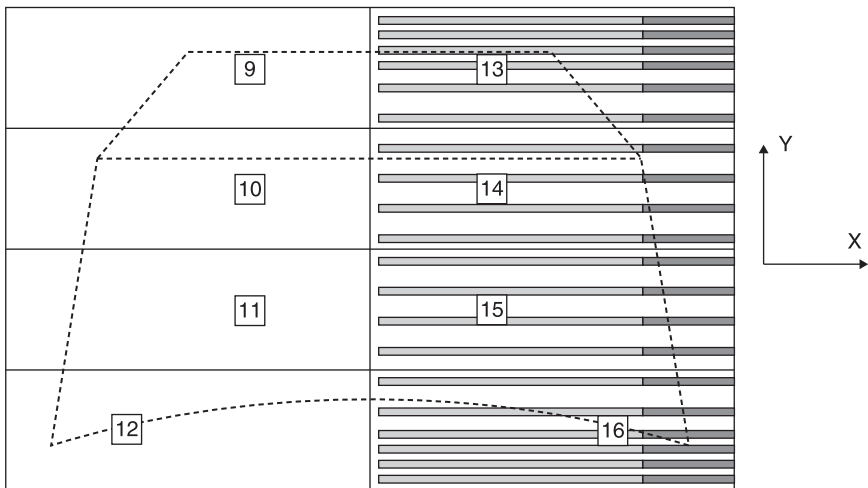
12.5.2 Heaters and zones

For this typical tool size and accompanying power requirement, 19 mm diameter heaters placed at about 75 mm intervals (center to center) and 75 mm below the working surfaces are sufficient to heat the tool. To promote temperature uniformity, the tool is divided into 16 zones: 8 zones in each tool half. The specific pattern of

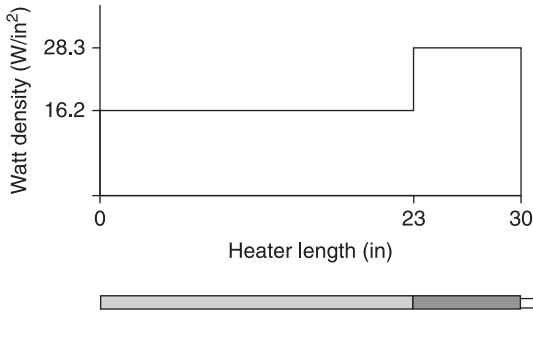
16 heating/control zones allows the tool corners to be controlled independently from the tool interior. This is important because the corners will tend to cool most rapidly due to the greater surface area per volume in those regions. Heater holes are gun-drilled through the entire tool and heaters wired from each side to divide the tool into two zones across its width. Some compromises must be used during positioning of the heaters, because the nominal 75 mm offset must be imposed between a complex three-dimensional surface and a series of linear gun-drilled holes. Generally, the desired distance is imposed as a minimum value except for very local areas. The control system uses a 480 V, 200 A power supply.

The fundamental goal in designing the heating system is to distribute the power that is developed locally in the heating elements evenly over large distances in the tool. Successful balance results in relatively uniform temperatures over large tool volumes controlled from a single thermocouple within each zone. Balance was attained through all three tool-dimensions in different ways. Consider Fig. 12.10, which illustrates a schematic plan view of a deck-lid tool. Heat is lost primarily through the outer edges of the tool when it is closed, so more heat must be introduced near the tool exterior than within the interior. Thermal balance was pursued in the x-direction by use of distributed wattage heaters in which greater wattage density is developed along the first 175 mm of each 760 mm heater rod (Fig. 12.11). In the y-dimension, greater heat input is provided for the outside edges of the tool by using six (closely spaced) elements in the outer zones and only four (more widely spaced) elements in the similarly-sized inner zones.

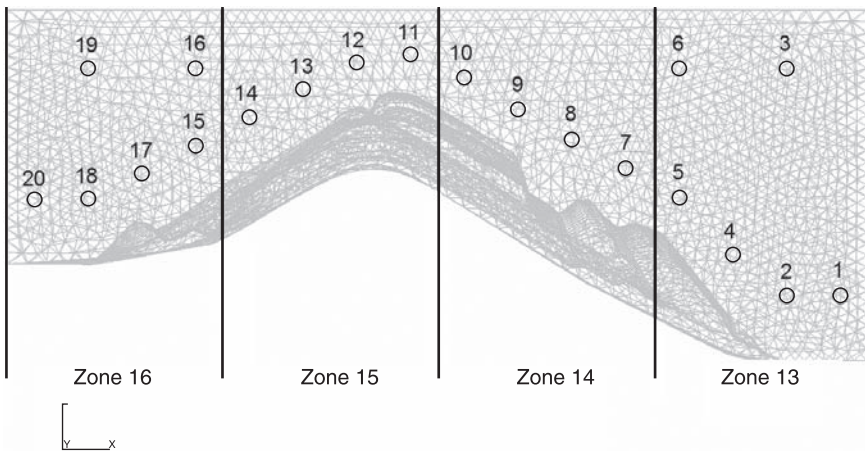
Although the majority of heaters are placed near the tool cavity surface, some additional heaters are placed further below the working surface of the



12.10 Cartridge heater plan view layout within a QPF tool for forming of a deck-lid inner panel.



12.11 Distributed wattage heaters were implemented to generate more power at the tool periphery, the site of maximum heat loss.



12.12 Side view of a deck-lid tool showing heater rod positions as indicated by the circles. Note that tool sides are symmetric since each gun-drilled hole contains two heater rods, each of which is wired from opposite sides of the tool. Note also that 16 heater rods (8 holes) are positioned away from the tool working surface, but add to overall temperature uniformity within the heated tool.

tool (Fig. 12.12). These heaters function to balance the heating wattage (and temperature) in the tool z-direction, particularly in light of the greater heat loss through the load-bearing insulation elements relative to the peripheral insulation.

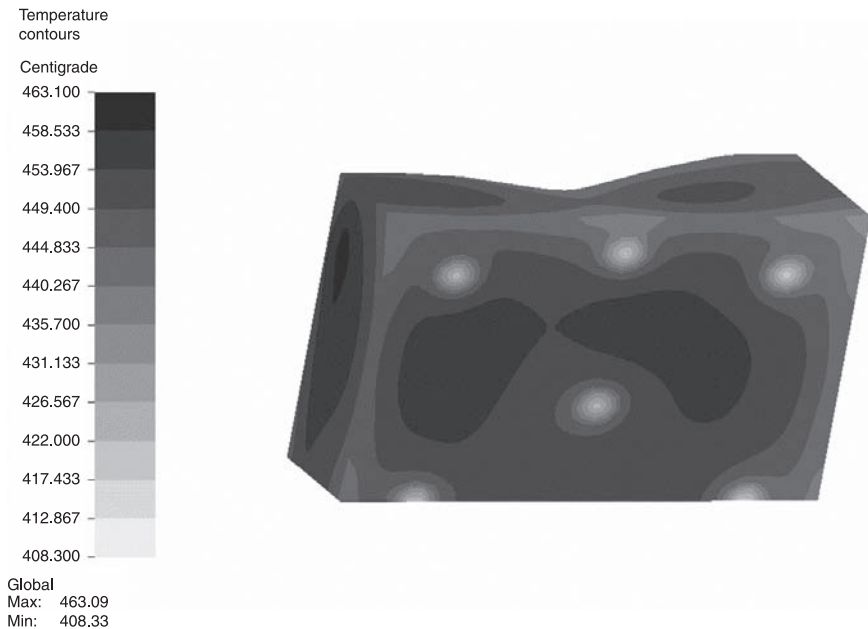
12.5.3 Control thermocouples

A major impetus for heated tool development was the desire to maintain more uniform temperatures at the tool's working surface. A temperature of $\pm 5^\circ\text{C}$ would

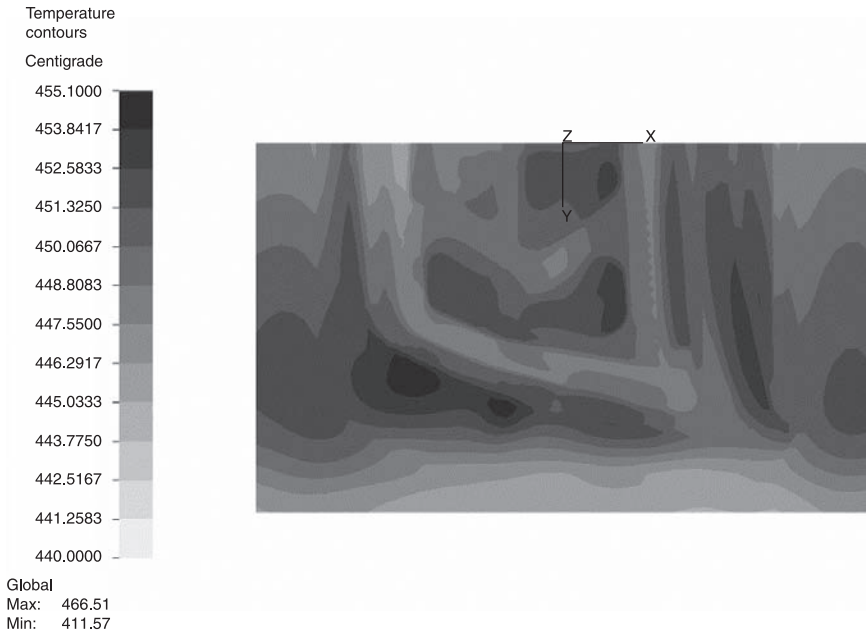
provide significant improvement over the existing press-based heating systems. Control thermocouples were placed near the center of the plan view of the zone, but within ~13 mm of the tool working surface. Closed loop proportional-integral-derivative (PID) controllers were used to maintain temperatures in each of the tool zones.

12.6 Temperature distribution in a deck-lid inner panel tool

Thermal modeling was used extensively to calculate time-averaged temperatures within tools. Extensive experimentation was carried out in order to define proper boundary conditions in order to assess thermal transport away from the tools. Figure 12.13 shows the predicted temperature distribution on the surface of a tool in contact with the load bearing insulation system. The locations of the load posts are apparent, and reflect the thermal losses associated with their presence. In early work, constant temperature set points were imposed at the desired target temperature. Modeling results in Fig. 12.14 indicate that with



12.13 Predicted temperature distribution on the outside surface of the (integrally heated) working portion of a tool. The tool surfaces shown interface with the insulation package. The load-bearing Ni-base alloy posts are more conductive than the surrounding insulation and produce the six 'cold spots' on the face of the tool.



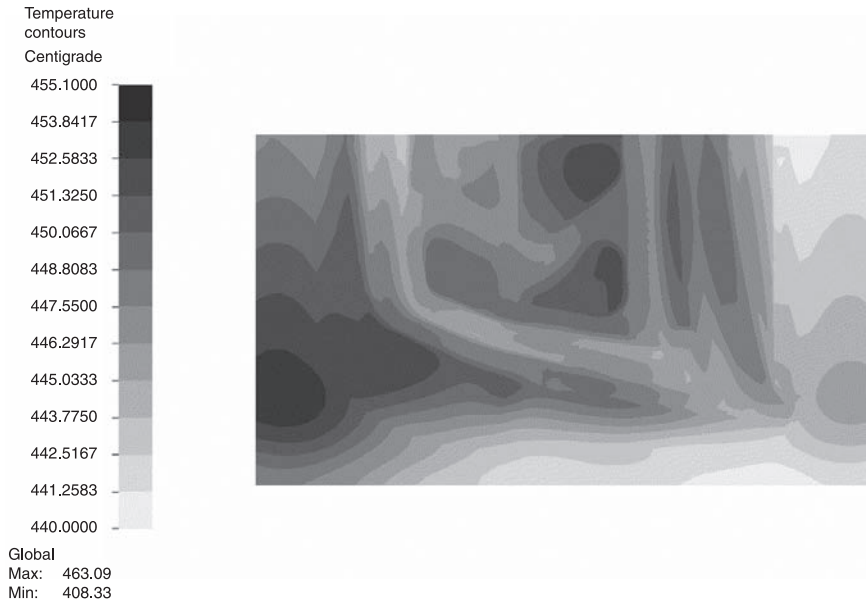
12.14 Predicted tool temperature distribution for identical 450 °C set points at all control thermocouples.

constant temperature set points a temperature variation of ~ 13 °C is obtained. In later work, a solver was introduced that allowed solution of the control set point temperatures that would minimize the average tool surface temperature deviation. Modeling results for the optimized set point temperatures are shown in Fig. 12.15. It can be seen that the average temperature is a bit higher (now exactly 450 °C), but that the temperature variation is only reduced slightly. Fundamentally, the use of a limited number of linear heater rods placed below a complex surface geometry limits the temperature uniformity that can be achieved. In practice, radiative heat transfer between opposing tool halves actually helps to even out these temperature gradients. The temperature variation in the incoming preheated blanks also influences steady state tool surface temperature gradients.

12.7 Ancillary benefits of integrally heated tools

12.7.1 Distortion

Integrally heated and insulated tools that have a relatively uniform tool temperature exhibit very little thermal distortion. Through the application of thermal modeling results, it has been shown that such tools are expected to show relative deviations in position at their working surfaces of only 0.1–0.15 mm due to inhomogeneities



12.15 Predicted tool temperature distribution for control thermocouple set points chosen to minimize average surface temperature deviation from 450 °C.

in temperature. In contrast, heated-platen tools of identical initial geometry exhibit dimensional variations of >0.50 mm at their parting surfaces. With such dimensional variations in both tool halves, the mating tool surfaces are prone to developing problems in obtaining a gas-tight seal in operation, which was a problem commonly encountered in previous heated press operations. Repeated thermal cycling provides much less potential for warping the tools when the temperatures remain nearly constant.

12.7.2 Improved tool mechanisms

Heated and insulated tools facilitate the use of external mechanisms to aid in the manufacturing process. One example is a clamping system. In a heated tool, provision was necessary to set and maintain the position of a hot blank after the loading robot released it, and during the press motion that closed the tool. An electrically actuated clamp system was chosen to serve this purpose (Fig. 12.7). Two clamps pinch the loaded blank to the lower pads at the peak of the tool before the robot releases the blank. The upper pads at those positions are hollowed out in a geometry that matches the clamp arm geometry. Those upper pads move past the clamp as the tool is closed, and pinch the blank between the pads. As the tool continues to close, the blank is carried below the clamp arm as it is firmly held

between the pads. The clamp is retracted once it is no longer needed to hold the blank in position. This clamping system would not be possible in a tool placed in a heated press.

A similar benefit has been introduced in the form of active or passive panel extraction systems. Rack-actuated systems have been installed outside of the load-bearing insulation, but with pass-through elements that act to lift the panel off the tool simultaneously at many points in order to maintain the as-formed panel shape.

12.8 Production validation experience

A number of observations can be made about the heated and insulated tool system based on several years of production experience at General Motors.

- Successful operation of the heated and insulated tool confirms the viability of the heated-tool approach as a replacement for heated presses.
- The combination of uniform tool surface temperatures (resulting from the integral heaters) reduced tool distortion and allowed fully formed panels to be completed in an acceptable production-viable cycle time.
- The power-supply/heater-system proved capable of maintaining the control thermocouples within ± 3 °C of the set point during ordinary use. Closed loop control was used to maintain the temperature at the desired level.
- The programmed forming temperature was maintained both for short press cycles and for duty cycles that included substantial press-open time. This behavior contrasts strongly with that of press-based platen-heating systems, which cool significantly under such conditions.
- The dimensions of panels formed by QPF are similar to those of a very well controlled stamping operation and allow trimmed panels to be manufactured into assemblies without any dimensional correction.
- Preheating of panels outside the press introduces additional flexibility with respect to maintaining the desired thermal conditions within the tools, even for situations of very short (e.g. <100-second) part-to-part cycle times.

12.9 Material development

12.9.1 Background

At the higher production volumes targeted by the QPF process, material cost becomes a larger percentage of the total cost of a component because the press, tooling, and other equipment are divided by a larger number, driving their relative costs per part down. As a result, there were two key drivers for developing the material used in the QPF process:

- *Material quality.* The materials must be capable of robustly making parts at the desired temperatures and strain rates for the QPF process. If the part cannot be successfully made, the cost is irrelevant.
- *Cost.* The cost of the material should be close to that for commercial commodity aluminum alloys that are used in conventional stamping applications.

The two items will be addressed in detail below.

12.9.2 Material quality

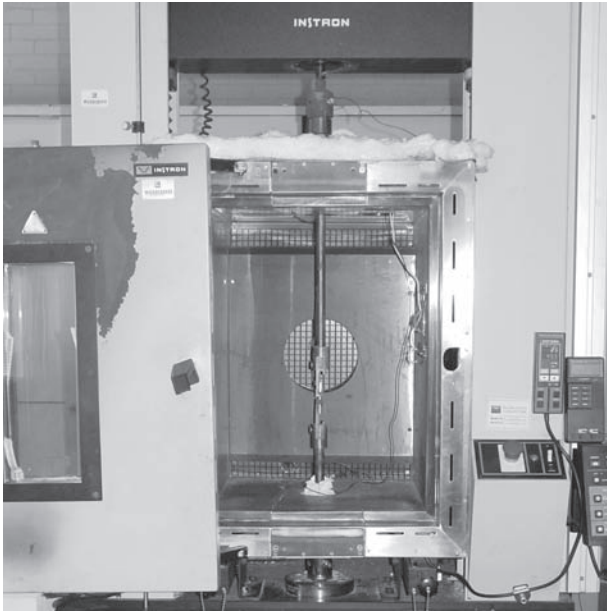
The first step in the successful development of a robust material for use in the QPF process was the creation of metrics ensuring that the material could be formed into the desired shapes. Two metrics were developed to support the QPF process:

- an elevated temperature tensile test to failure where total elongation was specified;
- a biaxial bulge test where height to failure was specified.

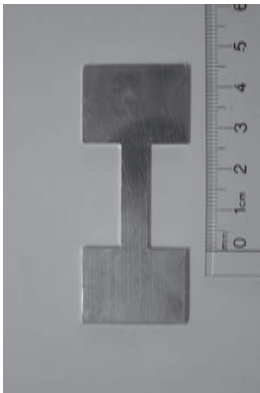
These metrics were independent of the material composition, processing route, etc.

The first metric, tensile elongation, has been used extensively in academic research to demonstrate the superplastic nature of a material. A photograph of the elevated temperature tensile test frame, grips, and specimen is shown in Fig. 12.16. A key element of the test is the loading fixture, which enables rapid insertion of the specimen. Samples are heated to temperature in less than five minutes and then tested, consistent with the QPF process. For the QPF material specification, samples were tested at 500 °C using a constant crosshead displacement speed, calculated to give an initial strain rate of 0.001/s. The total elongation to failure is measured by comparing the final length of the specimen after failure with the initial 25.4 mm length. The conditions used are both slightly slower and slightly hotter than the actual QPF process; however, it was found that these conditions provided a greater spread in the resulting elongation values and enabled better differentiation between ‘good’ and ‘bad’ material.

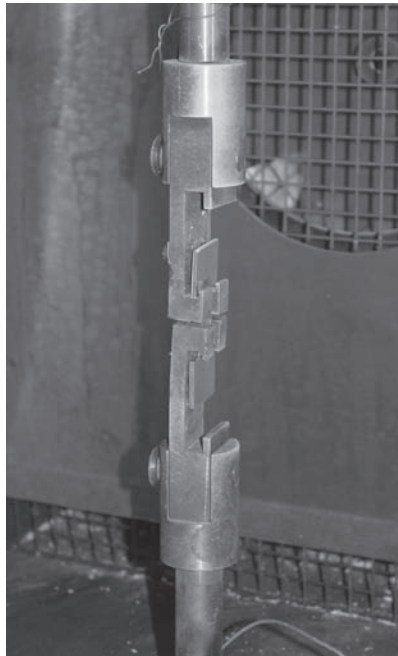
Numerous trials were performed to correlate the total elongation measured from the tensile tests described above with the performance of the measured materials in the QPF plant. One example of such a comparison is shown in Fig. 12.17, where deck-lid outer panels were formed from material which exhibited two different tensile elongations to failure: 296% and 382% (the value reported was the average of five measured samples). The material with the higher elongation material could successfully form a part, while the lower elongation material could not. Compilation of the results from many similar trials demonstrated that a minimum of 325% elongation was required for successful forming. Materials which exhibited higher elongations than this level were



(a)

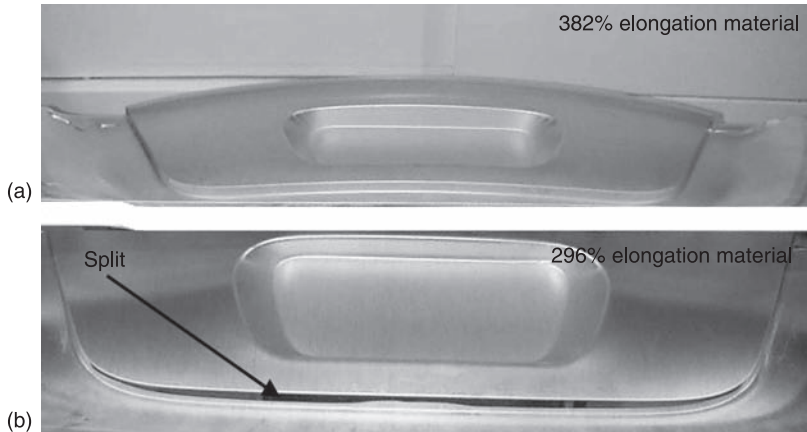


(b)



(c)

12.16 Photographs of: (a) test frame and furnace used for the tensile testing; (b) schematic representation of the specimen; and (c) grip fixture used to hold the specimen and apply the load.



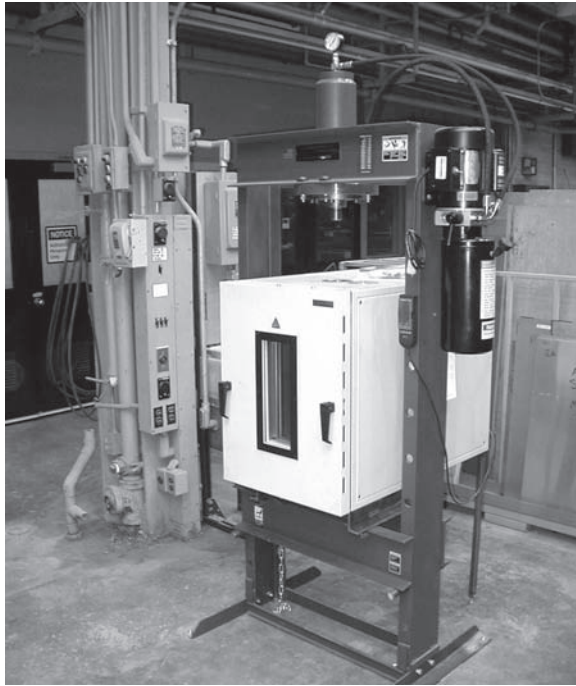
12.17 Photographs of: (a) a deck-lid outer panel made using material which exhibited 382% elongation showing no splitting and (b) a deck-lid outer panel made using material which exhibited 296% elongation and showed excessive splitting.

deemed 'acceptable' and used in the QPF process. Elements of this test were included in the ASTM standard E2448-06.¹⁰

The tensile test criteria were utilized during much of the development phase and early implementation phase for the QPF process. However, the tensile tests had limitations that necessitated the development of a second test method and criteria. The key drivers for the development of the new test were:

- Machining samples took too long to provide feedback on the quality of the material to the supplier.
- The tensile samples did not provide information in both the rolling and transverse material directions.
- Testing was not representative of forming, i.e. deformation was mechanical, not using gas pressure.
- There was a desire to construct a simple test that could be performed easily in the plant.

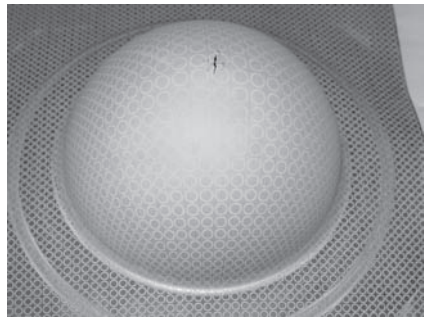
The biaxial bulge test was developed to address the issues described above. This test involves constant pressure forming at elevated temperature into a 100 mm diameter cylindrical die to form a dome. The test is described in detail elsewhere.¹¹ An example of the press, die, and resulting dome are shown in Fig. 12.18. The test is performed until the dome fails, releasing the gas pressure. The height of the dome is measured using a simple gage. The test can be performed on a sample of material sheared from a blank without any special machining. Establishing a common procedure for performing the test is critical for multi-location repeatability. In the case of the QPF specification, the material to be tested was not lubricated, the blank was allowed to preheat to the desired



(a)



(b)

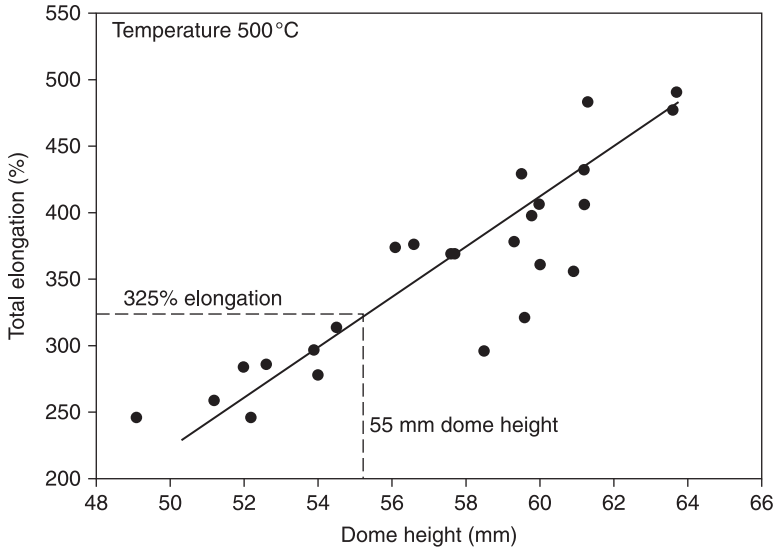


(c)

12.18 Photographs of: (a) biaxial bulge test frame; (b) biaxial bulge test die; and (c) biaxial bulge after forming and failure.

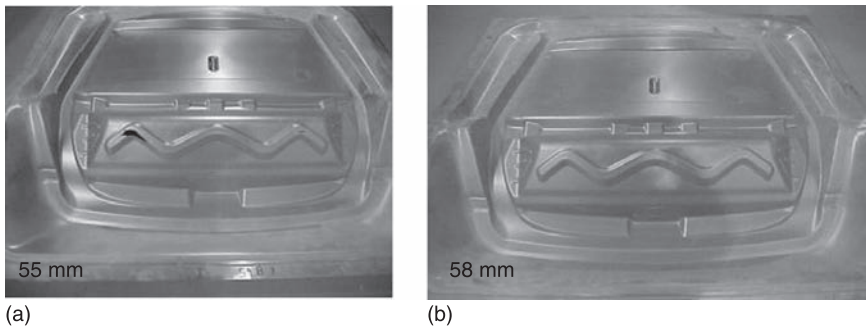
temperature prior to clamping the die, and pressure was applied instantaneously (no prescribed ramping). Subtle changes in the process, such as increasing the preheating time, affect the final bulge height, so it was important to perform a 'round robin' calibration of the tools before a new test fixture was used.

Two types of analyses were performed to develop a height criteria for the bulge test. The first, summarized in Fig. 12.19, established the relationship between uniaxial tensile elongation and biaxial dome height. This was done by measuring



12.19 The relationship between total elongation and biaxial dome height for AA5083, tensile tested parallel to the rolling direction.

both properties on a variety of sheet materials with different quality levels. A strong linear correlation was observed. A dome height of approximately 55 mm was identified to correlate to a 325% elongation value. Plant trials were then performed to determine whether such a criteria would be valid, similar to those reported in Fig. 12.17 above. An example of two parts formed with materials having different tested biaxial bulge heights, 55 mm and 58 mm, is shown in Fig. 12.20. The 55 mm material exhibited some localized tearing, while the 58 mm material successfully formed the part. After a series of trials, it was



12.20 Photographs of lift-gate inner panels formed from material have a biaxial bulge height of: (a) 55 mm, showing some tearing and (b) 58 mm, successfully forming.

determined that QPF material should exhibit a bulge height >55 mm for successful forming, with higher material providing more robust forming. This biaxial bulge testing methodology and bulge height specification was adopted for qualifying material and will be used for all future QPF applications.

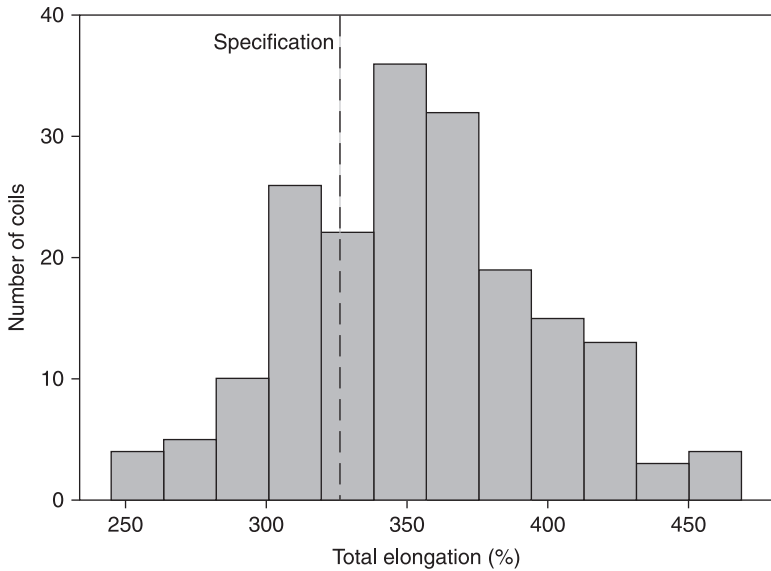
12.9.3 Material cost

The cost of hot blow forming material is driven by composition and processing. SPF-grade aluminum alloys are available in 2XXX, 5XXX, or 7XXX series compositions and can be purchased as-rolled (H temper) or annealed (O temper). The alloy chosen for QPF was AA5083 because of its improved corrosion resistance compared to 2XXX materials, lower cost than the 7XXX series materials, and relative commonality with traditional automotive aluminum alloys such as AA5182 and AA5754. Many suppliers in the aluminum industry produce AA5083 plate in non-SPF grades. Traditionally, SPF-grade AA5083 material is provided with a very low iron content (<0.10) to avoid the formation of coarse constituent particles which lead to cavitation and thereby lower ductility. In order to reduce the cost of the QPF material, the following decisions were made:

- the material should be provided in an H temper to save the cost of the annealing step;
- an Fe level of up to 0.25 w/o should be tolerated, consistent with commercial materials;
- 'exotic' alloy additions which would increase cost such as Sr and Sc were avoided.

Improvements in material performance were attained through optimization of the main alloying elements (Mg, Mn, Cr) and improving thermomechanical processing. The goal was to optimize composition within the target AA5083 specification with only slight modifications to the commercial production material. Data were collected on 200 coils of AA5083, which were used in the prototype development and early production phase of the QPF process. Elevated temperature tensile elongation was collected for each coil and is summarized in Fig. 12.21. Material showed a fairly normal distribution of elongation with an average elongation of approximately 350%, and a range between 250% and 450%. Approximately 20% of the coils would not meet the QPF specification.

The data from Fig. 12.21 were analyzed in more detail by examining the composition of each individual coil and trying to determine whether there were ranges of composition that were common in the higher performing materials. The first analysis, shown in Fig. 12.22(a), found no correlation between elongation and iron content. The material exhibiting the highest elongation had an iron content of 0.27 suggesting that commercial purity iron levels could be tolerated. Similar analyses were performed for all measurable compositions. The



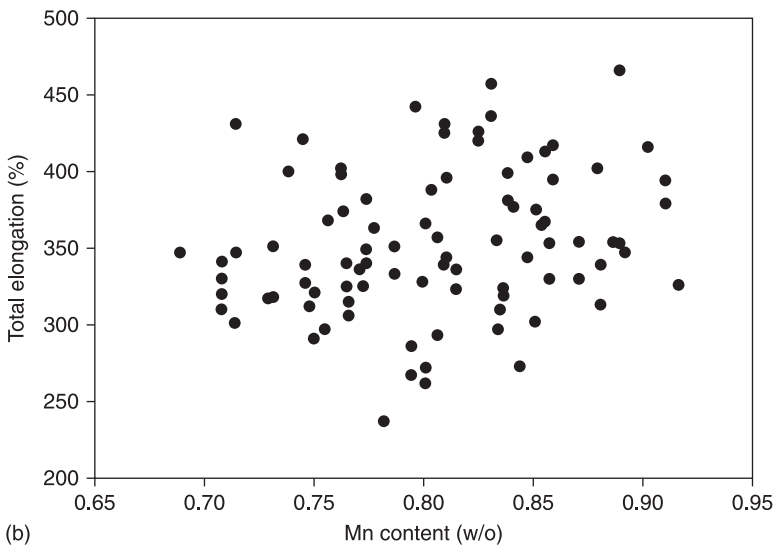
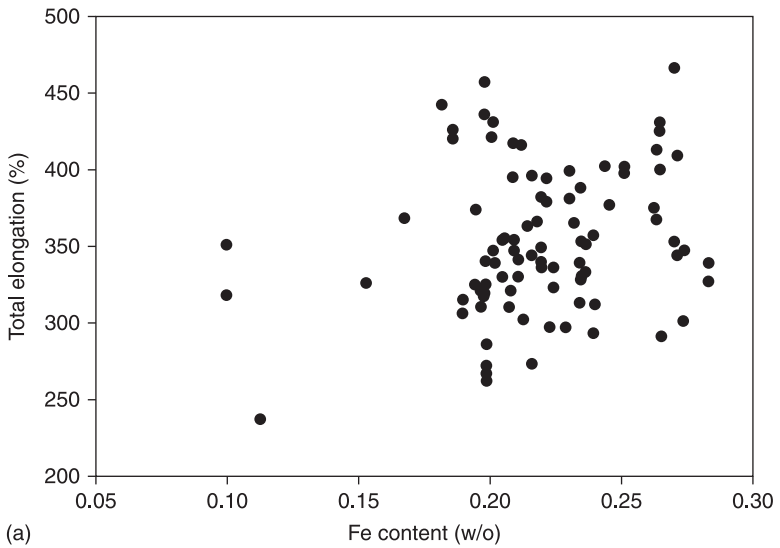
12.21 Distribution of total elongation behavior for material produced under the standard AA5083 composition specification. Each coil was sampled in three areas with an average of five measurements. A large fraction of coils fall below the target total elongation value.

alloying elements with the strongest correlations were Mn and Cr, as shown in Fig 12.22(b) and (c). Both showed positive correlations with total elongation, and led to change in the recommended composition range for the material as shown in Table 12.2.

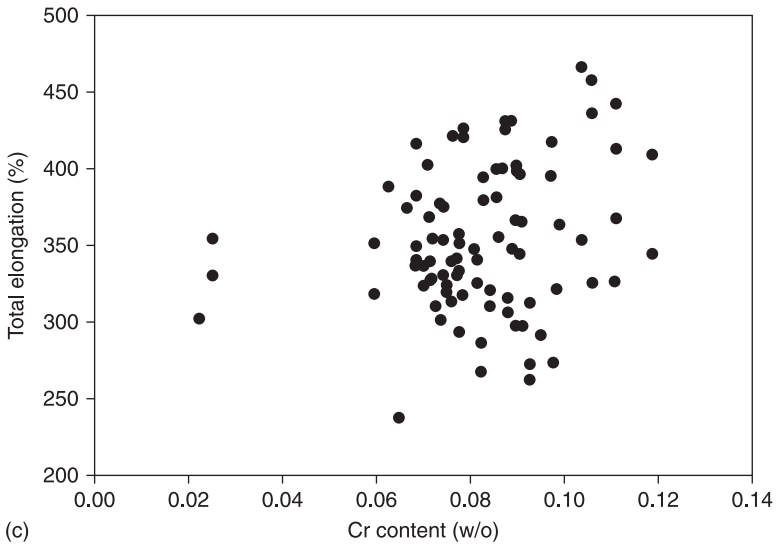
After the change in specification, shown in Table 12.2, data for the next 50+ coils after the change in composition is shown in Fig. 12.23. The performance of the material was clearly increased, with only a 4% rejection rate of the material. This analysis resulted in a QPF material which could be made at only a modest premium compared to commercial stamping grade 5XXX series materials. More details of this analysis including the effect of thermomechanical processing is discussed elsewhere.¹²

Table 12.2 Specifications for AA5083 sheet (composition shown in w/o)

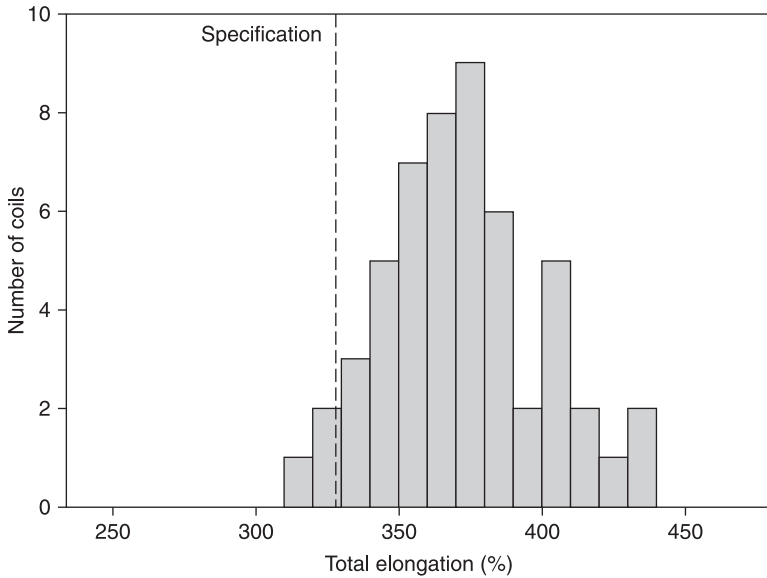
Specification	Mn \geq	Cr \geq	Mg \geq
Standard material specification	0.70	0.06	4.6
New QPF material specification	0.80	0.08	4.6



12.22 The relationship between composition in weight percent and total elongation for AA5083 for the following elements: (a) iron, Fe; (b) manganese, Mn; and (c) chromium, Cr.



12.22 Continued.



12.23 Distribution of total elongation behavior for material produced under the modified AA5083 composition specification. Each coil was sampled in three areas with an average of five measurements. Only 4% of the coils did not meet the specification.

12.9.4 Modeling

Finite element (FE) modeling of the QPF process was required to make the technology a 'viable' manufacturing process. A successful FE modeling approach must be able to predict both deformation and failure. More specifically, it should be able to predict the strain evolution during forming (constitutive equation) and identify regions of the formed part that may fail during forming (failure criteria or forming limit diagram). To be consistent with other sheet metal forming FE work at GM, the FE code selected for QPF was PAMSTAMP. General Motors worked with the code developers to create a PAMQPF module that could be used in analyzing QPF components and transferred to the mainstream engineering community.

The majority of FE analyses performed for hot blow forming such as SPF use a simple power-law equation that relates stress with strain rate through a stress exponent, n , or strain rate sensitivity m ($1/n$).

$$\sigma = K \dot{\epsilon}^m$$

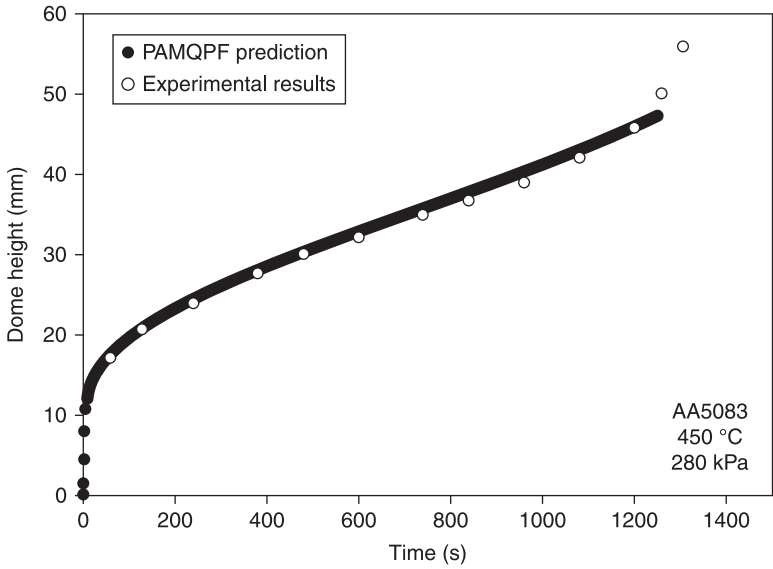
Initial QPF work used that same equation, and a failure criteria of 50% maximum thickness reduction. This criteria was developed to demonstrate the strain level above which internal damage through cavitation began to degrade mechanical properties.¹³ The criteria works very well when panels are formed very slowly (0.0001/s), and a single deformation mechanism such as grain boundary sliding (GBS) controls deformation. However, extensive work has shown that under QPF conditions, both GBS and dislocation creep contribute to deformation,^{14–16} and optimum forming occurs when the mix between mechanisms is approximately 50–50. As a result, the constitutive models assume a single mechanism are inaccurate, especially in predicting the cycle time necessary to make a given component.

The equation which has been developed for predicting QPF deformation is a two-term constitutive equation which accounts for both grain boundary sliding and dislocation.¹⁷ The equation is shown below:

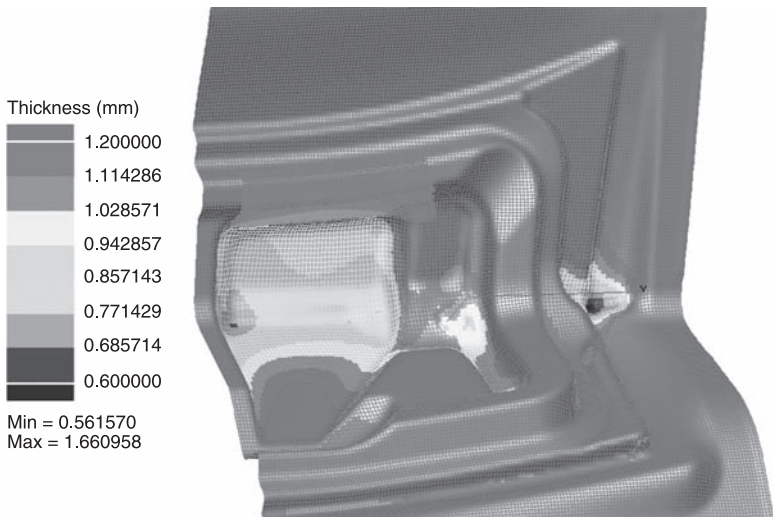
$$\dot{\epsilon} = 2.466 \times 10^{-6} (\sigma - 0.7)^{2.027} + 9.383 \times 10^{-9} \sigma^{3.917}$$

The equation has been successfully used to predict both strain evolution and forming cycle. An example of the prediction of a forming cycle is shown in Fig. 12.24. This equation can then be used to predict the strain distribution in a formed automotive panel such as the deck-lid inner panel shown in Fig. 12.25.

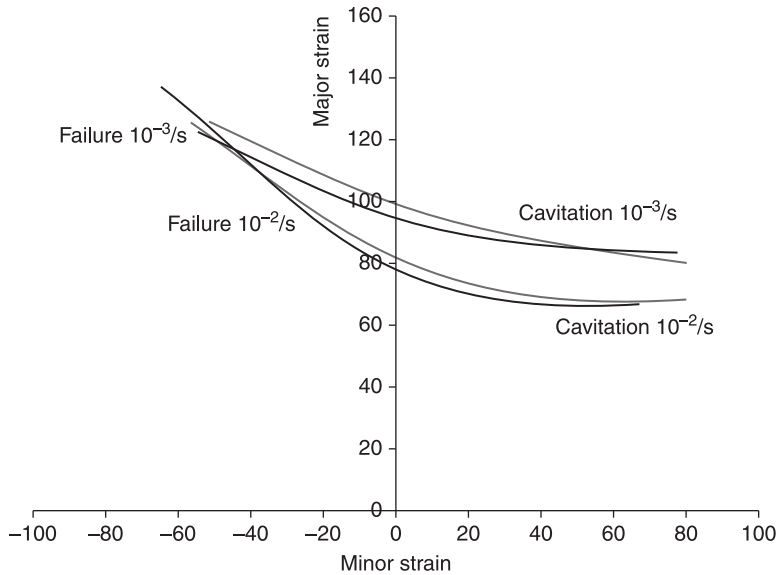
The 50% failure criteria that was initially used was developed based largely on a cavitation failure mode. In reality, necking is the most common failure mode during forming. As a result, a new failure criteria was developed, which showed the failure criteria as a function of temperature and strain rate. An example of a forming limit diagram at 450 °C is shown in Fig. 12.26, illustrating the forming limits at different strain rates when the failure criteria is either cavitation based (cavity level >2%) or failure, where the part has a physical tear. The development of these forming limit diagrams is discussed in detail elsewhere.¹⁸



12.24 Comparison of predicted dome height versus time with experimentally measured results using the two-term constitutive equation and PAMQPF finite element code.



12.25 Predicted thickness distribution for a deck-lid inner panel after QPF forming.



12.26 Forming limit diagram for AA5083 at 450 °C showing failure limits for two different strain rates (0.001/s and 0.01/s) and two different failure criteria (cavitation and failure).

12.10 Lubrication

Lubrication plays a key role in the QPF process. Proper lubrication will enable forming, facilitate part release from the die, and minimize surface quality issues. The key issues in lubrication for hot blow forming processes are addressed elsewhere in this book, and detail in other literature.¹⁹ This section will briefly provide specific details of the lubrication process used for QPF blanks. The aluminum sheet is blanked and stacked in skids of 200 blanks and shipped to a supplier for processing. The blanks are then hung on a conveyor as shown in Fig. 12.27 where they are processed. The cleanliness of the blanks is critical to achieving uniform lubricant application. Irregular oil, dirt, or metal fines can lead to issues with the lubrication distribution or adhesion. An example of a dirty coil is shown in Fig. 12.28. As a result, the first step in processing the blank is a detergent wash. The overhead chain conveyor then carries the blank into an oven where it is rapidly warmed to about 70 °C. This enables the lubricant to stick without beading, thus creating a uniform appearance. The warmed sheet then enters a spraying chamber where a robot applies the lubricant to both sides of the blank if needed. In most cases, a narrow strip around the sealbead on the air side of the blank during forming is lubricated, creating what appears like a picture frame. The lubricant is applied either thin (6 microns) or thick (20 microns) depending on the requirements of the part.



12.27 Blank lubrication conveyor. Blanks are hung on a conveyor and then processed through a wash station, heater, and robotic paint sprayer to apply the lubricant.



12.28 Photograph of a coil of AA5083 materials exhibiting dirt/debris streaks on the coil which must be removed to ensure proper paint application.

12.11 Conclusions

QPF is a hot blow forming process capable of producing complex panels at automotive volumes. This chapter provided an overview of the process and the drivers around the development of the technology. It also reviewed specific details around design of the dies for the process, as well as background for the development of materials, the lubrication system, and finite element modeling of the process. More details of the process can be found in a variety of publications referenced throughout this chapter.

12.12 References

1. J. G. Schroth, "General Motors' quick plastic forming process," in E. M. Taleff, P. A. Friedman, P. E. Krajewski, R. S. Mishra and J. G. Schroth (eds), *Advances in Superplasticity and Superplastic Forming*, TMS, Warrendale, PA, p. 9 (2004).
2. P. E. Krajewski and J. G. Schroth, "Overview of quick plastic forming technology," *Materials Science Forum*, 551–552: 3–12 (2007).
3. P. E. Krajewski, "The warm ductility of commercial aluminum sheet alloys," *SAE Paper* 2005-01-1388, 2005.
4. J. Hohnhaus and G. Obermaier, "Super plastic forming with new type of press," in K. Siegert (ed.), *New Developments in Sheet Metal Forming*, MAT INFO Werkstoff-Informationsgesellschaft mbH, Frankfurt, pp. 59–70 (2002).
5. S. Li, M. Chabin and A. Heath, "New developments in superplastic forming simulation and industrial applications," *Key Engineering Materials*, 433: 211–217 (2010).
6. D. Sorgente and L. Tricarico, "The role of the numerical simulation in superplastic forming process analysis and optimization," *Key Engineering Materials*, 433: 225–234 (2010).
7. A. Petiot and T. Favre, "Tool thermal behavior in SPF environment," *Materials Science Forum*, 551–552: 111–122 (2007).
8. M. R. Barone and D. A. Caulk, "A new method for thermal analysis of die casting," *ASME Transactions Journal of Heat Transfer*, 115: 284–293 (1993).
9. M. R. Barone and D. A. Caulk, "dieCAS – Thermal analysis software for die casting: modeling approach," *Transactions, 17th NADCA International Die Casting Congress and Exposition*, Cleveland, Ohio (1993).
10. ASTM E2448–06, *Standard Test Method for Determining the Superplastic Properties of Metallic Sheet Materials*, Copyright © ASTM International, West Conshohocken, PA, United States.
11. J. R. Bradley, "Bulge testing of superplastic AA5083 aluminum sheet", in E. M. Taleff, P. A. Friedman, P. E. Krajewski, R. S. Mishra and J. G. Schroth, (eds) *Advances in Superplasticity and Superplastic Forming*, TMS, pp. 109–118 (2004).
12. R. Verma and P. E. Krajewski, *Composition and Process Optimization of AA5083 Aluminum Sheet for Quick Plastic Forming*, TMS, New Orleans, (2008).
13. J. R. Bradley and J. E. Carsley, "Post-form properties of superplastically formed AA5083 aluminum sheet", in E. M. Taleff, P. A. Friedman, P. E. Krajewski, R. S. Mishra and J. G. Schroth, (eds) *Advances in Superplasticity and Superplastic Forming*, TMS, pp. 149–157 (2004).
14. M-A. Kulas, W. P. Green, E. M. Taleff, P. E. Krajewski and T. R. McNelley, *Metallurgical and Materials Transactions A*, 36A(5): 1249–1261A (2005).

15. M-A. Kulas, W. P. Green, E. M. Taleff, P. E. Krajewski and T. R. McNelley, *Metallurgical and Materials Transactions A*, 37A(3): 645 (2006).
16. T. R. McNelley, K. Oh-Ishi, A. P. Zhilyaev, S. Swaminathan, P. E. Krajewski and E. M. Taleff, "Characteristics of the transition from grain-boundary sliding to solute drag creep in superplastic AA5083," *Metallurgical and Materials Transactions A*, 3(1): 50–64 (2008).
17. L. G. Hector, Jr., P. E. Krajewski, E. M. Taleff and J. T. Carter, "High-temperature forming of a vehicle closure component in fine-grained aluminum alloy AA5083: Finite element simulations and experiments", *Key Engineering Materials*, 433: 197–210 (2010).
18. M-A. Kulas, P. E. Krajewski, J. R. Bradley and E. M. Taleff, "Forming limit diagrams for AA5083 under SPF and QPF conditions", *Materials Science Forum*, 551–552: 129–134 (2007).
19. P. E. Krajewski and A. T. Morales, "Tribological issues during quick plastic forming", *Journal of Materials Engineering and Performance*, 13(6): 700–709 (2004).

Superplastic forming of magnesium alloys

R. GRIMES, University of Warwick, UK

Abstract: For rather more than the last decade the world's car makers have been making major efforts to reduce the mass of their vehicles. As magnesium is the lightest structural metal, much attention has been devoted to increasing its use in motor cars and considerable success has been achieved with high pressure die castings. This chapter describes the excellent superplastic properties that can be obtained from magnesium alloys, but also outlines the problems such as corrosion and lack of ambient temperature ductility that, from a technical viewpoint, have restricted its application. The major economic and environmental issues (life cycle analyses (LCA)) holding back its use are also reviewed and prospects for future application considered.

Key words: twin roll casting, Pidgeon process, superplastic magnesium, life cycle analysis (LCA).

13.1 Introduction

Research into superplastic alloys began in earnest after the publication of the review by Underwood (1962) and magnesium alloys were amongst the first materials in which the phenomenon of superplastic deformation was subsequently observed (Backofen *et al.* 1968). The alloys in which it was observed (ZK60A and HM21A) had not been specially processed giving, perhaps, an early indication of the good potential for superplastic behaviour in magnesium alloys. However, although over the next three decades considerable effort was devoted to the development of superplasticity in titanium and aluminium alloys, very little further attention appears to have been given to magnesium alloys. Presumably this was because, despite their low density, there was not a large demand for magnesium alloys in sheet form and alloys existed that were capable of making very high quality die castings thus evading the problem of limited ductility in the wrought alloys.

However, growing concerns at diminishing fossil fuel reserves, together with unnecessary atmospheric pollution, led in the United States (in 1975) to the introduction of the CAFE (Corporate Average Fuel Economy) fuel economy regulations followed, in 1993, by the PNGV (Program for a New Generation of Vehicles) and consequential major efforts to reduce the mass of automobiles. In Europe, the vehicle builders entered a voluntary commitment to reduce fuel consumption by 25% from 1990 levels by 2005. The net result of all these regulations and agreements has been the initiation of numerous developments to investigate all the means by which vehicle mass might be reduced. Over the last ten years this has led to a growing surge in investigations into the possibilities for

greater use of magnesium alloys in automobile construction and this, in turn, has led to investigation into the possibilities of employing superplastic forming (SPF) for sheet applications. If viable superplastic magnesium alloys and manufacturing routes for the alloys are developed over the next few years, there is little doubt that the material would find uses in a range of applications. However, at present the driver for the current developments is the enormous potential of the automotive market and it is from this perspective that this chapter is written.

The following sections will consider the history of magnesium, the properties of magnesium that make it an attractive vehicle construction material, the availability for major vehicle use, the development of superplastic variants and their manufacturing route and the current and future outlook for superplastic applications of magnesium alloys in vehicle construction. Some of the economic issues will also be briefly addressed.

13.2 History

The existence of magnesium was demonstrated by Sir Humphrey Davy in 1808, but isolation of the metal was not achieved until 1828 when Bussy reduced magnesium chloride with potassium. Subsequently, industrial extraction techniques based upon electrolysis of molten salts and thermal reduction with ferrosilicon were developed and, essentially, these are the processes that remain in current production. Magnesium is one of the most abundant elements in the earth's crust, notably occurring in the minerals dolomite ($\text{MgCO}_3 \cdot \text{CaCO}_3$) and magnesite (MgCO_3). Ocean water, however, represents a virtually inexhaustible source with a content of about 0.17% magnesium. Growth in industrial production of the metal was erratic, increasing dramatically during the two world wars but falling back after the wars and for many years the major outlet for metallic magnesium was as an alloying addition to aluminium alloys.

Magnesium alloys tend to possess excellent casting properties and found early application in racing cars in the 1920s (Magnesium Elektron). However, the first major automotive application came in 1936 when Volkswagen employed magnesium alloys for the engine block and gearbox housing of the new Volkswagen Beetle. Production of the Beetle reached its peak in 1971 and was then consuming magnesium at the rate of 42 000 tonnes per annum (Friedrich and Schumann 2001). Magnesium and most of its alloys have close-packed hexagonal structures (some magnesium lithium alloys have a body centred cubic structure; they are considered further in Section 13.5.3 below) and, in consequence, in the form of rolled sheet they possess very limited cold formability compared with other structural sheet alloys such as steel or aluminium, thus making its fabrication into many parts considerably more difficult compared with these competing materials. When mass is all important, such as in helicopters, it has been used in significant quantities – consumption reaching a peak of more than 14 000 tonnes per annum in 1972 but declining to 7000 tonnes per annum by 1986 as the Vietnam



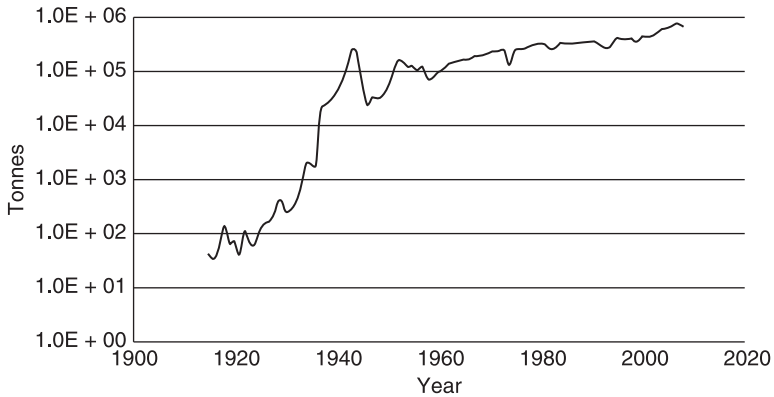
13.1 1955 Mercedes Benz 300 SLR racing car. The body panels were fabricated from magnesium sheet.

war declined. Sheet magnesium alloys have, however, found relatively recent (1955) niche automotive application in, for example, the Mercedes Benz 300 SLR racing car (Fig. 13.1) where the body panels were all fabricated from magnesium alloy sheet.

Current global economic problems have resulted in some recent decline but magnesium production is near to an all-time high at about 600 000 tonnes per annum (and the trend is to continuing growth, see Fig. 13.2). A large part of the current growth is contributed by magnesium alloy die castings for the automotive industry. However, sheet production has declined further and is estimated to be only slightly greater than 1000 tonnes per annum with the majority of this production going into printing plates (*Materials World* 2003).

13.3 Properties of magnesium

Magnesium is the lightest structural metal (density 1.74 gm/cm^3) giving it obvious immediate attractions for aerospace and automotive applications where mass is important. In addition to its low density, it has high specific strength and high specific stiffness. The combination of reasonable strength with relatively low modulus results in a high dent resistance. Moll *et al.* (2003) conducted simulated hail storms with wooden balls (each weighing 2.5 g and at impact speeds up to 95 km/h) onto steel, aluminium (AA6016T6) and AZ31B sheet. Across the range



13.2 Annual global production of primary magnesium since 1920. Note that the tonnage scale is logarithmic (derived from US Geological Survey data, *Historical Statistics for Mineral and Material Commodities in the United States*, Data Series 140: 2007).

of speeds investigated, the magnesium alloy performed the best with barely perceptible damage until 80 km/h impact velocity and less than 0.025 mm indentation depth at 95 km/h, compared with depths of about 0.13 mm and 0.25 mm for the aluminium alloy and steel respectively. However, the gauge of the steel used was about half that of the aluminium and magnesium and this would, presumably, have exaggerated the lower dent resistance of the steel. Noise, vibration and harshness (NVH) problems in vehicle design can be significantly reduced by use of magnesium alloys. Machining behaviour is excellent and the alloys are readily recyclable. While only limited investigation seems to have taken place into the possibilities of diffusion bonding, results reported by Somekawa *et al.* (2003) with AZ31 sheet report that good quality diffusion bonds were readily obtained. Against these good properties the greatest technical disadvantage of magnesium is its hexagonal crystal structure, which results in very limited ambient temperature ductility and hence a very restricted ability to form sheet into panels if any significant strain is involved. Where magnesium is joined to other metals, galvanic corrosion is a potential problem. Currently, and at existing production techniques and levels, it is suggested (USAMP 2006) that magnesium alloy sheet is five times more expensive than aluminium vehicle body sheet.

The very considerable success that magnesium alloys have achieved in recent years, in applications such as instrument panel cross-beams, derives from the fact that a high degree of part consolidation can be achieved as a consequence of the good casting properties of the material. Compared with a steel fabrication, a cast magnesium cross-beam can reduce the number of parts from about 30 to, perhaps, six achieving both weight and cost savings of around 50%. With sheet applications the benefits are far less clear-cut. The magnesium sheet component is likely to be being used in preference to aluminium so that the potential for mass saving is immediately reduced

to a maximum of 33%. However, because of the lower modulus of the magnesium alloy, the gauge may well have to be increased relative to the aluminium component in order to achieve equal stiffness. Das (2003) suggests that the mass saving may be as low as 10%. The complexity of large castings, and feeding difficulties during casting, frequently enforce the use of thicker gauges in parts of the casting than strict mechanical property requirements would dictate. Against this, no such limitations apply to sheet so the gauge can be as thin as the application requires, particularly as higher properties can be achieved in the wrought product. If SPF is used to convert the sheet into a component then some degree of part consolidation would generally be possible although, obviously, not to the extent possible with castings.

The magnesium alloy most commonly used in sheet form is AZ31B and, at the present stage of magnesium alloy development, this would be the alloy most likely to be employed in the manufacture of sheet automotive components. At present, the great majority of superplastically formed motor car parts in aluminium employ the alloy AA5083. The search for reduction of vehicle mass has led to the grades of sheet steel employed in vehicle construction becoming far wider than in the past, with increasing use of a wide range of higher strength alloys so that it is no longer possible to describe vehicle bodies as being constructed from deep drawing quality (DDQ) mild steel. Nevertheless DDQ steel is still employed for a significant proportion of the body in white and Table 13.1, therefore, compares some of the relevant properties of SPF variants of AZ31B, SPF AA5083 and DDQ vehicle body steel. It is not easy to give a numeric value to the corrosion performance of such different materials, but the AA5083 possesses an inherent resistance to corrosion. Unprotected DDQ steel will corrode rapidly, particularly in salt-containing environments, but the various forms of zinc coating that are now very widely employed have transformed the performance of DDQ steel in corrosive situations. Unprotected, AZ31B's corrosion resistance is not good, but it responds well to commercially available chrome-free treatments based on potassium permanganate or titanium/zircon fluoride and that confer sufficient resistance to pass standardised salt spray corrosion tests.

Table 13.1 Properties of a variety of competing body panel materials

Property	AZ31B	AA5083	DDQ Steel
Density (g/cm ³)	1.78	2.65	7.8
Modulus (GPa)	45	71	207
0.2% Proof stress (MPa)	140	145	165
Tensile strength (MPa)	240	290	310
Specific strength (MPa)	135	109	40
Specific stiffness (GPa)	25	27	26
Elongation (%)	10	25	45
Crystal structure	cph	fcc	bcc

cph, close-packed hexagonal; fcc, face-centred cubic; bcc, body-centred cubic.

13.4 Superplasticity in magnesium alloys

There is no internationally agreed system of designating magnesium alloys, although the system devised by the American Society for Testing and Materials (ASTM) is widely adopted. This consists of a three-part letter, number, letter description in which the first two letters indicate the major alloying elements and the numbers indicate, in weight per cent but rounded to the nearest whole number, the content of the additions. The code letters are shown in Table 13.2 while the nominal compositions of the alloys mentioned in the following sections are given in Table 13.3.

13.4.1 The earliest experiments

As mentioned above, magnesium alloys were among the first materials in which superplastic behaviour was reported, having been observed in sheet ZK60A and

Table 13.2 Element code letters used in the ASTM designation system for magnesium alloys

Letter	Alloying element
A	Aluminium
C	Copper
E	Rare earth metals
H	Thorium
K	Zirconium
L	Lithium
M	Manganese
Q	Silver
S	Silicon
W	Yttrium
Z	Zinc

Table 13.3 Nominal compositions (wt%) of alloys mentioned in the text

Alloy	Al	Mn	Zn	RE*	Zr	Th	Y
AZ31B	3.0	0.2	1.0				
AZ61	6.6	0.15	1.0				
AZ91	8.7	0.13	0.7				
HM21A		0.8				2.3	
WE43				3.4	0.7		4.0
ZK60A			5.5		0.45		

* RE indicates rare earths.

Elektron 21: 2.7%Nd, 1.3% HRD(Gd), 0.6%Zn, 0.5%Zr.

HM21A that had received no special processing (Backofen *et al.* 1968). However, there appears to have been no further interest in superplasticity in magnesium alloys for the following two to three decades. While not an investigation into superplasticity, Ion *et al.* (1982) studied the behaviour of Magnox (Mg–1%Al–0.005%Be) when deformed in uniaxial compression at temperatures and strain rates that would be associated with superplastic deformation. They reported the progressive refinement of the relatively coarse grained starting material by dynamic recrystallisation, thus giving an early pointer to means of achieving superplastically deformable microstructures in magnesium alloys.

13.4.2 High strain experiments

Although investigations into reducing vehicle mass by greater use of aluminium had commenced in earnest in the mid-1970s, real pressure to reduce fuel consumption has been driven by concerns over global warming and this was probably responsible for the surge in interest in superplastic magnesium alloys from the late 1990s onwards. The investigations into the development of superplasticity in aluminium alloys that had taken place from the mid-1970s to the mid-1980s had demonstrated that quite complex treatments, particularly involving large strains and/or special heat treatments, were frequently required. Initially the ‘new’ investigations into superplasticity in magnesium alloys tended to follow this earlier thinking and examine the influence of more complex thermo-mechanical treatment including rapid solidification and powder metallurgy. Thus, Watanabe *et al.* (2001) reported excellent ductilities in WE43 that had been subjected to a large strain by hot extrusion with a high extrusion ratio. They concluded that the deformation mechanism during superplastic straining was grain boundary sliding (GBS) accommodated by slip controlled grain boundary diffusion. Mabuchi *et al.* (1999) examined the influence of even bigger strains by subjecting AZ91 to numerous equal channel angular extrusion (ECAE) passes. Interestingly, although they achieved a grain size of about 0.7 μm in the ECAE material compared with 3.1 μm in an annealed material, the annealed material gave superior superplastic performance. However, both conditions gave good ductilities, albeit at very low strain rates ($\sim 10^{-5} \text{ s}^{-1}$), with the ECAE material showing the lower flow stress. As an alternative approach, Watanabe *et al.* (1999) hot extruded sintered AZ91 powder and achieved a reasonably thermally stable grain size of about 1 μm . Elongations to failure exceeded 300% at strain rates of 10^{-2} s^{-1} to 10^{-1} s^{-1} with optimum deformation temperatures of about 300 °C. Another novel, high strain approach was employed by W-J Kim *et al.* (2009) with ZK60. They subjected material that had been hot extruded and rolled to a final single pass of ‘high ratio differential speed rolling’ in which the top roll rotated counter-clockwise at three revolutions per minute while the bottom roll rotated clockwise at one revolution per minute thus imparting a reduction of 70%. The through thickness microstructure was fairly uniform with a grain size of 1.4 μm

and optimum superplastic elongation of ~1000% at 280 °C and a strain rate of $1 \times 10^{-3} \text{ s}^{-1}$. It is not obvious how such a process could be employed for the manufacture of commercial-sized sheets in commercial quantities.

13.4.3 Industrially relevant experiments

Much development work then turned to considerably simpler production routes to achieve superplastic behaviour, moving towards those that might be industrially relevant. Mohri *et al.* (2000) took an as-cast slice of AZ91 and hot rolled and annealed it, resulting in a grain size of about 40 μm before hot tensile testing material from the annealed sheet. During the hot tensile deformation, the grain size was refined to about 6 μm (with an elongation of about 600%) demonstrating that, in at least some magnesium alloys, dynamic recrystallisation (DRX) occurs relatively easily and could be employed to refine the grain structure. Tan and Tan (2002) followed this up by investigating the possibilities for refining the grain structure in relatively coarse grained, commercially manufactured AZ31B sheet. They demonstrated that by conducting deformation in two stages it was possible to grain refine the structure by an initial strain performed under the optimum conditions for DRX ($1 \times 10^{-4} \text{ s}^{-1}$ at 400 °C) and then achieve a greater overall strain by conducting the second stage under the optimum conditions for superplastic deformation ($2 \times 10^{-4} \text{ sec}^{-1}$ at 450 °C). Wei *et al.* (2003) examined the influence of strain rates $\geq 10^{-3} \text{ s}^{-1}$ to see whether it would be possible to achieve superplastic behaviour at strain rates that might be industrially acceptable. They started from cast AZ91 with a grain size of 78 μm and applied a number of warm rolling passes. This refined the grain size, presumably by DRX, to ~11 μm and the material then achieved a ductility of 455% at 350 °C and 10^{-3} s^{-1} . They concluded that GBS was the main deformation system operating during superplastic flow, with GBS accommodation through dislocation creep controlled by atom diffusion through grain boundaries. Some small grain coarsening accompanied the superplastic deformation. These papers all seemed to demonstrate that, far from needing complex, high strain routes to develop superplastically deformable magnesium alloys, quite simple routes either relying on hot/warm rolling to refine cast structure by DRX before commencing superplastic deformation, or even employing the early stage of superplastic deformation simultaneously to generate the superplastic structure from a coarse grained starting structure could be employed. It was also apparent that, while the level of superplastic performance differed from alloy to alloy, from a superplastic point of view the composition was relatively unimportant. This was then even further simplified when Pong (*Materials World*, 2006) demonstrated that it was possible to obtain superplastic behaviour starting directly from as-cast material. He electro-discharge machined 1.5 mm thick tensile test pieces from a 25 mm thick sand casting of the alloy Elektron 21 and obtained elongations over 300% at 500 °C over a range of initial strain rates from about $8 \times 10^{-4} \text{ s}^{-1}$ to $1.5 \times 10^{-3} \text{ s}^{-1}$. He suggested that these results pointed to twin roll

strip casting as being an obvious and relatively simple production route for the manufacture of superplastically deformable magnesium alloy strip. Follow-up work from Pong's observations by Grimes *et al.* (2008) then examined the superplastic behaviour of twin roll cast samples of both AZ31 and AZ91. Good superplastic behaviour was obtained from both alloys whether they were simply in the as-strip cast condition or whether they had been subsequently warm rolled. Both as-strip cast alloys had relatively coarse starting grain structures and these were refined simultaneously with the superplastic deformation. Since the twin roll strip casting process inevitably combines fairly rapid solidification with a certain amount of hot work, this series of experiments was continued with hot tensile tests on samples (full plate thickness) cut from a pressure die cast 'plate' of AZ31, 100 mm wide \times 150 mm long \times 5 mm thick, in order to remove any effects of hot working. In the as-cast condition, an optimum ductility over 520% was achieved at 450 °C and an initial strain rate of $\sim 8 \times 10^{-4} \text{ s}^{-1}$. Further strength was given to the argument that only a simple route should be required for the manufacture of superplastic magnesium alloy sheet by Watari *et al.* (2004), who produced material in a fairly wide range of magnesium alloys using an experimental twin roll caster to convert partially solidified alloys into sheet. Good superplastic behaviour was obtained in the as-cast condition with gauges ranging from 2.5 mm to 4 mm.

13.4.4 Mechanisms of superplastic flow in magnesium alloys

Earlier chapters in this book have considered the mechanisms by which metals deform superplastically and so this section will be confined to a limited number of comments describing situations where magnesium alloys appear to behave differently from other established superplastic alloys. Perhaps, from a superplastic deformation viewpoint, the most significant characteristic is the relative ease with which magnesium alloys recrystallise during hot/warm deformation. Magnesium has a high stacking fault energy and might, therefore, during hot/warm deformation be expected to recover rather than recrystallise. However, it appears that the limited number of slip systems that can operate as a consequence of its hexagonal structure result in some form of DRX (either continuous or discontinuous) occurring readily. This may then result in grain refinement or, indeed, grain coarsening and the grain structure resulting from the DRX is likely to determine the superplastic behaviour. Unlike aluminium alloys, particles seem neither to be required to stimulate recrystallisation by particle stimulated nucleation nor to control grain boundary movement by Zener pinning. The WE43 alloy examined by Watanabe *et al.* (2001) gave ductilities in excess of 1000% despite containing a significant volume fraction of intergranular spherical particles of about 0.2 μm diameter. Dislocations were observed to interact with the intragranular particles but the grain shape remained largely equi-axed. Superplastic behaviour has now been observed in a wide range of magnesium alloys and there is strong evidence

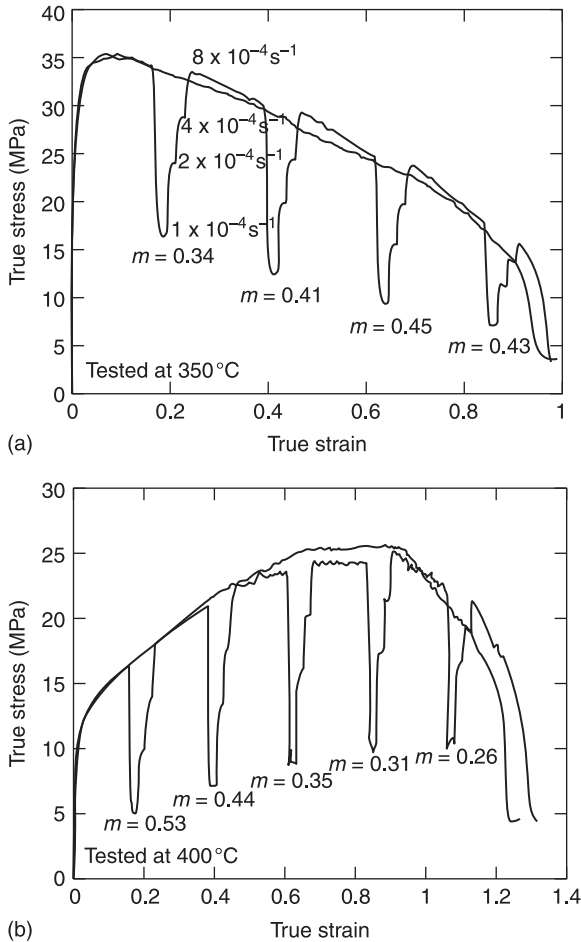
that this behaviour can be significantly different between different alloys. Kim *et al.* (2001) developed deformation mechanism maps (DMMs) by using constitutive equations for various creep mechanisms. They plotted grain size against normalised flow stress (σ/E) (where σ is flow stress and E is Young's modulus) for Mg–Al–Zn alloys, and suggested that for small grain sizes deformation would be dominated by GBS accommodated by grain boundary diffusion while at larger grain sizes the accommodation mechanism would change to lattice diffusion. At even larger grain sizes, solute drag creep or power law creep may dominate. Thus, from the appropriate DMM it can be seen how the deformation mechanism may change with strain according to whether grain size is refined by DRX or coarsened by grain growth. Dashwood *et al.* (2010) demonstrated that when relatively fine grained, die cast AZ31 was deformed at 350 °C and a constant strain rate of $8 \times 10^{-4} \text{ s}^{-1}$ the flow stress increased progressively throughout most of the test (Fig. 13.3(a)). A 'staircase' of jump strain rate tests performed under the same basic conditions showed that the m value progressively declined and it was postulated that the initial deformation was by GBS and that grain coarsening had resulted in the decline in m value. In contrast, when similar tests were performed on twin roll cast AZ91 (but at a temperature of 350 °C) the flow stress rapidly rose to a peak but then progressively declined (Fig. 13.3(b)). The associated jump strain rate tests showed the m value to be increasing with strain. While the initial grain structure of this material was dendritic and relatively coarse, after testing equi-axed grains of about 14 μm resulted implying that DRX had been responsible for the grain refinement.

13.5 Manufacture of superplastic magnesium alloy sheet

Whether superplastic magnesium alloy sheet achieves a breakthrough into volume vehicle manufacture will be dependent not simply upon the technical issues but also upon its carbon footprint and, particularly relative to aluminium alloys, its cost. The dramatic increase in Chinese magnesium production and concomitant decline in Western production over the last decade seems likely to have increased the cost competitiveness of magnesium but worsened its environmental impact. The following sections attempt to address these 'non-technical' issues, albeit since no generally agreed production route for such material exists, a high degree of uncertainty must attach to any conclusions.

13.5.1 Extraction of magnesium

As mentioned in Section 13.2, the early development of extraction techniques for magnesium resulted, essentially, in two techniques that have both, in essence, continued in use to the present. The electrolytic process is the more capital intensive of the two, but thermal reduction with ferrosilicon (the Pidgeon process)



13.3 Stress–strain plots from constant strain rate tests at $8 \times 10^{-4} \text{ s}^{-1}$ with superimposed strain rate jumps showing m values for (a) AZ91 and (b) AZ31B (from Dashwood *et al.* 2010).

is more labour intensive. In 1999, full operating costs for the Western world producers were lower for the electrolytic plants (Das 2003). At that time, global production of magnesium was about 415 000 tonnes per annum, with China accounting for about 115 000 tonnes (Ehrenberger *et al.* 2008). By 2007 Chinese production had risen from about 25% of global production to over 75% at 627 300 tonnes. Magnesium production in China is by the Pidgeon process and has been generally regarded as resulting in considerable atmospheric pollution. Initially the dolomite, from which the magnesium is to be extracted, is subjected to a calcining operation at about 1000 °C to remove carbon dioxide and the subsequent reduction process operates at about 1300 °C thus requiring a significant input of heat.

Production of the ferrosilicon is also energy intensive. Possibly worst of all, is the use of sulphur hexafluoride to protect the molten magnesium, but this is being phased out.

It is possible, however, that two fairly recent developments in the production of primary magnesium could result, in due course, in a significant reduction in both cost and the generation of green house gases. In Australia, CSIRO is developing a carbothermic reduction route for magnesite (Prentice *et al.* 2010). While the basic chemistry is well known, previous attempts to employ the carbothermic reduction route have been unsuccessful because of reversion of the carbothermal reaction:



The belief is that in the Australian development the reaction products are very rapidly quenched, thus suppressing the reversion reaction and allowing the magnesium to condense and solidify.

The other alternative to the 'traditional' extraction routes is much nearer to production reality. The Norwegian company, Hydro, is participating in a 50:50 venture with Advanced Metallurgical Group (AMG) to develop what is described as a low cost production route for magnesium and silica starting from the mineral olivine (a magnesium iron silicate abundant in Norway). An electrolytic process will be employed starting from olivine dissolved in hydrochloric acid with no CO₂ emissions and no solid waste. The intention is to use the mothballed Hydro Porsgrunn electrolytic (Norway) plant and the capacity should be 35 000 tonnes of magnesium and 35 000 tonnes of silica (Hydro press release December 19, 2008, and *International Magnesium Association Weekly*, May 30, 2008). The intention is that the silica would find use as a filler in vehicle tyres. Production is scheduled to commence in the autumn of 2013.

Ehrenberger *et al.* (2008) performed life cycle analyses (LCA) on Chinese magnesium plants and concluded that when all of the heating came from coal the overall emissions amount to 47 kg CO₂ equivalent per kilogram of magnesium produced. This figure reduced to about 25 kg CO₂ equivalent for an integrated plant employing natural gas for heating. The study was concluded by a theoretical assessment of the benefit to a car builder (and society) of substituting a magnesium alloy casting for a steel fabrication. Taking the total CO₂ emissions from extraction of the raw material, through fabrication of the component to driving the vehicle and comparing results for the best and worst magnesium production cases with the steel, they found that the best magnesium became better than the steel after about 136 000 kilometres whereas the coal route magnesium was still producing more CO₂ than the steel after 200 000 kilometres (assumed to be the typical lifetime mileage of a petrol-engined car). Thus, unless the production of magnesium in China can overall equal, or better, the CO₂ emissions from the integrated, natural gas fired plants, the resultant carbon footprint from its use in car construction is likely, at best, to be marginally acceptable. However, between

the years 2000 and 2006, energy consumption in extracting magnesium in China dropped by 40% and the Chinese government is supporting efforts to reduce energy consumption further and increase waste heat utilisation (Beals *et al.* 2007) so that there seem to be grounds for optimism in the medium term.

A more major investigation into the LCA consequences of substituting magnesium structure for steel in the front end of a 2007 GM-Cadillac CST was conducted by Das *et al.* (2009). This involved a magnesium structure made up from die castings (30 kg), sheet stampings (4 kg) and extrusions (11 kg) in place of 82 kg of steel. As with the earlier (Ehrenberger) study, benefits from reductions in energy consumption or reduced emissions of green house gases would only be achieved after several years of operation. The investigation did conclude, however, that the environmental benefit from use of magnesium would be likely to increase with improvements in materials management and recycling.

The Prentice *et al.* (2010) investigation of the carbothermal route suggests a global warming potential of between 6.4 and 21.3 tonnes CO₂ equivalent for their process, the actual value depending on the source of electricity used, and so at its worst roughly equates to the Ehrenberger best result (25 tonnes CO₂ equivalent) for the Chinese Pidgeon process. However, when the sensitivity of the Pidgeon process results to energy source is taken into account, it is not clear that the carbothermal route offers any major advantage.

13.5.2 Magnesium sheet production

Conversion of magnesium ingot into high pressure die castings (HPDC) is less costly than the metal working operations involved in converting ingot into a wrought alloy semi-fabricated product and converting the resultant sheet into a vehicle component. Thus, magnesium alloy sheet will not be used where an HPDC would be viable. However, the cost of producing the sheet product will have a very strong bearing on its competitiveness relative to aluminium.

Traditionally magnesium alloy sheet has been manufactured by a fairly conventional route of casting a rectangular cross-section ingot, scalping the major surfaces of the ingot and pre-heating for several hours followed by hot rolling on a reversing breakdown mill without re-heating. At an intermediate gauge, the hot blank is reheated to about 350 °C and warm rolled to final gauge and temper. Most of the industrially based development of SPF techniques that have been conducted so far (see below) has been performed using sheet manufactured by such a route. However, relative to steel or aluminium, only very small quantities of magnesium sheet are currently consumed globally. Since production of this sheet is divided between several plants around the world, it is inevitable that none can achieve the level of production efficiency that would be expected with volume production and a relatively expensive product results.

Potentially, however, twin roll strip casting offers a considerably simpler and cheaper route to the same product and it has been suggested (USAMP 2006) that

eventually there could be a premium of only 20% compared with aluminium alloy sheet. While twin roll strip casting is now (the process was originally invented by Bessemer in 1846) well established for the production of certain aluminium alloys, it has never been fully developed for magnesium alloys. An earlier programme by the Dow company in the 1980s, taking a Hunter caster designed for aluminium and coupling it with a proprietary magnesium feed system to produce coils at about 6–7 mm gauge, was discontinued for commercial reasons (Park *et al.* 2009). Nevertheless, as well as the obvious economic advantages of strip casting, technically it offers the benefits of considerably more rapid solidification and refined microstructure with reduced segregation. Against this, and compared with aluminium alloys, magnesium alloys freeze more rapidly resulting in greater difficulty in achieving uniform solidification across wide strip. Also the freezing range of magnesium alloys is generally wider than that of the aluminium alloys that are produced via strip casting and this makes control of centre line segregation and defects more difficult. Work at Brunel University (Bayandorian *et al.* 2009; Xia *et al.* 2009) has demonstrated that subjecting the melt to intensive shearing at just above the casting temperature can result in a much refined and more uniform microstructure in the cast product. The technique has produced good results with AZ31, AZ61 and AZ91 cast through a small, experimental, twin roll strip caster but has not yet been tried on a larger scale.

More recent investigations into the potential of twin roll strip casting for magnesium seem to have had their origin in the development at CSIRO in Australia, which began in 2000 with the specific objective of reducing the manufacturing costs of magnesium sheet (Liang and Cowley 2004). They have developed an industrial scale pilot plant complete with protected liquid metal feed capable of producing 3 mm thick strip. CSIRO estimate that, compared with conventional sheet production, industrial use of their process would reduce green house gases by 50% and overall sheet production costs by up to 60%. They also reported modest, but significant, improvements in both the strength and ductility of their twin roll cast material compared with conventionally cast and rolled AZ31B sheet.

Since 2000, several other magnesium twin roll casting developments have begun, including casters in Japan, China and Germany. However, at present, developments in Korea and Turkey appear to be nearest to commercial production. The POSCO/Research Institute of Industrial Science and Technology (RIST) development in Korea has an integrated melting, twin roll casting and rolling operation capable of continuously producing 600 mm wide strip in gauges from 3–7 mm and coils up to 1220 mm diameter (Jung *et al.* 2007). Sheet properties are reported to be at least as good as those from commercially (conventionally) produced sheet and the grain structures obtained are both finer and more uniform. Development work is continuing into the melting and casting technology, high speed warm rolling, stronger, more ductile alloys, welding and superplastic forming. While less appears to have been published about the TKS

(ThyssenKruppStahl) magnesium twin roll casting facility in Germany it, too, appears to be quite well advanced with a capability of casting 700 mm wide strip (ThyssenKrupp Steel, press release, 2002). In 2001 TKS set up an organisation, 'Magnesium Flachprodukte GmbH' (MgF), with the objective of expanding the application of sheet magnesium alloys and in June 2010 entered into collaboration with POSCO to exchange technology (*Magnesium Monthly Review* 2010, p. 10).

The other twin roll casting facility that appears to be near to being able to produce magnesium alloy sheet on an industrial scale is being developed in Turkey by the Materials Institute, TUBITAK MRC (Kaya *et al.* 2008; Duygulu *et al.* 2009). Their unit has cast a reasonably wide range of magnesium alloys in the gauge range 4.5 to 6.5 mm and 1.5 metres wide. They are developing techniques for casting thinner strip and other alloys. As part of the same development, work has also been conducted on the warm rolling of the as-cast strip down to final gauge (Duygulu *et al.* 2009) and demonstrates that the resultant strip is appreciably less anisotropic than strip produced via the ingot casting route.

13.5.3 Alloy development

While AZ31B is long established, and is the most commonly used magnesium alloy in structural applications of sheet, the investigations into the superplastic behaviour of magnesium alloys have included several other alloys that could, potentially, find automotive application. Alderman *et al.* (2006) reports a detailed comparison of the superplastic behaviour of AZ31B and ZK10, including manufacture of several vehicle components. Both alloys performed well, although the ZK10 exhibited a higher m value and, it was felt, might permit somewhat faster forming in commercial operations. However, the strength properties of the AZ31B were rather higher than the ZK10. Wang *et al.* (2008), using the analogy of the effects of zirconium plus scandium additions to aluminium alloys, demonstrated significant grain refinement by an addition of 0.15%Zr + 0.03%Sc to AZ31 and enabling warm forming of a demonstration PDA casing. Additionally, entirely new wrought alloys are under development and these are considered below. Certainly, there seems to be a current perception that it is only a matter of time before magnesium alloys achieve far wider utilisation in vehicle construction and this has resulted in major development activities into peripheral topics in addition to straightforward alloy development in Germany, China, Japan, Korea and the United States. Virtually every aspect of the application of magnesium alloys in vehicle construction is receiving, or has received, recent attention. Thus there have been programmes to improve response to precipitation hardening (Mendis *et al.* 2009; Shepelev *et al.* 2009), to develop surface treatments (Ohara *et al.* 2009), to investigate sheet formability (Letzig *et al.* 2009), to characterise warm forming lubricants (Rohatgi *et al.* 2010) and to examine ignition behaviour (Luo *et al.* 2009) and ignition proofing (Ji *et al.* 2009). While magnesium is always referred to as being readily recyclable, this is on the assumption that the

scrap that is to be recycled is clean and segregated. If magnesium alloys, in a variety of different forms (and therefore different alloys), find major automotive application they are likely to be shredded at the end of the vehicle's life raising the issue of how such mixed scrap could be dealt with. Gesing *et al.* (2010) and Fechner *et al.* (2009) have both worked on these problems.

Some success in improving ambient temperature ductility has been achieved by addition of 0.2% cerium to pure magnesium (Chino *et al.* 2008). Although this effect has been attributed in earlier work to the resulting reduction in the c/a ratio (where a and c are lattice constants) making non basal slip easier, they conclude that the cerium increases the stacking fault energy of the alloy. In turn this led to a reduction in the intensity of the basal plane texture and enhanced ductility. Early work by Chapman and Wilson (1962) demonstrated that by refining the grain size of pure magnesium to about 2 μm the ambient temperature tensile ductility was increased to well over 60%. As ambient temperature ductility problems in magnesium alloys tend to manifest themselves during bending operations when twinning can lead to failure, it is a pity that Chapman and Wilson's work was confined to uniaxial tensile testing. Fan *et al.* (2006) added 2% cerium to AZ91D achieving significant improvements in both tensile strength and ductility and also improvement in the corrosion behaviour. They believed that the addition refined the β phase but also left it in a more continuous form so acting as a corrosion barrier. In other experiments with AZ91, a calcium addition improved the corrosion resistance but reduced mechanical properties. However the strength loss was restored by a rare earth addition (Wu *et al.* 2005). Attention has also been devoted to modifying the surface layers to produce a very fine grained layer to improve corrosion resistance, either by surface mechanical attrition (Sun *et al.* 2007) or by laser treatment (Dube *et al.* 2001).

As mentioned above, Mg–Li based alloys with a lithium content greater than about 11wt% can exhibit a bcc structure that gives them greater ambient temperature ductility than other magnesium alloys. In the 1960s, this led to the development of several ultralight alloys of magnesium with lithium, and other additions such as aluminium, zinc or silicon. Densities as low as 1.35 g/cm^3 were achieved and limited aerospace and military sheet applications were found (*ASM Speciality Handbook: Magnesium and Magnesium Alloys*, 1999). However, the molten alloy was very reactive making manufacture difficult and the semi-fabricated product was also very susceptible to corrosion. These early alloys are not now commercially available. Given the price sensitivity of automotive materials and given the fact that the addition of only 2.5wt% Li to an aluminium alloy was sufficient to double the cost of the basic Al–Li alloy (Grimes *et al.* 1985) it is surprising to find that there seems to be a resurgence of interest in Mg–Li based alloys. Nevertheless there have been reports of recent work on Mg–10.3Li–2.4Al–0.7Zn (Yang *et al.* 2010), Mg–9Li–2Zn (Zu *et al.* 2009) and Mg–9wt%Li–1wt%Zn alloy with a small amount of Mn (0.1wt%) (Kim *et al.* 2009). The latter alloy exhibited superplastic behaviour between 150 °C and 250 °C.

13.6 Superplastic forming of magnesium components

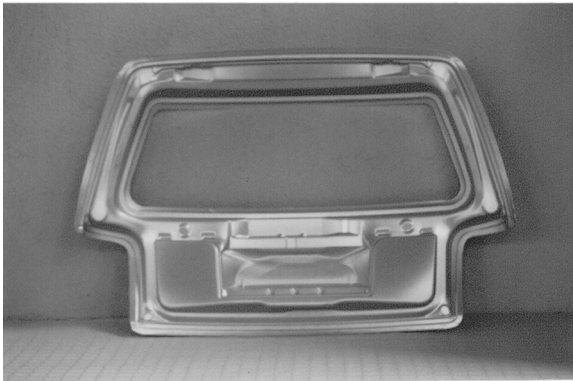
13.6.1 Current situation

While development activities with the ultimate aim of establishing magnesium alloy sheet components (whether fabricated conventionally or by warm forming or by superplastic forming) in motorcar construction have now been proceeding for well over a decade, actual applications remain very few.

Rather more than 10 years ago, Formtec AG manufactured a number of prototype inner tail gate doors (Fig. 13.4) for the Volkswagen Lupo by superplastically forming AZ31B sheet. The material was in the as-supplied condition and had received no special treatment to render it superplastic. It is understood that a satisfactory product resulted (Dunwoody 1999) but Volkswagen took the decision (Friedrich and Schumann 2001) to employ a magnesium HPDC for the door inner in conjunction with an aluminium alloy sheet outer panel for the production vehicle.

In the intervening years, Superform Aluminium, in conjunction with Magnesium Elektron, has conducted numerous full-scale SPF trials with various alloys and a wide range of trial components. They have concluded that sufficient knowledge now exists to be able to offer AZ31B as one of their standard available alloys and a brochure with the product details has been produced (Superform Aluminium). Figure 13.5 shows a prototype inner door panel in AZ31B being removed from the forming machine. This component was originally formed from SPF 5083 and use of SPF enabled a three component fabricated steel inner panel to be replaced with a single light aluminium part. Clearly the magnesium alloy could have achieved the same part consolidation with a reduction in mass.

As far as niche and exotic vehicles are concerned, and where the total numbers required are up to about 20000, AZ31B is certainly sufficiently well understood now to be employed for superplastically forming both inner and outer panels,



13.4 Prototype inner panel in AZ31B for the tail gate of the VW Lupo (courtesy of FormTec AG, 3965, Chippis, Switzerland).



13.5 Trial pressing of inner door panel in AZ31B (courtesy of Superform Aluminium).

albeit measures will have to be taken to prevent galvanic corrosion and any clinching operations in joining panels are liable to create difficulties.

At greater numbers, it is likely that some warm forming process combining initial mechanical forming with limited gas pressure forming, as in GM's Quick Plastic Forming, will come to be applied.

13.6.2 The future

Apart from technical issues, the future prospects for the use of magnesium alloy sheet in motor vehicle construction, whether by SPF or simply by warm forming, are critically dependent upon the price of magnesium sheet relative to that of aluminium alloy sheet. There are very good prospects that sheet manufacturing systems, based on twin roll continuous casting, will be developed that allow the conversion of molten magnesium into magnesium alloy sheet at a cost only marginally greater than that for converting molten aluminium into aluminium alloy sheet. However, great uncertainty attaches to the future costs of primary magnesium. In a quite short period, production of primary magnesium has been transformed (Pater 2010). Global capacity in 2001 is estimated to have been about 530 000 tonnes with Chinese production representing about 40% of this total. By 2008, global capacity is believed to have increased to 1113 000 tonnes – of which about 88% is Chinese. In the same period, Western capacity declined by 170 000 tonnes, or 53%. As described above (Section 13.5.1), with

production by the Pidgeon process and current Chinese fuel prices, LCA analyses show only marginal benefits from magnesium substitution even when the most favourable fuel prices are assumed. While this appears a fairly pessimistic assessment, it has to be recognised that there have been major improvements in the efficiency of the Chinese Pidgeon plants and further improvements are likely. It is also distinctly possible that the introduction of extraction techniques like the SilMag process will have lower production costs and be accompanied by less pollution than existing processes.

In the immediate future the situation is further confused by the imposition by the United States government of punitive antidumping tariffs upon Chinese and Russian imports of magnesium into the United States (*Magnesium Monthly Review* 2010, p. 1). This leaves the US die-casting industry with no alternative but to source their primary magnesium from the single remaining domestic producer, thus making them unable to compete internationally. The North American Die Casting Association (NADCA) has made representation to have the order lifted but the outcome remains uncertain. In the meantime NADCA claims that there have been 1675 direct job losses and 8000 indirect job losses as a consequence of the orders and some 50% of Chinese magnesium production capacity is idle (Patzner 2010).

Notwithstanding the above uncertainties, numerous organisations in Korea, Germany, the United States, the United Kingdom, Turkey, China and Japan continue with development work aimed at resolving the outstanding technical issues relating to sheet application in volume vehicles. In 2001, Friedrich and Schumann (2001) envisaged a 'new age of magnesium' in the automotive industry in which, in the near term use of castings, would increase; followed, progressively, by forgings, extrusions, interior sheet applications and exterior sheet applications. They imply a time scale of more than 10 years to resolve all the issues relating to sheet applications, these issues including corrosion and surface finish that they did not consider then to be good enough for exterior panels. Virtually 10 years have now passed and widespread automotive application of magnesium alloy sheet, however formed, does not appear to be imminent. High prices and pollution from the Pidgeon process combine to reduce the attraction of magnesium in applications unless, as with HPDC, there are significant immediate benefits from its use. Although major progress has been made in the development of the twin roll casting process, none of the development plants is yet in a position to supply magnesium alloy sheet in the quantities and of the quality and dimensions that would be required for use in volume motor cars. Issues remain relating to corrosion, secondary processing operations, scrap recycling and LCA. However, as far as more specialised vehicles are concerned, it is likely that there will be use of some superplastically formed AZ31B panels in the very near future.

While, eventually, the argument for the use of wrought (in addition to cast) magnesium alloys, including superplastically formed sheet, in volume vehicle manufacture seems overwhelming both technical and economic matters require further resolution and the time scale may well be protracted.

13.7 References

- Alderman M, Barnes A, Bhayani R and Cottam R, 2006, "Superplastic forming of magnesium alloys", presented at the 14th Automotive Magnesium Seminar at the Europäische Forschungsgemeinschaft Magnesium e.V.
- ASM Speciality Handbook: Magnesium and Magnesium Alloys*, ASM International, Metals Park, Ohio, 1999.
- Backofen W, Azzarto F, Murty G and Zehr S, 1968, "Superplasticity", Chapter 10 in *Ductility*, ASM, Metals Park, Ohio, 279–310.
- Bayandorian I, Bian Z, Xia M, Zhang H, Scamans G and Fan Z, 2009, "Magnesium alloy strip produced by melt conditioned twin roll casting (MC-TRC) process", in E Nyberg, S Agnew, N Neelameggham and M Pekguleryuz (eds), *Magnesium Technology*, TMS, 363–368.
- Beals R, Tissington C, Zhang X, Kainer K, Petrillo J, *et al.*, 2007, "Magnesium global development: outcomes from the TMS 2007 annual meeting", *JOM*: 59: 39–42.
- Chapman J and Wilson D, 1962, "The room temperature ductility of fine grain magnesium", *Journal of the Institute of Metals*, 91: 39–40.
- Chino Y, Kado M and Mabuchi M, 2008, "Enhancement of tensile ductility and stretch formability of magnesium by addition of 0.2wt%(0.035 at%)Ce", *Materials Science and Engineering*, A494: 343–349.
- Das S, 2003, "Magnesium for automotive applications: primary production cost assessment", *JOM*, 55: 22–26.
- Das S, Dubreuil A, Bushi L and Tharumarajah A, 2009, "A life cycle assessment of a magnesium automotive front end", in E Nyberg, S Agnew, N Neelameggham and M Pekguleryuz (eds), *Magnesium Technology 2009*, TMS, 179–184.
- Dashwood R, Klaumunzer D, Jackson M, Fan Z and Grimes R, 2010, "The development of superplastic magnesium alloy sheet", *Key Engineering Materials*, 433: 273–279.
- Dube D, Fiset M, Couture A and Nakatsugawa I, 2001, "Characterization and performance of laser melted AZ91D and AM60B", *Materials Science and Engineering*, A299: 38–45.
- Dunwoody B, 1999, Presentation at meeting of EURO SPF Group, Kings College London, July.
- Duygulu O, Ucuncuoglu S, Oktay G, Temur D, Yucel O and Kaya A, 2009, "Development of rolling technology for twin roll cast 1500 mm wide magnesium AZ31 alloy", in E Nyberg, S Agnew, N Neelameggham and M Pekguleryuz (eds), *Magnesium Technology 2009*, TMS, 379–384.
- Duygulu O, Ucuncuoglu S, Oktay G, Temur D, Yucel O and Kaya A, 2009, "Development of 1500 mm wide wrought magnesium alloys by twin roll casting technique in Turkey", in E Nyberg, S Agnew, N Neelameggham and M Pekguleryuz (eds), *Magnesium Technology 2009*, TMS, 385–390.
- Ehrenberger S, Schmid S, Song S and Friedrich H, 2008, "Status and potentials of magnesium production in China: Life cycle analysis focussing on CO_{2eq} emissions", World Magnesium Conference.
- Fan Y, Wu G and Zhai C, 2006, "Influence of cerium on the microstructure, mechanical properties and corrosion resistance of magnesium alloy", *Materials Science and Engineering*, A433: 208–215.
- Fechner D, Hort N and Kainer K, 2009, "Magnesium recycling system prepared by permanent mould- and high pressure die casting", in E Nyberg, S Agnew, N Neelameggham and M Pekguleryuz (eds), *Magnesium Technology 2009*, TMS, 110–111.

- Friedrich H and Schumann S, 2001, "Research for a 'new age of magnesium' in the automotive industry", *Journal of Materials Processing Technology*, 117: 276–281.
- Gesing A, Reade N, Sokolowski J, Blawert C, Fechner D and Hort N, 2010, "Development of recyclable magnesium based alloys: AZ91 and AZC1231 phase information derived from heating/cooling curve analysis", in E Nyberg, S Agnew, N Neelameggham and M Pekguleryuz (eds), *Magnesium Technology 2009*, TMS, 97–105.
- Grimes R, Cornish A, Miller W and Reynolds M, 1985, "Aluminium–lithium based alloys for aerospace applications", *Metals and Materials*, 1: 357–363.
- Grimes R, Jackson M, Moorhouse B and Dashwood R, 2008, "The manufacture of superplastic magnesium alloy sheet" *Materialwissenschaft und Werkstoff Technik*, 39: 340–346.
- Hydro press release, December 19, 2008: <http://www.hydro.com/en/Press-room/News/Archive/2008/12/Developing-new-silica-and-magnesium-technology/> International Magnesium Association Weekly Update, Edition 20, May 30, 2008.
- Ion S, Humphreys F and White S, 1982, "Dynamic recrystallisation and the development of microstructure during the high temperature deformation of magnesium", *Acta Metallurgica*, 30: 1909–1919.
- Ji H, Yao G, Liu L, Liu Y and Zu G, 2009, "Ignition-proof magnesium alloy and preparation of magnesium foam", in E Nyberg, S Agnew, N Neelameggham and M Pekguleryuz (eds), *Magnesium Technology 2009*, TMS, 203–207.
- Jung I-H, Bang W, Kim I, Sung H-J, Park W-J, *et al.*, 2007, "Mg coil production via strip casting and coil rolling technologies", in R Beals, A Luo, N Neelameggham and M Pekguleryuz (eds), *Magnesium Technology 2007*, TMS, 85–88.
- Kaya A, Duygulu O, Ucuncuoglu S, Oktay G, Temur, D and Yucel O, 2008, "Production of 150 cm wide AZ31 magnesium sheet by twin roll casting", *Trans Nonferrous Met Soc China*, 18: 185–188.
- Kim W, Kim M and Wang J, 2009, "Ultrafine-grained Mg–9Li–1Zn alloy sheets exhibiting low temperature superplasticity", *Materials Science and Engineering*, A516: 17–22.
- Kim W, Kim M and Wang J, 2009, "Superplastic behaviour of a fine-grained ZK60 magnesium alloy processed by high-ratio differential speed rolling", *Materials Science and Engineering*, A527: 322–327.
- Kim W-J, Chung S, Chung C and Kum D, 2001, "Superplasticity in thin magnesium alloy sheets and deformation mechanism maps for magnesium alloys at elevated temperatures", *Acta Materialia*, 49: 3337–3345.
- Letzig D, Fuskova L, Hantzschke K, Kurz G, Yi S and Bohlen J, 2009, "Formability of magnesium sheets", in E Nyberg, S Agnew, N Neelameggham and M Pekguleryuz (eds), *Magnesium Technology 2009*, TMS, 415–418.
- Liang D and Cowley C, 2004, "The twin-roll strip casting of magnesium", *JOM*, 5: 26–30.
- Luo H, Liu Y, Li T and Zhang Y, 2009, "The influence of calcium and cerium mischmetal on the ignition behaviour of magnesium", in E Nyberg, S Agnew, N Neelameggham and M Pekguleryuz (eds), *Magnesium Technology 2009*, TMS, 173–176.
- Mabuchi M, Ameyama K, Iwasaki H and Higashi K, 1999, "Low temperature superplasticity of AZ91 magnesium alloy with non-equilibrium grain boundaries", *Acta Materialia*, 47: 2047–2057.
- Magnesium Elektron web site, www.magnesium-elektron.com
- Magnesium Monthly Review*, 39(5): 10, June 28th 2010.
- Magnesium Monthly Review*, 39(5): 1, June 28th 2010.
- Materials World*, 2003, "The magnesium sheet casting process: The process, properties, economics, advantages and capabilities" *Materials World*, 11: 29–30.

- Materials World*, 2006, “Sustainable Scientists”, *Materials World*, 14: 26–27.
- Mendis C, Oh-ishi K and Hono K, 2009, “Age hardening response and microstructures of ZK60 alloy with Li additions”, in E Nyberg, S Agnew, N Neelameggham and M Pekguleryuz (eds), *Magnesium Technology 2009*, TMS, 393–398.
- Mohri T, Mabuchi M, Nakamura M, Asahina T, Iwasaki H, *et al.*, 2000, “Microstructural evolution and superplasticity of rolled Mg–9Al–1Zn”, *Materials Science and Engineering*, A290: 139–144.
- Moll F, Schumann S and Friedrich H, 2003, “Application of Mg sheets in car body structures”, Volkswagen AG paper, *Euromotor2003_vw_04112003_1510.doc*
- Ohara M, Takigawa Y and Higashi K, 2009, “New surface treatment for developing luster on AZ31 magnesium alloy in industrial scale”, in E Nyberg, S Agnew, N Neelameggham and M Pekguleryuz (eds), *Magnesium Technology 2009*, TMS, 343–345.
- Park S, Park W-J, Kim C, You B and Kim M, 2009, “The twin roll casting of magnesium alloys”, *JOM*, 61: 14–17.
- Patzner G, 2010, “The magnesium industry today . . . the global perspective”, in E Nyberg, S Agnew, N Neelameggham and M Pekguleryuz (eds), *Magnesium Technology 2010*, TMS, 85–90.
- Pong I, 2006, Results described in article “Sustainable Scientists”, *Materials World*, 14: 26–27.
- Prentice L, Poi N and Haque N, 2010, “Life Cycle Assessment of Carbothermal Production of Magnesium in Australia”, Presentation at 2010 World Magnesium Conference.
- Rohatgi A, Herling D and Nyberg E, 2010, “Characterisation of continuous cast AZ31B magnesium alloy sheets and lubricants for warm-forming-friction effects”, in E Nyberg, S Agnew, N Neelameggham and M Pekguleryuz (eds), *Magnesium Technology 2010*, TMS, 573–578.
- Shepelev D, Edelshtein G, Bamberger M and Katsman A, 2009, “Evolution of grain boundary depleted zones in Mg–Ca–Zn alloy stabilised by Zr additions”, in E Nyberg, S Agnew, N Neelameggham and M Pekguleryuz (eds), *Magnesium Technology 2009*, TMS, 151–154.
- Somekawa H, Hosokawa H, Watanabe H and Higashi K, 2003, “Diffusion bonding in superplastic magnesium alloys”, *Materials Science and Engineering*, A339: 328–333.
- Sun H, Shi Y-N, Zhang M-X and Lu K, 2007, “Plastic strain-induced grain refinement in the nanometer scale in a Mg alloy”, *Acta Materialia*, 55: 975–982.
- Superform Aluminium AZ31B Technical Brochure: <http://www.superformusa.com/TECHNICAL/datasheets/MagnesiumDataSheet.pdf>
- Tan J and Tan M, 2002, “Superplasticity in a rolled Mg–3Al–1Zn alloy by two-stage deformation method”, *Scripta Materialia*, 47: 101–106.
- Thyssen Krupp Steel, 2002, “World premiere: First magnesium strip produced by casting-rolling”, Press release, 26 September, 2002. http://www.thyssenkrupp.com/en/presse/art_detail.html&eid=tk_pnid648
- Underwood E, 1962, “A review of superplasticity”, *Journal of Metals*, 14: 914–919.
- US AMP Magnesium Vision 2020, Released 11 01 2006 www.uscar.org/commands/files_download.php?files_id=99
- Wang S and Chou C, 2008, “Effect of adding Sc and Zr on grain refinement and ductility of AZ31 magnesium alloy”, *Journal of Materials Processing Technology*, 197: 116–121.
- Watanabe H, Mukai T, Ishikawa K, Mohri T, Mabuchi M and Higashi K, 2001, “Superplasticity of a particle strengthened WE43 magnesium alloy”, *Materials Transactions of the Japanese Institute of Metals*, 42: 157–162.

- Watanabe H, Mukai T, Mabuchi M and Higashi K, 1999, "High-strain-rate superplasticity at low temperature in a ZK61 magnesium alloy produced by powder metallurgy", *Scripta Materialia*, 41: 209–213.
- Watari H, Davey K, Rasgado M, Haga T and Izawa S, 2004, "Semi-solid manufacturing process of magnesium alloys by twin-roll casting", *Journal of Materials Processing Technology*, 155–156: 1662–1667.
- Wei Y, Wang Q, Zhu Y, Zhou H, Ding W, *et al.*, 2003, "Superplasticity and grain boundary sliding in rolled AZ91 magnesium alloy at high strain rates", *Materials Science and Engineering*, A360: 107–115.
- Wu G, Fan Y, Gao H, Zhai C and Zhu Y, 2005, "The effect of Ca and rare earth elements on the microstructure, mechanical properties and corrosion behavior of AZ91D", *Materials Science and Engineering*, A408: 255–263.
- Xia X, Wang Y, Li H, Arumuganathar S, Zuo Y, *et al.*, 2009, "Refinement of solidification microstructures by MCAST process", in E Nyberg, S Agnew, N Neelameggham and M Pekguleryuz (eds), *Magnesium Technology 2009*, TMS, 135–140.
- Yang C-W, Lui T-S and Chen L-H, 2010, "Tensile mechanical properties and the ductile to brittle transition behaviour Mg–Li–Al–Zn alloy", in E Nyberg, S Agnew, N Neelameggham and M Pekguleryuz (eds), *Magnesium Technology 2009*, TMS, 455–459.
- Zu G, Li T and Yao G, 2009, "Study on Rolling Process of Mg–9Li–2Zn Alloy Plate", in E Nyberg, S Agnew, N Neelameggham and M Pekguleryuz (eds), *Magnesium Technology 2009*, TMS, 527–530.

Superplastic micro-tubes fabricated by dieless drawing processes

T. FURUSHIMA and K. MANABE,
Tokyo Metropolitan University, Japan

Abstract: This chapter describes a novel manufacturing process of micro-tubes utilizing a dieless drawing technique. The chapter first discusses the principle of a dieless drawing process for micro-tubes of superplastic and conventional materials. To achieve local heating for the tube, several heating systems (such as high frequency induction heating and laser heating) are discussed, and the advantages of the superplastic dieless drawing process from the viewpoints of productivity and quality, and its industrial applications are described. The chapter then describes the finite element model of this process. As another application, the chapter discusses advanced dieless forming, which can control various axial and cross-sectional profiles.

Key words: micro-tube, dieless drawing, local heating, superplasticity, product quality, profile control, geometrical similarity law in cross-section.

14.1 Introduction

Micro-tubes are commonly required for micro-components, e.g. micro-nozzles, painless injection and micro-exchangers. The manufacture of micro-tubes using die drawing techniques with tools such as dies, plugs and mandrels has advanced markedly. However, it is not easy to scale down the conventional process to the micro-scale. It is increasingly difficult to fabricate a micro-tool with high accuracy, and also to insert a plug and a mandrel into a micro-tube. In addition, the increase in frictional resistance between the tool and the micro-tube, due to the size effect with miniaturization, causes a decrease in the forming limit. Thus, the development of new drawing technologies for fabrication of micro-tubes without tools such as dies, plugs and mandrels has become necessary.

From this background, a dieless drawing process, utilizing the superplastic characteristic with great ductility, was initiated by the authors to fabricate micro-tubes. Tools are unnecessary in this process. Thus, there is no need to consider the technical issues of such tools in this process in contrast with the conventional die drawing process. Additionally, this process can be realized with a high flexibility.

In this chapter, the characteristics of a superplastic dieless drawing process for fabrication of micro-tubes are described. The effectiveness of superplastic dieless drawing for fabrication of micro-tubes is demonstrated. Specifically, the dieless drawing experiment was conducted to fabricate micro-tubes of Zn-22%Al alloy.

In addition, the effect of the number of drawing passes on the surface roughness, and the microstructure of superplastic micro-tubes fabricated by dieless drawing, was investigated and the effectiveness of the drawing process was demonstrated experimentally and numerically. Furthermore, finite element (FE) simulation coupled with thermo-mechanical analysis of superplastic dieless drawing is described to show the effect of each factor on the drawing behavior. In addition, the dieless drawing techniques for special applications, such as fabrication of non-circular tubes and taper tubes by controlling the deformation profile using a drawing speed control technique, are explained.

14.2 Industrial application of micro-tubes

Recently, the manufacture of ultrafine and high-precision processed components has led to the enhancement of the functions of medical and biological equipment, and equipment used for communication, measurement, and information storage, and has contributed to developments in the fields of microsystem technologies (MST) and micro-electro-mechanical systems (MEMS). Micro-forming is an important technology for fabricating very small metal components that are required in many industrial products (Engel and Eckstein, 2002; Vollertsen *et al.*, 2004). The current main micro-forming technology is very advanced in lithographic technologies (Rangelow and Hudek, 1995), but costs are comparatively high and the number of different materials is quite limited. Thus, metal forming technologies which can realize mass and high-speed production should be established in the fabrication of micro-parts and many research studies are being carried out in this field.

Conventional macro-scale metal tubes have been used for structural components in the automobile field for weight saving and high rigidity, and with plumbing pipes for fluid and gas. However, metal micro-tubes provide not only components for weight saving and high rigidity, but also special application for micro-parts by taking advantage of the micro-hollow structure of the metal micro-tubes. The metal micro-tubes are expected to be used in various apparatus, such as mechanical/structural components, electrode tubes for electrical discharge machining (EDM), cooling micro-nozzles used in micro-machines, laser accelerators, optical-fiber contact probes, and painless injection, sensors for fluid and gas as shown in Table 14.1. For example, in laser accelerators used in the optical engineering field, the electron is accelerated successfully into 100 million volts by passing laser beam through the micro-tube with an inner diameter of several tens of micrometers (Kitagawa, 2005). In addition, the micro-heat exchanger with many micro-channels using titanium decomplex micro-tubes is used for components such as marine facilities for cooling gas (Hallmark, 2008). Furthermore, as an important application of micro-tube technology, a painless injection is used. Miniaturizing of the injection into micro-scale becomes effective in eliminating pain (Tsuchiya, 2010). Thus, the mental and physical pain given by the

Table 14.1 Application of metal micro-tubes

Industrial fields	Applicable product	Materials
Medical	Painless injection needle	Stainless steel
	Catheter	Titanium/Ti alloy
	Stent	Magnesium/Mg alloy
	Needle for cosmetic surgery	
Electrical and electronics	Contact probe	Nickel/Ni alloy
	Electrode tube for EDM	Copper/Cu alloy
Optoelectronics	Optical fiber	Nickel/Ni alloy
	Laser accelerator	Kovar
Chemical parts	Micro-reactor	Stainless steel
	Micro-nozzle	Titanium/Ti alloy
Sensing parts	Differential pressure detector for gas	Platinum/Pt alloy
	Micro-quantitative analysis device	Tungsten/W alloy
Heat transfer field	Micro-heat exchanger	Titanium/Ti alloy Aluminum/Al alloy

administration of insulin can be reduced. In this way, metal micro-tubes may have many applications in various fields by taking advantage of the micro-hollow structure.

14.3 Fundamentals of dieless drawing processes

14.3.1 Principle of dieless drawing using a local heating technique

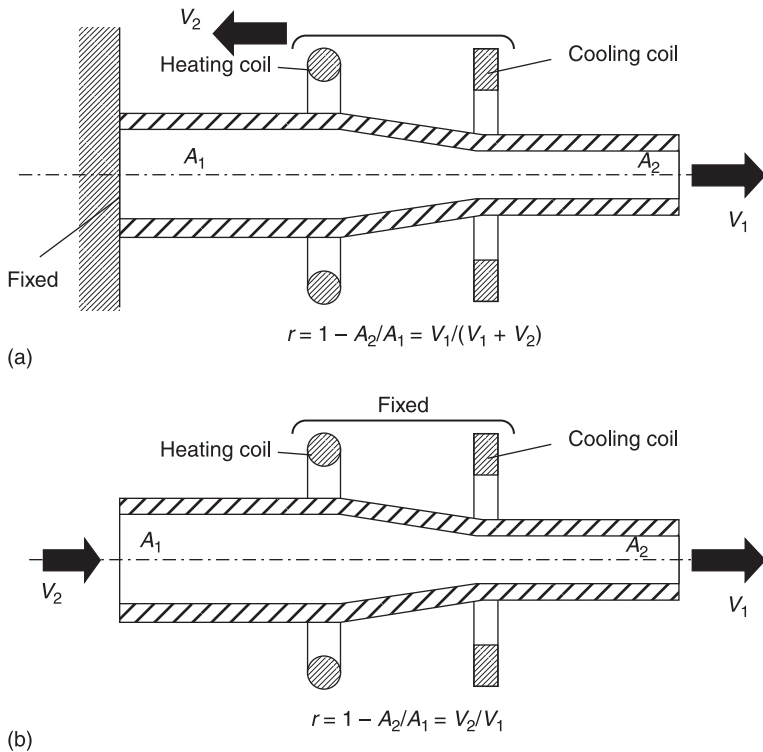
A drawing process, using tools such as dies, plugs and mandrels, etc., has been used as a conventional process for miniaturization of tubes. However, it is not easy to scale down the conventional process to the micro-scale. There are many problems related to the tools, and it is increasingly difficult to fabricate a micro-tool with high accuracy, and to insert a plug and a mandrel into a fine tube. Thus, the development of new drawing technologies to fabricate micro-tubes without tools such as dies, plugs and mandrels is necessary.

Meanwhile, the dieless drawing techniques have been investigated since 1969 by Weiss and Kot (1969). The dieless drawing is a unique deformation process without the need for conventional dies. The dieless drawing by the use of local heating and cooling devices of metal wires, bars and tubes replaces the conventional die drawing, which is subjected to tensile deformation. This technique can achieve a great reduction of materials in a single pass by the local heating and cooling approach compared with the conventional die drawing.

There are two typical types of dieless drawing process (Sekiguchi *et al.*, 1974). One is a non-continuous dieless drawing as shown in Fig. 14.1(a). In this process, a tube is fixed at one end, and is heated and cooled at the other. It is then pulled at the other end with tensile speed V_1 , while the heater and cooler are moved in the opposite direction at V_2 . Since the heated part of the tube has a low flow stress, necking occurs only in this region. The necking is diffused out by the continuous motion of the heater and cooler, achieving a large reduction in tube size in a single pass drawing. The relationship between the reduction in area r and the speed ratio V_1/V_2 is formulated as:

$$r = 1 - A_2/A_1 = V_1/(V_1 + V_2). \tag{14.1}$$

The other type of dieless drawing is a continuous dieless drawing process as shown in Fig. 14.1(b). The heating and cooling devices are fixed and the metal tube moves from left to right through the heating zone. Concurrently, the workpiece is subjected to tension by the difference in speed between pulling V_1 and feeding V_2 . The flow stress of materials is reduced significantly and the ductility is enhanced considerably at elevated temperature. The local temperature increase causes a plastic deformation. Necking occurs at the locally heated end,



14.1 Schematic illustration of dieless drawing processes: (a) non-continuous processing type and (b) continuous processing type.

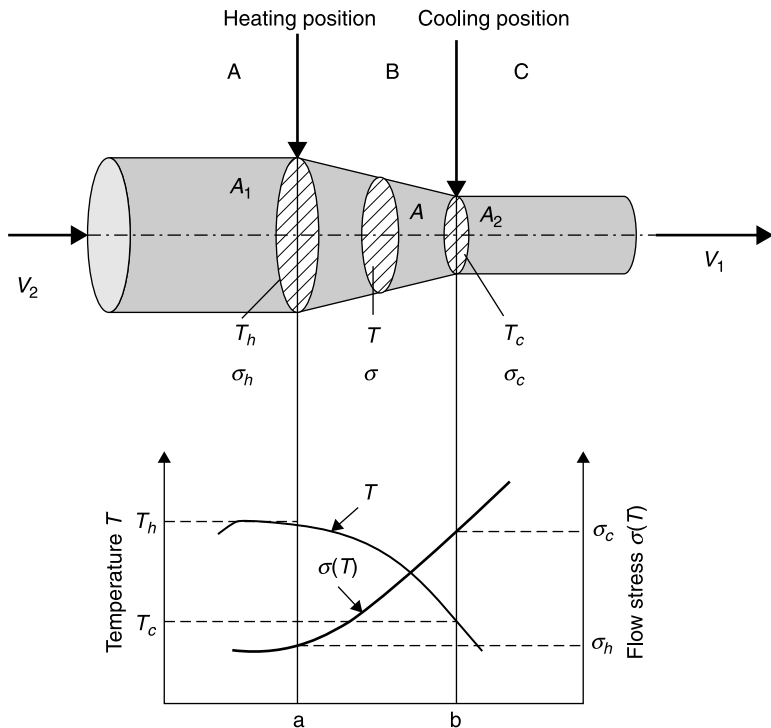
and diffuses out with the moving, heating and cooling devices, achieving a large reduction in area in a single pass drawing. The relationship between the reduction in area r and the speed ratio V_2/V_1 is as follows.

$$r = 1 - A_2/A_1 = 1 - V_2/V_1 \tag{14.2}$$

In general, the forming limit in the dieless drawing processes depends on the difference in the flow stress between the heated and cooled areas on the basis of basic equilibrium equation (Sekiguchi and Kobatake, 1987). Figure 14.2 shows the schematic illustration of deformation profile, temperature and flow stress distribution in the axial direction during the dieless drawing process. The relationship between the theoretical limiting reduction in area r_c , and the flow stresses at the heated and cooled parts, σ_h and σ_c respectively, can be expressed as

$$r_c = 1 - \sigma_h/\sigma_c \tag{14.3}$$

This means that by applying superplastic materials, which exhibit extremely low flow stress at the elevated temperatures in this process, further improvement of the forming limit can be achieved. Thus, a great reduction in area to the micro-scale is realized in the superplastic dieless drawing process.



14.2 Schematic illustration of temperature and flow stress distribution in the axial direction during a dieless drawing process.

14.3.2 History of dieless drawing processes

Table 14.2 shows the historical background of the study on dieless drawing processes. The concept of dieless drawing techniques was introduced by Weiss *et al.* (1969), who applied it to steel and titanium (Ti) alloy rods, and achieved a reduction in area of 50%. Alexander *et al.* (1974) used SUS304 and Ti alloy rods and bars in dieless drawing. Sekiguchi *et al.* (1974) investigated the dieless draw abilities of carbon steels, SUS304, and pure titaniums. They successfully

Table 14.2 History of the studies on dieless drawing processes

Date	Experimental work	Analytical and numerical work
~1970s	<p>First report of a dieless drawing process (Weiss and Kot, 1969)</p> <p>Dieless drawing for steel, titanium alloy and stainless steel (Weiss and Kot, 1969; Alexander <i>et al.</i>, 1974; Sekiguchi <i>et al.</i>, 1976)</p> <p>Manufacturing of a taper and stepped tube (Kobatake <i>et al.</i>, 1979)</p>	<p>Fundamental analysis of dieless drawing (Price <i>et al.</i>, 1977)</p>
1980s	<p>Development of a dieless drawing machine with computer control for superplastic materials (Saotome <i>et al.</i>, 1986)</p>	<p>FE simulation for temperature distribution in dieless drawing (Kobatake <i>et al.</i>, 1980)</p> <p>Analysis of limiting the reduction in area in dieless drawing under steady state (Sekiguchi <i>et al.</i>, 1985)</p>
1990s		<p>Coupled thermo-mechanical analysis of dieless drawing under steady state (Pawelski <i>et al.</i>, 1995; Fortunier <i>et al.</i>, 1997)</p> <p>Analysis of drawing load and velocity field in dieless drawing (Wang <i>et al.</i>, 1999)</p>
2000s	<p>Thermomechanical treatment using dieless drawing (Carolan <i>et al.</i>, 2004; Eynatten <i>et al.</i> 2004)</p> <p>Fabrication of metal micro-tubes using dieless drawing (Furushima <i>et al.</i>, 2004; 2007a; 2007b; 2008; 2011)</p> <p>Effective temperature distribution and drawing speed path for dieless drawing (Furushima and Manabe, 2009)</p>	<p>Fundamental analysis for controlling taper tube by dieless drawing (Wengenroth <i>et al.</i>, 2001)</p> <p>FE simulation coupled with thermo-mechanical analysis for dieless drawing under non-steady state (Furushima <i>et al.</i>, 2004; 2007a; 2007b; 2009)</p>

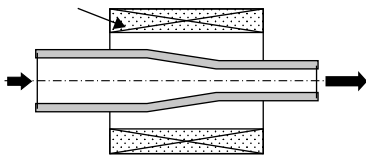
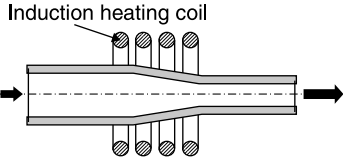
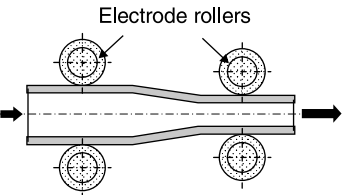
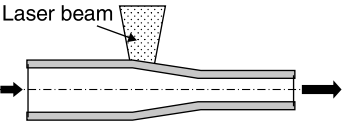
formed tapered rods, various cross-section bars, circular tubes and clad wire rods by using the flexibility of dieless drawing. Saotome *et al.* (1986) developed a continuous dieless drawing machine with computer control using the transformation superplasticity characteristics of titanium alloy. Carolan *et al.* (2004) and Eynatten and Reissner (2004) indicated that a wide variety of micro-structures and mechanical properties were obtained using different dieless drawing strategies. In addition, Furushima and Manabe (2007a) and Furushima *et al.* (2008a) applied dieless drawing to superplastic metal tubes for the fabrication of micro-tubes. In the main part, Section 14.4 of this chapter, fabrication of superplastic micro-tubes using a dieless drawing process is described. This section shows that dieless drawing techniques have wide applications.

Meanwhile, the dieless drawing process has many influencing factors on deformation behavior because of its high flexibility without using any dies. Thus, it takes time to obtain the effective forming conditions for a dieless drawing process experimentally. An analytical approach is required to speed up the development time and improve efficiency. Price and Alexander (1977) reported their fundamental analysis and FE simulation of deformation behavior in dieless drawing under steady state. Kobatake *et al.* (1977) calculated the temperature distribution by assuming a deformation profile using FE simulation. In addition, the velocity field and drawing force were analyzed by an energy method (Wang *et al.*, 1999). In the 1990s, a coupled thermo-mechanical analysis was reported by some researchers. In the studies, the deformation profile and temperature distribution were calculated during the dieless drawing under steady state to investigate the effect of temperature distribution on drawing speed, and the effect of drawing force on reduction in area (Pawelski and Kolling, 1995; Wengenroth *et al.*, 2001). In the 2000s, Furushima *et al.* developed the FE model with a coupled thermo-mechanical analysis to study deformation behavior and temperature distribution under non-steady state (Furushima *et al.*, 2004; Furushima and Manabe, 2007b; 2009). The detail of the FE simulation of superplastic dieless drawing is shown in Section 14.5.

14.3.3 Heating system

To make dieless drawing successful, appropriate local heating conditions should be required. To achieve the local heating condition, the heating and cooling system is very important for this process. In this section, the heating and cooling methods are described. Table 14.3 shows the heating and cooling method used in the process for fabrication of micro-tubes. As heating sources, there is electric furnace heating, high-frequency induction heating, direct resistance heating and laser heating. The high-frequency induction heating is more commonly used for the heating source of the process. Local and rapid heating can be realized by high-frequency induction heating. In recent years, laser heating has been used for

Table 14.3 Classification of heating methods for dieless drawing processes

Heating method	Local heating	Rapid heating	Heating efficiency	Controllability
Electric furnace heating Electric furnace 	Poor	Poor	Poor	Not good
Induction heating Induction heating coil 	Good	Good	Excellent	Good
Direct resistance heating Electrode rollers 	Bad	Excellent	Excellent	Good
Laser heating Laser beam 	Excellent	Not good	Good	Good

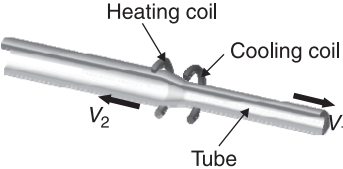
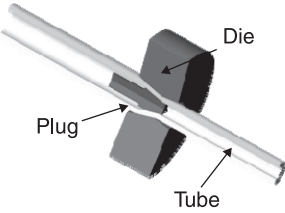
micro-tubes in the dieless drawing process (Li *et al.*, 2002a; 2002b; 2003). The small spot size of the laser for the micro-tube can be decreased easily by the design of the optical systems. The direct resistance heating method is highly effective because a workpiece is heated from the inside by electrifying it directly. Thus, direct resistance heating is suitable for continuous dieless drawing. At the same time, it is difficult to make a local heating condition using direct resistance heating. Each heating method has its advantages and disadvantages. Therefore, we should choose the right heating method for the right conditions in dieless drawing.

14.3.4 Advantages and disadvantages of dieless drawing

Conventional drawing processes with dies, plugs and mandrels have been used in the miniaturization of tubes. However, it is difficult to scale down the conventional process for the smaller sizes. There are many problems related to the tools as it is increasingly difficult to fabricate a micro-tool with high accuracy, and to insert a plug and a mandrel into a fine tube. Thus, the development of new drawing technologies to fabricate micro-tubes without tools such as dies, plugs and mandrels is necessary.

On the contrary, the dieless drawing has the advantage of a larger reduction in area, no tools and dies, and the flexibility of the process compared with die drawing processes. The dieless drawing is a unique deformation process without the need for conventional dies. However, the dieless drawing process has some considerable problems for fabrication of micro-tubes. For this process, the roughening phenomenon on the free surface is the overwhelmingly dominant factor, because the surface smoothing mechanism caused by sliding between the tube and the tool cannot be expected. Therefore, investigation of the roughening phenomenon on the free surface during the process is necessary. Furthermore, the heat transfer behavior is closely related to the deformation behavior in dieless drawing. It takes time to raise the temperature of tubes generally, thus it is difficult to draw the tube at high speed in the drawing region. Table 14.4 shows the advantages and issues of die drawing and superplastic dieless drawing.

Table 14.4 Advantages and disadvantages of dieless tube drawing processes compared with conventional die tube drawing processes

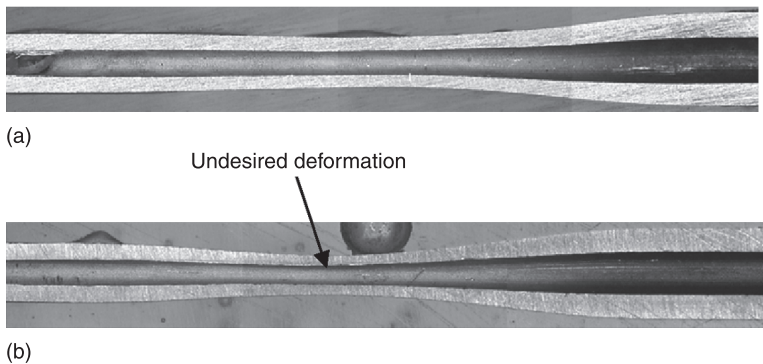
	Dieless drawing	Die drawing
Outline		
Advantage	Without tools High flexibility No friction Large reduction in area	High speed drawing High surface quality High accurate profile
Disadvantage	Free surface roughening Low drawing speed Low accurate profile Many control parameters	With tool Low flexibility With friction Low reduction in area

14.4 Superplastic dieless drawing processes

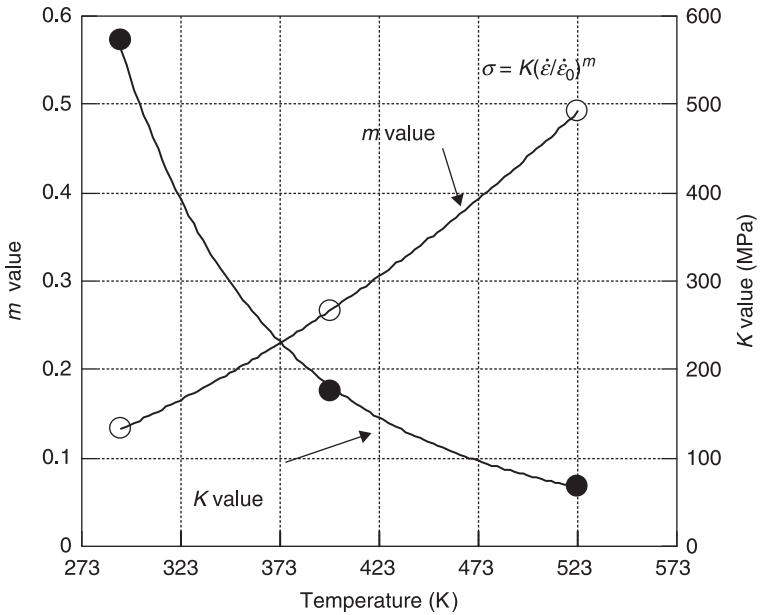
14.4.1 Effect of heating conditions

In the dieless drawing process, the heating conditions such as heating temperature and temperature distribution affect deformation behavior during dieless drawing. Here, the effect of the heating temperature on the deformation profile is described (Furushima *et al.*, 2008). The material used is Zn–22%Al, a superplastic alloy with outer and inner diameter of $D = 2$ mm and $d = 1$ mm, respectively. Photographs of longitudinal cross-sections of the Zn–22%Al superplastic tubes deformed by drawing at 473 K and 523 K are shown in Fig. 14.3. Here, dieless drawing was carried out under the conditions of $V_1 = 7.2$ mm/min and $V_2 = 3.6$ mm/min ($r = 66.7\%$) by non-continuous style. Although drawing was possible at both temperatures, necking was generated at the heating temperature $T_h = 473$ K in the initial stage of the fabrication owing to the undesired deformation, whereas undesired deformation is suppressed in the case of $T_h = 523$ K. From the temperature dependency of material properties based on $\sigma = K\dot{\epsilon}^m$ of a Zn–22%Al tube shown in Fig. 14.4, it is found that the values of m are approximately 0.5 and 0.4 at 523 K and 473 K, respectively. When a part of the material starts to undergo local deformation during drawing at $T_h = 523$ K, the flow stress increases with increasing strain rate at that part, suppressing the growth of the local deformation. As a result, the undesired deformation was suppressed in the case of $T_h = 523$ K when m was greater, but was locally generated in the case of $T_h = 473$ K. During this drawing, most of the fracture occurred in the initial stage. Therefore, for successful fabrication, it is important to select an appropriate temperature corresponding to a sufficiently large value of m .

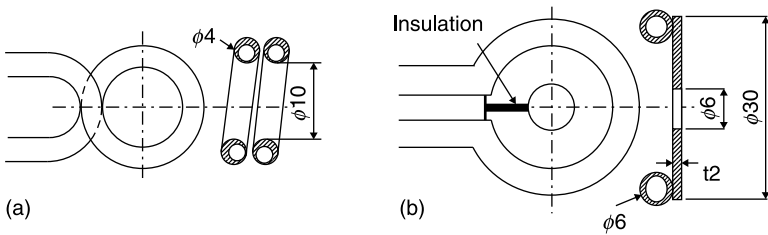
To investigate the effect of temperature distribution on the deformation behavior in dieless drawing, two types of heating coil were used. Figure 14.5(a)



14.3 Photograph of Zn–22%Al superplastic tubes after the dieless drawing process at heating temperature of (a) $T_h = 573$ K and (b) $T_h = 473$ K.

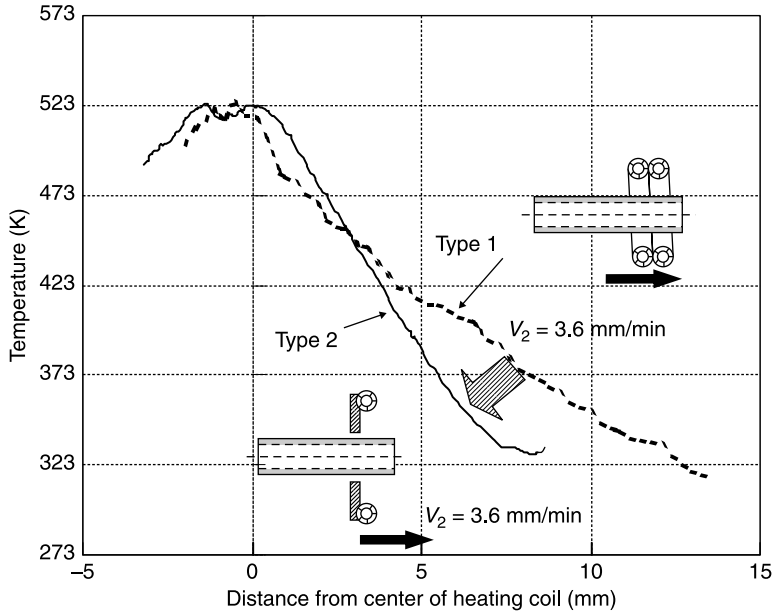


14.4 Temperature dependency of superplastic material properties for Zn-22%Al alloy tube obtained from jump tensile tests.

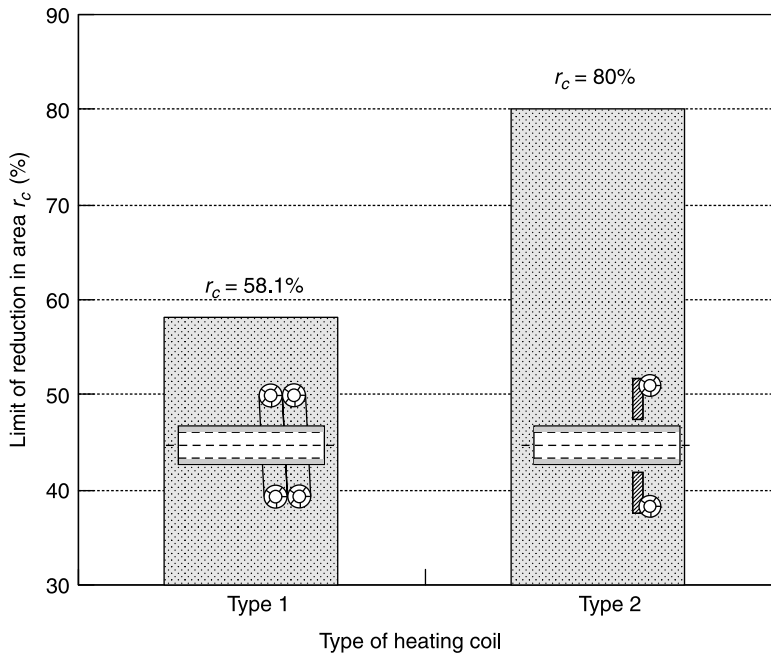


14.5 (a) A coil made of two loops of copper pipe with an inner diameter of 10 mm and a width of 6.5 mm (Type 1); (b) a special coil with an inner diameter of 6 mm and a width of 1 mm.

shows a coil made of two loops of copper pipe with an inner diameter of 10 mm and a width of 6.5 mm (Type 1). Figure 14.5(b) shows a special coil with an inner diameter of 6 mm and a width of 1 mm, which was made for the purpose of reducing the width of the heating region and the distance between the specimen and the coil (Type 2). Figure 14.6 shows the temperature distribution of the specimen under $V_1 = V_2 = 3.6$ mm/min. The heating length of Type 2 is shorter than that of Type 1. Figure 14.7 shows a comparison between the limiting reduction in area for Type 1 and Type 2 heating coils. The limiting reduction in area for Type 1 was 58.1% and that for Type 2 was 80%. As a result, this reveals that the limiting reduction in area is improved by decreasing the heating length.



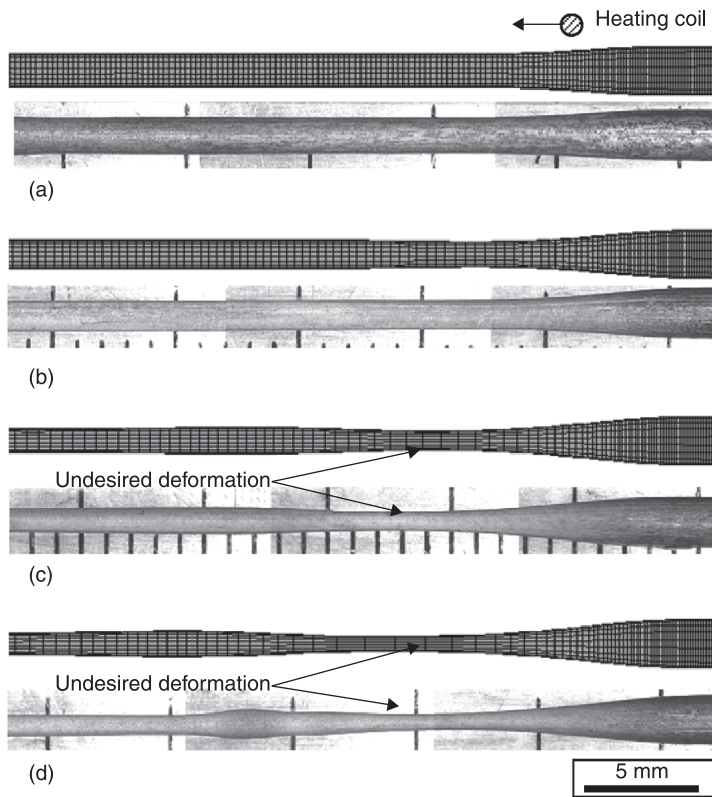
14.6 Effect of type of heating coil length on temperature distribution in dieless drawing.



14.7 Effect of length of heating coil on limiting reduction in area in dieless drawing.

14.4.2 Deformed shape after superplastic dieless drawing

The reduction in area can be controlled by speed ratio as shown in Eq. [14.1] or Eq. [14.2]. The deformation behavior of tubes with increasing r is described in a single pass drawing. Figure 14.8 shows the deformation profiles of tubes after a single pass drawing at various tensile speeds, V_1 (Furushima and Manabe, 2009). Undesired deformations are observed at early drawing stages at $r = 75$ and 80% , as shown in Fig. 14.8(c) and (d). Actually, the fracture of tubes may occur due to undesired deformation at the early drawing stages. The limiting reduction in area was 80% , and the tubes were fractured at greater reductions in area in the experiment. A tube with outer and inner diameters of $D = 894 \mu\text{m}$ and $d = 496 \mu\text{m}$, respectively, was fabricated at $r = 80\%$ in a single pass drawing. Undesired deformations occur if finer tubes are fabricated by a single pass drawing. Therefore, multi-pass dieless drawing is essential for fabricating finer micro-tubes.



14.8 Comparison of deformed shapes between FE simulation and experiment: (a) $V_1 = 3.6 \text{ mm/min}$, $V_2 = 3.6 \text{ mm/min}$, $r = 50\%$; (b) $V_1 = 7.2 \text{ mm/min}$, $V_2 = 3.6 \text{ mm/min}$, $r = 66.7\%$. (c) $V_1 = 10.8 \text{ mm/min}$, $V_2 = 3.6 \text{ mm/min}$, $r = 75\%$; and (d) $V_1 = 14.4 \text{ mm/min}$, $V_2 = 3.6 \text{ mm/min}$, $r = 80\%$.

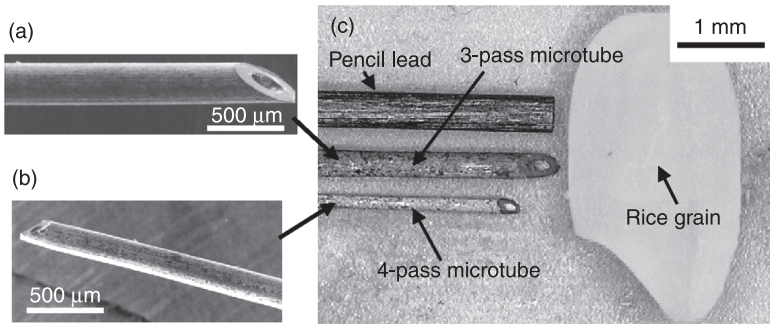
14.4.3 Fabrication of micro-tubes

The reduction in area of 66.7%, under which the deformation profile was stable at early drawing stages and a large reduction in area was obtained easily, was selected not only for a single pass drawing but also for multi-pass dieless drawing. After a 4-pass dieless drawing, a micro-tube with outer and inner diameters of $D = 190 \mu\text{m}$ and $d = 91 \mu\text{m}$, respectively, was fabricated successfully, as shown in Fig. 14.9 (Furushima and Manabe, 2007a). In addition, Fig. 14.10 shows the relationship between the diameter ratio d/D and outer diameter D from experimental results. It is confirmed that d/D remains a constant value in this process. In other words, the geometrical similarity law in the cross-section is satisfied when the tube is miniaturized to the micro-scale. Micro-tubes can be fabricated successfully without the closing phenomenon of a hollow tube and without any tools. Therefore the geometrical similarity law in the cross-section is an essential characteristic in this process. The experimental results also demonstrated that the multi-pass dieless drawing process is effective for the fabrication of fine micro-tubes.

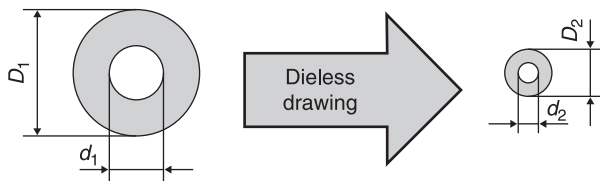
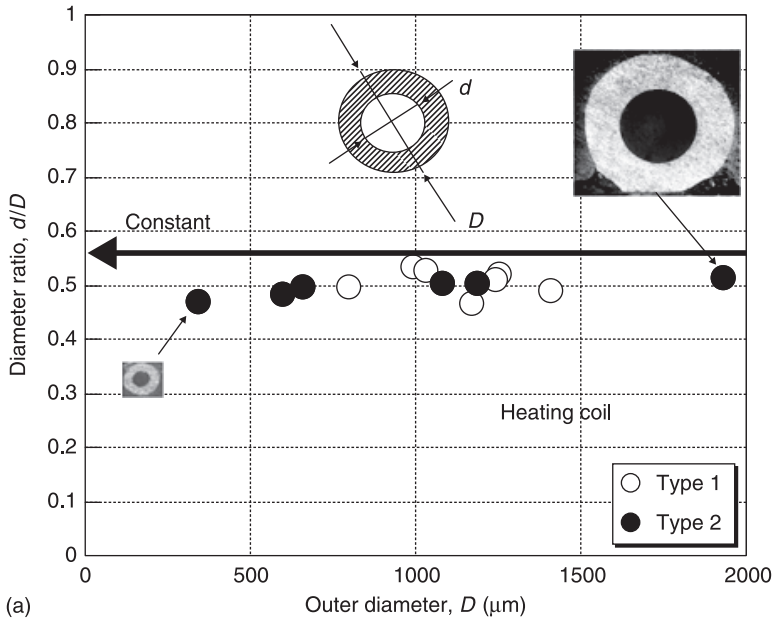
This process, as mentioned above, satisfies the geometrical similarity law in the cross-section. This mechanism for circular tubes can be explained on the basis of results in the following fundamental analysis (Furushima and Manabe, 2007b). The stress state of a tube locally heated in dieless drawing is assumed to be in a uniaxial stress state, and the material is considered isotropic in the model. The circumferential strain ε_θ and the thickness strain ε_t can be calculated using

$$\varepsilon_\theta = \ln(D_1/D_0), \quad \varepsilon_t = \ln(t_1/t_0) \quad [14.4]$$

where D and t represent the outer diameter and wall thickness of the tube, respectively. The suffixes 0 and 1 represent the inlet and outlet tubes in dieless



14.9 Photograph of superplastic micro-tubes fabricated by a multi-pass dieless drawing process: (a) 3-pass micro-tube with outer and inner diameters of $D = 343 \mu\text{m}$ and $d = 161 \mu\text{m}$; (b) 4-pass micro-tube with $D = 190 \mu\text{m}$ and $d = 91 \mu\text{m}$; and (c) comparison of micro-tube fabricated with pencil lead and rice grain.



Geometrical similarity law in cross-section
 $d_1/D_1 = d_2/D_2 = \text{constant}$

(b)

14.10 Satisfaction of the geometrical similarity law in cross-section in dieless drawing: (a) variation in tube diameter ratio, d/D , under various drawing conditions and (b) schematic illustration of geometrical similarity law in cross-section.

drawing, respectively. Using volume constancy, the relation between ϵ_θ and ϵ_t is represented as $\epsilon_\theta = \epsilon_t$, i.e.:

$$D_1/D_0 = t_1/t_0 \tag{14.5}$$

Therefore, Eq. [14.5] yields

$$d_0/D_0 = d_1/D_1 = \text{const.} \tag{14.6}$$

where d represents the inner diameter. Hence, Eq. [14.6] indicates the principle of satisfying the geometrical similarity law in the cross-section.

14.5 FE simulation of superplastic dieless drawing processes

14.5.1 Finite element model

Finite element simulation is a useful tool to clarify the effect of the forming condition on the deformation and heat transfer behaviors in the efficiency of the dieless drawing process. The FE model for superplastic dieless drawing, which is made by MSC Marc/Mentat, is described in this section. The coupled thermo-mechanical FE simulation was carried out (Furushima and Manabe, 2009). As shown in Fig. 14.11, an axisymmetric model was used in the FE model. The left end of the tube was fixed and tensile deformation was applied to the right end of the tube at tensile speed V_1 for modeling of the non-continuous dieless drawing process.

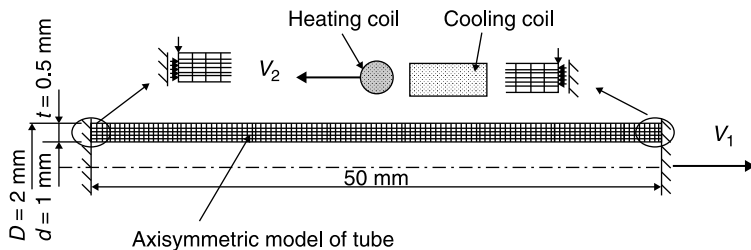
14.5.2 Boundary conditions

The temperature distribution of the tube during dieless drawing was changed in accordance with the heat supplied from the heating coil, the heat conduction inside the tube, and the heat transfer from the tube to the cooling air from the cooling coil and that from the tube to the atmosphere. The heat conduction equation of the axisymmetric model in an unsteady state considering the above factors is expressed as:

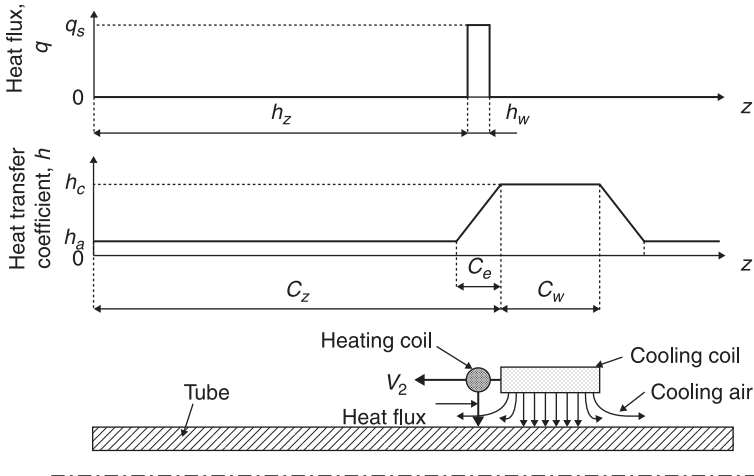
$$\lambda \left\{ \frac{1}{r} \frac{\partial}{\partial r} \left(r \frac{\partial T}{\partial r} \right) + \frac{\partial^2 T}{\partial z^2} \right\} - c\rho \frac{\partial T}{\partial t} + \dot{Q} = 0. \quad [14.7]$$

Here, λ is the thermal conductivity, c is the specific heat, ρ is the mass density, and \dot{Q} is the heat generated per unit time and unit volume.

The tube is heated by the heat supplied from the heating coil and cooled by the cooling air from the cooling coil and the atmosphere. In this analysis, the boundary conditions for the heat transfer at the tube boundaries are as shown in Fig. 14.12.



14.11 Axisymmetric FE model of the dieless drawing process (non-continuous processing type).



14.12 Heat transfer model on tube surface in FE simulation of the dieless drawing process.

The heat is transferred through these boundaries, where the following boundary conditions are satisfied.

Heat is transferred to the tube surface by the heating coil, and the following boundary condition is satisfied on the tube surface.

$$-\lambda \frac{\partial T}{\partial n} = q \tag{14.8}$$

The heat flux q outside the heating coil ($z < h_z$ and $h_z + h_w \leq z$) is defined as

$$q = 0 \tag{14.9}$$

and that inside the heating coil ($h_z \leq z < h_z + h_w$) is defined as

$$q = q_s \tag{14.10}$$

Here, h_z is the position coordinate of the heating coil on the z axis, h_w is the width of the heating coil, and q_s is the amount of heat flux supplied.

Because the heating coil is moved at speed V_2 in time t , h_z is expressed as

$$h_z = h_{z0} - V_2 t \tag{14.11}$$

Here, h_{z0} is the initial position coordinate of the heating coil on the z axis.

Heat transfer occurs between the tube surface and the cooling air from the cooling coil and between the tube surface and the atmosphere, and the following boundary condition is satisfied:

$$-\lambda \frac{\partial T}{\partial n} = h(T - T_c) \tag{14.12}$$

Here, h is the heat transfer coefficient and T_c is the atmospheric temperature. In the analysis, the air flowing from the inside to the outside of the cooling coil was modeled assuming that h gradually changes. Namely, h outside the cooling coil ($z < c_z - c_e$ and $c_z + c_w + c_e \leq z$) is defined as:

$$h = h_a, \quad [14.13]$$

Heat, h , in the region outside the cooling coil where the effect of cooling air is observed ($c_z - c_e < z < c_z$ and $c_z + c_w \leq z < c_z + c_w + c_e$) is defined as:

$$h = \frac{(h_c - h_a)}{c_e} \{z - (c_z - c_e)\} + h_a \quad (c_z - c_e \leq z < c_z), \quad [14.14]$$

$$h = \frac{(h_c - h_a)}{c_e} \{(c_z + c_w) - z\} + h_c \quad (c_z + c_w \leq z < c_z + c_w + c_e), \quad [14.15]$$

and h under the cooling coil ($c_z \leq z < c_z + c_w$) is defined as:

$$h = h_c. \quad [14.16]$$

Here, c_z is the position coordinate of the cooling coil on the z axis, c_e is the distance which is affected by the cooling air, c_w is the width of the cooling coil, h_a is the heat transfer coefficient between the tube surface and the atmosphere, and h_c is the heat transfer coefficient between the tube surface and the cooling air from the cooling coil.

Because the cooling coil moves at speed V_2 in time t , similar to the heating coil, c_z is expressed as:

$$c_z = c_{z0} - V_2 t. \quad [14.17]$$

Here, c_{z0} is the initial position coordinate of the cooling coil on the z axis.

In this analysis, the amount of heat (q_s) and the heat transfer coefficient (h_a, h_c) are assumed to be constant values. In the case of the analysis with a higher precision, it is better to set the amount of heat and the heat transfer coefficient on the basis of the actual heating and cooling sources. For example, when modeling the high-frequency-induced heating, a more precise analysis can be realized by adding the coupled electromagnetic-thermal analysis and calculating the amount of heat generated to this model. In this case, however, it is necessary to prepare a numerical model in which all of the electromagnetic-thermo-mechanical factors are coupled, which is very complicated. In this report, only the coupled thermo-mechanical analysis was taken into consideration for simplicity.

The thermal properties of the Zn-22%Al alloy are: a specific heat c of $383 \text{ J kg}^{-1} \text{ K}^{-1}$, a mass density ρ of 7130 kgm^{-3} , and a thermal conductivity λ of $113 \text{ Wm}^{-1} \text{ K}^{-1}$. The heat transfer coefficient between the material and the atmosphere h_a is $30 \text{ Wm}^{-2} \text{ K}^{-1}$, and the atmospheric temperature and the temperature of the cooling air are both 293 K .

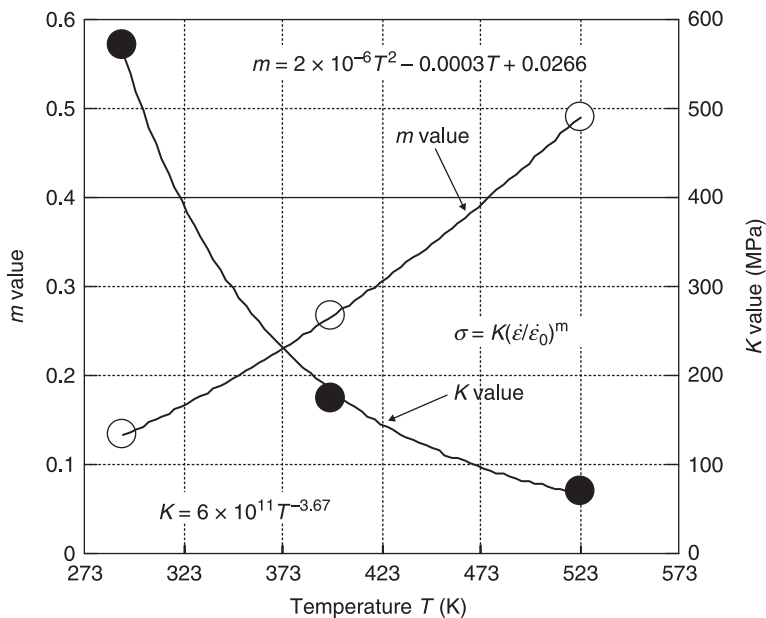
14.5.3 Material model

In dieless drawing process, a tube is fabricated by locally elevated temperature. In general, the flow stress of a material is greatly affected by the strain rate at a high temperature. Particularly in the case of the superplastic material used in this study, the strain rate sensitivity of the flow stress is very high. Now, we apply the following flow stress function taking the strain hardening dependence and the strain rate sensitivity into consideration for the material model dealt with in this analysis.

$$\sigma = K\epsilon^n (\dot{\epsilon}/\dot{\epsilon}_0)^m \tag{14.18}$$

Here, K is the strength coefficient, n is the drawing hardening index, and m is the strain rate sensitivity index. $\dot{\epsilon}_0$ is the scaling factor, which is generally taken as 1 s^{-1} . Moreover, K , m , and n are assumed, approximately, to be functions of temperature.

The Zn–22%Al superplastic alloy, which was used in the experiment, was used as the material in this analysis. Because this material rarely hardens even at room temperature, $n = 0$ was assumed in every temperature range. The other material properties, K and m , were obtained by the jump tensile test in the temperature region between room temperature and 523 K, in the range of strain rate between $4.17 \times 10^{-4} \text{ s}^{-1}$ and 10^{-2} s^{-1} , and were defined to be functions of temperature on the basis of the test result as shown Fig. 14.13.



14.13 Material properties as a function of temperature.

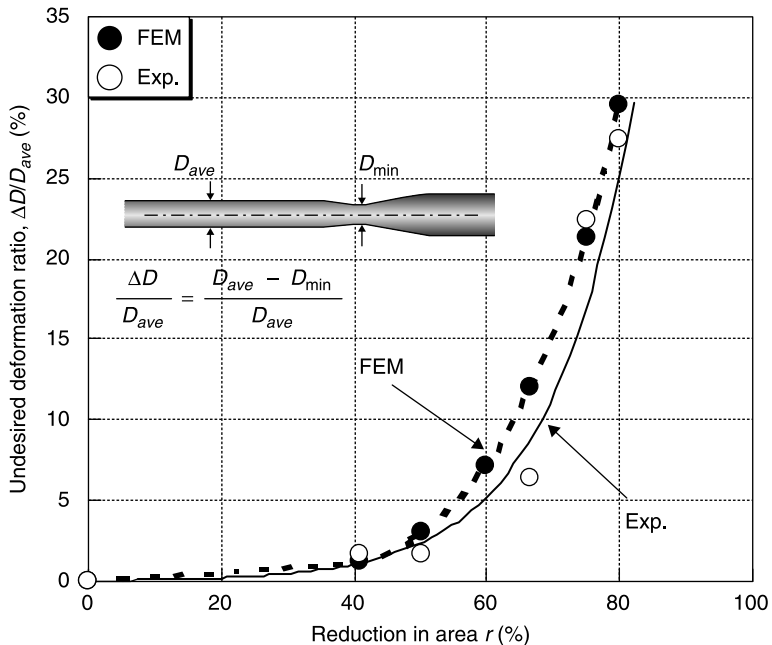
14.5.4 Validity of the FE simulation

The deformation profile was observed after superplastic dieless drawing while maintaining the moving speed of the heating coil V_2 at 3.6 mm/min and changing the tensile speed V_1 in the range of 3.6–14.4 mm/min. The analysis was carried out by setting $q_s = 1100 \text{ kWm}^{-2}$ such that the temperature of the heated part of the tube was approximately 523 K. Figure 14.8 shows the deformation profiles under the conditions of the experiment and the numerical analysis. With increasing V_1 , the reduction in area r increases and the outer diameter of the tube D decreases. Moreover, undesired deformation in the initial stage of dieless drawing can also be observed in the FE analysis results. The degree of undesired deformation is defined as the undesired deformation rate $\Delta D/D_{ave}$.

$$\frac{\Delta D}{D_{ave}} = \frac{D_{ave} - D_{min}}{D_{ave}} \quad [14.19]$$

Here, D_{ave} is the average outer diameter in the steady state and D_{min} is the minimum outer diameter of the unstable deformed part.

Figure 14.14 shows the relationship between $\Delta D/D_{ave}$ and r . $\Delta D/D_{ave}$ increases with increasing r . The higher the $\Delta D/D_{ave}$, the higher the risk of fracture in an unsteady state in the initial stage of drawing. In the experiment, drawing with r of



14.14 Relationship between the ratio of undesired deformation, $\Delta D/D_{ave}$ and reduction in area r .

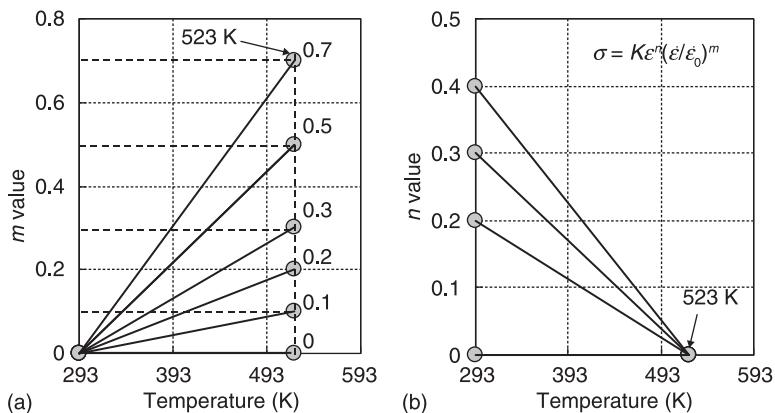
more than 80% failed and fracture occurred. Here, we judged that $\Delta D/D_{ave}$ can be used as an index for evaluating the risk of fracture. The analysis result shows good agreement with the experimental result, indicating that the behavior during dieless drawing in the unsteady state until reaching the steady state is well simulated.

14.5.5 Effect of material properties

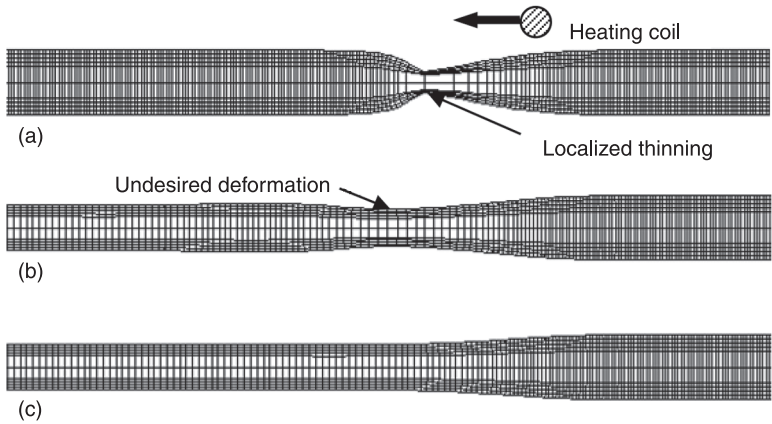
The effect of the temperature at the heated part on the deformation profile was examined, and it was found that the undesired deformation can be suppressed at an appropriate temperature. We considered this to be due to the effect of the n value with temperature dependent. However, some other parameters also depend on the temperature, and it is impossible to individually determine each effect of the various material characteristics, including the m value, experimentally. In the present analysis, we focused on the individual effect of the m and n values on the deformation profile. Figure 14.15 shows the temperature dependency of the m and n values. The relationship between the material characteristics and the temperature from room temperature to 523 K was approximated to be linear. The representative m and n values were the values at 523 K and room temperature, respectively. K value was set to be the same as that of the Zn–22%Al alloy shown in Fig. 14.13. The analysis was carried out under the conditions of $V_1 = 3.6$ mm/min, $V_2 = 3.6$ mm/min, and $r = 50\%$.

Figure 14.16 shows the effect of m value on the deformation profile. When the m value is 0.1 or less, the undesired deformation occurs locally, resulting in necking. The undesired deformation is suppressed with the increasing m value.

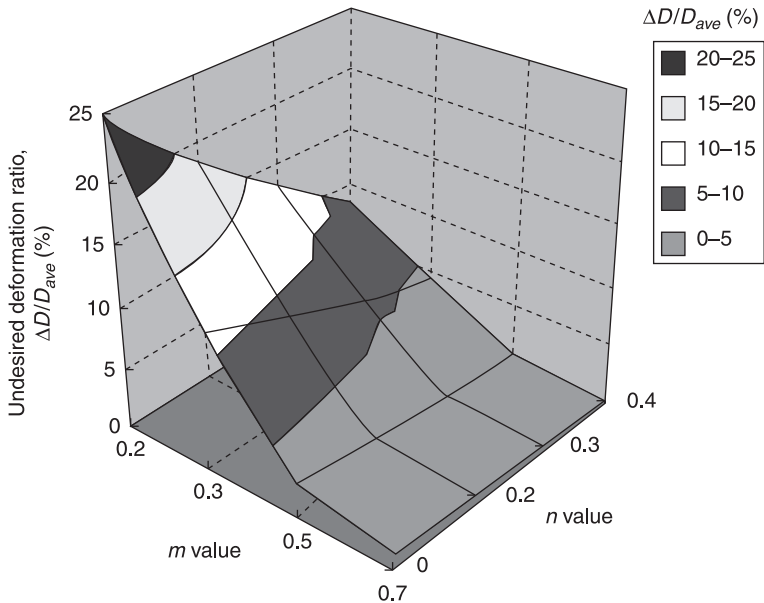
Figure 14.17 shows the effects of the m and n values on $\Delta D/D_{ave}$. As described above, the magnitude of the m value greatly affects $\Delta D/D_{ave}$. Generally, $\Delta D/D_{ave}$ is suppressed with a high m value regardless of the n value, suggesting a low



14.15 Temperature dependency of m and n values used in FEM simulation: (a) m value and (b) n value.



14.16 Effect of m value on the deformation profile in the dieless drawing process: (a) $m = 0.1$, $n = 0.2$; (b) $m = 0.2$, $n = 0.2$; and (c) $m = 0.5$, $n = 0.2$.



14.17 Effect of m and n values on the undesired deformation ratio, $\Delta D/D_{ave}$, in the dieless drawing process.

probability of breakage in the unsteady state. On the other hand, the n value affects $\Delta D/D_{ave}$ greatly in the case of a low m value but negligibly in the case of a high m value.

These results reveal that the m value under high-temperature conditions affects the deformation profile more greatly than the n value at room temperature during

dieless drawing. Here, the deformation behavior in the unsteady state is considered to be the same as that upon the occurrence of necking during tensile testing. Namely, in the case of a material with a high m value, when the strain rate of the necking part increases, the flow stress increases and further deformation is suppressed. This behavior also occurs in the unsteady state during dieless drawing and the undesired deformation behavior is suppressed. Most materials exhibit strain rate sensitivity at high temperatures, which also illustrates the importance of taking into consideration the strain rate sensitivity index m value in the analysis. Moreover, to achieve successful drawing without the undesired deformation, it is necessary to select a material with a high m , such as superplastic material, regardless of the magnitude of the n value at room temperature. The analytical results reveal the effectiveness of superplastic dieless drawing proposed in this study. Furthermore, for a material with a low m under high-temperature conditions, selecting a material with a high n value at room temperature is effective for achieving successful drawing.

14.6 Grain refinement process of metal tubes for superplastic dieless drawing process

14.6.1 Magnesium alloy tubes

The low density and considerably higher strength and stiffness of magnesium alloys contribute significantly to weight saving of the structures and parts in the automotive and aerospace industries. Furthermore, in recent years, the magnesium and its alloys are expected to be biodegradable metallic implants, because of good biocompatibility, non-toxicity, biodegradation and mechanical properties (Song, 2007). In particular, the use of tubular parts made of magnesium alloys is expected from the viewpoint of further weight saving and high stiffness in the automotive and aerospace industries. Additionally, the fine tubes of magnesium alloy can be used for medical and biodegradable parts, such as injection needles, stents and implants. In spite of the above mentioned advantages and applications, the use of magnesium alloy in industry is limited because of its low deformability by cold working, due to its hexagonal closed-packed (HCP) crystal structure.

In general, the cold drawing with dies and tools is used for shrinking the tubes to fabricate fine tubes. However, the large reduction in area cannot be obtained by cold drawing for magnesium alloy tubes. The limiting reduction in area is 5% in a 1-pass drawing at room temperature. In addition, in case of a warm drawing process with dies and tools at elevated temperature, the reduction in area is limit to 15%. Thus, it is difficult to fabricate a magnesium alloy fine tube.

14.6.2 Grain refinement process for a metal tube

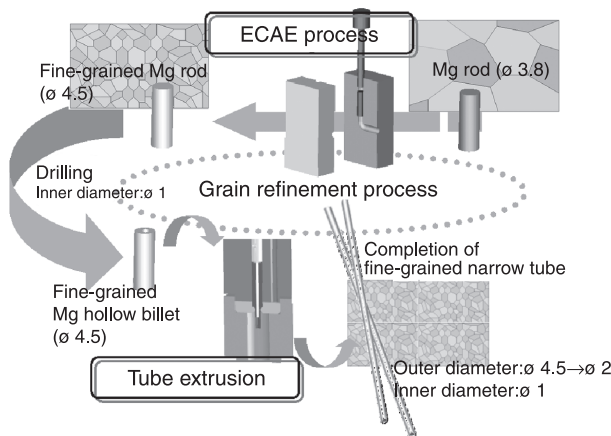
Grain refinement processing has become an attractive procedure for producing alloys with mechanical properties including high strength at room temperatures

and a superplasticity at elevated temperature. Many grain refinement methods have been suggested, such as ECAE (equal-channel angular extrusion) (Iwahashi *et al.*, 1996) and ARB (accumulative roll bonding) (Lee *et al.*, 2002). However, most conventional grain refinement methods covered bulk and sheet metals from the viewpoint of the shape of the target material. The grain refinement processing for tubular materials has not been studied.

In this section, the novel grain refinement method by combined ECAE and extrusion processes for tubular material was proposed. Additionally, to fabricate the magnesium alloy fine tube, the dieless drawing process is applied for a magnesium alloy tube with fine grain by use of the combined ECAE and extrusion processes. The effectiveness of the grain refinement and superplastic dieless drawing for fabricating magnesium alloy fine tubes is described.

In general, the extrusion process is a suitable method for producing complex cross-sectional shapes such as tubular and non-circular material as well as bulk material with complex shapes. However, plastic strain which can be given into the material in a process has a limit in the case of the extrusion process. Meanwhile, the ECAE process can cause strain to the material repeatedly, because the shape after the ECAE process is not changed. Thus, we apply the ECAE process to the billet used in the extrusion process. Figure 14.18 shows the schematic illustration of grain refinement by the combined ECAE/Extrusion process (Furushima *et al.*, 2010b). The billet with fine grain for the extrusion process is made by the ECAE process. The extrusion process is carried out for the billet with fine grain. In this way, the tubular material with fine grain can be fabricated by grain refinement using the combined ECAE/Extrusion process.

AZ31 magnesium alloy was used in the experiment. The billet used in the ECAE process has a diameter of 3.8 mm and length of 45 mm. The initial average

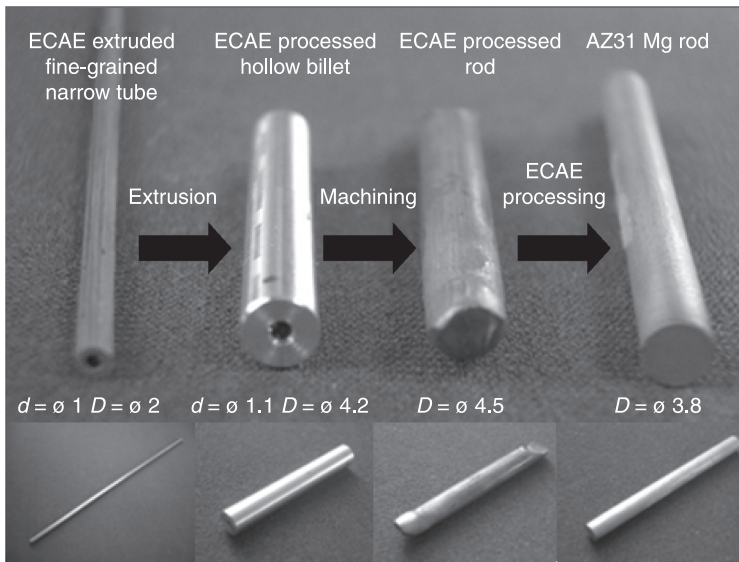


14.18 Schematic illustration of grain refinement using the combined ECAE/Extrusion process for alloy tubes (units are mm).

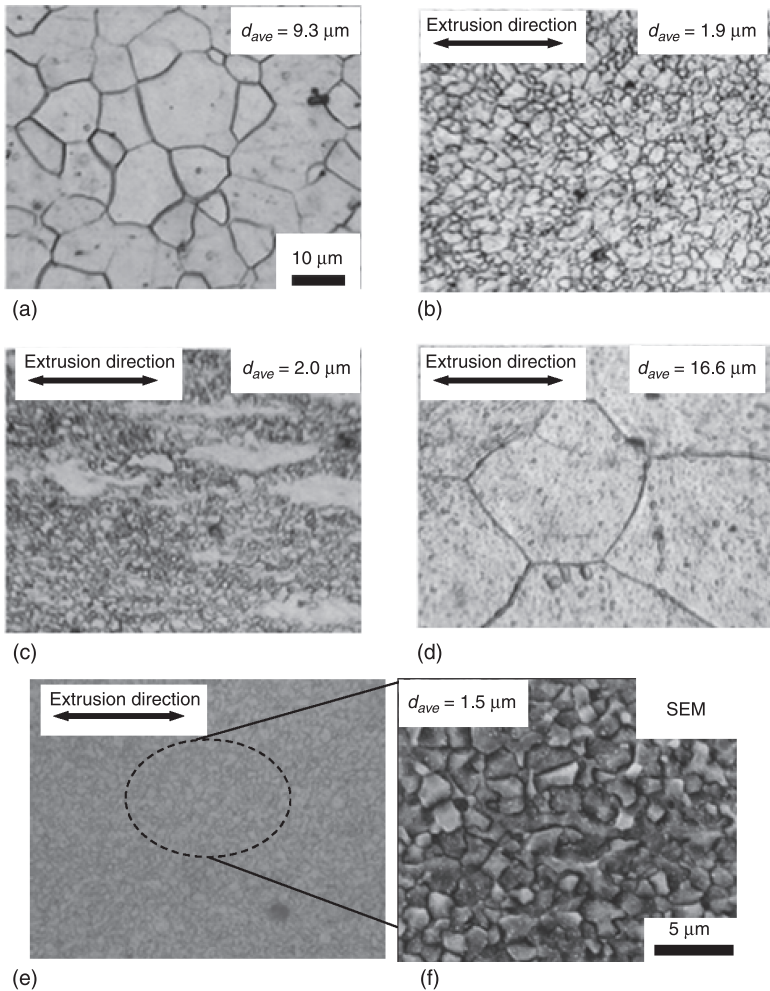
grain size of the billet is 9.3 μm . The ECAE process used is the technique of pressing specimens through a die containing two channels with diameter of 4.5 mm, equal in cross-section, intersecting at an angle of 90°. As a result of the pressing, the billet is subjected to simple shear state but retained the same cross-sectional area so that it was possible to repeat the pressings for several cycles. Billets were processed by ECAE at 473 K for four passes via route B_C (Iwahashi *et al.*, 1996). The extrusion process with a fixed mandrel for fabricating a tubular shape with outer and inner diameter of $D = 2$ mm and $d = 1$ mm, respectively, were carried out for the billets with fine grain after the ECAE process. For comparison, a billet not processed by ECAE was also processed by the extrusion. The forming temperature and extrusion ratio were 523 K and 6.4, respectively, in the experiment. To observe the microstructure of AZ31 magnesium alloy, the samples were etched by picric acid solution. The tensile tests at an elevated temperature of 673 K were performed under the condition of strain rate from $1.0 \times 10^{-4} \text{ s}^{-1}$ to $5.0 \times 10^{-2} \text{ s}^{-1}$ to investigate the superplastic characteristics such as strain rate sensitivity index m and elongation.

14.6.3 Microstructure

Figure 14.19 shows photographs of specimens obtained from each fabrication process of fine-grained magnesium alloy tubes. The tube, with outer and inner diameters of 2 mm and 1 mm respectively, can be fabricated successfully in the final stage. Figure 14.20 shows the microstructures of specimens obtained



14.19 Photographs of specimens obtained from each fabrication process of fine-grained magnesium.



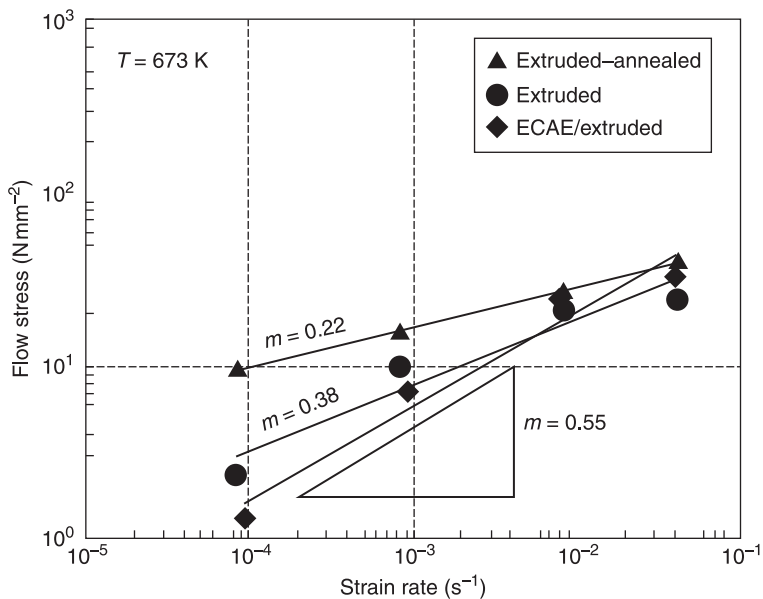
14.20 Microstructure of specimens obtained from each fabrication process of fine-grained magnesium alloy tubes: (a) as-received; (b) 4-pass ECAE processed; (c) Extruded; (d) Extruded-Annealed; and (e) 4-pass ECAE/Extruded.

from each fabrication process of the fine-grained magnesium alloy tubes observed by optical microscope (OM) and scanning electron microscope (SEM). Figure 14.20(a) is the microstructure of the billet with average grain size d_{ave} of $9.3 \mu\text{m}$. Figure 14.20(b) shows the micro-structures of the billet after the ECAE process at 4-pass with d_{ave} of $1.9 \mu\text{m}$. For comparison with the ECAE/Extrusion process, only the extrusion process without the ECAE process for the billet was carried out. In addition, annealing for the tube was only performed after the extrusion process. Figure 14.20(c) and (d) are the microstructures of the tubes

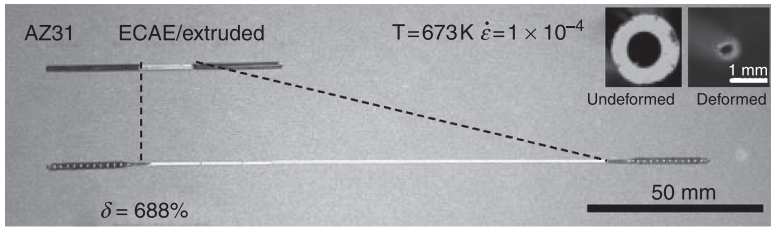
fabricated by the extrusion process only, with d_{ave} of 2.0 μm , and the annealed tube after extrusion with d_{ave} of 14.6 μm only. For the tube fabricated by the extrusion process only, the grains are inhomogeneous and extended in the extrusion direction. The microstructure of the tube fabricated by novel grain refinement using the combined ECAE/Extrusion process is shown in Fig. 14.20(e) and (f) as observed by OM and SEM. The finest grain d_{ave} of 1.5 μm can be obtained from the process (Furushima *et al.*, 2010b). It is confirmed that the grains of the tube refined by the ECAE/Extrusion process are of a fine, homogeneous and equi-axed structure.

14.6.4 Superplasticity

Figure 14.21 shows the relationship between flow stress and strain rate for ECAE/ Extruded, extruded-only, and annealed-only after extrusion tubes. The gradient of flow stress to strain gives a strain rate sensitivity index of m value. As a result, the highest m value of 0.55 can be obtained from ECAE/Extruded tubes with finest grain compared with extruded-only, and annealed-only after extrusion, tubes. Figure 14.22 shows the photograph of the fractured tensile test specimen deformed at strain rate $1.0 \times 10^{-4} \text{ s}^{-1}$ at 673 K for ECAE/Extruded tube. The maximum elongation of $\delta = 688\%$ can be obtained for ECAE/Extruded tube with fine grain (Furushima *et al.*, 2010b). These results indicate that the tube with fine grain fabricated by the ECAE/Extrusion process exhibits excellent superplastic potential. Therefore, the effectiveness of grain refinement combined



14.21 Relationship between flow stress and strain rate for extruded-annealed, extruded and ECAE/Extruded obtained from tensile test.

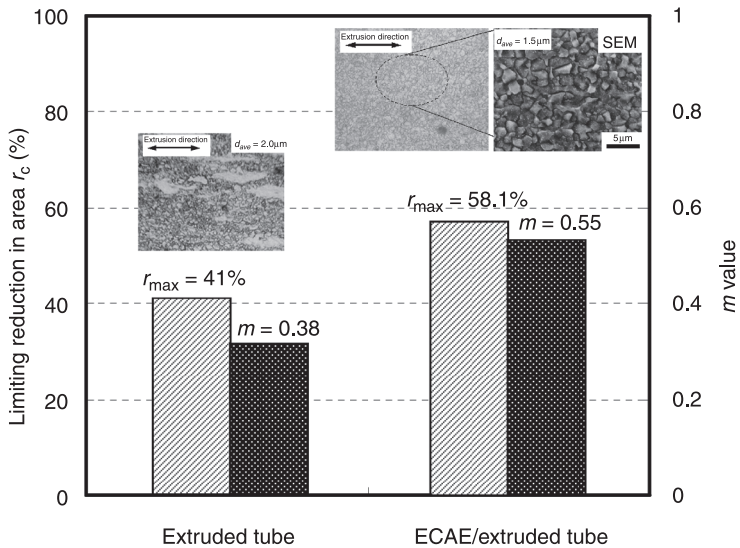


14.22 Photograph of fractured tensile test specimen deformed at strain rate $1.0 \times 10^{-4} \text{ s}^{-1}$ at 673 K.

by the ECAE/Extrusion process for fabrication of tubular material with a fine grain can be demonstrated.

14.6.5 Enhancement of the dieless drawing limit

For the fabrication of fine tubes, instead of conventional cold and warm die drawings with a low drawing limit, the dieless drawing process (which does not use any dies and tools, and which can realize the high reduction in area) was applied to the tubular materials with fine grain and excellent superplasticity fabricated by the ECAE/Extrusion process described above. For investigation of the effect of the m value on the limiting reduction in area, the dieless drawing limit of ECAE/Extruded tube with an m value of 0.55 was compared to that of the extruded-only tube with an m value of 0.38. Figure 14.23 shows the effect of



14.23 Effect of microstructure and m value on limiting reduction in area for extruded tube and ECAE/Extruded tube.

average grain size and m value of the tubes on the limiting reduction in area in the dieless drawing process. As a result, the limiting reduction in area of the ECAE/Extruded tube is larger than that of extruded-only tube. The limiting reduction in area is enhanced with an increasing m value due to grain refinement. The limiting reduction in the area of 58.1% for the ECAE/Extruded tube can be obtained (Furushima *et al.*, 2010b). Therefore, it is found that the grain refinement by the combined ECAE/Extrusion process for fabrication of tubes with a fine grain and a high m value is effective.

14.7 Other applications

14.7.1 Axial profile control: taper micro-tubes

Micro-tubes are commonly used not only as components of straight tubes but also of various axial profile tubes such as taper tubes. For example, the axial profile of a painless injection needle is advisable to be taper shaped, so that the inflow resistance of the medicinal solution can be reduced.

In the dieless drawing process, we know that the reduction in area can be controlled by the speed ratio as shown in Eq. [14.1] or Eq. [14.2]. This means that the reduction in area along the axial direction can change gradually because it changes the drawing speed during the forming process, and the shape of the tube can be controlled. In the case of the continuous dieless drawing process, it is assumed that V_1 can be shown by the following equation:

$$V_1(t) = V_2 + at \tag{14.20}$$

where a is the acceleration of drawing speed V_1 , t is time. The outer radius R of drawn tubes is given from the conventional study (Wengenroth and Pawelski, 2001) by the following equation:

$$R(t) = R_0 \sqrt{V_2/V_1(t)} = R_0 \sqrt{V_2/(V_2 + at)} \tag{14.21}$$

Thus, deformation time t can be expressed as shown in following equation:

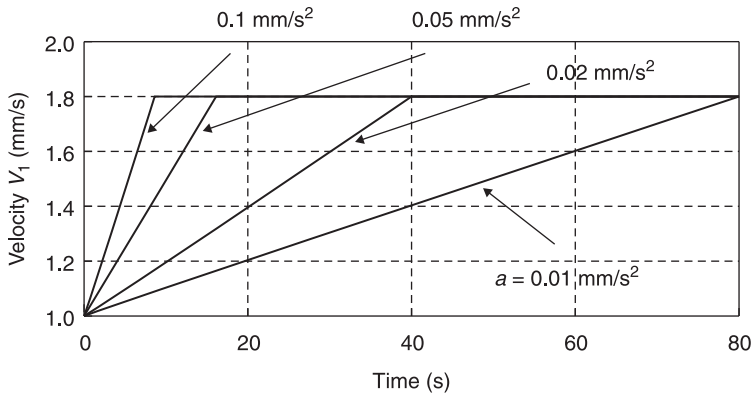
$$t = \sqrt{\frac{2x}{a}} \tag{14.22}$$

Equation [14.22] is substituted for Eq. [14.21]:

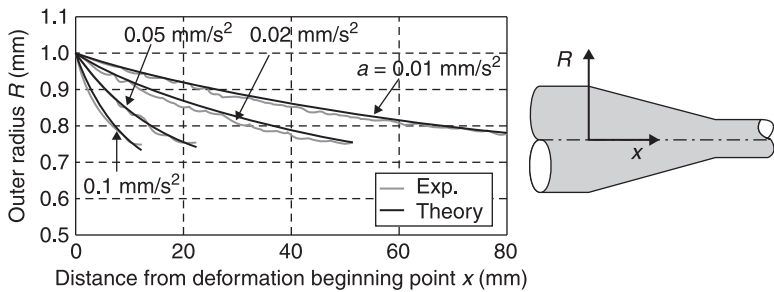
$$R(x) = R_0 (1 + 2ax/V_2^2)^{-1/4} \tag{14.23}$$

In this way, the axial taper profile can be controlled by changing acceleration a of drawing speed V_1 .

Figure 14.24 shows the input path of drawing speed V_1 . The gradient of drawing speed V_1 is defined as acceleration a of 0.005, 0.01, 0.02, 0.05 and 0.1 mm/s² for feeding speed V_2 of 1 mm/s. Figure 14.25 shows the comparison with the predicted



14.24 Drawing speed paths for controlling the axial profile by the dieless drawing process.

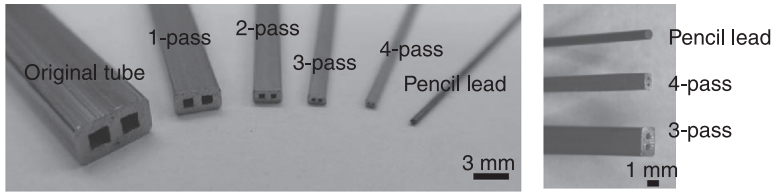


14.25 Fabrication of a taper tube by the dieless drawing process with variable drawing speed control.

profile obtained from Eq. [14.23] and the actual profile by experiment. The actual profile is in good agreement with the predicted profile. It has been found that the axial taper profile can be manufactured by the dieless drawing process with drawing speed control (Furushima *et al.*, 2010b).

14.7.2 Cross-section shape control: square and non-circular micro-tubes

Micro-non-circular tube with complex cross-sections such as a number of micro-holes or channels are used as micro-heat exchangers, micro-reactors and electrode tubes for EDM. Therefore, miniaturization of circular and non-circular tube is important and necessary in various fields. However, it is very difficult to scale down into micro-scale for non-circular tube using a conventional die drawing process with any dies, because the complex dies and tools are also needed for miniaturizing non-circular tubes; meanwhile, the dieless drawing process



14.26 Photograph of micro-non-circular tubes fabricated by superplastic dieless drawing.

has unique characteristics for the cross-section, called the geometrical similarity law in cross-section, as described in Section 14.4.3. The geometrical similarity law in cross-section can apply not only to circular tubes but also to non-circular tubes. Figure 14.26 shows the photograph of micro-non-circular tubes with double hollows in the cross-section fabricated by the superplastic dieless drawing process for the Zn–22%Al alloy. The micro-non-circular tube, with dimensions of outer tube of $533 \times 923 \mu\text{m}$ and inner square tubes of $335 \mu\text{m}$ on a side, can be fabricated successfully after a 4-pass superplastic dieless drawing process with $r = 60\%$ without closing the inner hollows (Furushima *et al.*, 2011). Furthermore, it is found that the geometrical similarity law in cross-section can be satisfied for non-circular tubes. Therefore, the effectiveness of the superplastic dieless drawing process for micro-non-circular tubes can be demonstrated.

14.8 Conclusion

In this chapter, the dieless drawing process for fabricating superplastic micro-tubes was discussed. The metal micro-tubes have many industrial applications, such as mechanical/structural components, electrode tubes for electrical discharge machining (EDM), cooling micro-nozzles used in micro-machines, laser accelerators, optical fibers, contact probes, painless injection, and sensors for fluid and gas. As a fabricating process of metal micro-tubes, the novel superplastic dieless drawing process is an effective process without using any dies and tools compared with a conventional die drawing process. Dieless drawing by the use of local heating and cooling devices of metal wires, bars and tubes replaces conventional die drawing which is subjected to tensile deformation. The metal micro-tube with outer and inner diameters of $D = 190 \mu\text{m}$ and $d = 91 \mu\text{m}$, respectively, was fabricated successfully by the superplastic dieless drawing process. The geometrical similarity law in cross-section is satisfied during the dieless drawing process. In addition, the modeling method of FE simulation with coupled thermo-mechanical analysis of the dieless drawing was described. The validity of this model can be verified. It is found that the strain rate sensitivity of material properties is an important factor in the dieless drawing process to enhance

the drawing limit. Furthermore, superplastic dieless drawing is an effective process for not only fabricating circular straight micro-tube but also fabricating taper micro-tube and non-circular micro-tube.

The most significant characteristic of superplastic dieless drawing is that dies and tools are not necessary. Therefore, the dieless drawing process enables the fabrication of micro-tube without friction, which would be a serious problem due to the size effect in micro-scale. Furthermore, the reduction in area ratio can be controlled by arbitrarily controlling the fabrication speed without using any special dies or tools. Moreover, as a benefit of the size effect due to miniaturization, the improvement of fabrication efficiency owing to the increase in heating and cooling speeds should also be noted. In the future, by realizing the accurate measurement and control of temperatures at a micro-scale, the use of dieless drawing as a highly flexible micro-forming process is a strong possibility. If many kinds of hollow micro-components can be fabricated by this process in the future, further development of micro-forming techniques can be expected.

14.9 References

- Alexander J M and Turner T W (1974), 'A preliminary investigation of the dieless drawing of titanium and some steels', *Proceedings of the Int. M. T. D. R. Conference: Advance in Machine Tool Design and Research*, 15: 525–537.
- Carolan R, Tierman P and Commerford P (2004), 'The dieless drawing of high carbon steel', *Material Science Forum*, 447–448: 513–520.
- Engel U and Eckstein R (2002), 'Microforming—from basic research to its realization', *Journal of Materials Processing Technology*, 125–126: 35–44.
- Eynatten K V and Reissner J (2004), 'Dieless drawing for flexible processing of microstructure and mechanical properties' *Proceedings of 34th Int. M. T. D. R. Conference*, 34: 187–192.
- Furushima T, Sakai T and Manabe K (2004), 'Finite element modeling of dieless tube drawing of strain rate sensitive material with coupled thermo-mechanical analysis', *Proceedings of the 8th International Conference on NUMIFORM*, 522–527.
- Furushima T and Manabe K (2007a), 'Experimental study on multi-pass dieless drawing process of superplastic Zn–22%Al alloy micro-tubes', *Journal of Materials Processing Technology*, 187–188: 236–240.
- Furushima T and Manabe K (2007b), 'Experimental and numerical study on deformation behavior in dieless drawing process of superplastic micro-tubes', *Journal of Materials Processing Technology*, 191: 59–63.
- Furushima T and Manabe K (2009), 'Finite element simulation with coupled thermo-mechanical analysis of superplastic dieless tube drawing considering strain rate sensitivity', *Materials Transactions*, 50: 161–166.
- Furushima T, Manabe K and Sakai T (2008), 'Fabrication of superplastic micro-tubes using dieless drawing process', *Materials Transactions*, 49: 1365–1371.
- Furushima T, Esaka Y and Manabe K (2010a), 'Fabrication of small taper-needles using dieless drawing process with drawing speed control', *Proceeding of the International Conference on Material Processing Technology 2010*, 68–71.

- Furushima T, Noda Y and Manabe K (2010b), 'Grain refinement by combined ECAE/ Extrusion and dieless drawing processes for AZ31 magnesium alloy tubes' *Materials Science Forum*, 654–656: 735–738.
- Furushima T, Shiravaki P and Manabe K (2011), 'Fabrication of micro-noncircular multicore tubes using superplastic dieless drawing process' *Journal of the Japan Society for Technology of Plasticity*, 52: 380–384.
- Hallmark B, Hornung H H, Broady D, P-Kuehne C and Mackley M R (2008), 'The application of plastic microcapillary films for fast transient micro-heat exchange', *I. J. Heat and Mass Transfer*, 51: 5344–5358.
- Iwahashi Y, Wang J, Horita Z, Nemoto M and Langdon T. G. (1996), 'Principle of equal-channel angular pressing for the processing of ultra-fine grained materials', *Scripta Materialia*, 35: 143–146.
- Kitagawa Y (2005), 'Capillary acceleration of electrons' *Journal of Plasma Fusion Research*, 81: 250–254.
- Kobatake K, Sekiguchi H, Osakada K and Yoshikawa K (1977), 'An analysis of temperature distribution in continuous dieless drawing', *Proceedings of the Int. M. T. D. R. Conference: Advance in Machine Tool Design and Research*, 18: 253–258.
- Lee S H, Saito Y, Sakai T and Utsunomiya H (2002), 'Microstructures and mechanical properties of 6061 aluminum alloy processed by accumulative roll-bonding', *Materials Science and Engineering A*, 325: 228–235.
- Li Y, Quick N R and Kar A (2002), 'Thermomechanical effects in laser microprocessing for dieless metal wire drawing', *Journal of Laser Application*, 14: 91–99.
- Li Y, Quick N R and Kar A (2002), 'Dieless laser drawing of fine metal wires', *Journal of Materials Processing Technology*, 123: 451–458.
- Li Y, Quick N R and Kar A (2003), 'Structural evolution and drawability in laser dieless drawing of fine nickel wires', *Materials Science and Engineering A*, 358: 59–70.
- Rangelow I W and Hudek P (1995), 'MEMS fabrication by Lithography and Reactive Ion Etching (LIRIE)', *Microelectronic Engineering*, 27: 471–474.
- Pawelski O and Kolling A (1995), 'Calculation of the temperature distribution in dieless drawing', *Steel Research*, 66: 50–54.
- Price J W H and Alexander J M (1977), 'An analytical solution for dieless drawing utilizing a method of equalisation of work rate', *Proceedings of the Int. M. T. D. R. Conference: Advance in Machine Tool Design and Research*, 18: 259–265.
- Tsuchiya K, Jinnin S, Yamamoto H, Uetsuji Y and Nakamachi E (2010), 'Design and development of a biocompatible painless microneedle by the ion sputtering deposition method', *Precision Engineering*, 34: 461–466.
- Saotome Y, Iguchi N, Mizusawa N and Kobayashi T (1986), 'The development of controlled die-less drawing machine and the deformation behaviour with dynamic superplasticity', *Journal of the Japan Society for Technology of Plasticity*, 27: 422–428 (in Japanese).
- Sekiguchi H, Kobatake K and Osakada K (1974), 'A fundamental study on dieless drawing', *Proceedings of the Int. M. T. D. R. Conference: Advance in Machine Tool Design and Research*, 15: 539–544.
- Sekiguchi H and Kobatake K (1987), 'Development of dieless drawing process', *Advanced Technology of Plasticity 1987*, 347–354.
- Song G (2007), 'Control of biodegradation of biocompatible magnesium alloys', *Corrosion Science*, 49: 1696–1701.
- Vollertsen F, Hu Z, Niehoff H S and Theiler C (2004), 'State of the art in micro-forming and investigations into micro-deep drawing', *Journal of Materials Processing Technology*, 151: 70–79.

- Wang Z T, Luan G F and Bai G R (1999), 'Study of the deformation velocity field and drawing force during the dieless drawing of tube', *Journal of Materials Processing Technology*, 94: 73–77.
- Weiss V and Kot R A (1969), 'Dieless wire drawing with transformation plasticity', *Wire Journal*, 9: 182–189.
- Wengenroth W, Pawelski O and Rasp W (2001), 'Theoretical and experimental investigations into dieless drawing', *Steel Research*, 72: 402–405.

- AA747, 14–15
 AA2004, 249–51
 cavitation with tensile strain, 260
 ductilities, 250
 influence of preheating conditions, 250
 AA5083, 15, 20, 255–8, 268, 294, 308
 architectural application, 257
 AA7075, 248
 AA7475, 248, 251–2, 257, 261, 262
 ambient temperature mechanical properties, 251
 production route on superplastic properties, 259
 AA8090, 255
 ABAQUS, 146, 175, 176, 207
 Accumulative Roll Bonding, 18–19, 350
 alloys, 11–16
 see also specific alloy
 aluminium alloys, 13–15
 AA2004 (Al–6Cu–0.4Zr), Supral 100, 13–14
 AA5083 (Al–4.5Mg–0.8Mn–0.1Cr), 15
 AA7475 (Al–5.5Zn–2.5Mg–1.5Cu–0.2Cr), 14–15
 Al–Li alloys, 15
 Rockwell Route, 14
 duplex (α/β) Ti alloys, 11–13
 composition, SPF temperatures, strain rate and elongation, 12
 elongation at deformation temperatures, 11
 fine grain microstructure, 12
 other processed alloys with superplasticity, 13
 magnesium alloys, 15–16
 aluminium alloys, 13–15
 see also superplastic aluminium alloys
 Quick Plastic Forming, 272–302
 superplastic flow, 29–30
 extension zones, 30
 superplastic forming, 247–69
 cavitation, 258–62
 exploitation, 264–9
 high strain rate superplasticity, 262–4
 history, 248–9
 superplastic aluminium alloys, 249–58
 aluminium–calcium based alloys, 252–4
 eutectic alloy microstructures, 253
 aluminium–lithium based alloys, 248, 254–5
 alloys exhibiting superplasticity, 254
 military aircraft door inner structure, 256
 aluminium–magnesium based alloys, 249
 ARB *see* Accumulative Roll Bonding
 ASTM B637, 282
 ASTM E21 2009, 37, 40–1
 ASTM E2448-06, 291
 ASTM E2448 2008, 36, 39
 AZ31, 350–1
 AZ31B, 308, 311, 318, 320
 biaxial bulge test, 291
 boron nitride, 73, 74
 bulging tests, 127–32
 conical die, 127–32
 schematic layout, 128
 V-shaped die, 130–2
 carbothermic reduction route, 315
 Cauchy–Green deformation tensor, 142
 Cauchy stress, 137, 139, 142
 cavitation, 258–62
 cavity nucleation, 258–9
 CDM *see* continuum damage mechanics
 ceramic based dies, 62–7
 coatings, 66–7
 non-reinforced ceramic materials, 64–5
 prototype, 64
 reinforced ceramic materials, 65–6
 fibre reinforced refractory concrete SPF die, 66
 titanium parts production, 65
 CETOL, 176
 clamping device, 39, 43–4
 quick mount grips, 43
 specimen mounting, 44
 co-operative grain boundary sliding, 28–9
 Considère condition, 185
 constitutive equations, 20–2
 Al–Zn–Mg
 computed vs experimental at various strain rates, 173
 material constants, 174
 determined set for superplasticity, 170–4
 fitted vs experimental stress–strain relationship, 171
 uni-axial power-law model, 170
 uni-axial sinh-law model, 170–1
 uni-axial superplastic-damage constitutive equations, 171–4
 void growth at grain boundaries, 172
 experimental data, 160–74
 features of Region I and Region III, 22–4

- logarithmic plot of stress-*versus*-strain rate, 23
 - Region I, 22–3
 - Region II, 24–7
 - Region III, 23–4
 - general objective function (OF_III), 168–9
 - objective function, 168–9
 - true error definition (logarithmic error), 168
 - weighting factors, 168
 - integration methods, 160–3
 - error estimation and step-size control, 162–3
 - implicit methods, 161–2
 - logarithmic plot of stress *versus* strain rate of an SP alloy, 22
 - modelling metals superplastic forming, 154–81
 - objective functions for optimisation, 163–9
 - problem, 163–4
 - optimisation methods for determining the material constants, 169–74
 - shortest distance method (OF_I), 164–6
 - error definition, 166
 - experimental vs computed stress-strain curves and errors analysis, 165
 - superplastic alloys, 154–60
 - cyclic hardening diagram, 155
 - grain growth, 158–9
 - isotropic hardening, 157–8
 - superplastic flow rule, 156–7
 - unified uni-axial superplastic constitutive equations, 159–60
 - superplastic forming simulation, 174–81
 - field plots, 178
 - finite element model, 175–7
 - gas-pressure histories, 179
 - integrated finite-element model for simulating the superplastic gas-blow forming, 176
 - material model implementation for FE analysis, 174–5
 - max – min histories, 180
 - modelling results, 177–81
 - Ti–6Al–4V
 - material constants at 900 °C, 171
 - material constants at 927 °C, 170
 - universal multi-objective function (OF_II), 166–8
 - error definition, 167
 - continuous dieless drawing, 330–1
 - continuum damage mechanics, 199
 - core and mantle model *see* grain boundary model
 - Corrosion RESistant Steel (CRES), 59–60
 - Coulomb friction, 77
 - Coulomb friction model, 177
 - coupled cyclic viscoplasticity, 68
 - CREEP, 176, 206, 207
 - damage mechanics model, 198–202, 214–15
 - deep drawing quality steel, 308
 - deformation mechanism maps, 313
 - delta Kronecker tensor, 143
 - dieless drawing process
 - see also* superplastic dieless drawing process
 - axisymmetric FE model, 342
 - fundamentals, 329–35
 - advantages and disadvantages, 335
 - heating system, 333–4
 - history, 332–3
 - principles using a local heating technique, 329–31
 - temperature and flow stress distribution, 331
 - heating methods classification, 334
 - schematic illustration, 330
 - superplastic micro-tubes fabrication, 327–58
 - diffusion bonding, 307
 - laser surface modification in combined superplastic forming and, 83–111
 - bonding process simulation, 99–109
 - laser surface modification effect on alloy surface, 84–91
 - laser surface modified alloys diffusion bonding, 91–9
 - real rough surface application, 100–1
 - titanium, 227–44
 - applications, 241–4
 - superplastic forming/diffusion bonding process, 235–41
 - titanium alloys, 228–35
- diffusion models, 26–7
 - grain switching model, 27
- DIN EN 10002-5 1991, 37, 41
- dislocation models, 24–6
 - grain boundary sliding, 25
- DISTOL, 175
- DMM *see* deformation mechanism maps
- dolomite (MgCO₃·CaCO₃), 305, 314
- DRX *see* dynamic recrystallisation
- duplex alloys, 9
- dynamic recrystallisation, 311
- ECAE *see* Equi-Channel Angular Extrusion
- elasticity theory, 118
- Equi-Channel Angular Extrusion, 17–18, 310, 350–1
 - Al alloy 1420, 18
 - schematic illustration of ECAE and HPT principles, 19
- Euler method, 161
- evolutionary algorithm-based optimisation method, 163, 173
- evolutionary programming-based optimisation technique, 170
- extrusion process, 350
- FEA *see* finite element analysis
- finite element analysis, 67, 77
- finite element modelling
 - applications, 146–51
 - automotive component, 148
 - Jack can, 147
 - orbital floor computational analysis, 150
 - orbital floor pressure cycle for different contact conditions, 150
 - RAM computational analysis, 149
 - RAM pressure cycle for different contact conditions, 149
 - commercial codes, 145–6
 - continuum model, 137–40
 - general 3-D constitutive equations, 139–40
 - superplastic forming constitutive behaviour, 138
 - uni-axial models, 137–9

- die representation and contact algorithms, 145
- finite element formulation and time integration schemes, 140–1
- future trends, 151
- incremental flow formulation, 141–4
- pressure cycle algorithms, 144–5
- thin metal sheet forming, 136–51
- FLD *see* forming limit diagram
- flow localisation factor, 190, 198–9
 - application, 211–12
- flow rule, 118
- Formal, 249
- Formal 545, 249
- forming dies, 59–70
 - ceramic based dies, 62–7
 - die design and lifetime simulation, 67–70
 - experimental vs simulated loops at different strain rates, 69
 - die environment constraints, 59
 - metallic dies, 59–62
- forming limit diagram, 185
- friction, 76
- friction coefficient, 177
- friction stir processing, 19–20
- friction stir welding, 221

- galvanic corrosion, 307
- GBS *see* grain boundary sliding
- general objective function (OF_III), 168–9
 - objective function, 168–9
 - true error definition (logarithmic error), 168
 - weighting factors, 168
- Gleeble 1500 thermal imaging machine, 91, 95
- Gradient-based Optimisation Method, 163, 170
- grain boundary model, 25
- grain boundary sliding, 249, 298, 310, 313
- grain refinement, 9–11
 - mechanical working, 9–10
 - duplex alloys, 9
 - pseudo-single phase alloys, 9–10
 - phase separation, 10
 - phase transformation, 10–11
- severe plastic deformation, 17–20
 - Accumulative Roll Bonding, 18–19
 - Equi-Channel Angular Extrusion, 17–18
 - Friction Stir Processing, 19–20
 - high pressure torsion, 18
- graphite, 73, 74

- hard chrome, 80
- Hart stability criterion, 189–90
- heating/holding time, 39–41, 46
 - stress/strain curves, 40
- heating platen technology, 56–8
 - ceramic heating platen technology, 58
 - metallic heating platen, 56, 58
 - metallic monolithic HRCS heating platen, 57
- Hexagonal Boron Nitride (HBN), 207
- hexagonal crystal structure, 307
- High Cycle Blow Forming, 54
- high pressure die castings (HPDC), 316
- high pressure torsion, 18
- high strain rate superplasticity, 16–17, 262–4
 - optimum SP strain rates for Al alloys, 17
- Hill equation, 187
- Hill–Swift FLD, 187

- hollow cavity forming, 51
 - steel tube after SPF, 52
- hot-isostatic-pressed (HIP), 84
- hot tensile deformation, 311
- Hydro Porsgrunn electrolytic plant, 315

- implicit methods, 161–2
- incremental flow formulation, 141–4, 146
- infrared heating lamps, 59
- instability
 - forming analyses and experiments, 202–9
 - constitutive model, 205–7
 - die geometry and die in SPF press, 203
 - FE-implementation of damage mechanics, 208
 - FEM boundary and loading conditions, 204
 - mechanisms-based sinh model implementation, 207
 - mesh refinement study, 205
 - parameter values for unified-constitutive sinh model, 206
 - SPF press with annotation, 208
 - SPFLD 2D section views, 209
 - superplastic forming trials, 207–9
 - future trends, 220–2
 - initial grain size range
 - ductility, 194
 - localisation and necking, 193
 - strain-rate sensitivity, 191
- results in superplastic forming of metals, 209–20
 - components formed at target strain rates, 210
 - damage mechanics model, 214–15
 - failed SPF part, 210
 - finite element model of truncated cone die and sheet, 211
 - finite element-predicted FLF predictions, 212
 - finite element-predicted major–minor strain paths, 213
 - finite element-predicted paths, 217
 - finite element-predicted paths vs SPFLD values, 219
 - FLF application, 211–12
 - predicted damage distributions, 215
 - predicted time histories of damage, 216
 - SPFLD approach, 215–18
 - SPFLD showing finite element predicted paths, 218
 - void growth models, 213–14
- superplastic forming of metals, 184–222
- theoretical considerations, 185–202
 - assumed neck imperfection, 201
 - assumed pre-existing geometric imperfection, 200
 - curve fits for Ti-64 and Ti-6242, 198
 - 3D superplastic forming limit diagram for Ti-64, 199
 - damage mechanics models, 198–202
 - failure and instability microstructural analysis, 190–4
 - FLDs schematic representation, 197
 - Hill–Swift forming limit diagram, 187
 - instability models, 185–90
 - neck formation under uni-axial SPF deformation, 192

- strain-rate sensitivity on growth of imperfections, 188
 - superplastic forming limit diagram concept, 197–8
 - superplastic fracture mechanism diagram schematic, 196
 - Ti–6Al–4V stress-life rupture data, 202
 - void growth models, 194–7
- INSTRON, 45
- ISO 783 1999, 37, 41
- ISO 20032 2007, 36, 39
- isotropic hardening, 157–8
- Jacobian matrix, 160, 161, 162
- JIS H7501 2002, 36
- Jovane model, 120
- κ -penalty approach, 142
- Kroll process, 232
- Lagrangian mesh, 140
- laser surface clad, 84
- laser surface modification
 - alloy surface, 84–91
 - bonding conditions effects, 102–5
 - model prediction illustrating different bonding pressure effects, 105
 - model prediction illustrating different bonding temperature effects, 104
 - variations in the contributions from each operating mechanism, 103
- bonding process simulation, 99–109
- combined superplastic forming and metals
 - bonding diffusion, 83–111
- diffusion bonding, 91–9, 105–9
 - different microstructures effects, 105–9
 - model prediction displaying diffusion ability effects, 106
 - model prediction revealing material hardness effects, 107
 - times needed for the voids closure in bonding, 107
 - variations in the contribution from operating mechanisms to the void closures, 108
- LSR γ -TiAl alloy, 84–8
 - alloy temperature and micro-hardness relationship, 88
 - dendritic structural transformation, 87
 - micro-hardness curve, 87
 - microstructural transformation, 86–8
 - substrate and melt zone DSC results, 86
- Ni–Cr–Ti–Al laser cladding layers, 88–91
 - casting Ni-based alloy, 90–1
 - cladding and transition zone metallographs, 89
 - K418 alloy representative structure, 91
 - materials chemical constitutions, 90
 - TiAl clad coating macrostructures, 89
 - TiAl cladding layer on deforming Ni-based alloy, 88–90
- remelted TiAl alloy, 84–8
 - LSR–TiAl alloy microstructural characteristics, 84–5
 - microstructural characteristics, 84
 - XD–TiAl alloy microstructure, 85
- TiAl/Ti alloys bonding, 98–9
 - TiAl/Ti bonds shear strength with different intended surface microstructures, 99
 - TiAl alloy bonding, 91–5
 - compression shear tests results, 92
 - couples sheared bonds treated with different process, 93–4
 - LSR effects on TiAl bonding couples strength, 91–2
 - LSR–TiAl alloy fracture characteristics, 93–5
 - TiAl/Ni alloys bonding
 - bonding of TiAl and casting Ni alloys, 96–8
 - bonding of TiAl and deforming Ni alloy, 95–6
 - elements across the LSM–TiAl/K418 joints interface, 97
 - TiAl/K418 direct bonding joint interfacial structure, 98
 - TiAl/GH3044 bonding couples shear strength, 95
 - voids shrinkage modelling, 100–2
 - contacting surface simulation results with elliptical voids, 101
 - contacting surface simulation results with irregular voids, 101
 - diffusion distance time limit effect during diffusion bonding, 101–2
 - mass transference along the surface, 102
 - real rough surface application in diffusion bonding, 100–1
- laser surface remelting, 84
- laser surface treatments, 84
- lasers, 59
- LCA *see* life cycle analyses
- Levy–Mises equations, 120, 186
- Levy–Mises flow rule, 118, 120
- life cycle analyses, 315
- LS-DYNA, 146
- LSC *see* laser surface clad
- LSM *see* laser surface modification
- LSR *see* laser surface remelting
- LST *see* laser surface treatments
- lubricants
 - high-temperature for metals superplastic forming, 72–81
 - influence of friction and lubricant on forming, 76–8
 - reported constant coefficients of friction, 78
 - thickness distribution for the SPF of a plane strain section, 76
 - mechanisms, 73–4
 - types of SPF dies, 74
 - production issues, 78–80
 - superplastic forming, 74–6
 - testing and evaluation, 78
- magnesite (MgCO_3), 305, 315
- magnesium alloys, 15–16
 - element code letters used in ASTM designation system, 309
 - history, 305–6, 307
 - 1955 Mercedes Benz 300 SLR racing car, 306
 - annual global production of primary magnesium since 1920, 307
 - manufacture of superplastic sheet, 313–19
 - alloy development, 318–19
 - magnesium extraction, 313–16
 - magnesium sheet production, 316–18

- properties of magnesium, 306–8
 - competing body panel materials, 308
- superplastic forming, 304–22
- superplastic forming of magnesium
 - components, 320–2
 - current situation, 320–1
 - future, 321–2
 - prototype inner panel in AZ31B for tailgate, 320
 - trial pressing of inner door panel in AZ31B, 321
- superplasticity, 309–13, 314
 - earliest experiments, 309–10
 - high strain experiments, 310–11
 - industrially relevant experiments, 311–12
 - nominal compositions of alloys in the text, 309
 - stress–strain plots, 314
 - superplastic flow mechanisms, 312–13
- Magnesium Elektron, 320
- magnesium hydroxide, 77
- Magnox, 310
- MARC, 146
- mathematical modelling
 - bulging tests, 127–32
 - conical die, 127–32
 - conical die schematic layout, 128
 - V-shaped die, 130–2
 - constant pressure application in free forming
 - from circular sheet
 - normalised pressure, 124
 - normalised strain rate, 123
 - normalised time, 125
 - flow rule, 118
 - free forming processes analysis
 - circular sheet clamped around its periphery and loaded by gas pressure, 120
 - non-uniformity factor during a free forming process, 122
 - normalised strain rate for constant pressure application from rectangular sheet, 127
 - rectangular sheet, 124–7
 - material constants from bulging tests, 127–34
 - experimental data for PbSn alloy, 133
 - free forming test, 132–4
 - membrane theory, 116–18
 - shells, 117
 - tangential stress acting on the shell, 117
 - superplastic free forming processes analysis, 119–27
 - bulged parts starting with circular or rectangular sheets, 119
 - circular sheet, 119–24
 - superplastic metal sheet forming processes, 115–34
- membrane theory, 116–18
 - shells, 117
 - tangential stress acting on the shell, 117
- MEMS *see* micro-electro-mechanical systems
- meridians, 116
- metallic dies, 59–62
 - composition and chemical elements effect, 60
 - typical heat-resistant cast steels, 61
 - mechanical strength and rupture, 61–2
 - thermomechanical properties of alloys, 61
 - typical heat-resistant cast steels mechanical and physical properties, 63
- oxidation and spallation, 60–1
- process, phases and ageing, 60
 - HRCS macrostructure and microstructure, 61
- weld repair and life extension, 62
- metals
 - constitutive equations for modelling
 - superplastic forming, 154–81
 - determination from experimental data, 160–74
 - superplastic alloys, 154–60
 - superplastic forming simulation, 174–81
 - high-temperature lubricants for superplastic forming, 72–81
 - friction and lubricants on forming, 76–8
 - lubricants mechanisms, 73–4
 - production issues, 78–80
 - SPF lubricants, 74–6
 - testing and evaluation, 78
 - predicting instability in superplastic forming, 184–222
 - forming analyses and experiments, 202–9
 - future trends, 220–2
 - results, 209–20
 - theoretical considerations, 185–202
 - superplastic forming, 3–31
 - grain refinement, 9–11
 - high strain rate, 16–17
 - historical aspects, 4–7
 - mechanisms, 20–30
 - processing of commercially significant alloy, 11–16
 - severe plastic deformation from grain refinement, 17–20
 - types of materials, 7–9
- micro-electro-mechanical systems, 328
- micro-forming, 328
- microsystem technologies, 328
- microtubes *see* superplastic microtubes
- molybdenum disulphide, 75
- MST *see* microsystem technologies
- MTS, 45
- multi-sheet forming and diffusion bonding, 51–3
 - four sheet SPF, 53
 - two sheet SPF, 53
- Newton–Raphson method, 142, 143
- Newton’s method, 161
- Nickel–Boron, 80
- non-Newtonian viscous flow, 137
- noncontinuous dieless drawing, 330
- Norton–Hoff power law, 137
- Norton–Hoff viscoplastic potential, 142
- objective functions, 163
- ODEs *see* ordinary differential equations
- OF *see* objective functions
- orbital cranioplasties, 149–50
- ordinary differential equations, 160
- PAMQPF module, 298
- PAMSTAMP, 146, 298
- particle stimulated nucleation, 252
- parting agents, 73, 75, 77
- pickling, 75
- PID controllers *see* proportional–integral–derivative controllers
- Pidgeon process, 313–15, 316, 322

- Piola-Kirchhoff stress tensor, 142
 plastic instability, 185–7
 Poisson coefficient, 118
 Positive Exponent Superplasticity, 16
 Power-law model, 159
 uni-axial, 170
 pressure cycle algorithms, 144–5
 proportional–integral–derivative controllers, 285
 ‘protect specimen’ 40
 pseudo-single phase alloys, 9–10
 PSN *see* particle stimulated nucleation
 Pureshield, 207
- Quick Plastic Forming, 15, 54
 aluminium alloys, 272–302
 ancillary benefits of integrally heated tools,
 286–8
 distortion, 286–7
 improved tool mechanisms, 287–8
 definition, 272
 development drivers, 272
 differences from superplastic forming, 273
 forming cell for parallel processing of two
 panels simultaneously, 274
 hot forming systems, 275–7, 278
 hot forming press with heated platens and
 insulated working volume, 275
 hydraulic press with heated and insulated
 tool system, 278
 temperature distribution of an unheated
 steel tool, 276
 temperature history within an unheated
 tool, 277
 integrally heated tool system, 277–82
 heated/insulated tool concept, 279
 peripheral insulation around the tool, 281
 peripheral insulation development, 280
 QPF tool, 279
 schematic of tool peripheral insulation
 system, 281
 tool exterior temperature target, 279
 top and bottom insulation, 280–2
 lubrication, 300–1
 AA5083 coil exhibiting dirt/debris, 301
 blank lubrication conveyor, 301
 material development, 288–300
 AA5083 sheet specifications, 295
 biaxial bulge test frame, die and biaxial
 bulge after forming and failure, 292
 composition in weight percent and total
 elongation for AA5083, 296–7
 cost, 294–7
 deck-lid outer panel, 291
 distribution of total elongation behaviour
 for material produced under modified
 AA5083, 297
 forming limit diagram for AA5083, 300
 lift-gate inner panels, 293
 modelling, 298–300
 predicted dome height vs time, 299
 predicted thickness distribution for
 deck-lid panel, 299
 quality, 289–94
 test frame and furnace used for tensile
 testing, 290
 total elongation and biaxial dome height
 relationship, 293
 total elongation distribution behaviour,
 295
 process overview, 273–5
 production validation experience, 288
 temperature distribution in deck-lid inner
 panel tool, 285–6, 287
 control thermocouple set points, 287
 identical 450 °C set points, 286
 tool surface, 285
 tool heating system, 282–5
 cartridge heater plan view layout, 283
 control thermocouples, 284–5
 deck-lid tool side view, 284
 distributed wattage heaters, 284
 heaters and zones, 282–4
 power requirements, 282
- RAM *see* Ridge Augmentation membrane
 refractory castable, 66
 Rice and Tracey model, 195
 Ridge Augmentation membrane, 149
 roughening phenomenon, 335
- sand casting, 60
 shortest distance method (OF_I), 164–6
 error definition, 166
 experimental vs computed stress–strain
 curves and errors analysis, 165
 single-sheet forming, 50–1
 die and sheet cross section, 50
 sinh model, 205, 206, 207
 SNAPFORM, 146
 SPF *see* superplastic forming
 SPFLD *see* superplastic forming limit diagram
 standard press-forming equipment, 54–6
 blank removal operation, 57
 characteristics, 55
 four column press furnace with manual blank
 removal, 55
 shuttle press with moving platen, 56
 strip casting, 317
 Struvite, 65
 sub-microcrystalline Ti–6Al–4V, 240
 Superform Aluminium, 265–6, 320
 superplastic aluminium alloys, 247–69,
 249–58
 AA2004, 249–51
 ductilities, 250
 influence of preheating conditions, 250
 AA5083, 255–8
 architectural application, 257
 AA7475, 251–2
 ambient temperature mechanical
 properties, 251
 production route on superplastic properties,
 259
 aluminium–calcium based alloys, 252–4
 eutectic alloy microstructures, 253
 aluminium–lithium based alloys, 254–5
 alloys exhibiting superplasticity, 254
 military aircraft door inner structure,
 256
 cavitation, 258–62
 cavity nucleation, 258–9
 control, 260–2
 development with tensile strain, 260
 influence on service properties, 261

- exploitation, 264–9
 - current Superform Aluminium parts, 268
 - early days, 264–6
 - future, 268–9
 - markets investigated before establishing superform metals, 265
 - parts made after Superform Aluminium operation, 267
 - present, 266–8
 - techno economic niche, 266
- high strain rate superplasticity, 262–4
 - Al–4%Mg–1%Zr alloy vs SPF AA5083, 264
 - grain size refinement and increase in optimum strain rate, 263
- history, 248–9
- superplastic properties under optimum deformation conditions, 251
- superplastic behaviour, 247
- superplastic deformation, 28
- superplastic dieless drawing process, 336–41
 - deformed shape after superplastic dieless drawing, 339
 - effect of heating conditions, 336–8
 - coil made of two loops of copper pipe, 337
 - length of heating coil, 338
 - temperature dependency of superplastic material properties for Zn–22%Al alloy tube, 337
 - type of heating coil length, 338
 - Zn–22%Al superplastic tubes after dieless drawing process, 336
- FE simulation, 342–9
 - axisymmetric FE model, 342
 - boundary conditions, 342–4
 - effect of m and n values on undesired deformation ratio, 348
 - effect of m value on deformation profile, 348
 - effect of material properties, 347–9
 - finite element model, 342
 - heat transfer model on tube surface, 343
 - material model, 345
 - material properties as function of temperature, 345
 - ratio of undesired deformation and reduction in area, 346
 - temperature dependency of m and n values, 347
 - validity, 346–7
- FE simulation vs experiment deformed shapes, 339
- grain refinement process of metal tubes, 349–55
 - dieless drawing limit enhancement, 354–5
 - flow stress and strain rate, 353
 - fractured tensile test specimen, 354
 - magnesium alloy tubes, 349
 - microstructure, 351–3
 - microstructure and m value effect on limiting reduction in area, 354
 - schematic illustration, 350
 - superplasticity, 353–4
- microtubes fabrication, 340–1
 - fabricated by multi-pass dieless drawing process, 340
 - satisfaction of geometrical similarity law in cross-section in dieless drawing, 341
- specimens from each fabrication process of fine grain magnesium microstructure, 352
 - photograph, 351
- superplastic flow rule, 156–7
- superplastic forming
 - aluminium alloys, 247–69
 - cavitation, 258–62
 - exploitation, 264–9
 - high strain rate superplasticity, 262–4
 - history, 248–9
 - superplastic aluminium alloys, 249–58
 - constitutive equations for modelling metals, 154–81
- differences from Quick Plastic Forming, 273
- forming dies, 59–70
 - ceramic based dies, 62–7
 - chemical composition, 61
 - die design and lifetime simulation, 67–70
 - die environment constraints, 59
 - macrostructure and microstructure of typical HRCS for a SPF die, 61
 - mechanical and physical properties of typical heat-resistant cast steels, 63
 - metallic dies, 59–62
- high-temperature lubricants for metals, 72–81
- laser surface modification in combined diffusion bonding and, 83–111
 - bonding process simulation, 99–109
 - laser surface modification effect on alloy surface, 84–91
 - laser surface modified alloys diffusion bonding, 91–9
- magnesium alloys, 304–22
 - components, 320–2
 - history, 305–6
 - manufacture of superplastic magnesium alloy sheet, 313–19
 - properties of magnesium, 306–8
 - superplasticity, 309–13
- metals, 3–31
 - Bi–Sn eutectic, 5
 - composition, SPF temperatures, strain rate and elongation, 8
 - grain refinement, 9–11
 - high strain rate, 16–17
 - historical aspects, 4–7
 - mechanisms, 20–30
 - Pb–Sn eutectic alloy, 6
 - processing of commercially significant alloy, 11–16
 - severe plastic deformation from grain refinement, 17–20
 - SP titanium alloy (IMI550), 3
 - types of materials, 7–9
- predicting instability in metals, 184–222
- forming analyses and experiments, 202–9
 - future trends, 220–2
 - results, 209–20
 - theoretical considerations, 185–202
- processes and equipment, 49–70
 - emerging innovative processes, 58–9
 - heating platen technology, 56–8

- hollow cavity forming, 51
- multi-sheet forming and diffusion bonding, 51–3
- new rapid forming processes, 54
- single-sheet forming, 50–1
- standard press-forming equipment, 54–6
- standards, 34–46
 - existing standards, 36–7
 - issues, 37–41
 - rationale, 35–6
 - temperature changes in furnace and test specimen, 45
 - testing standard, 41–6
- titanium, 227–44
 - applications, 241–4
 - superplastic forming/diffusion bonding process, 235–41
 - titanium alloys, 228–35
- superplastic forming limit diagram, 185, 195
 - approach, 215–18
 - concept, 197–8
- superplastic forming press, 207–9
- superplastic metal sheet forming processes
 - mathematical modelling, 115–34
 - flow rule, 118
 - material constants from bulging tests, 127–34
 - membrane theory, 116–18
 - superplastic free forming processes
 - analysis, 119–27
- superplastic microtubes
 - fabricated by dieless drawing processes, 327–58
 - industrial application, 328–9
 - metal microtubes application, 329
 - other applications, 355–7
 - axial profile control, 355–6
 - cross-section shape control, 356–7
 - drawing speed paths, 356
 - micro-non-circular tubes, 357
 - taper tube fabrication, 356
 - superplastic dieless drawing processes, 336–41
 - FE simulation, 342–9
 - fundamentals of dieless drawing processes, 329–35
 - grain refinement process of metal tubes, 349–55
- superplasticity, 6
- Supral 100, 7, 13–14
- tadpole seal, 280
- Taylor series expansions, 161, 162
- test specimen geometry, 37–8, 41–3
 - material flow for various gauge lengths, 42
 - material flow from grip to gauge region, 41
- tensile test specimen, 38
- testing procedure, 44–6
 - temperature changes in furnace and test specimen, 45
- thermal mechanical treatments, 252
- thin metal sheet forming
 - finite element modelling, 136–51
 - applications, 146–51
 - commercial codes, 145–6
 - continuum model, 137–40
 - die representation and contact algorithms, 145
 - finite element formulation and time integration schemes, 140–1
 - future trends, 151
 - incremental flow formulation, 141–4
 - pressure cycle algorithms, 144–5
- TI Superform *see* Superform Aluminium
- titanium alloys
 - aerospace industry, 228–9
 - applications, 241–4
 - 4-part SPF Ti pressing, 243
 - 4-sheet Ti–6Al–4V X core configuration, 244
 - girder structure in hollow wide-chord Ti–6Al–4V fan blade, 243
 - Ti-pressings multi-part assembly, 244
 - Ti–6Al–4V hollow, wide-chord fan blades, 242
- diffusion bonding, 234–5
 - Ti–6Al–4V membrane panel diffusion bond and microstructure, 235
- metallurgy, 229–31
 - alpha phase and beta phase unit cell, 230
 - quasi-vertical section for ternary titanium alloys, 231
 - Ti–6Al–4V from the same billet, 231
- production of titanium sheet products, 232–3
 - hot rolling, 233
 - vacuum arc remelted titanium ingot, 232
- superplastic forming and diffusion bonding, 227–44
 - 3-sheet lay-up, 238
 - low temperature, 239–41
 - submicron-grained Ti–6Al–4V sheet, 240
 - superplastic forming/diffusion bonding process, 235–41
 - Ti–6Al–4V hollow wide-chord fan blades, 228
 - titanium alloys, 228–35
 - two-sheet SPF/DB using matched metal tooling, 237
 - superplasticity, 233–4
- TMT *see* thermal mechanical treatments
- tolerance, 162
- transient thermal modelling, 67
 - experimental and calculated thermal cycles, 68
- trapezoid rule, 161
- truncation error, 162
- Twin Roll Casting, 15–16, 316–18
- uncoupled plasticity-creep model, 68
- uni-axial models, 137–9
 - superplastic forming constitutive behaviour, 138
- universal multi-objective function (OF_II), 166–8
 - error definition, 167
- URDFIL, 175
- void growth models, 194–7, 213–14
- Volkswagen Beetle, 305
- Volkswagen Lupo, 320

von Mises criterion, 118
von Mises equivalent stress, 139

WE43 alloy, 312

XD process, 84

Young's modulus, 159–60
yttria, 75, 77

Zener pinning, 8, 312
ZK10, 318